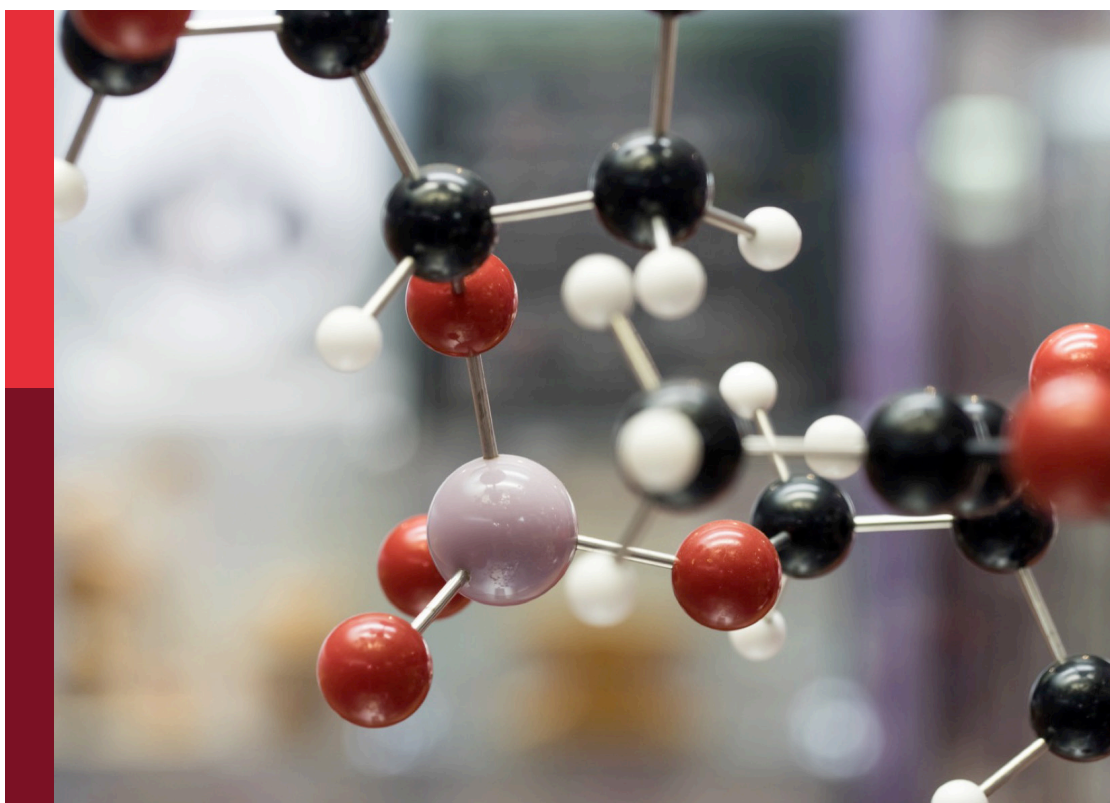


# Organic chemistry editor's pick 2024

**Edited by**  
Iwao Ojima

**Published in**  
Frontiers in Chemistry



## FRONTIERS EBOOK COPYRIGHT STATEMENT

The copyright in the text of individual articles in this ebook is the property of their respective authors or their respective institutions or funders. The copyright in graphics and images within each article may be subject to copyright of other parties. In both cases this is subject to a license granted to Frontiers.

The compilation of articles constituting this ebook is the property of Frontiers.

Each article within this ebook, and the ebook itself, are published under the most recent version of the Creative Commons CC-BY licence. The version current at the date of publication of this ebook is CC-BY 4.0. If the CC-BY licence is updated, the licence granted by Frontiers is automatically updated to the new version.

When exercising any right under the CC-BY licence, Frontiers must be attributed as the original publisher of the article or ebook, as applicable.

Authors have the responsibility of ensuring that any graphics or other materials which are the property of others may be included in the CC-BY licence, but this should be checked before relying on the CC-BY licence to reproduce those materials. Any copyright notices relating to those materials must be complied with.

Copyright and source acknowledgement notices may not be removed and must be displayed in any copy, derivative work or partial copy which includes the elements in question.

All copyright, and all rights therein, are protected by national and international copyright laws. The above represents a summary only. For further information please read Frontiers' Conditions for Website Use and Copyright Statement, and the applicable CC-BY licence.

ISSN 1664-8714  
ISBN 978-2-8325-5941-3  
DOI 10.3389/978-2-8325-5941-3

## About Frontiers

Frontiers is more than just an open access publisher of scholarly articles: it is a pioneering approach to the world of academia, radically improving the way scholarly research is managed. The grand vision of Frontiers is a world where all people have an equal opportunity to seek, share and generate knowledge. Frontiers provides immediate and permanent online open access to all its publications, but this alone is not enough to realize our grand goals.

## Frontiers journal series

The Frontiers journal series is a multi-tier and interdisciplinary set of open-access, online journals, promising a paradigm shift from the current review, selection and dissemination processes in academic publishing. All Frontiers journals are driven by researchers for researchers; therefore, they constitute a service to the scholarly community. At the same time, the *Frontiers journal series* operates on a revolutionary invention, the tiered publishing system, initially addressing specific communities of scholars, and gradually climbing up to broader public understanding, thus serving the interests of the lay society, too.

## Dedication to quality

Each Frontiers article is a landmark of the highest quality, thanks to genuinely collaborative interactions between authors and review editors, who include some of the world's best academicians. Research must be certified by peers before entering a stream of knowledge that may eventually reach the public - and shape society; therefore, Frontiers only applies the most rigorous and unbiased reviews. Frontiers revolutionizes research publishing by freely delivering the most outstanding research, evaluated with no bias from both the academic and social point of view. By applying the most advanced information technologies, Frontiers is catapulting scholarly publishing into a new generation.

## What are Frontiers Research Topics?

Frontiers Research Topics are very popular trademarks of the *Frontiers journals series*: they are collections of at least ten articles, all centered on a particular subject. With their unique mix of varied contributions from Original Research to Review Articles, Frontiers Research Topics unify the most influential researchers, the latest key findings and historical advances in a hot research area.

Find out more on how to host your own Frontiers Research Topic or contribute to one as an author by contacting the Frontiers editorial office: [frontiersin.org/about/contact](https://frontiersin.org/about/contact)

# Organic chemistry editor's pick 2024

## Topic editor

Iwao Ojima — Stony Brook University, United States

## Citation

Ojima, I., ed. (2025). *Organic chemistry editor's pick 2024*.  
Lausanne: Frontiers Media SA. doi: 10.3389/978-2-8325-5941-3

## Table of contents

- 04 **Efficient antibacterial AIEgens induced ROS for selective photodynamic treatment of bacterial keratitis**  
Wenting Cai, Tianyi Shen, Dong Wang, Tingting Li, Jing Yu, Chen Peng and Ben Zhong Tang
- 17 **A new chiral phenomenon of orientational chirality, its synthetic control and computational study**  
Shengzhou Jin, Ting Xu, Yao Tang, Jia-Yin Wang, Yu Wang, Junyi Pan, Sai Zhang, Qingkai Yuan, Anis Ur Rahman, Adelia J. A. Aquino, Hans Lischka and Guigen Li
- 28 **Cytotoxic hexadepsipeptides and anti-coronaviral 4-hydroxy-2-pyridones from an endophytic *Fusarium* sp.**  
Shanshan Chang, Biying Yan, Yuchuan Chen, Wuli Zhao, Rongmei Gao, Yuhuan Li, Liyan Yu, Yunying Xie, Shuyi Si and Minghua Chen
- 37 **Essential oils of *Psidium cattleianum* Sabine leaves and flowers: Anti-inflammatory and cytotoxic activities**  
Heba E. Elsayed, Eman M. El-Deeb, Heba Taha, Hussein S. Taha, Mohamed R. Elgindi and Fatma A. Moharram
- 50 **Hydrogen bonding-induced high-performance stretchable organic semiconductors: a Review**  
Jinhan Chen, Zheng Wang, Zhifeng Deng, Ligui Chen, Xuhui Wu, Yihan Gao, Yumeng Hu, Mei Li and Hongzhen Wang
- 56 **Design, synthesis, and unraveling the antibacterial and antibiofilm potential of 2-azidobenzothiazoles: insights from a comprehensive *in vitro* study**  
Tanzeela Qadir, Saadat A. Kanth, Mohammad Aasif, Abdalla N. Fadul, Gulam N. Yattoo, Kailash Jangid, Mushtaq A. Mir, Wajahat A. Shah and Praveen K. Sharma
- 77 **MOF-based stimuli-responsive controlled release nanopesticide: mini review**  
Shuhui Hu, Chang Yan, Qiang Fei, Bo Zhang and Wenneng Wu
- 87 **Structural tuning of  $\beta$ -enamino diketones: exploration of solution and crystalline state photochromism**  
Kiran B. Manjappa, Sheng-Chieh Fan and Ding-Yah Yang
- 98 **Aminothioloation of alkenes with azoles and Bunte salts**  
Bingqing Ouyang, Xing Chai, Zhe Li, Chunling Zhang and Xingmei Liu
- 106 **Choline chloride/urea as a green and efficient deep eutectic solvent in three-component and four-component synthesis of novel pyrazole and pyrano[2,3-c] pyrazole derivatives with antibacterial and antifungal activity**  
Israa Habeeb Naser, Hassan Thoulfikar A. Alamir, Ali Hisham Al-Shukarji, Batool Ali Ahmed, Talal Aziz Qassem, Maher Kamal, Tahani M. Almeleebia, Enas R. Alwaily, Eftikhaar Hasan Kadhum, Ahmed Alawadi and Ali Alsalamy
- 125 **Biologically active secondary metabolites from white-rot fungi**  
Orkun Pinar and Susana Rodríguez-Couto





## OPEN ACCESS

## EDITED BY

Jingjing Guo,  
Nanyang Technological University,  
Singapore

## REVIEWED BY

Fang Hu,  
Southern Medical University, China  
Yu Cai,  
Hangzhou Medical College, China  
Guorui Jin,  
Xi'an Jiaotong University, China  
Meng Gao,  
South China University of Technology,  
China

## \*CORRESPONDENCE

Chen Peng,  
✉ cpengrr@tongji.edu.cn  
Ben Zhong Tang,  
✉ tangbenz@cuhk.edu.cn

<sup>†</sup>These authors have contributed equally to this work

## SPECIALTY SECTION

This article was submitted to  
Organic Chemistry,  
a section of the journal  
Frontiers in Chemistry

RECEIVED 03 November 2022

ACCEPTED 28 November 2022

PUBLISHED 04 January 2023

## CITATION

Cai W, Shen T, Wang D, Li T, Yu J, Peng C  
and Tang BZ (2023), Efficient  
antibacterial AIEgens induced ROS for  
selective photodynamic treatment of  
bacterial keratitis.  
*Front. Chem.* 10:1088935.  
doi: 10.3389/fchem.2022.1088935

## COPYRIGHT

© 2023 Cai, Shen, Wang, Li, Yu, Peng  
and Tang. This is an open-access article  
distributed under the terms of the  
[Creative Commons Attribution License](#)  
(CC BY). The use, distribution or  
reproduction in other forums is  
permitted, provided the original  
author(s) and the copyright owner(s) are  
credited and that the original  
publication in this journal is cited, in  
accordance with accepted academic  
practice. No use, distribution or  
reproduction is permitted which does  
not comply with these terms.

# Efficient antibacterial AIEgens induced ROS for selective photodynamic treatment of bacterial keratitis

Wenting Cai<sup>1†</sup>, Tianyi Shen<sup>1†</sup>, Dong Wang<sup>2</sup>, Tingting Li<sup>1</sup>, Jing Yu<sup>1</sup>,  
Chen Peng<sup>1,3\*</sup> and Ben Zhong Tang<sup>2,4\*</sup>

<sup>1</sup>Department of Ophthalmology, Shanghai Tenth People's Hospital, School of Medicine, Tongji University, Shanghai, China, <sup>2</sup>College of Materials Science and Engineering, Shenzhen University, Shenzhen, China, <sup>3</sup>Department of Radiology, Shanghai Public Health Clinical Center, Fudan University, Shanghai, China, <sup>4</sup>Shenzhen Institute of Molecular Aggregate Science and Engineering, School of Science and Engineering, The Chinese University of Hong Kong, Shenzhen, Hong Kong SAR, China

Bacterial keratitis (BK) is an acute infection of the cornea, accompanied by uneven epithelium boundaries with stromal ulceration, potentially resulting in vision loss. Topical antibiotic is the regular treatment for BK. However, the incidence rate of multidrug-resistant bacteria limits the application of traditional antibiotics. Therefore, a cationic aggregation-induced emission luminogens (AIEgens) named TTVP is utilized for the treatment of BK. TTVP showed no obvious cytotoxicity in maintaining the normal cell morphology and viability under a limited concentration, and revealed the ability to selectively combine with bacteria in normal ocular environment. After light irradiation, TTVP produced reactive oxygen species (ROS), thus exerting efficient antibacterial ability *in vitro*. What's more, in rat models of *Staphylococcus aureus* (*S. aureus*) infection, the therapeutic intervention of TTVP lessens the degree of corneal opacity and inflammatory infiltration, limiting the spread of inflammation. Besides, TTVP manifested superior antibacterial efficacy than levofloxacin in acute BK, endowing its better vision salvage ability than conventional method. This research demonstrates the efficacy and advantages of TTVP as a photodynamic drug in the treatment of BK and represents its promise in clinical application of ocular infections.

## KEYWORDS

aggregation-induced emission (AIE), bacterial keratitis, *Staphylococcus aureus*, antimicrobial materials, photodynamic therapy

## 1 Introduction

Bacterial keratitis (BK) is the sixth leading cause of global vision loss, accounting for 3.2% of the  $36 \times 10^6$  cases in both developing and developed countries, which may be associated with trauma, contact lens wear, ocular surgery, or deficiency of corneal sensation (Davis et al., 2020; Khan et al., 2020; Blindness, 2021). BK is characterized by epithelial defect with corneal stromal inflammation and ulceration. As the progression

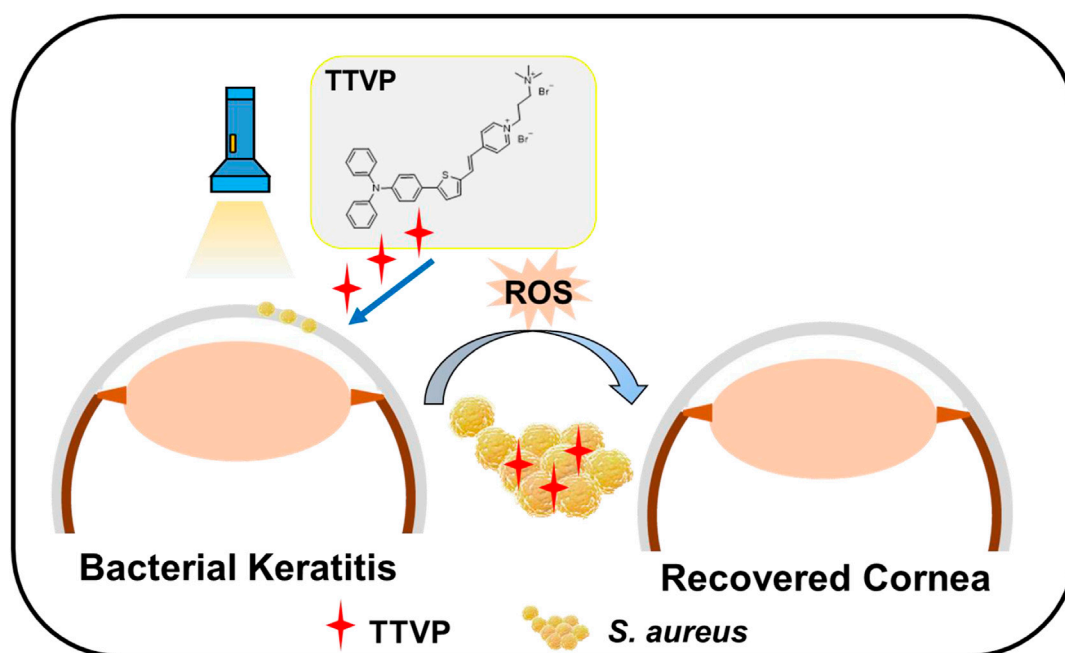
of BK or without timely and appropriate treatment, corneal abscess, stromal lysis and corneal perforation may lead to severe visual loss ultimately (Han et al., 2020; Tuft et al., 2022). Among bacterial pathogens, *Staphylococcus aureus* (*S. aureus*) is the predominant pathogen inducing keratitis since it is a common inhabitant on ocular surface (Silva et al., 2019; Zhang et al., 2019). The cornea of rats infected by *S. aureus* was therefore widely utilized to perform the experimental keratitis research (Zhang et al., 2021; Zhang et al., 2022b). At present, BK is commonly administrated with topical eye drops of broad-spectrum antibiotics such as levofloxacin (LVFX), ciprofloxacin and moxifloxacin (Li et al., 2020a). The overuse and misuse of antibiotics are the most important determinant for the occurrence of antibiotics resistance, even with super bacteria occurred (Zhou et al., 2020). In BK, the prognosis of the disease is severely affected by an increasing resistant trend towards widely used empirical antibiotics, such as combinations of cephalosporin or glycopeptide and aminoglycoside (Ung et al., 2019). Besides, norfloxacin was reported to mediate apoptosis by injuring mitochondrial transmembrane and activating death proteins, and eventually leading to necroptosis through RIPK1-RIPK3-MLKL pathway (Yang et al., 2020). In this regard, there is still an urgent need to explore new targets with low incidence of drug-resistance. Therefore, the development of alternative effective antibacterial strategy is urgently needed, which favors the reduction of emergency of the resistance of bacteria.

In response to such a severe situation of drug resistance, sterilization material based on light-to-heat conversion, photocatalysis, chemocatalysis and biological extraction were performed (Huo et al., 2021; Wang et al., 2022). Among them, photodynamic therapy (PDT) utilized reactive oxygen species (ROS) generation from photosensitizers (PSs) activated with light irradiation, which has been regarded as a vital strategy to deal with drug-resistant bacterial infections under the background of post-antibiotic era (Chen et al., 2019; Qi et al., 2019; Liu et al., 2021; Zhou et al., 2021). The generation of abundant ROS could destroy bacterial cell membrane, inducing necrosis and apoptosis of bacteria (Idris et al., 2012; Han et al., 2016). Several studies have reported that PDT performed excellent anti-bacterial ability in the treatment of periodontitis (Li et al., 2021b), diabetic wound healing (Huang et al., 2021), malignant tumor (Cheng et al., 2020), immunomodulatory effects (Ayaz et al., 2020), rheumatoid arthritis (Lu et al., 2018) and bacterial ocular infection (Peng et al., 2021; Li et al., 2022). Encouragingly, PDT has advantage of excellent light transmission property, which is appropriate in the application of ocular infectious therapy (Fan et al., 2021). Thus, PDT with good antibacterial ability and biocompatibility showed a promising potential in the treatment of ocular infectious diseases. However, traditional PSs suffer from fluorescence quenching under irradiation, and generate low ROS due to  $\pi$ - $\pi$  stacking in the aggregate state,

which severely hindered their development of practical application (Liu et al., 2013; Jiang et al., 2018).

Recently, luminogens with aggregation-induced emission (AIEgens) features showed broad application prospects for theranostic applications as PSs (Hu et al., 2018; Kang et al., 2019; Dai et al., 2020; Abrahamse et al., 2022). A delightful phenomenon could be observed that AIEgens exhibited excellent fluorescence and effective ROS creation during aggregation state while showing poor emission in the monomer state, which was resulting from the restriction of intramolecular motions (RIMs) (Mei et al., 2015; Wang et al., 2018a). AIEgens performed promising characteristics of high-efficiency of ROS production, low-toxicity and high-specificity targets (Li et al., 2020b). In addition, AIEgens have been broadly applied in fluorescent bioimaging due to splendid emission efficiency and large stokes shift (Yu et al., 2017). AIEgens have been reported to possess excellent biological applications, including granulomas tracking and targeted theranostics for tuberculosis (Liao et al., 2020), specific bacterial clearance and tumor elimination (Li et al., 2020b), and accelerated reduction of refractory internalized bacteria such as methicillin-resistant *Staphylococcus aureus* (MRSA) (Ni et al., 2020; Li et al., 2021a). Also, Hu et al. reported that M1-DPAN showed specific AIE ability, along with outstanding photostability and biosecurity, which take advantage of visualizing the occurrence of bacterial infection. Besides, it has been reported that AIEgens could selectively identify and aim at bacteria because of cationic charge and appropriate hydrophobicity, and exhibited vision defense *via* activating early intraocular immune response for bacterial endophthalmitis (Li et al., 2022). Such selective discrimination was attributed to the differences in membrane potential between bacteria and mammals (Yuan et al., 2014). Inspired by the previous studies, the design of cationic AIEgens, which performed selectively elimination of bacteria over normal cells is feasible.

In this study, we designed and synthesized a cationic AIEgens named TTVP, possessing the ability of identification and photodynamic antibacterial of Gram-positive bacteria (Lee et al., 2020), for the therapeutic schedule of bacterial keratitis. For the predominant position of *S. aureus* in pathogen of keratitis, we work on *S. aureus* to evaluate the killing efficiency of TTVP both *in vitro* and *in vivo* (Scheme 1). First of all, TTVP exhibited no obvious cytotoxicity in maintaining the normal cell morphology and viability under a limited concentration, and selectively combined with bacteria rather than normal ocular cells, which confirmed its biosafety in our following research. Under white light irradiation, TTVP generated abundant ROS production, leading to the death of *S. aureus*. The excellent killing efficiency of TTVP to *S. aureus* was further assessed *via in vitro* antibacterial activity studies. Furthermore, TTVP was applied to treat *S. aureus*-induced keratitis on a rat model, and excitingly, the infection recovery treated with TTVP was faster than that with LVFX *in vivo*.



**SCHEME 1**  
Schematic illustration of AIEgen TTVP for efficient photodynamic antibacterial therapy of BK.

Attracted by these results, the outstanding treatment efficiency and good biosafety make TTVP promising for the clinical treatment of bacterial keratitis.

## 2 Experimental section

## 2.1 Materials and reagents

TTVP was synthesized in complying with the literature mentioned (Wang et al., 2018b). Other chemicals and reagents were bought from J&K Scientific and Sigma-Aldrich. DMEM/F12 cell medium, penicillin, streptomycin and fetal bovine serum (FBS) were obtained from HyClone (United States). Yeasen (Shanghai, China) provided cell counting kit (CCK)-8. *S. aureus* was acquired from China General Microbiological Culture Collection Center. SD rats were purchased from Beijing Vital River Laboratory Animal Technology Co., Ltd. (Beijing, China).

## 2.2 Characterization

Mother solution (5 mM) of TTVP was obtained through dimethyl sulfoxide (DMSO) initially, and then mixed with PBS to certain concentration. The aqueous dispersibility of TTVP in water, PBS and DMEM at the concentration of 5  $\mu$ M was

displayed excellently (**Supplementary Figure S1**). Ultraviolet-visible (UV-Vis) absorption and fluorescence (FL) spectra were measured by the Perkin Elmer Lambda 25 spectrophotometer and fluorescence spectrometry (Agilent Cary Eclipse), respectively.

### 2.3 Preparation of bacterial solution

A single *S. aureus* colony on solid agar plate was added to 10 ml liquid Luria broth (LB) culture medium. After incubation at 37°C overnight at 220 rpm, the bacteria were gathered by centrifugation (9,000 rpm, 3 min) and washed twice. After being resuspended with sterile normal saline, the concentrations were measured at 600 nm (1.0 OD = 10<sup>8</sup> CFU ml<sup>-1</sup>). Finally, the *S. aureus* suspensions were diluted with PBS for further use.

## 2.4 *In vitro* antibacterial analysis

A standard plate counting method was carried out to evaluate sterilization effect of TTVP *in vitro* at concentrations of 0, 0.02, 0.05, 0.1 and 0.2  $\mu\text{M}$ . The mixture was exposed to white light lamp for certain min (5, 10, 15 and 30 min), while the control group was exposed in dark. The treated bacterial suspension was diluted (1:5000) and incubated on the agar plate at  $37^{\circ}\text{C}$  for 24 h, followed by quantification and photo taking.

## 2.5 Assay for reactive oxygen species

ROS accumulation of TTVP was assessed According to a given standard protocol. The mixture of TTVP (0.1  $\mu\text{M}$ ) and DCFH-DA was incubated under a white light lamp (20  $\text{mW}/\text{cm}^2$  power) for 15 min. The fluorescence intensity was recorded *via* a microplate reader before irradiation and every 1 min interval for 16 times ( $\lambda_{\text{ex}} = 480 \text{ nm}$ ,  $\lambda_{\text{em}} = 525 \text{ nm}$ ). Meanwhile, OD values of DCFH-DA solution and PBS were recorded as control.

## 2.6 Zeta potential measurement

*S. aureus* was collected and resuspended with PBS, followed by incubating with different concentrations of TTVP (0, 0.02, 0.05, 0.1 and 0.2  $\mu\text{M}$ ) for 15 min. Then Zeta potential was measured *via* a Malvern Zetasizer.

## 2.7 Co-culture of bacteria and cells

*S. aureus* was co-cultured with human corneal epithelial cells (HCECs) to test the selective affinity of TTVP against bacteria. *S. aureus* suspension was added to pre-cultured adherent HCECs, along with different concentrations (0, 0.02, 0.05, 0.1  $\mu\text{M}$ ) of TTVP for 15 min. The slides were sealed and photographed using a fluorescence microscope.

## 2.8 *In vitro* cytotoxicity

The possible cytotoxicity of TTVP is a crucial issue to be examined before application. In general, cell viability, cell morphology and live/dead staining were performed to evaluate the biosafety of TTVP *in vitro*. In order to explore the biosafety of TTVP in keratopathy, research based on normal cells of ocular surface was necessary. Hence, HCECs were selected to evaluate the toxicity of TTVP.

Adherent HCECs were cultured in 96-well plates, being divided into irradiation group (20  $\text{mW}/\text{cm}^2$ , group a) and dark group (group b). After co-cultured with TTVP (0–1.0  $\mu\text{M}$ ) for 15 min, HCECs were placed in light or dark environment during the following 15 min. HCECs were continued culturing in the incubator for 24 h after removal of TTVP. Also, the cells were incubated for 24 h at the same concentration of TTVP in dark (group c) to detect the intrinsic cytotoxicity. Afterward, CCK-8 reagent was incubated for 2 h to obtain the fluorescence intensity at 450 nm. In addition, the cellular morphology of HCECs after incubation for 24 h was also recorded *via* optical microscopy.

For the live/dead staining analysis, HCECs were intervened with TTVP (0, 0.05, 0.1, 0.2  $\mu\text{M}$ ) for 24 h. Live and dead cells were labeled with calcein AM and PI, which excited green and red fluorescence under microscope, respectively.

## 2.9 Hemolysis assay

The hemocompatibility of TTVP was detected through hemolysis assay. Saline was added to the whole blood to wash several times until the supernatant was colorless. After diluting with saline to 2% red cell suspension, different TTVP concentrations (0, 0.02, 0.05, 0.1, and 0.2  $\mu\text{M}$ ) were added to the above red cell suspension, and heated at 37°C for 1 h. After centrifugation (3,000 rpm, 5 min), the images were captured and the ratio of hemolysis was calculated by the absorbance of supernatants at 540 nm recorded by a microplate reader. The erythrocytes treated with distilled water were regarded as positive control.

## 2.10 Animal experiments of antibacterial test

### 2.10.1 *In vivo* antibacterial test on infected keratitis

The animal procedures involved were in accordance with the Association for Research in Vision and Ophthalmology Statement of Shanghai Tenth People's Hospital. Six weeks of SD male rats were used to simulate the occurrence of BK as previously described with minor adjustments (Josyula et al., 2021). After general anesthetization by chloralhydrate, 0.5% proparacaine hydrochloride ophthalmic solution was performed for local anesthesia. Prior to any operation, the images of rat corneas were captured. The operative eye was then scratched using a blade, and then *S. aureus* suspension (50  $\mu\text{l}$ ,  $1 \times 10^8 \text{ CFU}/\text{ml}$ ) was placed over the ocular surface.

After being inoculated for 24 h, the rats were classified into four groups: 1) *S. aureus*-infected eyes treated by PBS, 2) *S. aureus*-infected eyes treated by TTVP under dark condition, 3) *S. aureus*-infected eyes treated by TTVP with light irradiation (20  $\text{mW}/\text{cm}^2$  power, 15 min), and 4) *S. aureus*-infected eyes treated by LVFX. Photographs of the ocular surface were captured before treatment, as well as 1, 3 and 7 days after intervention to observe the infection and inflammation. The clinical inflammatory scores were calculated to qualify the severity. Seven days after treatment, eyeballs were fixed for H&E staining, Masson staining and immunohistochemistry staining analysis, or homogenized for spread plate assay.

### 2.10.2 Clinical inflammatory scores

Clinical inflammatory scores of anterior segments, including size of corneal opacity area (grades 1–4, less than 25% to more than 75%), opacity density of cornea (grades 1–4, slightly misty to dense opacity) and hypopyon (grades 1 and 2, paracentral cornea involved or not) were performed to evaluate the severity of BK as previously reported (Zhang et al., 2019). Thus, the score of normal cornea was 0, while that of different groups was between 0 and 10.

### 2.10.3 Spread plate test

The isolated corneas were homogenized in 0.5 ml of sterile PBS, diluted and cultured on agar plates for 24 h, followed by quantification and photo taking.

### 2.10.4 HE, Masson and immunohistochemistry staining analysis

Eyeballs were fixed 7 days after infection for H&E and Masson staining to describe the bacterial histopathological reaction. Meanwhile, tumor necrosis factor- $\alpha$  (TNF- $\alpha$ ) is the common primary inflammatory protein. Immunohistochemical staining of TNF- $\alpha$  was performed to display the inflammation at the site of the infected corneal lesions at 7 d follow-up. All photos were collected under the optical microscope.

## 2.11 *In vivo* biosafety

### 2.11.1 Organ structure

At the end time points, the rats were sacrificed to harvest the heart, spleen, kidney, liver and lung for histopathology *in vivo*. After being fixed overnight, the tissues were embedded, sectioned, and stained with H&E, following standardized protocol. Neutral gum was applied to immobilize the sections, then the slides were imaged under an optical microscope.

### 2.11.2 Serological assay

Whole blood of rats was reversed and centrifuged to obtain serum. Functions were measured according to the instructions. Liver and kidney functions including alanine aminotransferase (ALT) and aspartate aminotransferase (AST) and creatinine (CRE) were measured. Total cholesterol (T-CHO) and triglyceride (TG) reflected blood lipids, while potassium (K<sup>+</sup>), calcium (Ca<sup>2+</sup>), and chlorine (Cl<sup>-</sup>) represented electrolytic levels.

## 2.12 Statistical analysis

SPSS 23.0 software and GraphPad Prism 5 were utilized for statistical analyses. ImageJ version 1.48 was used for quantification of bacterial colonies. One-way ANOVA was carried out between multiple groups.  $p < 0.05$  were identified as statistically significant.

## 3 Results and discussions

### 3.1 Optical property

The synthesis and purification of TTVP were under the guidance to the previous study (Wang et al., 2018b). As represented in Figure 1, UV–Vis and FL spectra were performed to verify the optical characteristics of TTVP. After incubating TTVP in *S. aureus* for 15 min, red fluorescence was obviously visible under 365 nm UV

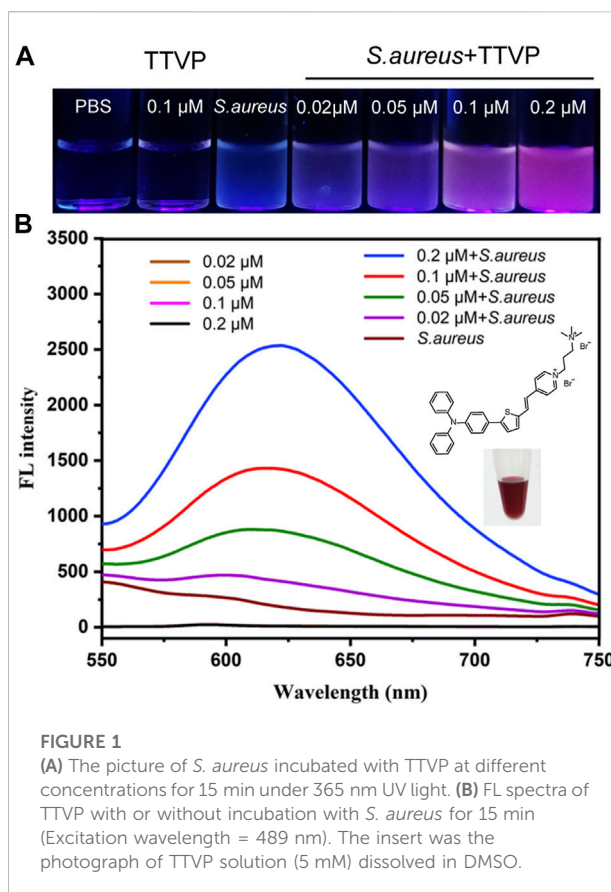


**FIGURE 1**  
(A) The picture of *S. aureus* incubated with TTVP at different concentrations for 15 min under 365 nm UV light. (B) FL spectra of TTVP with or without incubation with *S. aureus* for 15 min (Excitation wavelength = 489 nm). The insert was the photograph of TTVP solution (5 mM) dissolved in DMSO.

irradiation, indicating that TTVP had a remarkable bioimaging effect on *S. aureus* (Figure 1A). Afterward, as shown in Figure 1B, TTVP solutions alone photoexcited by 489 nm showed no obvious difference in FL intensity under different concentrations. After a mixture with *S. aureus* at room temperature for 15 min, FL intensity showed the emission maximum wavelength at around 620 nm under concentration-dependent manner. The phenomenon might be due to the change of TTVP aggregation states of TTVP in response to *S. aureus*. TTVP has a strong affinity for *S. aureus* and may become a valuable visualization reagent for bacterial research.

### 3.2 *In vitro* antibacterial test

The antibacterial property *in vitro* was tested through traditional spread plate method, and the bacteriostasis was evaluated intuitively by comparing the number of viable bacteria (Zhang et al., 2022a). The bacterial growth in the plate was recorded and the antimicrobial rate of TTVP was calculated. First of all, as shown in Figure 2A, TTVP exerted negligible toxicity without light irradiation process after various concentrations of TTVP intervened. Next, the *S. aureus* incubated with TTVP was irradiated in an intensity of 40 mW/cm<sup>2</sup> for 15 min, showing good bactericidal ability at



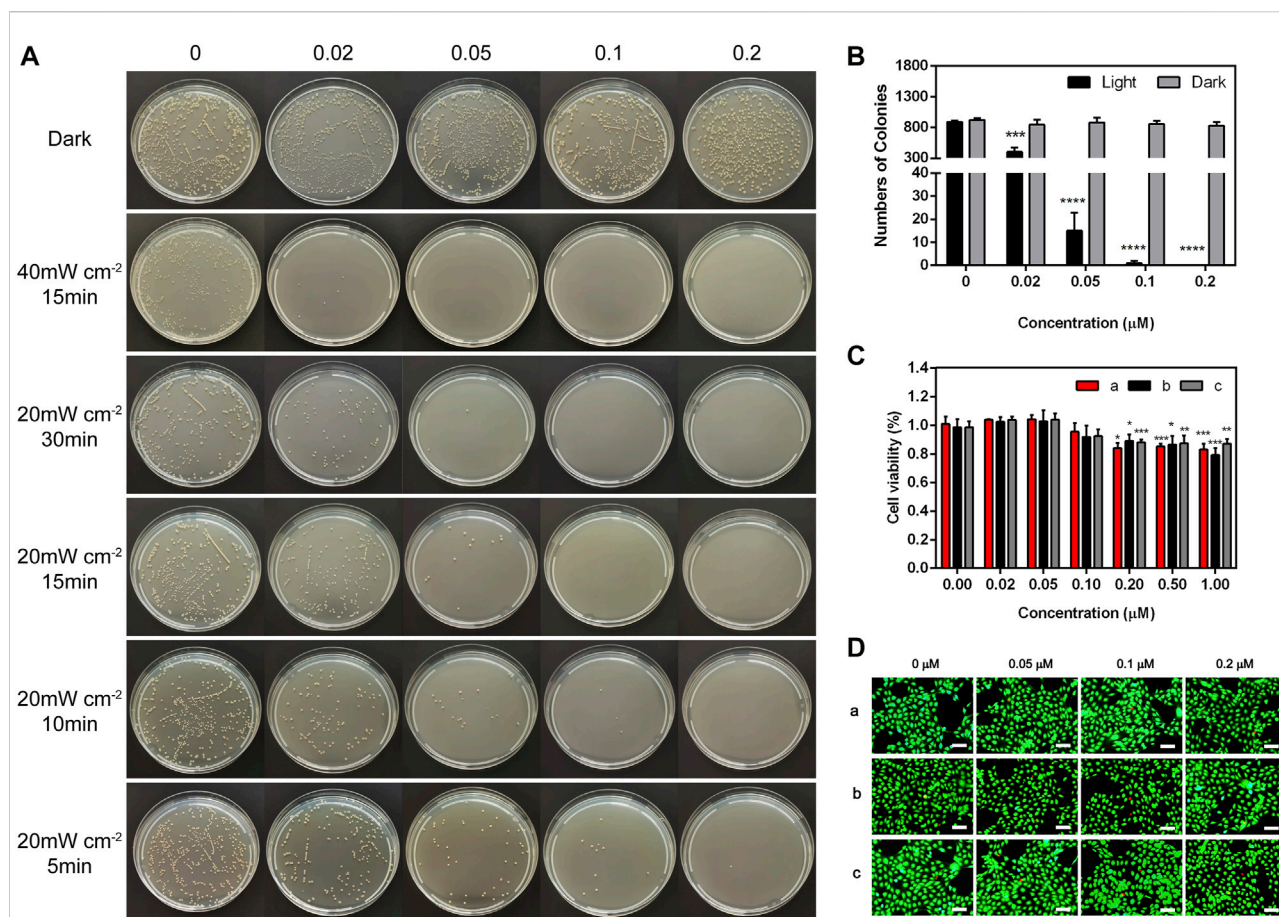


FIGURE 2

(A) Representative photographs of *S. aureus* treated by TTVP at different concentrations and irradiation conditions. (B) The surviving colony count of *S. aureus* treated by TTVP in light condition (20 mW/cm<sup>2</sup>) for 15 min. (C,D) Cell viability and Live/dead staining images of HCECs treated with TTVP, (a) with light after incubation with TTVP for 15 min and (b) without light after incubation with TTVP for 15 min (c) treated by TTVP for 24 h without light (scale bar: 100 μm). \*for comparison among different concentrations of TTVP (0.02, 0.05, 0.1, 0.2, 0.5 and 1 μM) versus TTVP (0 μM) in light and dark conditions. \**p* < 0.05, \*\**p* < 0.01, \*\*\**p* < 0.001 and \*\*\*\**p* < 0.0001.

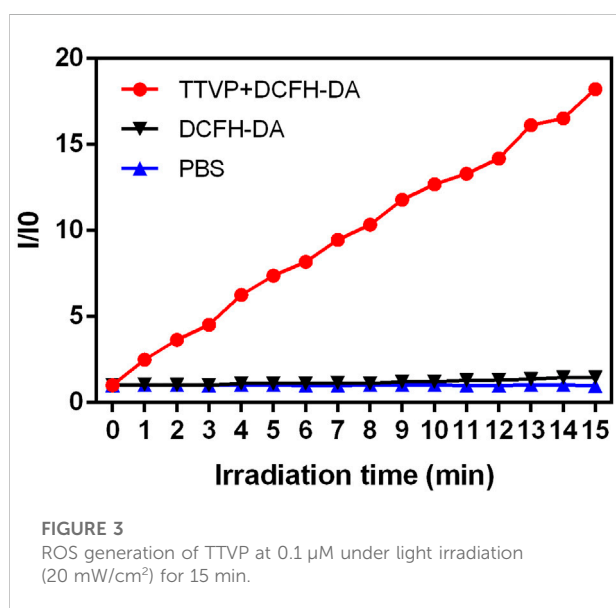


FIGURE 3

ROS generation of TTVP at 0.1 μM under light irradiation (20 mW/cm<sup>2</sup>) for 15 min.

the concentration of 0.02 μM. In order to optimize the illuminance, we halved the light intensity of 20 mW/cm<sup>2</sup> and performed at different durations including 5, 10, 15 and 30 min. As shown in Figure 2A, the antibacterial effect of TTVP exhibited a dose-dependency feature, and enhanced gradually along with the increased concentrations ranging from 0 to 0.2 μM. Amazingly, *S. aureus* was killed effectively with irradiation (20 mW/cm<sup>2</sup>) for 15 min, along with 0.1 μM TTVP co-cultured (Figure 2B). In order to better bactericidal effect, this intervention method was applied for further experiments.

### 3.3 Antibacterial mechanisms of TTVP

Under light irradiation (20 mW/cm<sup>2</sup>), we further explored the mechanisms of TTVP killing *S. aureus* by measuring the ROS generation ability within 15 min. As shown in Figure 3, Supplementary Figure S2, abundant ROS was generated by TTVP

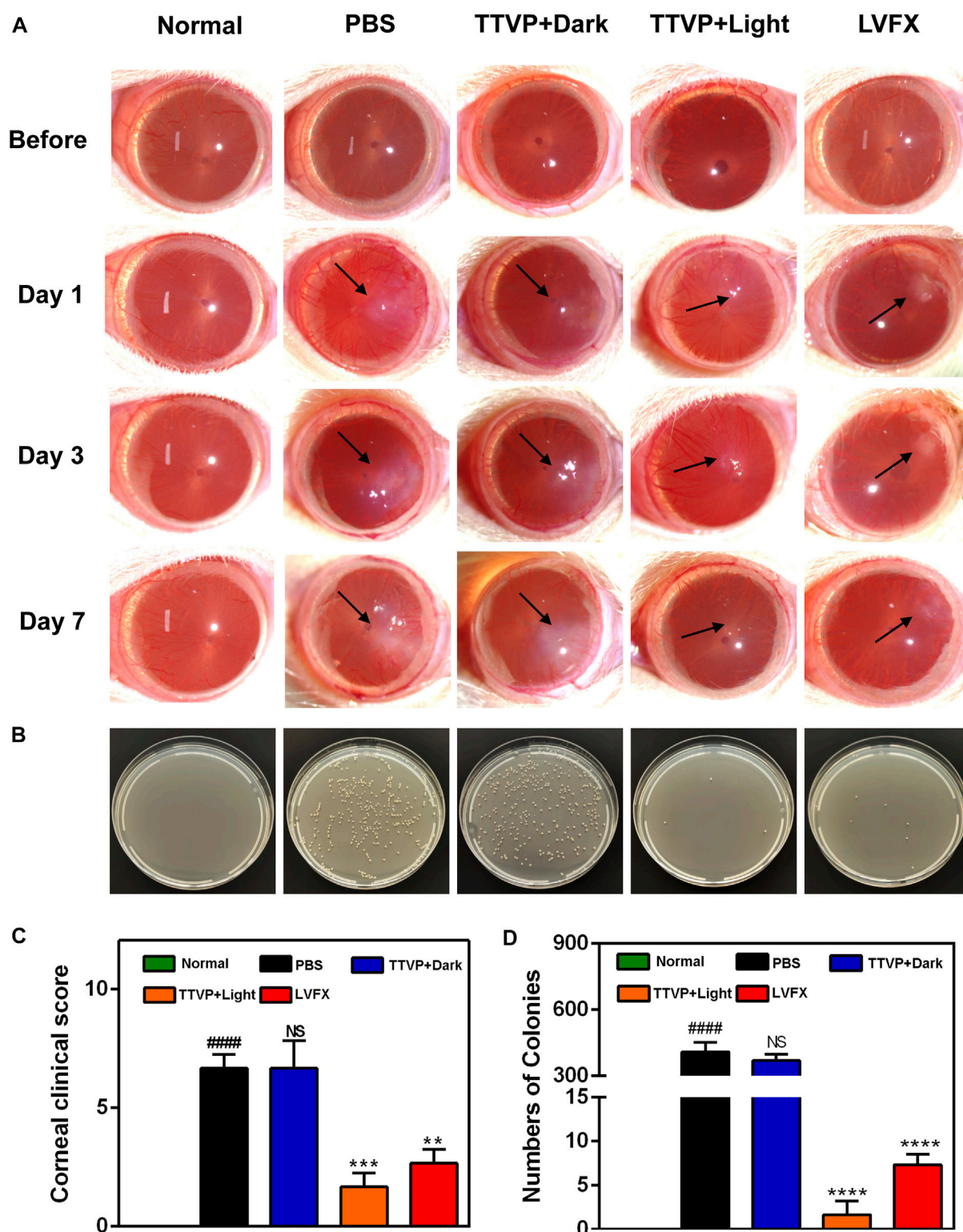
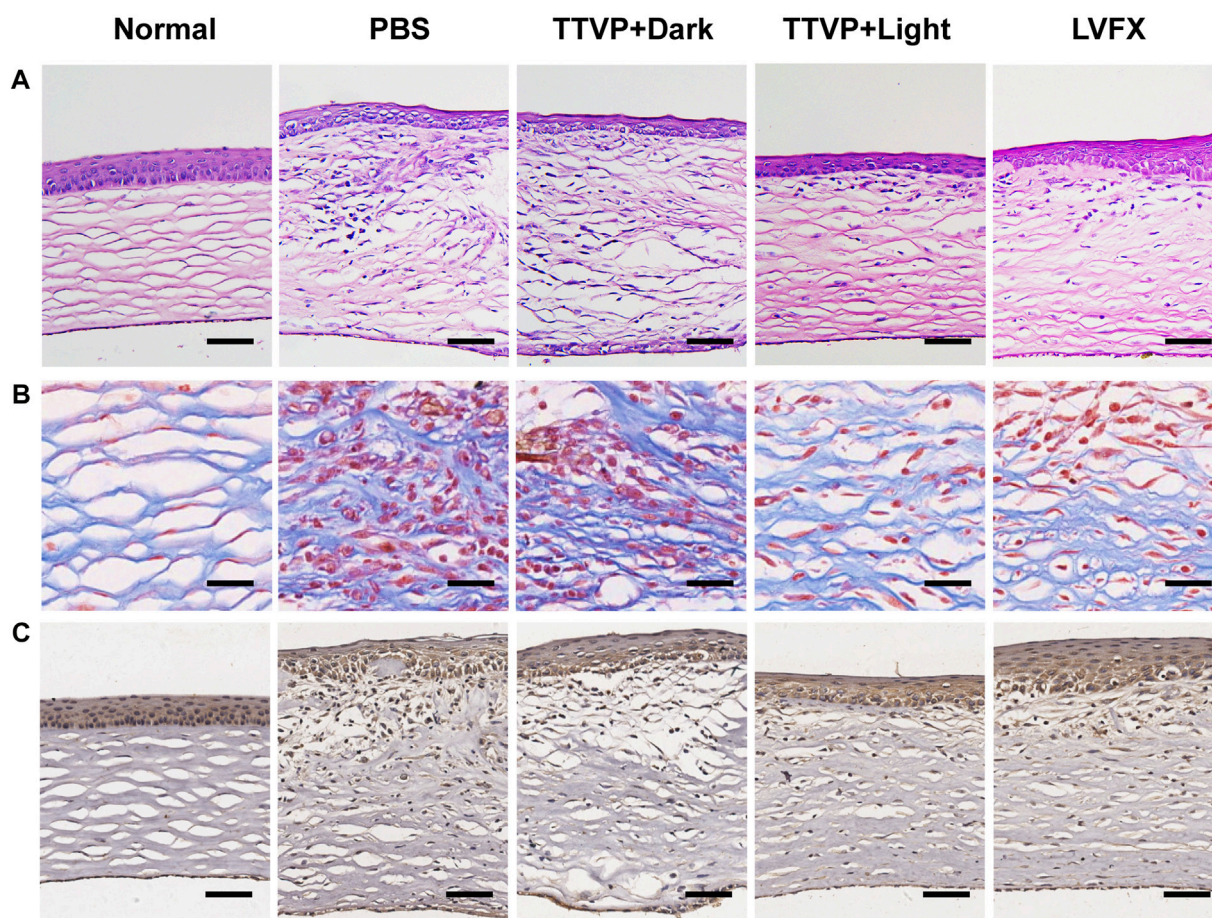


FIGURE 4

(A) Representative photographs of rat eyes before and at 1, 3 and 7 days after treatment. (B) The bacterial cultures on agar plates from the corresponding cornea. (C) Clinical score of rat eyes after different treatments; (D) the number of surviving *S. aureus* in corneas after different treatments at 7 days. # for group PBS versus group Normal, \* for group TTVP + Dark, TTVP + Light, LVFX versus group PBS, \* $p$  or # $p$  < 0.05, \*\* $p$  or ## $p$  < 0.01, \*\*\* $p$  or ### $p$  < 0.001, \*\*\*\* $p$  or #### $p$  < 0.0001, and NS for not significant.





**FIGURE 5**  
(A) H&E staining (scale bar: 100  $\mu$ m), (B) Masson staining (scale bar: 25  $\mu$ m), and (C) Immunohistochemistry staining of TNF- $\alpha$  (scale bar: 100  $\mu$ m) of cornea in different groups.

at the concentration of 0.1  $\mu$ M under white light irradiation, which demonstrated that AIEgens could generate efficient ROS in an aggregation state. The possible mechanism was the block of energy consumption by the way of non-radiative channels and aggregation-induced intersystem crossing (AI-ISC), inducing the transfer of facilitated energy state between singlet (S1) and triplet (T1) (Xu et al., 2015b; Yang et al., 2016). What's more, our previous research has shown a terrific generation of singlet oxygen in the aggregation state, inducing the antibacterial ability of TTVP (Lee et al., 2020). Thus, TTVP was expected to be a meaningful photosensitizer for PDT evolvement.

### 3.4 Imaging of HCECs cells and *S. aureus* mixture

The zeta potential value of pure *S. aureus* was  $-25.31 \pm 0.54$  mV, while the values were increased to  $-21.76 \pm 1.04$ ,  $-21.06 \pm 1.13$ ,  $-20.71 \pm 0.90$  mV, and  $-18.99 \pm 1.50$  mV

after incubated with TTVP (0.02, 0.05, 0.1 and 0.2  $\mu$ M), which verified the affinity of TTVP to *S. aureus* (Supplementary Figure S3). The co-culture method of HCECs and *S. aureus* was further employed to verify the selective killing ability of TTVP. As shown in Supplementary Figure S4, in a co-culture system of HCECs and *S. aureus*, red fluorescence was observed in *S. aureus* (area circled) and extremely weak in HCECs. TTVP could bind *S. aureus* specifically under certain concentrations for the surface charge discrepancy. Such a high selectivity reduced the damage on the normal corneal cells, thus implying promising application in BK treatment.

### 3.5 Biocompatibility evaluation

The biocompatibility of AIEgens should be taken into serious consideration prior to biological application. Since TTVP was administrated on the cornea, HCECs were performed to evaluate



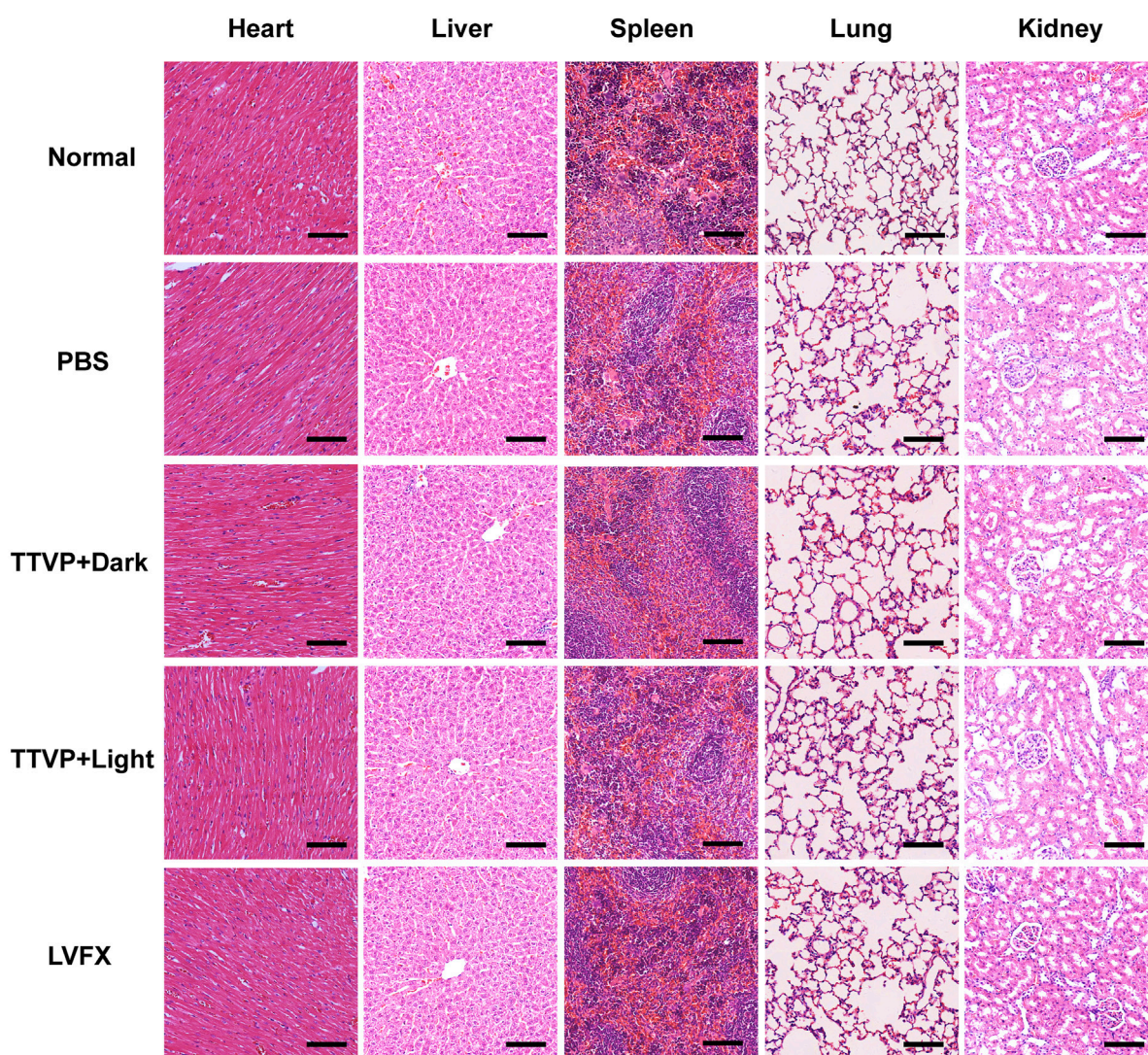


**FIGURE 6**  
H&E staining of main visceral organs at 7 days post treatment (heart, liver, spleen, lung and kidney, scale bar: 100  $\mu$ m).

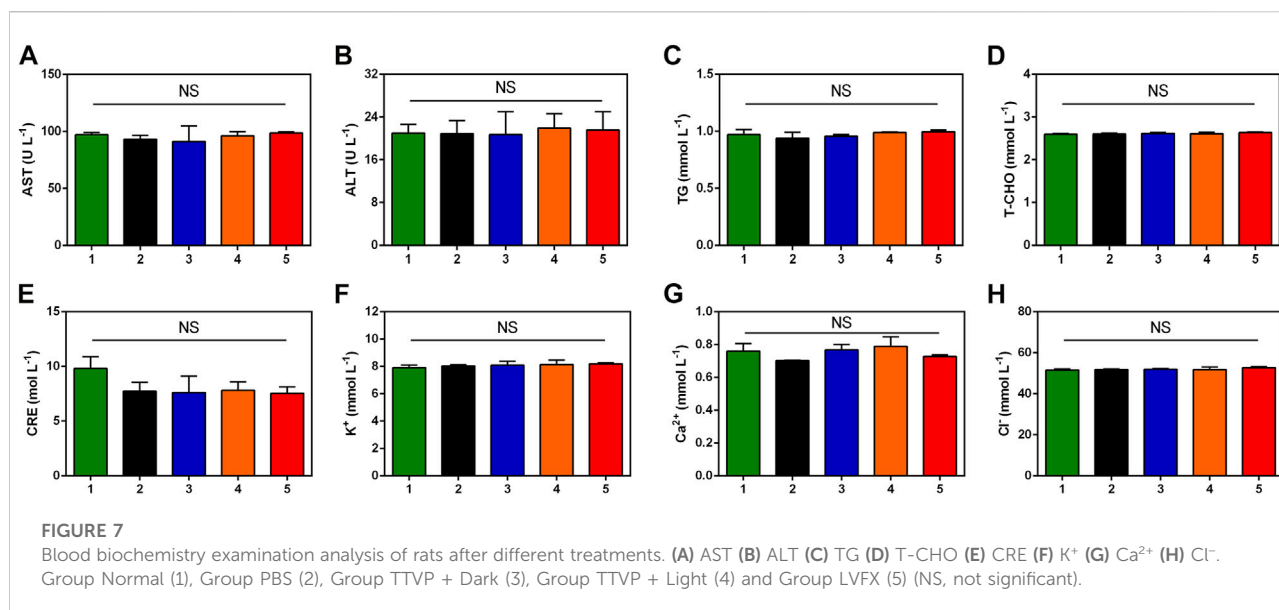
the biosafety. In **Figure 2C**, no significant difference was observed in cell viability of HCECs incubated with TTVP at concentrations under 0.1  $\mu$ M in dark and light condition. Meanwhile, the cellular morphology and density were observed visually by optical microscope. In **Supplementary Figure S5**, no obvious cell morphology change and density decrease were observed after TTVP incubation. What's more, live/dead staining of HCECs was performed to evaluate the cytotoxicity of TTVP. As shown in **Figure 2D**, the results showed no meaningful differences between live and dead fluorescence after being treated with TTVP (0–0.2  $\mu$ M) under dark or light condition (20 mW/cm<sup>2</sup>, 15 min), indicating low cytotoxicity of TTVP. In general, a hemolysis ratio no more than 10% was considered safe and acceptable for biological application (Xu et al., 2015a). It was

found that the hemolysis rates were less than 1% after TTVP was added to blood, and calculated to be  $0.27\% \pm 0.001\%$  at the concentration of 0.2  $\mu$ M (**Supplementary Figure S6**). Therefore, TTVP in our study was expected to be a promising option *in vitro* for further application.

### 3.6 *In vivo* treatment of BK

#### 3.6.1 Clinical observation

Encouraged by the high antibacterial activity, we employed TTVP to treat severe BK, which is prone to relapse and often leads to refractory ocular damage and blindness. Based on the promising antibacterial efficacy and reliable security of TTVP, we



established an experimental keratitis rat model to investigate whether TTVP could be applied for bacterial keratitis treatment. As shown in Figure 4A, after inoculation for 24 h, all rats appeared conjunctival congestion, corneal opacity and decreased corneal transparency to the same extent. Then, after different treatments, obvious differences in ocular manifestation were observed in these groups. In the PBS and TTVP under dark condition groups, the infection worsened severely over time. Three days after infection, the rat cornea exhibited prominent clinical manifestations of edema and muddiness at the damaged lesions. On the contrary, in TTVP with light group (20 mW/cm<sup>2</sup> power, 15 min) and LVFX group, the severity of infection was well-controlled, while the TTVP under light condition exhibited better antibacterial efficacy. At day 7, the groups treated with PBS and TTVP without light irradiation showed severe bacterial infection, displaying a more pyknotic corneal opacity. Amazingly, the eye symptoms were alleviated and the transparency of the ocular surface was enhanced in the TTVP with light irradiation group, which was superior to the LVFX groups.

In Figure 4C, the groups treated by TTVP with light irradiation showed significantly lower clinical scores than dark or PBS groups. This demonstrates that light activation of TTVP could effectively reduce the degree of infection, which was consistent with the photographs of rats' corneas. The strengthened antibacterial ability may be attributed to the ROS potency after light irradiation.

In addition, the corneal tissues were isolated from each group, and then homogenized and distributed on the spread plate to quantitatively evaluate the surviving bacterial colonies. The plates displayed nearly no colony formation in TTVP with light irradiation group, which showed better therapeutic effects

than LVFX, further indicating the remarkable therapeutic efficacy of TTVP against BK (Figures 4B, D). Due to the incidence of bacteria resistance after antibiotics application, the sterilization process of TTVP under light condition showed great potential for the treatment of *S. aureus*-infected keratitis.

### 3.6.2 Histopathological analysis

Figure 5 displayed photomicrographs of corneal tissue sections stained with H&E, Masson and immunohistochemistry staining of different groups. The normal cornea is composed of five layers, with continuous corneal epithelium and endothelial layer, as well as stromal connective tissue layer with no inflammatory-cell infiltration (Bharti and Kesavan, 2017). Masson staining is used to display the fibers in the tissue and visualize the structure of collagen in the stromal tissue (Meng et al., 2019). However, in PBS and TTVP without light irradiation groups, the epithelial layer was dense and stratified, the stromal layer was apparent edema and massive inflammatory infiltration, and the endothelial layer was focally dense. In comparison with these two groups, TTVP under light irradiation group revealed less severity of corneal edema and reduced inflammatory cell infiltration, which could be attributed to rapid sterilization via ROS generation to alleviate inflammatory response. And the groups treated with LVFX showed less antibacterial ability than TTVP with light irradiation. Next, immunohistochemistry staining of TNF-α was performed to assess the therapeutic efficacy, which was a vital index to evaluate the Inflammation levels. The results showed that the cornea treated with TTVP under light condition exhibited a significant reduction in inflammation levels. All the

histopathological results were consistent with the ocular manifestations.

### 3.7 *In vivo* biosafety

In order to assess the biosafety of TTVP *in vivo*, H&E staining was conducted on heart, liver, spleen, lung and kidney to detect the structural damage, while several biochemical indexes were applied to test the major functions of organs. H&E staining and biochemical indexes are extensively used to visually appraise the structural and functional change respectively (Abdelhalim et al., 2018; Zhang et al., 2018; Nguyen et al., 2019). As shown in Figure 6, no histomorphological changes were revealed in main organs *in vivo*, which proved the safety of TTVP in organ structure. Meanwhile, no obvious discrepancy was shown in the content of AST, ALT, TG, T-CHO, CRE, K<sup>+</sup>, Ca<sup>2+</sup> and Cl<sup>-</sup> among all groups, which indicated excellent liver and renal functions, lipid levels, and electrolyte stabilization in this study (Figure 7). TTVP was thus expected to be a promising option *in vivo* for BK application.

## 4 Conclusion

To sum up, a TTVP-mediated and ROS-induced PDT therapy was estimable in bactericidal research of BK. TTVP displayed low toxicity and excellent biocompatibility, ensuring further biological applications. TTVP could selectively combine with *S. aureus* over corneal cells. TTVP possessed excellent ROS release capacity, and showed specific antibacterial function without apparent cytotoxicity. TTVP exhibited vital status of photodynamic antibacterial therapy over BK injury. Our findings demonstrated that TTVP showed promising possibility as antimicrobials, which may take advantage of clinical application of BK treatment. This work will stimulate extensive application of TTVP as a novel therapy against BK infection.

## Data availability statement

The original contributions presented in the study are included in the article/Supplementary Material, further inquiries can be directed to the corresponding authors.

## References

Abdelhalim, M. A. K., Qaid, H. A., Al-Mohy, Y., and Al-Ayed, M. S. (2018). Effects of quercetin and arginine on the nephrotoxicity and lipid peroxidation induced by gold nanoparticles *in vivo*. *Int. J. Nanomedicine* 13, 7765–7770. doi:10.2147/IJN.S183281

## Ethics statement

The animal study was reviewed and approved by the Shanghai Tenth People's Hospital Animal Ethics Committee.

## Author contributions

CP and DW designed the project and experiments. WC, TS, and TL have carried out the experiments. JY and BT participated in the discussion and revision of the manuscript. All authors contributed to the article and approved the submitted version.

## Funding

This research was supported by Shenzhen Key laboratory of Functional Aggregate Materials (ZDSYS20211021111400001), Shenzhen Peacock Team Project (KQTD20210811090142053), and the Youth Program of National Natural Science Foundation of China (No. 82101130).

## Conflict of interest

The authors declare that the research was conducted in the absence of any commercial or financial relationships that could be construed as a potential conflict of interest.

The handling editor declared a past co-authorship with the author BT.

## Publisher's note

All claims expressed in this article are solely those of the authors and do not necessarily represent those of their affiliated organizations, or those of the publisher, the editors and the reviewers. Any product that may be evaluated in this article, or claim that may be made by its manufacturer, is not guaranteed or endorsed by the publisher.

## Supplementary material

The Supplementary Material for this article can be found online at: <https://www.frontiersin.org/articles/10.3389/fchem.2022.1088935/full#supplementary-material>

Abrahamse, H., Hamblin, M. R., and George, S. (2022). Structure and functions of Aggregation-Induced Emission-Photosensitizers in anticancer and antimicrobial theranostics. *Front. Chem.* 10, 984268. doi:10.3389/fchem.2022.984268



- Ayaz, F., Demirbag, B., and Ocakoglu, K. (2020). Immunoactive photosensitizers had photodynamic immunostimulatory and immunomodulatory effects on mammalian macrophages. *Photodiagnosis Photodyn. Ther.* 32, 102034. doi:10.1016/j.pdpdt.2020.102034
- Bharti, S. K., and Kesavan, K. (2017). Phase-transition W/O microemulsions for ocular delivery: Evaluation of antibacterial activity in the treatment of bacterial keratitis. *Ocul. Immunol. Inflamm.* 25 (4), 463–474. doi:10.3109/09273948.2016.1139136
- Blindness, G. B. D., Steinmetz, J. D., Flaxman, S., Briant, P. S., Taylor, H. R., Resnikoff, S., et al. (2021). Vision impairment, C., and vision loss expert group of the global burden of disease, STrends in prevalence of blindness and distance and near vision impairment over 30 years: An analysis for the global burden of disease study. *Lancet Glob. Health* 9 (2), e130–e143. doi:10.1016/S2214-109X(20)30425-3
- Chen, H., Yang, J., Sun, L., Zhang, H., Guo, Y., Qu, J., et al. (2019). Synergistic chemotherapy and photodynamic therapy of endophthalmitis mediated by zeolitic imidazolate framework-based drug delivery systems. *Small* 15 (47), e1903880. doi:10.1002/smll.201903880
- Cheng, J., Wang, W., Xu, X., Lin, Z., Xie, C., Zhang, Y., et al. (2020). AgBiS2 nanoparticles with synergistic photodynamic and bioimaging properties for enhanced malignant tumor phototherapy. *Mater. Sci. Eng. C* 107, 110324. doi:10.1016/j.msec.2019.110324
- Dai, J., Wu, X., Ding, S., Lou, X., Xia, F., Wang, S., et al. (2020). Aggregation-induced emission photosensitizers: From molecular design to photodynamic therapy. *J. Med. Chem.* 63 (5), 1996–2012. doi:10.1021/acs.jmedchem.9b02014
- Davis, S. A., Bovel, R., Han, G., and Kwagyan, J. (2020). Corneal collagen cross-linking for bacterial infectious keratitis. *Cochrane Database Syst. Rev.* 6, CD013001. doi:10.1002/14651858.CD013001.pub2
- Fan, W., Han, H., Chen, Y., Zhang, X., Gao, Y., Li, S., et al. (2021). Antimicrobial nanomedicine for ocular bacterial and fungal infection. *Drug Deliv. Transl. Res.* 11 (4), 1352–1375. doi:10.1007/s13346-021-00966-x
- Han, H., Gao, Y., Chai, M., Zhang, X., Liu, S., Huang, Y., et al. (2020). Biofilm microenvironment activated supramolecular nanoparticles for enhanced photodynamic therapy of bacterial keratitis. *J. Control. Release* 327, 676–687. doi:10.1016/j.jconrel.2020.09.014
- Han, H., Jin, Q., Wang, H., Teng, W., Wu, J., Tong, H., et al. (2016). Intracellular dual fluorescent lightup bioprobes for image-guided photodynamic cancer therapy. *Small* 12 (28), 3870–3878. doi:10.1002/smll.201600950
- Hu, F., Xu, S., and Liu, B. (2018). Photosensitizers with aggregation-induced emission: Materials and biomedical applications. *Adv. Mat.* 30 (45), e1801350. doi:10.1002/adma.201801350
- Huang, J., Wu, S., Wu, M., Zeng, Q., Wang, X., and Wang, H. (2021). Efficacy of the therapy of 5-aminolevulinic acid photodynamic therapy combined with human umbilical cord mesenchymal stem cells on methicillin-resistant *Staphylococcus aureus*-infected wound in a diabetic mouse model. *Photodiagnosis Photodyn. Ther.* 36, 102480. doi:10.1016/j.pdpdt.2021.102480
- Huo, J., Jia, Q., Huang, H., Zhang, J., Li, P., Dong, X., et al. (2021). Emerging photothermal-derived multimodal synergistic therapy in combating bacterial infections. *Chem. Soc. Rev.* 50 (15), 8762–8789. doi:10.1039/d1cs00074h
- Idris, N. M., Gnanasammandhan, M. K., Zhang, J., Ho, P. C., Mahendran, R., and Zhang, Y. (2012). *In vivo* photodynamic therapy using upconversion nanoparticles as remote-controlled nanotransducers. *Nat. Med.* 18 (10), 1580–1585. doi:10.1038/nm.2933
- Jiang, M., Kwok, R. T. K., Li, X., Gui, C., Lam, J. W. Y., Qu, J., et al. (2018). A simple mitochondrial targeting AIEgen for image-guided two-photon excited photodynamic therapy. *J. Mat. Chem. B* 6 (17), 2557–2565. doi:10.1039/c7tb02609a
- Josyula, A., Omiadze, R., Parikh, K., Kanvinde, P., Appell, M. B., Patel, P., et al. (2021). An ion-paired moxifloxacin nanosuspension eye drop provides improved prevention and treatment of ocular infection. *Bioeng. Transl. Med.* 6 (3), e10238. doi:10.1002/btm2.10238
- Kang, M., Zhou, C., Wu, S., Yu, B., Zhang, Z., Song, N., et al. (2019). Evaluation of structure-function relationships of aggregation-induced emission luminogens for simultaneous dual applications of specific discrimination and efficient photodynamic killing of gram-positive bacteria. *J. Am. Chem. Soc.* 141 (42), 16781–16789. doi:10.1021/jacs.9b07162
- Khan, M., Stapleton, F., and Willcox, M. D. P. (2020). Susceptibility of contact lens-related *Pseudomonas aeruginosa* keratitis isolates to multipurpose disinfecting solutions, disinfectants, and antibiotics. *Transl. Vis. Sci. Technol.* 9 (5), 2. doi:10.1167/tvst.9.5.2
- Lee, M. M. S., Xu, W., Zheng, L., Yu, B., Leung, A. C. S., Kwok, R. T. K., et al. (2020). Ultrafast discrimination of Gram-positive bacteria and highly efficient photodynamic antibacterial therapy using near-infrared photosensitizer with aggregation-induced emission characteristics. *Biomaterials* 230, 119582. doi:10.1016/j.biomaterials.2019.119582
- Li, G., Xu, L., Jiang, M., and Wu, X. (2020a). Eye drops and eye gels of levofloxacin: Comparison of ocular absorption characterizations and therapeutic effects in the treatment of bacterial keratitis in rabbits. *Drug Dev. Ind. Pharm.* 46 (4), 673–681. doi:10.1080/03639045.2020.1750626
- Li, Q., Li, Y., Min, T., Gong, J., Du, L., Phillips, D. L., et al. (2020b). Time-dependent photodynamic therapy for multiple targets: A highly efficient AIE-active photosensitizer for selective bacterial elimination and cancer cell ablation. *Angew. Chem. Int. Ed.* 59 (24), 9470–9477. doi:10.1002/anie.201909706
- Li, T., Wu, Y., Cai, W., Wang, D., Ren, C., Shen, T., et al. (2022). Vision defense: Efficient antibacterial AIEgens induced early immune response for bacterial endophthalmitis. *Adv. Sci. (Weinh.)* 9 (25), e2202485. doi:10.1002/advs.202202485
- Li, Y., Liu, F., Zhang, J., Liu, X., Xiao, P., Bai, H., et al. (2021a). Efficient killing of multidrug-resistant internalized bacteria by AIEgens *in vivo*. *Adv. Sci. (Weinh.)* 8 (9), 2001750. doi:10.1002/advs.202001750
- Li, Z., Pan, W., Shi, E., Bai, L., Liu, H., Li, C., et al. (2021b). A multifunctional nanosystem based on bacterial cell-penetrating photosensitizer for fighting periodontitis via combining photodynamic and antibiotic therapies. *ACS Biomater. Sci. Eng.* 7 (2), 772–786. doi:10.1021/acsbomaterials.0c01638
- Liao, Y., Li, B., Zhao, Z., Fu, Y., Tan, Q., Li, X., et al. (2020). Targeted theranostics for tuberculosis: A rifampicin-loaded aggregation-induced emission carrier for granuloma tracking and anti-infection. *ACS Nano* 14 (7), 8046–8058. doi:10.1021/acsnano.0c00586
- Liu, K., Liu, Y., Yao, Y., Yuan, H., Wang, S., Wang, Z., et al. (2013). Supramolecular photosensitizers with enhanced antibacterial efficiency. *Angew. Chem. Int. Ed.* 52 (32), 8285–8289. doi:10.1002/anie.201303387
- Liu, Y. S., Wei, X., Zhao, X., Chen, L. J., and Yan, X. P. (2021). Near-Infrared photothermal/photodynamic-in-one agents integrated with a guanidinium-based covalent organic framework for intelligent targeted imaging-guided precision chemo/PTT/PDT sterilization. *ACS Appl. Mat. Interfaces* 13 (24), 27895–27903. doi:10.1021/acsami.1c05705
- Lu, Y., Li, L., Lin, Z., Wang, L., Lin, L., Li, M., et al. (2018). A new treatment modality for rheumatoid arthritis: Combined photothermal and photodynamic therapy using Cu<sub>7</sub>S<sub>4</sub> nanoparticles. *Adv. Healthc. Mat.* 7 (14), e1800013. doi:10.1002/adhm.201800013
- Mei, J., Leung, N. L., Kwok, R. T., Lam, J. W., and Tang, B. Z. (2015). Aggregation-induced emission: Together we shine, united we soar. *Chem. Rev.* 115 (21), 11718–11940. doi:10.1021/acs.chemrev.5b00263
- Meng, E., Chen, C. L., Liu, C. C., Liu, C. C., Chang, S. J., Cherng, J. H., et al. (2019). Bioapplications of bacterial cellulose polymers conjugated with resveratrol for epithelial defect regeneration. *Polym. (Basel)* 11 (6), 1048. doi:10.3390/polym11061048
- Nguyen, V. P., Li, Y., Qian, W., Liu, B., Tian, C., Zhang, W., et al. (2019). Contrast agent enhanced multimodal photoacoustic microscopy and optical coherence tomography for imaging of rabbit choroidal and retinal vessels *in vivo*. *Sci. Rep.* 9 (1), 5945. doi:10.1038/s41598-019-42324-5
- Ni, J. S., Min, T., Li, Y., Zha, M., Zhang, P., Ho, C. L., et al. (2020). Planar AIEgens with enhanced solid-state luminescence and ROS generation for multidrug-resistant bacteria treatment. *Angew. Chem. Int. Ed.* 59 (25), 10179–10185. doi:10.1002/anie.202001103
- Peng, C., Sun, W., Zhou, C., Qiang, S., Jiang, M., Lam, J. W. Y., et al. (2021). Vision redemption: Self-reporting AIEgens for combined treatment of bacterial keratitis. *Biomaterials* 279, 121227. doi:10.1016/j.biomaterials.2021.121227
- Qi, M., Chi, M., Sun, X., Xie, X., Weir, M. D., Oates, T. W., et al. (2019). Novel nanomaterial-based antibacterial photodynamic therapies to combat oral bacterial biofilms and infectious diseases. *Int. J. Nanomedicine* 14, 6937–6956. doi:10.2147/IJN.S212807
- Silva, C. N. D., Silva, F. R. D., Dourado, L. F. N., Reis, P., Silva, R. O., Costa, B. L. D., et al. (2019). A new topical eye drop containing LyTxI-b, A synthetic peptide designed from A *Lycosa erithrognata* venom toxin, was effective to treat resistant bacterial keratitis. *Toxins (Basel)* 11 (4), 203. doi:10.3390/toxins11040203
- Tuft, S., Somerville, T. F., Li, J. O., Neal, T., De, S., Horsburgh, M. J., et al. (2022). Bacterial keratitis: Identifying the areas of clinical uncertainty. *Prog. Retin. Eye Res.* 89, 101031. doi:10.1016/j.preteyeres.2021.101031
- Ung, L., Bispo, P. J. M., Shanbhag, S. S., Gilmore, M. S., and Chodosh, J. (2019). The persistent dilemma of microbial keratitis: Global burden, diagnosis, and antimicrobial resistance. *Surv. Ophthalmol.* 64 (3), 255–271. doi:10.1016/j.survophthal.2018.12.003
- Wang, B., Zhou, L., Guo, Y., Guo, H., Zhong, Y., Huang, X., et al. (2022). Cyanobacteria-based self-oxygenated photodynamic therapy for anaerobic infection treatment and tissue repair. *Bioact. Mat.* 12, 314–326. doi:10.1016/j.bioactmat.2021.10.032
- Wang, D., Lee, M. M. S., Xu, W., Kwok, R. T. K., Lam, J. W. Y., and Tang, B. Z. (2018a). Theranostics based on AIEgens. *Theranostics* 8 (18), 4925–4956. doi:10.7150/thno.27787
- Wang, D., Su, H., Kwok, R. T. K., Hu, X., Zou, H., Luo, Q., et al. (2018b). Rational design of a water-soluble NIR AIEgen, and its application in ultrafast wash-free

cellular imaging and photodynamic cancer cell ablation. *Chem. Sci.* 9 (15), 3685–3693. doi:10.1039/c7sc04963c

Xu, H., Yang, D., Cai, C., Gou, J., Zhang, Y., Wang, L., et al. (2015a). Dual-responsive mPEG-PLGA-PGlu hybrid-core nanoparticles with a high drug loading to reverse the multidrug resistance of breast cancer: An *in vitro* and *in vivo* evaluation. *Acta Biomater.* 16, 156–168. doi:10.1016/j.actbio.2015.01.039

Xu, S., Yuan, Y., Cai, X., Zhang, C. J., Hu, F., Liang, J., et al. (2015b). Tuning the singlet-triplet energy gap: A unique approach to efficient photosensitizers with aggregation-induced emission (AIE) characteristics. *Chem. Sci.* 6 (10), 5824–5830. doi:10.1039/c5sc01733e

Yang, L., Wang, X., Zhang, G., Chen, X., Zhang, G., and Jiang, J. (2016). Aggregation-induced intersystem crossing: A novel strategy for efficient molecular phosphorescence. *Nanoscale* 8 (40), 17422–17426. doi:10.1039/c6nr03656b

Yang, T., Fan, T. J., and Xu, B. (2020). Norfloxacin induces apoptosis and necroptosis in human corneal epithelial cells. *Toxicol. Vitro* 66, 104868. doi:10.1016/j.tiv.2020.104868

Yu, C. Y., Xu, H., Ji, S., Kwok, R. T., Lam, J. W., Li, X., et al. (2017). Mitochondrion-anchoring photosensitizer with aggregation-induced emission characteristics synergistically boosts the radiosensitivity of cancer cells to ionizing radiation. *Adv. Mat.* 29 (15), 1606167. doi:10.1002/adma.201606167

Yuan, H., Liu, Z., Liu, L., Lv, F., Wang, Y., and Wang, S. (2014). Cationic conjugated polymers for discrimination of microbial pathogens. *Adv. Mat.* 26 (25), 4333–4338. doi:10.1002/adma.201400636

Zhang, H., Jiang, W., Peng, Y., Yang, J., Chu, X., Long, Z., et al. (2022a). Killing three birds with one stone: Near-infrared light triggered nitric oxide release for

enhanced photodynamic and anti-inflammatory therapy in refractory keratitis. *Biomaterials* 286, 121577. doi:10.1016/j.biomaterials.2022.121577

Zhang, H., Liu, S., Yue, J., Sun, S., Lv, Q., Jian, S., et al. (2019). *In vitro* antimicrobial activity of diacerein on 76 isolates of gram-positive cocci from bacterial keratitis patients and *in vivo* study of diacerein eye drops on *Staphylococcus aureus* keratitis in mice. *Antimicrob. Agents Chemother.* 63 (4), 018744–18. doi:10.1128/AAC.01874-18

Zhang, L., Chang, J., Zhao, Y., Xu, H., Wang, T., Li, Q., et al. (2018). Fabrication of a triptolide-loaded and poly- $\gamma$ -glutamic acid-based amphiphilic nanoparticle for the treatment of rheumatoid arthritis. *Int. J. Nanomedicine* 13, 2051–2064. doi:10.2147/IJN.S151233

Zhang, Y., Li, G., Zhang, X., and Lin, L. (2022b). ROS-scavenging glyco-nanoplatform for synergistic antibacterial and wound-healing therapy of bacterial keratitis. *J. Mat. Chem. B* 10 (24), 4575–4587. doi:10.1039/d2tb00667g

Zhang, Y., Yu, Y., Li, G., Zhang, X., Wu, Z., and Lin, L. (2021). Epithelium-penetrable nanoplatform with enhanced antibiotic internalization for management of bacterial keratitis. *Biomacromolecules* 22 (5), 2020–2032. doi:10.1021/acs.biomac.1c00139

Zhou, T., Hu, R., Wang, L., Qiu, Y., Zhang, G., Deng, Q., et al. (2020). An AIE-active conjugated polymer with high ROS-generation ability and biocompatibility for efficient photodynamic therapy of bacterial infections. *Angew. Chem. Int. Ed.* 59 (25), 9952–9956. doi:10.1002/anie.201916704

Zhou, Y., Deng, W., Mo, M., Luo, D., Liu, H., Jiang, Y., et al. (2021). Stimuli-Responsive nanoplatform-assisted photodynamic therapy against bacterial infections. *Front. Med.* 8, 729300. doi:10.3389/fmed.2021.729300



## OPEN ACCESS

## EDITED BY

Zhendong Jin,  
The University of Iowa, United States

## REVIEWED BY

Wanbin Zhang,  
Shanghai Jiao Tong University, China  
Guanzhao Wu,  
Qilu Hospital of Shandong University  
(Qingdao), China

## \*CORRESPONDENCE

Guigen Li,  
✉ [guigen.li@ttu.edu](mailto:guigen.li@ttu.edu)  
Hans Lischka,  
✉ [hans.lischka@univie.ac.at](mailto:hans.lischka@univie.ac.at)

<sup>†</sup>These authors have contributed equally to  
this work

## SPECIALTY SECTION

This article was submitted to Organic  
Chemistry,  
a section of the journal  
Frontiers in Chemistry

RECEIVED 28 November 2022

ACCEPTED 19 December 2022

PUBLISHED 05 January 2023

## CITATION

Jin S, Xu T, Tang Y, Wang J-Y, Wang Y,  
Pan J, Zhang S, Yuan Q, Rahman AU,  
Aquino AJA, Lischka H and Li G (2023), A  
new chiral phenomenon of orientational  
chirality, its synthetic control and  
computational study.  
*Front. Chem.* 10:1110240.  
doi: 10.3389/fchem.2022.1110240

## COPYRIGHT

© 2023 Jin, Xu, Tang, Wang, Wang, Pan,  
Zhang, Yuan, Rahman, Aquino, Lischka and  
Li. This is an open-access article  
distributed under the terms of the [Creative  
Commons Attribution License \(CC BY\)](#).  
The use, distribution or reproduction in  
other forums is permitted, provided the  
original author(s) and the copyright  
owner(s) are credited and that the original  
publication in this journal is cited, in  
accordance with accepted academic  
practice. No use, distribution or  
reproduction is permitted which does not  
comply with these terms.

# A new chiral phenomenon of orientational chirality, its synthetic control and computational study

Shengzhou Jin<sup>1†</sup>, Ting Xu<sup>1†</sup>, Yao Tang<sup>2†</sup>, Jia-Yin Wang<sup>3</sup>, Yu Wang<sup>1</sup>,  
Junyi Pan<sup>1</sup>, Sai Zhang<sup>2</sup>, Qingkai Yuan<sup>2</sup>, Anis Ur Rahman<sup>2</sup>,  
Adelia J. A. Aquino<sup>4</sup>, Hans Lischka<sup>2\*</sup> and Guigen Li<sup>1,2\*</sup>

<sup>1</sup>School of Chemistry and Chemical Engineering, Nanjing University, Nanjing, China, <sup>2</sup>Department of Chemistry and Biochemistry, Texas Tech University, Lubbock, TX, United States, <sup>3</sup>Continuous Flow Engineering Laboratory of National Petroleum and Chemical Industry, Changzhou University, Changzhou, Jiangsu, China, <sup>4</sup>Department of Mechanical Engineering, Texas Tech University, Lubbock, TX, United States

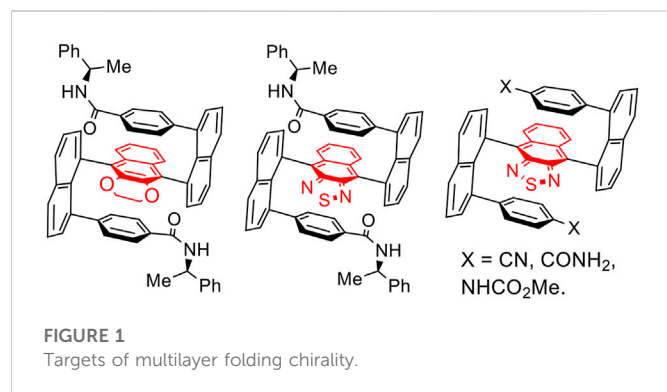
A new type of chirality, orientational chirality, consisting of a tetrahedron center and a remotely anchored blocker, has been discovered. The key structural element of this chirality is characterized by multiple orientations directed by a through-space functional group. The multi-step synthesis of orientational chiral targets was conducted by taking advantage of asymmetric nucleophilic addition, Suzuki-Miyaura cross-coupling and Sonogashira coupling. An unprecedented catalytic species showing a five-membered ring consisting of C (sp<sup>2</sup>)-Br-Pd-C (sp<sup>2</sup>) bonds was isolated during performing Suzuki-Miyaura cross-coupling. X-ray diffraction analysis confirmed the species structure and absolute configuration of chiral orientation products. Based on X-ray structures, a model was proposed for the new chirality phenomenon to differentiate the present molecular framework from previous others. DFT computational study presented the relative stability of individual orientatiomers. This discovery would be anticipated to result in a new stereochemistry branch and to have a broad impact on chemical, biomedical, and material sciences in the future.

## KEYWORDS

orientational chirality, atropisomerism, rotamer, suzuki-miyaura coupling, and sonogashira coupling

## 1 Introduction

Chirality and its control have been among the most active topics in science, technology, and public society for over a century (Wang et al., 1983; Dunitz, 2001; Ojima, 2010; Taniguchi et al., 2011; Bao et al., 2020; Bryliakov, 2020; Zhang and Kürti, 2021). Chirality widely exists in functional biomolecules, such as peptides/proteins, DNA/RNA, and carbohydrates, and has been heavily involved in biological mechanisms in human beings, animals, and plants on the Earth (Wagner and Musso, 1983; Pace and Scholtz, 1998; Williams and Perlmutter, 2013). It has been becoming increasingly important since a large number of modern drugs and their building blocks exhibit chirality in their structures and subunits. The chirality of molecular medicine often governs medical treatments in regard to potency and selectivity of drugs in regard to reducing dosages and unwanted side effects (Lung et al., 1995; Hruby et al., 1997; Markwell, 2008; Rouh et al., 2022). In modern materials science, the control of chirality is necessitated so as to achieve challenging optoelectronic properties (Huang et al., 2018; Feng et al., 2019; Li et al., 2020; Zhao et al., 2020; Liu et al., 2021; Oki et al., 2021). It is worth noting that the progress of aforementioned fields should be greatly attributed to achievements made in asymmetric synthesis and catalysis (Dai et al., 2003; Zeng and Chemler, 2007; Cui et al., 2011; Zhou,



2011; Lorion et al., 2017; Song et al., 2017; Liao et al., 2018; Wang and Tan, 2018; Guo et al., 2019; Chen et al., 2020; Ge et al., 2020; Liu et al., 2020; Ma et al., 2020; Zhang et al., 2020; Huang et al., 2021; Wang et al., 2021; Zhao et al., 2021).

Chirality is commonly divided into the following categories: central (Zhao et al., 2021), axial (Wang and Tan, 2018; Zhang et al., 2020), spiral (Zhou, 2011), metallic (Dai et al., 2003) and organo (Wu et al., 2019; Liu Y. et al., 2020) sandwich-type, rigid helical (Shen and Chen, 2012; Shirakawa et al., 2016) and flexible folding (Wu, et al., 2019; Wu et al., 2020; Tang et al., 2022; Wang et al., 2022) multilayered chirality (Figure 1). Among these categories,  $C_2$  symmetry has been occupying a special position concerning chirality control, catalyst design and applications (Zhou, 2011; Zhao et al., 2021). Meanwhile, pseudo or quasi  $C_2$  symmetry has also become an interesting and important addition to chirality documents. For instance, organo sandwich chirality shows unique “S” and “Z” (*anti* S) patterns of pseudo  $C_2$  symmetry (Tang et al., 2022b; Jin et al., 2022), and their chiral aggregates displayed various spectroscopic properties (Figure 2).

Very recently, we reported a new chirality pattern stabilized by aromatic/aromatic interaction (w in Figure 3), as proven by X-ray diffraction analysis (Wu et al., 2021). Interestingly, the new target showed a new chiral subunit containing a pseudo chiral center (x in Figure 3) and orientational axis (y in Figure 3A). The pseudo chiral center on the phosphorus atom was directly connected to naphthalenyl ring and two Ph groups which are differentiated by internally paralleled packing. This pseudo phosphorous center would be extended to other similar centers of tetrahedron (e.g., C and Si) or polyhedron. The atropisomerism along the C-P axis would be made possible not only by Ar-Ar interaction, but also by the special arrangement of the layered phenyl ring on the bottom. Concurrently, Sparr and Jørgensen labs have successfully designed and achieved asymmetric catalytic approaches to stable atropisomers containing C ( $sp^2$ )-C ( $sp^3$ )  $\sigma$  bonds as axes [y in Figures 3B, C] (Wu X. et al., 2021; Bertuzzi et al., 2022). In fact, the tetrahedron-plane based rotamers had not become atropisomers until when the aforementioned labs were involved in this research (Wu X. et al., 2021; Wu et al., 2021; Bertuzzi et al., 2022), this is due to the fact that rotational barriers around the tetrahedron-plane axis is not large enough.

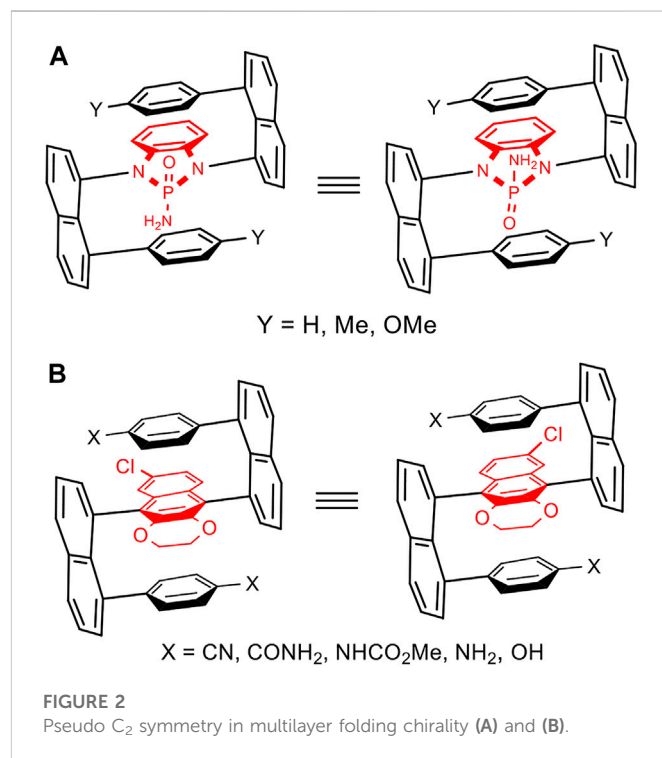
While continuing the project on multi-layer folding chirality, we found a new pattern of chirality-orientational chirality in which both the chiral center and stereochemical blocker are remotely anchored. The orientational chiral isomers have been stabilized and

asymmetrically synthesized through structural analysis and design. Herein, we would like to report our preliminary results of this discovery.

## 2 Discussion and results

This project was initiated by our vision that chirally layered structures would lead to asymmetric control of synthetic reactions by taking advantage of through-space asymmetric induction. For instance, using a chirally attached para-carbon center on the right phenyl ring would generate stereospecific control for reactions on mesitylene subunit nearby. 8-(Mesitylethynyl)naphthalen-1-yl phenyl-derived sulfonamide was thus generated in the formation of crystalline solids. We pleasingly found that two different rotamers co-exist in their crystals, as revealed by X-ray diffraction analysis (Figure 4). This observation would indicate the possibility of achieving individual atropisomers centered on  $sp^3$  carbon. It is worth noting that this atropisomerism is based on four independent flexible motifs on  $sp^3$  carbon, which made the present atropisomerism to be differentiated from previous systems containing cyclized rigid substituents centered on  $sp^3$  carbon (Wu X. et al., 2021; Bertuzzi et al., 2022).

This encouraging observation inspired us to conduct the structural analysis, design and synthesize derivatives of (IA) or (IB) to increase energy barriers to prevent individual isomers from rotating. To our pleasant, the stable orientationomers were successfully achieved through structural design, as shown in Figure 5. The first crystals of IA showed the co-existence of two rotamers in a ratio of 1:1, in which n-butyl- and sulfinyl-amino groups are directed away from the shielding mestyl plane, respectively. This indicates that low energy barriers led to freely rotating along  $sp^2$ - $sp^3$   $\sigma$  bond in solution prior to forming crystals. Rotational barriers heavily depend on the distance between two





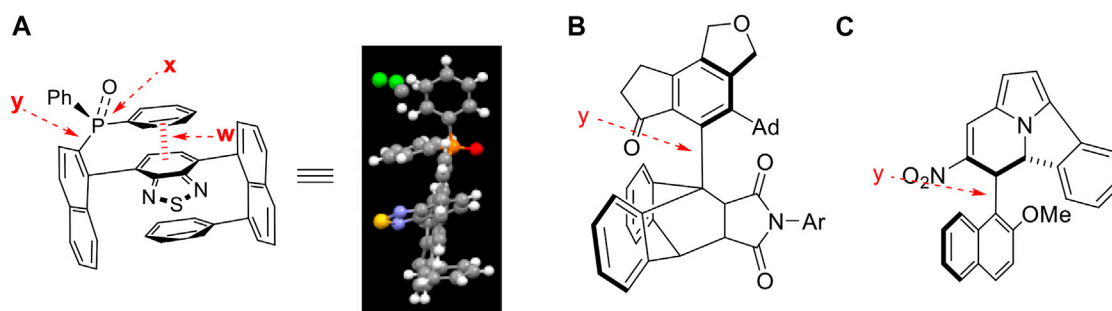


**FIGURE 3**  
Targets with pseudo chiral center (A) and orientational axis (A–C).

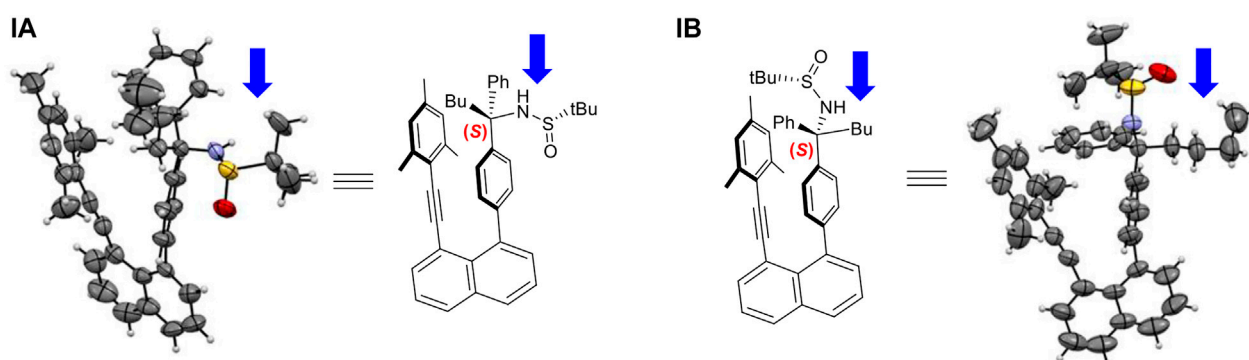


**FIGURE 4**  
Two differentiated orientational isomers of (IA) and (IB).

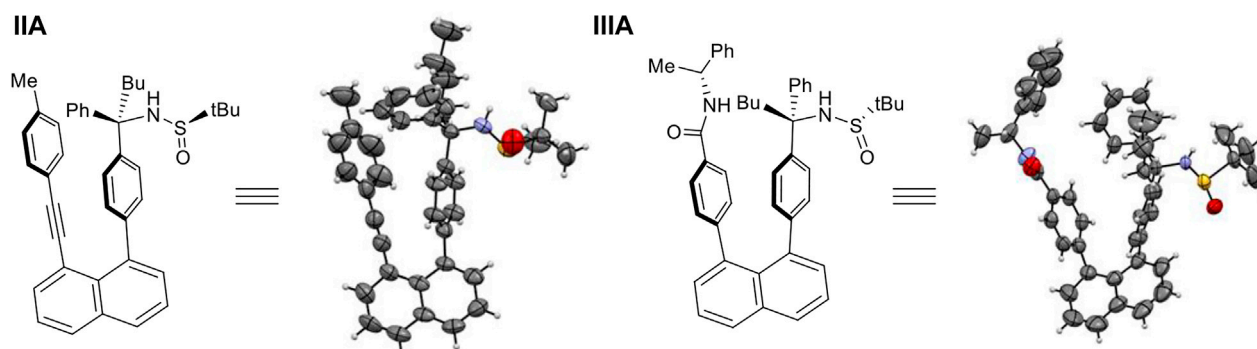


**FIGURE 5**  
Stabilized individual orientational isomers (IIA) and (IIIA).

anchored levers/arms on 1,8-positions of naphthalene which is opened wider gradually toward the two ends on top of the structural framework. While the *p*-methyl group on the mesityl ring plays a crucial role in controlling rotation along  $sp^2$ - $sp^3$   $\sigma$  bond, its 2,5-methyl groups widen the distance between two levers/arms (Figure 6); this is attributed to  $sp^3$  hybridization of methyl groups appearing as two

round balls connected on two sides of aromatic ring symmetrically. For this reason, we utilized the *p*-methylphenyl group to replace its mesityl counterpart to avoid the steric effects by two symmetric round balls on the left arms/levers. (*R*)-2-Methyl-*N*-((*R*)-1-phenyl-1-(4-(8-(*p*-tolylethynyl)naphthalen-1-yl)phenyl)pentyl)propane-2-sulfonamide (IIA) was thus designed and synthesized to give



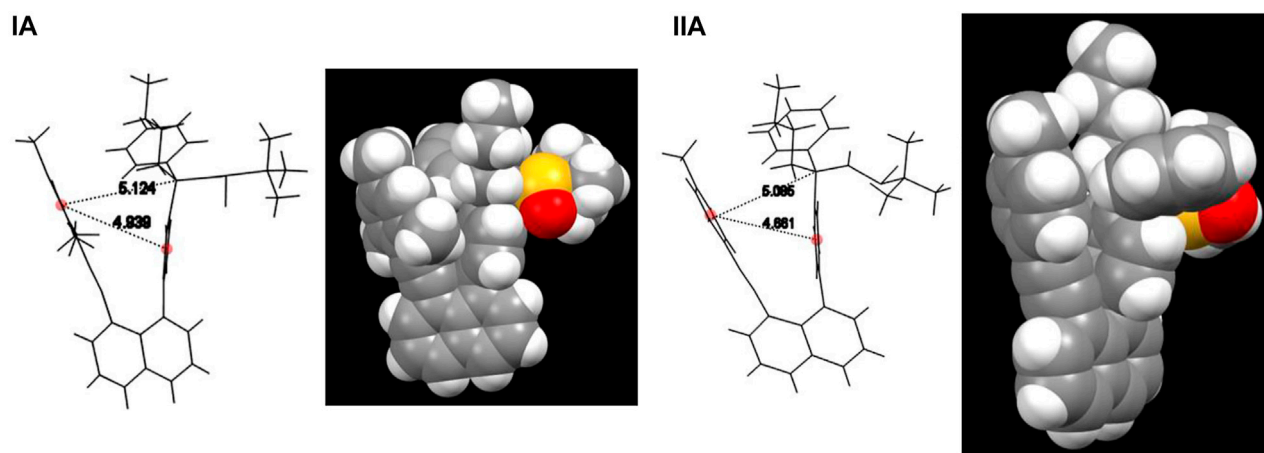


**FIGURE 6**  
Models and distances of orientational isomers (IA) and (IIA).

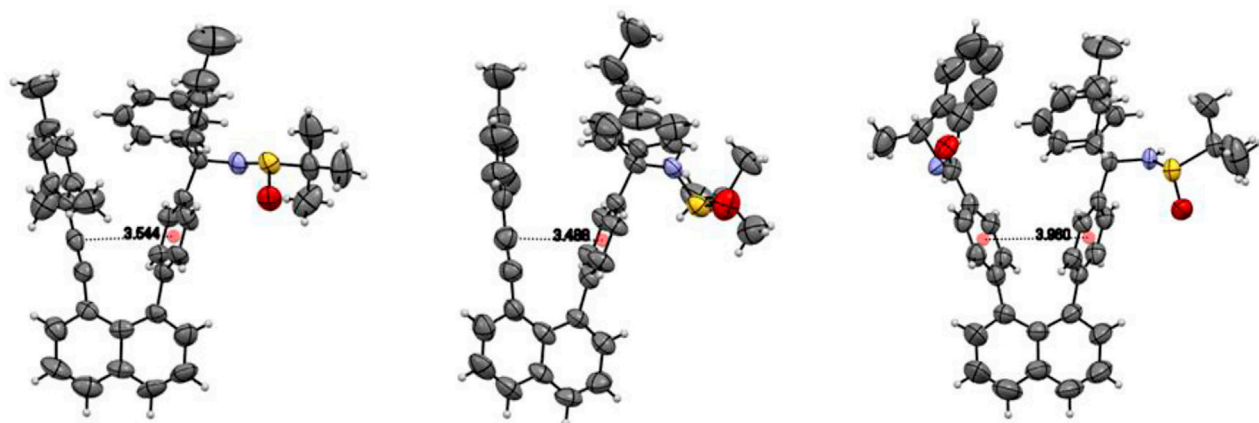


**FIGURE 7**  
Comparison of distances of anchor centers.

crystalline solids. X-ray diffraction analysis of single crystals has proven the aforementioned hypothesis, *i.e.*, removing the two methyl groups on mesityl ring did shorten the distance of Ph-to-Ph (phenyl rings' center-to-center) from 4.939 Å to 4.661 Å, and  $sp^3$  chiral center to the left phenyl ring center from 5.124 Å to 5.095 Å, respectively (Figure 6). The shortened distance enabled the steric effect by tolyl blocker to be large enough leading to the formation of an atropisomer (IIA). In this atropisomer, the sulfinyl amino group is directed away from the *p*-tolyl plane of the left lever.

Next, we make efforts to replace 1-ethynyl-4-methylphenyl lever by using (*R*)-4-*N*-(1-phenylethyl)benzamide counterpart, which has been widely employed for multi-layer chirality investigation. Similarly, the stable atropisomer (IIIA) has been designed, synthesized, and analyzed by X-ray diffraction analysis. In this atropisomer, the sulfinyl amino group is also pushed away from the blocking group, (*R*)-4-*N*-(1-phenylethyl)amide on benzene ring of the left arm (Figure 5).

Lines were drawn and measured between two centers of phenyl rings on two arms/levers parallel to the line between 1,8-positions of

naphthalenyl anchor. The distance from two ring centers of (IIIA) was measured to be 3.960 Å. Similar lines of (IA) and (IIA) were drawn for the comparing purpose, which is also nearly parallel to that between 1,8-positions of naphthalenyl ring. These two lines were measured to be 3.544 Å and 3.488 Å, respectively. Interestingly, the two levers/arms in (IIIA) are more widely opened than those in (IA) and (IIA), but chiral carbon's free rotation cannot occur in (IIIA). This is due to the fact that (*R*)-4-*N*-(1-phenylethyl)amide is much bulkier than the methyl group, particularly, the phenyl ring on the amide group is directed toward the chiral center side. This phenyl ring could partially shield groups on  $sp^3$  carbon, making it even more difficult to rotate (Figure 7).

### 3 Orientational chirality model

The conformationally stable architectures containing axial C ( $sp^2$ )–C ( $sp^3$ ) stereogenic axis was achieved *via* asymmetric

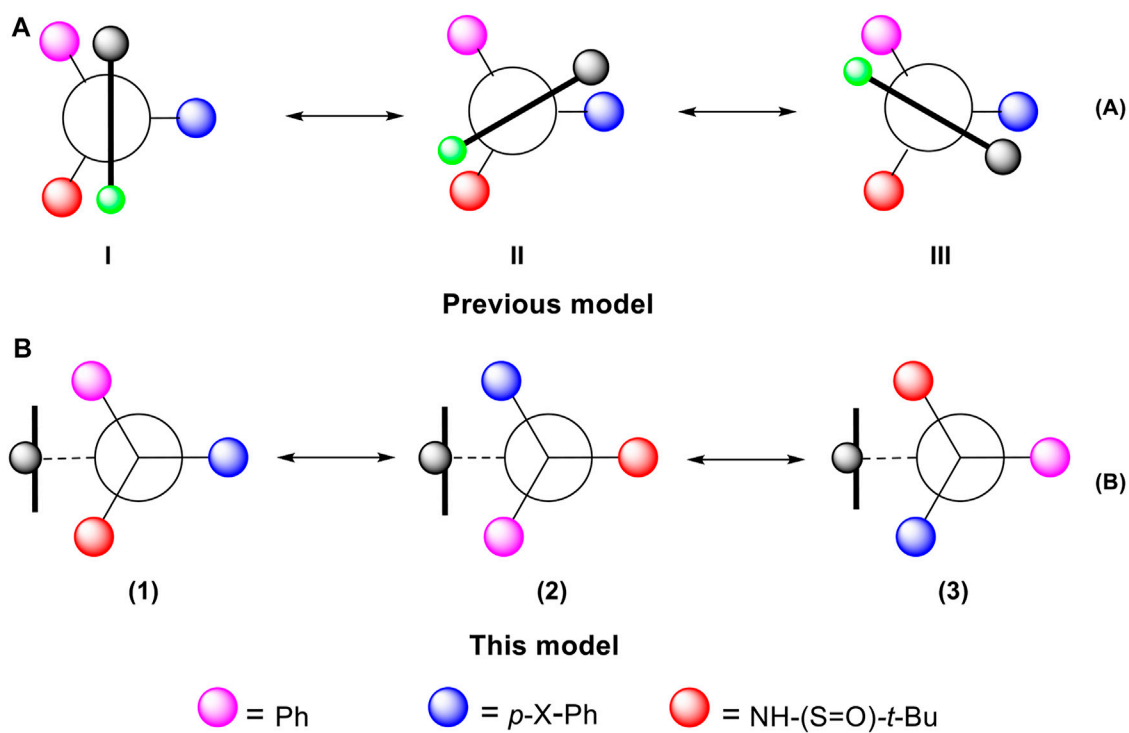


**FIGURE 8**  
Orientantion chirality models: previous I-III and present 1-3.

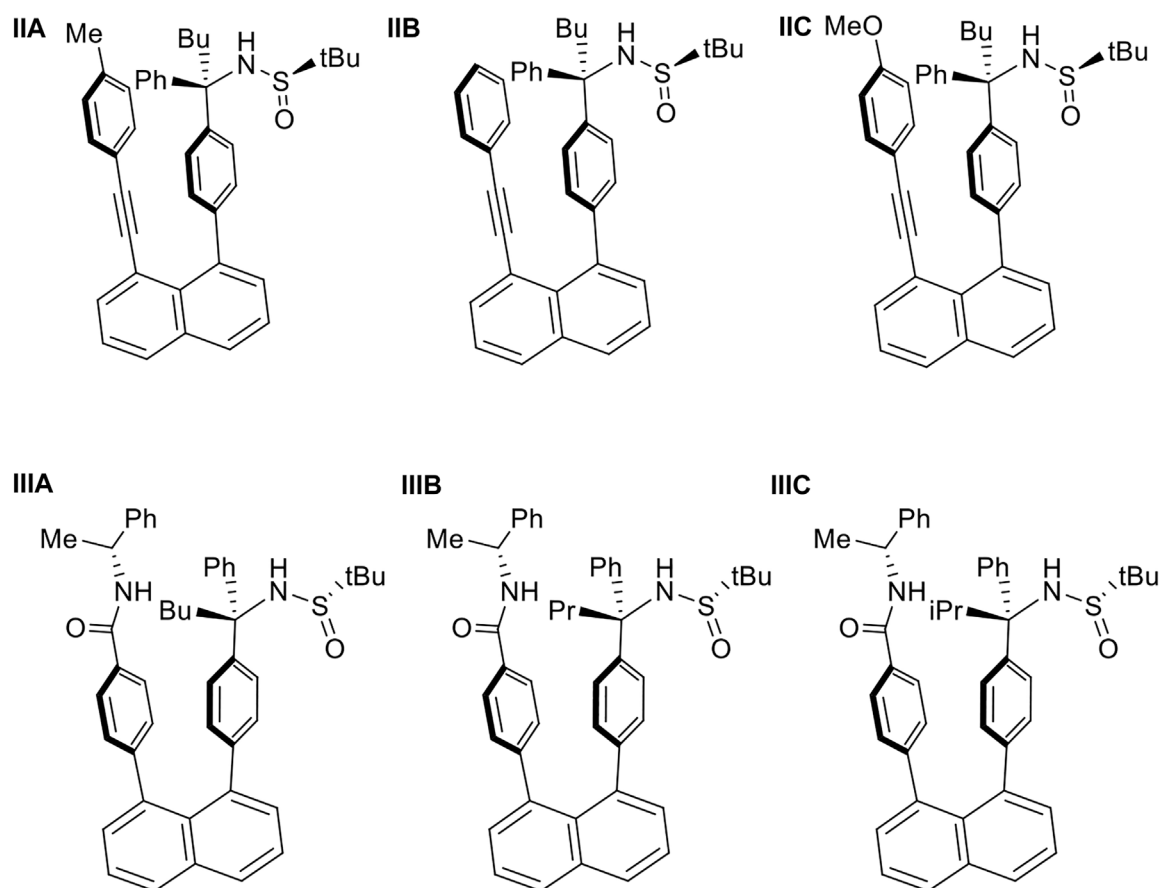
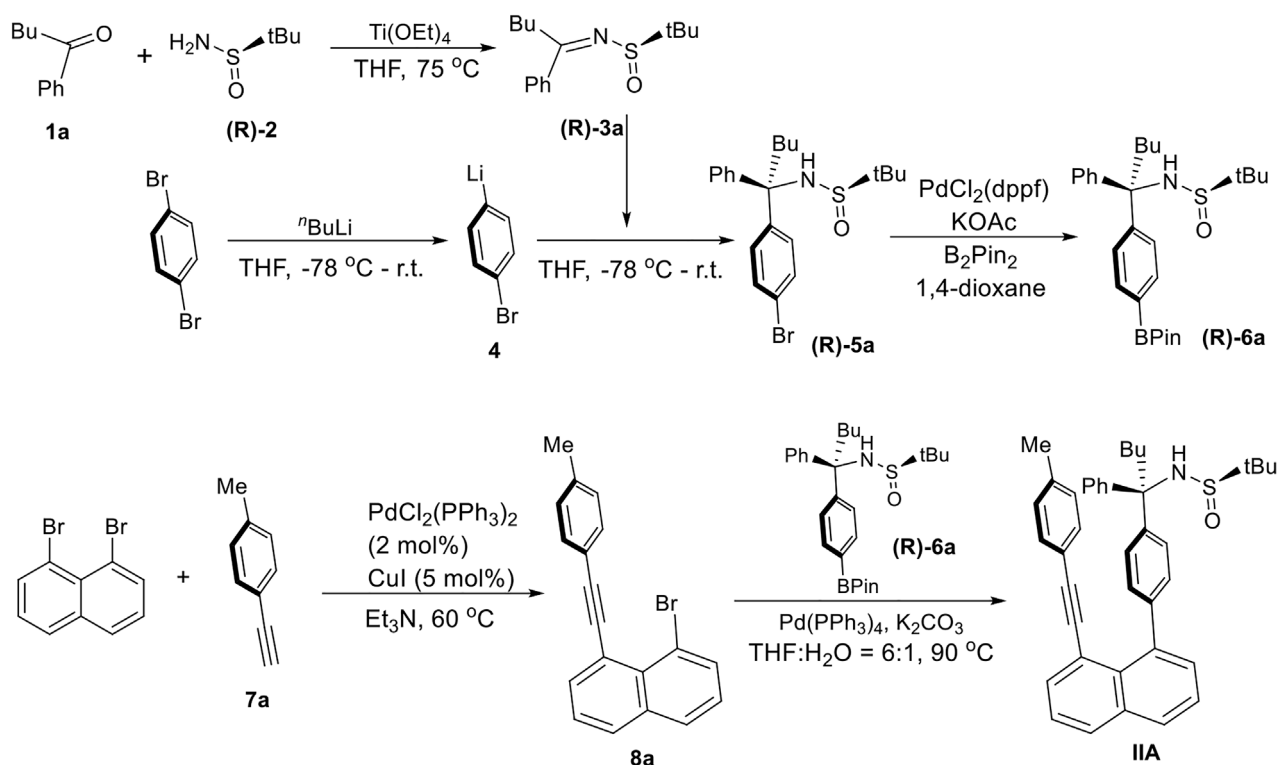
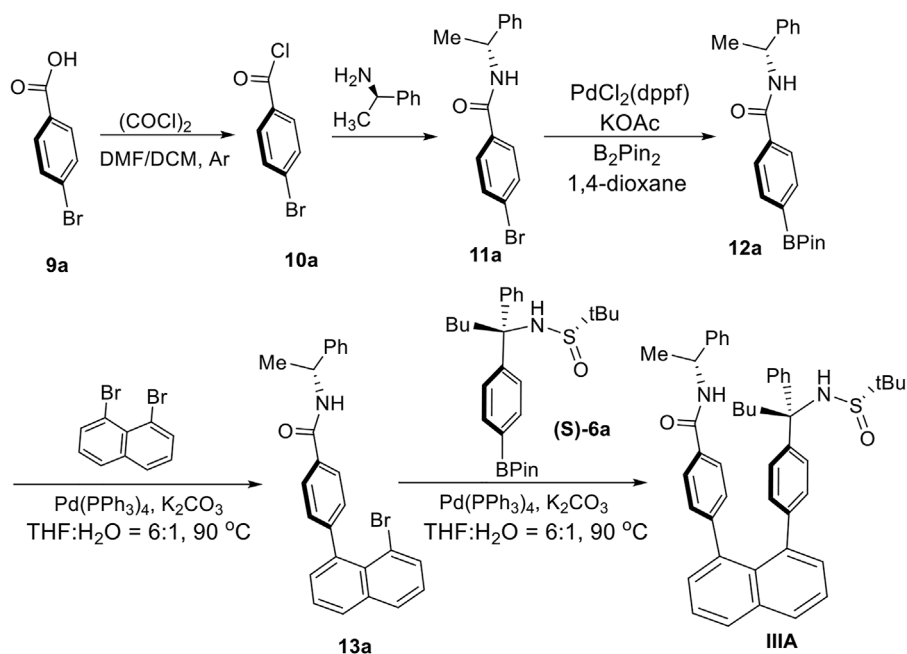


**FIGURE 9**  
Targets of orientational chirality: (IIA-IIC) and (IIIA-IIIC).



SCHEME 1

Asymmetric synthesis of orientational chirality with different anchors.



SCHEME 2

Asymmetric synthesis of orientational chirality with two aryl anchors.

catalytic [2 + 2 + 2] cyclotrimerization leading to forming one of six rotamers (Wu X. et al., 2021). The resulting axial C (sp<sup>2</sup>)–C (sp<sup>3</sup>) atropisomers have been proven by X-ray diffraction analysis to

follow Felkin-Ahn-type model, *i.e.*, one of the three groups on C (sp<sup>3</sup>) is arranged perpendicularly to C (sp<sup>2</sup>) plane (Figure 8A). There are six energy barriers existing during the rotating process.

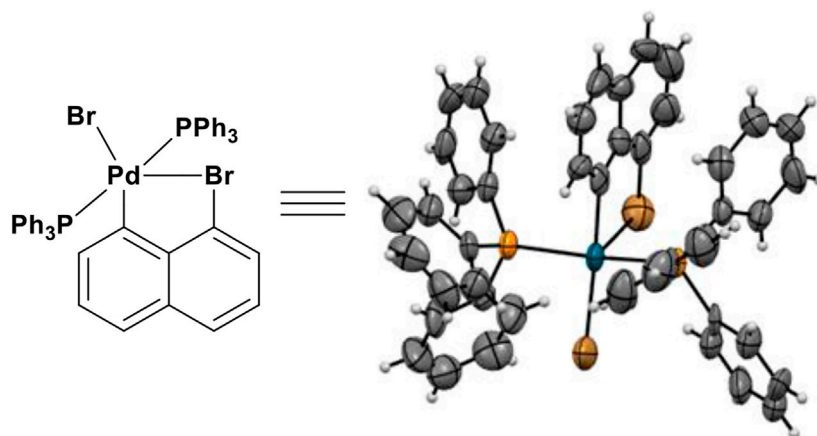


**FIGURE 10**  
X-ray structure of a new catalytic species.

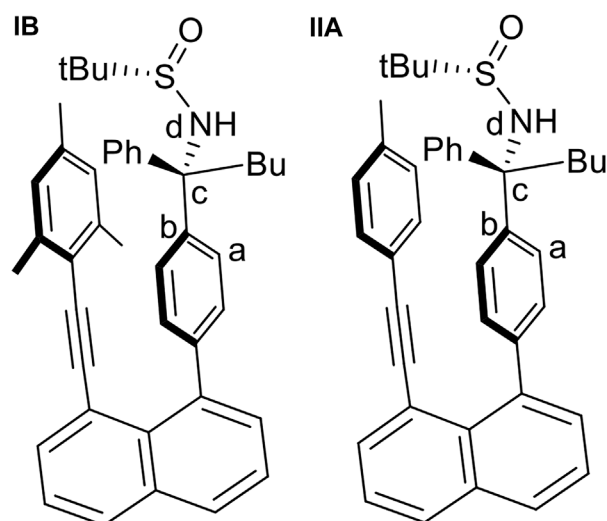


**FIGURE 11**  
The two initial structures, (IB) and (IIA), used for geometry optimization and the definition of the torsional angle  $\tau(a,b,c,d)$  used for the calculation of the rotational potential energy curves.

This multi-fold chirality is focused on the dialog relationship between two adjacent blocking  $C(sp^2)$  and chiral  $C(sp^3)$  scaffolds. However, in our chirality framework, there is no direct controlling force between chiral  $C(sp^3)$  stereogenicity and blocking  $C(sp^2)$  subunit. The remotely anchored aromatic ring is the only functional group that blocks rotation along  $C(sp^2)-C(sp^3)$  axis (Figure 8B). Therefore, the present orientational chirality is focused on the dialog relationship between  $C(sp^3)$  center and a remotely anchored functional group. Since there is only a single interaction (the heavy black line in the model, Figure 8B) existing in each of the three atropisomers, there are three energy barriers instead of six in the previous atropisomerism to be expected.

It should be pointed out that the nomenclature of previous molecular architectures follows the Cahn–Ingold–Prelog (CIP) rules (Tang et al.,

2022b; Jin et al., 2022). However, finding a nomenclature rule for the present chirality framework seems difficult. The relationship among three atropisomers (I, II and III in Figure 8A) would not belong to the classical enantiomeric or diastereomeric isomerism. For comparison, a representative example is given in Figure 8B for three atropisomers, (1)–(3). In these cases, there exist three pairs of enantiomers and six pairs of diastereomers, which is very rare in stereochemistry.

Consequently, the stereochemical measurements for the atropisomers, (1), (2) and (3), would not fit the classical *ee/er* or *de/dr* descriptions. Therefore, new descriptions would be temporally suggested for measuring outcomes of asymmetric synthesis and catalysis for assembling these three chiral atropisomers, e.g., orientatiomeric selectivity of orientatiomeric excess (*oe*) and orientatiomeric ratios (*or*) would be utilized, respectively.

## 4 Asymmetric synthesis

Asymmetric syntheses of atropisomers IIA are represented by assembling (*R*)-2-Methyl-*N*-((*R*)-1-phenyl-1-(4-(8-(*p*-tolylethynyl)naphthalen-1-yl)phenyl)pentyl)propane-2-sulfonamide ((*R,R*)-6a) (Scheme 1). The preparation of (*R*)-2-methyl-*N*-(1-phenylpentylidene)propane-2-sulfonamide ((*R*)-3a) was performed by dehydration of 1-phenylpentan-1-one (1a) with (*R*)-2-methylpropane-2-sulfonamide ((*R*)-2) by using  $Ti(OEt)_4$  in dry THF at 75°C to room temperature to give 93% yield (Zhang et al., 2019). 1,4-Dibromobenzene was converted into (4-bromophenyl)lithium precursor *via* the treatment with *n*-BuLi in THF at the same temperatures followed by reacting with (*R,Z*)-2-methyl-*N*-(1-phenylpentylidene)propane-2-sulfonamide ((*R*)-3a) to give (*R*)-*N*-((*R*)-1-(4-bromophenyl)-1-phenylpentyl)-2-methylpropane-2-sulfonamide ((*R*)-5a, 75% yield), which was then transformed into its BPin derivative ((*R*)-6a) by reacting with  $B_2Pin_2$  in the presence of  $PdCl_2(dppf)$  as the catalyst and KOAc as an additive in 1,4-dioxane to give a yield of 58%.

1,8-Dibromonaphthalene was subjected to Sonogashira coupling reaction (Sonogashira, 2002) with 1-ethynyl-4-methylbenzene in the presence of  $PdCl_2(PPh_3)_2$  and Cu(I) iodide as co-catalysts in  $Et_3N$  solution to afford 1-bromo-8-(*p*-tolylethynyl)naphthalene (8a) in 74% chemical yield. Suzuki–Miyaura cross-coupling (Miyaura and Suzuki,

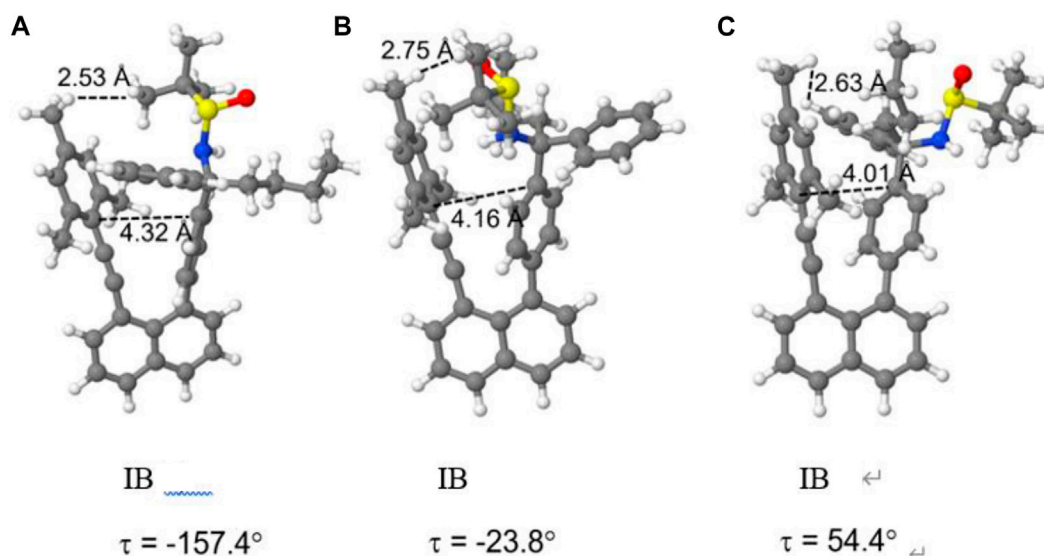


**FIGURE 12**  
Fully optimized structures of the three rotamers of structure IB (A–C).

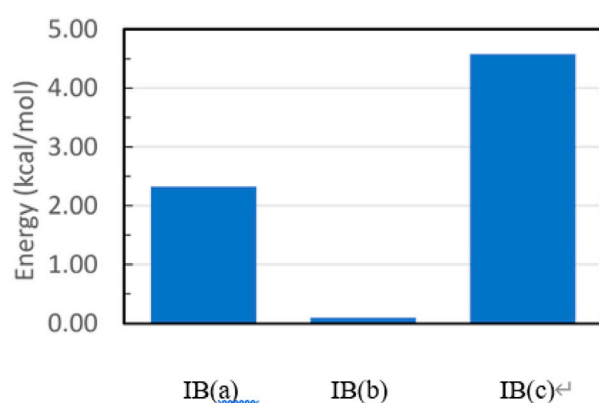


**FIGURE 13**  
Relative energies of the three fully optimized geometries for Structure (IB).

1995) of 1-bromo-8-(*p*-tolylethynyl)naphthalene (**8a**) with (*R*)-2-methyl-*N*-((*R*)-1-phenyl-1-(4-(4,4,5,5-tetramethyl-1,3,2-dioxaborolan-2-yl)phenyl)pentyl)propane-2-sulfinamide ((*R*)-**6a**) resulted in the final product, (*R*)-2-methyl-*N*-((*R*)-1-phenyl-1-(4-(8-(*p*-tolylethynyl)naphthalen-1-yl)phenyl)pentyl)propane-2-sulfinamide (**IIA**) in a yield of 67%.

Atropisomers **IIIA** was assembled from three building blocks (Scheme 2): (*R*)-*N*-(1-phenylethyl)-4-(4,4,5,5-tetramethyl-1,3,2-dioxaborolan-2-yl)benzamide (**12a**), 1,8-dibromonaphthalene, and (*S*)-2-methyl-*N*-((*S*)-1-phenyl-1-(4-(4,4,5,5-tetramethyl-1,3,2-dioxaborolan-2-yl)phenyl)pentyl)propane-2-sulfinamide ((*S*)-**6a**). The synthesis of (*S*)-2-methyl-*N*-((*S*)-1-phenyl-1-(4-(4,4,5,5-tetramethyl-1,3,2-dioxaborolan-2-yl)phenyl)pentyl)propane-2-sulfinamide ((*S*)-**6a**) is similar to that described above for **IIA**. (*R*)-4-(8-Bromonaphthalen-1-yl)-*N*-(1-phenylethyl)benzamide (**13a**) was obtained by reacting (*R*)-*N*-(1-

phenylethyl)-4-(4,4,5,5-tetramethyl-1,3,2-dioxaborolan-2-yl)benzamide (**12a**) with 1,8-dibromonaphthalene under the Suzuki-Miyaura cross-coupling condition (Miyaura and Suzuki, 1995). The precursor (**12a**) was generated by treating (*R*)-4-bromo-*N*-(1-phenylethyl)benzamide with  $B_2Pin_2$  in the presence of  $PdCl_2(dppf)$  as the catalyst and KOAc as an additive in 1,4-dioxane to give a yield of 54%.

According to the above procedures, the derivatives of **IIA** and **IIIA** were synthesized as the two pairs of **IIB/IIC** and **IIIB/IIIC**, respectively (Figure 9). Not only *p*-MeO substituent on benzene ring is anticipated to block the rotation along the C (chiral  $sp^3$ )-C ( $sp^3$ ) bond as *p*-Me group does, but also the none-substituent benzene group (*p*-H) still can perform blocking as revealed by spectra analysis. For cases **IIIB** and **IIIC** in which *n*-butyl group in **IIIA** was replaced by propyl and isopropyl groups, respectively, showed stable rotamers as expected.

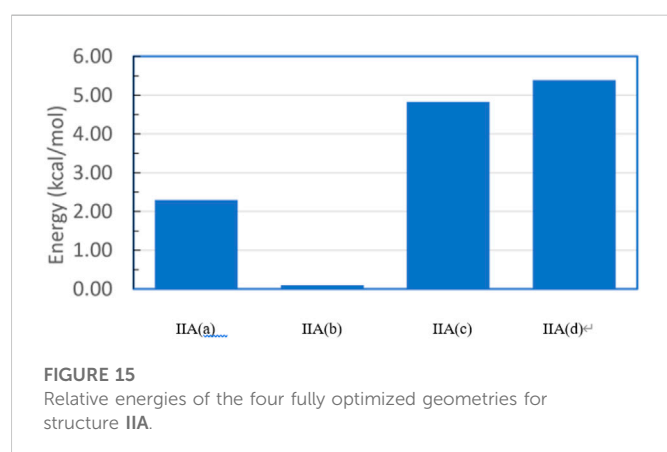
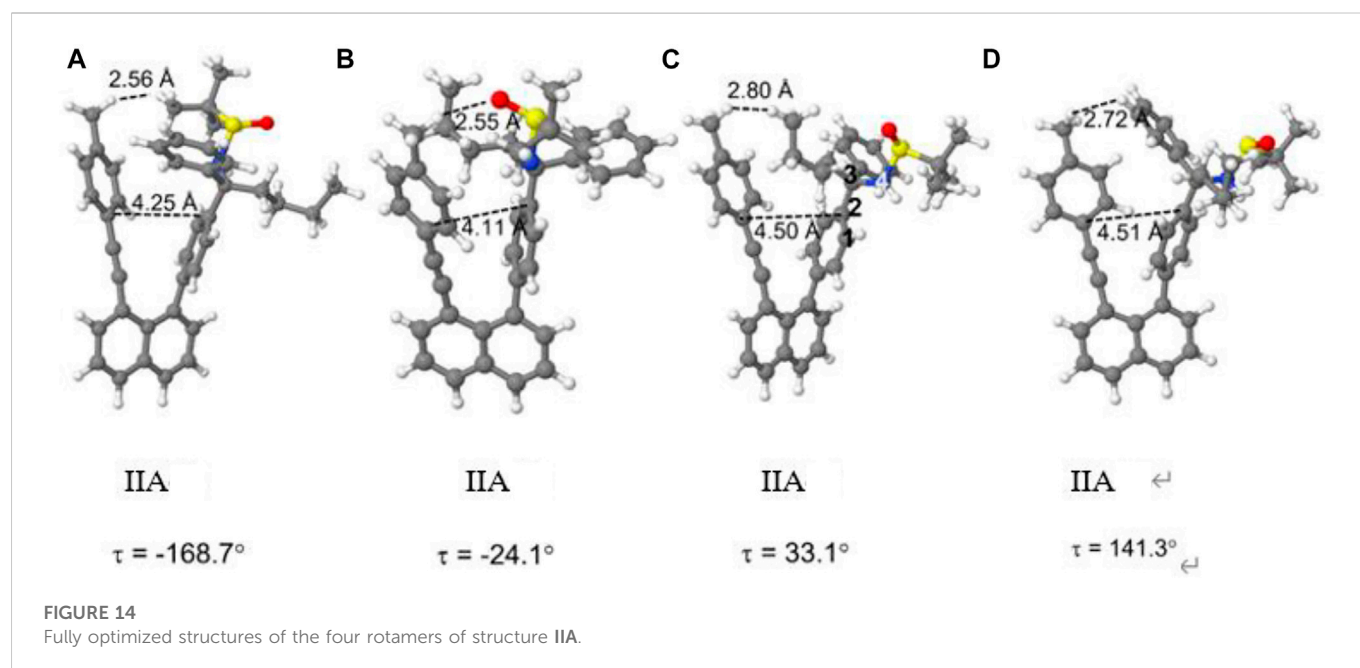
During the Suzuki-Miyaura cross-coupling involving 1,8-dibromonaphthalene, a key catalytic species was successfully isolated. Its x-ray diffraction analysis revealed that this metal-ligand species displays a five-membered ring system consisting of C ( $sp^2$ )-Br-Pd-C ( $sp^2$ ) bonds (Figure 10), which has not been documented in the literature to the best of our knowledge. A CSD search revealed that there has been only one similar catalytic species of five-membered ring complex formed during the catalytic synthesis of tetrahydrobenzo [b] azepines (THBAs), but it is based on C ( $sp^3$ )-Br-Pd-C ( $sp^3$ ) bonds (Liu X. et al., 2021). We believe this new catalytic complex would find applications in future, especially, when two phosphine ligands are replaced by their chiral counterparts (Figure 10).

## 5 Computational Studies

### 5.1 Computational details

The quantum chemical calculations have been performed at density functional theory (DFT) level using the Becke, 3-





parameter, Lee–Yang–Par (B3-LYP functional including the D3 dispersion correction (Becke, 1993; Grimme et al., 2010) and the 6-31G\* basis set (Hariharan and Pople, 1973). Calculations were performed for a solvent consisting of a 1:1 mixture of tetrahydrofuran and water with an average dielectric constant  $\epsilon$  of 42.89. The crystal structure of Structure IB (Figure 11) was used as starting geometry for a full geometry optimization. Starting from this geometry, the torsional angle  $\tau$  defined in Figure 11 was increased in steps of 20° to obtain an energy profile on the different rotated structures. Keeping  $\tau$  fixed for each value, the remaining geometry was optimized, and potential energy curves (PECs) were computed. Using the geometries of the minima in the PEC as starting points, full geometry optimizations were performed. The PEC for structure IIA (Figure 11) in which the mesityl group was replaced by the p-methylphenyl group (see also structure 9aa, Figure 5) has been obtained in an analogous way. All calculations were carried out using the Gaussian 09 program suite (Gaussian 09 Citation, 2022).

## 5.2 Theoretical results

The PEC (Supplementary Figures S1, S2 of the Supplementary Material S1) for the torsion around the bc bond (Figure 11) for structure IB shows an energy profile with several minima. The most stable ones are found for  $\tau$  values of -25° and -165°. Another one is located at 55° with a relative energy of ~3.5 kcal/mol. The region with positive  $\tau$  values shows a broad peak with a height of around 6–8 kcal/mol and a shallow minimum at 55°. The structures corresponding to these three minima are displayed in Supplementary Figure S2. The analogous PEC for structure II (Supplementary Figure S3) looks similar with the difference that the broad region of positive torsional values has only shallower formation of two minima.

For structure IB, the three geometries obtained by restricted optimization were used as starting points for complete optimization without any restriction in the torsional angle  $\tau$ . This optimization led to the final three rotamer structures displayed in Figure 12. The corresponding energetic stabilities are given in Figure 13. The most stable structure is IB(b) where the butyl and sulfamide groups interact with the opposite benzene ring and the phenyl ring is turned to the outside. The next stable structure (at relative energy of 2.3 kcal/mol) is IB(a) showing the interaction of the t-butyl group and the phenyl ring in contact with the opposite benzene ring. Finally, the least stable structure at 4.6 kcal/mol is the one with the butyl and phenyl ring oriented toward the opposite benzene ring.

The PEC for structure IIA shows a similar, but slightly more extended manifold of energetic minima and structures (Supplementary Figures S3, S4). Full geometry optimization of these structures shows a similar, but slightly more extended manifold of energetic minima (Figure 14). Structures IIA (a–c) resemble closely the three structures IB cases. Structure IIA(b) is the most stable structure (Figure 15), followed by structures IIA(a) and IIA(c). The fourth structure IIA(d), is slightly higher in energy than IIA(c).

For both structures IB and IIA, the most stable structure is of type (b) where the polar S=O bond is directly oriented toward the opposite phenyl ring, interacting with its aromatic  $\pi$  system. In both cases, the

second stable structure involves the sulfinyl-amino group as well; it is, however, not directly oriented toward the opposing phenyl ring. In the least stable structures, the sulfinyl-amino group is oriented completely away from this phenyl ring. Selected non-bonded distances are displayed in Figures 12, 14 as well. Most interesting is the comparison of the distance of the mesityl group to the opposing ring in comparison to case where two of the methyl groups had been removed. For the most stable structures (a) and (b), the distance between the two rings, as measured by the C...C distances shown in Figures 12, 14, is larger for the mesitylene substitution (4.32 Å vs. 4.25 Å for structures (a), and 4.16 Å vs. 4.11 Å for structures (b) indicating the repulsive effect of the bulkier methyl groups pushing the two aromatic rings a bit farther away. This structural opening up due to the methyl groups agrees well with the widening between the two levers/arms as shown in Figure 6 for the X-ray structures.

## 6 Summary

We have discovered the orientational chirality showing that multiple orientations can be controlled by remotely anchored and through-space functional blockers. The multi-step synthesis of several orientational chiral targets were achieved by conducting asymmetric nucleophilic addition, Suzuki-Miyaura cross-coupling and Sonogashira coupling reactions. Single orientational atropisomers were obtained in modest to good yields as crystalline solids. A novel catalytic complex was isolated during performing Suzuki-Miyaura cross-coupling, and analyzed by X-ray diffraction analysis displaying a five-membered ring consisting of C (sp<sup>2</sup>)-Br-Pd-C (sp<sup>2</sup>) bonds. The present orientational chirality is focused on the dialog relationship between C (sp<sup>3</sup>) center and a remotely anchored functional group. X-ray structures of orientational chiral targets leads to a conceptually new stereochemistry model which is differentiated from the previous Felkin-Ahn-type of models containing adjacent C (sp<sup>2</sup>)-C (sp<sup>3</sup>) σ bonds. In this new model, there are three main energy barriers during orientational rotation instead of six barriers in previous multi-fold systems. DFT computational study was carried out, and present the relative stability with rotating of individual orientationomers. This discovery would be anticipated to result in a new stereochemistry area, and to have a broad impact on chemical, biomedical and material sciences in future.

## References

- Bao, J., Liu, N., Tian, H., Wang, Q., Cui, T., Jiang, W., et al. (2020). Chirality enhancement using Fabry-Pérot-like cavity. *Res. (Wash D C)* 2020, 7873581–7873589. doi:10.34133/2020/7873581
- Becke, A. D. (1993). Density-functional thermochemistry. III. The role of exact exchange. *J. Chem. Phys.* 98, 5648–5652. doi:10.1063/1.464913
- Bertuzzi, G., Corti, V., Izzo, J. A., Ričko, S., Jessen, N. I., and Jørgensen, K. A. (2022). Organocatalytic enantioselective construction of conformationally stable C(sp<sup>2</sup>)-C(sp<sup>3</sup>) atropisomers. *J. Am. Chem. Soc.* 144, 1056–1065. doi:10.1021/jacs.1c12619
- Bryliakov, K. P. (2020). Chemical mechanisms of prebiotic chirality amplification. *Res. (Wash D C)* 2020, 1–8. doi:10.34133/2020/5689246
- Chen, X.-Y., Gao, Z.-H., and Ye, S. (2020). Bifunctional N-heterocyclic carbenes derived from l-pyrogutamic acid and their applications in

## Data availability statement

The original contributions presented in the study are included in the article/Supplementary Material, further inquiries can be directed to the corresponding authors.

## Author contributions

GL directed research and wrote the paper. SJ, TX, YT, J-YW, YW, JP, SZ, QY, and AR, J. McDonald performed and repeated all synthetic experiments and data analysis. AA and HL performed computations and wrote the relevant sections.

## Funding

Robert A. Welch Foundation (D-1361-20210327, United States), the National Natural Science Foundation of China (Nos 22071102 and 91956110).

## Conflict of interest

The authors declare that the research was conducted in the absence of any commercial or financial relationships that could be construed as a potential conflict of interest.

## Publisher's note

All claims expressed in this article are solely those of the authors and do not necessarily represent those of their affiliated organizations, or those of the publisher, the editors and the reviewers. Any product that may be evaluated in this article, or claim that may be made by its manufacturer, is not guaranteed or endorsed by the publisher.

## Supplementary material

The Supplementary Material for this article can be found online at: <https://www.frontiersin.org/articles/10.3389/fchem.2022.1110240/full#supplementary-material>

enantioselective organocatalysis. *Acc. Chem. Res.* 53, 690–702. doi:10.1021/acs.accounts.9b00635

Cui, X., Xu, X., Lu, H., Zhu, S., Wojtas, L., and Zhang, X. P. (2011). Enantioselective cyclopropanation of alkynes with acceptor/acceptor-substituted diazo reagents via Co(II)-based metalloradical catalysis. *J. Am. Chem. Soc.* 133, 3304–3307. doi:10.1021/ja111334j

Dai, L.-X., Tu, T., You, S.-L., Deng, W.-P., and Hou, X.-L. (2003). Asymmetric catalysis with chiral ferrocene ligands. *Acc. Chem. Res.* 36, 659–667. doi:10.1021/ar020153m

Dunitz, J. D. (2001). Pauling's left-handed α-helix. *Angew. Chem. Int. Ed. Engl.* 40, 4167–4173. doi:10.1002/1521-3773(20011119)40:22<4167::aid-anie4167>3.0.co;2-q

Feng, H.-T., Liu, C., Li, Q., Zhang, H., Lam, J. W. Y., and Tang, B. Z. (2019). Structure, assembly, and function of (latent)-chiral AIEgens. *ACS Mater. Lett.* 1, 192–202. doi:10.1021/acsmaterialslett.9b00116

- Gaussian 09 Citation (2022). *Gaussian 09 citation*. Edu.tw. Available at: [http://wild.life.nctu.edu.tw/~jsyu/compchem/g09/g09ur/m\\_citation.htm](http://wild.life.nctu.edu.tw/~jsyu/compchem/g09/g09ur/m_citation.htm) (Accessed November 25, 2022).
- Ge, Y., Qin, C., Bai, L., Hao, J., Liu, J., and Luan, X. (2020). A dearomatization/debromination strategy for the [4+1] spiroannulation of bromophenols with  $\alpha$ ,  $\beta$ -unsaturated imines. *Angew. Chem. Int. Ed. Engl.* 59, 18985–18989. doi:10.1002/anie.202008130
- Grimme, S., Antony, J., Ehrlich, S., and Krieg, H. (2010). A consistent and accurate *ab initio* parametrization of density functional dispersion correction (DFT-D) for the 94 elements H–Pu. *J. Chem. Phys.* 132, 154104. doi:10.1063/1.3382344
- Guo, J., Wang, H., Xing, S., Hong, X., and Lu, Z. (2019). Cobalt-catalyzed asymmetric synthesis of gem-bis(silyl)alkanes by double hydrosilylation of aliphatic terminal alkynes. *Chem* 5, 881–895. doi:10.1016/j.chempr.2019.02.001
- Hariharan, P. C., and Pople, J. A. (1973). The influence of polarization functions on molecular orbital hydrogenation energies. *Theor. Chim. Acta* 28, 213–222. doi:10.1007/bf00533485
- Hruby, V. J., Li, G., Haskell-Luevano, C., and Shenderovich, M. (1997). Design of peptides, proteins, and peptidomimetics in chi space. *Pept. Sci.* 43, 219–266. doi:10.1002/(sici)1097-0282(1997)43:3<219:aid-bip3>3.0.co;2-y
- Huang, G., Wen, R., Wang, Z., Li, B. S., and Tang, B. Z. (2018). Novel chiral aggregation induced emission molecules: self-assembly, circularly polarized luminescence and copper(ii) ion detection. *Mater. Chem. Front.* 2, 1884–1892. doi:10.1039/c8qm00294k
- Huang, S., Wen, H., Tian, Y., Wang, P., Qin, W., and Yan, H. (2021). Organocatalytic enantioselective construction of chiral azepine skeleton bearing multiple-stereogenic elements. *Angew. Chem. Int. Ed. Engl.* 60, 21486–21493. doi:10.1002/anie.202108040
- Jin, S., Wang, J.-Y., Tang, Y., Rouh, H., Zhang, S., Xu, T., et al. (2022). Central-to-folding chirality control: Asymmetric synthesis of multilayer 3D targets with electron-deficient bridges. *Front. Chem.* 10, 860398. doi:10.3389/fchem.2022.860398
- Li, J., Hou, C., Huang, C., Xu, S., Peng, X., Qi, Q., et al. (2020). Boosting circularly polarized luminescence of organic conjugated systems via twisted intramolecular charge transfer. *Res. (Wash D C)* 2020, 1–10. doi:10.34133/2020/3839160
- Liao, G., Yao, Q.-J., Zhang, Z.-Z., Wu, Y.-J., Huang, D.-Y., and Shi, B.-F. (2018). Scalable, stereocontrolled formal syntheses of (+)-Isoschizandrin and (+)-Steganone: Development and applications of palladium(II)-Catalyzed atroposelective C–H alkynylation. *Angew. Chem. Wein. Bergstr. Ger.* 130, 3723–3727. doi:10.1002/ange.201713106
- Liu, D., Li, B., Chen, J., Gridnev, I. D., Yan, D., and Zhang, W. (2020). Ni-catalyzed asymmetric hydrogenation of N-aryl imino esters for the efficient synthesis of chiral  $\alpha$ -aryl glycines. *Nat. Commun.* 11, 5935. doi:10.1038/s41467-020-19807-5
- Liu, Y., Wu, G., Yang, Z., Rouh, H., Katakam, N., Ahmed, S., et al. (2020b). Multi-layer 3D chirality: new synthesis, AIE and computational studies. *Sci. China Chem.* 63, 692–698. doi:10.1007/s11426-019-9711-x
- Liu, T.-T., Yan, Z.-P., Hu, J.-J., Yuan, L., Luo, X.-F., Tu, Z.-L., et al. (2021). Chiral thermally activated delayed fluorescence emitters-based efficient circularly polarized organic light-emitting diodes featuring low efficiency roll-off. *ACS Appl. Mater. Interfaces* 13, 56413–56419. doi:10.1021/acsami.1c16223
- Liu, X., Wang, J., and Dong, G. (2021b). Modular entry to functionalized tetrahydrobenzo[b]azepines via the palladium/norbornene cooperative catalysis enabled by a C7-modified norbornene. *J. Am. Chem. Soc.* 143, 9991–10004. doi:10.1021/jacs.1c04575
- Lorion, M. M., Maindan, K., Kapdi, A. R., and Ackermann, L. (2017). Heterometallic catalysis for sustainable organic syntheses. *Chem. Soc. Rev.* 46, 7399–7420. doi:10.1039/c6cs00787b
- Lung, F.-D. T., Meyer, J.-P., Li, G., Lou, B.-S., Stropova, D., Davis, P., et al. (1995). Highly. kappa. receptor-selective dynorphin A analogs with modifications in position 3 of dynorphin A(1-11)-NH<sub>2</sub>. *J. Med. Chem.* 38, 585–586. doi:10.1021/jm00004a002
- Ma, C., Sheng, F.-T., Wang, H.-Q., Deng, S., Zhang, Y.-C., Jiao, Y., et al. (2020). Atroposelective access to oxindole-based axially chiral styrenes via the strategy of catalytic kinetic resolution. *J. Am. Chem. Soc.* 142, 15686–15696. doi:10.1021/jacs.0c00208
- Markwell, J. (2008). *Molecules and medicine* by E.J. Corey, B. czakó, and L. Kürti. *Biochem. Mol. Biol. Educ.* 36, 245–246. doi:10.1002/bmb.20179
- Miyaura, N., and Suzuki, A. (1995). Palladium-catalyzed cross-coupling reactions of organoboron compounds. *Chem. Rev.* 95, 2457–2483. doi:10.1021/cr00039a007
- Ojima, I. (2010). in *Catalytic asymmetric synthesis*. Editor I. Ojima 3rd ed. (Hoboken, NJ: Wiley-Blackwell).
- Oki, O., Kulkarni, C., Yamagishi, H., Meskers, S. C. J., Lin, Z.-H., Huang, J.-S., et al. (2021). Robust angular anisotropy of circularly polarized luminescence from a single twisted-bipolar polymeric microsphere. *J. Am. Chem. Soc.* 143, 8772–8779. doi:10.1021/jacs.1c03185
- Pace, C. N., and Scholtz, J. M. (1998). A helix propensity scale based on experimental studies of peptides and proteins. *Biophys. J.* 75, 422–427. doi:10.1016/s0006-3495(98)77529-0
- Rouh, H., Tang, Y., Xu, T., Yuan, Q., Zhang, S., Wang, J.-Y., et al. (2022). Aggregation-induced synthesis (AIS): Asymmetric synthesis via chiral aggregates. *Res. (Wash D C)* 2022, 1–9. doi:10.34133/2022/9865108
- Shen, Y., and Chen, C.-F. (2012). Helicenes: synthesis and applications. *Chem. Rev.* 112, 1463–1535. doi:10.1021/cr200087r
- Shirakawa, S., Liu, S., and Kaneko, S. (2016). Organocatalyzed asymmetric synthesis of axially, planar, and helical chiral compounds. *Chem. Asian J.* 11, 330–341. doi:10.1002/asia.201500951
- Song, J., Chen, D.-F., and Gong, L.-Z. (2017). Recent progress in organocatalytic asymmetric total syntheses of complex indole alkaloids. *Natl. Sci. Rev.* 4, 381–396. doi:10.1093/nsr/nwx028
- Sonogashira, K. (2002). Development of Pd–Cu catalyzed cross-coupling of terminal acetylenes with sp<sup>2</sup>-carbon halides. *J. Organomet. Chem.* 653, 46–49. doi:10.1016/s0022-328x(02)01158-0
- Tang, Y., Jin, S., Zhang, S., Wu, G.-Z., Wang, J.-Y., Xu, T., et al. (2022). Multilayer 3D chiral folding polymers and their asymmetric catalytic assembly. *Res. (Wash D C)* 2022, 1–8. doi:10.34133/2022/9847949
- Tang, Y., Wu, G., Jin, S., Liu, Y., Ma, L., Zhang, S., et al. (2022b). From center-to-multilayer chirality: Asymmetric synthesis of multilayer targets with electron-rich bridges. *J. Org. Chem.* 87, 5976–5986. doi:10.1021/acs.joc.2c00234
- Taniguchi, K., Maeda, R., Ando, T., Okumura, T., Nakazawa, N., Hatori, R., et al. (2011). Chirality in planar cell shape contributes to left-right asymmetric epithelial morphogenesis. *Science* 333, 339–341. doi:10.1126/science.1200940
- Wagner, I., and Musso, H. (1983). New naturally occurring amino acids. *Angew. Chem. Int. Ed. Engl.* 22, 816–828. doi:10.1002/anie.198308161
- Wang, Y.-B., and Tan, B. (2018). Construction of axially chiral compounds via asymmetric organocatalysis. *Acc. Chem. Res.* 51, 534–547. doi:10.1021/acs.accounts.7b00602
- Wang, A. H., Fujii, S., van Boom, J. H., and Rich, A. (1983). Right-handed and left-handed double-helical DNA: structural studies. *Cold Spring Harb. Symp. Quant. Biol.* 47, 33–44. doi:10.1101/sqb.1983.047.01.006
- Wang, Q., Zhang, W.-W., Zheng, C., Gu, Q., and You, S.-L. (2021). Enantioselective synthesis of azoniahelices by Rh-catalyzed C–H annulation with alkynes. *J. Am. Chem. Soc.* 143, 114–120. doi:10.1021/jacs.0c11735
- Wang, J.-Y., Tang, Y., Wu, G.-Z., Zhang, S., Rouh, H., Jin, S., et al. (2022). Asymmetric catalytic assembly of triple-columned and multilayered chiral folding polymers showing aggregation-induced emission (AIE). *Chemistry* 28, e202104102. doi:10.1002/chem.202104102
- Williams, R. M., and Perlmutter, P. (2013). *Synthesis of optically active alpha-amino acids*. London, England: Elsevier Science.
- Wu, G., Liu, Y., Yang, Z., Katakam, N., Rouh, H., Ahmed, S., et al. (2019). Multilayer 3D chirality and its synthetic assembly. *Res. (Wash D C)* 2019, 1–11. doi:10.34133/2019/6717104
- Wu, G., Liu, Y., Yang, Z., Jiang, T., Katakam, N., Rouh, H., et al. (2020). Enantioselective assembly of multi-layer 3D chirality. *Natl. Sci. Rev.* 7, 588–599. doi:10.1093/nsr/nwz203
- Wu, G., Liu, Y., Rouh, H., Ma, L., Tang, Y., Zhang, S., et al. (2021). Asymmetric catalytic approach to multilayer 3D chirality. *Chemistry* 27, 8013–8020. doi:10.1002/chem.202100700
- Wu, X., Witzig, R. M., Beaud, R., Fischer, C., Häussinger, D., and Sparr, C. (2021b). Catalytic control over sixfold stereogenicity. *Nat. Catal.* 4, 457–462. doi:10.1038/s41929-021-00615-z
- Zeng, W., and Chemler, S. R. (2007). Copper(II)-catalyzed enantioselective intramolecular carboamination of alkenes. *J. Am. Chem. Soc.* 129, 12948–12949. doi:10.1021/ja0762240
- Zhang, J., and Kürti, L. (2021). Multi-layer 3D chirality: Its enantioselective synthesis and aggregation-induced emission. *Natl. Sci. Rev.* 8, nwaa205. doi:10.1093/nsr/nwaa205
- Zhang, M., Lu, T., Zhao, Y., Xie, G., and Miao, Z. (2019). K<sub>3</sub>PO<sub>4</sub>-promoted domino reactions: Diastereoselective synthesis of trans-2, 3-dihydrobenzofurans from silyl N-tert-butanedisulfonyl imines and sulfur ylides. *RSC Adv.* 9, 11978–11985. doi:10.1039/c9ra00309f
- Zhang, Y.-C., Jiang, F., and Shi, F. (2020). Organocatalytic asymmetric synthesis of indole-based chiral heterocycles: Strategies, reactions, and outreach. *Acc. Chem. Res.* 53, 425–446. doi:10.1021/acs.accounts.9b00549
- Zhao, T., Han, J., Duan, P., and Liu, M. (2020). New perspectives to trigger and modulate circularly polarized luminescence of complex and aggregated systems: Energy transfer, photon upconversion, charge transfer, and organic radical. *Acc. Chem. Res.* 53, 1279–1292. doi:10.1021/acs.accounts.0c00112
- Zhao, P., Li, Z., He, J., Liu, X., and Feng, X. (2021). Asymmetric catalytic 1, 3-dipolar cycloaddition of  $\alpha$ -diazesters for synthesis of 1-pyrazoline-based spirochromanones and beyond. *Sci. China Chem.* 64, 1355–1360. doi:10.1007/s11426-021-1027-7
- Zhou, Q. L. (2011). in *Privileged chiral ligands and catalysts*. Editor Q.-L. Zhou (Weinheim, Germany: Wiley-VCH Verlag). Available at: [https://books.google.at/books?id=PhkVage\\_dRAC](https://books.google.at/books?id=PhkVage_dRAC).





## OPEN ACCESS

## EDITED BY

Fushuang Li,  
Massachusetts Institute of Technology,  
United States

## REVIEWED BY

Zhigang She,  
Sun Yat-sen University, China  
Guo-Dong Chen,  
Jinan University, China

## \*CORRESPONDENCE

Shuyi Si,  
✉ sisymb@hotmail.com  
Minghua Chen,  
✉ chenminghua@imb.pumc.edu.cn

<sup>†</sup>These authors have contributed equally to  
this work

## SPECIALTY SECTION

This article was submitted to  
Organic Chemistry,  
a section of the journal  
Frontiers in Chemistry

RECEIVED 24 November 2022

ACCEPTED 28 December 2022

PUBLISHED 12 January 2023

## CITATION

Chang S, Yan B, Chen Y, Zhao W, Gao R,  
Li Y, Yu L, Xie Y, Si S and Chen M (2023),  
Cytotoxic hexadepsipeptides and anti-  
coronaviral 4-hydroxy-2-pyridones from  
an endophytic *Fusarium* sp.  
*Front. Chem.* 10:1106869.  
doi: 10.3389/fchem.2022.1106869

## COPYRIGHT

© 2023 Chang, Yan, Chen, Zhao, Gao, Li,  
Yu, Xie, Si and Chen. This is an open-  
access article distributed under the terms  
of the [Creative Commons Attribution  
License \(CC BY\)](#). The use, distribution or  
reproduction in other forums is permitted,  
provided the original author(s) and the  
copyright owner(s) are credited and that  
the original publication in this journal is  
cited, in accordance with accepted  
academic practice. No use, distribution or  
reproduction is permitted which does not  
comply with these terms.

# Cytotoxic hexadepsipeptides and anti-coronaviral 4-hydroxy-2-pyridones from an endophytic *Fusarium* sp.

Shanshan Chang<sup>†</sup>, Biying Yan<sup>†</sup>, Yuchuan Chen, Wuli Zhao,  
Rongmei Gao, Yuhuan Li, Liyan Yu, Yuning Xie, Shuyi Si\* and  
Minghua Chen\*

Institute of Medicinal Biotechnology, Chinese Academy of Medical Sciences & Peking Union Medical College,  
Beijing, China

Three new hexadepsipeptides (**1–3**), along with beauvericin (**4**), beauvericin D (**5**), and four 4-hydroxy-2-pyridone derivatives (**6–9**) were isolated from the endophytic fungus *Fusarium* sp. CPCC 400857 that derived from the stem of tea plant. Their structures were determined by extensive 1D and 2D NMR, and HRESIMS analyses. The absolute configuration of hexadepsipeptides were elucidated by the advanced Marfey's method and chiral HPLC analysis. Compounds **4**, and **7–9** displayed the cytotoxicity against human pancreatic cancer cell line, AsPC-1 with IC<sub>50</sub> values ranging from 3.45 to 29.69 μM, and **7** and **8** also showed the antiviral activity against the coronavirus (HCoV-OC43) with IC<sub>50</sub> values of 13.33 and 6.65 μM, respectively.

## KEYWORDS

*Fusarium* sp., hexadepsipeptides, 4-hydroxy-2-pyridone, advanced Marfey's method, anti-coronavirus activity

## Introduction

*Fusarium*, a common genus of filamentous fungi, is considered as a treasure trove of bioactive secondary metabolites. About 280 compounds, including alkaloids, peptides, amides, terpenoids, quinones, and pyranones have been discovered from the *Fusarium* genus (Li J. et al., 2020; Zhen et al., 2021; Chen et al., 2022; Gu et al., 2022; Zhao et al., 2022). These compounds exhibited a broad spectrum of bioactivities, such as antibacterial, antifungal, antiviral, anti-angiogenic, phytotoxic, and cytotoxic effects (Li M. et al., 2020). Hexadepsipeptides, including typical amide bonds and at least one or two ester bonds, is a typical class of constituents of this genus (Xu et al., 2007; Urbaniak et al., 2020). Beauvericins represent a kind of conventional cyclo-hexadepsipeptides, being composed of three N-methyl amino acids and three hydroxy acid moieties, and displaying a variety of biological activities, such as cytotoxic (Ivanova et al., 2006), antifungal (Fukuda et al., 2004; Zhang et al., 2007), and insecticidal (Urbaniak et al., 2020) activity. Among of them, the beauvericin not only can be used as a co-drug to enhance the antifungal activities of ketoconazole (Nilanonta et al., 2002; Supothina et al., 2004; Zhang et al., 2007), but also exhibited the growth inhibition of human-pathogenic bacteria (Meca et al., 2010). In addition, 4-hydroxy-2-pyridone alkaloids bearing the central 4-hydroxy-2-pyridone moiety linked to two additional substituents at C-3 and C-5 positions are widely distributed in the genus *Fusarium* (Zhan et al., 2007; Jessen et al., 2010). Examples such as (–)-sambutoxin (Kim et al., 1995), (–)-4,6'-anhydrooxysporidinone (Zhan et al., 2007), (–)-oxysporidinone (Jayasinghe et al., 2006), funiculosin (Ando et al., 1969),

TABLE 1 <sup>1</sup>H NMR (600 MHz) and <sup>13</sup>C NMR (150 MHz) Data for Compounds 1-3 in DMSO-*d*<sub>6</sub> (δ in ppm, *J* in Hz).

	No.	1		2		3	
		δ <sub>C</sub> type	δ <sub>H</sub> ( <i>J</i> in Hz)	δ <sub>C</sub> type	δ <sub>H</sub> ( <i>J</i> in Hz)	δ <sub>C</sub> type	δ <sub>H</sub> ( <i>J</i> in Hz)
N-Me-Phe	1	169.5, C		169.3, C		169.3, C	
	2	56.8, CH	5.47, m	56.5, CH	5.43, dd (5.4, 12.0)	60.9, CH	4.45, dd (5.4, 11.4)
	3	33.9, CH <sub>2</sub>	3.20, m	34.4, CH <sub>2</sub>	3.03, m; 3.19, m	34.0, CH <sub>2</sub>	3.13, m; 3.01, m
	4	137.0, C		136.7, C		137.6, C	
	5	126.3–129.1, CH	7.13–7.28, m	126.6–129.7, CH	7.13–7.26, m	129.5, CH	7.04–7.28, m
	6	126.3–129.1, CH		126.6–129.7, CH		128.3, CH	
	7	126.3–129.1, CH		126.6–129.7, CH		126.6, CH	
	8	126.3–129.1, CH		126.6–129.7, CH		128.3, CH	
	9	126.3–129.1, CH		126.6–129.7, CH		129.5, CH	
	10-NCH <sub>3</sub>	31.1, CH <sub>3</sub>	2.85, s	31.5, CH <sub>3</sub>	2.94, s	34.9, CH <sub>3</sub>	2.62, s
Hiv	10	173.8, C		169.3, C		168.1, C	
	11	71.7, CH	3.94, d (4.2)	74.8, CH	4.88, d (8.4)	73.7, CH	5.11, d (9.6)
	12	30.5, CH	1.41, m	29.3, CH	1.73, m	29.2, CH	1.91, m
	13	15.5, CH <sub>3</sub>	0.29, d (6.6)	16.8, CH <sub>3</sub>	0.29, d (6.0)	17.8, CH <sub>3</sub>	0.71, d (6.6)
	14	19.1, CH <sub>3</sub>	0.61, d (6.6)	16.3, CH <sub>3</sub>	0.62, d (7.2)	16.9, CH <sub>3</sub>	0.25, d (7.2)
N-Me-Phe/Phe	15	169.7, C		170.8, C		169.6, C	
	16	57.0, CH	5.47, m	52.7, CH	4.57, m	55.1, CH	5.50, dd (5.4, 12.0)
	17	33.9, CH <sub>2</sub>	3.26, m	36.6, CH <sub>2</sub>	3.01, m; 2.86, m	34.4, CH <sub>2</sub>	3.05, m
	18	136.9, C		136.8, C		136.4, C	
	19	126.3–129.1, CH	7.13–7.28, m	126.6–129.7, CH	7.13–7.26, m	128.8, CH	7.04–7.28, m
	20	126.3–129.1, CH		126.6–129.7, CH		128.2, CH	
	21	126.3–129.1, CH		126.6–129.7, CH		126.4, CH	
	22	126.3–129.1, CH		126.6–129.7, CH		128.2, CH	
	23	126.3–129.1, CH		126.6–129.7, CH		128.8, CH	
	24-NCH <sub>3</sub>	31.5, CH <sub>3</sub>				31.0, CH <sub>3</sub>	3.08, s
	24-NH				8.32, d (8.4)		
Hiv/HL	24	168.9, C		167.6, C		168.9, C	
	25	74.8, CH	5.07, d (8.4)	78.3, CH	4.66, d (7.8)	67.4, CH	5.20, q (6.6)
	26	28.6, CH	1.49, m	28.9, CH	1.89, m	15.4, CH <sub>3</sub>	1.16, d (6.6)
	27	18.8, CH <sub>3</sub>	0.66, d (7.2)	17.8, CH <sub>3</sub>	0.74, d (6.6)		
	28	15.8, CH <sub>3</sub>	0.30, d (7.2)	18.0, CH <sub>3</sub>	0.62, d (7.2)		
N-Me-Phe/Phe	29	171.6, C		170.5, C		169.4, C	
	30	58.9, CH	5.02, m	52.8, CH	4.61, m	55.5, CH	5.58, dd (5.4, 11.4)
	31	33.5, CH <sub>2</sub>	3.03, m; 2.93, m	37.0, CH <sub>2</sub>	3.01, m; 2.86, m	33.0, CH <sub>2</sub>	3.12, m; 3.01, m
	32	137.7, C		136.8, C		136.9, C	
	33	126.3–129.1, CH	7.13–7.28, m	126.6–129.7, CH	7.13–7.26, m	128.9, CH	7.04–7.28, m
	34	126.3–129.1, CH		126.6–129.7, CH		128.2, CH	
	35	126.3–129.1, CH		126.6–129.7, CH		126.5, CH	

(Continued on following page)

TABLE 1 (Continued) <sup>1</sup>H NMR (600 MHz) and <sup>13</sup>C NMR (150 MHz) Data for Compounds 1–3 in DMSO-*d*<sub>6</sub> (δ in ppm, *J* in Hz).

	No.	1		2		3	
		$\delta_C$ type	$\delta_H$ ( <i>J</i> in Hz)	$\delta_C$ type	$\delta_H$ ( <i>J</i> in Hz)	$\delta_C$ type	$\delta_H$ ( <i>J</i> in Hz)
	36	126.3–129.1, CH		126.6–129.7, CH		128.2, CH	
	37	126.3–129.1, CH		126.6–129.7, CH		128.9, CH	
	38-NCH <sub>3</sub>	32.7, CH <sub>3</sub>	2.87, s			30.9, CH <sub>3</sub>	3.00, s
	38-NH				8.29, d (8.4)		
Hiv	38	168.7, C		168.0, C		168.8, C	
	39	75.4, CH	5.06, d (8.4)	78.4, CH	4.65, d (7.8)	73.2, CH	5.07, d (9.0)
	39-OH		4.15, d (8.4)				
	40	28.7, CH	1.68, m	29.4, CH	1.80, m	29.4, CH	1.74, m
	41	18.6, CH <sub>3</sub>	0.77, d (6.6)	17.7, CH <sub>3</sub>	0.47, d (6.6)	17.9, CH <sub>3</sub>	0.66, d (6.6)
	42	15.9, CH <sub>3</sub>	0.50, d (6.6)	17.7, CH <sub>3</sub>	0.60, d (7.2)	16.3, CH <sub>3</sub>	0.15, d (7.2)

sambutoxins A and B (Yang et al., 2021), and related analogues displayed a range of biological activities including antibacterial, antifungal, antiviral, and antitumor properties.

During our ongoing search for the bioactive products from the special habitat fungi (Chen et al., 2019; Li J. et al., 2020; Chang et al., 2022; Wang et al., 2022), *Fusarium* sp. CPCC 400857, an endophytic fungus isolated from a stem of tea plant, was investigated. A chemical investigation on the fungus led to three new hexadepsipeptides (1–3), along with six known compounds including beauvericin (4), beauvericin D (5), and four 4-hydroxy-2-pyridinone derivatives (6–9). The absolute configurations of hexadepsipeptides were assigned by the advanced Marfey's method and chiral HPLC analysis. Herein, the isolation, structural elucidation, and their cytotoxic and anti-coronavirus activity of the compounds 1–9 are described.

## Results

### Structural elucidation of the isolated compounds

Secobauvericin A (1) was obtained as a white amorphous powder. Its molecular formula was assigned as C<sub>45</sub>H<sub>59</sub>N<sub>3</sub>O<sub>10</sub> by the positive HR-ESI-MS ion [M + H]<sup>+</sup> at *m/z* 802.4282 (calcd. For C<sub>45</sub>H<sub>60</sub>N<sub>3</sub>O<sub>10</sub> 802.4279), corresponding for 18 degrees of unsaturation. The NMR spectrum of 1 (Table 1) displayed resonances of three monosubstituted benzenes, three pairs of vicinal methyls, three *N*-methyl groups, three methylenes, nine methines involving six peptidic α-methines, together with six amide and/or ester carbonyl carbons (δ<sub>C</sub> 168.7, 168.9, 169.5, 169.7, 171.6, 173.8). A comparison of the molecular composition and NMR data of compounds 1 and beauvericin (4) revealed that compound 1 could be a linear hexadepsipeptide (Yuan et al., 2021).

Comprehensive analysis of 2D NMR spectra (Figure 1) revealed the presence of three hydroxyisovaleric acids (Hiv) and three *N*-methyl phenylalanine (*N*-Me-Phe) moieties. HMBC correlations from *N*-CH<sub>3</sub>-10 to C-10, H-11 to C-15, *N*-CH<sub>3</sub>-24 to C-24, H-25 to C-29, and *N*-CH<sub>3</sub>-38 to C-38 established the sequence of Hiv-(*N*-Me-Phe)-Hiv-(*N*-Me-Phe)-Hiv-(*N*-Me-Phe), which was supported by

NOESY correlations from *N*-CH<sub>3</sub>-10 to H-11, H-11 to H-17, *N*-CH<sub>3</sub>-24 to H-25, H-25 to H-31, and *N*-CH<sub>3</sub>-38 to H-39. Furthermore, the connection of these hydroxy acid and amino acid residues was confirmed by the HR-MS/MS fragments at *m/z* 663.3252 [M-(*N*-Me-Phe)+OH + Na]<sup>+</sup>, 563.2729 [M-(*N*-Me-Phe)-Hiv + OH + Na]<sup>+</sup>, 402.1890 [M-(*N*-Me-Phe)-Hiv-(*N*-Me-Phe)+OH + Na]<sup>+</sup>, 302.1373 [M-(*N*-Me-Phe)-Hiv-(*N*-Me-Phe)-Hiv + OH + Na]<sup>+</sup> and 141.0530 [M-(*N*-Me-Phe)-Hiv-(*N*-Me-Phe)-Hiv-(*N*-Me-Phe)+OH + Na]<sup>+</sup> (Figure 2). Thus, the planar structure of 1 was determined as shown in Figure 1.

After acid hydrolysis, the absolute configuration of Hiv in 1 was determined to be *R* (Supplementary Figure S4; Supplementary Table S2) by chiral HPLC analysis in comparison to the authentic *R/S* Hiv units, while the advanced Marfey's analysis of the hydrolysate of 1 revealed the *N*-Me-Phe residues was *L*-configuration (Supplementary Figure S1) (Tripathi et al., 2009; Wang et al., 2017). Therefore, the structure of compound 1 was determined and designated as secobauvericin A (Figure 3).

Beauvericin M (2) was determined as C<sub>43</sub>H<sub>53</sub>N<sub>3</sub>O<sub>9</sub>, based on the HRESIMS peak at 756.3886 [M + H]<sup>+</sup> (calcd for C<sub>43</sub>H<sub>54</sub>N<sub>3</sub>O<sub>9</sub>, 756.3860), implying 19 degrees of unsaturation. The NMR data of 2 was closely correlated with beauvericin (4). The extensively analysis of the NMR data (Table 1) revealed that two *N*-CH<sub>3</sub> in beauvericin were replaced to NH in 2, which were verified by <sup>1</sup>H-<sup>1</sup>H COSY correlations of NH-24/H-16/H-17, NH-38/H-30/H-31, together with the HMBC correlations from NH-24 to C-16 and C-24, NH-38 to C-30 and C-38. The above related information shows that compound 2 contained two phenylalanine residues. In addition, the HMBC correlations from *N*-CH<sub>3</sub>-10 to C-10, H-11 to C-15, NH-24 to C-24, H-25 to C-29, NH-38 to C-38, and H-39 to C-1 indicated that the cyclic structure of 2 was Hiv-Phe-Hiv-Phe-Hiv-(*N*-Me-Phe). This connection was confirmed by cross peaks in the NOESY spectra with the correlations *N*-CH<sub>3</sub>-10 to H-11, NH-24 to H-25 and NH-38 to H-39. The cleavage method of the MS/MS spectrometer further verified the above connection of groups (Figure 2). The absolute configuration of *N*-Me-Phe, Phe, and Hiv units were determined as *L*, *L*, and *R* by advanced Marfey's method and chiral HPLC (Supplementary Figures S2, S4).

Beauvericin N (3) was obtained as the white amorphous powder. On the basis of (+)-HRESIMS data, the formula of 3

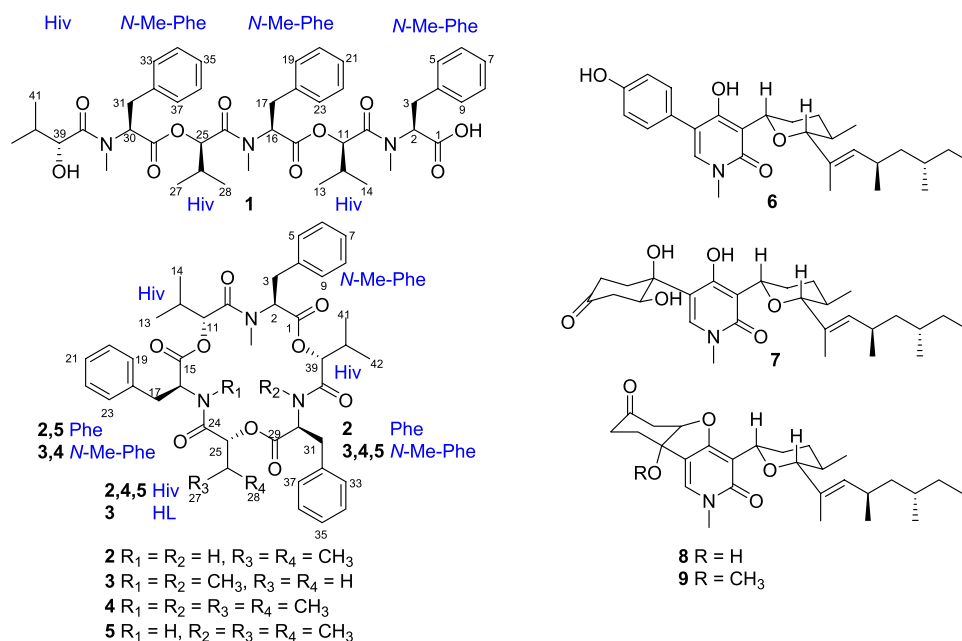


**FIGURE 1**  
Structures of compounds 1–9.

was established as  $C_{43}H_{53}N_3O_9$ . The comparison of NMR data of **3** and **4** suggested that an Hiv unit in **4** was replaced by a 2-hydroxypropionic acid (HL) moiety in **3**, which was verified by the  $^1H$ - $^1H$  COSY correlations of H-25/H-26, together with the HMBC correlations from H-26 to C-24. The connection of those  $\alpha$ -amino acids and  $\alpha$ -hydroxy acids in **3** was deduced by the HMBC correlations from *N*-CH<sub>3</sub>-10 to C-10, H-11 to C-15, *N*-CH<sub>3</sub>-24 to C-24, H-25 to C-29, *N*-CH<sub>3</sub>-38 to C-38 and H-39 to C-1, as well as NOESY correlations and HRESIMS/MS analysis (Figures 1, 2). The absolute configurations of the  $\alpha$ -hydroxy acids were determined as *R*-Hiv, *R*-HL by using the chiral HPLC, and the amino acids were assigned as *L*-*N*-Me-Phe by the advanced Marfey's method. Accordingly, compound **3** was corroborated and named as beauvericin N (Figure 3).

Secobeaubericin A (**1**) is assembled from three *R*-Hiv-*N*-methyl-*L*-Phe acid dipeptidol monomers. Beauvericin M (**2**) is formed as cyclic combined with two *R*-Hiv-*L*-Phe acid dipeptidol monomers and one *R*-Hiv-*N*-methyl-*L*-Phe acid monomer, while beauvericin N (**3**) is formed as cyclic with two *R*-Hiv-*N*-methyl-*L*-Phe acid dipeptidol monomers and one *R*-HL-*N*-methyl-*L*-Phe acid monomer (Urbaniak et al., 2020) (Figure 4).

The known compounds **4–9** were identified as beauvericin (Isaka et al., 2011), beauvericin D (Fukuda et al., 2004), (–)-sambutoxin (Kim et al., 1995), (–)-oxysporidinone (Jayasinghe et al., 2006), fusapyridon A (Wijeratne et al., 2011), and (–)-fusoxypyridone (Jayasinghe et al., 2006) by comparison of MS and 1D NMR data in the literature, respectively.

## Physicochemical properties and spectroscopic data of compounds 1–3

Secobeaubericin A (**1**): White amorphous powder; mp. 90°C–91°C;  $[\alpha] -73.3$  (c .4, MeOH); UV (LC): 210 nm; IR  $\nu_{max}$ : 3441, 2966, 2933, 2876, 1739, 1659, 1633, 1456, 1285, 1091, 1023, 828, 748, 700  $cm^{-1}$ ;  $^1H$

(600 MHz) and  $^{13}C$  NMR (150 MHz), see Table 1; HRESIMS  $m/z$   $[M + H]^+$  802.4282 (calcd for  $C_{45}H_{59}N_3O_{10}$ , 802.4279).

Beauvericin M (**2**): White amorphous powder; mp. 85°C–86°C;  $[\alpha] +6.7$  (c .2, MeOH); UV (LC) 217 nm; IR  $\nu_{max}$ : 3358, 3279, 2927, 1742, 1679, 1457, 1421, 1203, 1134, 1026, 802, 722, 700  $cm^{-1}$ ;  $^1H$  (600 MHz) and  $^{13}C$  NMR (150 MHz), see Table 1; HRESIMS  $m/z$   $[M + H]^+$  756.3886 (calcd for  $C_{43}H_{53}N_3O_9$ , 756.3860).

Beauvericin N (**3**): White amorphous powder; mp. 82°C–83°C;  $[\alpha] +13.3$  (c .2, MeOH); UV (LC) 217 nm; IR  $\nu_{max}$ : 3400, 3306, 2967, 2935, 1738, 1664, 1640, 1457, 1422, 1203, 1134, 1083, 1029, 835, 722, 700  $cm^{-1}$ ;  $^1H$  (600 MHz) and  $^{13}C$  NMR (150 MHz), see Table 1; HRESIMS  $m/z$   $[M + H]^+$  756.3830 (calcd for  $C_{43}H_{54}N_3O_9$ , 756.3860).

## Cytotoxicity and anti-coronavirus activity compounds 1–9

Beauvericins and 4-hydroxy-2-pyridones were shown to display potent cytotoxic activity against different human cell lines. Therefore, compounds **1–9** were evaluated the cytotoxic activity *in vitro*. Compounds **4**, and **7–9** showed the cytotoxicity against human pancreatic adenocarcinoma cell line AsPC-1 with IC<sub>50</sub> values of 3.45, 17.62, 29.69, and 18.81  $\mu M$ , respectively, while compounds **1–3**, **5**, and **6** were inactive at 90  $\mu M$  (Table 2). Compared with the positive drug, compounds **4**, and **7–9** exhibited weaker cytotoxicity than the gemcitabine. In addition, funiculosin could inhibited both the RNA and DNA virus in previous report (Ando et al., 1969). Therefore, the 4-hydroxy-2-pyridones (**6–9**) were tested for the inhibition against the coronavirus (HCoV-OC43). Compounds **7** and **8** displayed the antiviral activity against the coronavirus (HCoV-OC43) with IC<sub>50</sub> values of 13.33 and 6.67  $\mu M$ , and SI values of 1.7 and 1.7, respectively, and showed slightly better than the positive drug ribavirin (Table 3).

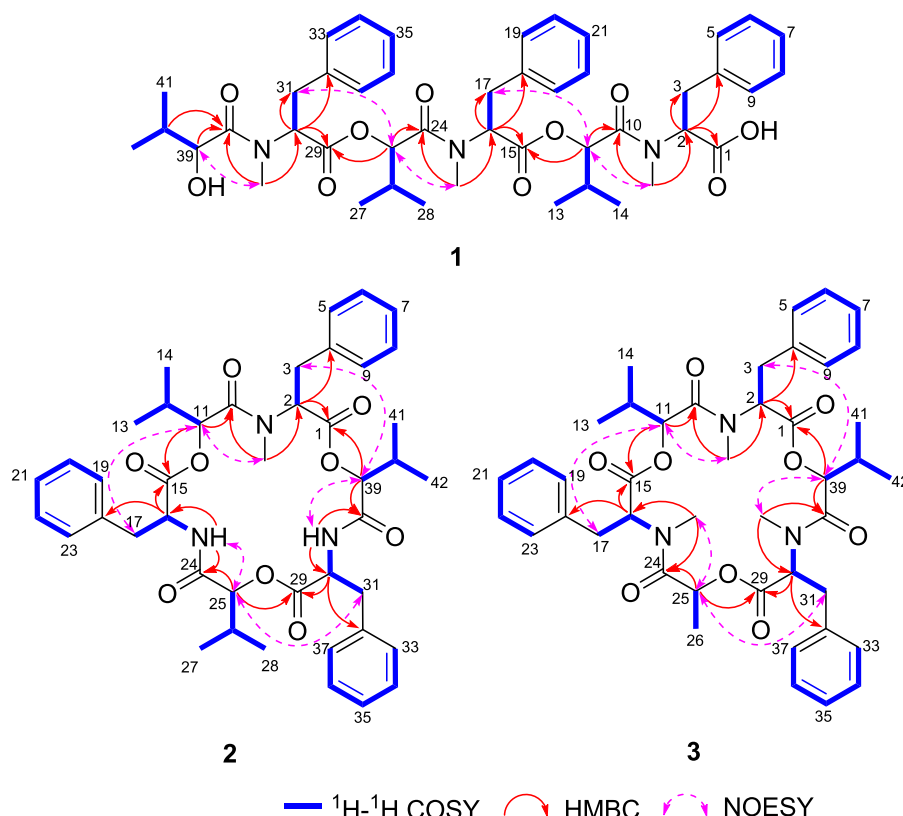


FIGURE 2

$^1\text{H}$ - $^1\text{H}$  COSY, HMBC, and NOESY correlations of compounds 1–3.

## Materials and methods

### Fungal materials

The fungus *Fusarium* sp. CPCC400857 was isolated from a stem of tea plant collected from Shaanxi Province, China. The strain was deposited in the China Pharmaceutical Culture Collection (Institute of Medicinal Biotechnology, Chinese Academy of Medical Sciences and Peking Union Medical College, No. CPCC 400857).

### Fermentation and extraction

The fungal strain was cultured on slants of potato dextrose agar (PDA) at 25°C for 7 days. Subsequently, the spores were used to inoculate in 500 ml Erlenmeyer flasks, each containing 100 ml of potato dextrose broth at 25°C (180 rpm) for 4 days to obtain the seed culture. The large-scale fermentation proceeded in 30 Erlenmeyer flasks (500 mL) containing 100 g of rice and 100 ml of distilled water, which were autoclaved at 121°C for 15 min. After being cooled to room temperature, each flask was inoculated with 5 ml of seed culture and incubated at 25°C for 30 days.

The fermented material was extracted with 95% EtOH (12 L for 2 times) and with 50% EtOH (12 L for 1 time). The solution was combined and evaporated under the reduced pressure to yield an aqueous suspension (4.0 L). The aqueous suspension was partitioned

with EtOAc (3 × 4.0 L). The organic solution was concentrated to dryness, and yielded a dark brown extract (124.3 g).

### Isolation and purification

The EtOAc extract (124.3 g) was subjected to silica gel column chromatography using  $\text{CH}_2\text{Cl}_2/\text{MeOH}$  gradient elution (50:1, 35:1, 25:1, 20:1, 15:1, 10:1, 1:1, and 1:0) to afford 10 fractions (Fr.1–Fr.10).

Fr. 2 (890 mg) was fractionated by Sephadex LH-20 column chromatography with  $\text{CH}_2\text{Cl}_2/\text{MeOH}$  (1:1) to afford three subfractions (Fr. 2-1–Fr. 2-3). Fr. 2-2 (41.0 mg) was further purified by reversed-phase semipreparative HPLC (Capcell Pak PFP column, 5  $\mu\text{m}$ , 10 × 250 mm, 1.5 mL/min, 60%  $\text{CH}_3\text{CN}/\text{H}_2\text{O}$ ) to yield 2 (3.1 mg).

Fr. 5 (1.7 g) was separated to seven subfractions (Fr. 5-1–Fr. 5-7) with reversed-phase (RP) flash column chromatography (5 mL/min, 5%–100%  $\text{MeOH}/\text{H}_2\text{O}$ ), then Fr. 5-3 (27 mg) was further purified by reversed-phase semipreparative HPLC (Capcell Pak PFP column, 5  $\mu\text{m}$ , 10 × 250 mm, 1.5 mL/min, 66%  $\text{CH}_3\text{CN}$  in 0.1% trifluoroacetic acid) to yield 1 (4.1 mg). Subsequently, the purification of Fr. 5-7 (192 mg) with Sephadex LH-20 column chromatography ( $\text{CH}_2\text{Cl}_2/\text{MeOH}$ , 1:1) yielded to seven subfractions (Fr. 5-7-1–Fr. 5-7-7). Then, the compound 4 (46.6 mg) was purified by reversed-phase semipreparative HPLC (Capcell Pak PFP column, 5  $\mu\text{m}$ , 10 × 250 mm, 1.5 mL/min, 80%  $\text{CH}_3\text{CN}/\text{H}_2\text{O}$  containing 0.1% TFA) from the subfraction Fr. 5-7-1 (72 mg). The subfraction of Fr. 5-7-5 (51 mg) was further isolated by

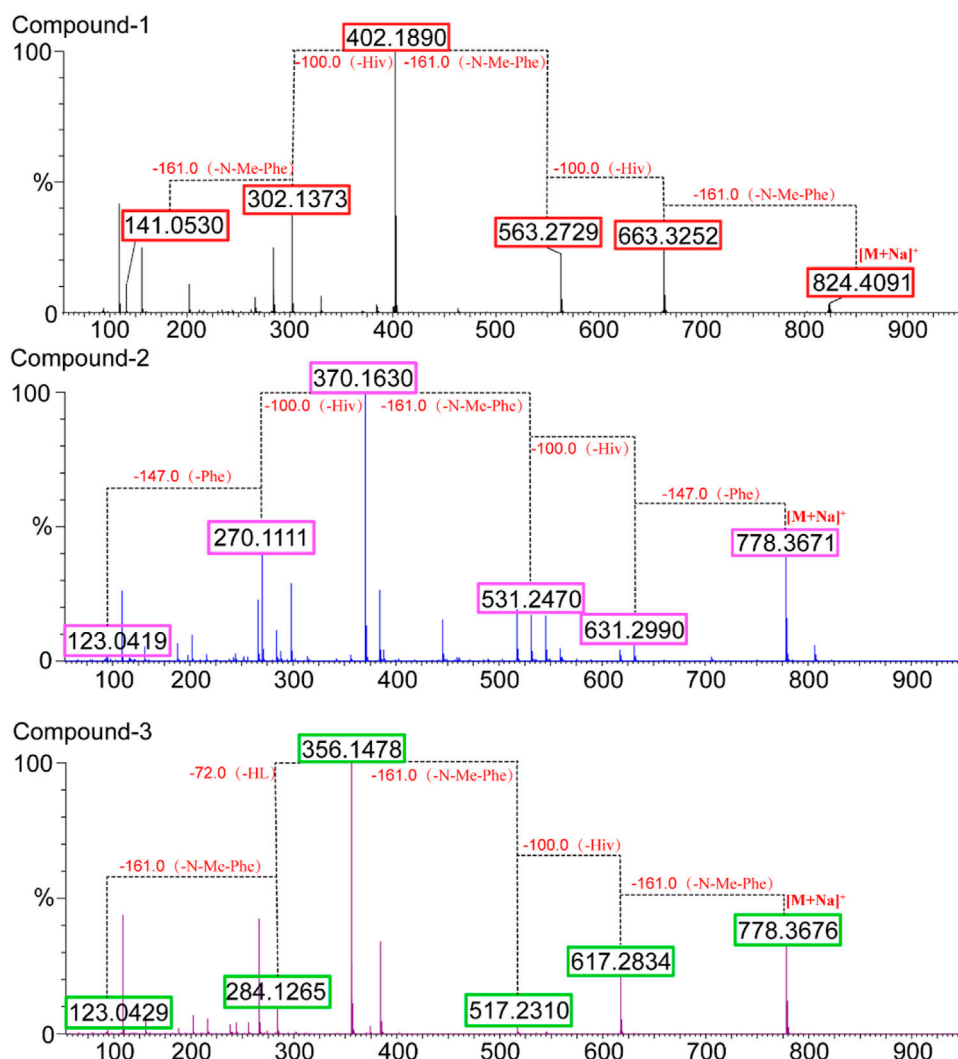


**FIGURE 3**  
Fragments observed for compounds 1–3 by HR-ESI-MS/MS.

reversed-phase semipreparative HPLC (Capcell Pak MGII column, 5  $\mu$ m, 10  $\times$  250 mm, 1.5 mL/min, 78% CH<sub>3</sub>CN/H<sub>2</sub>O) to yield **3** (2.7 mg), **5** (2.5 mg), and **9** (3.7 mg).

Fr. 10 (1.3 g) was fractionated by reversed-phase (RP) flash column chromatography with 5–100% MeOH to obtain **8** (3.1 mg) and six subfractions. Then Fr. 10–3 (33 mg) was isolated by reversed-phase semipreparative HPLC (Capcell Pak MGII column, 5  $\mu$ m, 10  $\times$  250 mm, 1.5 mL/min, 69% CH<sub>3</sub>CN in 0.1% trifluoroacetic acid) to get **6** (9.6 mg), and **7** (4.2 mg).

### Advanced Marfey's method (Tripathi et al., 2009; Wang et al., 2017)

Each of the compounds **1–3** (2 mg) in 1 mL of 6 M HCl were heated at 110°C for 18 h. The crude hydrolysate was divided into three portions and evaporated to dryness separately. Two of them were added to 50  $\mu$ L of 1% (w/v) *L* and *L/D*-FDLA (Marfey's reagent) and 100  $\mu$ L 1 M NaHCO<sub>3</sub> solution, respectively, and the mixtures were incubated at 40°C for 1 h. After being cooled to the room temperature,

the reactions were quenched by additional 100  $\mu$ L 1 M HCl, and diluted with 250  $\mu$ L MeOH. The *L*- and *L/D*-FDLA derivatives were analyzed by LC/MS on an Agilent 1100 LC/MSD spectrometer using the following conditions: Capcell Pak MGII column (3  $\mu$ m, 2.0  $\times$  100 mm); column temperature at 30°C; mobile phase, solvent A (0.1% FA in H<sub>2</sub>O) and solvent B (0.1% FA in CH<sub>3</sub>CN); flow rate, 0.5 mL/min; UV detection at 340 nm; compounds **1** and **3**, under isocratic ratio of A/B (34:66); compound **2**, under a linear gradient elution mode (5–100% B for 30 min). The retention times of the corresponding *L/D*-FDLA derivatives (*m/z* 474) for **1** and **3** were 23.6 min (*L*-*N*-Me-Phe-*L*-FDLA) and 28.7 min (*L*-*N*-Me-Phe-*D*-FDLA), respectively, while the *L*-FDLA derivatives for **1** and **3** were 23.6 min. The retention times of the corresponding *L/D*-FDLA derivatives for **2** were 5.6 min (*L*-*N*-Me-Phe-*L*-FDLA, *m/z* 474), 9.5 min (*L*-*N*-Me-Phe-*D*-FDLA, *m/z* 474), 4.6 min (*L*-Phe-*L*-FDLA, *m/z* 460), and 14.0 min (*L*-Phe-*D*-FDLA, *m/z* 460), respectively, while the *L*-FDLA derivatives for **2** were 5.6 min (*L*-*N*-Me-Phe-*L*-FDLA, *m/z* 474) and 4.6 min (*L*-Phe-*L*-FDLA, *m/z* 460), respectively. Consequently, the absolute configuration of the *N*-Me-Phe and Phe moieties in **1–3** were assigned as *L* (Supplementary Figures S1, S3).



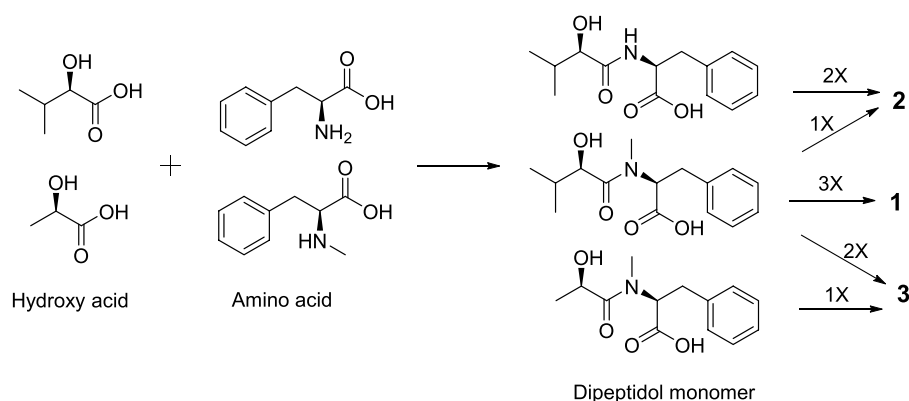


**FIGURE 4**  
Postulated biogenetic pathway of 1–3.

**TABLE 2 Cytotoxicity of compounds 1–9**

	IC <sub>50</sub> , $\mu$ M									Positive control
	1	2	3	4	5	6	7	8	9	Gemcitabine
AsPC-1	>90	>90	>90	3.45	>90	>90	17.62	29.69	18.81	1.53

**TABLE 3 Anti-coronavirus (HCoV-OC43) activity of compounds 7–9.**

Compd	TC <sub>50</sub> ( $\mu$ g/mL)	IC <sub>50</sub> ( $\mu$ g/mL)	SI (TC <sub>50</sub> /IC <sub>50</sub> )
6	<0.02	-	-
7	23.09	13.33	1.7
8	11.55	6.67	1.7
9	11.55	>6.67	-
Ribavirin	100	19.24	5.2

## Antiviral activity assessment (Song et al., 2022)

Briefly, the H460 cells were inoculated into 96 well culture plates and cultured at 35°C under 5% CO<sub>2</sub> condition, and infected by HCoV-OC43 virus with 100 times 50% tissue culture infective dose (TCID<sub>50</sub>) 24 h later; then the positive control drugs and test compounds were added. The half inhibitory concentration (IC<sub>50</sub>) and the half toxic concentration (TC<sub>50</sub>) were determined by the Reed and Muench method. The selectivity index (SI) was calculated as the ratio of TC<sub>50</sub>/IC<sub>50</sub>. The ribavirin (IC<sub>50</sub>, 19.24  $\mu$ g/mL; SI, 5.2) was used as the positive drug.

## Chiral HPLC analysis of the hydrolyzate

Above the third portion of hydrolysate was performed by HPLC analysis using a ligand-exchange-type chiral column: MCI gel CRS10W, 4.6  $\times$  50 mm, 5  $\mu$ m; flow rate 1 mL/min, eluent 2 mM aqueous CuSO<sub>4</sub>, UV detection at 254 nm (Chen et al., 2018). Standard *R*-Hiv, *S*-Hiv, *R*-HL and *S*-HL were used co-injection experiments and their retention times (*t<sub>R</sub>*, min) were as follows: *R*-Hiv (43.4), *S*-Hiv (69.7), *R*-HL (5.9), *S*-HL (7.8). These results of the HPLC analysis established the *R*-configuration for Hiv and HL units in 1–3 (Supplementary Figure S4).

## Cytotoxic activity assessment (Chen et al., 2018)

The cytotoxic effects of all compounds against human pancreatic cancer cell line (ASPC-1) were evaluated by CCK-8 method. The gemcitabine (IC<sub>50</sub>, 1.53  $\mu$ M) was used as the positive drug.

## Conclusion

In conclusion, three undescribed hexadepsipeptides, together with six known compounds were separated from the fungus *Fusarium* sp. CPCC400857. Their structures including the absolute configuration were determined by the extensive analysis of spectroscopic data, advanced Marfey's method, and chiral HPLC analysis. Pancreatic cancer is one of the most difficult and invasive tumors of digestive system, with low resection rate (Wang et al., 2022). But recent years, few active molecules have been found for pancreatic cancer from microorganisms. Leucinostatin Y, a peptaibiotic isolated from the entomoparasitic fungus *Purpureocillium lilacinum* selectively suppressed the growth of human pancreatic cancer cells, including PANC-1, BxPC-3, PSN-1, and PK-8 (Momose et al., 2019). Two benzophenone derivatives, pestalones C and E were found to suppress the pancreatic cancer cell line PANC-1 with IC<sub>50</sub> values of 7.6 and 7.2  $\mu$ M, respectively (Wang et al., 2019). In our previous study, we have found secoemestrin C, an epipolythiodioxopiperazine compound, displayed significant cytotoxicity against several

pancreatic adenocarcinoma cells, and enhanced the endoplasmic reticulum stress by a unique mechanism with downregulation of the YAP via the destruction complex (YAP-Axin-GSK- $\beta$ TrCP) (Wang et al., 2022). Beauvericin (4) had shown cytotoxicity to the hepatocellular carcinoma-line Hep G2 and fibroblast-like foetal lung cell line MRC-5 in previous report (Ivanova et al., 2006). In this work, compounds 4, and 7–9 exhibited moderate cytotoxicity against the human pancreatic cancer cell ASPC-1, which indicated that beauvericins and 4-hydroxy-2-pyridones may be used as the leading molecules of anti-pancreatic cancer, providing clues for pharmaceutical chemists and pharmacologists. Comparison of the cytotoxicity of 1–5 demonstrated that the cyclo-form and nitrogen methylation at L-phe residue are important for the cytotoxic activity. Compounds 7–9 showed more cytotoxic than 6 indicating that the 5-aromatic ring may decrease the toxicity to the ASPC-1 cell.

The global outbreak of the COVID-19 pandemic has caused serious public health and social problems. Although several drugs, such as remdesivir, molnupiravir, nirmatrelvir/ritonavir, and azvudine have been successively approved (Zhang et al., 2021; Zhang et al., 2022), the effective anti-COVID-19 drugs is still one of the major researches focuses. Here, we firstly discovered compounds 7 and 8 displayed the antiviral activity against the coronavirus (HCoV-OC43), but this type of compounds would need further structural modification, to lower toxicity and improve their values of selectivity index (SI).

## Data availability statement

The original contributions presented in the study are included in the article/Supplementary Material, further inquiries can be directed to the corresponding authors.

## Author contributions

SC and BY. performed most of the chemical experiments and wrote the manuscript, and both authors contributed equally to this

work. YC and YX. helped to complete the chemical experiments. WZ, RG, and YL. performed the pharmacological experiments. LY. supplied the strain. SS and MC. designed the research and revised the manuscript. All authors have read and agreed to the published version of the manuscript.

## Funding

This work was supported by the CAMS Innovation Fund for Medical Sciences (CIFMS, 2021-I2M-1-028, and 2022-I2M-2-002), National Natural Science Foundation of China (NNSFC, 81302675, and 82104047).

## Conflict of interest

The authors declare that the research was conducted in the absence of any commercial or financial relationships that could be construed as a potential conflict of interest.

## Publisher's note

All claims expressed in this article are solely those of the authors and do not necessarily represent those of their affiliated organizations, or those of the publisher, the editors and the reviewers. Any product that may be evaluated in this article, or claim that may be made by its manufacturer, is not guaranteed or endorsed by the publisher.

## Supplementary material

The Supplementary Material for this article can be found online at: <https://www.frontiersin.org/articles/10.3389/fchem.2022.1106869/full#supplementary-material>

## References

- Ando, K., Suzuki, S., Saeki, T., Tamura, G., and Arima, K. (1969). Funiculosin, a new antibiotic. I. Isolation, biological and chemical properties. *J. Antibiot.* 22, 189–194. doi:10.7164/antibiotics.22.189
- Chang, S., Cai, M., Xiao, T., Chen, Y., Zhao, W., Yu, L., et al. (2022). Prenylemestriins A and B: Two unexpected epipolythiodioxopiperazines with a thioethanothio bridge from *Emericella* sp. isolated by genomic analysis. *Org. Lett.* 24, 5941–5945. doi:10.1021/acs.orglett.2c02187
- Chen, M. H., Chang, S. S., Dong, B., Yu, L. Y., Wu, Y. X., Wang, R. Z., et al. (2018). Ahmpatinin 'Bu, a new HIV-1 protease inhibitor, from *Streptomyces* sp. CPEC 202950. *RSC Adv.* 8, 5138–5144. doi:10.1039/C7RA13241G
- Chen, M., Wang, R., Zhao, W., Yu, L., Zhang, C., Chang, S., et al. (2019). Isocoumarindole A, a chlorinated isocoumarin and indole alkaloid hybrid metabolite from an endolichenic fungus *Aspergillus* sp. *Org. Lett.* 21, 1530–1533. doi:10.1021/acs.orglett.9b00385
- Chen, Y., Wang, G., Yuan, Y., Zou, G., Yang, W., Tan, Q., et al. (2022). Metabolites with cytotoxic activities from the mangrove endophytic fungus *Fusarium* sp. 2ST2. *Front. Chem.* 10, 842405. doi:10.3389/fchem.2022.842405
- Fukuda, T., Arai, M., Tomoda, H., and Omura, S. (2004). New beauvericins, potentiators of antifungal miconazole activity produced by *Beauveria* sp. FKI-1366. II. Structure elucidation. *J. Antibiot.* 57, 117–124. doi:10.7164/antibiotics.57.117
- Gu, H., Zhang, S., Liu, L., Yang, Z., Zhao, F., and Tian, Y. (2022). Antimicrobial potential of endophytic fungi from *Artemisia argyi* and bioactive metabolites from *Diaporthe* sp. AC1. *Front. Microbiol.* 13, 908836. doi:10.3389/fmicb.2022.908836
- Isaka, M., Yangchum, A., Sappan, M., Suvannakad, R., and Srikitikulchai, P. (2011). Cyclohexadepsipeptides from *acremonium* sp. BCC 28424. *Tetrahedron* 67, 7929–7935. doi:10.1016/j.tet.2011.08.041
- Ivanova, L., Skjerve, E., Eriksen, G. S., and Uhlig, S. (2006). Cytotoxicity of enniatins A, A1, B, B1, B2 and B3 from *Fusarium avenaceum*. *Toxicon* 47, 868–876. doi:10.1016/j.toxicon.2006.02.012
- Jayasinghe, L., Abbas, H. K., Jacob, M. R., Herath, W. H. M. W., and Nanayakkara, N. P. D. (2006). N-Methyl-4-hydroxy-2-pyridinone analogues from *Fusarium oxysporum*. *J. Nat. Prod.* 69, 439–442. doi:10.1021/np050487v
- Jessen, H. J., and Gademann, K. (2010). 4-Hydroxy-2-pyridone alkaloids: Structures and synthetic approaches. *Nat. Prod. Rep.* 27, 1168–1185. doi:10.1039/b911516c
- Kim, J. C., Lee, Y. W., Tamura, H., and Yoshizawa, T. (1995). Sambutoxin: A new mycotoxin isolated from *Fusarium sambucinum*. *Tetrahedron Lett.* 36, 1047–1050. doi:10.1016/0040-4039(94)02450-p
- Li, J., Chen, M., Hao, X., Li, S., Li, F., Yu, L., et al. (2020). Structural revision and absolute configuration of burnettramic acid A. *Org. Lett.* 22, 98–101. doi:10.1021/acs.orglett.9b04008
- Li, M., Yu, R., Bai, X., Wang, H., and Zhang, W. (2020). *Fusarium*: A treasure trove of bioactive secondary metabolites. *Nat. Prod. Rep.* 37, 1568–1588. doi:10.1039/d0np00038h
- Meca, G., Sospedra, I., Soriano, J. M., Ritieni, A., Moretti, A., and Manes, J. (2010). Antibacterial effect of the bioactive compound beauvericin produced by *Fusarium*



- proliferatum* on solid medium of wheat. *Toxicon* 56, 349–354. doi:10.1016/j.toxicon.2010.03.022
- Momose, I., Onodera, T., Doi, H., Adachi, H., Iijima, M., Yamazaki, Y., et al. (2019). Leucinosatin Y: A peptaibiotic produced by the entomoparasitic fungus *Purpureocillium lilacinum* 40-H-28. *J. Nat. Prod.* 82, 1120–1127. doi:10.1021/acs.jnatprod.8b00839
- Nilanonta, C., Isaka, M., Kittakoop, P., Trakulnaleamsai, S., Tanticharoen, M., and Thebtaranonth, Y. (2002). Precursor-directed biosynthesis of beauvericin analogs by the insect pathogenic fungus *Paecilomyces tenuipes* BCC 1614. *Tetrahedron* 58, 3355–3360. doi:10.1016/S0040-4020(02)00294-6
- Song, Y., Deng, Y., Wang, H., Bei, Z., Gu, H., Zhao, H., et al. (2022). Naphthoquinone: A potent broad-spectrum anti-coronavirus drug *in vitro*. *Molecules* 27, 712. doi:10.3390/molecules27030712
- Supothina, S., Isaka, M., Kirtikara, K., Tanticharoen, M., and Thebtaranonth, Y. (2004). Enniatin production by the entomopathogenic fungus *Verticillium hemipterigenum* BCC 1449. *J. Antibiot.* 57, 732–738. doi:10.7164/antibiotics.57.732
- Tripathi, A., Puddick, J., Prinsep, M. R., Lee, P. P., and Tan, L. T. (2009). Hantupeptin A, a cytotoxic cyclic depsipeptide from a Singapore collection of *Lyngbya majuscula*. *J. Nat. Prod.* 72, 29–32. doi:10.1021/np800448t
- Urbaniak, M., Waśkiewicz, A., and Stepień, Ł. (2020). *Fusarium* cyclodepsipeptide mycotoxins: Chemistry, biosynthesis, and occurrence. *Toxins* 12, 765. doi:10.3390/toxins12120765
- Wang, J., Chen, M., Wang, M., Zhao, W., Zhang, C., Liu, X., et al. (2022). The novel ER stress inducer Sec C triggers apoptosis by sulfating ER cysteine residues and degrading YAP via ER stress in pancreatic cancer cells. *Acta Pharm. Sin. B* 12, 210–227. doi:10.1016/j.apsb.2021.07.004
- Wang, Q., Zhang, Y., Wang, M., Tan, Y., Hu, X., He, H., et al. (2017). Neo-actinomycins A and B, natural actinomycins bearing the 5*H*-oxazolo[4, 5-*b*] phenoxazine chromophore, from the marine derived *Streptomyces* sp. IMB094. *Sci. Rep.* 7, 3591. doi:10.1038/s41598-017-03769-8
- Wang, W., Park, C., Oh, E., Sung, Y., Lee, J., Park, K. Y., et al. (2019). Benzophenone compounds, from a marine-derived strain of the fungus *Pestalotiopsis neglecta*, inhibit proliferation of pancreatic cancer cells by targeting the MEK/ERK pathway. *J. Nat. Prod.* 82, 3357–3365. doi:10.1021/acs.jnatprod.9b00646
- Wijeratne, E. M. K., and Gunatilaka, A. A. L. (2011). Biomimetic conversion of (–)-fusoxypyridone and (–)-oxysporidinone to (–)-sambutoxin: Further evidence for the structure of the tricyclic pyridone alkaloid, (–)-fusoxypyridone. *Bioorg. Med. Chem. Lett.* 21, 2327–2329. doi:10.1016/j.bmcl.2011.02.091
- Xu, Y., Zhan, J., Wijeratne, E. M. K., Burns, A. M., Gunatilaka, A. A. L., and Molnár, I. (2007). Cytotoxic and antihaptotactic beauvericin analogues from precursor-directed biosynthesis with the insect pathogen *Beauveria bassiana* ATCC 7159. *J. Nat. Prod.* 70, 1467–1471. doi:10.1021/np070262f
- Yang, W., Tan, Q., Yin, Y., Chen, Y., Zhang, Y., Wu, J., et al. (2021). Secondary metabolites with  $\alpha$ -glucosidase inhibitory activity from mangrove endophytic fungus *Talaromyces* sp. CY-3. *Mar. Drugs* 19, 492. doi:10.3390/md19090492
- Yuan, Y., Li, T., Wang, T., Naman, C. B., Ye, J., Wu, X., et al. (2021). Targeted isolation of a cytotoxic cyclic hexadepsipeptide from the mesophotic zone sponge-associated fungus *Cymostachys* sp. NBUF082. *Mar. Drugs* 19, 565. doi:10.3390/md19100565
- Zhan, J., Burns, A. M., Liu, M. X., Faeth, S. H., and Gunatilaka, A. A. L. (2007). Search for cell motility and angiogenesis inhibitors with potential anticancer activity: Beauvericin and other constituents of two endophytic strains of *Fusarium oxysporum*. *J. Nat. Prod.* 70, 227–232. doi:10.1021/np060394t
- Zhang, J. L., Li, Y. H., Wang, L. L., Liu, H. Q., Lu, S. Y., Liu, Y., et al. (2021). Azvudine is a thymus-homing anti-SARS-CoV-2 drug effective in treating COVID-19 patients. *Signal Transduct. Target Ther.* 6, 414. doi:10.1038/s41392-021-00835-6
- Zhang, J., Yang, Q. L., Li, X., Wang, Y. Y., and Huang, M. L. (2022). Analysis of the clinical application of four novel antiviral drugs for coronavirus disease 2019 (COVID-19). *Chin. J. Clin. Pharmacol.* 38, 1392–1397. doi:10.13699/j.cnki.1001-6821.2022.12.021
- Zhang, L., Yan, K., Zhang, Y., Huang, R., Bian, J., Zheng, C., et al. (2007). High-throughput synergy screening identifies microbial metabolites as combination agents for the treatment of fungal infections. *Proc. Natl. Acad. Sci. U.S.A.* 104, 4606–4611. doi:10.1073/pnas.0609370104
- Zhao, D. L., Liu, J., Han, X. B., Wang, M., Peng, Y. L., Ma, S. Q., et al. (2022). Decalintetracids A and B, two pairs of unusual 3-decalinoyltetramic acid derivatives with phytotoxicity from *Fusarium equiseti* D39. *Phytochemistry* 197, 113125. doi:10.1016/j.phytochem.2022.113125
- Zhen, X., Mao, M. J., Wang, R. Z., Chang, S. S., Xiao, T. M., Wu, Y. X., et al. (2021). Fusapyrone A, a  $\gamma$ -pyrone derived from a desert *Fusarium* sp. *J. Asian Nat. Prod. Res.* 23, 504–511. doi:10.1080/10286020.2020.1794857



## OPEN ACCESS

## EDITED BY

Igor Jerkovic,  
University of Split, Croatia

## REVIEWED BY

Latifa Bouissane,  
Université Sultan Moulay Slimane,  
Morocco  
Vijai Agnihotri,  
Institute of Himalayan Bioresource  
Technology (CSIR), India

## \*CORRESPONDENCE

Fatma A. Moharram,  
✉ famoharram1@hotmail.com

<sup>†</sup>These authors have contributed equally to  
this work

## SPECIALTY SECTION

This article was submitted  
to Organic Chemistry,  
a section of the journal  
Frontiers in Chemistry

RECEIVED 09 December 2022

ACCEPTED 13 January 2023

PUBLISHED 06 February 2023

## CITATION

Elsayed HE, El-Deeb EM, Taha H, Taha HS,  
Elgindi MR and Moharram FA (2023),  
Essential oils of *Psidium cattleianum*  
Sabine leaves and flowers: Anti-  
inflammatory and cytotoxic activities.  
*Front. Chem.* 11:1120432.  
doi: 10.3389/fchem.2023.1120432

## COPYRIGHT

© 2023 Elsayed, El-Deeb, Taha, Taha,  
Elgindi and Moharram. This is an open-  
access article distributed under the terms  
of the [Creative Commons Attribution  
License \(CC BY\)](#). The use, distribution or  
reproduction in other forums is permitted,  
provided the original author(s) and the  
copyright owner(s) are credited and that  
the original publication in this journal is  
cited, in accordance with accepted  
academic practice. No use, distribution or  
reproduction is permitted which does not  
comply with these terms.

# Essential oils of *Psidium cattleianum* Sabine leaves and flowers: Anti-inflammatory and cytotoxic activities

Heba E. Elsayed<sup>1†</sup>, Eman M. El-Deeb<sup>2†</sup>, Heba Taha<sup>3</sup>, Hussein S. Taha<sup>4</sup>,  
Mohamed R. Elgindi<sup>1</sup> and Fatma A. Moharram<sup>1\*</sup>

<sup>1</sup>Pharmacognosy Department, Faculty of Pharmacy, Helwan University, Cairo, Egypt, <sup>2</sup>Pharmacognosy Department, Faculty of Pharmacy, October 6 University, Giza, Egypt, <sup>3</sup>Biochemistry and Molecular Biology Department, Faculty of Pharmacy, Helwan University, Cairo, Egypt, <sup>4</sup>Department of Plant Biotechnology, Genetic Engineering Division, National Research Centre, Cairo, Egypt

**Introduction:** *Psidium cattleianum* Sabine is a Brazilian native shrub cultivated for its edible fruit araçá (strawberry guava). *P. cattleianum* is recognized for health and food applications, although the essential oils (EOs) from the Egyptian inhabitant are not fully explored. The current study investigated the anti-inflammatory and cytotoxic activities of EOs from *P. cattleianum* leaves and flowers.

**Materials and methods:** The EOs were obtained by three different methods viz; the conventional hydro-distillation, microwave assisted hydro-distillation, and supercritical fluid extraction, while their analysis was accomplished using GC/MS. The derived EOs were screened for their anti-inflammatory activity in the 5-lipoxygenase, COX-1, and COX-2 enzyme based assays, while the anticancer potential was deduced from MTT cytotoxic assay, cell cycle, and western blotting analysis.

**Results and discussion:** Among other methods, supercritical fluid extraction offered the highest EO yield, 0.62% (leaves) and 1.4% (flowers). GC/MS identified  $\beta$ -caryophyllene and  $\alpha$ -humulene in both organs with high but variable percentages. The leaves demonstrated strong activity in inhibiting the 5-lipoxygenase enzyme (IC<sub>50</sub> 2.38), while the flowers, in inhibiting COX-2 (IC<sub>50</sub> 2.575). Moreover, the leaves showed potent, selective cytotoxicity to MCF-7 cells (IC<sub>50</sub> 5.32) via apoptosis by modulating the p53/Bax/Bcl2 axis. The deduced activities are possible due to the synergism between the volatile components that endorses *P. cattleianum* leaves' EOs in the management of breast cancer and inflammatory disorders.

## KEYWORDS

anti-inflammatory, caryophyllene, cytotoxicity, MCF-7, *Psidium cattleianum*, supercritical fluid extraction

## 1 Introduction

Essential oils (EOs) are presently attracting interest in the scientific community, owing to their imperative pharmacological activities (Amorim et al., 2009). They have been traditionally used by ancient cultures as a complementary holistic health approach, which was later termed aromatherapy, as they possess an array of unique health-fostering benefits. Currently, hundreds of EOs have been identified as commercially important crude drugs in the therapeutic, horticultural, cosmetic, and food industries (Shakeri et al., 2016). In addition, their unique

chemical framework is accredited to a variety of effective biological activities, such as antioxidant, antimicrobial, antinociceptive, anti-inflammatory, and anticancer activities (Amorim et al., 2009; Singh et al., 2013). To date, species of the family Myrtaceae are among the recognized plants that provide many valuable products including EOs (Araim et al., 2019). Notably, *Psidium* is one of the economically important genera because of its distinguished edible, essential oil-rich species such as *P. guajava* L. and *P. cattleianum* Sabine (Beltrame et al., 2021). *P. cattleianum* Sabine is a Brazilian native shrub, where it is commonly known as “araçá” (Faleiro et al., 2016); however, it is cultivated through the tropics and subtropics for its juicy, purple-red fruits known as strawberry guava or Cattle guava (Patel, 2012). The fruit has a strawberry-like flavor with a spicy touch and is rich in vitamin C, which is 3–4 times more than citrus fruits (Chalannavar et al., 2013). The characteristic flavor is due to the presence of essential oils (EOs), which were previously extracted by the hydro-distillation method from *P. cattleianum* grown in different countries and extensively studied by several researchers (Chalannavar et al., 2013; Soliman et al., 2016; dos Santos et al., 2018; Chrystal et al., 2020; Silvestre et al., 2022). On the other hand, only one report was conducted on the EOs from Egyptian species (Soliman et al., 2016). The relevant literature stated that the EOs derived from *P. cattleianum* leaves possessed significant *in vitro* antioxidant, antimicrobial, anti-inflammatory, and anticancer activities (Castro et al., 2015; Chrystal et al., 2020; de Souza et al., 2021). To the best of our knowledge, no prior study has investigated the volatile metabolites from the flowers; hence, it is interesting to investigate the chemical nature of its derived EOs in comparison with those obtained from the leaves, in an attempt, to discover a new active essential oil-based remedy for the management of cancer and inflammatory disorders.

Cancer is considered one of the most severe diseases worldwide and is expected to increase due to the lifestyle adopted nowadays (Bray and Moller, 2006). The World Health Organization (WHO) revealed that cancer was responsible for nearly 30% of deaths from non-chronic diseases among adults in 2020. Drug resistance to cancer and the toxicity of available chemotherapeutic agents are currently the main limitations in its treatment. So, the discovery of innovative and safe treatments is considered a big challenge (Abdullaev, 2001). However, this mission is not impossible with natural products. Natural products have played a pivotal role in cancer chemotherapy and chemoprevention for over half a century and established anticancer drugs, e.g., camptothecin, doxorubicin, paclitaxel, vinblastine, and vincristine (Sarker et al., 2020). Hence, the discovery of new anticancer hits derived from natural sources is a feasible strategy and is in dire need.

The functional correlation between inflammation and cancer is not new. It is now becoming clear that the cancer micro-environment, which is largely composed of inflammatory cells, is an indispensable participant in neoplastic development, encouraging proliferation, survival, and migration. COX-1 and COX-2 are two important isoforms of the cyclooxygenase family in which COX-2, the inducible isoform of COX, has developed as the key enzyme in the regulation of inflammation and cancer (Agrawal and Mishra, 2010). Other reports mentioned the disposition of COX-2 and lipoxygenases (LOX) in the regulation of different normal physiological processes and inflammation, in addition to cancer (Wang and Du Bois, 2010). These insights are raising new anti-inflammatory therapeutic approaches for the development of cancer. Natural products play a significant role in human health in relation to the prevention and treatment of inflammatory conditions witnessed by curcumin, cucurbitacins, and 1,8-cineole, in which the latter is an essential oil-

derived terpene oxide (Juergens et al., 2020). Hence, searching for new anti-inflammatory active agents derived from natural products or even essential oils is a propitious approach.

In continuation to our research into the discovery of anti-inflammatory and anticancer bioactive hits from natural sources, we aimed to identify the chemical composition of the EOs obtained from *P. cattleianum* leaves and flowers cultivated in Egypt for the first time using three different techniques. Moreover, it was deemed of interest to validate their cytotoxicity potential in different cancer cell lines and unravel their detailed underlying mechanisms in terms of cell cycle analysis and apoptosis-related proteins. Furthermore, the inhibitory activities of the derived EOs to 5-LOX, COX-1, and 2 were investigated to expand the conception that inflammation may be a serious factor in cancer progression.

## 2 Material and methods

### 2.1 Plant material

Both leaves and flowers of *Psidium cattleianum* Sabine were collected at the fruiting stage from March to April 2021 from Mazhar Botanic Garden, Cairo, Egypt. The plant was identified by Dr. Trease Labib, Senior Botanist at Mazhar Botanic Garden, Cairo, Egypt. Plant voucher samples (01Pca/2021) were represented at the herbarium of Pharmacognosy Department, Faculty of Pharmacy, Helwan University, Cairo, Egypt.

### 2.2 Extraction of essential oils of flowers and leaves

#### 2.2.1 Conventional hydro-distillation method

Small pieces of fresh leaves (200 g) and flowers (50 g) were mixed with double distilled water before hydro-distillation (HD) using Clevenger apparatus for 4 h.

#### 2.2.2 Microwave-assisted hydro-distillation method

The microwave-assisted hydro-distillation (MAHD) was achieved using a microwave oven (CEM Corporation, Matthews, NC, United States) and a model (MARS 240/50, No. 907511, 1,200 W) operated at a frequency of 2,450 MHz. In brief, small pieces of fresh leaves (200 g) and flowers (50 g) were placed in 1L- and 500-mL flask and mixed with 500 and 250 mL deionized water, respectively. After that, the Clevenger apparatus was set up within the microwave oven cavity, while the cooling system connected to the outside of the oven to condense the distillate volatiles continuously. The microwave oven was operated at an 800-W power level for 60 min (Ghazanfar et al., 2020).

#### 2.2.3 Supercritical fluid extraction

The supercritical fluid extraction (SFE) using supercritical carbon dioxide was accomplished as per the procedure described by Suetsugu et al. (2013) using Speed TM SFE-2/4, applied separations, and constructed in conjunction with the USDA1-USA. About 200 g and 50 g of dried and milled leaves and flowers were extracted at 40°C and 15.0 MPa. First, the apparatus was operated in a static mode for 60 min and then in dynamic mode for 60 min with a final total processing time of 180 min. The main drawback of SCE is its low

polarity; this problem is overcome by employing polar modifiers by the addition of absolute ethanol with a flow rate of 0.2 mL/min as a co-solvent to alter the polarity and increase its solvating power. The oil obtained from the three methods was dried in anhydrous Na<sub>2</sub>SO<sub>4</sub> and stored in amber, sealed bottles at 4°C until GC/MS analysis.

Moreover, the oil percentage was calculated as an essential oil volume (mL)/100 g of fresh plant material.

## 2.3 Gas chromatography coupled with mass spectrometry analysis

Gas chromatography-mass spectrometry (GC/MS) investigation was conducted using Shimadzu GCMS-QP2010 (Kyoto, Japan) coupled with quadrupole mass spectrometer (Shimadzu Corporation, Kyoto, Japan). Separation of oil compounds was achieved using an Rtx-5MS column (30 m × 0.25 mm i.d. × 0.25-μm film thickness, Restek, United States) with a flame ionization injector. The temperature of the column was kept at 50°C for 3 min in the beginning (isothermal), then planned to increase it to 300°C at a rate of 5°C/min, and then continuously kept for 10 min at 300°C (isothermal). The temperature of the injector was adjusted to 280°C. The flow rate of the helium carrier gas is 1.37 mL/min for HD and MAHD samples, while that of SCE sample is 1.41 mL/min. The mass spectra were recorded as follows: the temperatures of the interface and ion source are 280°C and 200°C, respectively; the mode of electron ionization is 70 eV with a scanning range of 35–500 amu. The split mode (1: 15) was used for injecting the oil samples (1 μL).

## 2.4 Identification of volatile oil components

The obtained volatile constituents were identified by comparing their Kovats retention indices (RI) with that of standard *n*-alkane series (C<sub>8</sub>–C<sub>28</sub>) and their mass spectra with those reported in the NIST (National Institute of Standards and Technology) and Wiley mass spectral databases (similarity index >90%) (Adams, 2005).

## 2.5 In vitro biological evaluation

All *in vitro* assays were accomplished on the EOs isolated from *P. cattleianum* leaves and flowers using the SFE method as this extraction method offered the highest oil yield.

### 2.5.1 Enzyme-based anti-inflammatory assays

#### 2.5.1.1 5-Lipoxygenase inhibitory screening assay

It was performed using a BioVision 5-lipoxygenase inhibitor screening assay kit (catalog no. K980-100; Milpitas, CA, United States). Four concentrations of the EOs (0.1, 1, 10, and 100 μL/mL) were prepared in DMSO (Sigma-Aldrich, Steinheim, Germany). Then, 2 μL of each EO stock solution, 5-LOX enzyme (enzyme control), DMSO (negative control), or zileuton (positive control) were added separately to a 96-well plate; then, 38 μL of LOX buffer was added. Subsequently, 40 μL of the reaction mixture (34 μL LOX buffer, 2 μL LOX probe, and 4 μL 5-LOX enzyme) was added to each well except for the enzyme control well, which will receive a reaction mixture composed of 38 μL LOX buffer and 2 μL

LOX probe only. The plate was incubated for 10 min at room temperature before the addition of 20 μL of 5% LOX substrate (prepared in LOX buffer) to each well. The experiment was performed recurrently in triplicate, and the percentage inhibitions of EOs were measured fluorometrically using the following equation:

$$\% \text{ Inhibition} = [(\text{slope of enzyme control} - \text{slope of tested EO}) / \text{slope of enzyme control}] \times 100.$$

IC<sub>50</sub> represents the EO concentration that causes 50% enzyme inhibition from the dose-response curve using non-linear regression analysis.

#### 2.5.1.2 COX-1 and COX-2 inhibitory screening assays

It was accomplished using BioVision COX-1 and 2 inhibitor screening assay kits (catalog no K548-100 and K547-100, respectively; Milpitas, CA, United States), according to the manufacturer's instructions. Briefly, four different concentrations of EOs (0.1, 1, 10, and 100 μL/mL) were prepared in DMSO. Thereafter, in a 96-well plate, 10 μL of each EO stock solution or assay buffer was added separately to the wells that were assigned as sample screen [SC] and enzyme control [EC], respectively. Thereafter, 80 μL of the reaction mixture (76 μL COX assay buffer, 1 μL COX probe, 2 μL COX cofactor, and 1 μL COX-1) was added to each well, and then, 10 μL of arachidonic acid/NaOH was added. SC560 (COX-1 inhibitor), celecoxib (COX-2 inhibitor), and indomethacin (non-steroidal anti-inflammatory drug) were considered as standard control drugs. The inhibition percentage of tested EOs was measured fluorometrically and calculated as follows:

$$\% \text{ Inhibition} = [(\text{slope of EC} - \text{slope of SC}) / \text{slope of EC}] \times 100.$$

IC<sub>50</sub> represents the concentration of EOs that causes 50% enzyme inhibition deduced from the dose-response curve using non-linear regression analysis.

### 2.5.2 Anticancer assays

#### 2.5.2.1 Cell lines and culture conditions

The human hepatocellular (HepG2), breast (MCF-7), and immortalized myelogenous leukemia (K562) cancer cell lines and the normal fibroblast lung cells (WI-38) were supplied from the company for biological products and vaccines (VACSERA, Egypt). The HepG2 and MCF-7 cells were sustained in Dulbecco's modified Eagle's medium (DMEM), K562 in Roswell Park Memorial Institute medium (RPMI-1640), and WI-38 were preserved in Eagle's Minimum Essential Medium (EMEM). All media were supplemented with 10% fetal calf serum (FCS), 2 mM glutamine, 100 U/mL penicillin, and 100 μg/mL streptomycin at 37°C at 5% CO<sub>2</sub> (v/v) atmosphere.

#### 2.5.2.2 Cytotoxicity assay

Cell viability was evaluated using the MTT reagent (3-(4, 5-dimethylthiazolyl)-2,5-diphenyltetrazolium bromide, Sigma-Aldrich, Steinheim, Germany) colorimetric assay (Papadimitriou et al., 2019). Briefly, MCF-7, HepG2 and K562, and WI 38 cell lines were added to a 96-well culture plate (1.2–1.8 × 10<sup>3</sup> cells/well). The cells were incubated for 24 h and then treated with an increasing concentration of tested EOs (3.125, 6.25, 12.5, 25, and 100 μL/mL) for 48 h. Then, the supernatant of the culture was removed followed by the addition of 40 μL of an MTT solution. The formazan crystals of MTT were dissolved by the addition of DMSO (180 μL). Finally, color absorbance was measured using a microplate reader at λ<sub>570</sub> nm (Sunrise, TECAN, Inc, United States), and doxorubicin<sup>®</sup> (Sigma Company, Suffolk County, NY, United States) was



used as a standard cytotoxic agent. Triplicate repeats were performed, and the cell viability percentage was measured as follows:

Cell viability percentage = (treated cell absorbance/control cell absorbance)  $\times$  100.

IC<sub>50</sub> was calculated by non-linear regression analysis.

### 2.5.2.3 Cell cycle analysis

Since the EO of *P. cattleianum* leaves displayed potent cytotoxic activity toward the MCF-7 cell line, the following assays were carried out to extensively evaluate its mode of cytotoxicity and identify the downstream signaling pathway. So, to assess the leaves' EO effects on MCF-7 cell distribution *via* different stages of the cell cycle, the DNA content of the propidium iodide (PI)-stained nuclei was evaluated by flow cytometry, according to Ormerod (1994). The cells were treated with a dose equivalent to the IC<sub>50</sub> of the EOs of the leaves (IC<sub>50</sub> 5.32  $\mu$ L/mL) for 48 h, followed by washing with ice-cold phosphate-buffered saline (PBS) twice and then collected by centrifugation. Then, the cell pellets were mixed with ethanol (75%,  $-20^{\circ}$ C) and stained with the kit of PI flow cytometry (ab139418, Abcam, United States), according to the manufacturer's instructions. Cell cycle distribution was recognized using a FACSCalibur flow cytometer (BD Biosciences, San Jose, CA) and measured using CellQuest software (Becton Dickinson Immunocytometry Systems, San Jose, CA).

### 2.5.2.4 Apoptosis assay

Necrosis cell populations and early and late apoptosis were measured using the annexin V-FITC/PI apoptosis/necrosis kit (Cat No: K101; BioVision, Inc., United States) to evaluate the effects of leaves' EOs on programmed cell death. Briefly, MCF-7 cells were treated for 48 h with the IC<sub>50</sub> concentration of EOs of leaves (5.32  $\mu$ L/mL) and then collected by trypsinization, washed twice with ice-cold PBS, re-suspended in annexin V-binding buffer (500  $\mu$ L), and finally, 5  $\mu$ L of annexin V-FITC was added and incubated in the dark at  $25^{\circ}$ C for 10 min. The investigation was achieved by using a FACSCalibur flow cytometer and CellQuest software.

### 2.5.2.5 Western blot analysis

MCF-7 cells were seeded, cultured, and treated with IC<sub>50</sub> of the EOs of leaves (5.32  $\mu$ L/mL) for 48 h. Cell protein lysates were prepared by radio immunoprecipitation assay buffer (RIPA buffer, Cell Signaling, Danvers, MA), and the concentration of the total protein in the supernatant was measured calorimetrically using the Bradford method (Sambrook et al., 1989) before Western blot, which was assessed by mixing and boiling equal amounts of protein samples (20  $\mu$ g) with sodium dodecyl sulfate (SDS) buffer for 10 min, cooled on ice, loaded into SDS polyacrylamide gel, and then separated by electrophoresis (Cleaver, United Kingdom). Then, the bands were transported by semi-dry electroblotting (Bio-Rad, United States) at 2.5 A and 25 V for 30 min to the polyvinylidene fluoride (PVDF) membranes (Bio-Rad, United States) which were blocked with non-fat dry milk in TBS-T (5%) for 2 h and incubated with anti-Bax, anti-Bcl-2, anti-p53 (Cell Signaling Technology, Inc. United States), and anti- $\beta$ -actin (Sigma-Aldrich, United States) antibodies (1:1000) overnight, and washed with TBS-T (three times), followed by incubation with horseradish peroxidase (HRP)-linked secondary antibody (1:5000) for 1 h. Progress was carried out using a chemiluminescent ECL substrate (Perkin Elmer, United States), following the manufacturer's recommendation, and chemiluminescent signals were taken using a CCD camera-based

imager, and the intensities of bands were measured using Image Lab (Bio-Rad, United States).

### 2.5.3 Statistical analyses

All experimental data were obtained from three separate experiments performed in three replicates. Data were expressed as the mean  $\pm$  SD in both *in vitro* cytotoxic and *in vitro* anti-inflammatory assays. GraphPad Prism version 5.0 (GraphPad Software, San Diego, CA, United States) was used to calculate mean inhibitory concentrations and IC<sub>50</sub> values using non-linear regression analysis.

## 3 Results and discussion

Essential oils are odorous products of complex compositions, obtained from natural sources by various methods. They possess the characteristic taste and odor of the source from which it was derived. Such organoleptic properties are principally dependent on chemical composition, which is greatly affected by intrinsic and extrinsic factors (Dhifi et al., 2016). The intrinsic factors include, but are not limited to, the plant organ, genetics, and maturity stage, while the extrinsic factors include the extraction methods and environmental conditions (Dhifi et al., 2016). In the present study, the variations in *P. cattleianum* EOs cultivated in Egypt were comparatively investigated in terms of different plant organs and extraction methods. Herein, the leaves and flowers were extracted for the first time using three different methods, namely, HD, MAHD, and SFE. The HD method is the most common and low-priced method, although the obtained oil may undergo saponification, polymerization, and/or isomerization, especially for its labile components (Koedam et al., 1979). Meanwhile, MAHD and SFE represent one of the most applied green technology and environmentally friendly methods that produce good EOs in a little time with slight environmental degradation (Abbas et al., 2022). However, the SFE method is privileged by its diffusion coefficient, high oil yield, and low oil viscosity. Hence, it is obvious that each extraction method differs in its basic principle and adjusted conditions, which subsequently affect the yield and physical and chemical composition of the obtained volatile. By the aforementioned information, the EOs derived from the leaves and flowers by HD were almost pale-yellow liquids with a fruity, acidic flavor, while those obtained from SEF exhibited brown color and fruity, aromatic flavor. Moreover, it was found that the oil's yield was affected not only by the extraction method but also according to the plants' organs. The measured yield was 0.14, 0.31, and 0.62 v/w (*P. cattleianum* leaves) and 0.20, 0.31, and 1.40 v/w (*P. cattleianum* flowers) for HD, MAHD, and SFE, respectively. From the obtained results, it was found that SFE corresponded to the highest oil yield, an observation that may be correlated with the unique characteristics of the SFE. SF is considered a liquid–gas intermediate phase: it is non-viscous with low or no surface tension and possesses the characteristics of both liquid and gas, which results in a great diffusion rate and solvation power, allowing faster extraction and worthy yield (Sargenti and Lancas, 1997).

### 3.1 GC/MS analysis for the extracted essential oils

The effects of the techniques used in the oil extraction from various plants' organs were reflected in the qualitative and quantitative compositions of *P. cattleianum* EOs. Regarding,

TABLE 1 Identified compounds of *P. cattleianum* leaves' essential oil extracted by different methods.

Peak	R <sub>t</sub>	Compound	M.F.	RI <sub>exp</sub>	RI <sub>lit</sub>	%Content			Identifications
						HD	MAHD	SFE	
1	7.13	α-Thujene	C <sub>10</sub> H <sub>16</sub>	908	908	0.10	0.07	-	MS, RI
2	7.31	α-Pinene	C <sub>10</sub> H <sub>16</sub>	915	915	6.29	4.51	0.43	MS, RI
3	8.58	β-Pinene	C <sub>10</sub> H <sub>16</sub>	961	961	0.49	0.29	-	MS, RI
4	9.05	β-Myrcene	C <sub>10</sub> H <sub>16</sub>	978	978	0.19	0.06	-	MS, RI
5	10.20	D-Limonene	C <sub>10</sub> H <sub>16</sub>	1017	1017	1.22	0.61	0.23	MS, RI
6	10.51	<i>trans</i> -β-Ocimene	C <sub>10</sub> H <sub>16</sub>	1027	1027	0.19	0.08	-	MS, RI
7	10.83	<i>cis</i> -β-Ocimene	C <sub>10</sub> H <sub>16</sub>	1038	1038	1.15	0.43	0.18	MS, RI
8	11.15	γ-Terpinene	C <sub>10</sub> H <sub>16</sub>	1048	1048	0.09	-	-	MS, RI
10	14.84	Terpinen-4-ol	C <sub>10</sub> H <sub>18</sub> O	1167	1167	0.16	0.07	-	MS, RI
11	19.85	α-Cubebene	C <sub>15</sub> H <sub>24</sub>	1339	1339	-	0.07	-	MS, RI
12	20.05	α-Longipinene	C <sub>15</sub> H <sub>24</sub>	1346	1347	-	0.06	-	MS, RI
13	20.33	(+)-Cyclosativene	C <sub>15</sub> H <sub>24</sub>	1356	1358	-	-	0.04	MS, RI
14	20.49	Ylangene	C <sub>15</sub> H <sub>24</sub>	1362	1362	0.10	0.14	0.09	MS, RI
15	20.59	Copaene	C <sub>15</sub> H <sub>24</sub>	1365	1365	2.16	2.57	2.39	MS, RI
16	20.79	Nerol acetate	C <sub>12</sub> H <sub>20</sub> O <sub>2</sub>	1372	1372	1.04	0.59	0.56	MS, RI
17	21.05	β-Elemene	C <sub>15</sub> H <sub>24</sub>	1380	1380	0.62	0.67	0.45	MS, RI
18	21.42	7- <i>epi</i> -Sesquithujene	C <sub>15</sub> H <sub>24</sub>	1392	1391	0.15	0.20	-	MS, RI
19	21.54	α-Gurjunene	C <sub>15</sub> H <sub>24</sub>	1398	1398	0.20	0.28	0.17	MS, RI
20	21.64	<i>cis</i> -α-Bergamotene	C <sub>15</sub> H <sub>24</sub>	1402	1403	0.30	0.38	-	MS, RI
21	21.69	<i>trans</i> -α-Bergamotene	C <sub>15</sub> H <sub>24</sub>	1404	1405	-	-	0.31	MS, RI
22	21.90	β-Caryophyllene	C <sub>15</sub> H <sub>24</sub>	1414	1414	11.77	12.56	13.20	MS, RI
23	22.17	γ-Elemene	C <sub>15</sub> H <sub>24</sub>	1423	1423	2.38	-	2.36	MS, RI
24	22.35	Aromandendrene	C <sub>15</sub> H <sub>24</sub>	1429	1429	0.54	0.77	0.74	MS, RI
25	22.73	α-Humulene	C <sub>15</sub> H <sub>24</sub>	1445	1445	14.65	15.00	10.90	MS, RI
26	22.85	β-Santalene	C <sub>15</sub> H <sub>24</sub>	1449	1449	0.58	0.65	0.07	MS, RI
27	22.95	Alloaromadendrene	C <sub>15</sub> H <sub>24</sub>	1452	1452	0.44	0.58	0.55	MS, RI
28	23.08	Muurolo-4,11-diene	C <sub>15</sub> H <sub>24</sub>	1458	1458	-	-	0.37	MS, RI
29	23.32	γ-Muuroloene	C <sub>15</sub> H <sub>24</sub>	1467	1467	2.00	2.89	1.01	MS, RI
30	23.45	Germacrene D	C <sub>15</sub> H <sub>24</sub>	1473	1473	0.44	1.00	0.51	MS, RI
31	23.61	γ-Selinene	C <sub>15</sub> H <sub>24</sub>	1479	1479	1.06	1.29	3.75	MS, RI
32	23.81	γ-Maaliene	C <sub>15</sub> H <sub>24</sub>	1487	1435	1.59	1.82	-	MS, RI
33	24.09	β-Bisabolene	C <sub>15</sub> H <sub>24</sub>	1498	1498	1.42	2.30	2.48	MS, RI
34	24.16	β-Curcumene	C <sub>15</sub> H <sub>24</sub>	1501	1504	0.52	-	-	MS, RI
26	22.85	β-Santalene	C <sub>15</sub> H <sub>24</sub>	1449	1449	0.58	0.65	0.07	MS, RI
27	22.95	Alloaromadendrene	C <sub>15</sub> H <sub>24</sub>	1452	1452	0.44	0.58	0.55	MS, RI
28	23.08	Muurolo-4,11-diene	C <sub>15</sub> H <sub>24</sub>	1458	1458	-	-	0.37	MS, RI
29	23.32	γ-Muuroloene	C <sub>15</sub> H <sub>24</sub>	1467	1467	2.00	2.89	1.01	MS, RI
30	23.45	GermacreneD	C <sub>15</sub> H <sub>24</sub>	1473	1473	0.44	1.00	0.51	MS, RI

(Continued on following page)

TABLE 1 (Continued) Identified compounds of *P. cattleianum* leaves' essential oil extracted by different methods.

Peak	R <sub>t</sub>	Compound	M.F.	RI <sub>exp</sub>	RI <sub>lit</sub>	%Content			Identifications
						HD	MAHD	SFE	
31	23.61	γ-Selinene	C <sub>15</sub> H <sub>24</sub>	1479	1479	1.06	1.29	3.75	MS, RI
32	23.81	γ-Maaliene	C <sub>15</sub> H <sub>24</sub>	1487	1435	1.59	1.82	-	MS, RI
33	24.09	β-Bisabolene	C <sub>15</sub> H <sub>24</sub>	1498	1498	1.42	2.30	2.48	MS, RI
34	24.16	β-Curcumene	C <sub>15</sub> H <sub>24</sub>	1501	1504	0.52	-	-	MS, RI
26	22.85	β-Santalene	C <sub>15</sub> H <sub>24</sub>	1449	1449	0.58	0.65	0.07	MS, RI
27	22.95	Alloaromadendrene	C <sub>15</sub> H <sub>24</sub>	1452	1452	0.44	0.58	0.55	MS, RI
46	26.46	Humulene epoxide I	C <sub>15</sub> H <sub>24</sub> O	1591	1592	0.19	0.19	0.27	MS, RI
47	26.56	Ledol	C <sub>15</sub> H <sub>26</sub> O	1595	1595	1.23	1.06	1.12	MS, RI
48	26.71	(-)-Humulene epoxide II	C <sub>15</sub> H <sub>24</sub> O	1601	1602	1.47	1.41	1.94	MS, RI
49	27.14	Di- <i>epi</i> -1,10-cubenol	C <sub>15</sub> H <sub>26</sub> O	1619	1619	1.81	1.72	2.07	MS, RI
50	27.27	Humulenol-II	C <sub>15</sub> H <sub>24</sub> O	1624	1620	1.50	1.53	-	MS, RI
51	27.37	Caryophylla-4(12),8(13)-dien-5-α-ol	C <sub>15</sub> H <sub>24</sub> O	1629	1632	0.67	0.69	-	MS, RI
52	27.47	<i>T</i> -Muurolol	C <sub>15</sub> H <sub>26</sub> O	1633	1634	4.09	3.39	3.73	MS, RI
53	27.52	α-Cadinol	C <sub>15</sub> H <sub>26</sub> O	1635	1635	1.34	1.36	3.19	MS, RI
54	28.40	α-Bisabolol	C <sub>15</sub> H <sub>26</sub> O	1673	1673	6.39	7.46	7.48	MS, RI
55	28.82	Eudesm-7(11)-en-4-ol	C <sub>15</sub> H <sub>26</sub> O	1692	1692	1.19	0.47	1.10	MS, RI
56	29.22	Farnesol	C <sub>15</sub> H <sub>26</sub> O	1710	1711	0.59	0.87	1.24	MS, RI
57	31.81	<i>trans</i> -Farnesyl acetate	C <sub>17</sub> H <sub>28</sub> O <sub>2</sub>	1824	1824	1.19	0.47	1.10	MS, RI
		Total identified compounds				95.48	93.85	86.73	
		Non-oxygenated							
		Monoterpene hydrocarbons (MH)				9.72	6.05	0.84	
		Sesquiterpene hydrocarbons (SH)				56.47	61.15	54.53	
		Oxygenated							
		Oxygenated monoterpenes (OM)				1.20	0.66	0.56	
		Oxygenated sesquiterpenes (OS)				28.09	25.99	30.8	

R<sub>t</sub>, retention time; RI<sub>exp</sub>, experimental refractive index; RI<sub>lit</sub>, reference refractive index; MF: molecular formula.

the leaves' essential oil, a total of 51 (95.57%), 50 (93.85%), and 41 (86.73%) volatile compounds were identified in HD, MAHD, and SEF oil samples, respectively (Table 1, Supplementary Figures S1–S3). Interestingly, careful interpretation of the data showed that there is no major difference among the three extraction methods in the percentage of the major identified components. For instance, it was found that humulene represented 10.9%–15.00%, β caryophyllene 11.77%–13.2%, germacrene B 6.02%–8.19%, and α-bisabolol 6.39%–7.46% in HD, MAHD, and SEF methods, respectively. On the other hand, there is a significant difference in the main EO classes as the percentage of the oxygenated compounds was 29.38, 26.65, and 31.36% for HD, MAHD, and SFE, respectively, while the percentage of non-oxygenated compounds was double the percentage of the oxygenated compounds being 66.19% (HD), 67.20% (MAHD), and 55.37% (SFE). Moreover, there is an additional exciting difference in the chemical subclass of the identified volatiles.

Herein, the monoterpene (MH) and sesquiterpene (SH) hydrocarbon percentages were different among the implemented extraction methods. For instance, all oil samples displayed a low percentage of MH being 9.72, 6.05, and 0.84% in HD, MAHD, and SFE, respectively, while SH represented the highest percentage, which was calculated as 56.47% (HD), 61.15% (MAHD), and 54.53% (SFE). Concerning the oxygenated sesquiterpenes (OS), it was found that the leaves' EOs encompass considerable contents of OS being 28.09, 25.99, and 30.8% in HD, MAHD, and SFE, respectively, in comparison with oxygenated monoterpenes (OM), which represented a very low percentage in the three extraction methods.

The EOs obtained from *P. cattleianum* flowers, which were investigated here for the first time, displayed a total of 30 (87.55%), 49 (81.96%), and 27 (68.46%) volatile compounds in the HD, MAHD, and SFE derived samples, respectively (Table 2, Supplementary Figures S4–S6). Keen analysis of the obtained data has shown that

TABLE 2 Identified compounds of *P. cattleianum* flowers' essential oil extracted by different methods.

Peak	R <sub>t</sub>	Compound	M.F.	RI <sub>exp</sub>	RI <sub>lit</sub>	%Content			Identifications
						HD	MAHD	SFE	
1	7.31	α-Pinene	C <sub>10</sub> H <sub>16</sub>	915	915	3.45	2.90	-	MS, RI
2	8.59	β-Pinene	C <sub>10</sub> H <sub>16</sub>	961	961	-	0.26	-	MS, RI
3	9.05	β-Myrcene	C <sub>10</sub> H <sub>16</sub>	978	978	-	0.21	-	MS, RI
4	9.44	Pseudolimonen	C <sub>10</sub> H <sub>16</sub>	992	996	-	0.05	-	MS, RI
5	10.20	D-Limonene	C <sub>10</sub> H <sub>16</sub>	1017	1027	0.59	0.06	-	MS, RI
6	10.51	trans-β-Ocimene	C <sub>10</sub> H <sub>16</sub>	1027	1027	-	0.14	-	MS, RI
7	10.83	cis-β-Ocimene	C <sub>10</sub> H <sub>16</sub>	1038	1038	-	0.51	-	MS, RI
8	12.44	β-Linalool	C <sub>10</sub> H <sub>18</sub>	1090	1090	1.25	1.66	-	MS, RI
9	12.68	trans-Dihydrocarvone	C <sub>10</sub> H <sub>16</sub> O	1097	1193	-	0.07	-	MS, RI
10	13.65	Isopinocarveol	C <sub>10</sub> H <sub>16</sub> O	1129	1136	-	0.04	-	MS, RI
11	14.84	Terpinen-4-ol	C <sub>10</sub> H <sub>18</sub> O	1167	1167	-	0.07	-	MS, RI
12	15.26	α-Terpineol	C <sub>10</sub> H <sub>18</sub> O	1180	1180	-	0.25	-	MS, RI
13	18.06	trans-Linalool oxide acetate	C <sub>12</sub> H <sub>20</sub> O <sub>3</sub>	1277	1282	-	0.04	-	MS, RI
14	19.85	α-Cubebene	C <sub>15</sub> H <sub>24</sub>	1339	1339	-	0.06	-	MS, RI
15	20.05	α-Longipinene	C <sub>15</sub> H <sub>24</sub>	1346	1347	-	0.05	-	MS, RI
16	20.37	(+)-Cyclosativene	C <sub>15</sub> H <sub>24</sub>	1358	1358	-	0.06	-	MS, RI
17	20.49	Ylangene	C <sub>15</sub> H <sub>24</sub>	1362	1362	-	0.13	-	MS, RI
18	20.59	Copaene	C <sub>15</sub> H <sub>24</sub>	1365	1365	1.85	1.95	0.64	MS, RI
19	20.97	Geranyl acetate	C <sub>12</sub> H <sub>20</sub> O <sub>2</sub>	1372	1372	-	0.74	-	MS, RI
20	21.42	7-epi-Sesquithujene	C <sub>15</sub> H <sub>24</sub>	1394	1391	-	0.18	-	MS, RI
21	21.54	α-Gurgujene	C <sub>15</sub> H <sub>24</sub>	1398	1398	0.19	-	-	MS, RI
22	21.56	β-Maaliene	C <sub>15</sub> H <sub>24</sub>	1399	1381	-	0.32	-	MS, RI
23	21.64	cis-α-Bergamotene	C <sub>15</sub> H <sub>24</sub>	1402	1403	0.25	-	-	MS, RI
24	21.82	β-Caryophyllene	C <sub>15</sub> H <sub>24</sub>	1409	1409	18.85	8.18	14.99	MS, RI
25	22.33	Aromadendrene	C <sub>15</sub> H <sub>24</sub>	1429	1429	0.61	0.76	0.57	MS, RI
26	22.73	α-Humulene	C <sub>15</sub> H <sub>24</sub>	1445	1445	14.46	11.02	7.21	MS, RI
27	22.95	Alloaromadendrene	C <sub>15</sub> H <sub>24</sub>	1452	1452	0.38	0.49	0.75	MS, RI
28	23.31	γ-Muurolene	C <sub>15</sub> H <sub>24</sub>	1467	1467	0.59	1.09	0.59	MS, RI
29	23.45	Germacrene D	C <sub>15</sub> H <sub>24</sub>	1473	1473	-	0.97	0.24	MS, RI
30	23.59	Eudesma-4(14),11-diene	C <sub>15</sub> H <sub>24</sub>	1478	1478	0.91	3.74	0.55	MS, RI
31	23.84	β-Cyclogermacrene	C <sub>15</sub> H <sub>24</sub>	1488	1488	-	-	1.84	MS, RI
32	24.09	β-Bisabolene	C <sub>15</sub> H <sub>24</sub>	1498	1498	1.31	2.07	1.14	MS, RI
33	24.16	β-Curcumene	C <sub>15</sub> H <sub>24</sub>	1501	1504	0.57	-	-	MS, RI
34	24.28	cis-γ-Bisabolene	C <sub>15</sub> H <sub>24</sub>	1505	1507	1.06	1.09	0.75	MS, RI
35	24.50	Cadina-1(10),4-diene	C <sub>15</sub> H <sub>24</sub>	1514	1514	3.11	3.07	2.15	MS, RI
36	24.57	Cadina-3,9-diene	C <sub>15</sub> H <sub>24</sub>	1517	1518	-	3.07	-	MS, RI
37	24.83	Eudesma-4(14),7(11)-diene	C <sub>15</sub> H <sub>24</sub>	1527	1544	1.47	1.92	0.92	MS, RI
38	25.00	Selina-3,7(11)-diene	C <sub>15</sub> H <sub>24</sub>	1533	1532	1.64	1.92	1.44	MS, RI

(Continued on following page)



TABLE 2 (Continued) Identified compounds of *P. cattleianum* flowers' essential oil extracted by different methods.

Peak	R <sub>t</sub>	Compound	M.F.	RI <sub>exp</sub>	RI <sub>lit</sub>	%Content			Identifications
						HD	MAHD	SFE	
39	25.41	Germacrene B	C <sub>15</sub> H <sub>24</sub>	1549	1549	9.22	2.49	4.30	MS, RI
40	25.91	Spatulenol	C <sub>15</sub> H <sub>26</sub> O	1569	1569	-	-	0.32	MS, RI
41	26.07	Caryophyllene oxide	C <sub>15</sub> H <sub>26</sub> O	1575	1575	3.42	-	-	MS, RI
42	26.29	Viridiflorol	C <sub>15</sub> H <sub>26</sub> O	1584	1584	0.59	-	0.2	MS, RI
43	26.56	Ledol	C <sub>15</sub> H <sub>26</sub> O	1594	1595	-	0.16	0.69	MS, RI
44	26.57	(-)-Globulol	C <sub>15</sub> H <sub>26</sub> O	1594	1580	1.23	-	1.75	MS, RI
45	26.71	Humulene 6,7-epoxide	C <sub>15</sub> H <sub>26</sub> O	1600	1600	1.07	2.14	0.24	MS, RI
46	27.13	Di- <i>epi</i> -1,10-cubenol	C <sub>15</sub> H <sub>26</sub> O	1619	1619	1.99	2.97	0.98	MS, RI
47	27.26	Cis-2,3,4,4a,5,6,7,8-octahydro-1,1,4a,7-tetramethyl-, 1H-benzocyclohepten-7-ol	C <sub>15</sub> H <sub>26</sub> O	1624	1616	1.09	-	-	MS, RI
48	27.34	Acorenone B	C <sub>15</sub> H <sub>24</sub> O	1624	1620	-	0.85	-	MS, RI
49	27.47	<i>tau</i> -Muurolool	C <sub>15</sub> H <sub>26</sub> O	1633	1634	1.21	2.27	-	MS, RI
50	27.52	α-Cadinol	C <sub>15</sub> H <sub>26</sub> O	1635	1635	2.36	4.07	1.50	MS, RI
51	27.78	Neointermedeol	C <sub>15</sub> H <sub>24</sub> O	1646	1656	-	4.07	1.5	MS, RI
52	28.09	<i>cis</i> -Sesquisabinene hydrate	C <sub>15</sub> H <sub>26</sub> O	1660	1590	1.84	2.56	0.89	MS, RI
53	28.40	α-Bisabolol	C <sub>15</sub> H <sub>26</sub> O	1673	1673	9.05	8.03	7.65	MS, RI
54	28.77	Eudesm-7(11)-en-4-ol	C <sub>15</sub> H <sub>26</sub> O	1690	1690	1.94	0.86	0.98	
55	29.26	Farnesol	C <sub>15</sub> H <sub>26</sub> O	1711	1711	-	1.66	-	
56	30.04	α-Cyperone	C <sub>15</sub> H <sub>22</sub> O	1745	1755	-	0.07	-	MS, RI
57	30.40	6-Isopropenyl-4,8a-dimethyl-1,2,3,5,6,7,8,8a-octahydro-naphthalen-2-ol	C <sub>15</sub> H <sub>26</sub> O	1760	1714	-	0.29	-	MS, RI
58	31.81	<i>trans</i> -Farnesyl acetate	C <sub>17</sub> H <sub>28</sub> O <sub>2</sub>	1824	1824	-	0.33	-	MS, RI
59	31.98	β-Sitosterol	C <sub>29</sub> H <sub>50</sub> O	3277	3203	-	-	13.68	MS, RI
		Total identified compounds				87.55	81.96	68.46	
		Non-oxygenated							
		Monoterpene hydrocarbons (MH)				5.29	5.79	-	
		Sesquiterpene hydrocarbons (SH)				56.47	44.63	38.08	
		Sterols				-	-	13.68	
		Oxygenated							
		Oxygenated monoterpenes (OM)				-	1.21	-	
		Oxygenated sesquiterpenes (OS)				25.79	30.33	16.7	

R<sub>t</sub>, retention time; RI<sub>exp</sub>, experimental refractive index; RI<sub>lit</sub>, reference refractive index; M.F., molecular formula.

β-caryophyllene (18.85%), humulene (14.46), germacrene B (9.22%), and α-bisabolol (9.05%) represented the major volatile components in the flower's HD EO, while in the case of MAHD, humulene (11.02%), β-caryophyllene (8.18%), and α-bisabolol (8.03%) were the most abundant volatiles. However, β-caryophyllene (14.99%), humulene (7.02%), and α-bisabolol (7.65%) represented the major volatile components in SFE. These values were reflected in the total percentage of non-oxygenated volatile compounds, which in all methods, showed high percentages (61.76%, 50.42%, and 51.76% in

HD, MAHD, and SFE, respectively) than the oxygenated compounds (25.79% (HD), 31.54% (MAHD), and 16.7% (SFE)). Moreover, the percentage of monoterpene hydrocarbons (MH) is nearly the same in HD and MAHD (5.29%–5.79%), while completely absent in SFE samples. Interestingly, the sesquiterpene hydrocarbons (SH) represented the major percentage in HD (56.47%), followed by MAHD (44.63%) and SFE (38.08%). Also, it was noticed that β-sitosterol was detected only in SFE oil with 13.68%, while oxygenated monoterpenes were detected only in MAHD (1.21%). Lastly, OS

**TABLE 3** IC<sub>50</sub> of *P. cattleianum* leaves (L) and flowers' (F) essential oils against 5-LOX, COX-1, and COX-2 enzymatic activities.

Tested EO	IC <sub>50</sub> ± SD (μL/mL)		
	5-LOX	COX-1	COX-2
L	2.38 ± 0.10	45.96 ± 2.32	9.116 ± 0.25
F	7.69 ± 0.22	19.08 ± 0.96	2.575 ± 0.07
Indomethacin (μg/mL)	—	1.067 ± 0.05	6.653 ± 0.18
SC560 (nM)	—	6.45 ± 0.05	—
Celecoxib (μM)	—	11.34 ± 0.57	0.547 ± 0.01
Zileuton (μM)	0.42 ± 0.02	-	—

represents the major percentage in HD (25.79%) and MAHD (30.33%) than that present in SEF oil (16.33%).

From the analysis of our results, it was found that  $\beta$  caryophyllene, humulene, germacrene B, and  $\alpha$ -bisabolol (Supplementary Figure S7) represented the major components in both leaves and flowers' EOs but with variable percentages based either on the investigated organ or the preparation method. Moreover, the SEF oil of the flower showed a high percentage of  $\beta$ -sitosterol. Yet, in comparison to the previously published data about *P. cattleianum*, it was found that  $\beta$ -caryophyllene represents the major compound in most HD-based reports about leaves' EOs (Soliman et al., 2016), while caryophyllene oxide (Chalannavar et al., 2013) was detected as a major compound in few reports. Conclusively, the qualitative and quantitative variations in the essential oils derived from the leaves and flowers of *P. cattleianum* compared to other prior studies may be attributed to various factors, such as genetic variations, environmental conditions, harvesting time, drying period, or extraction temperature (Patel et al., 2016).

## 3.2 Biological activity

As it was revealed from the EO yield extracted by the three methods, it was found that SFE offered the highest yield being 0.62% and 1.4% from the leaves and flowers, respectively, so it was selected for further biological assessment.

### 3.2.1 In vitro anti-inflammatory activity

The lipoxygenase (LOX) pathway is the main source of potent proinflammatory leukotrienes (LTs) supplied from arachidonic acid metabolism (AA). Therefore, its inhibition can help with anti-inflammatory effects (Hu and Ma, 2017). In the current study, the EOs from the leaves and flowers of *P. cattleianum* cultivated in Egypt were screened against the 5-LOX enzyme, and the results (Table 3) showed that leaves' EOs exerted a strong 5-LOX inhibitory effect with IC<sub>50</sub> 2.380 μL/mL, while the flowers' EOs displayed weak activity (IC<sub>50</sub>, 7.697 μL/mL) in comparison with the positive control, zileuton (IC<sub>50</sub>, 0.423 μM/mL). Other recognized enzymes that significantly mediate the inflammatory response are the cyclooxygenase isozymes COX-1 and COX-2; the first isozyme is constitutively stated in all organs and particularly responsible for the gastrointestinal protection, while the other isozyme is prevailing at inflammation sites (COX-2) (Hawkey, 2001). In the current investigation, both organs' SFE oils were screened

**TABLE 4** IC<sub>50</sub> of *P. cattleianum* leaves (L) and flowers' (F) essential oils against cancer cell lines (MCF-7, HepG2, K562) and normal cell line (WI38).

Tested EO	IC <sub>50</sub> ± SD (μL/mL)			
	Cancer cell lines			Normal cells
	MCF-7	HepG2	K562	
L	5.32 ± 0.29	25.70 ± 1.38	12.30 ± 0.66	59.70 ± 3.22
F	36.20 ± 1.95	58.10 ± 3.13	31.70 ± 1.71	43.40 ± 2.34
Doxorubicin (μg/mL)	4.46 ± 0.24	7.5 ± 0.4	0.72 ± 0.04	13.8 ± 0.74

for their COX inhibitory activities, and the results showed that the leaves' EOs exerted low COX-1 inhibitory activity (IC<sub>50</sub> 45.96 μL/mL) in comparison with SC560 (standard, selective COX-1 inhibitor, IC<sub>50</sub> 0.12 nM), moderate COX-2 inhibitory activity (IC<sub>50</sub> 9.116 μL/mL) in comparison with indomethacin (IC<sub>50</sub>, 6.653 μg/mL), and finally almost no significant effect in comparison with celecoxib (IC<sub>50</sub>, 0.547 μM/mL). It is noteworthy that the flower's EOs showed moderate COX-1 activity (IC<sub>50</sub>, 19.08 μL/mL) in comparison with celecoxib (IC<sub>50</sub>, 11.34 μg/mL) and SC560 (IC<sub>50</sub>, 6.34 nM), while high IC<sub>50</sub> in comparison with indomethacin (IC<sub>50</sub>, 1.067 μg/mL). Moreover, in the case of COX-2, it exhibited strong inhibitory activity (IC<sub>50</sub>, 2.575 μL/mL) as compared to indomethacin (IC<sub>50</sub>, 6.653 μg/mL) and celecoxib (IC<sub>50</sub>, 0.547 μM/mL).

### 3.2.2 In vitro cytotoxic activity

The Eos of the leaves and flowers of *P. cattleianum* were initially screened for their cytotoxic potential against the available in-house cancer cell lines, namely, MCF-7, HepG2, and K562, and the normal cell line WI38. The results (Table 4) revealed that both organs' EOs exhibited strong anticancer activity against the three cell lines to a different extent. Yet, the leaves' oil displayed selective potent growth inhibitory activity to MCF-7 cells (IC<sub>50</sub>, 5.32 μL/mL), followed by K562 (IC<sub>50</sub>, 12.30 μL/mL) and lastly HepG2 (IC<sub>50</sub>, 25.7 μL/mL). However, it showed far low IC<sub>50</sub> on the normal WI38 cells (IC<sub>50</sub>, 59.7 μL/mL), demonstrating its selectivity to the cancer cell lines, exclusively MCF-7 (SI, 11.2), which is better than the SI of doxorubicin (SI, 13.8). On the other hand, the screening of the flowers' EOs in the same assay demonstrated that K562 (IC<sub>50</sub>, 31.70 μL/mL) is the most sensitive cell line, followed by MCF-7 (IC<sub>50</sub>, 36.20 μL/mL), while HepG2 is the least sensitive cell line to the applied treatment (IC<sub>50</sub>, 58.10 μL/mL). Even though this is the first time in reporting the screening of the flowers' EOs on various cancer cell lines, the promising, selective anticancer potential of leaves' EOs was our compelling rationale. Hence, a complete mechanistic study was accomplished to understand the mode of cell death and the proposed molecular targets involved in the observed anticancer potential.

### 3.2.3 Cell cycle analysis and detection of apoptosis in MCF-7 cells

Propidium iodide (PI) is commonly used in combination with annexin V to measure if the cells are viable, apoptotic, or necrotic via observing the changes in the integrity and permeability of the plasma membrane (Rieger et al., 2011). The intact cell and nuclear membranes inhibit PI entrance; hence, they do not stain either live or early

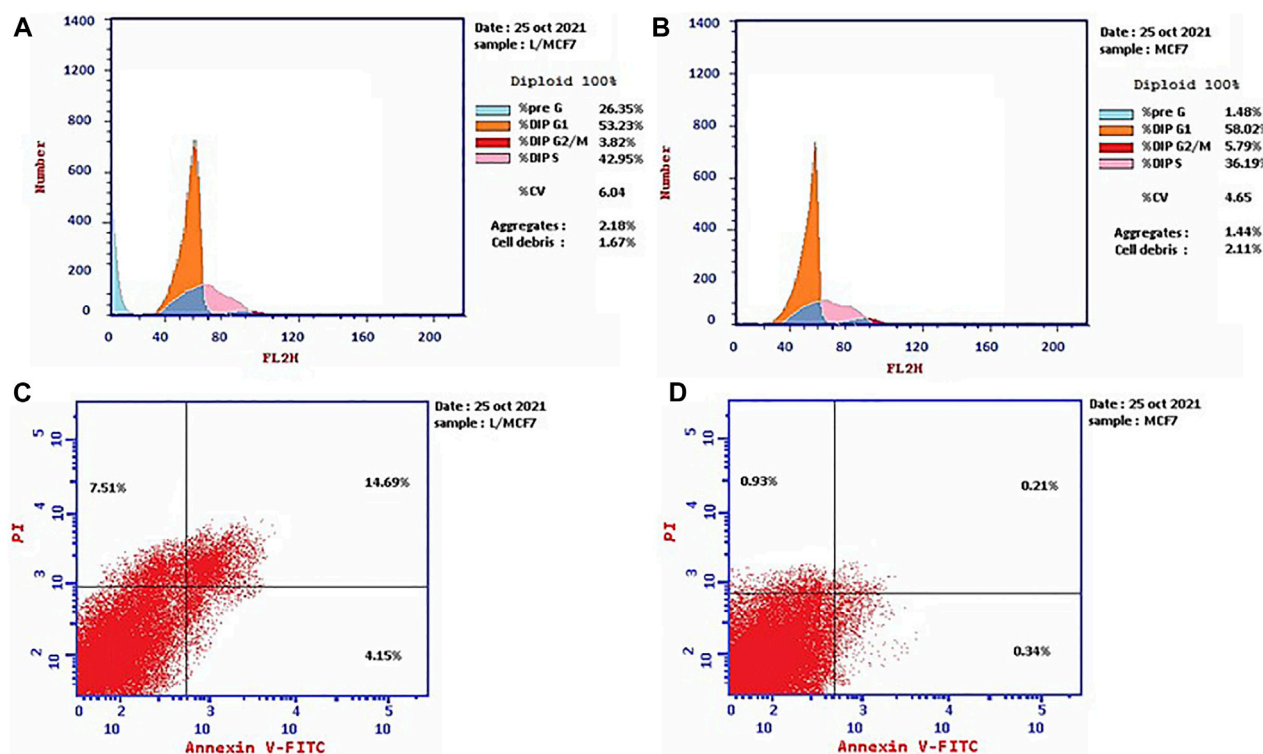


FIGURE 1

Cell cycle distributions of MCF-7 cells (A) treated with EOs obtained from *P. cattleianum* Sabine leaves compared to (B) untreated, control cells.

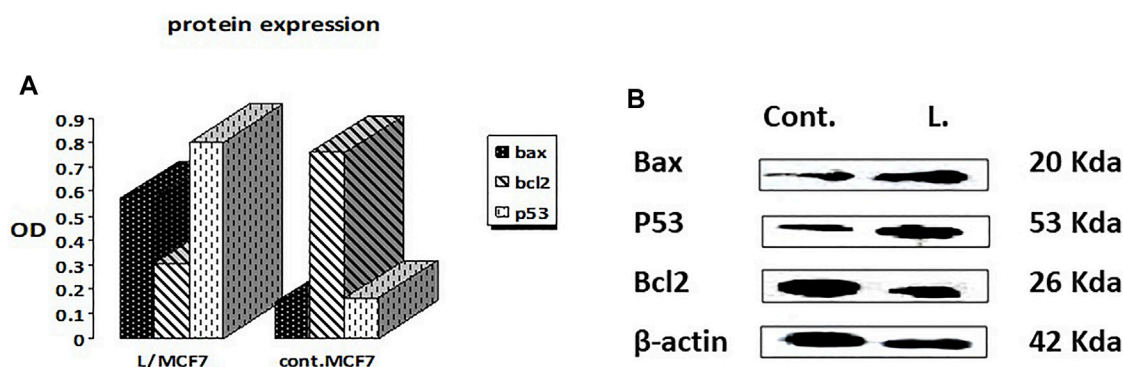
Percentage of early, late apoptotic, and necrotic cells in MCF-7 cells (C) treated with EOs obtained from *P. cattleianum* leaves compared to (D) untreated, control.

apoptotic cells; on the other hand, in late apoptotic and necrotic cells, the integrity of the plasma and nuclear membranes is reduced, allowing PI to permit and intercalate into nucleic acids, and revealed red fluorescence (Rieger et al., 2011). In this study, the MCF-7 cells, treated with the leaves' EOs, were subjected to cell cycle analysis to gain understanding of the cytotoxicity mechanism and mode of cell death. The results (Figure 1, Supplementary Table S1) demonstrated that the cell percentage in the  $G_0$ - $G_1$  and  $G_2/M$  phases decreased upon treatment, being 53.23% and 3.82%, respectively, in comparison with the untreated control group. Moreover, it exhibited an increase in the cellular population of the S and pre- $G_1$  phases to 42.95% and 26.35% compared to the control (36.19% and 1.48%, respectively). Subsequently, the apoptosis percentage increased from 1.48% in the control cells to 26.35%, whereas the percentage of necrotic cells increased to 7.51% compared to 0.93% in untreated cells (Figure 1, Supplementary Table S1).

### 3.2.4 Expression of apoptosis-related proteins using the Western blot technique

The Western blotting technique was adopted to quantify the total levels of the apoptosis-mediated proteins, namely, Bax, Bcl2, and p53 (Mahmood and Yang, 2012). The results showed that the leaves' EOs significantly overexpressed the Bax and p53 protein levels by 3.9 and 4.8 folds, respectively, in comparison with the control and untreated group, while the level of the Bcl-2 protein level was decreased to about 0.4 in the control (Figure 2, Supplementary Figure S8). Therefore, we expect that leaves' EOs modulated the apoptotic pathway by regulating

the p53-Bax/Bcl2 axis in MCF-7. Several reports were conducted on the biological activities of *cattleianum* leaves' EOs, which revealed its significant antioxidant, antifungal, antibacterial (Castro et al., 2014), and anticancer activities against HeLa (human cervical adenocarcinoma cells), HepG2, AGS (human gastric cancer cells), SNU-1 (colorectal cancer cells), and SNU-16 (human stomach cancer cells) (Fidy et al., 2016). Meanwhile, there are no studies about the anti-inflammatory and anticancer activities of flower-derived EOs and the anti-inflammatory and anticancer activities of leaves' EOs, especially against MCF-7 and K562. The chemical components of leaves and flowers' EOs prepared by the SFE method are responsible for their biological activities. It was found that both oils pioneered principally with  $\beta$ -caryophyllene (BCP), representing 13.2% and 14.99% for leaves and flowers, respectively, together with  $\alpha$ -humulene ( $\alpha$ -caryophyllene), which represented 10.9% (leaves) and 7.21% (flower). Moreover, the leaves' EOs are also traced with caryophyllene oxide (BCPO, the oxidation derivative of  $\beta$ -caryophyllene) being 4.81%, which is almost absent from the flowers' EOs. BCPO is one of the major active components in various EOs derived from numerous food and spices. It possessed different biological effects such as anti-inflammatory (Medeiros et al., 2007) and anticarcinogenic (Langhasova et al., 2014) effects. BCP belongs to cannabinoid compounds (CBS), especially phytocannabinoids. However, cannabinoids could stimulate the cannabinoid receptors ( $CB_1$  and  $CB_2$ ), while BCP activates only  $CB_2$  and has no affinity to  $CB_1$ , which explains that BPC action is lacking psychoactive side effects allied with cannabinoids and recommends its potential use in medicine (Fidy et al., 2016). Moreover,  $\alpha$ -humulene and BCPO have no affinity to

**FIGURE 2**

Effects of treatment by the EOs obtained from *P. cattleianum* Sabine leaves on the protein expression levels of (A) p53, Bax, Bcl-2, and  $\beta$ -actin; (B) protein relative abundance as measured from band intensity compared to  $\beta$ -actin.

CB<sub>1</sub> and CB<sub>2</sub>, which explain that both compounds exhibited their biological activities through partially different mechanisms such as apoptosis induction, repression of the cell cycle, and inhibition of angiogenesis and metastasis (Carracedo et al., 2006). Many investigations have been performed to unravel the anticancer mechanism of BCPO, while that of BCP has hardly been studied (Fidyt et al., 2016). Many reports have mentioned the strong anti-proliferative activity of BCP against many cell lines due to its antiangiogenic properties, which are attributed to its interaction with the hypoxia-inducible transcription factor-1 $\alpha$  (HIF-1 $\alpha$ ) that controls the biological pathways associated with hypoxia, tumor metastasis, tumor-mediated angiogenesis, and vascular endothelial growth factor transcription (VEGF) (Ghosh et al., 2022). Moreover, it was reported that BCPO possessed methylene and epoxide exocyclic functional groups, which bind covalently to the DNA nitrogenous bases and proteins by sulfhydryl and amino groups. Thus, BCPO exhibited great potential as a signaling modulator in tumor cancer cells (Park et al., 2011). Other reports revealed that BCPO has anticancer effects on MCF-7 and prostate cancer cell lines through the indication of ROS generation, MAPK activation, and inhibition of the PI3K/AKT/mTOR/S6K1 signaling pathway, which is vital to cell survival, proliferation, and angiogenesis of the tumor (Lo Piccolo et al., 2008). Additionally, it significantly decreases key protein levels involved in proliferation (cyclinD1), metastasis, angiogenesis (VEGF), and apoptosis inhibitors Bcl-2 (B-cell lymphoma 2) and IAP-1/2 (inhibitor of apoptosis 1 and 2) (Ryu et al., 2012). Moreover, it was reported that BCOP can exert pro-apoptotic activity in cancer cells through a reduction in NF- $\kappa$ B as a key transcription factor in the development of tumors through monitoring cancer cell proliferation, tumorigenesis, angiogenesis, and metastasis (Sain et al., 2014), and it regulated several genes implicated in cellular proliferation, apoptosis, and inflammation. Furthermore, it was reported that  $\alpha$ -humulene and BCPO exhibited significant anti-proliferative activities against different cell lines witnessed by their combination with BCP in decreasing MCF-7 proliferation compared to when used separately (Legault et al., 2007). An observation that is in good agreement with our results is that leaves' EOs exerted more potent cytotoxic effects than flowers' EOs which may be due to the absence of BCPO from the flower. Moreover, it was stated

that there is a possibility of a synergistic effect between the volatile components in EOs instead of only one major component or isolated compounds in modulating the cancer pathway. Additionally, it was reported that the strength of the cellular response induced after treatment with BCP(O) compounds differs significantly among cancer cells, which was also figured out from our results.

## 4 Conclusion

Essential oils (EOs) from *P. cattleianum* leaves and flowers, cultivated in Egypt, have been extracted by three different methods and evaluated in terms of their chemical composition and biological significance. The implemented extraction methods greatly affected the yield, in addition to the qualitative and quantitative chemical properties of the EOs. Supercritical fluid extraction (SFE), represented an environment-friendly method and offered the highest EO yield from both organs with minimal degradation drawbacks, while the least yield was indicated by the conventional hydro-distillation method. *P. cattleianum* EOs were superlative by terpenoid hydrocarbons such as  $\alpha$ -humulene,  $\beta$ -caryophyllene, and germacrene B, while  $\alpha$ -bisabolol and caryophyllene oxide represented the major, identified oxygenated terpenes. The leaves' EOs showed potent, anti-inflammatory capacity *via* inhibiting the 5-LOX enzyme, while the flowers inhibited the COX-2 enzyme. In addition, the leaves' EOs induced apoptosis in the MCF-7 breast cancer cell line by modulating the P53-Bax/Bcl2 axis. The observed promising activities is, at least in part, due to the synergism between the volatile components; hence, *P. cattleianum*-derived EOs may be promoted as dietary supplements for the management of breast malignancies and inflammatory disorders.

## Data availability statement

The original contributions presented in the study are included in the article/Supplementary Materials; further inquiries can be directed to the corresponding author.



## Author contributions

FM, HE, ME, HeT, and HuT expressed the research point and experimental design. EE-D prepared the essential oils. EE-D, HE, FM, and ME identified the essential oil components. HeT carried out the *in vitro* biological studies. FM, HE, EE-D, and HeT have written the manuscript. All authors approved writing and revising the manuscript.

## Conflict of interest

The authors declare that the research was conducted in the absence of any commercial or financial relationships that could be construed as a potential conflict of interest.

## References

- Abbas, A., Anwar, F., Alqahtani, S. M., Ahmad, N., Al-Mijalli, S. H., Shahid, M., et al. (2022). Hydro-distilled and supercritical fluid extraction of *Eucalyptus camaldulensis* essential oil: Characterization of bio-actives along with antioxidant, antimicrobial and antibiofilm activities. *Dose-Response* 20 (3), 155932582211254. doi:10.1177/15593258221125477
- Abdullaev, F. I. (2001). "Plant-derived agents against cancer," in *Pharmacology and therapeutics in the new millennium*. Editor S. K. Gupta (New Delhi, India: Narosa Publishing House), 345–354.
- Adams, R. P. (2005). Identification of essential oil components by gas chromatography/quadrupole mass spectroscopy Robert P. Adams. *Journal of the American Society for Mass Spectrometry* 16, 1902–1903. doi:10.1016/j.jasms.2005.07.008
- Agrawal, D. K., and Mishra, P. K. (2010). Curcumin and its analogues: Potential anticancer agents. *Medicinal Research Reviews* 30 (5), 818–860. doi:10.1002/med.20188
- Amorim, A., Hovell, A. M. C., Miranda, A. L. P., Kleiton, C., Lima, F., Hovell, H. A., et al. (2009). Antinociceptive and hypothermic evaluation of the leaf essential oil and isolated terpenoids from *Eugenia uniflora* L. (Brazilian Pitanga). *Phytomedicine* 16 (10), 923–928. doi:10.1016/j.phymed.2009.03.009
- Araim, A., Sherazi, S. T. H., Mahesar, S. A., and Sirajuddin (2019). Essential oil from psidium guajava leaves: An excellent source of  $\beta$ -caryophyllene. *Natural Product Communications* 14 (5), 1934578X1984300–5. doi:10.1177/1934578X19843007
- Beltrame, B. M., Klein-Junior, L. C., Schwanz, M., and Henriques, A. T. (2021). Psidium L. genus: A review on its chemical characterization, preclinical and clinical studies. *Phytotherapy Research* 35 (9), 4795–4803. doi:10.1002/ptr.7112
- Bray, F., and Møller, B. (2006). Predicting the future burden of cancer. *Nature Reviews Cancer* 6 (1), 63–74. doi:10.1038/nrcr1781
- Carracedo, A., Gironella, M., Lorente, M., Garcia, S., Guzmán, M., Velasco, G., et al. (2006). Cannabinoids induce apoptosis of pancreatic tumor cells via endoplasmic reticulum stress-related genes. *Cancer Research* 66 (13), 6748–6755. doi:10.1158/0008-5472.CAN-06-0169
- Castro, M. R., Victoria, F. N., Oliveira, D. H., Jacob, R. G., Savegnago, L., and Alves, D. (2015). Essential oil of *Psidium cattleianum* leaves: antioxidant and antifungal activity. *Biology* 53 (2), 242–250. doi:10.3109/13880209.2014.914231
- Chalannavar, R. K., Narayanaswamy, V. K., Bajinath, H., and Odhav, B. (2013). Chemical constituents of the essential oil from leaves of *Psidium cattleianum* var. *cattleianum*. *Journal of Medicinal Plants Research* 7 (13), 783–789. doi:10.5897/JMPR12.929
- Chrystal, P., Pereira, A. C., Fernandes, C. C., De Souza, J. M., Martins, C. H. G., Potenza, J., et al. (2020). Essential oil from *Psidium cattleianum* Sabine (Myrtaceae) fresh leaves: Chemical characterization and *in vitro* antibacterial activity against endodontic pathogens. *Brazilian Archives of Biology and Technology* 63 (4), e20190196. doi:10.1590/1678-4324-2020190196
- De Souza, W. F. C., De Lucena, F. A., De Castro, R. J. S., De Oliveira, C. P., Quirino, M. R., and Martins, L. P. (2021). Exploiting the chemical composition of essential oils from *Psidium cattleianum* and *Psidium guajava* and its antimicrobial and antioxidant properties. *Journal of Food Science* 86 (10), 4637–4649. doi:10.1111/1750-3841.15889
- Dhifi, W., Bellili, S., Jazi, S., Bahloul, N., and Mnif, W. (2016). Essential oils' chemical characterization and investigation of some biological activities: A critical review. *Medicines* 3 (4), 25. doi:10.3390/medicines3040025
- Dos Santos Pereira, E., Vinholes, J., Franzon, R. C., Dalmazo, G., Vizzotto, M., and Nora, L. (2018). *Psidium cattleianum* fruits: A review on its composition and bioactivity. *Food Chemistry* 258, 95–103. doi:10.1016/j.foodchem.2018.03.024
- Faleiro, J. H., Gonçalves, R. C., Dos Santos, M. N. G., Da Silva, D. P., Naves, P. L. F., and Malafaia, G. (2016). The chemical featuring, toxicity, and antimicrobial activity of *Psidium cattleianum* (Myrtaceae) leaves. *New Journal of Science* 2016, 1–8. doi:10.1155/2016/7538613
- Fidy, K., Fiedorowicz, A., Strzdała, L., and Szumny, A. (2016).  $\beta$ -caryophyllene and  $\beta$ -caryophyllene oxide-natural compounds of anticancer and analgesic properties. *Cancer Medicine* 5 (10), 3007–3017. doi:10.1002/cam4.816
- Ghazanfari, N., Mortazavi, S. A., Yazdi, F. T., and Mohammadi, M. (2020). Microwave-assisted hydrodistillation extraction of essential oil from coriander seeds and evaluation of their composition, antioxidant and antimicrobial activity. *Heliyon* 6 (9), e04893. doi:10.1016/j.heliyon.2020.e04893
- Ghosh, R., Samanta, P., Sarkar, R., Biswas, S., Saha, P., Hajra, S., et al. (2022). Targeting HIF-1 $\alpha$  by natural and synthetic compounds: A promising approach for anti-cancer therapeutics development. *Molecules* 27, 5192. doi:10.3390/molecules27165192
- Hawkey, C. J. (2001). COX-1 and COX-2 inhibitors. *Journal of Clinical Gastroenterology* 15 (5), 801–820. doi:10.1053/bega.2001.0236
- Hu, C., and Ma, S. (2017). Recent development of lipoxygenase inhibitors as anti-inflammatory agents. *MedChemComm* 9 (2), 212–225. doi:10.1039/c7md00390k
- Juergens, L. J., Worth, H., and Juergens, U. R. (2020). New perspectives for mucolytic, anti-inflammatory and adjunctive therapy with 1,8-cineole in COPD and asthma: Review on the new therapeutic approach. *Advances in Therapy* 37, 1737–1753. doi:10.1007/s12325-020-01279-0
- Koedam, A., Scheffer, J. C. S., and Svendsen, A. B. (1979). Comparison of isolation procedures for essential oils. *Zeitschrift für Lebensmittel-Untersuchung und-Forschung* 168, 106–111. doi:10.1007/BF01127514
- Langhasova, L., Hanusova, V., Rezek, J., Stohanska, B., Ambroz, M., Kralova, V., et al. (2014). Essential oil from *Myrica rubra* leaves inhibits cancer cell proliferation and induces apoptosis in several human intestinal lines. *Industrial Crops and Products* 59, 20–26. doi:10.1016/j.indcrop.2014.04.018
- Legault, J., and Pichette, A. (2007). Potentiating effect of  $\beta$ -caryophyllene on anticancer activity of  $\alpha$ -humulene, isocaryophyllene, and paclitaxel. *Journal of Pharmacy and Pharmacology* 59, 1643–1647. doi:10.1211/jpp.59.12.0005
- Lo Piccolo, J., Blumenthal, G. M., Bernstein, W. B., and Dennis, P. A. (2008). Targeting the PI3K/Akt/mTOR pathway: Effective combinations and clinical considerations. *Drug Resistance Updates* 11 (1–2), 32–50. doi:10.1016/j.drug.2007.11.003
- Mahmood, T., and Yang, P. C. (2012). Western blot: Technique, theory, and trouble shooting. *North American Journal of Medical Sciences* 4 (9), 429–434. doi:10.4103/1947-2714.100998
- Medeiros, R., Passos, G. F., Vitor, C. E., Koepp, J., Mazzuco, T. L., Pianowski, L. F., et al. (2007). Effect of two active compounds obtained from the essential oil of *Cordia verbenacea* on the acute inflammatory responses elicited by LPS in the rat paw. *British Journal of Pharmacology* 151 (5), 618–627. doi:10.1038/sj.bjp.0707270
- Ormerod, M. G. (1994). "Analysis of DNA – general methods," in *Flow cytometry: A practical approach*. 2 (Oxford, United Kingdom: IRL at Oxford University Press), 119–135. 9780199638246.
- Papadimitriou, M., Hatzidaki, E., and Papasotiriou, I. (2019). Linearity comparison of three colorimetric cytotoxicity assays. *Journal of Cancer Therapy* 10, 580–590. doi:10.4236/jct.2019.107047
- Park, K. R., Nam, D., Yun, H. M., Lee, S. G., Jang, H. J., Sethi, G., et al. (2011).  $\beta$ -Caryophyllene oxide inhibits growth and induces apoptosis through the suppression of PI3K/AKT/mTOR/S6K1 pathways and ROS-mediated MAPKs activation. *Cancer Letters* 312 (2), 178–188. doi:10.1016/j.canlet.2011.08.001
- Patel, R. P., Singh, R., Rao, B. R., Singh, R., Srivastava, A., and Lal, R. (2016). Differential response of genotype  $\times$  environment on phenology, essential oil yield and quality of natural aroma chemicals of five *Ocimum* species. *Industrial Crops and Products* 87, 210–217. doi:10.1016/j.indcrop.2016.04.001

## Publisher's note

All claims expressed in this article are solely those of the authors and do not necessarily represent those of their affiliated organizations, or those of the publisher, the editors, and the reviewers. Any product that may be evaluated in this article, or claim that may be made by its manufacturer, is not guaranteed or endorsed by the publisher.

## Supplementary material

The Supplementary Material for this article can be found online at: <https://www.frontiersin.org/articles/10.3389/fchem.2023.1120432/full#supplementary-material>

- Patel, S. (2012). Exotic tropical plant psidium cattleianum: A review on prospects and threats. *Reviews in Environmental Science and Bio/Technology*. 11, 243–248. doi:10.1007/s11157-012-9269-8
- Rieger, A. M., Nelson, K. L., Konowalchuk, J. D., and Barreda, D. R. (2011). Modified annexin V/propidium iodide apoptosis assay for accurate assessment of cell death. *Journal of Visualized Experiments*. 50, 2597. doi:10.3791/2597
- Ryu, N. H., Park, K. R., Kim, S. M., Yun, H. M., Nam, D., Lee, S. G., et al. (2012). A hexane fraction of guava Leaves (*Psidium guajava* L.) induces anticancer activity by suppressing AKT/mammalian target of rapamycin/ribosomal p70 S6 kinase in human prostate cancer cells. *Journal of Medicinal Food*. 15 (3), 231–241. doi:10.1089/jmf.2011.1701
- Sain, S., Naoghare, P. K., Devi, S. S., Daiwile, A., Krishnamurthi, K., Arrigo, P., et al. (2014). Beta caryophyllene and caryophyllene oxide, isolated from *Aegle marmelos*, as the potent anti-inflammatory agents against lymphoma and neuroblastoma cells. *Anti-Inflammatory & Anti-Allergy Agents in Medicinal Chemistry*. 13 (1), 45–55. doi:10.2174/18715230113129990016
- Sambrook, J., Fritsch, E. F., and Maniatis, T. (1989). *Molecular cloning: A laboratory manual*. New York, United States: Cold Spring Harbor Laboratory.
- Sargenti, S., and Lancas, F. N. (1997). Supercritical fluid extraction of *Cymbopogon citratus* (DC) Stapf. *Stapp. Chromatogr.* 46, 285–290. doi:10.1007/BF02496320
- Sarker, S. D., Nahar, L., Miron, A., and Guo, M. (2020). Anticancer natural products. *Annual Reports in Medicinal Chemistry*. 55, 45–75. doi:10.1016/bs.armc.2020.02.001
- Shakeri, A., Sahebkar, A., and Javadi, B. (2016). *Melissa officinalis* L. A review of its traditional uses, phytochemistry, and pharmacology. *Journal of Ethnopharmacology*. 188, 204–228. doi:10.1016/j.jep.2016.05.010
- Silvestre, W. P., Mazzotti, L., and Fernandes Pauletti, G. (2022). Bioprospecting of strawberry guava leaf essential oil in Caxias do Sul region, South Brazil. *Pesquisa Agropecuária Gaúcha*. 28 (1), 58–69. doi:10.36812/pag.202228158-69
- Singh, B. R., Singh, V., Ebibeni, N., and Singh, R. K. (2013). Antimicrobial and herbal drug resistance in enteric bacteria isolated from faecal droppings of common house lizard/gecko (*Hemidactylus frenatus*). *International Journal of Microbiology*. 2013, 1–8. doi:10.1155/2013/340848
- Soliman, F. M., Fathy, M. M., Salama, M. M., and Saber, F. R. (2016). Comparative study of the volatile oil content and antimicrobial activity of *Psidium guajava* L. and *Psidium cattleianum* Sabine leaves. *Bulletin of Faculty of Pharmacy, Cairo University*. 54 (2), 219–225. doi:10.16/j.bfopcu.2016.06.003
- Suetsugu, T., Tanaka, M., Iwai, H., Matsubara, T., Kawamoto, Y., Saito, C., et al. (2013). Supercritical CO<sub>2</sub> extraction of essential oil from Kabosu (*Citrus sphaerocarpa* Tanaka) peel. *Flavour* 2, 18. doi:10.1186/2044-7248-2-18
- Wang, D., and Dubois, R. N. (2010). The role of COX-2 in intestinal inflammation and colorectal cancer. *Oncogene* 29 (6), 781–788. doi:10.1038/onc.2009.421



## OPEN ACCESS

## EDITED BY

Maning Liu,  
Lund University, Sweden

## REVIEWED BY

Zhao Li,  
Xi'an Shiyu University, China  
Yiqun Wang,  
Chengdu University of Technology,  
China

## \*CORRESPONDENCE

Zhifeng Deng,  
✉ dengzf@snut.edu.cn  
Hongzhen Wang,  
✉ 02998@qust.edu.cn

<sup>†</sup>These authors have contributed equally  
to this work

RECEIVED 05 April 2023

ACCEPTED 14 April 2023

PUBLISHED 21 April 2023

## CITATION

Chen J, Wang Z, Deng Z, Chen L, Wu X,  
Gao Y, Hu Y, Li M and Wang H (2023),  
Hydrogen bonding-induced high-  
performance stretchable organic  
semiconductors: a Review.  
*Front. Chem.* 11:1200644.  
doi: 10.3389/fchem.2023.1200644

## COPYRIGHT

© 2023 Chen, Wang, Deng, Chen, Wu,  
Gao, Hu, Li and Wang. This is an open-  
access article distributed under the terms  
of the [Creative Commons Attribution  
License \(CC BY\)](#). The use, distribution or  
reproduction in other forums is  
permitted, provided the original author(s)  
and the copyright owner(s) are credited  
and that the original publication in this  
journal is cited, in accordance with  
accepted academic practice. No use,  
distribution or reproduction is permitted  
which does not comply with these terms.

# Hydrogen bonding-induced high-performance stretchable organic semiconductors: a Review

Jinhan Chen<sup>1†</sup>, Zheng Wang<sup>2†</sup>, Zhifeng Deng<sup>1\*</sup>, Ligui Chen<sup>1</sup>,  
Xuhui Wu<sup>2</sup>, Yihan Gao<sup>1</sup>, Yumeng Hu<sup>1</sup>, Mei Li<sup>1</sup> and  
Hongzhen Wang<sup>2\*</sup>

<sup>1</sup>National and Local Joint Engineering Laboratory for Slag Comprehensive Utilization and Environmental Technology, School of Materials Science and Engineering, Shaanxi University of Technology (SNUT), Hanzhong, Shaanxi, China, <sup>2</sup>Key Laboratory of Rubber-Plastic of Ministry of Education (QUST), School of Polymer Science and Engineering, Qingdao University of Science and Technology, Qingdao, China

Semiconductors are widely used in electron devices. With the development of wearable soft-electron devices, conventional inorganic semiconductors are unable to meet the demand because of their high rigidity and high cost. Thus, scientists construct organic semiconductors with high charge mobility, low cost, eco-friendly, stretchable, etc. Due to the excellent performance of stretchable organic semiconductors, they can be widely used as wearable soft-electron devices, such as stretchable organic field-effect transistors (OFETs), organic solar cells (OSCs), etc. Contains flexible display devices and flexible power sources, which are of great interest for applications of future electron devices. However, there are still some challenges that need to be solved. Commonly, enhancing the stretchability may cause the degradation of charge mobility, because of the destruction of the conjugated system. Currently, scientists find that hydrogen bonding can enhance the stretchability of organic semiconductors with high charge mobility. Thus in this review, based on the structure and design strategies of hydrogen bonding, various hydrogen bonding induced stretchable organic semiconductors are introduced. In addition, the applications of the hydrogen bonding induced stretchable organic semiconductors are reviewed. Finally, the stretchable organic semiconductors design concept and potential evolution trends are discussed. The final goal is to outline a theoretical scaffold for the design of high-performance wearable soft-electron devices, which can also further advance the development of stretchable organic semiconductors for applications.

## KEYWORDS

hydrogen bonding, stretchable organic semiconductors, charge mobility, soft-electron devices, OSCs, OFETs

## 1 Introduction

Organic semiconductors are organic materials with semiconductor properties (Chen et al., 2023). Compared with inorganic semiconductors, organic semiconductors have many advantages, such as being tailorable, easy to modify, and having low energy consumption (Zheng et al., 2022). Researchers have developed many meaningful organic semiconductor molecules, such as thiophenes, azole, fullerenes, perylene, phthalocyanines, etc. (Dai et al., 2022; Miao et al., 2023) With the further development of organic semiconductor devices, people are concentrating more on the stretchability of organic semiconductors with high

charge mobility (Yang J. C. et al., 2019). The stretchable organic semiconductors make the flexible display, flexible organic sensors, and stretchable organic solar cells possible, which have shown great potential for commercialization (Yu et al., 2019).

In application, stretchable organic semiconductors will experience the recycling of stretch and retract. Therefore, for practical application, stretchable organic semiconductors need to function more than just single stretchable, but rather high elasticity and reversibility (Yu et al., 2021). However, organic semiconductor materials commonly are conjugated structures with high rigidity. Enhancing the stretchability may destroy the rigid  $\pi$ -conjugated system, then cause the reduction of charge mobility. Thus, designing high-stretch organic semiconductors with high charge mobility becomes a challenge (Pei et al., 2022). In addition, it is crucial to maintain high charge mobility upon the stretching status. To solve these problems, scientists have developed many useful strategies, such as embedding the crystallites into the amorphous regions, introducing side-chain, etc. (Yang Y. et al., 2019). Currently, many scientists use hydrogen bonding as the non-covalent cross-linking sites to design stretchable organic semiconductors, which have great performance in application (Charron et al., 2018).

Hydrogen bonding is an interaction force formed between hydrogen atoms and strongly electronegative atoms, which is widely existing in nature, including DNA (deoxyribonucleic acid), water, amino acid, etc. (Aakerøy and Seddon, 1993). Hydrogen bonding makes these structures more stable (Arunan et al., 2011). Same as them, hydrogen bonding can significantly enhance the stability and performance of organic semiconductor devices (Wang et al., 2018b). On the one hand, hydrogen bonding can enhance the intermolecular force and reduce the distance between molecules, which results in better  $\pi$ - $\pi$  accumulation (Zhang et al., 2022). Because of the better  $\pi$ - $\pi$  accumulation, the carrier mobility of stretchable organic semiconductors is elevated, which also solves the charge mobility reduction by the destruction of  $\pi$ -conjugation. On the other hand, the hydrogen bonds between molecules can significantly improve the stretchable properties of the systems. Thus, the design strategies of conjugated systems capable of hydrogen bonding are expected to both have high charge mobility and high stretchable properties (Lee et al., 2020).

In this review, we first summarize the recent advances in hydrogen bonding stretchable organic semiconductors in practical applications. Although some articles have reviewed the stretchable materials, only a few articles have discussed the hydrogen bonding-induced stretchable organic semiconductors. Herein, different hydrogen bonding design strategies in applications such as OSCs and OFETs are reviewed. Moreover, high-stretchable materials which are potentially used for these territories are introduced. In the end, the future outlook is highlighted. The final goal is to outline a theoretical scaffold for the design of high-performance hydrogen bonding stretchable organic semiconductors that can at the same time further the development of the applications of stretchable organic semiconductors.

## 2 OSCs

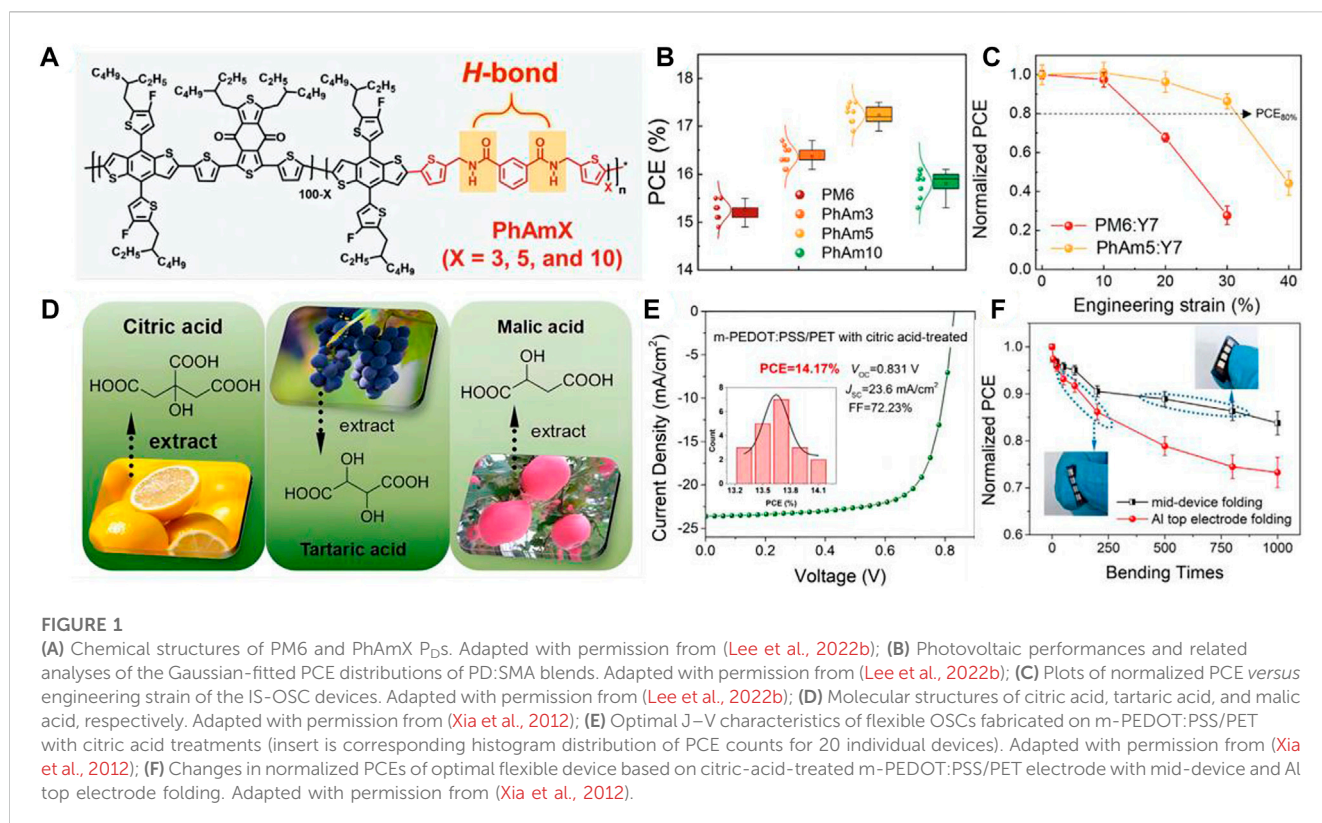
Organic solar cells as a green energy technology are attracting the attention of many scientists. Compared to conventional

silicon-based solar cells, OSCs have many advantages, such as light-weight, low-cost, low pollution, etc. (Chen et al., 2021). Moreover, conventional silicon-based solar cells commonly are high rigidity, which restricts the development of soft-electronic devices (Wang et al., 2021). Relatively, because of the designability and softness of the organic materials, the OSCs are potential to be the most powerful source of soft-electronic devices (Lee et al., 2022a). The active layer of OSCs can generate the exciton when illuminated by light, then the exciton will separate into a hole and an electron. The hole and the electron can transport by the corresponding hole transport layer or electron transport layer. In this way, the current can be generated in the system. In a word, the active layer is one of the most important structures in the OSCs, which directly influences the performance of the OSCs (Liu et al., 2021). However, the active layer materials commonly are high rigidity. Thus, to promote the development of stretchable OSCs, exploiting high-charge mobility active layers with high stretchability is immediate.

Kim et al. developed a series of new polymer donors (P<sub>DS</sub>, PhAmX) featuring phenyl amide (N<sup>1</sup>, N<sup>3</sup>-bis((5-bromothiophen-2-yl)methyl) isophthalamide, PhAm)-based flexible spacer (FS) (Figure 1A) (Lee et al., 2022b). The PhAmX have different hydrogen bonding densities to pursue appropriate intermolecular hydrogen bonding interaction, which both have great charge mobility and excellent stretchability. Among them, the IS-OSCs based on the PhAm5 reached a high power conversion efficiency (PCE) of 12.73% (Figure 1B). Significantly, the PhAm5:Y7-based IS-OSC maintained over 90% of the initial PCE at 20% strain, which is much higher than the frequently-used PM6:Y7-based IS-OSC (68% of the initial PCE at 20% strain) (Figure 1C). In addition, the performance of the device under cyclic stretching/releasing is crucial for the sustainability of the IS-OSC. The PhAm5-based device maintained 86% of the initial PCE after 120 times stretching, nonetheless the PM6-based device showed only 41% of the initial PCE after the same number of cycles. In the PhAm5 system, although the  $\pi$ -conjugated system of the chain is destroyed by the introduction of the acid amides units, the hydrogen bonding induces the reduction of the intermolecular distances and makes better accumulation. The hydrogen bonding compensates for efficiency degradation due to the destruction of the  $\pi$ -conjugated system. Thus, the high durability and excellent performance under cyclic stretching of the hydrogen-bonding-based IS-OSC show high potential as the powerful source for soft-electronic devices in practical applications.

Except for the active layer, developing the highly stretchable transparent electrode material is also inevitable. Nevertheless, conventional OSCs usually utilized indium tin oxide (ITO) as the transparent electrode material, which with a high price and high rigidity (Xia et al., 2012). These factors have limited the practical applications of ITO on soft-electron devices. Thus, designing stretchable, foldable, and transparent electrodes also is meaningful for the development of wearable soft-electron devices. Recently, scientists have utilized a number of emerging flexible transparent electrodes to replace the ITO, including graphene, ultrathin metal, conducting polymers, etc. Among these materials, poly (3,4-ethylene dioxythiophene):poly (styrene sulfonate) (PEDOT:PSS) has been broadly used in flexible





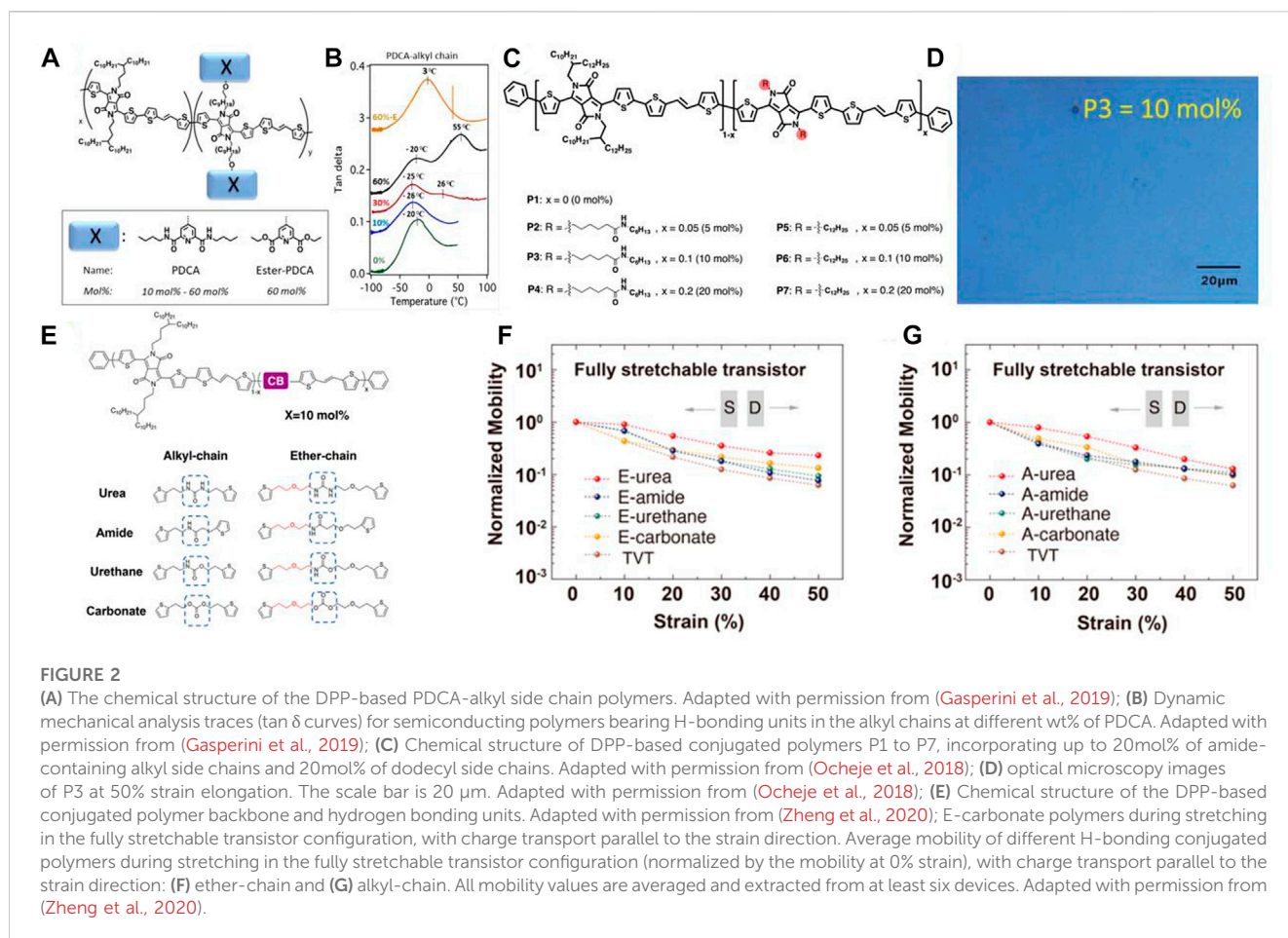
transparent electrodes, which possess well film-forming properties, high grade of transparency, and low cost (Chen et al., 2019). In addition, by doping with some acids in PEDOT:PSS films are confirmed as an effective strategy to enhance the performance of the devices. Wei Song et al. have designed the flexible OSCs by using the PEDOT:PSS (m-PEDOT:PSS)/polyethylene terephthalate (PET) films as the flexible transparent electrodes, which are doped with the eco-friendly acids, including citric acid, malic acid, and tartaric acid (Figure 1D) (Song et al., 2020). The carbonyl of the PET and the hydroxyl the acid can form hydrogen bonding in the system. Hydrogen bonding can significantly improve interfacial adhesion and reduce interface mechanical wear. Moreover, the deformation resistance and the environmental sustainability of the stretchable OSCs are obviously enhanced, which is caused by the intermolecular hydrogen bonding interaction. Thus, the green-acid-treated folding-flexible OSCs showed a high performance (PCE of 14.17%,  $V_{OC}$  of 0.831 V,  $J_{SC}$  of 23.60 mA cm<sup>2</sup>, and FF of 72.23%) with excellent stretchability (Figures 1E,F). This work is great potential for further implementation of stretchable, low-cost, and eco-friendly OSCs.

### 3 OFETs

Organic field-effect transistor (OFET) is an active device that uses an electric field to control the conductivity of solid organic materials. In electron devices, the OFETs are indispensable, which can transmit signals and control the operation of the devices (Fusco et al., 2022). Through molecular design and aggregate structural engineering, scientists have developed many high-charge mobility conjugated polymers for OFETs.

With the development of soft-electron devices, designing corresponding stretchable OFETs are inevitable. Recently, many high-charge mobility with high stretchable OFETs have been successfully developed by hydrogen bonding designing strategies (Zhang et al., 2018), which may meet the requirement of emerging flexible electronics such as electronic skin, flexible displaying, etc. further improving charge mobility and promoting conjugated polymers to the flexible device are running in the fast lane (Wang et al., 2018a; Tien et al., 2021).

Incorporating side chains into the polymer is a mature design strategy to enhance the performance of OFETs. For example, Bao's group introduced hydrogen bonding units PDCA (2,6-pyridine carboxamide) into Diketopyrrolopyrrole (DPP)-based donor-acceptor conjugated polymer OFETs (Figure 2A) (Gasparini et al., 2019). Compared with commonly DPP-based OFETs, the hydrogen bonding interaction reduced the intermolecular distance (from 24.02 to 22.87 Å) and induced better  $\pi$ - $\pi$  accumulation. They found that the hydrogen bonding is more sturdy than the backbone in the hydrogen bonding system (Figure 2B). That means the hydrogen bonding can buffer the effect while the materials are strained, which can significantly improve the stretchability and resistance to strain. Samely, Ocheje's group incorporated amide-containing alkyl chains in DPP-based conjugated polymers as stretchable OFETs (Figure 2C) (Ocheje et al., 2018). The resulting polymers with 10% hydrogen bonding units showed a maximum stretchability of 75% elongation (Figure 2D), which maintains a high retention rate of the morphology under the tensile state. Nonetheless, the hydrogen bonding side chains also can be extended to other polymer backbone structures to develop various high-performance OFETs.



Besides introducing hydrogen bonding side chains in the OFETs system, developing different hydrogen bonding densities in the backbone also is a popular research direction (Oh et al., 2016). The hydrogen bonding is able to induce better aggregation and crystallinity in as-casted thin films, which can result in a higher modulus and crack on-set strain. This property is highly correlated with the density and strength of hydrogen bonding. On this basis, Bao's group designed various diketopyrrolopyrrole (DPP)-based conjugated polymer backbones with various densities and intensities of hydrogen bonding units, and systematically investigate the effects of hydrogen bonding interactions on the performance of OFETs (Figure 2E) (Zheng et al., 2020). They found that the hydrogen bonding self-association constant  $>0.7$  (the Urea) can significantly improve the resistance to deformation and crack on-set strain. Additionally, introducing the ether chain contributes to better hydrogen bonding interaction and better electrical performance under strain. Then they fabricated the stretchable OFETs to evaluate their electrical performances under the strain states. The result shows that the hydrogen bonding induced better crystallization and improved the modulus of the system (Figures 2F,G). Nevertheless, the higher modulus leads to better charge mobility. Thus, regulating the densities and intensities of hydrogen bonding in the backbone can provide guidelines for designing various stretchable OFETs.

## 4 Conclusions and outlook

Hydrogen bonding-induced organic semiconductors have many advantages in stretchable electron devices, including designability, low cost, stretchability, etc. Moreover, through different design strategies, we can develop various functional stretchable organic semiconductors as we want. The development of stretchable organic semiconductors could promote the development of wearable soft-electron devices. On one hand, stretchable organic semiconductors can provide power for soft-electron devices such as stretchable OSCs. On the other hand, designing various stretchable organic semiconductors let the development of soft-electron devices quicker and more diversified.

Although hydrogen bonding-induced stretchable organic semiconductors have developed for many years, this technology is still in its infancy. For further development of soft-electron devices, there are still some problems that need to be solved. (i) At present, many hydrogen bonding-induced stretchable organic semiconductors lack deep-level research. (ii) Developing more practical applications, such as artificial skin, wearable electronic devices, electronic wallpaper, etc. (iii) Developing different types of hydrogen bonding-induced organic semiconductors, such as chemical hydrogen bonding, physical hydrogen bonding and dielectric hydrogen bonding. (iv) Designing Hydrogen bonding-induced organic semiconductors with multiple advantages,

including sustainability, stretchability, charge mobility, foldability, etc.

## Author contributions

JC and ZW prepared the manuscript. LC and XW collected and organized the OSCs part, YG and YH collected and organized the OFETs part, ML helped to revise the manuscript, ZD provided the overall working ideas and revised the manuscript, HW supervised the whole work. All authors discussed and commented on the paper.

## Funding

This study was financially supported by the Special research project of Shaanxi Provincial Department of Education (21JK0563), Key research and development project of Science and Technology Department of Shaanxi Province (2023-YBGY-004), Research projects of Shaanxi University of Technology (SLGRCQD2216,

SLG1901), National innovation and entrepreneurship training program for college students (No. 202210720027).

## Conflict of interest

The authors declare that the research was conducted in the absence of any commercial or financial relationships that could be construed as a potential conflict of interest.

The handling editor ML declared a past co-authorship with the author ZD.

## Publisher's note

All claims expressed in this article are solely those of the authors and do not necessarily represent those of their affiliated organizations, or those of the publisher, the editors and the reviewers. Any product that may be evaluated in this article, or claim that may be made by its manufacturer, is not guaranteed or endorsed by the publisher.

## References

- Aakeröy, C. B., and Seddon, K. R. (1993). The hydrogen bond and crystal engineering. *Chem. Soc. Rev.* 22, 397–407. doi:10.1039/CS9932200397
- Arunan, E., Desiraju, G. R., Klein, R. A., Sadlej, J., Scheiner, S., Alkorta, I., et al. (2011). Defining the hydrogen bond: An account (IUPAC Technical Report). *Pure Appl. Chem.* 83, 1619–1636. doi:10.1351/PAC-REP-10-01-01
- Charron, B. P., Ocheje, M. U., Selivanova, M., Hendsbee, A. D., Li, Y., and Rondeau-Gagné, S. (2018). Electronic properties of isoindigo-based conjugated polymers bearing urea-containing and linear alkyl side chains. *J. Mater. Chem. C* 6, 12070–12078. doi:10.1039/C8TC03438A
- Chen, J., Zhang, W., Wang, L., and Yu, G. (2023). Recent research progress of organic small-molecule semiconductors with high electron mobilities. *Adv. Mater.* 35, 2210772. doi:10.1002/adma.202210772
- Chen, R., Sun, K., Zhang, Q., Zhou, Y., Li, M., Sun, Y., et al. (2019). Sequential solution polymerization of poly(3,4-ethylenedioxythiophene) using V2O5 as oxidant for flexible touch sensors. *iScience* 12, 66–75. doi:10.1016/j.isci.2019.01.003
- Chen, Z., Song, W., Yu, K., Ge, J., Zhang, J., Xie, L., et al. (2021). Small-molecular donor guest achieves rigid 18.5% and flexible 15.9% efficiency organic photovoltaic via fine-tuning microstructure morphology. *Joule* 5, 2395–2407. doi:10.1016/j.joule.2021.06.017
- Dai, Z., Tian, J., Li, J., Liu, M., Vivo, P., and Zhang, H. (2022). Side-chain engineering by thymine groups enables hydrogen bond in P-type donor-acceptor polymers with enhanced optoelectronic properties. *Dyes Pigments* 205, 110565. doi:10.1016/j.dyepig.2022.110565
- Fusco, S., Barra, M., Gontrani, L., Bonomo, M., Chianese, F., Galliano, S., et al. (2022). Novel thienyl DPP derivatives functionalized with terminal electron-acceptor groups: Synthesis, optical properties and OFET performance. *Chem. A Eur. J.* 28, e202104552. doi:10.1002/chem.202104552
- Gasparini, A., Wang, G.-J. N., Molina-Lopez, F., Wu, H.-C., Lopez, J., Xu, J., et al. (2019). Characterization of hydrogen bonding formation and breaking in semiconducting polymers under mechanical strain. *Macromolecules* 52, 2476–2486. doi:10.1021/acs.macromol.9b00145
- Lee, J., Kim, G., Kim, D. J., Jeon, Y., Li, S., Kim, T., et al. (2022a). Intrinsically-stretchable, efficient organic solar cells achieved by high-molecular-weight, electroactive polymer acceptor additives. *Adv. Energy Mater.* 12, 2200887. doi:10.1002/aenm.202200887
- Lee, J., Seo, S., Lee, S., Kim, G., Han, S., Phan, T. N., et al. (2022b). Intrinsically stretchable, highly efficient organic solar cells enabled by polymer donors featuring hydrogen-bonding spacers. *Adv. Mater.* 34, 2207544. doi:10.1002/adma.202207544
- Lee, M. Y., Dharmapurikar, S., Lee, S. J., Cho, Y., Yang, C., and Oh, J. H. (2020). Regular H-Bonding-Containing polymers with stretchability up to 100% external strain for self-healable plastic transistors. *Chem. Mater.* 32, 1914–1924. doi:10.1021/acs.chemmater.9b04574
- Liu, T., Yang, T., Ma, R., Zhan, L., Luo, Z., Zhang, G., et al. (2021). 16% efficiency all-polymer organic solar cells enabled by a finely tuned morphology via the design of ternary blend. *Joule* 5, 914–930. doi:10.1016/j.joule.2021.02.002
- Miao, C., Liang, D., Gu, L., Li, C., Liu, M., Li, J., et al. (2023). Naphthodipyrrolopyrrole-based Aza-BODIPY dye for N-type organic field-effect transistors. *Dyes Pigments* 209, 110855. doi:10.1016/j.dyepig.2022.110855
- Ocheje, M. U., Selivanova, M., Zhang, S., Van Nguyen, T. H., Charron, B. P., Chuang, C.-H., et al. (2018). Influence of amide-containing side chains on the mechanical properties of diketopyrrolopyrrole-based polymers. *Polym. Chem.* 9, 5531–5542. doi:10.1039/C8PY01207E
- Oh, J. Y., Rondeau-Gagné, S., Chiu, Y.-C., Chortos, A., Lissel, F., Wang, G.-J. N., et al. (2016). Intrinsically stretchable and healable semiconducting polymer for organic transistors. *Nature* 539, 411–415. doi:10.1038/nature20102
- Pei, D., An, C., Zhao, B., Ge, M., Wang, Z., Dong, W., et al. (2022). Polyurethane-based stretchable semiconductor nanofilms with high intrinsic recovery similar to conventional elastomers. *ACS Appl. Mater. Interfaces* 14, 33806–33816. doi:10.1021/acsami.2c07445
- Song, W., Peng, R., Huang, L., Liu, C., Fanady, B., Lei, T., et al. (2020). Over 14% efficiency folding-flexible ITO-free organic solar cells enabled by eco-friendly acid-processed electrodes. *iScience* 23, 100981. doi:10.1016/j.isci.2020.100981
- Tien, H.-C., Huang, Y.-W., Chiu, Y.-C., Cheng, Y.-H., Chueh, C.-C., and Lee, W.-Y. (2021). Intrinsically stretchable polymer semiconductors: Molecular design, processing and device applications. *J. Mater. Chem. C* 9, 2660–2684. doi:10.1039/D0TC06059C
- Wang, S., Oh, J. Y., Xu, J., Tran, H., and Bao, Z. (2018a). Skin-inspired electronics: An emerging paradigm. *Acc. Chem. Res.* 51, 1033–1045. doi:10.1021/acs.accounts.8b00015
- Wang, S., Xu, J., Wang, W., Wang, G.-J. N., Rastak, R., Molina-Lopez, F., et al. (2018b). Skin electronics from scalable fabrication of an intrinsically stretchable transistor array. *Nature* 555, 83–88. doi:10.1038/nature25494
- Wang, Z., Xu, M., Li, Z., Gao, Y., Yang, L., Zhang, D., et al. (2021). Intrinsically stretchable organic solar cells beyond 10% power conversion efficiency enabled by transfer printing method. *Adv. Funct. Mater.* 31, 2103534. doi:10.1002/adfm.202103534
- Xia, Y., Sun, K., and Ouyang, J. (2012). Solution-processed metallic conducting polymer films as transparent electrode of optoelectronic devices. *Adv. Mater.* 24, 2436–2440. doi:10.1002/adma.201104795
- Yang, J. C., Mun, J., Kwon, S. Y., Park, S., Bao, Z., and Park, S. (2019). Electronic skin: Recent progress and future prospects for skin-attachable devices for health

monitoring, robotics, and prosthetics. *Adv. Mater.* 31, 1904765. doi:10.1002/adma.201904765

Yang Y., Y., Liu, Z., Zhang, G., Zhang, X., and Zhang, D. (2019). The effects of side chains on the charge mobilities and functionalities of semiconducting conjugated polymers beyond solubilities. *Adv. Mater.* 31, 1903104. doi:10.1002/adma.201903104

Yu, X., Li, C., Gao, C., Zhang, X., Zhang, G., and Zhang, D. (2021). Incorporation of hydrogen-bonding units into polymeric semiconductors toward boosting charge mobility, intrinsic stretchability, and self-healing ability. *SmartMat* 2, 347–366. doi:10.1002/smm2.1062

Yu, Y., Ma, Q., Ling, H., Li, W., Ju, R., Bian, L., et al. (2019). Small-molecule-based organic field-effect transistor for nonvolatile memory and artificial synapse. *Adv. Funct. Mater.* 29, 1904602. doi:10.1002/adfm.201904602

Zhang, H., Liu, K., Wu, K.-Y., Chen, Y.-M., Deng, R., Li, X., et al. (2018). Hydrogen-bonding-mediated solid-state self-assembled isopindolidiones (isoEpi) crystal for organic field-effect transistor. *J. Phys. Chem. C* 122, 5888–5895. doi:10.1021/acs.jpcc.7b11992

Zhang, Q., Huang, J., Wang, K., and Huang, W. (2022). Recent structural engineering of polymer semiconductors incorporating hydrogen bonds. *Adv. Mater.* 34, 2110639. doi:10.1002/adma.202110639

Zheng, Y., Ashizawa, M., Zhang, S., Kang, J., Nikzad, S., Yu, Z., et al. (2020). Tuning the mechanical properties of a polymer semiconductor by modulating hydrogen bonding interactions. *Chem. Mater.* 32, 5700–5714. doi:10.1021/acs.chemmater.0c01437

Zheng, Y., Zhang, S., Tok, J. B.-H., and Bao, Z. (2022). Molecular design of stretchable polymer semiconductors: Current progress and future directions. *J. Am. Chem. Soc.* 144, 4699–4715. doi:10.1021/jacs.2c00072





## OPEN ACCESS

## EDITED BY

Siva S. Panda,  
Augusta University, United States

## REVIEWED BY

Tao Shi,  
The Scripps Research Institute,  
United States  
Ajeet Kumar,  
University of Florida, United States  
Bubun Banerjee,  
Akal University, India

## \*CORRESPONDENCE

Praveen K. Sharma,  
✉ pk\_pandit1982@yahoo.com,  
✉ praveen.14155@lpu.co.in  
Wajahat A. Shah,  
✉ doctorwajaht@gmail.com

RECEIVED 21 July 2023

ACCEPTED 25 August 2023

PUBLISHED 07 September 2023

## CITATION

Qadir T, Kanth SA, Aasif M, Fadul AN,  
Yatoo GN, Jangid K, Mir MA, Shah WA and  
Sharma PK (2023), Design, synthesis, and  
unraveling the antibacterial and  
antibiofilm potential of  
2-azidobenzothiazoles: insights from  
a comprehensive *in vitro* study.  
*Front. Chem.* 11:1264747.  
doi: 10.3389/fchem.2023.1264747

## COPYRIGHT

© 2023 Qadir, Kanth, Aasif, Fadul, Yatoo,  
Jangid, Mir, Shah and Sharma. This is an  
open-access article distributed under the  
terms of the [Creative Commons  
Attribution License \(CC BY\)](#). The use,  
distribution or reproduction in other  
forums is permitted, provided the original  
author(s) and the copyright owner(s) are  
credited and that the original publication  
in this journal is cited, in accordance with  
accepted academic practice. No use,  
distribution or reproduction is permitted  
which does not comply with these terms.

# Design, synthesis, and unraveling the antibacterial and antibiofilm potential of 2-azidobenzothiazoles: insights from a comprehensive *in vitro* study

Tanzeela Qadir<sup>1</sup>, Saadat A. Kanth<sup>2</sup>, Mohammad Aasif<sup>3</sup>,  
Abdalla N. Fadul<sup>4</sup>, Gulam N. Yatoo<sup>3</sup>, Kailash Jangid<sup>5</sup>,  
Mushtaq A. Mir<sup>4</sup>, Wajahat A. Shah<sup>7\*</sup> and Praveen K. Sharma<sup>1\*</sup>

<sup>1</sup>Department of Chemistry, School of Chemical Engineering and Physical Sciences, Lovely Professional University, Phagwara, India, <sup>2</sup>Centre of Research for Development and P.G Programme in Microbiology, School of Biological Sciences, University of Kashmir, Srinagar, Jammu and Kashmir, India, <sup>3</sup>Department of Chemistry, National Institute of Technology, Srinagar, Jammu and Kashmir, India, <sup>4</sup>Department of Clinical Laboratory Sciences, College of Applied Medical Science, King Khalid University, Abha, Saudi Arabia, <sup>5</sup>Department of Chemistry, Central University of Punjab, Bathinda, Punjab, India, <sup>6</sup>Department of Bio-Resources, Amar Singh College Campus, Cluster University Srinagar, Srinagar, Jammu and Kashmir, India, <sup>7</sup>Laboratory of Natural Product and Designing Organic Synthesis, Department of Chemistry, University of Kashmir, Srinagar, Jammu and Kashmir, India

The present study reports the synthesis of 2-azidobenzothiazoles from substituted 2-aminobenzothiazoles using sodium nitrite and sodium azide under mild conditions. All the synthesized compounds were examined for their antibacterial activity against Gram (+) bacteria, *Staphylococcus aureus* (ATCC 25923), *Enterococcus faecalis* (ATCC 51299), *Bacillus cereus* (ATCC 10876) and Gram (–) bacteria, *Escherichia coli* (ATCC 10536), *Pseudomonas aeruginosa* (ATCC 10145), *Klebsiella pneumonia* (ATCC BAA-2146) and clinical isolates of Gram (+) Methicillin Resistant *S. aureus* (MRSA) and Multi Drug Resistant *E. coli*. The Minimum Inhibitory Concentration (MIC) and Minimum Bactericidal Concentration (MBC) values by broth dilution method revealed that compound **2d** exhibited significant antibacterial potential against *E. faecalis* and *S. aureus* with MIC of 8 µg/mL, while other synthesized compounds had only moderate effects against all the tested species. The compound significantly inhibited the biofilm formation of the bacterial strains below its MIC. The selective cytotoxicity of Compound **2d** towards bacterial cells was evidenced on extended exposure of Human Embryonic Kidney-293 cell line to higher concentrations of the compound. Hence, the present study confirmed that compound **2d** can be a potential drug candidate for future development as an antibacterial drug.

## KEYWORDS

synthesis, 2-azidobenzothiazoles, antibacterial activity, biofilm inhibition assay, cytotoxicity assay, benzothiazoles

## 1 Introduction

Aromatic azides are most frequently used as reagents for the photoaffinity labeling of biomolecules despite their unusual uses in synthetic organic chemistry. A relatively small number of transformations are used to synthesize aryl azides (Nicholls et al., 1991; Scriven and Turnbull, 1998; Ali et al., 2014; Lima et al., 2015; Faraji et al., 2017; De la Torre et al., 2018; Almehmadi et al., 2021; Zhilitskaya et al., 2021). This chemistry, while helpful for relatively straightforward ligands, is not necessarily permissive to additional functional groups. It has been investigated to use other techniques, such as *p*-tosylazide reacting with lithium reagents or aryl Grignard made from the appropriate aryl halides (Tariq et al., 2018). Similar to this, it has been demonstrated that *p*-tosylazide can react with aryl amide salts to produce the required azides. The general application of this transformation has been constrained by somewhat harsh conditions (Fischer and Anselme, 1967). In contrast to aromatic azides, aliphatic azides can be made using a variety of ways. A high-yielding reaction with triflyl azide can easily transform aliphatic amines into the corresponding azides, apart from simple substitution reactions utilizing the azide ion and different electrophiles ( $\text{TfN}_3$ ) (Wu et al., 2004). This reaction, recently popularized by Wong, has drawn a lot of attention and found several uses (Wang et al., 2003; Siddiki et al., 2013). It has been discovered that aryl azides can be produced from organoboron compounds employing a copper (II) catalyst (Nomiya et al., 2000). The diazotization of  $[\text{ArN}_2][\text{BF}_4]$  salts immobilized in [BMIM][PF<sub>6</sub>] ionic liquid is an effective way to produce azido-derivatives (Artyushin et al., 2008). However, only a small number of transformations are used in the synthesis of aryl azides (Warmuth and Makowiec, 2005). They are frequently made from the equivalent amines using the diazonium salts of those amines (Yamazaki et al., 2005). Depending on whether or not there are incompatible functional groups present, this could occasionally be an issue. Alternative approaches have been researched, such as interactions between organometallic aryls and *p*-tosyl azide, which have been studied (derived from the corresponding aryl halide) (Yalcin et al., 1992). More recently, Liu and Tor have successfully prepared aryl azides using Wong's ( $\text{TfN}_3$ ) technique (Moorhouse et al., 2006). Even though it works, this approach has several shortcomings. First, the highly reactive  $\text{Tf}_2\text{O}$  is used. Second, it has been discovered that  $\text{TfN}_3$  is explosive on its own (Kleinhofs et al., 1978). Tertbutyl nitrite (*t*-BuONO) and  $\text{NaN}_3$  have recently been reported to be used in the synthesis of aromatic azides by Das et al. (Kini et al., 2007). Phenyl hydrazine derivatives can also be used as a starting material in various processes to produce aromatic azides, including (Palmer et al., 1971) which uses  $\text{Br}_2/\text{PPh}_3$ , (Burger and Sawhney, 1968), which uses  $\text{N}_2\text{O}_4/\text{CCl}_4$ , and (Soni et al., 2010) which uses  $\text{O}_2/\text{NO}$ . Using diazonium salt and sulfonamide, Dutt et al. described the synthesis of aryl azide; however, a significant drawback of this technique is the production of sulfonic acid as a byproduct (Liu and Tor, 2003).

In click chemistry, organic azides play a key role (Telvekar et al., 2012). Applications for the cycloaddition of organic azides and terminal alkynes are numerous, including combinatorial drug development, and bioconjugation. The synthesis of triazoles begins with organic azides, one type of 1,3-dipole that is particularly significant (Kolb and Sharpless, 2003). These

heterocyclic derivatives have important uses in chemical biology (Siddiki et al., 2013), pharmaceuticals, and material science (Faraji et al., 2017), among others. Additionally, several benzothiazole analogs bearing triazole moiety have been investigated as potential anticancer (Katritzky and Rachwal, 2010; Almehmadi et al., 2021), anti-inflammatory, anti-nociceptive, FGFR1 inhibitors, analgesic and antimicrobial agents (Keri et al., 2015). Fluconazole, other antifungal medications, voriconazole, and albaconazole all include 1,2,4-triazole. However, no commercially available medications include the 1,2,3-triazole ring. Sincere efforts have been made to incorporate 1,2,3-triazole into currently available medications, further study is required to identify the lead molecule (Shafi et al., 2012; Ali et al., 2017; Ashour et al., 2020). Moreover, benzothiazole analogs serve as an important scaffold for further molecular research to produce novel compounds (Weekes and Westwell, 2009; Lauria et al., 2014). Hence, we were intrigued by the opportunity to design new compounds that would be very useful in click chemistry, for which Carolyn R. Bertozzi, Morten Meldal, and K. Barry Sharpless got the *Noble Prize in 2022*, and would be utilized for the formation of biologically significant scaffolds. Recently, Singh et al. synthesized triazoles derived from benzothiazole as promising antimicrobial agents and various substituted aryl azides were reacted with dialkyne substituted 2-aminobenzothiazole to generate desired compounds by click chemistry. The compounds showed maximum potency against all Gram (+)/Gram (−) bacterial strains with a MIC value of 3.12 µg/mL, which is two times more active as compared to the standard drug ciprofloxacin (MIC 6.25 µg/mL) (Singh et al., 2013). Similarly, Jakopcic et al. synthesized and evaluated the cytotoxicity activity of 1,2,3-triazoles of benzothiazole derivatives (Jakopcic et al., 2022). Both methodologies utilized dialkyne substituted 2-aminobenzothiazoles. Here in, we synthesized 2-azidobenzothiazole derivatives which can react with different mono-propargylated and bis-propargylated compounds. The immense importance of 2-azidobenzothiazoles will further proceed when we apply them to the synthesis of pharmacologically significant heterocyclic scaffolds. This may provide an extra credential for the development of innovative protocols which might be worthy to cure diseases of new origin.

## 2 Materials and methods

### 2.1 Chemistry

Chemicals and solvents used in this study were purchased from E. Merck (India) and Sigma Aldrich chemicals and used without further purification. Precoated aluminum sheets (Silica gel 60 F254, Merck Germany) were employed for thin-layer chromatography (TLC). The synthesized compounds were visualized on TLC using ultraviolet (UV) light ( $\lambda = 254 \text{ nm}$ ). The melting points of all the compounds were observed on a Veego instrument with model specifications REC-22038 A2 and are uncorrected.  $^1\text{H}$  NMR was recorded on Bruker Advance DX spectrometer at 400 MHz, respectively with chemical shifts reported relative to residual deuterated solvent peaks. Splitting patterns are indicated by s (singlet), d (doublet), t (triplet), q (quartet), dd (doublet of doublet), or m (multiplet). Mass spectra were recorded by

ESI-MS (AB-Sciex 2000; Applied Biosystem) and on a GCMS-QP 5000 (Shimadzu) mass spectrometers; Infra-red spectra were recorded on Perkin Elmer FT-IR spectrometer in the range of 4,000–600  $\text{cm}^{-1}$  as neat samples.

## 2.2 In Vitro antibacterial activity

### 2.2.1 Chemicals and reagents

Mueller Hinton Broth (MHB), Nutrient Agar (NA), Gram Staining Kit, and Crystal Violet (cell culture tested) used in the study were supplied by HiMedia. Dimethyl sulfoxide (DMSO), Methanol, Glycerol [Aqueous] acetic acid, Sodium Chloride (NaCl), Isopropanol, Absolute Ethanol, Resazurin, and 3-(4,5-dimethylthiazol-2-yl)-2,5-diphenyl tetrazolium bromide (MTT) was purchased from Merck (India). 4',6-diamidino-2-phenylindole (DAPI) Stain and Propidium Iodide counter stain (PI) were purchased from Thermo Fischer Scientific. Foetal Bovine Serum (FBS), Bovine Serum Albumin (BSA), Dulbecco's Modified Eagle Medium (DMEM), Trypsin, phosphate-buffered saline (PBS) were obtained from Gibco (Thermo Fischer Scientific). All chemicals used were of analytical research grade.

### 2.2.2 Bacterial strains

Gram (+) bacteria; *Staphylococcus aureus* (ATCC 25923), *Enterococcus faecalis* (ATCC 51299), *Bacillus cereus* (MTCC 121) and Gram (–) bacteria; *Escherichia coli* (ATCC 10536), *Pseudomonas aeruginosa* (ATCC 10145), *Klebsiella pneumonia* (NCTC 13440) were frozen as glycerol stocks and stored at  $-80^{\circ}\text{C}$ . For each experiment, the frozen bacterial stock had been thawed and grown in MHB to the mid-logarithmic phase of growth under proper incubated conditions and then used.

### 2.2.3 Determination of minimum inhibitory concentration (MIC)

To determine the MIC, the broth micro-dilution method was used, as described previously (Ali et al., 2022). The 96-well plates were labeled with the compound name, reference antibiotics (two wells/compound), and name of bacterial strains. 200  $\mu\text{L}$  of MHB were dispensed into the wells except for the first column. 200  $\mu\text{L}$  of the respective compounds (2a–2h) and drugs (CIP, AMK, and STR) were pipetted into the first column with a concentration equal to 128  $\mu\text{g/mL}$  2-fold serial dilution was performed so that the concentration from the first to 10th well ranges from 128–0.25  $\mu\text{g/mL}$ . This was followed by inoculation of 50  $\mu\text{L}$  of  $10^5$  CFU/mL cells of *S. aureus*, *E. faecalis*, *B. cereus*, *E. coli*, *P. aeruginosa*, and *K. pneumonia* to wells in individual 96-well plates. The last two wells were taken as Growth Control (GC) and Media Control (MC), one lacking the drug and the other lacking both drug and compound as an indicator of contamination. The plates were sealed with parafilm. After 24 h of incubation at  $37^{\circ}\text{C}$ , plates were checked for the presence or absence of visible growth by comparing them with the Culture Control (CC) and MC Wells which also act as indicators of contamination. MIC was defined as the lowest concentration of compound at which no bacterial growth was visualized.

### 2.2.3.1 Spectrophotometric analysis

The Optical Density (OD) of each well was measured at a wavelength of 600 nm using a microplate reader. The OD values for each well were recorded and the percentage of growth inhibition was calculated as described. In the calculation of percentage inhibition, the control well containing the bacterial culture but without any compound (GC) was used as the reference for comparison. This control well was used to determine the baseline OD value of the bacterial culture and considered as 100% growth or metabolic activity. The OD value of each well was then compared to the OD value of the control well to calculate the percentage inhibition of bacterial growth or metabolic activity. The percentage of growth inhibition in each well was calculated by comparing the OD of each well to that of the growth control wells using the following formula:

$$\text{Percentage inhibition} = [(\text{OD control} - \text{OD treated}) / \text{OD control}] \times 100 \quad (1)$$

The data was plotted to determine the percentage of inhibition (plotting the percentage of inhibition *versus* the concentration of the antibiotic). The  $\text{IC}_{50}$  value was determined from the curve as the concentration of the antibiotic that inhibits 50% of bacterial growth.

### 2.2.4 Determination of minimum bactericidal concentration (MBC)

To ascertain if the compounds are bactericidal, the MBC assay was performed as per CSLI, 2016 guidelines (Mir et al., 2023). MBC is the lowest concentration of compound that leads to a 3 log<sub>10</sub>-fold decrease in CFU units or the lowest drug concentration that results in 99.9% killing of bacterial cells in initial inoculums. It is important to determine MBC as it provides insights into the optimal dosing regimen and identifies potential resistance mechanisms. The MBC was performed by broth micro dilution. The experiment was performed in duplicates. Briefly, 2 sterile 96-well plates were filled with MHB containing serial two-fold dilutions ranging from 1x– 4x MIC of compounds (2a–2h) and Ampicillin (4–16  $\mu\text{g/mL}$ ) as standard in a set of 2. Drug-free controls were also included. The plates were inoculated with 50  $\mu\text{L}$  of *S. aureus* and *E. faecalis* respectively with a final density equal to  $10^5$  CFU. The initial CFU of inoculums was verified by plating onto NA media. After 24 h, the drug-containing wells showing no sign of growth compared to growth culture tubes were appropriately diluted to sub-MIC levels by 10-fold serial dilution in MHB. 100  $\mu\text{L}$  of each dilution was plated onto NA plates in duplicates. CFU was enumerated after 24 h of incubation at  $37^{\circ}\text{C}$ . CFU/mL was calculated using the formula:

$$\text{No. of Colonies} \times \text{Dilution Factor} \div \text{Volume of Culture Plated} \quad (2)$$

Then log<sub>10</sub> values of an average number of colonies and log reduction were calculated using log calculator Omni Calculator to determine if there is a 3-log reduction in cell number. Ampicillin (AMP) was used as a control drug. Colonies ranging from 30–300 were considered countable. The lowest concentration of the drug which caused 99.9% killing with a 3-log reduction in CFU was taken as MBC of the drug.

## 2.2.5 Time kill kinetics

To ascertain the bactericidal mechanism, i.e., the Time v/s Concentration dependent-killing of the lead compound **2d**, the kill curve kinetics assay, was performed using the CFU/mL method as per CSLI guidelines with slight modifications. Another method adapted from the protocol described by Wang was also used to study the kill curve to provide insights into the degree of killing (concentration dependence) and rate of killing (time dependence) (Tsuji et al., 2008).

### 2.2.5.1 Assessment of 24-hour time-kill kinetics via CFU/mL evaluation

To determine the kill kinetics of lead **2d** compound, *E. faecalis* and *S. aureus* cultures with cell density  $1 \times 10^5$  CFU/mL (confirmed by plate count) were exposed to 8 µg/mL MIC, 16 µg/mL (2xMIC) and 32 µg/mL (4xMIC) of **2d**. A growth control CC was included as negative control (devoid of the compound). 2xMIC of AMP was taken as a standard drug. The log CFU/mL for all groups was determined at time 0 and at a subsequent time interval of 4 h (taken up to 24 h). Aliquots (100 µL) of drug-exposed cultures were pipetted out at predetermined time intervals of 4 h in 1 day, i.e., at 0, 4, 8, 9, 12, 16, 20, and 24 h and serially diluted, then plated onto NA for CFU enumeration. First, the colonies at different dilutions for each concentration were enumerated then the average colony count at dilutions  $10^{-1}$ ,  $10^{-2}$ ,  $10^{-3}$ , and  $10^{-4}$  was calculated and then converting the value into  $\log_{10}$  (Note: the colonies on plates showing 30–300 colonies were only considered). The curve was generated by plotting  $\log_{10}$  CFU values at each concentration against time. Time-kill curves were plotted and analyzed for the rate and extent of bacterial killing. The rate of killing was determined from the start of 0 h to maximal reduction in  $\log_{10}$  CFU/mL.

### 2.2.5.2 Evaluation of time-kill kinetics based on MTT-reduction on a 360-min scale

For this assay, working solutions of **2d** were prepared in a series of conical tubes containing MIC, 2xMIC, and 4xMIC in 5 mL MHB. For each concentration, a set of tubes labeled with the time point were taken. 100 µL of  $10^5$  CFU/mL of *E. faecalis* and *S. aureus* were dispensed in their respective set of tubes and incubated at 37°C. At the various time points 0, 60, 120, 180, 240, 300, and 360 min, the incubated tubes containing culture-molecule mixtures were treated with 150 µL of MTT and incubated for 20 min. After incubation, the tubes were centrifuged at 10,000 rpm at 10°C for 10 min. The supernatant was discarded and the pellet containing formazan crystals at the bottom was dissolved in 1.5 mL of Isopropanol and absorption was measured at 550 nm. For positive control, the cells were treated with 2xMIC of STR. The untreated cultures were taken as a negative control. MTT can be reduced to purple formazan crystals by a dehydrogenase system of active cells which can be quantified through spectrophotometric analysis by dissolving in organic solvent Isopropanol. OD550 nm can be directly correlated to the number of metabolically active cells and this was used to determine the bacterial killing at various concentrations over time.

## 2.2.6 Post-antibiotic effect (PAE)

The PAE was determined as per the described protocol (Proma et al., 2020). Bacterial samples can have persistent subpopulations that remain dormant under antibiotic

treatment and lead to disease recurrence following cessation of antibiotic therapy. The PAE was determined by the viable count method and the procedure adopted was the slight modification of protocol as reported previously. Briefly, an exponentially grown culture of *E. faecalis* and *S. aureus* with a final density of  $10^6$  CFU/mL were exposed to **2d** and control drug Ampicillin (AMP) at x, 2x, and 4xMIC for 2 h. After drug exposure, the drugs were removed by three cycles of centrifugation at 10,000 rpm for 10 min. The pellet obtained was resuspended in MHB. Antibiotics were removed immediately after drug exposure (2 h) and taken as 0-h readings and then after 1, 2, 3, 4, 5, 6, 7, 8, 12, and 24 h by centrifugation. Aliquots removed at predetermined time points were serially diluted 10-fold (N,  $10^{-1}$ ,  $10^{-2}$ ,  $10^{-3}$ ,  $10^{-4}$ ,  $10^{-5}$ , and  $10^{-6}$ ) and plated on NA media in triplicates. Growth Controls with inoculums but no antibiotics were similarly processed and included to monitor the killing effect due to antibiotics to avoid any error in CFUs during processing.

The PAE was defined following Craig and Gudmundsson as

$$PAE = T - C \quad (3)$$

where T is the time required for the viability count of an antibiotic-exposed culture to increase by 1  $\log_{10}$  above the count observed immediately after dilution and C is the corresponding time for the growth control.

## 2.2.7 Fluorescent microscopy

DAPI and PI staining is commonly used to assess cell viability and the effect of antibiotics on cells. DAPI (4',6-diamidino-2-phenylindole) is a fluorescent dye that binds to DNA and emits blue fluorescence upon excitation by ultraviolet light. PI (propidium iodide) is also a fluorescent dye that binds to DNA, but it emits red fluorescence upon excitation by ultraviolet light. In live cells, the DAPI stain enters the nucleus and binds to DNA, whereas PI is excluded from the cell. However, in dead or damaged cells, the cell membrane becomes permeable to PI, which enters the cell and binds to DNA, causing it to emit red fluorescence. When using DAPI and PI staining to assess cell viability and the effect of antibiotics on cells, the cells are typically treated with the antibiotic and then stained with DAPI and PI. Live cells will appear blue, whereas dead cells will appear red. The staining was done as per the described protocol (Zotta et al., 2012). This staining method was used to study the effect of lead compound **2d** on the viability of *E. faecalis* and *S. aureus* using DAPI and PI stains. Bacterial cells were grown to an OD600 of 0.5. 1 mL of the actively growing cultures was pipetted into Eppendorf tubes with MIC and 2xMIC of compound **2d**. After incubation of 2 h at 37°C, the cultures in tubes containing **2d** were centrifuged at 10,000 rpm for 10 min supernatant was decanted and the pellet was resuspended in 200 µL Normal Saline Solution (NSS). 20 µL of PI (5 µg/mL) were added to the tubes and incubated in the dark at 0°C for 15 min. The unbound PI was removed by centrifuging the tubes at 10,000 rpm for 10 min and washing the pellet thrice with 200 µL of NSS. This was followed by 15-min incubation with 2 µL of DAPI (10 µg/mL) at 0°C in the dark. Finally, 100 µL of cultures were mounted onto the clean well-labeled slides, left to dry, and methanol fixed. For negative controls, the corresponding bacterial cells that did not receive **2d** treatment were processed under similar conditions. The stained bacterial



cells were visualized under a fluorescent microscope and photographed using an inbuilt digital camera.

## 2.2.8 Microtiter plate biofilm inhibition assay

To determine whether compound **2d** can inhibit the formation of biofilms, the Microtiter Plate Biofilm Assay was utilized as per described procedure (O'Toole, 2011; Mir et al., 2023). Firstly, the compound was prepared as a working stock (200  $\mu$ L of compound in first well) and was serially diluted two-fold to obtain a concentration ranging from 0.25 to 128  $\mu$ g/mL in 8 individual 96-well plates (1 plate for inoculation of each bacterium) already containing 100  $\mu$ L MHB (final volume of 200  $\mu$ L). 50  $\mu$ L of bacterial suspension containing  $10^5$  CFU/mL bacteria cells were added to the wells of their respective plates (*S. aureus*, *E. faecalis*, *B. cereus*, *E. coli*, *P. aeruginosa*, *K. pneumonia*). Culture control and Media control were included, in which only bacterial culture and growth media, respectively, were dispensed. The plates were then incubated at 37°C for 24 h to allow bacterial growth and understand if biofilm formation was inhibited in the presence of the compounds, as specified. No visible growth was observed in wells that correspond to the minimum inhibitory concentration (MIC) of the compound for the bacterial strains tested. After the incubation period, the planktonic bacterial cells in the wells were removed by washing three times with phosphate-buffered saline (PBS), and aliquots from the wells were serially diluted and plated onto NA to correlate the further findings. Next, 125  $\mu$ L of 30% of 0.5% crystal violet (CV) that included methanol was added to all the wells of the 96-well plates. The plate was then incubated at 37°C for 20 min to stain the biofilm formed by microorganisms that are adherent to the abiotic surface of a microtiter plate. The unbound CV was removed by washing the wells with distilled water, and the wells were air-dried at room temperature. The wells were then visualized and photographed under a microscope to determine the extent of biofilm formation. To quantify the amount of biofilm formed, 200  $\mu$ L of 30% [aqueous] acetic acid was added to each well to dissolve the crystal violet. The optical density (OD) of the dissolved CV was measured at 470 nm using a microplate reader. This protocol was repeated thrice to achieve optimal results and correct any background interference that may be present. The percentage of inhibition of biofilm formation was calculated using the following formula:

$$[100 - (\text{TreatedOD}_{470\text{nm}} \div \text{Growth ControlOD}_{470\text{nm}}) \times 100] \quad (4)$$

This formula compares the optical density of the treated wells to that of the culture control wells and expresses the result as a percentage of inhibition.

## 2.2.9 Biofilm eradication assay

A modified methodology incorporating diverse methods used earlier was implemented to determine the potential of compound **2d** for biofilm eradication and assess the minimum concentration required for biofilm eradication (Kreth et al., 2005). 12 well plates were employed for this assay. To begin with, the bacterial strains (*S. aureus*, *E. faecalis*, *B. cereus*, *P. aeruginosa*, *E. coli*, and *K. pneumonia*) were grown to mid-log phase and diluted to obtain  $10^5$  CFU/mL of cells. 3 mL of MHB was pipetted into the 12 well plates and subsequently inoculated with 100  $\mu$ L of the bacterial suspension.

Media Control well was taken as a positive control containing only MHB. For each bacterial strain, separate plates were utilized and subjected to incubation for 24, 48, and 72 h to assess the effect of different concentrations on various stages of bacterial biofilm formation. After the incubation at given time points the plates were washed thrice with PBS to remove the planktonic bacterial cells. After washing x, 2x, 4x, 8x, and 16x MIC concentrations of **2d** compound were added to the wells and incubated for 24 h at 37°C. Culture Control well taken as a negative control was not incubated with the compound. After incubation plates the drug-containing plates were washed with PBS. This was followed by the addition of 30% of 0.5% CV stain. The plates were further incubated for 1 h at room temperature. In the next step, the CV was removed by thorough washing. Each well was observed under a microscope and photographed. To quantify the percentage of eradication 30% [aqueous] acetic acid was added to the wells to dissolve CV-staining adherent cells. This was done by recording the OD at 470 nm using a spectrophotometer. The percentage of biofilm eradication was calculated using formula (4). The percentages were calculated by taking the mean of three OD readings obtained for each concentration.

## 2.2.10 Cytotoxicity assay

The critical factor that allows any compound to proceed successfully during drug discovery is selective toxicity to pathogens and non-toxicity to human cells. The assay was performed under the standards set by International Organization for Standardization (ISO) and Economic Cooperation and Development (OECD), to ensure accurate and reproducible results. The cytotoxicity of the lead compound **2d** was evaluated against HEK-293. Before evaluating the cytotoxicity of the compound, the cells were grown to reach a confluency of 70%–80%. The culture techniques used were in accordance with the cell culture technique guidelines regulated by the International Cell Line Authentication Committee (ICLAC), American Type Culture Collection (ATCC), and the European Collection of Authenticated Cell Cultures (ECACC).

### 2.2.10.1 Cell lines

Human Embryonic Kidney Cell lines, HEK-293 were purchased from National Centre for Cell Sciences (NCCS), Pune, India. The cell lines were cultured in DMEM (supplemented with 10% foetal bovine serum) in a Carbon Dioxide incubator with 98% humidity and 5% CO<sub>2</sub> at 37°C.

### 2.2.10.2 Preparation of HEK-293 for cytotoxicity evaluation

Thawing of frozen cells: HEK-293 cells stored at –80°C were thawed by removing the frozen cryovial and thawing it in 37°C water for 1–2 min until no visible was seen in the vial. The vials were swirled gently to ensure that the cells are fully thawed. Once the cells were thawed, the vial was removed from the water bath and wiped with 70% ethanol to sterilize the outside of the vial.

Cell Culture and Expansion: The thawed HEK-293 cells were then transferred to a sterile hood and the contents of the vial were transferred into a sterile tube containing 9 mL of pre-warmed growth medium Dulbecco's Modified Eagle's Medium (DMEM) supplemented with 10% FBS, and 1% penicillin-streptomycin. This was followed by centrifuging the tube at 1,000 rpm for 5 min to

pellet the cells. The supernatant was aspirated and the cell pellet and resuspended in 2 mL of fresh pre-warmed growth medium. The cell suspension was transferred to a T75 culture flask and incubated at 37°C with 5% CO<sub>2</sub> until they reached the desired confluency of 70%–80%.

**Harvesting of cells:** Once the cells had reached the desired confluency, they were harvested using standard trypsinization techniques. A small volume of Trypsin-EDTA solution was added to the culture flask and incubated at 37°C for 2 min. During incubation, the Trypsin cleaves the proteins that attach the cells to the culture surface, causing the cells to detach from the surface. The culture medium was removed from the culture dish, and the cells were washed with phosphate-buffered saline (PBS) to remove any residual serum. After incubation, an equal volume of culture medium containing FBS and DMEM was added to neutralize the Trypsin and stop the enzymatic activity. The cells were then collected by gently tapping or swirling the culture dish and transferred to a centrifuge tube. The cells were again pelleted by centrifugation, and the supernatant is discarded. The cells were resuspended in a fresh culture medium, counted, and seeded into a new culture flask. The harvested cells were then counted using a hemocytometer. A predetermined number of cells were seeded into 96-well optimized for the cytotoxicity assay being performed.

### 2.2.10.3 Cytotoxicity assay using MTT

The method was carried out as described earlier (Adan et al., 2016). The 100 µL of HEK-293 cells were seeded into the 96-well microtiter plate and allowed to grow for 24 h at 37°C with 5% CO<sub>2</sub>. The cells were treated with 6 concentrations of the **2d** compound 4, 8, 16, 32, 64, and 128 µg/mL dissolved in DMSO for time points 24, 48, and 72 h to determine the time and dose dependent effect of the compound on cell viability. Untreated control wells received only DMSO. After the given time points, the number of viable cells was determined. Briefly, the tissue culture medium was removed from the 96-well plate and replaced with 100 µL of fresh medium then 20 µL of the MTT stock solution (5 mg of MTT in 1 mL of PBS) was added to each well including the untreated controls. The 96-well plates were then incubated at 37°C and 5% CO<sub>2</sub> for 4 h. An aliquot (85 µL) of the medium was removed from the wells, and 150 µL of dimethyl sulfoxide was added to each well to dissolve the insoluble formazan crystals formed by viable cells and mixed thoroughly with the pipette and incubated at 37°C for 10 min. The optical density was measured at 590 nm with a microplate reader to determine the number of viable cells based on the selective ability of viable cells to reduce the tetrazolium component of MTT into purple-colored formazan crystals. The colored formazan intensity was measured at 570 nm absorbance in the micro-plate reader and growth percentage inhibition was calculated using the formula:

$$\text{Mean OD}_{570} \text{ Treated Well} \div \text{Mean OD}_{570} \text{ Control well} \times 100 \quad (5)$$

The results expressed were the average values of three experiments (±SD). Reduction of MTT to formazan crystals is mediated by the mitochondrial enzyme succinate dehydrogenase of cells the viable cells. The color of the formazan crystals that form after the reduction of MTT by viable cells indicates the level of cell viability and, hence, the cytotoxicity of the test compound. The formazan crystals appear as purple or dark blue precipitates in viable cells. The intensity of the color is directly proportional to the number of viable cells in the culture.

Conversely, a decrease in the intensity of the color indicates a decrease in the number of viable cells and, hence, an increase in cytotoxicity. A complete absence of color indicates that all the cells in the culture have died, and the test compound is highly cytotoxic to the cells.

### 2.2.11 General procedure for the synthesis of 2-azidobenzothiazoles

2-aminobenzothiazole (0.5 mmol) was dissolved in water (10 mL) in a 50 mL round bottom flask under a magnetic stirrer at room temperature; to this solution, hydrochloric acid was added dropwise until 2-aminobenzothiazole gets completely dissolved in water. In the next step solutions of sodium nitrite, (2 mmol), sodium acetate (2 mmol), and sodium azide (2 mmol) were added dropwise after every 5 min respectively and the reaction was stirred for further 30 min. The reaction progress was checked by thin layer chromatography which confirmed the completion of the reaction within 1 h. The solid precipitate was filtered, washed with water, and recrystallized from ethanol which did not require any further purification. (Note: NaNO<sub>2</sub>, NaOAc, and NaN<sub>3</sub> were first dissolved in water, and then added dropwise to the reaction mixture respectively. Also, the role of sodium acetate is to neutralize the acidic medium).

### 2.2.12 Spectroscopic data

#### 2.2.12.1 2-Azido-4, 6-difluorobenzothiazole (2a)

Brown solid, yield: 93%; mp 170°C–173°C; IR (neat)  $\nu$ : 2,124 cm<sup>−1</sup>. <sup>1</sup>H NMR (400 MHz, DMSO-*d*<sub>6</sub>)  $\delta$  (ppm): 7.98 (m, 1H), 7.63 (m, 1H). MS (*m/z*) 234.88 (M.F.: C<sub>7</sub>H<sub>2</sub>F<sub>2</sub>N<sub>4</sub>S).

#### 2.2.12.2 2-Azido-6-methoxybenzothiazole (2b)

Brown solid, yield: 93%; mp 155°C–158°C; IR (neat)  $\nu$ : 2,113 cm<sup>−1</sup>. <sup>1</sup>H NMR (400 MHz, DMSO-*d*<sub>6</sub>)  $\delta$  (ppm): 8.25 (d, 1H), 7.94 (d, 1H), 7.35 (dd, 1H), 3.93 (s, 3H). MS (*m/z*) 207.03 (M.F.: C<sub>8</sub>H<sub>6</sub>N<sub>4</sub>OS).

#### 2.2.12.3 Ethyl 2-azidobenzothiazole-6-carboxylate (2c)

White solid, yield: 89%; mp 145°C–148°C; IR (neat)  $\nu$ : 2,126 cm<sup>−1</sup>. <sup>1</sup>H NMR (400 MHz, CDCl<sub>3</sub>)  $\delta$  (ppm): 8.08 (d, 1H), 7.47 (dd, 1H), 7.39 (d, 1H), 3.74 (q, 2H), 1.28 (t, 3H).

#### 2.2.12.4 2-Azido-6-nitro-benzothiazole (2d)

Creamy white solid, yield: 95%; mp 190°C–193°C; IR (neat)  $\nu$ : 2,120 cm<sup>−1</sup>. <sup>1</sup>H NMR (400 MHz, CDCl<sub>3</sub>)  $\delta$  (ppm): 8.77 (d, 1H), 8.40 (dd, 1H), 8.10 (d, 1H). MS (*m/z*) 222.03 (M.F.: C<sub>7</sub>H<sub>3</sub>N<sub>5</sub>O<sub>2</sub>S).

#### 2.2.12.5 2-Azidobenzothiazole (2e)

Brown solid, yield: 80%; mp 153°C–156°C; IR (neat)  $\nu$ : 2,119 cm<sup>−1</sup>. <sup>1</sup>H NMR (400 MHz, CDCl<sub>3</sub>)  $\delta$  (ppm): 8.22 (d, 1H), 7.74 (d, 1H), 7.70–7.58 (m, 2H). MS (*m/z*) 176 (M.F.: C<sub>7</sub>H<sub>4</sub>N<sub>4</sub>S).

#### 2.2.12.6 2-Azido-4-methylbenzothiazole (2f)

Orange solid; yield: 80%; mp 117°C–120°C; IR (neat)  $\nu$ : 2,120 cm<sup>−1</sup>. <sup>1</sup>H NMR (400 MHz, CDCl<sub>3</sub>)  $\delta$  (ppm): 7.73 (d, 1H), 7.30 (d, 1H), 7.18 (t, 1H), 2.70 (s, 3H). MS (*m/z*) 191 (M.F.: C<sub>8</sub>H<sub>6</sub>N<sub>4</sub>S).

#### 2.2.12.7 2-Azido-6-ethoxybenzothiazole (2g)

Brown solid, yield: 92%; mp 161°C–164°C; IR (neat)  $\nu$ : 2,107 cm<sup>−1</sup>. <sup>1</sup>H NMR (400 MHz, CDCl<sub>3</sub>)  $\delta$  (ppm): 8.07 (d, 1H),

7.70 (d, 1H), 7.02 (dd, 1H), 4.06 (q, 2H), 1.44 (t, 3H). MS ( $m/z$ ) 221 (M.F.:  $C_9H_8N_4OS$ ).

#### 2.2.12.8.2-Azido-5-bromobenzothiazole (2h)

Brown solid; yield: 82%; mp 180°C–183°C; IR (neat)  $\nu$ : 2,110  $cm^{-1}$ .  $^1H$  NMR (400 MHz, DMSO- $d_6$ )  $\delta$  (ppm): 8.32 (d, 1H), 8.16 (d, 1H), 7.66 (dd, 1H).

## 3 Results and Discussion

### 3.1 Chemistry

This study presents a simple approach for the synthesis of 2-azidobenzothiazoles through the transformation of substituted 2-aminobenzothiazoles. The method involves the utilization of sodium nitrite and sodium azide as key reagents under mild reaction conditions (Scheme 1). The introduction of azide groups into organic molecules, facilitated by sodium nitrite and sodium azide, is a significant chemical transformation that opens doors to diverse functionalization and subsequent applications. The mild reaction conditions employed, in conjunction with these reagents, contribute to the synthesis's accessibility and potential applicability across a range of substrates. The synthesis of 2-azidobenzothiazoles via (Figure 1) this methodology adds to the toolbox of functional group transformations. The ability to incorporate azide functionality onto the benzothiazole scaffold is noteworthy due to the versatile reactivity of azides, which can be harnessed for further derivatization and diversification of the synthesized compounds. Additionally, the utilization of substituted 2-aminobenzothiazoles as starting materials allows for the introduction of specific substituents that can influence the resulting compound's properties and behaviors. The mild conditions employed in this synthesis are advantageous for maintaining the integrity of sensitive functional groups and minimizing unwanted side reactions. This feature is particularly beneficial when working with complex or delicate molecules, where harsher conditions might lead to undesired chemical transformations or yield losses. Further analysis of the equal amounts of sodium nitrite, sodium acetate, and sodium azide necessary for the reaction revealed that 4 equivalents of each were suitable to achieve the desired product in excellent yield. The synthesis of 2-azidobenzothiazoles in an isolated yield of 80%–95% results from the smooth, rapid, and quantitative progression of the reaction. It is evident that both electron donating and electron withdrawing substrates are acceptable for this transformation and generated good to excellent yields of the intended product in 1 h, establishing the further scope of the reaction. It was intriguing to learn that free ester and halogen groups might withstand the conditions of a reaction without producing hydrazide.

The choice of substituents and substitution patterns in the synthesis of 2-azidobenzothiazoles, as well as the subsequent antibacterial activity studies, seems to be guided by specific factors aimed at enhancing the antibacterial potential of the compounds while minimizing cytotoxicity. The selection of certain substituents and substitution patterns has been inspired by previous studies or analogs that have shown promising

antimicrobial activities. The presence of electron-withdrawing groups like  $-NO_2$  at the *meta* position increases the antibacterial activity by influencing interactions with bacterial targets. In this context, the introduction of a nitro group ( $-NO_2$ ) on the benzothiazole ring might enhance antibacterial potential. Replacement of the *meta* substituent of benzothiazole ring with methoxy group (2b), carboxylate (2c), hydrogen (2e), or ethoxy decreased the activity. Conversely, introducing a 4,6-difluoro group (2a) on the benzothiazole ring did not show any enhancement in the activity. In addition to this, the presence of the halogen group at the *ortho* position and a methyl group at the *para* position of the benzothiazole ring do not exhibit significant effects on the activity. The capability of 2-azido-6-nitro-benzothiazole to inhibit biofilm formation is noteworthy. This indicates potential interference with bacterial adhesion and colonization, an important factor in bacterial pathogenicity. The study's focus on extended exposure of a human cell line (Human Embryonic Kidney-293) to higher concentrations of 2-azido-6-nitro-benzothiazole suggests an attempt to determine the compound's selectivity for bacterial cells over human cells. The fact that the compound demonstrates selective cytotoxicity towards bacterial cells even at higher concentrations is promising for potential therapeutic applications.

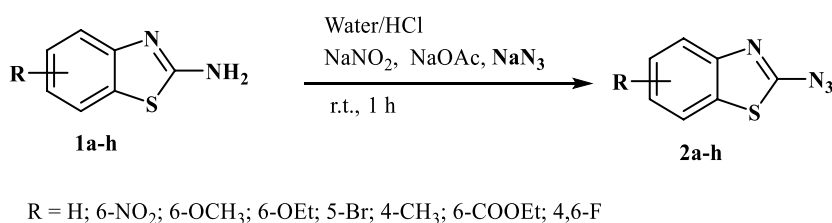
### 3.2 In Vitro antibacterial activity

#### 3.2.1 Minimum inhibitory concentration (MIC)

The Antibacterial Activity and MIC of all the synthesized compounds were determined using the Broth Micro dilution method as described in the methodology. All the synthesized compounds were tested for their antibacterial activity against the American Type Culture Collection (ATTC) strains of *S. aureus*, *E. faecalis*, *B. cereus*, *K. pneumonia*, *P. aeruginosa* and *E. coli* and clinical isolates of Methicillin Resistant *S. aureus* and Multidrug Resistant *E. coli*. It was found that compound 2d showed good antibacterial activity against the Gram (+) bacterial strains. It was elucidated that the compounds are more active against the Gram (+) bacterial strains, *E. faecalis*, and *S. aureus* with MIC of 8  $\mu g/mL$  (Table 1). However, it was moderately active against Gram (–) bacteria *P. aeruginosa* and Gram (+) bacteria *B. cereus* with a MIC value of 64  $\mu g/mL$ . Substantially the compound showed activity even against the Resistant strains, MRSA, and MDR *E. coli* of clinical origin with a MIC value of 128  $\mu g/mL$  (Tables 1, 2). These results were found to be consistent with several other benzothiazole derivatives, which inhibited the growth of Gram (+) and Gram (–) bacteria (Catalano et al., 2013; Singh et al., 2013). The MIC values of control drugs of known MIC values against the bacterial strains were also similar to the range given by CSLI (Clinical And Laboratory Standards Institute).

#### 3.2.2 Minimum bactericidal concentration (MBC)

As MIC only measures the ability of antimicrobial agents to inhibit bacterial growth, we performed an MBC assay which determines the lowest concentration of antimicrobial compound that can kill 99.9% of bacterial cells. MBC is required by regulatory agencies for approval of new antimicrobials. The MBC of the series



SCHEME 1

2-aminobenzothiazoles converted into 2-azidobenzothiazoles using sodium nitrite and sodium azide.

**TABLE 1 MIC (μg/mL) of the compounds and antibiotics tested against Gram (+) bacterial strains. Amikacin (AMK), Streptomycin (STR) and Ciprofloxacin (CIP) were used as controls.**

S. No.	Compound	<i>S. aureus</i>	<i>E. faecalis</i>	<i>B. cereus</i>	MRSA
1	<b>2a</b>	128	64	128	128
2	<b>2b</b>	128	128	128	128
3	<b>2c</b>	64	64	128	128
4	<b>2d</b>	<b>8</b>	<b>8</b>	64	128
5	<b>2e</b>	128	32	64	128
6	<b>2f</b>	128	>128	128	128
7	<b>2g</b>	128	128	128	128
8	<b>2h</b>	128	128	128	128
9	AMK	2.5	2.5	1.25	>128
10	STR	2.5	2.5	2.5	>128
11	CIP	1.25	0.3125	2.5	>128

The bold values in the tables depict MIC, MBC in low range.

of compounds **2a-h** was assessed against the Gram (+) bacterial strains *E. faecalis* and *S. aureus* as the compounds exhibited comparatively better MIC values against these strains compared to other strains. The MBC values must not be more than four times the MIC, which is consistent with our results (Gonzalez et al., 2013). For both *S. aureus* and *E. faecalis* MBC of the lead compound **2d**, was equal to 2xMIC, i.e., 16 μg/mL. The other compounds tested had bactericidal effects (led to 99.9% killing) rather than bacteriostatic effects, with MBC values of 128 μg/mL. Compound **2a** showed bactericidal activity at 2xMIC (128 μg/mL) against *E. faecalis*. Compound **2b** exhibited bactericidal activity at its MIC values, indicating their potential as promising antimicrobial agents that can effectively inhibit and kill bacterial pathogens. **2c** showed bactericidal potential against both Gram (+) bacteria at 2xMIC. **2e** showed bactericidal potential only against *E. faecalis* at 4x MIC. Ampicillin was used as a control drug and its MIC and MBC values against *S. aureus* were found to be 4 and 8 μg/mL and for *E. faecalis* the MIC and MBC values were 2 and 4 μg/mL. Negative controls for both strains, devoid of compounds were used to validate the CFU counts. CFU enumeration indicated a 3-log reduction, 99.9%

**TABLE 2 MIC (μg/mL) of the compounds and antibiotics tested against Gram (–) bacterial strains. Amikacin (AMK), Streptomycin (STR) and Ciprofloxacin (CIP) were used as controls.**

S. No.	Compound	<i>P. aeruginosa</i>	<i>K. pneumonia</i>	<i>E. coli</i>	MDR <i>E. Coli</i>
1	<b>2a</b>	128	128	128	128
2	<b>2b</b>	128	64	64	128
3	<b>2c</b>	128	128	64	128
4	<b>2d</b>	64	128	128	128
5	<b>2e</b>	64	128	128	128
6	<b>2f</b>	128	128	128	128
7	<b>2g</b>	128	128	128	128
8	<b>2h</b>	128	128	128	128
9	AMK	2.5	2.5	2.5	>128
10	STR	2.5	2.5	2.5	>128
11	CIP	5	1.25	0.015	>128

The bold values in the tables depict MIC, MBC in low range.



**TABLE 3** MBC ( $\mu\text{g/mL}$ ) of 2-azidobenzothiazoles against *Staphylococcus aureus* and *E. faecalis*.

S. No.	Compound name	<i>E. faecalis</i>	<i>S. aureus</i>
1	<b>2a</b>	128	128
2	<b>2b</b>	128	128
3	<b>2c</b>	128	128
4	<b>2d</b>	<b>16</b>	<b>16</b>
5	<b>2e</b>	128	>128
6	<b>2f</b>	128	128
7	<b>2g</b>	128	128
8	<b>2h</b>	128	128
9	Ampicillin	<b>4</b>	<b>8</b>

The bold values in the tables depict MIC, MBC in low range.

killing in both Gram (+) bacteria compared to the CFU count of Growth control which is indicative of the MBC. Overall, these findings suggest that the tested compounds have potent bactericidal activity against *E. faecalis* and *S. aureus*, which could be crucial in eradicating bacterial infections. The MBC values obtained after the enumeration of the CFU/mL are given in [Table 3](#).

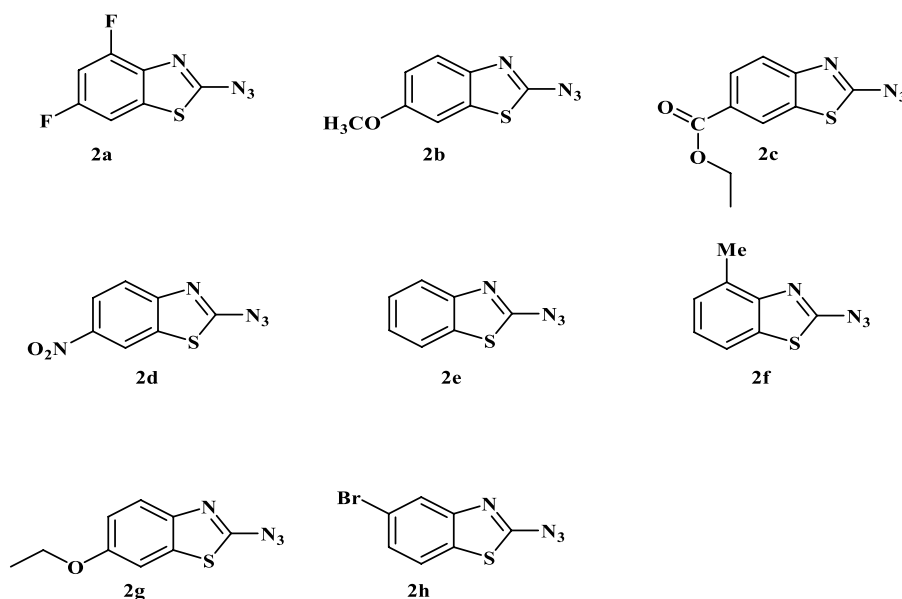
### 3.2.3 Time kill kinetics

To study the dynamics of *in vitro* activity, we assessed the kill curve kinetics of our lead compound **2d** against *S. aureus* and *E. faecalis* at concentrations of MIC (8  $\mu\text{g/mL}$ ), 2xMIC (16  $\mu\text{g/mL}$ ) and 4xMIC (32  $\mu\text{g/mL}$ ) for 24 h at seven time points (0, 4, 8, 12, 16, 20 and 24 h of exposure) using the two methods as described in methodology.

#### 3.2.3.1 Assessment of 24-hour time-kill kinetics via CFU/mL evaluation

**3.2.3.1.1 Staphylococcus aureus.** [Figure 2A](#) represents the time kill curve of the compound **2d** against *S. aureus* at different concentrations (MIC, 2xMIC, and 4xMIC) at the given time points, compared to ampicillin (2xAMP) and growth control (GC). The colonies were counted and converted into log<sub>10</sub> values in Excel. At time zero, all cultures showed similar bacterial counts ranging from 5.08 to 5.10 log<sub>10</sub> CFU/mL. As time progressed, the bacterial counts decreased in all cultures except GC. The compound **2d** at 4xMIC showed the most potent activity, reducing the bacterial counts to 0.08 log<sub>10</sub> CFU/mL after 12 h of incubation (more than 3 log reductions). In comparison, at 2xMIC, compound **2d** reduced the bacterial counts to 0.4 log<sub>10</sub> CFU/mL within 16 h, and at MIC, the reduction was modest, with bacterial counts remaining at 2.403 log<sub>10</sub> CFU/mL after 24 h of incubation indicating the bacteriostatic nature of the compound at a lower concentration. When comparing the activity of compound **2d** to ampicillin (2xAMP), the results showed that at 4xMIC and 2xAMP, the bacterial counts reduced to similar levels after 12 h of incubation. Moreover, at the time interval of 4–12 h maximum killing was observed at all three concentrations. In conclusion, compound **2d** showed a concentration-dependent as well as time-dependent bactericidal activity against *S. aureus*, with the highest bactericidal activity observed at 4xMIC within 12 h.

**3.2.3.1.2 Enterococcus faecalis.** [Figure 2B](#) represents the time-kill curve of *E. faecalis*, with various concentrations of **2d**, MIC, 2xMIC, 4xMIC, and 2xAMP at different time points. The bacteria appear to be highly susceptible to the compound as evidenced by the significant decrease in the growth rate at higher concentrations over time. After an interval of 4 h, a significant reduction in the growth

**FIGURE 1**

Depiction of the synthesized 2-azidobenzothiazoles. Reaction conditions: Substrate (0.5 mmol, 1equiv),  $\text{NaNO}_2$  (2 mmol, 4equiv),  $\text{NaOAc}$  (2 mmol, 4equiv),  $\text{NaN}_3$  (2 mmol, 4equiv),  $\text{H}_2\text{O}/\text{HCl}$ , r.t., 1 h. Isolated yield and structure were confirmed by comparison of IR, mp, MS, and  $^1\text{H}$  NMR. (**Note:** Although we have not experienced any problem in handling this compound, precautions should be taken due to its explosive nature).

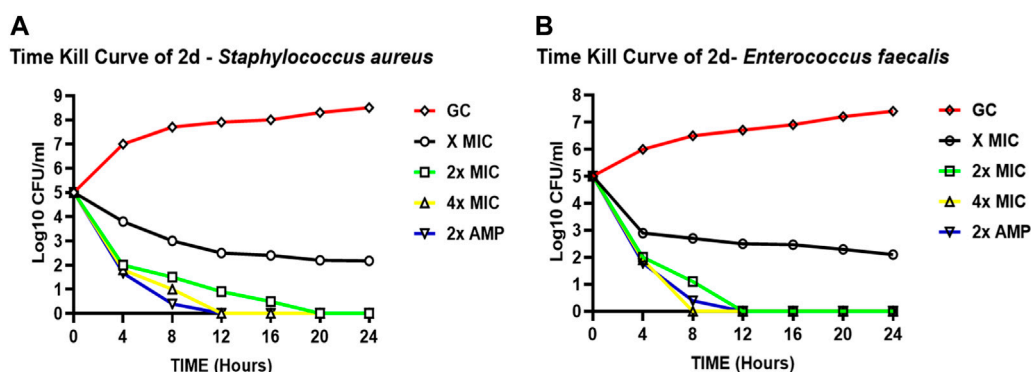


FIGURE 2

Time-kill curves of compound **2d**. The killing activity of **2d** against two bacterial strains *S. aureus* (A) and *E. faecalis* (B) monitored for 24 hours by CFU Enumeration method. The compound concentration used in the experiment were MIC (green), 2x MIC (pink), and 4x MIC (blue). Ampicillin indicated by the yellow line was used as a positive control. For negative control (Black line), the cultures were incubated under the similar condition without any drug.

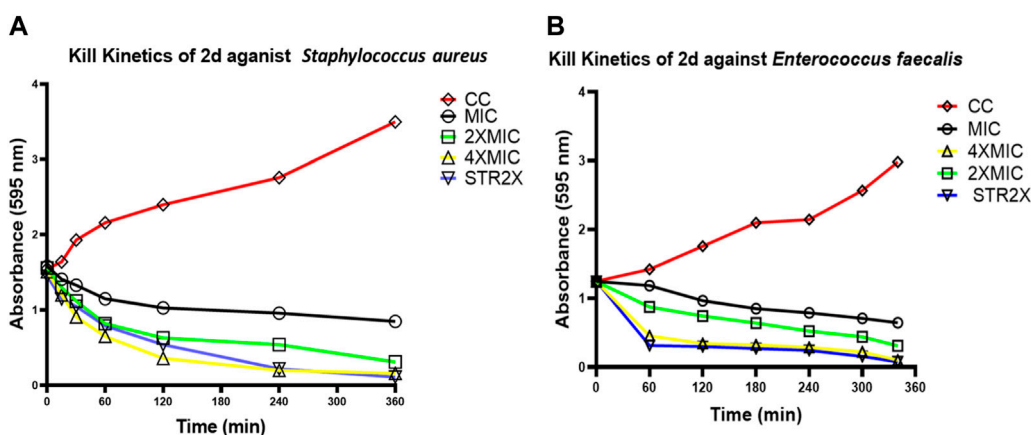


FIGURE 3

Time kill curves of **2d**. The killing activity of **2d** against two bacterial strains *S. aureus* (A) and *E. faecalis* (B) was monitored for 360 min. The compound concentration used in the experiment were MIC (Black), 2xMIC (Green), and 4xMIC (Yellow). Streptomycin (STR) indicated by the Blue line was used as a positive control. For negative control (Red line), the cultures were incubated under similar conditions without any drug.

rate was observed at all concentrations (approximately 2-log reduction across all concentrations). After 8 h, there was a significant decrease in CFU/mL count, at higher concentrations of 2x and 4xMIC, while as for MIC the activity remained static. 4xMIC exhibited bactericidal activity achieving 99.9% killing within 8 h. At MIC the compound exhibited a bacteriostatic activity at all time points. At 2xMIC the bactericidal activity was achieved after 12 h which is similar to that of Ampicillin. The results suggest that *E. faecalis* was highly susceptible to the compound at higher concentrations and the bactericidal effect was observed at 2xMIC and 4xMIC within 12 and 8 h respectively. Overall, we can deduce from the results that the activity of compound **2d** is concentration dependent as well as time dependent killing.

### 3.2.3.2 Evaluation of time-kill kinetics based on MTT-reduction on a 360-minute scale

To determine whether the effect of compound **2d** on the growth of *S. aureus* and *E. faecalis* is dose dependent, the time kill kinetic

assay was carried out using MTT on the minute scale as described in the methodology. Both the bacterial strains were incubated individually with compound **2d** at its final concentration of MIC, 2xMIC, and 4xMIC. The optical density of the cultures was recorded at time intervals of 60 min. It is clear from Figure 3 that the compound showed bactericidal activity against both strains in a dose dependent manner. The killing pattern of compound **2d** against *S. aureus* was comparable to that of Streptomycin with over 75% of bacterial death within 4 h of the treatment. For *E. faecalis*, however, the compound showed a similar rate of death after 2 h of treatment compared to Streptomycin.

### 3.2.4 Post-antibiotic effect (PAE)

To investigate the effect of compound **2d**, post its withdrawal, and assess whether the suppression in the growth of bacterial cells, *S. aureus* and *E. faecalis* persist after this brief exposure, the post-antibiotic effect (PAE) was calculated. PAE was deduced by the viable count method as described. *Staphylococcus aureus* and

**TABLE 4** Post antibiotic activity of **2d** at MIC, 2xMIC, and 4xMIC and Ampicillin against *Staphylococcus aureus*.

Compound	MIC	Time (hours)	PAE = T-C
	1X	6	5.00
<b>2d</b>	2X	7	6.00
	4X	6	5.00
Ampicillin	2X	6	5.00

The culture controls took, C= 1.00 h to grow in the absence of the antimicrobial agent. The average of the PAE, of **2d** at different concentrations was around 5.33 h.

**TABLE 5** Post antibiotic activity of **2d** at MIC, 2xMIC, and 4xMIC and Ampicillin against *E. faecalis*.

Compound	MIC	Time (hours)	PAE = T-C
	1X	7	5.00
<b>2d</b>	2X	8	6.00
	4X	8	6.00
Ampicillin	2X	8	6.00

The culture controls took, C= 2 h to grow in the absence of the antimicrobial agent. The average of the PAE, of **2d** at different concentrations was around 5.66 h.

*E. faecalis* were individually treated with MIC (8 µg/mL), 2xMIC (16 µg/mL), and 4xMIC (32 µg/mL) concentrations of the compound **2d** and MIC of Ampicillin for 2 h. The growth was monitored by CFU enumeration after a time interval of 1 h. The PAE results represented here are determined at a higher inoculum size of  $1 \times 10^6$  CFU/mL as against the routine inoculum size of  $1 \times 10^5$  CFU/mL more commonly used for susceptibility testing (MIC). To avoid the ambiguity in PAE results owing to the higher inoculum effect, MIC assay was first performed at a higher inoculum size ( $1 \times 10^6$  CFU/mL) to select the correct concentrations of antibacterial agents (**2d** & AMP) for PAE determination. No change in MIC of **2d** as well as Ampicillin was determined at higher inoculum size. PAE was calculated using formula (3) as described in the methodology.

### 3.2.4.1 Staphylococcus aureus

The cells took an average of 5.33 h to increase their CFU by 1 log<sub>10</sub> post-withdrawal of compound **2d**, irrespective of the concentration of compound **2d**. After treatment and removal of 8 and 32 µg/mL of **2d**, the growth was suppressed for around 6 h. The recovery period after **2d** treatment was almost identical to that of MIC of Ampicillin treatment. The PAE results indicate that compound **2d**, at concentrations ranging from 8, 16, and 32 µg/mL, demonstrates a significant and sustained inhibitory effect on bacterial regrowth even after the removal of the antibiotic. The consistent PAE duration across the tested concentrations suggests that compound **2d** exhibits a concentration-independent PAE (Table 4).

### 3.2.4.2 Enterococcus faecalis

In the case of *E. faecalis*, the cells took an average of 5.66 h to increase their CFU by 1 log<sub>10</sub> post-withdrawal of compound **2d**, which was comparable to that of Ampicillin. In this case, also the results indicate that the post-compound effect is independent of

drug concentration as there is not much variation in time taken by the bacteria to increase their CFU by 1 log<sub>10</sub> at all three concentrations tested (Table 5).

The results reveal that both *S. aureus* and *E. faecalis* exhibited similar post-treatment growth characteristics in response to compound **2d**. The average time required for a 1 log<sub>10</sub> CFU increase was 5.33 h (±0.577) for *S. aureus* and 5.66 h (±0.617) for *E. faecalis* when treated with MIC, 2xMIC, and 4xMIC concentrations of compound **2d** (Figure 4). These results suggest a consistent and predictable post-treatment effect independent of the drug concentration, indicating the potential effectiveness of compound **2d**. The sustained inhibitory effect of concentration-independent PAE can reduce the selection pressure for antibiotic-resistant bacterial strains. By maintaining a prolonged suppression of bacterial growth even after sub-MIC levels, the development and spread of resistance mechanisms may be hindered, preserving the effectiveness of the antibiotic over an extended period. Concentration-independent PAE offers advantages in terms of flexibility in dosing, extended suppression of bacterial regrowth, reduced resistance development, and optimized antibiotic therapy. These benefits contribute to the potential improvement in treatment outcomes and the management of bacterial infections.

### 3.2.5 Fluorescent microscopy

To further explore the mechanism by which the compound targeted the bacterial cells, fluorescent microscopy was performed on the bacterial cells treated with the compound. Post **2d** treatment, *E. faecalis* and *S. aureus* were treated with two fluorescent dyes 4',6-diamidino-2-phenylindole (DAPI), and propidium iodide (PI). DAPI is a fluorescent dye that binds to DNA and emits blue fluorescence upon excitation by ultraviolet light and PI is also a fluorescent dye that binds to DNA, but it emits red fluorescence upon excitation by ultraviolet light. PI is a membrane-impermeable DNA binding fluorescent dye whereas DAPI is a membrane-permeable DNA binding dye. PI only enters cells with compromised membranes and stains the nucleic acid of dead cells. DAPI is permeable to the cell wall and fluoresces upon binding to chromosomal DNA, whether the cells are dead or alive. For control, the cells were treated with DAPI and PI without prior treatment with compound **2d**. The DAPI/PI staining results revealed the presence of red fluorescence in both *S. aureus* and *E. faecalis* bacterial strains. The red fluorescence observed in the bacterial cells indicates the uptake and binding of PI, suggesting compromised cell membrane integrity. This red fluorescence was visually distinguishable from the blue fluorescence emitted by DAPI, which stains the DNA of both live and dead bacteria. The identification of compromised membrane integrity is of significance as it can indicate the susceptibility of *S. aureus* and *E. faecalis* strains to antimicrobial treatments. The presence of red fluorescence provides evidence of cell damage and potential loss of viability, suggesting that these strains may be more susceptible to the effects of **2d** targeting the cell membrane. From Figures 5A,B, it is evident that the antibacterial activity of compound **2d** was due to damage to the cell wall of the bacterial cells. These findings suggest that compound **2d** targets the cell wall of bacterial cells, leading to compromised membrane integrity and ultimately cell death.

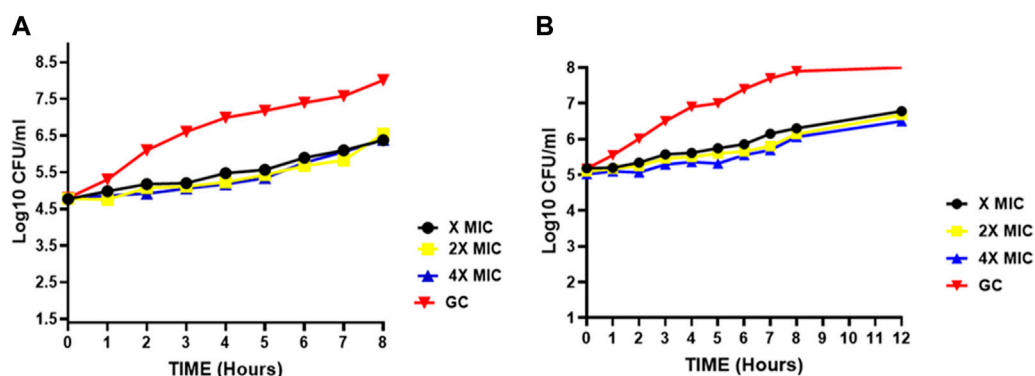


FIGURE 4

Post-antibiotic effect of compound **2d** at various concentrations against (A) *Staphylococcus aureus* (B) *E. faecalis* indicating the time points at which a 1 log<sub>10</sub> CFU/mL increase was observed for *Staphylococcus aureus* and *E. faecalis* after a brief exposure (2 h) to compound **2d** at different concentrations (x, 2x, and 4xMIC) and subsequent removal of the antimicrobial agent.

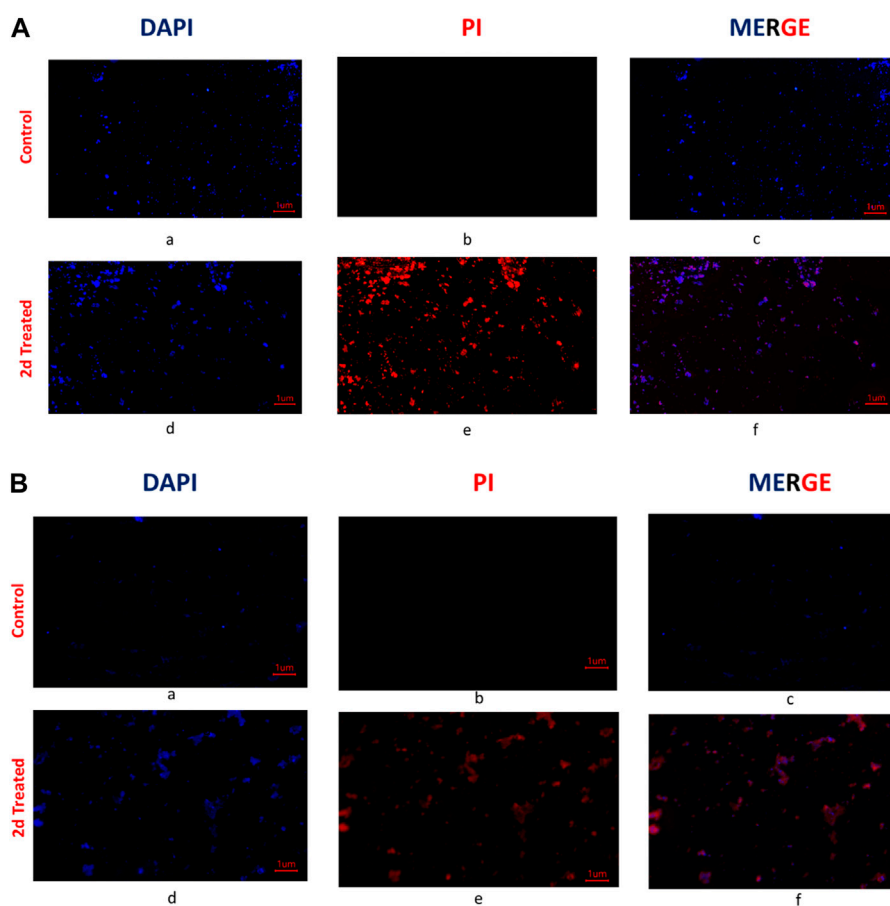


FIGURE 5

(A) Fluorescent images of *Staphylococcus aureus*: The untreated cells were stained with DAPI and PI and visualized under a fluorescent microscope. The photographed images of cells for DAPI (a) and PI (b) were merged (c). Under similar conditions **2d** (2x) treated *Staphylococcus aureus* cells were photographed for DAPI (d) and PI (e) and the images were merged using Image (f); (B) Fluorescent microscopy images of *E. faecalis*: The untreated cells were stained with DAPI and PI and visualized under a fluorescent microscope (Magnus). The photographed images of cells for DAPI (a) and PI (b) were merged (c). Under similar conditions, **2d** (2x) treated *E. faecalis* cells were photographed for DAPI (d) and PI (e), and the images were merged using Image (f).



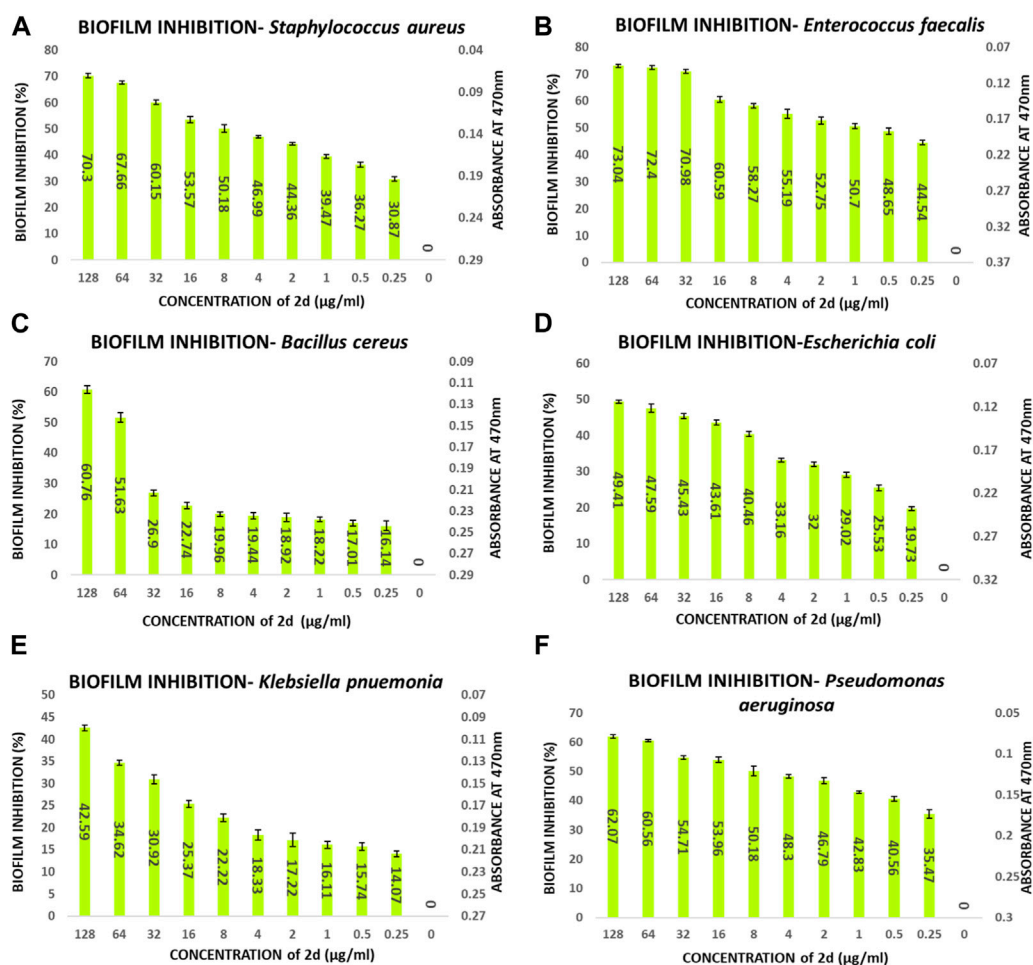


FIGURE 6

Quantitative analysis of biofilm percentage inhibition- (A) *Staphylococcus aureus*; (B) *E. faecalis*; (C) *Bacillus cereus*; (D) *E. coli*; (E) *Pseudomonas aeruginosa*; (F) *Klebsiella pneumonia*.

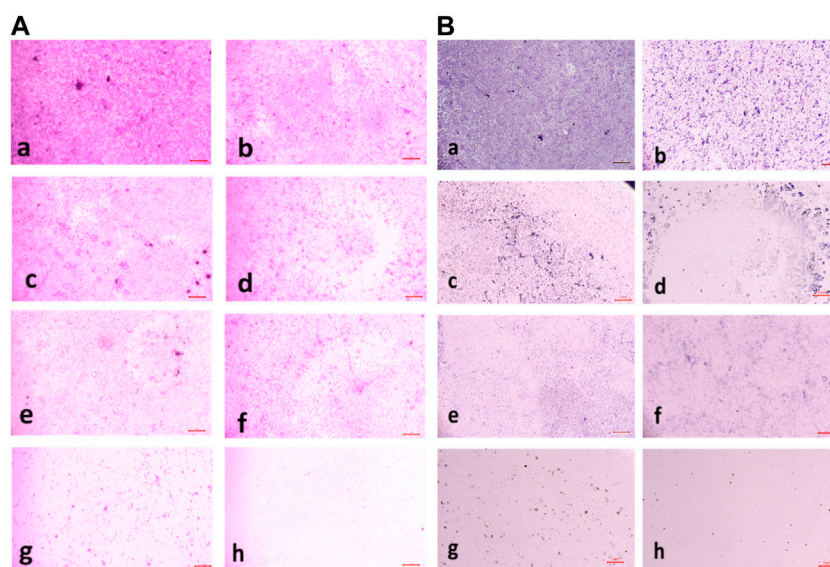
Conducting cell membrane-related studies on synthesized derivatives is a reasonable approach to understand their mechanisms of action. The cell membrane plays a critical role in regulating the passage of molecules and ions in and out of the cell, as well as in cell signalling and communication. Therefore, studying how the synthesized derivatives interact with the cell membrane can provide valuable insights into their potential mechanisms of action. However, we understand it is important to note that cell membrane-related studies alone may not provide a comprehensive understanding of the mechanisms of action of the synthesized derivatives. There could be additional mechanisms involved in their effects on cell viability that are independent of the cell membrane but DAPI and PI are commonly used fluorescent dyes that can be used to assess cell viability and membrane integrity. DAPI stains the nuclei of both live and dead cells, while PI is excluded from live cells but stains the DNA of dead or damaged cells with compromised membrane integrity. DAPI/PI staining allows for the differentiation between live cells (DAPI-positive, PI-negative). By using DAPI/PI staining, we wanted to assess the overall cell viability and determine whether the synthesized derivative have any

detrimental effects on cell membrane integrity, which may lead to cell death.

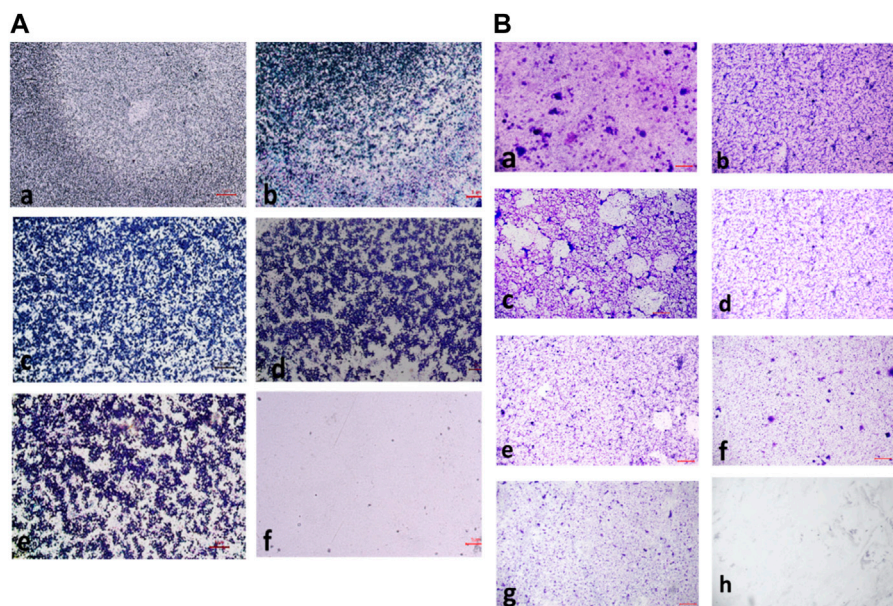
### 3.2.6 Biofilm inhibition assay

The compound **2d**, with the strong antibacterial activity, was tested against American Type Culture Collection (ATCC) strains of biofilm-forming Gram (+) bacteria, *S. aureus*, *E. faecalis*, *B. cereus* and Gram (–) bacteria, *E. coli*, *P. aeruginosa*, *K. pneumonia*. The Quantitative assessment of biofilm inhibition was done by calculating the percentage inhibition of the compound through spectrophotometric analysis for each bacterial strain by Microtiter Plate Biofilm Assay. The Qualitative assessment was done by CV staining and visualization under the microscope.

The percentage of biofilm inhibition was determined at various concentrations of compound **2d** (0.25–128 µg/mL), and the values reported are the means of three optical density (OD) measurements to ensure more reliable and accurate results. Compound **2d** exhibited significant biofilm inhibitory activity against all tested bacterial strains in a concentration-dependent manner. The percentage of biofilm inhibition varied across different

**FIGURE 7**

(A) Light microscopic images of biofilm (10x- Magnus) in *Staphylococcus aureus* at (a) Growth Control (b) 4 µg/mL (c) 8 µg/mL (d) 16 µg/mL (e) 32 µg/mL (f) 64 µg/mL (g) 128 µg/mL treated wells (h) media control; (B) Light microscopic images of biofilm (10x- Magnus) in *E. faecalis* at (a) Growth Control (b) 4 µg/mL (c) 8 µg/mL (d) 16 µg/mL (e) 32 µg/mL (f) 64 µg/mL (g) 128 µg/mL treated wells (h) media control.

**FIGURE 8**

(A) Light microscopic images of biofilm (10x- Magnus) in *Bacillus cereus* at (a) Growth Control (b) 4 µg/mL (c) 16 µg/mL (d) 32 µg/mL (e) 128 µg/mL (f) media control; (B) Light Microscopic Images of Biofilm (10x- Magnus) in *E. coli* at (a) Growth Control (b) 4 µg/mL (c) 8 µg/mL (d) 16 µg/mL (e) 32 µg/mL (f) 64 µg/mL (g) 128 µg/mL treated wells (h) media control.

concentrations and bacterial species. For *S. aureus*, compound **2d** displayed increasing biofilm inhibition percentages with higher concentrations. At the highest tested concentration of 128 µg/mL, the biofilm inhibition was 70.30%. Similarly, for *E. faecalis*, the biofilm inhibition reached 73.04% at the same concentration.

*Bacillus cereus* showed a distinct trend, with biofilm inhibition percentages of 61.23% and 53.09% at the highest concentration (128 µg/mL) and half that concentration (64 µg/mL), respectively. However, the inhibitory effect decreased significantly at lower concentrations. Among the Gram (–) bacteria, *Pseudomonas*



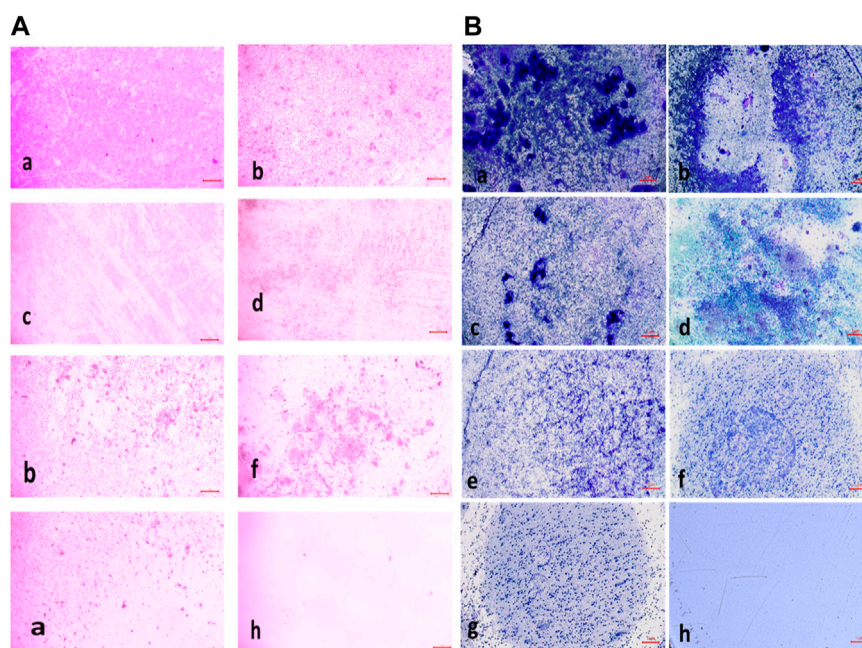


FIGURE 9

(A) Light Microscopic Images of Biofilm (10x- Magnus) in *Pseudomonas aeruginosa* at (a) Growth Control (b) 4  $\mu\text{g/mL}$  (c) 8  $\mu\text{g/mL}$  (d) 16  $\mu\text{g/mL}$  (e) 32  $\mu\text{g/mL}$  (f) 64  $\mu\text{g/mL}$  (g) 128  $\mu\text{g/mL}$  treated wells (h) media control; (B) Light Microscopic Images of Biofilm (10x- Magnus) in *Klebsiella pneumonia* at (a) Growth Control (b) 4  $\mu\text{g/mL}$  (c) 8  $\mu\text{g/mL}$  (d) 16  $\mu\text{g/mL}$  (e) 32  $\mu\text{g/mL}$  (f) 64  $\mu\text{g/mL}$  (g) 128  $\mu\text{g/mL}$  treated wells (h) media control.

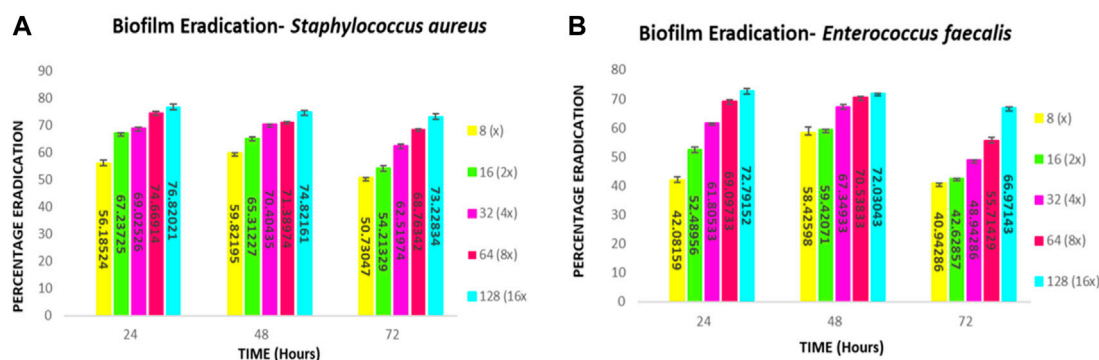


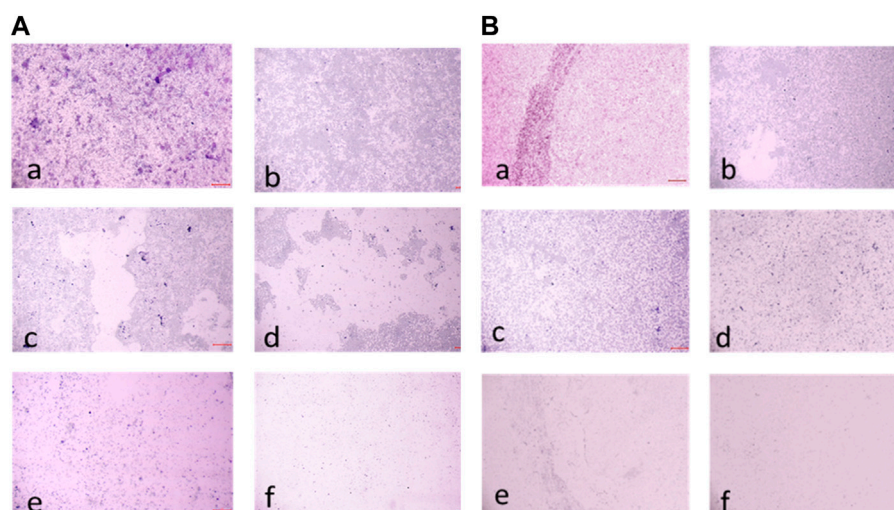
FIGURE 10

Quantitative Analysis: Biofilm eradication percentage (A) *Staphylococcus aureus* (B) *E. faecalis* at different concentrations of compound **2d** effecting the preformed 24-, 48- and 72-h biofilms.

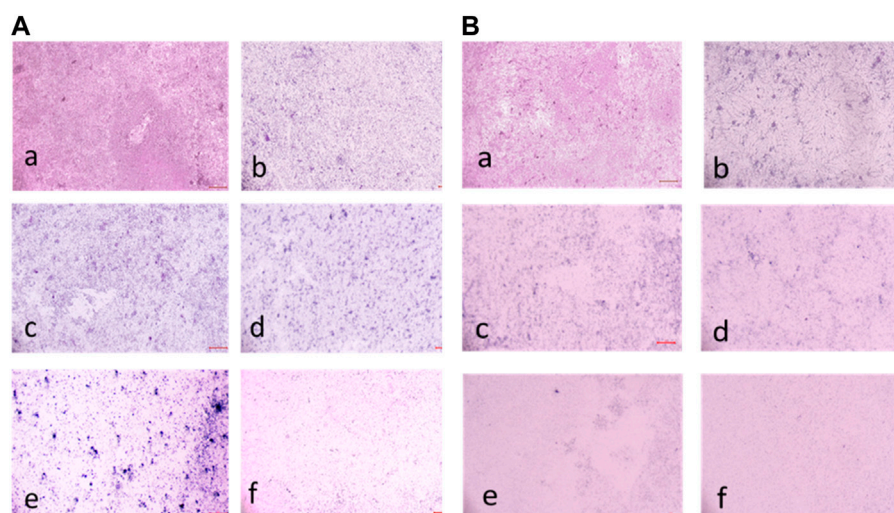
*aeruginosa* demonstrated substantial biofilm inhibition, with percentages ranging from 62.07% at 128  $\mu\text{g/mL}$  to 35.47% at 0.25  $\mu\text{g/mL}$ . *Escherichia coli* and *K. pneumonia* exhibited lower biofilm inhibition percentages, ranging from 19.73% to 49.41% and from 14.07% to 45.59%, respectively, across the tested concentrations. Overall, these results indicate that compound **2d** possesses significant biofilm inhibitory activity against a range of biofilm-forming bacterial strains with the most significant inhibitory potential against *S. aureus* and *E. faecalis*.

The percentage of biofilm inhibition at different concentrations of compound **2d** was consistent with the qualitative analysis

conducted using light microscopy. Microscopic examination revealed disrupted biofilm architecture and reduced biofilm biomass in the presence of compound **2d**, supporting the quantitative findings. The microscopic analysis provided visual confirmation of the biofilm inhibitory potential of compound **2d**. The growth control revealed a thick and compact biofilm structure, indicating the successful formation of mature biofilms by the tested bacterial strains. In contrast, the microscopic images of the biofilms treated with compound **2d** at different concentrations displayed notable differences compared to the growth control. The biofilms exposed to compound **2d** exhibited reduced biomass and disrupted

**FIGURE 11**

(A) Light microscopic images (20X) of biofilm eradication in 24 hour-preformed biofilm of *Staphylococcus aureus* by compound **2d**, (a) Growth control-showing initial attachment to surface (devoid of compound exhibiting biofilm formation after 24 h) (b) 8 µg/mL (c) 16 µg/mL (d) 32 µg/mL (e) 64 µg/mL (f) 128 µg/mL; (B) Biofilm of *Staphylococcus aureus* by compound **2d**, (a) Growth control-showing aggregation of cells (devoid of compound exhibiting biofilm formation after 48 h) (b) 8 µg/mL (c) 16 µg/mL (d) 32 µg/mL (e) 64 µg/mL (f) 128 µg/mL.

**FIGURE 12**

(A) Light Microscopic images (20X) of biofilm eradication in 72 hour-preformed biofilm of *S. aureus* by compound **2d**, (a) Growth control-showing mat formation (devoid of compound exhibiting biofilm formation after 72 h) (b) 8 µg/mL (c) 16 µg/mL (d) 32 µg/mL (e) 64 µg/mL (f) 128 µg/mL. (B) Light Microscopic images (20X) of biofilm eradication in 24 hour-preformed biofilm of *E. faecalis* by compound **2d**, (a) Growth control-showing initial attachment to surface (devoid of compound exhibiting Biofilm Formation after 24 h) (b) 8 µg/mL (c) 16 µg/mL (d) 32 µg/mL (e) 64 µg/mL (f) 128 µg/mL.

biofilm architecture. The qualitative analysis corroborated the quantitative results, confirming that compound **2d** has a significant impact on biofilm formation across different bacterial strains. The visual evidence of reduced biomass and disrupted biofilm architecture shown in the figures at various concentrations supports the notion that compound **2d** interferes with the crucial steps of biofilm development (Figures 6–9).

### 3.2.7 Biofilm eradication assay

The compound **2d** exhibited strong biofilm inhibition potential against both *E. faecalis* and *S. aureus* that prompted the evaluation of Biofilm Eradication potential against these two strains. The antibiofilm effect of the compound was evaluated both qualitatively and quantitatively by Light Microscopy and Crystal Violet method at concentrations 8, 16, 32, 64, and 128 µg/mL to



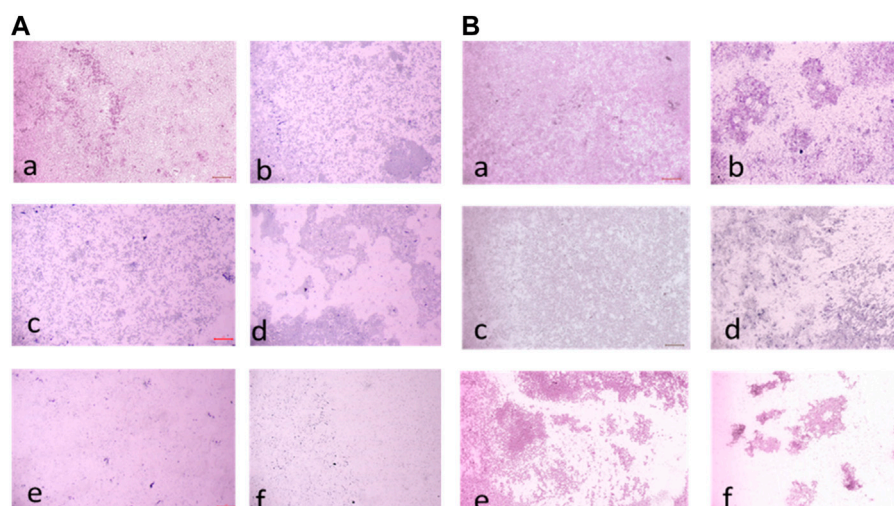


FIGURE 13

(A) Light microscopic images (20X) of biofilm eradication in 48 hour-preformed biofilm of *E. faecalis* by compound **2d**, (a) Growth control-showing aggregation of cells (devoid of compound exhibiting biofilm formation after 48 h) 8 µg/mL (c) 16 µg/mL (d) 32 µg/mL (e) 64 µg/mL (f) 128 µg/mL. (B) Light microscopic images (20X) of biofilm eradication in 72 hour-preformed biofilm of *E. faecalis* by compound **2d**, (a) Growth control-showing mat formation (devoid of compound exhibiting biofilm formation after 72 h) (b) 8 µg/mL (c) 16 µg/mL (d) 32 µg/mL (e) 64 µg/mL (f) 128 µg/mL.

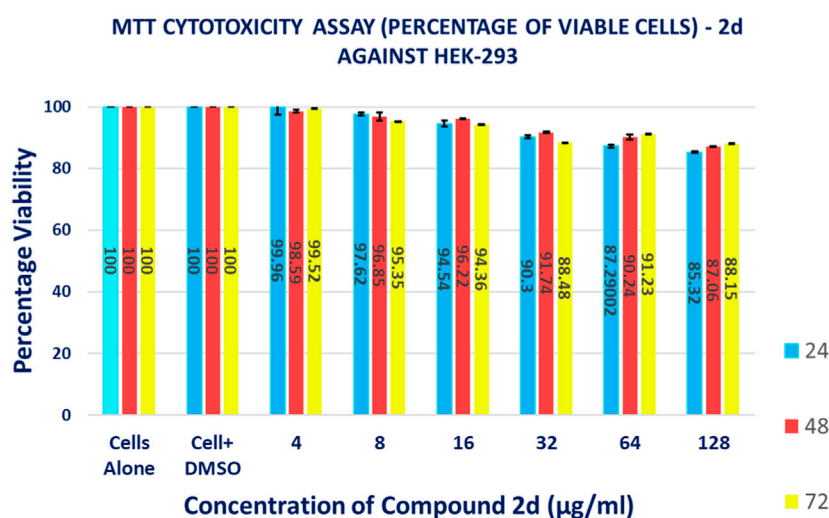


FIGURE 14

Graphical representation of the results of MTT cytotoxicity assay.

evaluate the effect of the compound on various stages of biofilm formed at 24, 48 and 72 h. Light microscopic images revealed that the growth control wells exhibited significant biofilm formation at all three-time points. At 24 h, cell attachment was observed, followed by cell aggregation at 36 h, and extensive biofilm formation or mat formation at 48 h. However, in wells incubated with compound **2d** at different concentrations, non-aggregation of cells was observed during all stages of biofilm formation for both bacterial strains. This indicates the compound's ability to inhibit cell aggregation, a critical step in biofilm development.

This qualitative finding was further investigated with the crystal violet staining method by comparing the absorbance

between the growth control wells and the wells incubated with the compound. The percentage of biofilm Eradication at various concentrations is shown (Figures 10A, B) which indicates a strong antibiofilm potential of the compound eradicating up to more than 40% of the biofilm at all concentrations. The crystal violet staining method confirmed the qualitative findings, demonstrating the compound's antibiofilm potential. The absorbance measurements showed that compound **2d** eradicated over 40% of the biofilm at all tested concentrations. Notably, at higher concentrations, the compound exhibited substantial eradication potential against both *E. faecalis* and *S. aureus*, eliminating 70%–77% of the preformed biofilm at all

**TABLE 6** Percentage of HEK-293 cell viability after treatment with different concentrations 2d for different time points (percentages expressed are the average values of three experiments  $\pm$ SD).

Average percentage of viable cells after exposure with 2d for different time durations			
Conc. ( $\mu$ g/mL)	24 h	48 h	72 h
4	99.96 $\pm$ 2.532	98.59 $\pm$ 0.501	99.52 $\pm$ 0.001
8	97.62 $\pm$ 0.475	96.85 $\pm$ 1.269	95.35 $\pm$ 0.010017
16	94.54 $\pm$ 0.989	96.22 $\pm$ 0.173	94.36 $\pm$ 0.006429
32	90.30 $\pm$ 0.557	91.74 $\pm$ 0.289	88.48 $\pm$ 0.002309
64	87.29 $\pm$ 0.428	90.24 $\pm$ 0.765	91.23 $\pm$ 0.024664
128	85.32 $\pm$ 0.164	87.06 $\pm$ 0.153	88.15 $\pm$ 0.005774

three-time points. These results suggest that compound **2d** has a strong biofilm eradication capability. The qualitative and quantitative evaluation of biofilm eradication correlated with each other. The eradication potential of the compound on the densely pre-biofilm at 72 h against both bacterial strains indicates that the compound can be a promising agent for biofilm eradication. The quantitative evaluation of the percentage of biofilm eradication was done as per the formula mentioned in the methodology and the results represented are the mean values of the three OD readings taken for each concentration in different wells. The compound effectively inhibited cell aggregation and eradicated preformed biofilms in a dose-dependent manner.

The biofilm eradication percentages of compound **2d** against 24-h formed *S. aureus* biofilms were found to be 59% at 8  $\mu$ g/mL, 67% at 16  $\mu$ g/mL, 69% at 32  $\mu$ g/mL, 74% at 64  $\mu$ g/mL, and 76% at 128  $\mu$ g/mL. For 48-h biofilms, the eradication percentages were 59%, 65%, 70%, 71%, and 74% at the corresponding concentrations. In the case of mature biofilms formed for 72 h, compound **2d** exhibited eradication percentages of 50%, 54%, 62%, 68%, and 73% at the respective concentrations.

The biofilm eradication percentages of compound **2d** against 24-h formed *E. faecalis* biofilms were found to be 42% at 8  $\mu$ g/mL, 52% at 16  $\mu$ g/mL, 61% at 32  $\mu$ g/mL, 69% at 64  $\mu$ g/mL, and 72% at 128  $\mu$ g/mL. For 48-h biofilms, the eradication percentages were 58%, 59%, 67%, 70%, and 72% at the corresponding concentrations. In the case of mature biofilms formed for 72 h, compound **2d** exhibited eradication percentages of 40%, 42%, 48%, 55%, and 66% at the respective concentrations.

These values represent the average mean of three independent experiments. The results of this study demonstrate the potent antibiofilm activity of compound **2d** against *S. aureus* and *E. faecalis* biofilms. The compound exhibited remarkable efficacy in eradicating biofilms at various time points and concentrations. Compound **2d** effectively eradicated a significant proportion of the 24-h formed biofilms. Even at the lowest concentration tested (8  $\mu$ g/mL), the compound achieved a substantial eradication percentage. As the concentration increased the eradication percentages also increased, reaching 72%–76% at the highest concentration (128  $\mu$ g/mL). These findings highlight the concentration-dependent efficacy of compound **2d** in disrupting and eliminating early-stage *S. aureus* and *E. faecalis* biofilms. Furthermore, compound **2d** demonstrated consistent efficacy in eradicating biofilms formed over 48 h. The eradication percentages

indicated its ability to penetrate and disrupt biofilm structures at various concentrations. Notably, even at lower concentrations, the compound achieved eradication percentages above 50%–65%, demonstrating its potency against established biofilms in both bacteria. Compound **2d** also exhibited substantial efficacy in eradicating mature biofilms formed over 72 h. The eradication percentages ranged from 50% to 73% for *S. aureus* and 40%–66% for *E. faecalis*, indicating its ability to target and disrupt the mature biofilm matrix. These results suggest that compound **2d** possesses strong biofilm-eradicating properties, even in the presence of a mature biofilm structure. The findings from this study highlight the potential of compound **2d** as an effective antibiofilm agent against *S. aureus* and *E. faecalis*. The ability of the compound to significantly reduce biofilm density and disrupt biofilm architecture is consistent with the qualitative observations made during the study. The strong correlation between the qualitative and quantitative evaluations supports the robustness of the antibiofilm activity of compound **2d**. The compound effectively inhibited cell adhesion, auto-aggregation, and mat formation, as observed under light microscopy. These findings suggest that compound **2d** may target key stages of biofilm development and inhibit biofilm formation (Figures 11–13).

### 3.2.8 Cytotoxicity assay

The MTT-based cell viability assay performed on HEK-293 verified that cells exposed to **2d** compound at varying concentrations for different time durations have a non-toxic effect on the human embryonic kidney cell lines. The results of the MTT-based cell viability assay were conducted on HEK-293 cells. Surprisingly, the findings indicate that the cells exposed to **2d** exhibited a non-toxic response, demonstrating higher percentages of viable cells even at higher concentrations and longer exposure durations (Figure 14). This suggests that the **2d** compound is cytocompatible and does not have a concentration- or time-dependent effect on cell viability. The MTT assay revealed that cell viability was significantly higher even at higher concentration ranges of 16–128  $\mu$ g/mL. The percentage viability was calculated using formula (5).

The data presented in Table 6 demonstrate the favorable impact of the **2d** compound on HEK-293 cell viability. At the lowest concentration tested (4  $\mu$ g/mL), the average viability percentages remained consistently high across all concentration and time point combinations. At the highest

concentration tested (128 µg/mL), the average viability percentage after 72 h of exposure was  $88.15\% \pm 0.005774\%$ , indicating that even at this relatively elevated concentration, the **2d** compound did not significantly compromise cell viability. This trend of high viability percentages persisted throughout the experiment, irrespective of the exposure duration. It is important to note that these results are specific to HEK-293 cells and should not be generalized to other cell types without further experimentation.

## 4 Conclusion, scope and limitations

In summary, we successfully synthesized 2-azidobenzothiazoles by employing sodium nitrite and sodium azide in a brief reaction time and established a straightforward, effective, and high-yielding method. The promising antibacterial activity of benzothiazole derivatives prompted us to perform *in vitro* antibacterial activity of the synthesized compounds. The experimental results revealed that compound **2d** exhibited potential antibacterial activity against various bacterial strains. As a result, compound **2d** could be exploited as a potential antimicrobial target for many drug-resistant microorganisms.

Our comprehensive *in vitro* study holds significant implications and contributions to the scientific community. It addresses the issue of antibiotic resistance which is fuelled by the decline in the development of new antibiotics that necessitates the exploration of novel therapeutic agents. Our study provides valuable insights into the antibacterial activity of 2-azidobenzothiazoles, demonstrating their potency against both Gram (+) and Gram (–) bacteria, including drug-resistant strains. Moreover, biofilm-associated infections pose a significant challenge in clinical settings due to their inherent resistance to conventional antibiotics. Our study reveals the remarkable ability of the lead compound **2d**, to inhibit and eradicate biofilms formed by various bacterial strains. This finding has important implications for developing effective strategies to manage chronic and persistent infections associated with biofilms. The identification of a potent lead compound **2d**, with selective cytotoxicity towards bacterial cells while sparing human cells, highlights its potential for therapeutic applications. This finding offers promising prospects for the development of safe and effective antimicrobial treatments. Further optimization and exploration of the lead compound, along with other compounds in the series, may lead to the development of novel antibiotics or antimicrobial agents. Our study further exemplifies the importance of drug discovery efforts in combating antibiotic resistance and biofilm-associated infections.

Although our study provides valuable insights into the antibacterial and antibiofilm potential, it is essential to acknowledge some limitations. Firstly, our experiments were conducted *in vitro*, and further investigations should include *in vivo* models to assess the compound's efficacy and safety in more complex biological systems. Our experiments were conducted solely *in vitro*, using laboratory-based assays. While these provide a controlled environment for evaluating the

compound's efficacy, they may not fully represent the complexity of bacterial infections *in vivo*. Further investigations using animal models or clinical studies are necessary to validate the potential therapeutic applications of these compounds. Although we performed a comprehensive analysis, focusing on multiple aspects such as MIC, MBC, kill kinetics, post-antibiotic effect, cytotoxicity, biofilm inhibition, and biofilm eradication, numerous other factors could influence the efficacy and safety of these compounds. Factors such as pharmacokinetics, tissue penetration, drug metabolism, and potential drug-drug interactions were not specifically addressed in our study. While our study identified one potent lead compound **2d** with significant antibacterial and antibiofilm activity, it is crucial to explore a broader range of compounds and structural modifications. The development of multiple lead compounds with diverse chemical scaffolds can increase the chances of finding more effective and selective antimicrobial agents. Our study focused primarily on *in vitro* assessments, and clinical data regarding the safety and efficacy of these compounds in human subjects are lacking. Clinical trials are needed to evaluate the compounds' performance in real-world scenarios and assess factors such as dosage, treatment duration, and potential side effects. Addressing these limitations and conducting further research will enhance our understanding of the potential of 2-azidobenzothiazoles as antimicrobial agents and pave the way for their future development and clinical application.

## Data availability statement

The original contributions presented in the study are included in the article/[Supplementary Material](#), further inquiries can be directed to the corresponding authors.

## Ethics statement

Ethical approval was not required for the studies on animals in accordance with the local legislation and institutional requirements because only commercially available established cell lines were used.

## Author contributions

TQ: Conceptualization, Formal Analysis, Methodology, Validation, Writing—original draft. SAK: Formal Analysis, Writing—original draft. MA: Writing—original draft. AF: Funding acquisition, Writing—review and editing. GY: Writing—review and editing. KJ: Software, Writing—review and editing. MM: Funding acquisition, Writing—review and editing. WS: Visualization, Writing—review and editing. PS: Conceptualization, Methodology, Writing—original draft.

## Funding

The author(s) declare financial support was received for the research, authorship, and/or publication of this article.

## Acknowledgments

The authors gratefully acknowledge, School of Chemical Engineering and Physical Sciences, Lovely Professional University, Punjab for providing the needed facilities during the course of the research. The authors extend their appreciation to the Deanship of Scientific Research, King Khalid University, Abha, Saudi Arabia, for funding this work under Grant No. RGP.1/304/44.

## Conflict of interest

The authors declare that the research was conducted in the absence of any commercial or financial relationships that could be construed as a potential conflict of interest.

## References

- Abe, H., Jeelani, I., Yonoki, A., Imai, H., and Horino, Y. (2021). Synthesis of Chloro-Substituted 6H-Dibenzo[b,d]pyran-6-one Natural Products, Graphis lactone G, and Palmariols A and B. *Chem. Pharm. Bull.* 69, 781–788. doi:10.1248/cpb.c21-00316
- Adan, A., Kiraz, Y., and Baran, Y. (2016). Cell proliferation and cytotoxicity assays. *Curr. Pharm. Biotechnol.* 17, 1213–1221. doi:10.2174/1389201017666160808160513
- Ahmed, K., and Jeelani, I. (2019). Synthesis and *in vitro* antimicrobial screening of 3-acetyl-4-hydroxycoumarin hydrazones. *Int. J. Pharm. Biol. Sci.* 9, 1000–1005.
- Ali, A. A., Gogoi, D., Chaliha, A. K., Buragohain, A. K., Trivedi, P., Saikia, P. J., et al. (2017). Synthesis and biological evaluation of novel 1, 2, 3-triazole derivatives as anti-tubercular agents. *Bioorg. Med. Chem. Lett.* 27, 3698–3703. doi:10.1016/j.bmcl.2017.07.008
- Ali, A., Correa, A. G., Alves, D., Zukerman-Schpector, J., Westermann, B., Ferreira, M. A., et al. (2014). An efficient one-pot strategy for the highly regioselective metal-free synthesis of 1, 4-disubstituted-1, 2, 3-triazoles. *ChemComm* 50, 11926–11929. doi:10.1039/c4cc04678a
- Ali, J., Mubarak, M. M., Samuel, C., Kantroo, H. A., Malik, A., Ahmad, Z., et al. (2022). Stibonic acids and related stibonate-phosphonate clusters: Synthesis, characterization and bioactivity evaluation. *J. Inorg. Biochem.* 235, 111909. doi:10.1016/j.jinorgbio.2022.111909
- Almehmadi, M. A., Aljuhani, A., Alraqa, S. Y., Ali, I., Rezki, N., Aouad, M. R., et al. (2021). Design, synthesis, DNA binding, modeling, anticancer studies and DFT calculations of Schiff bases tethering benzothiazole-1, 2, 3-triazole conjugates. *J. Mol. Struct.* 1225, 129148. doi:10.1016/j.molstruc.2020.129148
- Almehmadi, M. A., Aljuhani, A., Alraqa, S. Y., Ali, I., Rezki, N., Aouad, M. R., and Hagar, M. (2021). Design, synthesis, DNA binding, modeling, anticancer studies and DFT calculations of Schiff bases tethering benzothiazole-1, 2, 3-triazole conjugates. *J. Mol. Struct.* 1225, 129148. doi:10.1016/j.molstruc.2020.129148
- Amin, A., Qadir, T., Salhotra, A., Sharma, P. K., Jeelani, I., and Abe, H. (2022). Pharmacological significance of synthetic bioactive thiazole derivatives. *Curr. Bioact. Compd.* 18, 77–89. doi:10.2174/1573407218666220303100501
- Artyushin, O. I., Vorob'eva, D. V., Vasil'eva, T. P., Osipov, S. N., Röschenthaler, G. V., and Odinet, I. L. (2008). Facile synthesis of phosphorylated azides in ionic liquids and their use in the preparation of 1, 2, 3-triazoles. *Heteroat. Chem.* 19, 293–300. doi:10.1002/hc.20420
- Ashour, H. F., Abou-Zeid, L. A., Magda, A. A., and Selim, K. B. (2020). 1, 2, 3-Triazole-Chalcone hybrids: Synthesis, *in vitro* cytotoxic activity and mechanistic investigation of apoptosis induction in multiple myeloma RPMI-8226. *Eur. J. Med. Chem.* 189, 112062. doi:10.1016/j.ejmech.2020.112062
- Burger, A., and Sawhney, S. N. (1968). Antimalarials. III. Benzothiazole amino alcohols. *J. Med. Chem.* 11, 270–273. doi:10.1021/jm00308a018
- Catalano, A., Carocci, A., Defrenza, I., Muraglia, M., Carrieri, A., Van Bambeke, F., et al. (2013). 2-Aminobenzothiazole derivatives: Search for new antifungal agents. *Eur. J. Med. Chem.* 64, 357–364. doi:10.1016/j.ejmech.2013.03.064
- De la Torre, A. F., Ali, A., Westermann, B., Schmeda-Hirschmann, G., andertino, M. W. (2018). An efficient cyclization of lapachol to new benzo [h] chromene hybrid compounds: a stepwise vs. one-pot esterification-click (CuAAC) study. *New J. Chem.* 42, 19591–19599. doi:10.1039/c8nj03699c
- Faraji, L., Shahkarami, S., Nadri, H., Moradi, A., Saeedi, M., Foroumadi, A., et al. (2017). Synthesis of novel benzimidazole and benzothiazole derivatives bearing a 1, 2, 3-triazole ring system and their acetylcholinesterase inhibitory activity. *J. Chem. Res.* 41, 30–35. doi:10.3184/174751917x14836231670980
- Faraji, L., Shahkarami, S., Nadri, H., Moradi, A., Saeedi, M., Foroumadi, A., et al. (2017). Synthesis of novel benzimidazole and benzothiazole derivatives bearing a 1, 2, 3-triazole ring system and their acetylcholinesterase inhibitory activity. *J. Chem. Res.* 41, 30–35. doi:10.3184/174751917x14836231670980
- Fischer, W., and Anselme, J. P. (1967). Reaction of amine anions with p-toluenesulfonyl azide. Novel azide synthesis. *J. Am. Chem. Soc.* 89, 5284–5285. doi:10.1021/ja00996a036
- Gonzalez, N., Sevillano, D., Alou, L., Cafini, F., Gimenez, M. J., Gomez-Lus, M. L., et al. (2013). Influence of the MBC/MIC ratio on the antibacterial activity of vancomycin versus linezolid against methicillin-resistant *Staphylococcus aureus* isolates in a pharmacodynamic model simulating serum and soft tissue interstitial fluid concentrations reported in diabetic patients. *J. Antimicrob. Chemother.* 68, 2291–2295. doi:10.1093/jac/dkt185
- Itaya, K., Jeelani, I., and Abe, H. (2021). Total synthesis of urolithin C 3-glucuronide. *Heterocycles* 103, 1038. doi:10.3987/com-20-s(k)51
- Jakopec, S., Pantalon Juraj, N., Brozovic, A., Jadresko, D., Peric, B., Kirin, S. I., et al. (2022). Ferrocene conjugates linked by 1, 2, 3-triazole and their Zn (II) and Cu (II) complexes: Synthesis, characterization and biological activity. *Appl. Organomet. Chem.* 36, e6575. doi:10.1002/aoc.6575
- Jeelani, I., Itaya, K., and Abe, H. (2021). Total synthesis of hyalodendriol C. *Heterocycles* 102, 102. doi:10.3987/com-21-14480
- Katritzky, A. R., and Rachwal, S. (2010). Synthesis of heterocycles mediated by benzotriazole. 1. Monocyclic systems. *Chem. Rev.* 110, 1564–1610. doi:10.1021/cr900204u
- Keri, R. S., Patil, M. R., Patil, S. A., and Budagumpi, S. (2015). A comprehensive review in current developments of benzothiazole-based molecules in medicinal chemistry. *Eur. J. Med. Chem.* 89, 207–251. doi:10.1016/j.ejmech.2014.10.059
- Kini, S., Swain, S. P., and Am, G. (2007). Synthesis and evaluation of novel benzothiazole derivatives against human cervical cancer cell lines. *Indian J. Pharm. Sci.* 69, 46. doi:10.4103/0250-474x.32107
- Kleinhof, A., Owais, W. M., and Nilan, R. A. (1978). Azide. *Mutat. Res/Rev Genet. Toxicol.* 55, 165–195. doi:10.1016/0165-1110(78)90003-9
- Kolb, H. C., and Sharpless, K. B. (2003). The growing impact of click chemistry on drug discovery. *Drug Discov. Today* 8, 1128–1137. doi:10.1016/s1359-6446(03)02933-7
- Kreth, J., Merritt, J., Shi, W., and Qi, F. (2005). Competition and coexistence between *Streptococcus mutans* and *Streptococcus sanguinis* in the dental biofilm. *J. Bacteriol.* 187, 7193–7203. doi:10.1128/jb.187.21.7193-7203.2005
- Lauria, A., Delisi, R., Mingoia, F., Terenzi, A., Martorana, A., Barone, G., et al. (2014). 1, 2, 3-Triazole in heterocyclic compounds, endowed with biological activity, through 1, 3-dipolar cycloadditions. *Eur. J. Org. Chem.* 2014, 3289–3306. doi:10.1002/ejoc.201301695
- Lima, C. G., Ali, A., van Berkel, S. S., Westermann, B., and Paixao, M. W. (2015). Emerging approaches for the synthesis of triazoles: beyond metal-catalyzed and strain-promoted azide-alkyne cycloaddition. *ChemComm* 51, 10784–10796. doi:10.1039/c5cc04114g
- Liu, Q., and Tor, Y. (2003). Simple conversion of aromatic amines into azides. *Org. Lett.* 5, 2571–2572. doi:10.1021/ol034919+
- Mir, M. A., Altuhami, S. A., Mondal, S., Bashir, N., Dera, A. A., and Alfhili, M. A. (2023). Antibacterial and antibiofilm activities of  $\beta$ -lapachone by modulating the catalase enzyme. *Antibiotics* 12, 576. doi:10.3390/antibiotics12030576
- Mir, M. A., Altuhami, S. A., Mondal, S., Bashir, N., Dera, A. A., and Alfhili, M. A. (2023). Antibacterial and antibiofilm activities of  $\beta$ -lapachone by modulating the catalase enzyme. *Antibiotics* 12, 576. doi:10.3390/antibiotics12030576

## Publisher's note

All claims expressed in this article are solely those of the authors and do not necessarily represent those of their affiliated organizations, or those of the publisher, the editors and the reviewers. Any product that may be evaluated in this article, or claim that may be made by its manufacturer, is not guaranteed or endorsed by the publisher.

## Supplementary material

The Supplementary Material for this article can be found online at: <https://www.frontiersin.org/articles/10.3389/fchem.2023.1264747/full#supplementary-material>



- Moorhouse, A. D., Santos, A. M., Gunaratnam, M., Moore, M., Neidle, S., and Moses, J. E. (2006). Stabilization of G-quadruplex DNA by highly selective ligands via click chemistry. *J. Am. Chem. Soc.* 128, 15972–15973. doi:10.1021/ja0661919
- Nicholls, D., Gescher, A., and Griffin, R. J. (1991). Medicinal azides. Part 8. The *in vitro* metabolism of p-substituted phenyl azides. *Xenobiotica* 21, 935–943. doi:10.3109/00498259109039533
- Nomiya, K., Takahashi, S., Noguchi, R., Nemoto, S., Takayama, T., and Oda, M. (2000). Synthesis and characterization of water-soluble silver(I) complexes with l-histidine (H<sub>2</sub>his) and (S)-(-)-2-Pyrrolidone-5-carboxylic acid (H<sub>2</sub>pyrrld) showing a wide spectrum of effective antibacterial and antifungal activities. Crystal structures of chiral helical polymers [Ag(Hhis)]<sub>n</sub> and {[Ag(Hpyrrld)]<sub>2</sub>]<sub>n</sub> in the solid state. *Inorg. Chem.* 39, 3301–3311. doi:10.1021/ic990526o
- O'Toole, G. A. (2011). Microtiter dish biofilm formation assay. *JoVE* 47, 2437. doi:10.3791/2437
- Palmer, P. J., Trigg, R. B., and Warrington, J. V. (1971). Benzothiazolines as antituberculous agents. *J. Med. Chem.* 14, 248–251. doi:10.1021/jm00285a022
- Proma, F. H., Shourav, M. K., and Choi, J. (2020). Post-antibiotic effect of ampicillin and levofloxacin to *Escherichia coli* and *Staphylococcus aureus* based on microscopic imaging analysis. *Antibiotics* 9, 458. doi:10.3390/antibiotics9080458
- Qadir, T., Amin, A., Salhotra, A., Sharma, P. K., Jeelani, I., and Abe, H. (2022). Recent advances in the synthesis of benzothiazole and its derivatives. *Curr. Org. Chem.* 26, 189–214. doi:10.2174/138527282666211229144446
- Qadir, T., Amin, A., Sharma, P. K., Jeelani, I., and Abe, H. (2022). A review on medically important heterocyclic compounds. *Open J. Med. Chem.* 16, 2022. doi:10.2174/18741045-v16-e2022280
- Scriven, E. F. V., and Turnbull, K. (1998). Azides: Their preparation and synthetic uses. *Chem. Rev.* 88, 297–368. doi:10.1021/cr00084a001
- Shafi, S., Alam, M. M., Mulakayala, N., Mulakayala, C., Vanaja, G., Kalle, A. M., et al. (2012). Synthesis of novel 2-mercapto benzothiazole and 1, 2, 3-triazole based bis-heterocycles: Their anti-inflammatory and anti-nociceptive activities. *Eur. J. Med. Chem.* 49, 324–333. doi:10.1016/j.ejmech.2012.01.032
- Sharma, B. K., Sharma, P. K., and Kumar, M. (2010). One-pot, multicomponent sequential synthesis of benzothiazoloquinazolinones. *Synth. Commun.* 40, 2347–2352. doi:10.1080/00397910903243807
- Sharma, P. K., Kumar, M., and Mohan, V. (2010). Synthesis and antimicrobial activity of 2H-pyrimido [2, 1-b]benzothiazol-2-ones. *Res. Chem. Intermed.* 36, 985–993. doi:10.1007/s1164-010-0211-9
- Siddiki, A. A., Takale, B. S., and Telvekar, V. N. (2013). One pot synthesis of aromatic azide using sodium nitrite and hydrazine hydrate. *Tetrahedron Lett.* 54, 1294–1297. doi:10.1016/j.tetlet.2012.12.112
- Siddiki, A. A., Takale, B. S., and Telvekar, V. N. (2013). One pot synthesis of aromatic azide using sodium nitrite and hydrazine hydrate. *Tetrahedron Lett.* 54, 1294–1297. doi:10.1016/j.tetlet.2012.12.112
- Singh, M. K., Tilak, R., Nath, G., Awasthi, S. K., and Agarwal, A. (2013). Design, synthesis and antimicrobial activity of novel benzothiazole analogs. *Eur. J. Med. Chem.* 63, 635–644. doi:10.1016/j.ejmech.2013.02.027
- Soni, B., Ranawat, M. S., Sharma, R., Bhandari, A., and Sharma, S. (2010). Synthesis and evaluation of some new benzothiazole derivatives as potential antimicrobial agents. *Eur. J. Med. Chem.* 45, 2938–2942. doi:10.1016/j.ejmech.2010.03.019
- Tariq, S., Kamboj, P., Alam, O., and Amir, M. (2018). 1,2,4-Triazole-based benzothiazole/benzoxazole derivatives: Design, synthesis, p38α MAP kinase inhibition, anti-inflammatory activity and molecular docking studies. *Bioorg. Chem.* 81, 630–641. doi:10.1016/j.bioorg.2018.09.015
- Telvekar, V. N., Bairwa, V. K., Satardekar, K., and Bellubi, A. (2012). Novel 2-(2-(4-aryloxybenzylidene) hydrazinyl) benzothiazole derivatives as anti-tubercular agents. *Bioorg. Med. Chem. Lett.* 22, 649–652. doi:10.1016/j.bmcl.2011.10.064
- Tsuji, B. T., Yang, J. C., Forrest, A., Kelchlin, P. A., and Smith, P. F. (2008). *In vitro* pharmacodynamics of novel rifamycin ABI-0043 against *Staphylococcus aureus*. *J. Antimicrob. Chemother.* 62 (1), 156–160. doi:10.1093/jac/dkn133
- Wang, Q., Chan, T. R., Hilgraf, R., Fokin, V. V., Sharpless, K. B., and Finn, M. G. (2003). Bioconjugation by copper (I)-catalyzed azide-alkyne [3+2] cycloaddition. *J. Am. Chem. Soc.* 125, 3192–3193. doi:10.1021/ja021381e
- Warmuth, R., and Makowiec, S. (2005). The Phenylnitrene Rearrangement in the inner phase of a hemisarcander. *J. Am. Chem. Soc.* 127, 1084–1085. doi:10.1021/ja044557g
- Weekes, A. A., and Westwell, A. D. (2009). 2-Arylbenzothiazole as a privileged scaffold in drug discovery. *Curr. Med. Chem.* 16, 2430–2440. doi:10.2174/092986709788682137
- Wu, P., Feldman, A. K., Nugent, A. K., Hawker, C. J., Scheel, A., Voit, B., et al. (2004). Efficiency and fidelity in a click-chemistry route to triazole dendrimers by the copper (I)-catalyzed ligation of azides and alkynes. *Angew. Chem.* 116, 3928–3932. doi:10.1002/anie.200454078
- Yalçin, İ., Ören, İ., Şener, E., Akin, A., and Uçartürk, N. (1992). The synthesis and the structure-activity relationships of some substituted benzoxazoles, oxazolo (4, 5-b) pyridines, benzothiazoles and benzimidazoles as antimicrobial agents. *Eur. J. Med. Chem.* 27, 401–406. doi:10.1016/0223-5234(92)90154-s
- Yamazaki, K., Kaneko, Y., Suwa, K., Ebara, S., Nakazawa, K., and Yasuno, K. (2005). Synthesis of potent and selective inhibitors of *Candida albicans* N-myristoyltransferase based on the benzothiazole structure. *Bioorg. Med. Chem.* 13, 2509–2522. doi:10.1016/j.bmc.2005.01.033
- Zhilitskaya, L. V., Shainyan, B. A., and Yarosh, N. O. (2021). Modern approaches to the synthesis and transformations of practically valuable benzothiazole derivatives. *Molecules* 26, 2190. doi:10.3390/molecules26082190
- Zotta, T., Guidone, A., Tremonte, P., Parente, E., and Ricciardi, A. (2012). A comparison of fluorescent stains for the assessment of viability and metabolic activity of lactic acid bacteria. *World J. Microbiol. Biotechnol.* 28, 919–927. doi:10.1007/s11274-011-0889-x



## OPEN ACCESS

## EDITED BY

Jiwen Zhang,  
Northwest A&F University, China

## REVIEWED BY

Li Hao,  
Zhongkai University of Agriculture and  
Engineering, China  
Yu Luo,  
Shanghai University of Engineering  
Sciences, China  
Xingang Meng,  
Jingdezhen University, China

## \*CORRESPONDENCE

Bo Zhang,  
✉ zb830216@shnu.edu.cn  
Wenneng Wu,  
✉ wuwenneng123@126.com

RECEIVED 04 August 2023

ACCEPTED 28 August 2023

PUBLISHED 12 September 2023

## CITATION

Hu S, Yan C, Fei Q, Zhang B and Wu W  
(2023), MOF-based stimuli-responsive  
controlled release nanopesticide:  
mini review.  
*Front. Chem.* 11:1272725.  
doi: 10.3389/fchem.2023.1272725

## COPYRIGHT

© 2023 Hu, Yan, Fei, Zhang and Wu. This  
is an open-access article distributed  
under the terms of the [Creative  
Commons Attribution License \(CC BY\)](#).  
The use, distribution or reproduction in  
other forums is permitted, provided the  
original author(s) and the copyright  
owner(s) are credited and that the original  
publication in this journal is cited, in  
accordance with accepted academic  
practice. No use, distribution or  
reproduction is permitted which does not  
comply with these terms.

# MOF-based stimuli-responsive controlled release nanopesticide: mini review

Shuhui Hu<sup>1</sup>, Chang Yan<sup>1</sup>, Qiang Fei<sup>1</sup>, Bo Zhang<sup>2\*</sup> and Wenneng Wu<sup>1\*</sup>

<sup>1</sup>Food and Pharmaceutical Engineering Institute, Guiyang University, Guiyang, China, <sup>2</sup>Shanghai Engineering Research Center of Green Energy Chemical Engineering, College of Chemistry and Materials Science, Shanghai Normal University, Shanghai, China

By releasing an adequate amount of active ingredients when triggered by environmental and biological factors, the nanopesticides that respond to stimuli can enhance the efficacy of pesticides and contribute to the betterment of both the environment and food safety. The versatile nature and highly porous structure of metal-organic frameworks (MOFs) have recently garnered significant interest as drug carriers for various applications. In recent years, there has been significant progress in the development of metal-organic frameworks as nanocarriers for pesticide applications. This review focuses on the advancements, challenges, and potential future enhancements in the design of metal-organic frameworks as nanocarriers in the field of pesticides. We explore the various stimuli-responsive metal-organic frameworks carriers, particularly focusing on zeolitic imidazolate framework-8 (ZIF-8), which have been successfully activated by external stimuli such as pH-responsive or multiple stimuli-responsive mechanisms. In conclusion, this paper presents the existing issues and future prospects of metal-organic frameworks-based nanopesticides with stimuli-responsive controlled release.

## KEYWORDS

**nanopesticide, controlled release, stimuli-responsive, metal-organic frameworks, bioactivity**

## 1 Introduction

Pesticides have an indispensable function in enhancing the quality and productivity of crops, as well as fulfilling the increasing food demands of the world's population. According to Reichenberger and others (Reichenberger et al., 2007), the global production of pesticides has reached 4.6 million tons per year. However, over 90% of these pesticides end up in the environment and agricultural products, with less than 0.1% effectively targeting pests. According to Hussain and Kah (Kah and Hofmann, 2014; Hussain et al., 2019), nanopesticides have advantages in enhancing the scattering, durability, and effectiveness of pesticides on the intended subjects. Additionally, they aid in the attachment, longevity, and penetration of pesticides while minimizing their residual contamination in non-target regions and the surroundings.

By responding to particular microenvironmental stimuli, the release of pesticides can be controlled intelligently and accurately, leading to improved drug effectiveness and decreased toxic and adverse effects, as demonstrated by Ahmadi and Sun (Sun et al., 2014; Ahmadi et al., 2020). The innovation of pesticide formulations has gained more attention due to the emergence of smart pesticide delivery systems (PDS) utilizing nanomaterials (Sun et al.,

2014; Ahmadi et al., 2020; Zhang et al., 2020; Song et al., 2021; Wu H et al., 2021; Wu W et al., 2021; Zhou et al., 2021). Selecting intelligent nanocarriers, such as permeable nanomaterials, plays a crucial role in enhancing the effectiveness of nano-pesticide compositions (Lawson H. D et al., 2021; Wang et al., 2022a; Ma et al., 2023). Metal-organic frameworks (MOFs) are a novel type of porous nanomaterials characterized by their well-organized crystalline framework structures. These frameworks possess distinctive attributes, such as a well-arranged composition, remarkable surface area, and substantial pore volume, which facilitate the adsorption of functional molecules on their outer surface or within their interconnected channels. This capability allows for the entrapment of these molecules within the framework (Furukawa et al., 2013; Wang S et al., 2020; Mallakpour et al., 2022). Furthermore, rational design and control of organic ligands, metal nodes, and synthesis conditions enable the flexible regulation of MOFs structure and associated properties, catering to specific application scenarios (Qu et al., 2022; Wang et al., 2022b). In particular, for the altered MOFs, it has the potential to facilitate the attainment of controlled release of pesticides in response to stimuli (Dong et al., 2021). Furthermore, metal-organic frameworks (MOFs) have shown significant promise in the fields of biomedicine and pesticide usage due to their limited ability to accumulate within the body (Teplensky et al., 2019; Qiangqiang et al., 2020; Mahmoudi et al., 2022). Even though much attention has been paid to the development of MOF preparation methods and their application in pesticide adsorption, loading, and detection (Huiping et al., 2021; Rojas et al., 2022; Chenyu et al., 2023), in this review, we mainly focus on the latest advancements in the creation of controlled release nanopesticides utilizing MOFs, particularly remarkable progress has been made in the research of stimulus-responsive controlled release nanopesticides using ZIF-8 as the carrier.

## 2 Characteristics and preparation of MOFS-based environmentally responsive nanopesticides

Different types of stimuli-responsive nanopesticides are developed using MOFs: 1) Active ingredients (AIs) are encapsulated by MOFs through the one-pot method, resulting in stimuli-responsive nanopesticides like ZIF-8-based pH-responsive delivery nanoparticles. This prevents premature losses in the environment and ensures specific release of  $\beta$ -Cypermethrin in acidic environments associated with termite infestation pesticide (Ma et al., 2022a). 2) Initially, MOFs are fabricated to encapsulate pesticides, which are then coated with special materials like zain to facilitate stimuli-triggered pesticide release (Ma et al., 2022b). 3) An integrated pesticide-fertilizer system is constructed by combining MOF with hollow mesoporous silica and polydopamine, enabling simultaneous encapsulation of multiple pesticides and provision of micronutrient  $\text{Zn}^{2+}$  (Ji et al., 2021). 4) MOF-based nanopesticides are formed by directly using pesticide molecules as organic ligands and combining them with metal ions. For example, 2D-MOF can be prepared by chelating the herbicide glufosinate and  $\text{Cu}^{2+}$  (Sierra-Serrano et al., 2022). The above MOFs can be tailored to respond to microenvironmental stimuli, such as pH, redox,

enzymes to achieve precision agriculture. Moreover, most MOFs materials are pH-responsive.

## 3 Progress of MOFS-based environmentally responsive nanopesticides

### 3.1 Application of ZIF-8 in stimulus-responsive nanopesticides

Two primary techniques utilized in the synthesis of MOFs are the solvothermal approach (Hu et al., 2015) and the non-solvothermal technique (Lawson S et al., 2021). The one-pot method, as a typical of non-solventothermal method, has series of advantages of containing simple in operation, mild reaction conditions, which facilitate ZIF-8 preparation.

ZIF-8, a well-known MOF that is responsive to stimuli, is composed of a zeolitic imidazole acid skeleton consisting of  $\text{Zn}^{2+}$  and 2-methylimidazolate. According to Zhang, Sun and Saliba (Saliba et al., 2018; Sun et al., 2019; Zhang W et al., 2022), ZIF-8 decomposes in acidic conditions due to the dissociation of coordination bonds at pH 5.0–6.0. Consequently, it can serve as a carrier material that responds to acidity, as mentioned by Chen, Zhang and Mejías. (Chen et al., 2021; Mejías et al., 2021; Zhang X et al., 2022). Significantly, ZIF-8 releases zinc ions upon breakdown, which enhance plant development, establishing it as an eco-friendly carrier material in contrast to MOFs that contain toxic metals like copper, zirconium, and chromium (Yan et al., 2017; Yang J et al., 2017). Consequently, ZIF-8 exhibits great potential as an intelligent pesticide delivery system.

Harmful organisms such as termites and *Staphylococcus griseus* can produce a slightly acidic environment, which enables controlled release of pesticides by degrading ZIF-8. The study conducted by Ma and others,  $\beta$ -CYP/ZIF-8 was synthesized in a single step according to Ma's method (Ma et al., 2022a), as shown in Figure 1. The micro-acidic environment, in which termites flourish, can enhance the release of  $\beta$ -CYP through the decomposition of ZIF-8, leading to improved targeting of pesticides and reduced toxic side effects (Sun et al., 2019). This favorable acidic environment supports termite life and enhances the specific release. Furthermore,  $\beta$ -CYP/ZIF-8 diminished the harmful impacts on organisms that are not the intended target. Therefore, the nanoformulations prepared using the one-pot technique hold immense promise for utilization in both the sustainable control of pests and the preservation of the environment.

Likewise, a site-specific nano-release system containing dazomet (DZ@ZIF-8) was synthesized using ZIF-8 through a one-pot approach (Ren et al., 2022). Due to the production of acid compounds come from *Botrytis cinerea*, caused the breakdown of the DZ@ZIF-8 framework and the subsequent localized release of DZ (Figure 2). Additionally, the utilization of DZ@ZIF-8 can prevent the harmful effects of DZ on plants, enabling its use throughout the growth of plants. Consequently, employing ZIF-8 as a nanocarrier enhanced the efficiency of pesticide utilization while mitigating its harmful side effects.

The study conducted by Ma and others. In their study, Ma (Ma et al., 2022a) developed a hybrid material (DNF@ZIF-8@PMMA/zein) that responds to changes in pH and is triggered by protease.

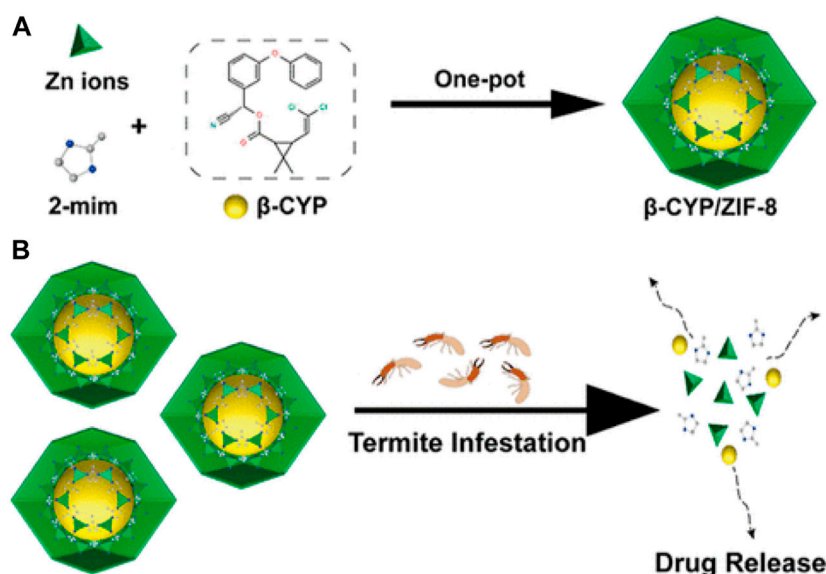


FIGURE 1

(A) The one pot method was employed for the synthesis of  $\beta$ -CYP/ZIF-8, (B) which subsequently facilitated the targeted drug release in response to termite infestation (Ma et al., 2022b).

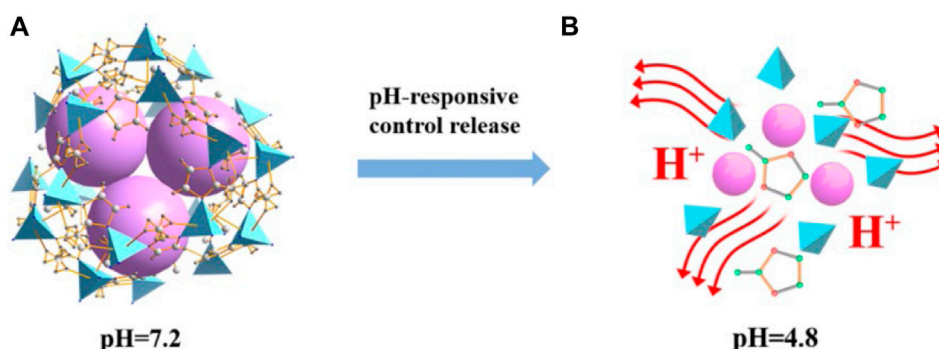


FIGURE 2

The release of DZ@ZIF-8 is controlled by the pH response (Ren et al., 2022).

This material was designed for delivering dinotefuran (DNF), as shown in Figure 3. ZIF-8 was initially fabricated for encapsulating DNF, and then hydrophobic poly (methyl methacrylate) (PMMA) was polymerized *in situ*. In the end, an additional coating of zein is applied to the outer layer in order to aid in the release of cargo triggered by protease. The UV resistance of DNF was enhanced by nearly 10 times (Figure 4) and pest control efficiency was significantly improved when using the nano formulation in comparison to free DNF. This hybrid MOF can be targeted against pests and diseases and has promising applications in sustainable agriculture.

An intriguing development in the field involved the creation of a pesticide-fertilizer blend that is eco-friendly. This blend utilized ammonium zinc phosphate (ZNP) and *in situ* synthesized ZIF-8 as sources of nutrients, along with dinotefuran (DNF) as the pesticide (Ma et al., 2021). Instead of being loaded through additional

adsorption, DNF was enclosed *in situ* while the ZIF-8 synthesis process took place, resulting in enhanced stability and prevention of premature or rapid release. Figure 5 illustrates the pH-sensitive sustained release characteristic of the water-repellent ZIF-8. The system combining pesticide and fertilizer had notable impacts on pre-cultivation of corn seeds, cultivation of soil, and control of pests.

Using ZnO nanomaterials as Zn source, ZnO-ZIF-8 (ZnO-Z) nanocomposite carriers with core-shell structure can be prepared using *in situ* crystal growth strategy. ZnO-Z, a pH-responsive core-shell nanocarrier, was prepared by Liang and others (Liang et al., 2022), using ZnO nanosphere as the core and ZIF-8 as the shell. Figure 6 illustrates the formation of nano-formulation Ber@ZnO-Z, where the berberine (Ber) was incorporated. In an acidic environment, Ber@ZnO-Z has the ability to quickly release Ber, which is consistent with the pH of the soil where the occurrence of tomato bacterial wilt disease is frequent. By binding to DNA, RNA



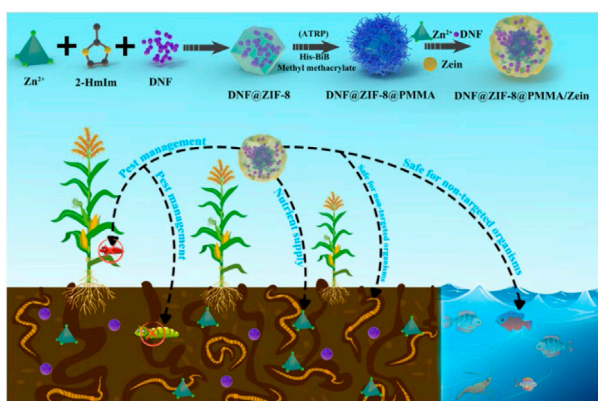


FIGURE 3

Utilization and implementation plan of the MOF composite (DNF@ZIF-8@PMMA/Zein) for delivering pesticides and fertilizers (Ma et al., 2022b).

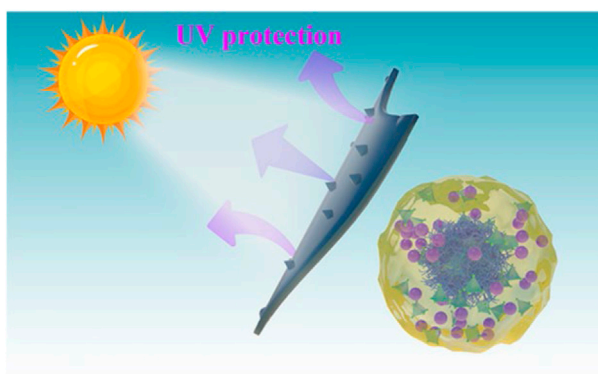


FIGURE 4

The possible mechanism for the MOF hybrid's ability to protect against ultraviolet radiation (Ma et al., 2022a).

and proteins, Ber inhibits DNA replication, RNA transcription, and protein synthesis, rendering it a secure medication that does not induce drug resistance (Li et al., 2018). Zinc oxide and titanium dioxide have been widely used in various applications due to their unique properties. ROS production can be triggered by ZnO, MgO, and CuO (Applerot et al., 2009; Applerot et al., 2012; Cai et al., 2018), consequently, ZnO-Z also exhibits a specific antimicrobial impact. Hence, this task holds significance in managing bacterial diseases that affect the soil.

### 3.2 Application of Fe-based MOFs in stimuli-responsive nanopesticide

Fe-based MOFs, particularly MIL-101(Fe) and MIL-101(Fe)-NH<sub>2</sub>, are frequently employed in the field of agriculture. Crop growth relies on iron, a crucial micronutrient that plays a vital part in photosynthetic reactions (Armin et al., 2014). Insufficient iron levels can significantly impact plant development and metabolic

processes, including chlorophyll production, nitrogen fixation, and respiration (Bindra et al., 2019). Moreover, Fe-based MOFs are utilized as an iron fertilizer to augment plant growth. (Anstoetz et al., 2016; Abdelhameed et al., 2019).

MIL-101(Fe) is composed of Fe<sub>3</sub>O<sub>4</sub> and 1,4-benzenedicarboxylate (BDC) (Horcajada et al., 2010; Dong et al., 2017). It possesses a high surface area, extensive porosity, and favorable biocompatibility (Lebedev et al., 2005; Wu and yang, 2017), making it suitable as a carrier for pesticide loading. Nevertheless, the premature release of pesticide occurs in Fe-based MOFs nanoparticles (Shan et al., 2020). The Fe-based MOFs surface underwent modification to attain its responsive characteristics to stimuli, including particular triggers within cells (e.g., the redox). The disintegration of the Fe-based MOFs framework structure was induced by, leading to the stimuli-responsive behavior of cargoes (Wang et al., 2022a).

Alkaline pH-responsive properties are exhibited by MOFs formed by combining high-valent metal ions with ligands based on carboxylic acid, such as PCN-222 and MIL-101. This is due to the self-decomposition of the carboxylic acid-based backbone in alkaline conditions, as mentioned in the studies by Taylor-Pashow and Yuan (Taylor-Pashow et al., 2009; Yuan et al., 2018). Additionally, Fe-based MOFs have the potential to serve as a fertilizer, enhancing the growth of plants (Anstoetz et al., 2016; Abdelhameed et al., 2019). The authors Gao and others (Gao et al., 2021) developed a clever nanocarrier called MIL-101(Fe)@silica that served two purposes: targeted delivery and plant nourishment. This nanocarrier effectively transported chlorantraniliprole (CAP) for eco-friendly pest control, leading to enhanced UV resistance and insecticidal efficacy against small cabbage moth larvae. Figure 7 illustrates the potential process of formation and the mechanism of release. SiO<sub>2</sub> can undergo hydrolysis to form soluble silanols (≡Si-OH) in the presence of alkali catalysis (Yang G.Z et al., 2017). In addition, lepidopteran pests that feed on plants have a highly basic digestive system (with a pH of up to 12), which serves as a mechanism for the controlled release of CAP (Gao et al., 2019; Wang X.G et al., 2020). Furthermore, MIL-101(Fe) and silica have the potential to serve as sources of iron (Fe) and silicon (Si) for enhancing plant development (El-Shetehy et al., 2021). This work offers promising strategies for efficient pesticide application and precise control of pests.

Liang and others (Liang et al., 2022b) utilized carboxymethyl starch (CMS) in conjunction with MIL-101(Fe)-NH<sub>2</sub> containing chlorantraniliprole (CAR) to create a nano-release system CAR@MIL-101(Fe)-NH<sub>2</sub>-CMS, which responds to pH, redox, and α-amylase stimuli (Figure 8). Carboxymethyl starch, a cheap polymeric carbohydrate composed of glucose units connected by glucose bonds, can be broken down by α-amylase in the insects' midgut (Holtot et al., 2019; Yu et al., 2021; Siemińska-Kuczer et al., 2022). The alkaline gut of insects contains both α-amylase and glutathione, which play a role in breaking down ingested substances. This enables CAR@MIL-101(Fe)-CMS nanoparticles to break apart in the insect intestine and promptly release CAR for precise targeting, as demonstrated by Khandelwal, Sharifloo and Banerjee et al. (Khandelwal et al., 2016; Sharifloo et al., 2016; Banerjee et al., 2022). By combining the digestive mechanism of bugs with the response-regulated discharge technology of insecticides, an efficient approach to pest control is achieved.

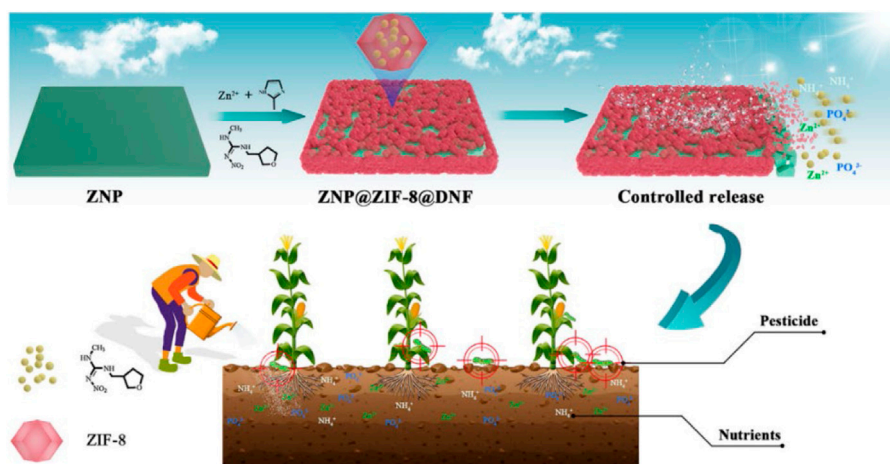


FIGURE 5

This stimuli-response contains a depiction of the creation of a slow-release pesticide-fertilizer combination (ZNP@ZIF-8@DNF) that responds to pH, along with its possible implementation in the field of sustainable farming (Ma et al., 2021).

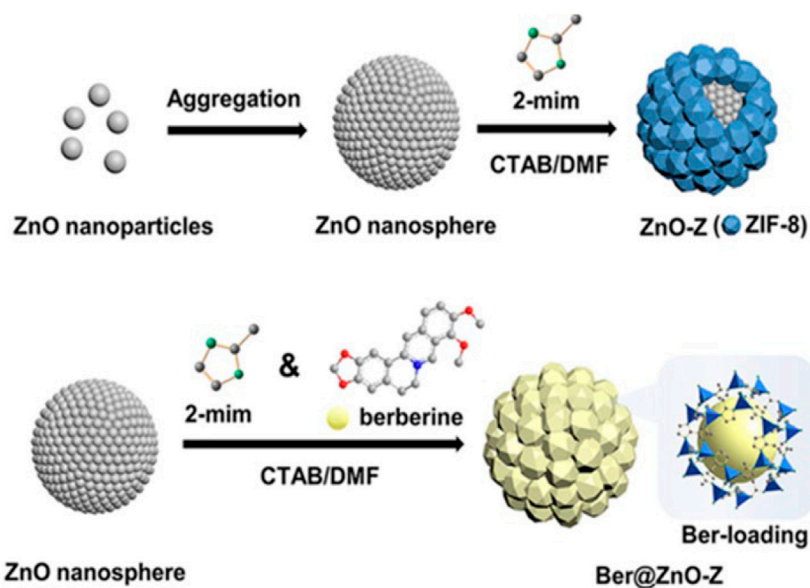
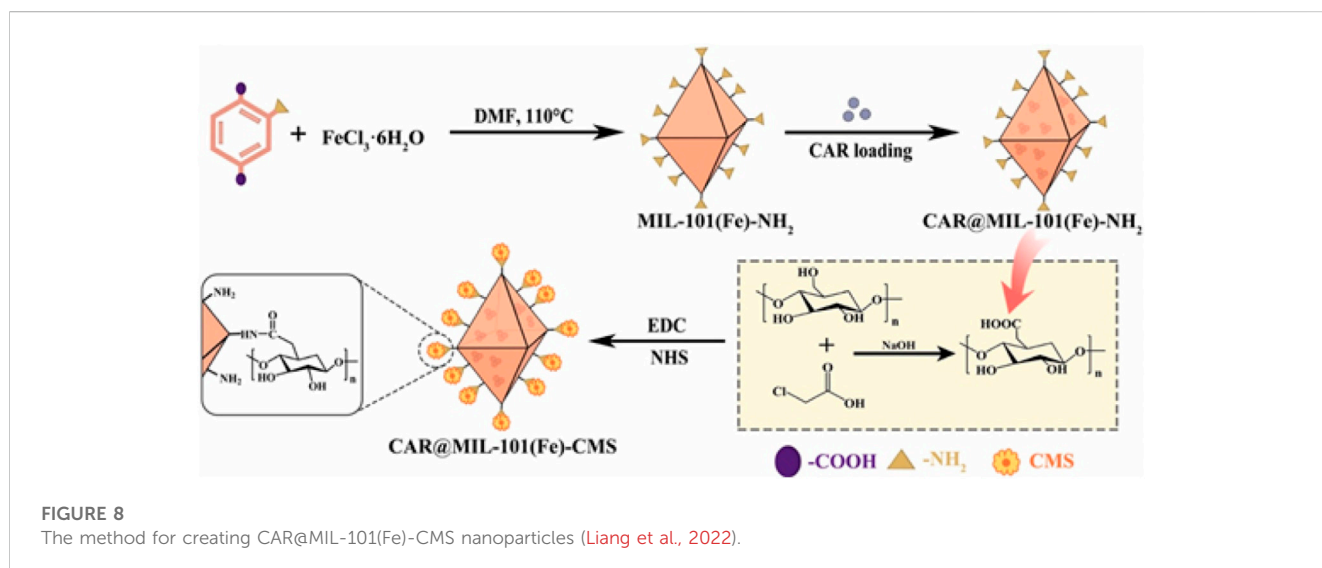
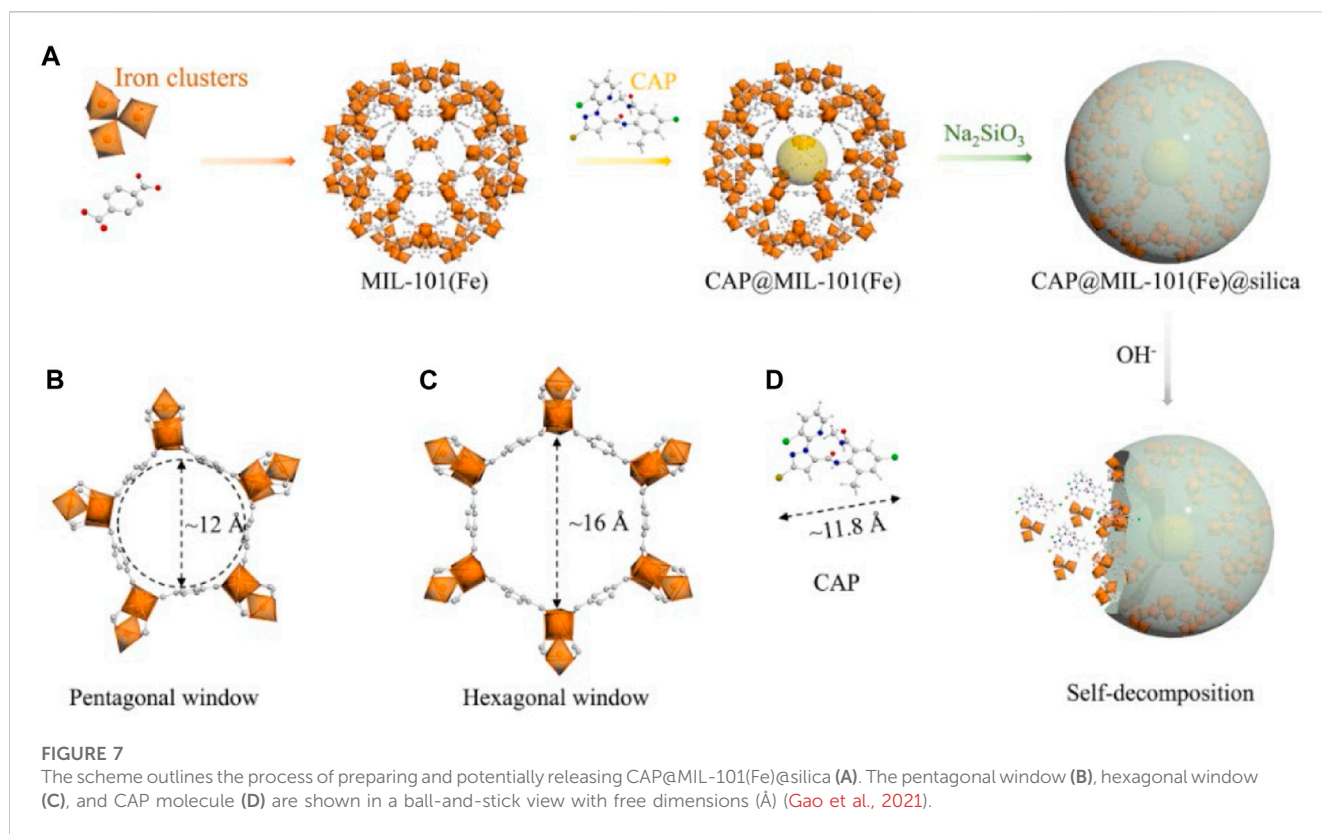


FIGURE 6

Preparation of ZnO-Z and Ber@ZnO-Z nanosphere depicted in the illustration (Liang et al., 2022a).

Liang and others (Liang et al., 2022a) synthesized PYR@FeMOF-pectin by incorporating pectin into MIL-101(Fe)-NH<sub>2</sub> along with pyraclostrobin (PYR), resulting in a composite material exhibiting dual responsiveness to redox and pectinase stimuli. Pectin, being a natural polymer, constitutes a significant portion of plant cell walls and possesses favorable water solubility and biocompatibility (Broxterman and Schols, 2018; Mohammadinejad et al., 2019). Moreover, it offers distinct benefits compared to alternative substances in agricultural practices (Bellemjid et al., 2021). Moreover, the pectin's carboxyl group can undergo cross-linking with the amino amide of MIL-101(Fe)-NH<sub>2</sub>, as stated by Shitrit and co-

workers (Shitrit et al., 2019). Consequently, when plants are infected, pectinases secreted by plant pathogenic microorganisms swiftly degrade it. On the other hand, *P. aeruginosa* possesses a robust antioxidant defense mechanism that generates glutathione during host plant infection. This glutathione helps in neutralizing reactive oxygen species produced by the host defense response. The design of PYR@FeMOF-pectin nanopesticide is accurately tailored to the specific surroundings in which it operates, resulting in a precise delivery of PYR that targets (Kubicek et al., 2014; Samalova et al., 2014; Chiniyuy et al., 2019; Sabbadin et al., 2021), as demonstrated earlier.

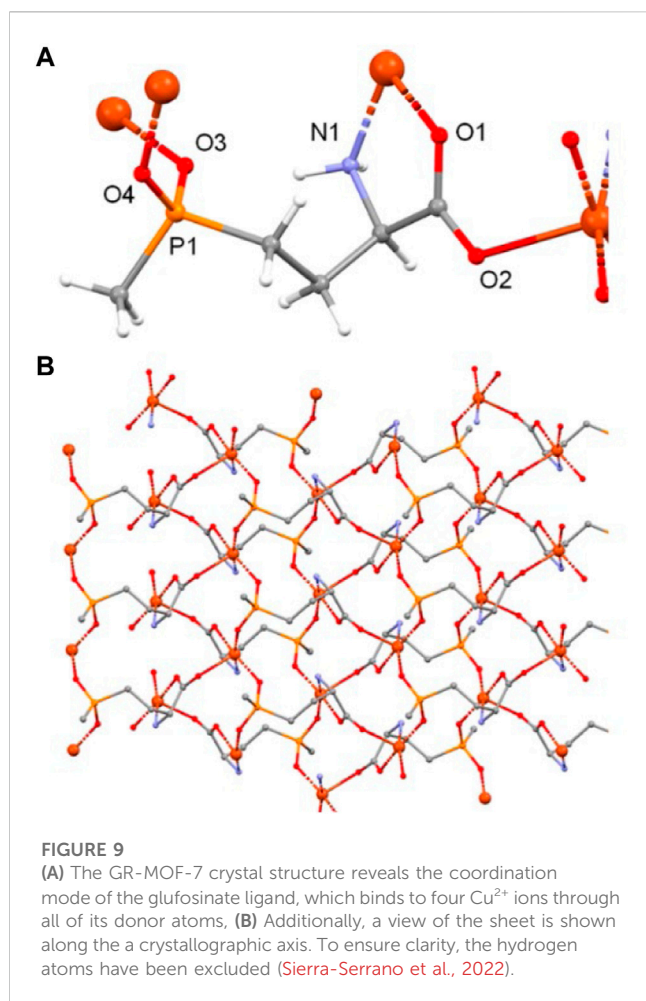


### 3.3 Other types of MOFs in stimuli-responsive nanopesticides

Agriculture can benefit from the promising potential of various other MOFs. Cobalt-imidazole metal-organic framework (MOF) ZIF-67 is produced by combining cobalt nitrate hexahydrate and 2-methylimidazole, possessing a larger pore size compared to ZIF-8. This larger pore size makes it a more suitable option as a carrier and delivery platform for pesticides, as stated by Tsalaporta and others (Tsalaporta and MacElroy, 2020).

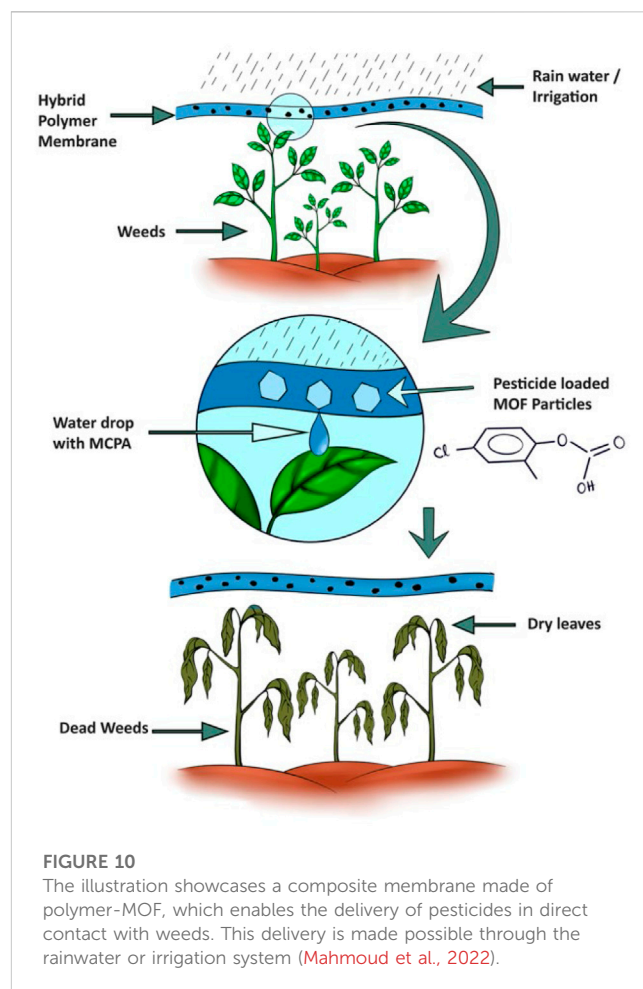
The authors Zhang and others (Zhang W et al., 2022) synthesized a carrier-based acetamiprid with pH sensitivity by utilizing ZIF-67. The pH-responsive release of acetamiprid occurs because of the ZIF-67's weak acidic group. Early in the infestation of host plants, griseus produces acidic substances such as oxalic acid, which facilitates the rapid disintegration and release of acetamiprid (Zhang X et al., 2022). The study not only showcases the potential of ZIF-67 as a nanocarrier for effectively managing gray mold, but also enhances the conventional approach to addressing agricultural diseases.





Creating multifunctional agrochemicals shows promise through the synthesis of MOFs using herbicide and antimicrobial components. Sierra-Serrano and others prepared a kind of Cu-based MOFs (2D-MOF), called GR-MOF-7, using glufo-sinate and  $\text{Cu}^{2+}$  (Sierra-Serrano et al., 2022) (Figure 9). The findings indicated that GR-MOF-7 exhibits outstanding antimicrobial efficacy against *Staphylococcus aureus* and *Escherichia coli*. Furthermore, GR-MOF-7 employs pesticides as ligands during MOF synthesis, thereby creating opportunities for the secure and effective utilization of MOF in the field of agriculture.

According to Song and others (Song et al., 2022), UiO-66 is a zirconium-based MOF that exhibits excellent durability and a notable rate of loading. Intelligent nanocarriers with better performance, such as UiO-66 derivatives include UiO-66- $\text{NH}_2$ , UiO-66- $(\text{COOH})_2$ . Mahmoud and others (Mahmoud et al., 2022) obtained the amino or carboxyl groups by introduction. In order to enhance biodegradability, Mahmoud and others incorporated 2-methyl-4-chlorophenoxyacetic acid (MCPA) into various zirconium-based MOFs (UiO-66, UiO-66- $\text{NH}_2$ , and UiO-67). During the synthesis of MOFs, MCPA is either loaded *in situ* or loaded afterwards. Subsequently, the MOFs loaded with MCPA are integrated into composite membranes made of biodegradable polycaprolactone (PCL) (Figure 10). The completion of research experiments has identified various



concentrations that can effectively impede the growth of different plant species at various stages. This discovery suggests that these composites hold great potential for future agricultural applications.

The authors of the song and others, in their study, Song and others (Song et al., 2022) developed pH-sensitive PDSs by utilizing carboxymethyl starch (CMC)-modified UiO-66- $\text{NH}_2$ , a zirconium-based organic framework, as a nanocarrier for acetaminophen (ATP). The surface area of UiO-66- $\text{NH}_2$ -CMC is extensive and it contains numerous pores, enabling efficient loading of ATP at a rate of 90.79%. The release behavior of ATP@UiO-66- $\text{NH}_2$ -CMC was responsive to changes in pH. In a separate investigation, researchers utilized the temperature-responsive polymer N-isopropyl acrylamide (PNIPAm) that had been altered with UiO-66- $(\text{COOH})_2$  to serve as a transporter for the highly effective insecticide indoxacarb (IDC). The PNIPAm polymer chains underwent contraction as the temperature surpassed the lower critical solution temperature (LCST), resulting in the nanoparticles collapsing. This collapse, as reported by Karakasyan and Guo (Guo and Gao, 2007; Karakasyan et al., 2008), led to a notable enhancement in the release rate of IDC. Due to its affordability, uncomplicated preparation process, effectiveness, and safety, this approach shows great potential for advancing pesticide formulation innovation and plant protection (Mahmoud et al., 2022; Song et al., 2022; Wan et al., 2022).



## 4 Summary and outlook

Due to their abundant functional properties, MOFs nanomaterials have found extensive applications in diverse fields. By utilizing them as carriers for pesticides and incorporating them with changes in microenvironmental stimulation (such as pH, redox, light, and other conditions) caused by the interaction among pests (such as pests, weeds, molds, etc.). This review provides a summary of the benefits, release mechanism triggered by stimuli, and bioactive characteristics of ZIF-8 and FeMOFs as carriers in the development of nanopesticides with stimulus-responsive properties. These carriers enable the intelligent and targeted release of pesticides, leading to enhanced utilization and efficiency in pest control while significantly mitigating environmental pollution. Furthermore, MOFs-based nanopesticides possess not only the characteristics of pesticides, but also can also function as nutrients for crop growth. This integrated pesticide-fertilizer approach offers substantial benefits in agriculture. Nevertheless, the present study encounters two issues. Firstly, the investigation on the absorption and transportation of MOF nanomaterials in plants remains limited, and the assessment of MOF materials' safety is still incomplete. Therefore, it is crucial to maintain focus on future toxicological and safety studies. Secondly, the current encapsulation rate of the majority of pesticides loaded with MOFs is inadequate. Enhancing the encapsulation rate of specific pesticides holds immense importance for the effective utilization of MOF pesticides. Moving forward, our focus will be on advancing MOFs nanopesticides and enhancing the encapsulation rate. Additionally, we will dedicate further resources to enhancing the safety evaluation system. To sum up, the utilization of MOF nanocarriers offers significant benefits in achieving a prompt release of pesticides when stimulated, thereby promoting the advancement of 'intelligent pesticides'.

## References

- Abdelhameed, R. M., Abdelhameed, R. E., and Kamel, H. A. (2019). Iron-based metal-organic-frameworks as fertilizers for hydroponically grown *Phaseolus vulgaris*. *Mater Lett.* 237, 72–79. doi:10.1016/j.matlet.2018.11.072
- Ahmadi, S., Rabiee, N., Bagherzadeh, M., Elmi, F., Fatahi, Y., Farjadian, F., et al. (2020). Stimulus-responsive sequential release systems for drug and gene delivery. *Nano today* 34, 100914. doi:10.1016/j.nantod.2020.100914
- Anstoetz, M., Sharma, N., Clark, M., and Yee, L. H. (2016). Characterization of an oxalate-phosphate-amine metal-organic framework (OPA-MOF) exhibiting properties suited for innovative applications in agriculture. *J. Mater. Sci.* 51, 9239–9252. doi:10.1007/s10853-016-0171-6
- Applerot, G., Lellouche, J., Lipovsky, A., Nitzan, Y., Lubart, R., Gedanken, A., et al. (2012). Understanding the antibacterial mechanism of CuO nanoparticles: revealing the route of induced oxidative stress. *Small* 8 (21), 3326–3337. doi:10.1002/sml.201200772
- Applerot, G., Lipovsky, A., Dror, R., Perkash, N., Nitzan, Y., Lubart, R., et al. (2009). Enhanced antibacterial activity of nanocrystalline ZnO due to increased ROS-mediated cell injury. *Adv. Funct. Mater.* 19 (6), 842–852. doi:10.1002/adfm.200801081
- Armin, M., Akbari, S., and Mashhadi, S. (2014). Effect of time and concentration of nano-Fe foliar application on yield and yield components of wheat. *Int. J. Biosci.* 4 (9), 69–75. doi:10.12692/ijb/4.9
- Banerjee, S., Maiti, T. K., and Roy, R. N. (2022). Enzyme producing insect gut microbes: an unexplored biotechnological aspect. *Crit. Rev. Biotechnol.* 42 (3), 384–402. doi:10.1080/07388551.2021.1942777
- Bellemjid, N., Assifaoui, A., Moussaif, A., Mesfioui, A., and Iddar, A. (2021). Silica-coated calcium pectinate formulations for controlling carbendazim release: water and soil release studies. *J. Env. Sci. Heal C-Tox.* 56 (7), 613–622. doi:10.1080/03601234.2021.1927603
- Bindra, P., Kaur, K., Rawat, A., Sarkar, A. D., Singh, M., and Shanmugam, V. (2019). Nano-hives for plant stimuli controlled targeted iron fertilizer application. *Chem. Eng. J.* 375, 121995. doi:10.1016/j.cej.2019.121995
- Broxterman, S. E., and Schols, H. A. (2018). Interactions between pectin and cellulose in primary plant cell walls. *Carbohydr. Polym.* 192, 263–272. doi:10.1016/j.carbpol.2018.03.070
- Cai, L., Chen, J., Liu, Z., Wang, H., Yang, H., and Ding, W. (2018). Magnesium oxide nanoparticles: effective agricultural antibacterial agent against *Ralstonia solanacearum*. *Front. Microbiol.* 9, 790. doi:10.3389/fmicb.2018.00790
- Chen, Y., Wu, H., Yang, T., Zhou, G., Chen, Y., Wang, J., et al. (2021). Biomimetic nucleation of Metal-Organic frameworks on silk fibroin nanoparticles for designing Core-Shell-Structured pH-Responsive anticancer drug carriers. *ACS Appl. Mat. Interfaces* 13 (40), 47371–47381. doi:10.1021/acsami.1c13405
- Chenyu, Q., Jie, Z., Yao, Z., Donghui, X., and Guangyang, L. (2023). Advances in preparation of metal-organic frameworks-based nanocarrier for sustained and controlled release of pesticides. *Chin. J. Pestic. Sci.* 25 (1), 51–61. doi:10.16801/j.issn.1008-7303.2022.0125
- Chiniy, D., Underwood, W., Corwin, J., Ryan, A., Szemenyei, H., Lim, C. C., et al. (2019). PMR 5, an acetylation protein at the intersection of pectin biosynthesis and defense against fungal pathogens. *Plant J.* 100 (5), 1022–1035. doi:10.1111/tpj.14497
- Dong, J., Chen, W., Feng, J., Liu, X., Xu, Y., Wang, C., et al. (2021). Facile, smart, and degradable metal-organic framework nanopesticides gated with FeIII-tannic acid

## Author contributions

SH: Writing-original draft, CY. Qiang Fei: Writing-original draft. BZ: Writing-review and editing. WW: Writing review and editing.

## Funding

The authors declare financial support was received for the research, authorship, and/or publication of this article. This research was financially supported by the Science and Technology Planning Project of Guizhou Province [No. QKHZC (2022)]132, the Science and Technology Fund Project of Guizhou [No. Qian Ke He Pingtai Rencai-CXTD (2022) 002], Education Department of Guizhou Province-Natural Science Research Project [QJ(2023)042], and Guiyang University Innovation and Entrepreneurship Category Cultivation Programs [GUIECCG(2023)].

## Conflict of interest

The authors declare that the research was conducted in the absence of any commercial or financial relationships that could be construed as a potential conflict of interest.

## Publisher's note

All claims expressed in this article are solely those of the authors and do not necessarily represent those of their affiliated organizations, or those of the publisher, the editors and the reviewers. Any product that may be evaluated in this article, or claim that may be made by its manufacturer, is not guaranteed or endorsed by the publisher.

- networks in response to seven biological and environmental stimuli. *ACS Appl. Mat. Interfaces*. 13 (16), 19507–19520. doi:10.1021/acsami.1c04118
- Dong, Z., Sun, Y., Chu, J., Zhang, X., and Deng, H. (2017). Multivariate metal–organic frameworks for dialing-in the binding and programming the release of drug molecules. *J. Am. Chem. Soc.* 139 (40), 14209–14216. doi:10.1021/jacs.7b07392
- El-Shetehy, M., Moradi, A., Macaroni, M., Reinhardt, D., Petri-Fink, A., Rothen-Rutishauser, B., et al. (2021). Silica nanoparticles enhance disease resistance in Arabidopsis plants. *Nat. Nanotechnol.* 16 (3), 344–353. doi:10.1038/s41565-020-00812-0
- Furukawa, H., Cordova, K. E., O’Keeffe, M., and Yaghi, O. M. (2013). The chemistry and applications of metal-organic frameworks. *Science* 341 (6149), 1230444. doi:10.1126/science.1230444
- Gao, Y., Liang, Y., Zhou, Z., Yang, J., Tian, J., Niu, J., et al. (2021). Metal-organic framework nanohybrid carrier for precise pesticide delivery and pest management. *Chem. Eng. J.* 422, 130143. doi:10.1016/j.cej.2021.130143
- Gao, Y., Zhang, Y., He, S., Xiao, Y., Qin, X., Zhang, Y., et al. (2019). Fabrication of a hollow mesoporous silica hybrid to improve the targeting of a pesticide. *Chem. Eng. J.* 364, 361–369. doi:10.1016/j.cej.2019.01.105
- Guo, B. L., and Gao, Q. Y. (2007). Preparation and properties of a pH/temperature-responsive carboxymethyl chitosan/poly (N-isopropylacrylamide) semi-IPN hydrogel for oral delivery of drugs. *Carbohydr Res.* 342 (16), 2416–2422. doi:10.1016/j.carres.2007.07.007
- Holtfo, M., Lenaerts, C., Cullen, D., and Broeck, J. V. (2019). Extracellular nutrient digestion and absorption in the insect gut. *Cell Tissue Res.* 377, 397–414. doi:10.1007/s00441-019-03031-9
- Horcajada, P., Chalati, T., Serre, C., Gillet, B., Sebrie, C., Baati, T., et al. (2010). Porous metal-organic-framework nanoscale carriers as a potential platform for drug delivery and imaging. *Nat. Mater* 9 (2), 172–178. doi:10.1038/nmat2608
- Hu, Z., Peng, Y., Kang, Z., Qian, Y., and Zhao, D. (2015). A modulated hydrothermal (MHT) approach for the facile synthesis of UiO-66-type MOFs. *Inorg. Chem.* 54 (10), 4862–4868. doi:10.1021/acs.inorgchem.5b00435
- Huiping, C., Lidong, C., Chunli, X., Bo, X., Gangchao, R., and Qiliang, H. (2021). Research progress of metal organic frameworks (MOFs) as adsorbents and carriers of pesticides. *Mod. Agrochem.* 20 (1), 13–18. doi:10.3969/j.issn.1671-5284.2021.01.003
- Hussain, H. A., Men, S., Hussain, S., Chen, Y., Ali, S., Zhang, S., et al. (2019). Interactive effects of drought and heat stresses on morpho-physiological attributes, yield, nutrient uptake and oxidative status in maize hybrids. *Sci. Rep-UK* 9 (1), 3890. doi:10.1038/s41598-019-04362-7
- Ji, Y., Ma, S., Lv, S., Wang, Y., Lü, S., and Liu, M. (2021). Nanomaterials for targeted delivery of agrochemicals by an all-in-one combination strategy and deep learning. *ACS Appl. Mat. Interfaces*. 13 (36), 43374–43386. doi:10.1021/acsami.1c11914
- Kah, M., and Hofmann, T. (2014). Nanopesticide research: Current trends and future priorities. *Environ. Int.* 63, 224–235. doi:10.1016/j.envint.2013.11.015
- Karakasyan, C., Lack, S., Brunel, F., Maingault, P., and Hourdet, D. (2008). Synthesis and rheological properties of responsive thickeners based on polysaccharide architectures. *Biomacromolecules* 9 (9), 2419–2429. doi:10.1021/bm800393s
- Khandelwal, N., Barbole, R. S., Banerjee, S. S., Chate, G. P., Biradar, A. V., Khandare, J. J., et al. (2016). Budding trends in integrated pest management using advanced micro- and nano-materials: Challenges and perspectives. *J. Environ. Manage* 184, 157–169. doi:10.1016/j.jenvman.2016.09.071
- Kubicek, C. P., Starr, T. L., and Glass, N. L. (2014). Plant cell wall-degrading enzymes and their secretion in plant-pathogenic fungi. *Annu. Rev. Phytopathol.* 52, 427–451. doi:10.1146/annurev-phyto-102313-045831
- Lawson, S., Siemers, A., Kostlenick, J., Al-Naddaf, Q., Newport, K., Rownaghi, A. A., et al. (2021). Mixing Mg-MOF-74 with Zn-MOF-74: A facile pathway of controlling the pharmacokinetic release rate of curcumin. *ACS Appl. Bio Mat.* 4 (9), 6874–6880. doi:10.1021/acsabm.1c00585
- Lawson, H. D., Walton, S. P., and Chan, C. (2021). Metal-organic frameworks for drug delivery: a design perspective. *ACS Appl. Mat. Interfaces*. 13 (6), 7004–7020. doi:10.1021/acsami.1c01089
- Lebedev, O. I., Millange, F., Serre, C., Tendeloo, G. V., and Férey, G. (2005). First direct imaging of giant pores of the metal-organic framework MIL-101. *Chem. Mat.* 17 (26), 6525–6527. doi:10.1021/cm051870o
- Li, Y., Yin, Y. M., Wang, X. Y., Wu, H., and Ge, X. (2018). Evaluation of berberine as a natural fungicide: Biodegradation and antimicrobial mechanism. *J. Asian Nat. Prod. Res.* 20 (2), 148–162. doi:10.1080/10286020.2017.1329300
- Liang, W., Cheng, J., Zhang, J., Xiong, Q., Jin, M., and Zhao, J. (2022). pH-Responsive on-demand alkaloids release from core-shell ZnO@ ZIF-8 nanosphere for synergistic control of bacterial wilt disease. *ACS Nano* 16 (2), 2762–2773. doi:10.1021/acsnano.1c09724
- Liang, Y., Wang, S., Jia, H., Yao, Y., Song, J., Dong, H., et al. (2022b). Pectin functionalized metal-organic frameworks as dual-stimuli-responsive carriers to improve the pesticide targeting and reduce environmental risks. *Colloid Surf. B* 219, 112796. doi:10.1016/j.colsurf.2022.112796
- Liang, Y., Wang, S., Jia, H., Yao, Y., Song, J., Yang, W., et al. (2022a). pH/redox/α-amylase triple responsive metal-organic framework composites for pest management and plant growth promotion. *Micropor Mesopor Mat.* 344, 112230. doi:10.1016/j.micromeso.2022.112230
- Ma, S., Ji, Y., Dong, Y., Chen, S., Wang, Y., and Lü, S. (2021). An environmental-friendly pesticide-fertilizer combination fabricated by *in-situ* synthesis of ZIF-8. *Sci. Total Environ.* 789, 147845. doi:10.1016/j.scitotenv.2021.147845
- Ma, S., Wang, Y., Yang, X., Ni, B., and Lü, S. (2022a). MOF hybrid for long-term pest management and micronutrient supply triggered with protease. *ACS Appl. Mat. Interfaces*. 14 (15), 17783–17793. doi:10.1021/acsami.2c01187
- Ma, Y., Zhao, R., Shang, H., Zhen, S., Li, L., Guo, X., et al. (2022b). pH-responsive ZIF-8-based metal-organic-framework nanoparticles for termite control. *ACS Appl. Nano Mat.* 5 (8), 11864–11875. doi:10.1021/acsanm.2c02856
- Ma, Y., Yu, M., Wang, Y., Pan, S., Sun, X., Zhao, R., et al. (2023). A pH/cellulase dual stimuli-responsive cellulose-coated metal-organic framework for eco-friendly fungicide delivery. *Chem. Eng. J.* 462, 142190. doi:10.1016/j.cej.2023.142190
- Mahmoud, L. A. M., Telford, R., Livesey, T. C., Katsikogianni, M., Kelly, A. L., Terry, L. R., et al. (2022). Zirconium-based MOFs and their biodegradable polymer composites for controlled and sustainable delivery of herbicides. *ACS Appl. Bio Mat.* 5 (8), 3972–3981. doi:10.1021/acsabm.2c00499
- Mahmoudi, Z., Ghasemzadeh, M. A., Kabiri-Fard, H., and Ganjali, S. T. (2022). Multicomponent Synthesis of pyrimidoquinolinetriones and pyridodipyrimidines in the presence of triethylenediamine-based ionic liquid/MIL-101 (Cr) metal-organic framework composite. *Polycycl. Aromat. Comp.* 42 (10), 7526–7545. doi:10.1080/10406638.2021.2005638
- Mallakpour, S., Nikkhoo, E., and Hussain, C. M. (2022). Application of MOF materials as drug delivery systems for cancer therapy and dermal treatment. *Coord. Chem. Rev.* 451, 214262. doi:10.1016/j.ccr.2021.214262
- Mejias, F. J. R., Trasobares, S., Varela, R. M., Molinillo, J. M. G., Calvino, J. J., and Macías, F. A. (2021). One-step encapsulation of ortho-disulfides in functionalized zinc MOF. Enabling metal-organic frameworks in agriculture. *ACS Appl. Mat. Interfaces*. 13 (7), 7997–8005. doi:10.1021/acsami.0c21488
- Mohammadinejad, R., Maleki, H., Larraneta, E., Fajardo, A., Nik, A. B., Shavandi, A., et al. (2019). Status and future scope of plant-based green hydrogels in biomedical engineering. *Appl. Mater Today* 16, 213–246. doi:10.1016/j.apmt.2019.04.010
- Qiangqiang, H., Heze, G., and Hongjing, D. (2020). Size control and biomedical applications of ZIF-8 nanoparticles. *Prog. Chem.* 32 (5), 656. doi:10.7536/PC190929
- Qu, J., Bi, F., Li, S., Feng, Z., Li, Y., Zhang, G., et al. (2022). Microwave-assisted synthesis of polyethylenimine-grafted nanocellulose with ultra-high adsorption capacity for lead and phosphate scavenging from water. *Bioresour. Technol.* 362, 127819. doi:10.1016/j.biortech.2022.127819
- Reichenberger, S., Bach, M., Skitschak, A., and Frede, H. G. (2007). Mitigation strategies to reduce pesticide inputs into ground-and surface water and their effectiveness (A Review). *Sci. Total Environ.* 384 (1–3), 1–35. doi:10.1016/j.scitotenv.2007.04.046
- Ren, L., Zhao, J., Li, W., Li, Q., Zhang, D., Fang, W., et al. (2022). Site-specific controlled-release imidazole Framework-8 for dazomet smart delivery to improve the effective utilization rate and reduce biotoxicity. *J. Agric. Food Chem.* 70 (20), 5993–6005. doi:10.1021/acs.jafc.2c00353
- Rojas, S., Rodríguez-Diéguez, A., and Horcajada, P. (2022). Metal-organic frameworks in agriculture. *ACS Appl. Mat. Interfaces*. 14 (15), 16983–17007. doi:10.1021/acsami.2c00615
- Sabbadin, F., Urresti, S., Henrissat, B., Avrova, A. O., Welsh, L. R. J., Lindley, P. J., et al. (2021). Secreted pectin monooxygenases drive plant infection by pathogenic oomycetes. *Science* 373 (6556), 774–779. doi:10.1126/science.abj1342
- Saliba, D., Ammar, M., Rammal, M., Al-Ghoul, M., and Hmadeh, M. (2018). Crystal growth of ZIF-8, ZIF-67, and their mixed-metal derivatives. *J. Am. Chem. Soc.* 140 (5), 1812–1823. doi:10.1021/jacs.7b11589
- Samalova, M., Meyer, A. J., Gurr, S. J., and Fricker, M. K. (2014). Robust anti-oxidant defences in the rice blast fungus *Magnaporthe oryzae* confer tolerance to the host oxidative burst. *New Phytol.* 201 (2), 556–573. doi:10.1111/nph.12530
- Shan, Y., Cao, L., Muhammad, B., Xu, B., Zhao, P., Cao, C., et al. (2020). Iron-based porous metal-organic frameworks with crop nutritional function as carriers for controlled fungicide release. *J. Colloid Interf. Sci.* 566, 383–393. doi:10.1016/j.jcis.2020.01.112
- Sharifloo, A., Zibae, A., Sendi, J. J., and Jahroumi, K. T. (2016). Characterization of a digestive α-amylase in the midgut of pieris brassicae L. (Lepidoptera: Pieridae). *Front. Physiol.* 7, 96. doi:10.3389/fphys.2016.00096
- Shitrit, Y., Davidovich-Pinhas, M., and Bianco-Peled, H. (2019). Shear thinning pectin hydrogels physically cross-linked with chitosan nanogels. *Carbohydr Polym.* 225, 115249. doi:10.1016/j.carbpol.2019.115249
- Siemińska-Kuczer, A., Szymańska-Chargot, M., and Zdunek, A. (2022). Recent advances in interactions between polyphenols and plant cell wall polysaccharides as studied using an adsorption technique. *Food Chem.* 373, 131487. doi:10.1016/j.foodchem.2021.131487
- Sierra-Serrano, B., García-García, A., Hidalgo, T., Ruiz-Camino, D., Rodríguez-Diéguez, A., Amariei, G., et al. (2022). Copper glufoinate-based metal-organic framework as a novel multifunctional agrochemical. *ACS Appl. Mat. Interfaces*. 14 (30), 34955–34962. doi:10.1021/acsami.2c07113

- Song, S., Jiang, X., Shen, H., Wu, W., Shi, Q., Wan, M., et al. (2021). MXene (Ti<sub>3</sub>C<sub>2</sub>) based pesticide delivery system for sustained release and enhanced pest control. *ACS Appl. Bio Mat.* 4 (9), 6912–6923. doi:10.1021/acsabm.1c00607
- Song, S., Wan, M., Feng, W., Tian, Y., Jiang, X., Luo, Y., et al. (2022). Environmentally friendly Zr-based MOF for pesticide delivery: Ultrahigh loading capacity, pH-responsive release, improved leaf affinity, and enhanced antipest activity. *Langmuir* 38 (35), 10867–10874. doi:10.1021/acs.langmuir.2c01556
- Sun, K., Sun, J., Lu, G. P., and Cai, C. (2019). Enhanced catalytic activity of cobalt nanoparticles encapsulated with an N-doped porous carbon shell derived from hollow ZIF-8 for efficient synthesis of nitriles from primary alcohols in water. *Green Chem.* 21 (16), 4334–4340. doi:10.1039/C9GC01893J
- Sun, W., Jiang, T., Lu, Y., Reiff, M., Mo, R., and Gu, Z. (2014). Cocoon-like self-degradable DNA nanoclew for anticancer drug delivery. *J. Am. Chem. Soc.* 136 (42), 14722–14725. doi:10.1021/ja508802a
- Taylor-Pashow, K. M. L., Della, Rocca, J., Xie, Z., Tran, S., and Lin, W. (2009). Postsynthetic modifications of iron-carboxylate nanoscale metal-organic frameworks for imaging and drug delivery. *J. Am. Chem. Soc.* 131 (40), 14261–14263. doi:10.1021/ja906198y
- Teplensky, M. H., Fantham, M., Poudel, C., Hockings, C., Lu, M., Guna, A., et al. (2019). A highly porous metal-organic framework system to deliver payloads for gene knockdown. *Chem* 5 (11), 2926–2941. doi:10.1016/j.chempr.2019.08.015
- Tsalaporta, E., and MacElroy, J. M. D. (2020). A comparative study of the physical and chemical properties of pelletized HKUST-1, ZIF-8, ZIF-67 and UiO-66 powders. *Heliyon* 6 (9), e04883. doi:10.1016/j.heliyon.2020.e04883
- Wan, M., Song, S., Feng, W., Shen, H., Luo, Y., Wu, W., et al. (2022). Metal-organic framework (UiO-66)-Based temperature-responsive pesticide delivery system for controlled release and enhanced insecticidal performance against *spodoptera frugiperda*. *ACS Appl. Bio Mat.* 5 (8), 4020–4027. doi:10.1021/acsabm.2c00549
- Wang, D., Saleh, N. B., Byro, A., Zepp, R., Sahle-Demessie, E., Luxton, T. P., et al. (2022a). Nano-enabled pesticides for sustainable agriculture and global food security. *Nat. Nanotechnol.* 17 (4), 347–360. doi:10.1038/s41565-022-01082-8
- Wang, L., Lu, D., Huo, M., and Xu, H. (2022b). Oligomycin A induces apoptosis-to-pyoptosis switch against melanoma with sensitized immunotherapy. *Adv. Funct. Mater.* 32 (4), 2106332. doi:10.1002/adfm.202106332
- Wang, S., Ma, Q., Wang, R., Zhu, Q., Yang, L., and Zhang, Z. (2020). Preparation of sodium alginate-poly (vinyl alcohol) blend beads for base-triggered release of dinotefuran in *Spodoptera litura* midgut. *Ecotox Environ. Safe* 202, 110935. doi:10.1016/j.ecoenv.2020.110935
- Wang, X. G., Xu, L., Li, M. J., and Zhang, X. Z. (2020). Construction of flexible-on-rigid hybrid-phase metal-organic frameworks for controllable multi-drug delivery. *Angew. Chem. Int. Ed.* 59 (41), 18078–18086. doi:10.1002/anie.202008858
- Wu H, H., Hu, P., Xu, Y., Xiao, C., Chen, Z., Liu, X., et al. (2021). Phloem delivery of fludioxonil by plant amino acid transporter-mediated polysuccinimide nanocarriers for controlling fusarium wilt in banana. *J. Agric. Food Chem.* 69 (9), 2668–2678. doi:10.1021/acs.jafc.0c07028
- Wu, W., Wan, M., Fei, Q., Tian, Y., Song, S., Shen, H., et al. (2021). PDA@Ti<sub>3</sub>C<sub>2</sub>T<sub>x</sub> as a novel carrier for pesticide delivery and its application in plant protection: NIR-responsive controlled release and sustained antipest activity. *Pest Manag. Sci.* 77 (11), 4960–4970. doi:10.1002/ps.6538
- Wu, M. X., and Yang, Y. W. (2017). Metal-organic framework (MOF)-based drug/cargo delivery and cancer therapy. *Adv. Mater* 29 (23), 1606134. doi:10.1002/adma.201606134
- Yan, L., Chen, X., Wang, Z., Zhang, X., Zhu, X., Zhou, M., et al. (2017). Size controllable and surface tunable zeolitic imidazolate framework-8-poly (acrylic acid sodium salt) nanocomposites for pH responsive drug release and enhanced *in vivo* cancer treatment. *ACS Appl. Mat. Interfaces* 9 (38), 32990–33000. doi:10.1021/acsami.7b10064
- Yang, G. Z., Wibowo, D., Yun, J. H., Wang, L., Middelberg, A. P. J., and Zhao, C. X. (2017). Biomimetic silica nanocapsules for tunable sustained release and cargo protection. *Langmuir* 33 (23), 5777–5785. doi:10.1021/acs.langmuir.7b00590
- Yang J, J., Trickett, C. A., Alahmadi, S. B., Alshammari, A. S., and Yaghi, O. M. (2017). Calcium L-lactate frameworks as naturally degradable carriers for pesticides. *J. Am. Chem. Soc.* 139 (24), 8118–8121. doi:10.1021/jacs.7b04542
- Yu, M., Ji, N., Wang, Y., Dai, L., Xiong, L., and Sun, Q. (2021). Starch-based nanoparticles: Stimuli responsiveness, toxicity, and interactions with food components. *Compr. Rev. Food Sci. F.* 20 (1), 1075–1100. doi:10.1111/1541-4337.12677
- Yuan, S., Feng, L., Wang, K., Pang, J., Bosch, M., Lollar, C., et al. (2018). Stable metal-organic frameworks: Design, synthesis, and applications. *Adv. Mater* 30 (37), 1704303. doi:10.1002/adma.201704303
- Zhang, W., Zhou, Y., Fan, Y., Cao, R., Xu, Y., Weng, Z., et al. (2022). Metal-organic-framework-based hydrogen-release platform for multieffective *Helicobacter pylori* targeting therapy and intestinal flora protective capabilities. *Adv. Mater* 34 (2), 2105738. doi:10.1002/adma.202105738
- Zhang, X., Tang, X., Zhao, C., Yuan, Z., Zhang, D., Zhao, H., et al. (2022). A pH-responsive MOF for site-specific delivery of fungicide to control citrus disease of *Botrytis cinerea*. *Chem. Eng. J.* 431, 133351. doi:10.1016/j.cej.2021.133351
- Zhang, Y., Yan, J., Avellan, A., Gao, X., Matyjaszewski, K., Tilton, R. D., et al. (2020). Temperature- and pH-responsive star polymers as nanocarriers with potential for *in vivo* agrochemical delivery. *ACS Nano* 14 (9), 10954–10965. doi:10.1021/acsnano.0c03140
- Zhou, Z., Gao, Y., Chen, X., Li, Y., Tian, Y., Wang, H., et al. (2021). One-pot facile synthesis of double-shelled mesoporous silica microcapsules with an improved soft-template method for sustainable pest management. *ACS Appl. Mat. Interfaces* 13 (33), 39066–39075. doi:10.1021/acsami.1c10135



## OPEN ACCESS

## EDITED BY

Kamaldeep Paul,  
Thapar Institute of Engineering and  
Technology, India

## REVIEWED BY

Borys Ośmiatowski,  
Nicolaus Copernicus University in Toruń,  
Poland  
Arindam Mukhopadhyay,  
Idaho National Laboratory (DOE),  
United States

## \*CORRESPONDENCE

Kiran B. Manjappa,  
✉ kiran@thu.edu.tw  
Ding-Yah Yang,  
✉ yang@thu.edu.tw

RECEIVED 16 September 2023

ACCEPTED 24 October 2023

PUBLISHED 07 November 2023

## CITATION

Manjappa KB, Fan S-C and Yang D-Y  
(2023), Structural tuning of  $\beta$ -enamino  
diketones: exploration of solution and  
crystalline state photochromism.  
*Front. Chem.* 11:1295347.  
doi: 10.3389/fchem.2023.1295347

## COPYRIGHT

© 2023 Manjappa, Fan and Yang. This is  
an open-access article distributed under  
the terms of the [Creative Commons  
Attribution License \(CC BY\)](#). The use,  
distribution or reproduction in other  
forums is permitted, provided the original  
author(s) and the copyright owner(s) are  
credited and that the original publication  
in this journal is cited, in accordance with  
accepted academic practice. No use,  
distribution or reproduction is permitted  
which does not comply with these terms.

# Structural tuning of $\beta$ -enamino diketones: exploration of solution and crystalline state photochromism

Kiran B. Manjappa<sup>1\*</sup>, Sheng-Chieh Fan<sup>2</sup> and Ding-Yah Yang<sup>1,2\*</sup>

<sup>1</sup>Graduate Program for Biomedical and Materials Science, Tunghai University, Taichung, Taiwan,

<sup>2</sup>Department of Chemistry, Tunghai University, Taichung, Taiwan

A library of  $\beta$ -enamino diketones was prepared via base-mediated, three-component reaction of 4-hydroxycoumarins with various aromatic/aliphatic amines and  $\beta$ -nitrostyrenes under microwave irradiation conditions to investigate their photochemical properties. Among the prepared compounds, a thiophene derived  $\beta$ -enamino diketone was found to be light-sensitive and to exhibit unique photochromic behavior, that is, positive photochromism in solution and negative photochromism in crystalline phase. In addition, this prepared photochromic compound was further covalently linked to a structure-related, piezochromic  $\beta$ -enamino diketone moiety to explore its potential multi-stimuli responsive properties.

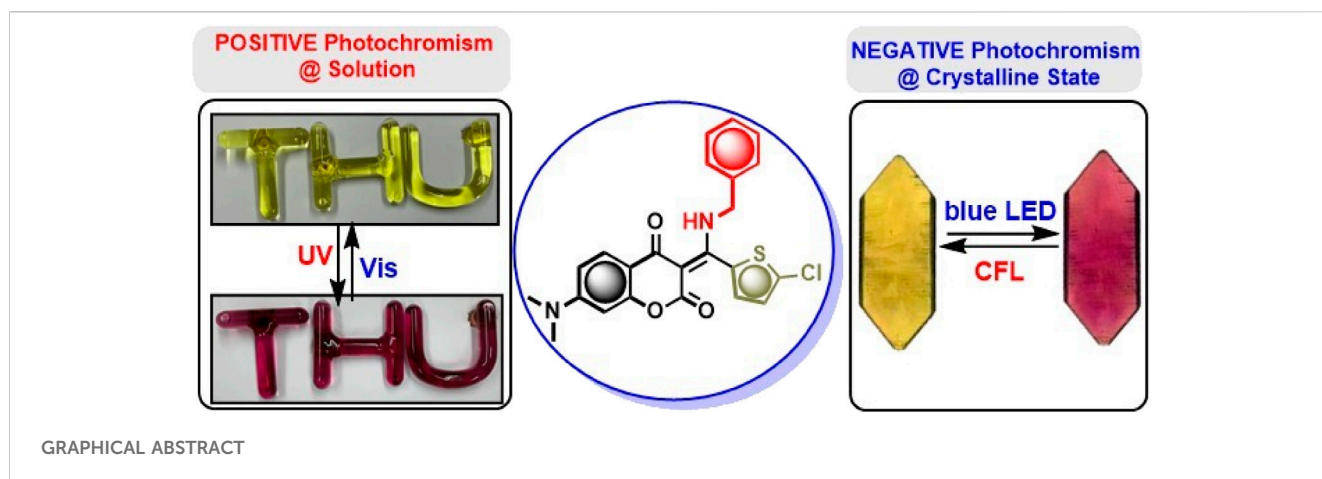
## KEYWORDS

$\beta$ -enamino diketones, thiophene, photochromism, piezochromism, multi-responsive, photosensitive, microwave, functional property

## 1 Introduction

The  $\beta$ -enamino diketones represent important and versatile synthons for the synthesis of natural products and other heterocycles (Michael et al., 2001; Valduga et al., 1998; Ferraz et al., 1995; White and Lhle, 2006; Li et al., 2007). Compounds bearing  $\beta$ -enamino diketone moiety, especially six-membered cyclic ones, were found to possess many biological properties. For instance, as shown in Figure 1,  $\beta$ -enamino diketone 1 is an antioxidant agent (Mladenovic et al., 2009). Compound 2 possesses strong inhibitory activity against fungus *C. albicans* (Vukovic et al., 2010). Compound 3 exhibits potent cytotoxicity against A546, HeLa, and K562 cells (Budzisz et al., 2004). Owing to their diverse biological activities, a plethora of multi-component reaction methodologies for the synthesis of  $\beta$ -enamino diketones have been reported in the literature (Kuo et al., 2009; Ghabraie et al., 2011; Ye et al., 2015). While most efforts were focused on the biological activities of the prepared compounds, their potential photochemical and functional properties were much less explored. Recently, we have reported that coumarin-based *N*-aryl- $\beta$ -enamino diketone 4 (Figure 1) exhibits piezochromic properties (Hsieh et al., 2019); that is, upon grinding, compound 4 changes from yellow to red and can be swiftly reverted to the original color when exposed to methylene chloride vapor. Further, the furan-derived enaminones 5 serve as amine-protected compounds for primary alkyl amines protection. These acid/base stable amine-protected 5 can be readily deprotected by treating with ethylene diamine under reflux conditions (Chithanna and Yang, 2019). Similarly, the phenyl-derived enaminones 6 function as amine-protected products for aryl amines and amino acids in both solution and solid phase peptide synthesis. The free aryl amines and amino



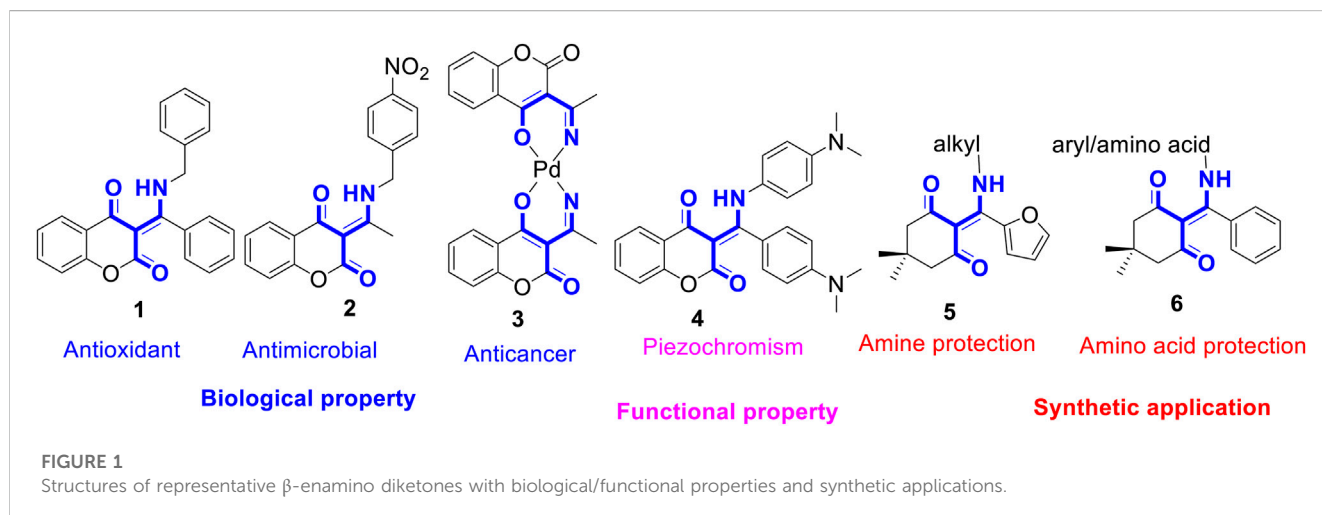


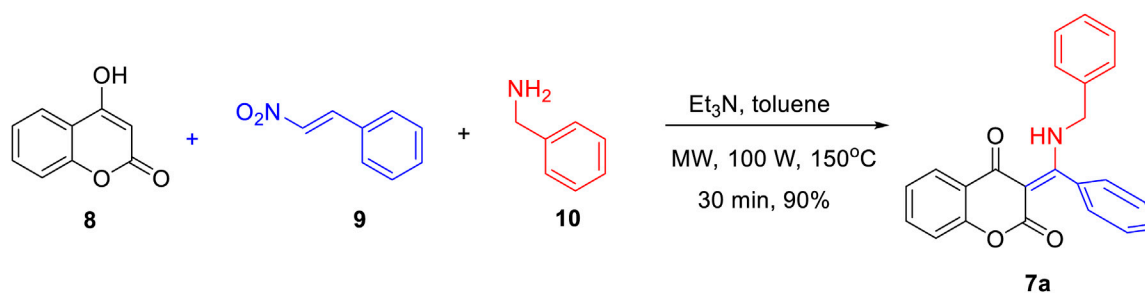
acids can be regenerated by treating with hydrazine hydrate in ethanol under mild conditions (Chithanna et al., 2020). These successful examples prompted us to speculate that new or unique functional behavior of  $\beta$ -enamino diketones via structural tuning of their three major molecular scaffolds, namely, cyclic diketone, aryl/alkyl amine, and aryl group. Further, we envisioned that the  $\beta$ -enamino diketones are prone to undergo the excited state intramolecular proton transfer (ESIPT) process upon photoirradiation by means of proton transfer from amine to nearby keto-group of coumarin. Thus, in our continuous efforts to unearth novel functional properties from the heterocycles synthesized via multi-component reaction, herein we reported the preparation of a library of  $\beta$ -enamino diketones from a microwave-assisted, three-component reaction of 4-hydroxycoumarins with various aromatic/aliphatic amines and  $\beta$ -nitrostyrenes in toluene under basic conditions. Their stimuli responses towards UV and visible light in solution, thin film, and crystalline state were examined. Further, the photochromic compound prepared from 7-*N,N*-dimethylamino-4-hydroxycoumarin, benzylamine, and 5-chlorothiophene-2-carbaldehyde was further linked to a structure-related, pressure-sensitive  $\beta$ -enamino diketone scaffold to investigate its potential multi-stimuli responsive properties.

## 2 Results and discussion

Scheme 1 outlines the microwave-assisted, three-component preparation of  $\beta$ -enamino diketone **7a**. With slight modifications from the literature reported procedure (Manjappa et al., 2018; Hsieh et al., 2019), it could be easily obtained via triethylamine-mediated coupling of 4-hydroxycoumarin (**8**),  $\beta$ -nitrostyrene (**9**), and benzylamine (**10**) in toluene under microwave conditions for 30 min in 90% yield.

Figure 2 lists the structures and yields of the prepared **7a–o**. Most of the reactions gave good to excellent yields, except for compound **7k** in which 4-bromofuran-2-carbaldehyde was used as the aldehyde source. This observation could be attributed to the furan's high propensity to be attacked by a nucleophilic amine (Helmy et al., 2014; Chithanna and Yang, 2019). In the present investigation, we focused mainly on 7-*N,N*-dimethylamino-4-hydroxycoumarin, benzylamine, and thiophene aldehydes derived  $\beta$ -enamino diketones. The molecular structures of diketones **7a–o** were elucidated by spectroscopic data along with X-ray crystal analysis (**7b**, **7g**, **7i**, and **7m**) (CCDC No, 2023). A broad signal appearing around 13–14 ppm in the proton NMR spectrum was detected for all prepared compounds, indicating the presence of an intramolecular hydrogen bond in the molecular scaffold. Indeed, an





SCHEME 1

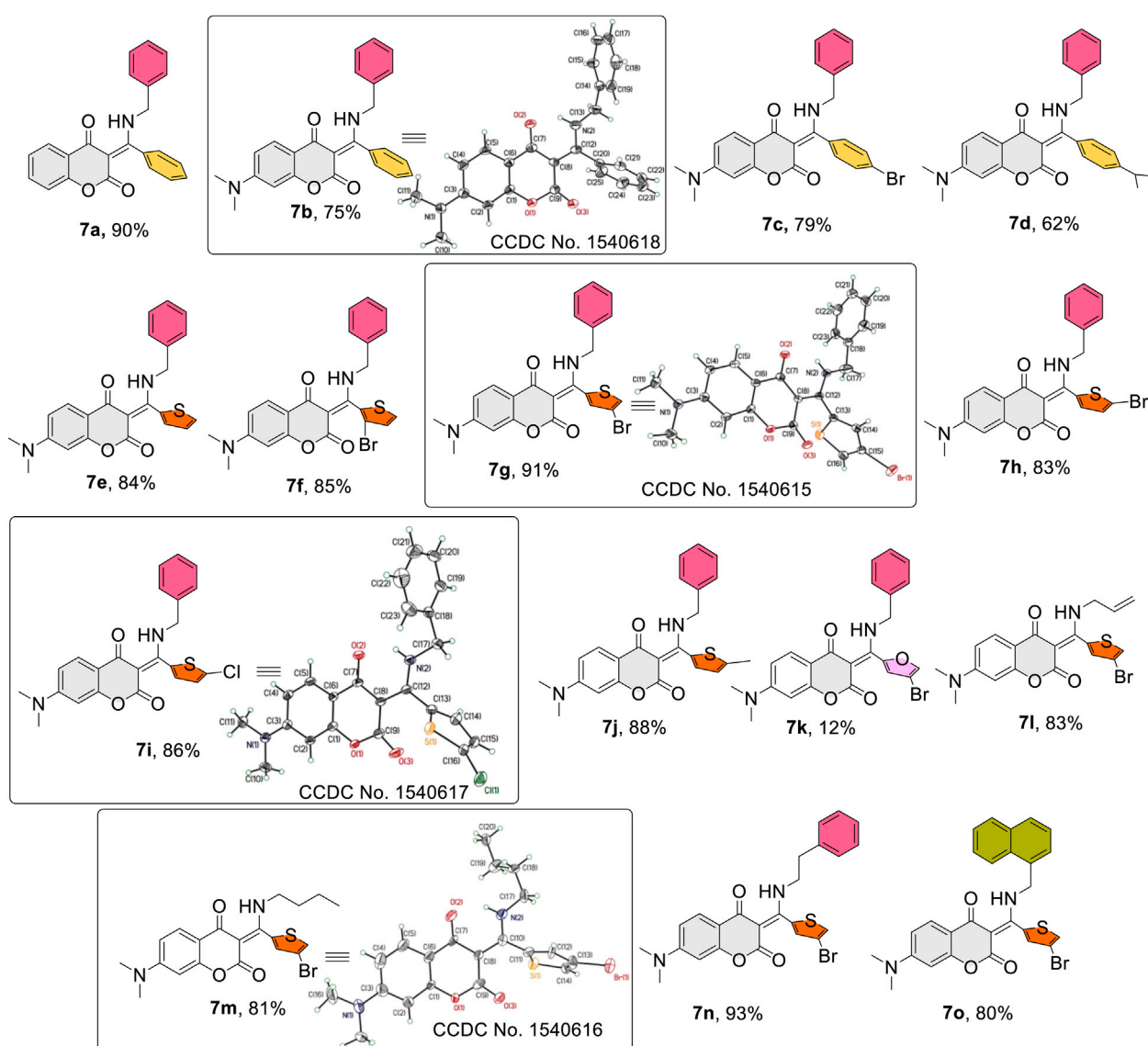
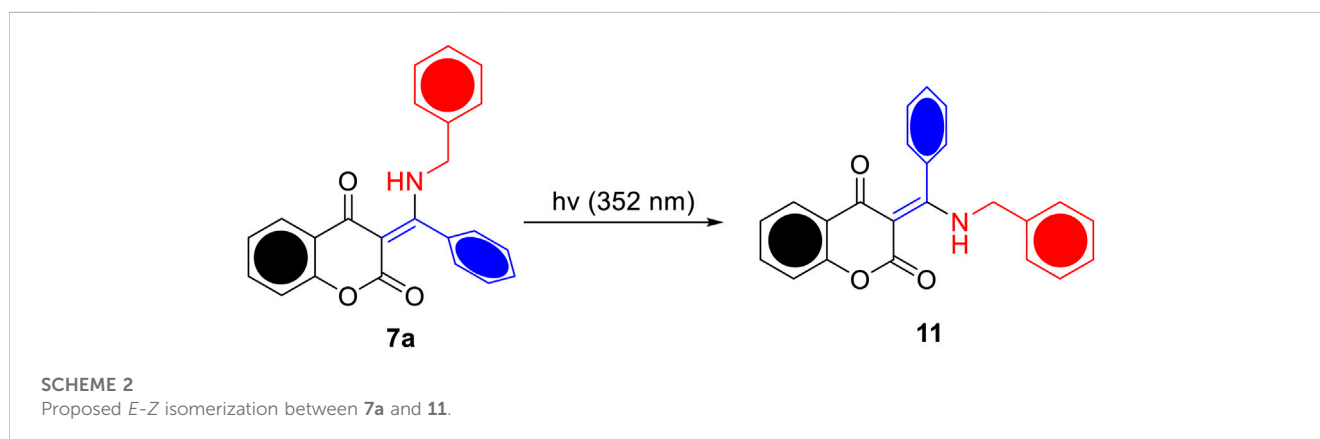
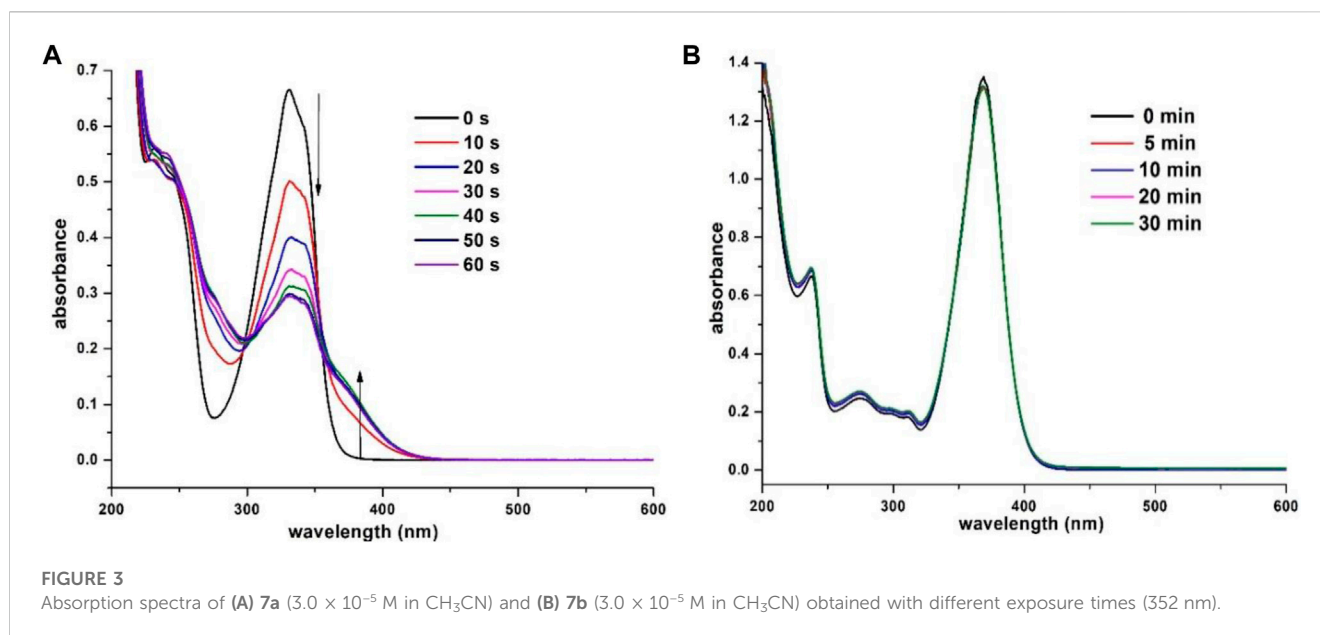
Three-component synthesis of  $\beta$ -enaminone diketone 7a.

FIGURE 2

Structures and yields of the prepared  $\beta$ -enamino diketones (7a–o) and ORTEP crystal structures of (7b, 7g, 7i, 7m) with atomic displacement shown at 50% probability.



intramolecular hydrogen bonding between the amine hydrogen (*N*-H) and carbonyl oxygen (*C*=O) of coumarin was distinctly observed in the ORTEP diagrams shown in Figure 2. Generally, changes of amines (aryl or aliphatic) or aromatic/heterocyclic aldehydes had little effect on product yields.

To investigate the potential ESIPT behavior, the prepared  $\beta$ -enaminone diketones **7a–o** were subjected to photoirradiation and their photochemical properties were explored. Compound **7a**, in which benzaldehyde was used as the aldehyde substrate, was found to be sensitive to UV light. Figure 3 shows the absorption spectra of **7a** in acetonitrile when exposed to UV irradiation (352 nm) for 60 s. With the increase of exposure time, the absorbance at wavelength of 330 and 342 nm gradually decreased, along with the emergence of broad shoulder at around 380 nm. Also, two isosbestic points located at 305 and 355 nm were clearly observed. Presumably, upon UV irradiation, compound **7a** undergoes *E-Z* isomerization of the central carbon-carbon double bond to generate the isomer **11**, as shown in Scheme 2. To further support this hypothesis, a time-dependent proton NMR study was carried out. Prior to irradiation, a small doublet appeared at 4.42 ppm and a broad singlet appeared at

14.34 ppm which correspond to the respective benzylic  $-\text{CH}_2$  and the intramolecular hydrogen bonding absorptions were observed in the proton NMR spectrum of **7a**. During the process of UV irradiation (up to 60 min), these peaks gradually diminished and the concomitant emergence of two new peaks at 4.83 and 9.03 ppm which correspond to the benzylic  $-\text{CH}_2$  and intramolecular hydrogen bonding absorptions of **11** was witnessed (see the Supporting Information). These observations suggest that indeed compound **7a** undergoes *E-Z* isomerization to give the compound **11** upon UV irradiation. On the other hand, when an *N,N*-dimethylamino group was introduced onto the 7-position of the coumarin moiety, the resulting compound **7b** became light-insensitive. Prolonged irradiation of **7b** did not exhibit considerable changes in the UV-vis absorption profiles (Figure 3B). This observation implies that the photochemical property of the  $\beta$ -enaminone diketones can be influenced by the substituents on the coumarin moiety.

Interestingly, compound **7i** bearing a 5-chlorothiophene moiety was found to be highly sensitive to UV light and exhibit unique photochemical properties. As shown in Figure 4, it turned from light

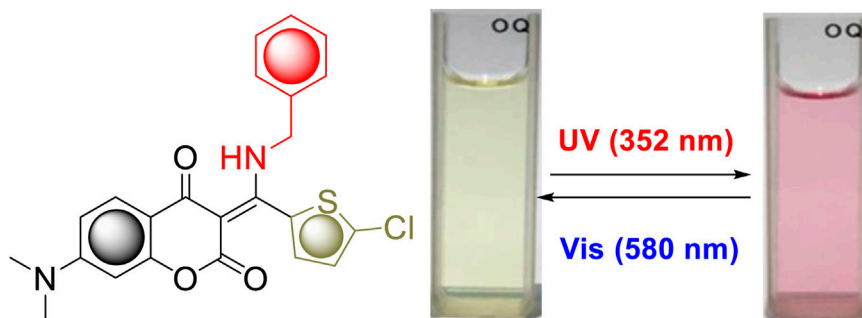


**FIGURE 4**  
Photochromic behavior of **7i** in acetonitrile.

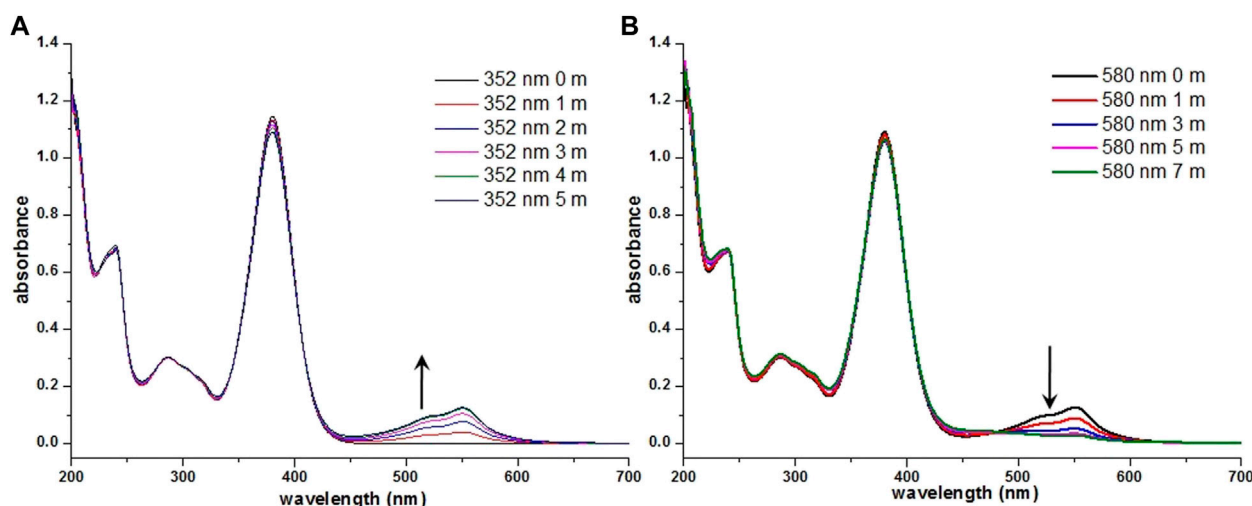


**FIGURE 5**  
Absorption spectra of (A) **7i** ( $3.0 \times 10^{-5}$  M in  $\text{CH}_3\text{CN}$ ) obtained with different exposure times (352 nm), 0–5 min, in increments of 1 min (B) the photogenerated product obtained with different exposure times (580 nm), 0–7 min, in increments of 2 min.

yellow to red within seconds when exposed to UV irradiation in solution. **Figure 5A** displays the time course of the UV–vis absorption spectra of **7i** in acetonitrile under continuous irradiation (352 nm) for 5 min. With the increase of exposure time, two broad absorbance peaks which centered at 527 and 551 nm exhibited smooth continuous growth. This process could be reverted by visible light irradiation (580 nm), indicating that compound **7i** possesses photochromic property (**Figure 5B**).

Isolation of the photogenerated product and subsequent characterization of its molecular structure proved to be difficult since prolonged UV irradiation of **7i** resulted in the *E-Z* isomerization to be the dominant process. **Figure 6** depicts the evolution of absorbance profile of **7i** during the prolonged UV irradiation. Starting from the initial 5 min of UV irradiation, there was a surge in a broad absorption band around 520–560 nm, indicating the formation of photogenerated products. However, as the irradiation time was further extended (up to 120 min), the decrease in absorption at 372 nm and the appearance of a broad shoulder near 455 nm were also recorded. This observation suggests

that prolonged irradiation of compound **7i** renders the *E-Z* isomerization to be a dominant process over the formation of photogenerated product. Therefore, current efforts to characterize the photogenerated product resulting from this photochromic behavior were futile.

Inspired by the photochromic behavior in solution, we chose to investigate the photosensitivity of **7i** in solid phase. The thin film of **7i** was prepared by spin coating on a quartz plate and then irradiated with light. When exposed to blue LED for 60 min, no apparent color change of **7i** was observed. Conversely, compound **7i** (thin film) changed from colorless to red in 5 min upon UV (352 nm) irradiation. **Figure 7** shows the color change and absorption profile of **7i** (thin film) prior to and after irradiation. As UV exposure increased, the absorbance centered at 388 nm decreased along with a smooth enhancement of the shoulders near 450 nm and 530 nm. This evolution of the absorbance resulted in the formation of two isosbestic points at 366 and 412 nm, which indicates the presence of two distinguishable species in the film. The fact that UV–vis spectra of **7i** in thin film (solid state) exhibited strong



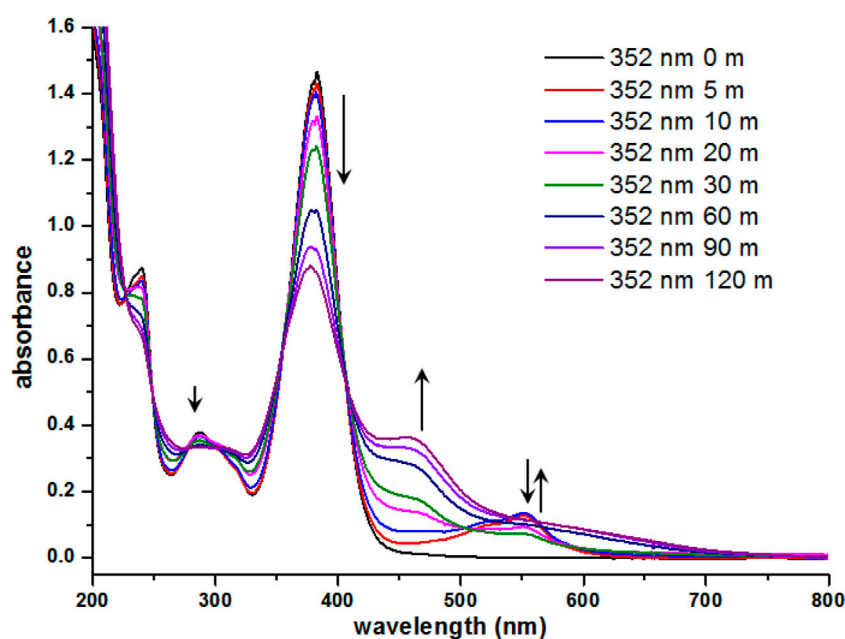


FIGURE 6

UV-vis spectra of **7i** ( $3.0 \times 10^{-5}$  M in  $\text{CH}_3\text{CN}$ ) after continuous irradiation at 352 nm for 120 min.

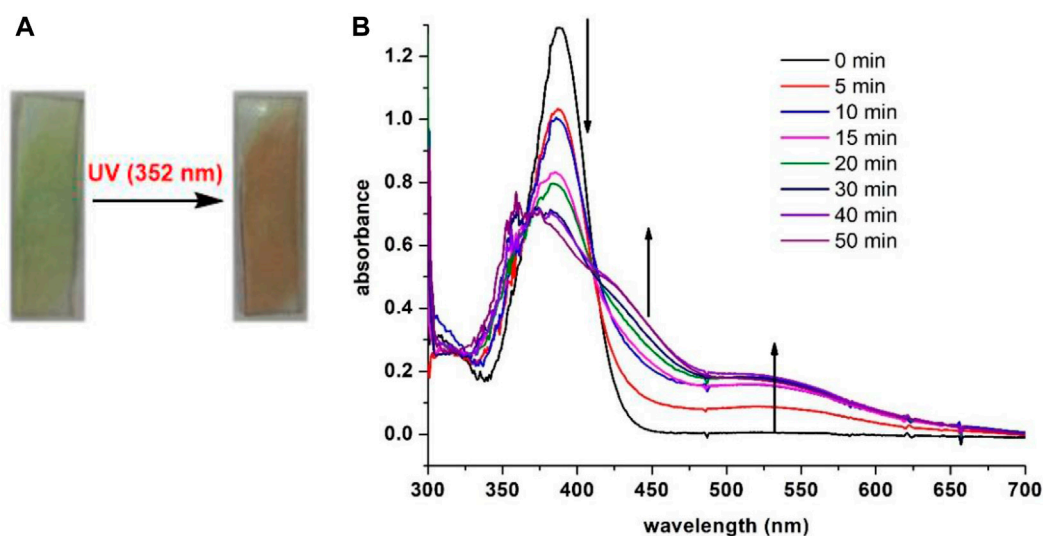


FIGURE 7

(A) Color change prior to and after UV irradiation of **7i** (thin film). (B) UV-vis spectra of **7i** (spin-coated on quartz plate) after continuous irradiation at 352 nm for 50 min.

resemblance to that of **7i** in solution phase (Figure 6) implies that similar photochromic mechanisms may be involved for **7i** in solution and solid state.

After discovering the photochromism of **7i** in both solution and solid state, we embarked upon our investigations on its photochromic behavior in crystalline state (Avadanei et al., 2014; Irie et al., 2014; Funasako et al., 2019; Zhang et al., 2021; Sun et al., 2022; Loan et al., 2023). A fine, moderate-sized crystal of **7i** was grown and subjected to photoirradiation. To our surprise, **7i** was

found to be highly sensitive to visible light in crystalline state. When exposed to blue LED (465 nm), the crystal of **7i** changed from yellow to violet within 15 s. Gratifyingly, this process was reversible upon exposure to the compact fluorescent lamp (CFL) for 2 h. Figure 8 shows the color transition of **7i** at crystalline state as well as UV-vis absorption profiles of **7i** prior to and after the blue LED irradiation. Before the exposure, **7i** displayed a maximum absorbance ( $\lambda_{\text{max}}$ ) around 416 nm. After blue LED exposure (40 min), the  $\lambda_{\text{max}}$  was red-shifted to 425 nm along with the broad absorbance increase

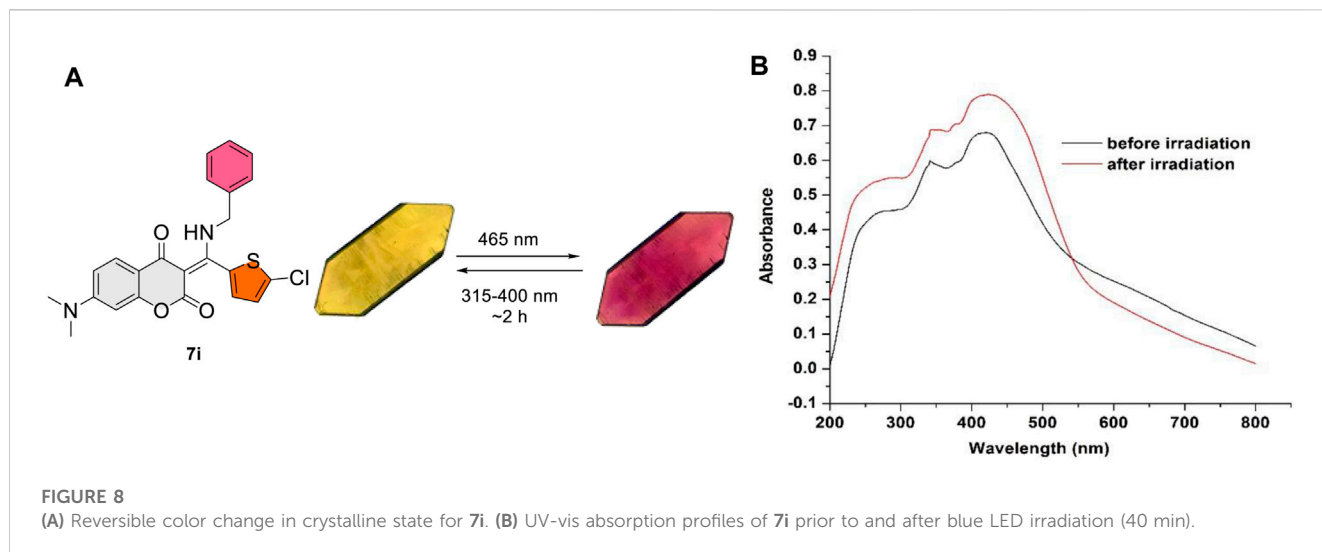


FIGURE 8 (A) Reversible color change in crystalline state for **7i**. (B) UV-vis absorption profiles of **7i** prior to and after blue LED irradiation (40 min).

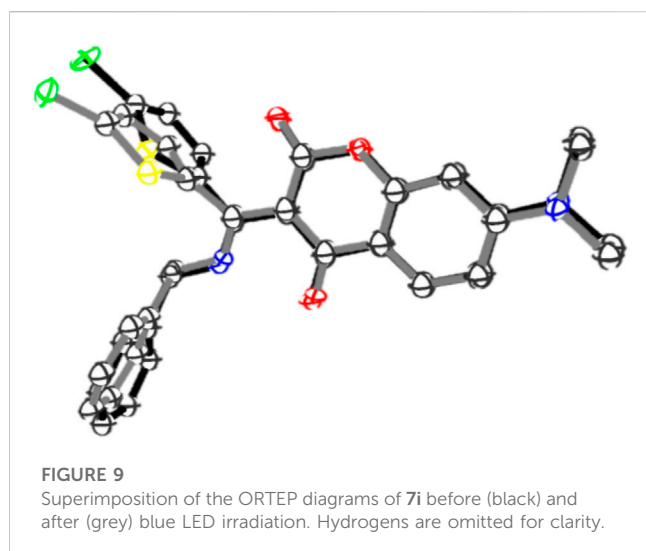


FIGURE 9 Superimposition of the ORTEP diagrams of **7i** before (black) and after (grey) blue LED irradiation. Hydrogens are omitted for clarity.

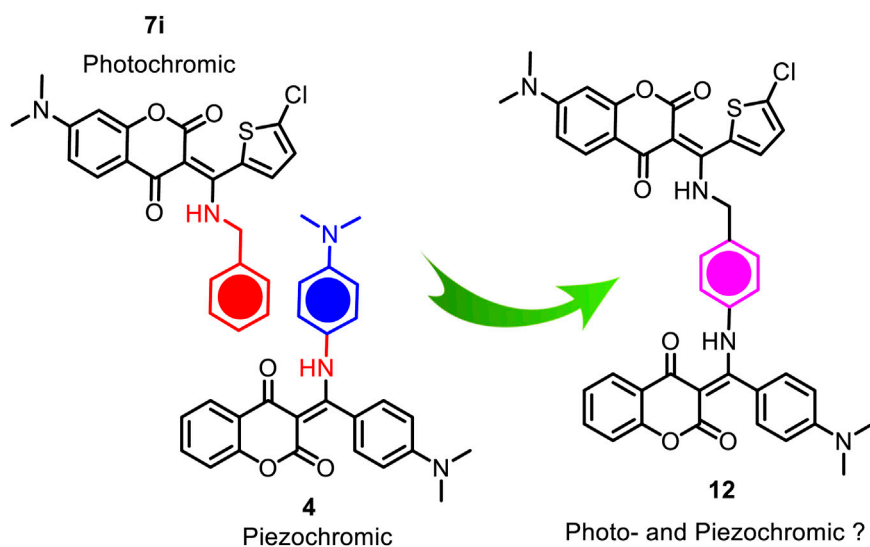
from 425 to 550 nm. This change in the absorbance was visible to the naked eye as blue LED imparted dark violet color to the **7i** crystal. The violet crystal of **7i** gradually returned to yellow upon exposure to CFL light (315–400 nm for UVA), suggesting possible reversibility. In the case of color change of **7i** in solution photochromism, the number of cycles is limited to 3–4 times only. On the other hand, the number of photochromic cycles for **7i** in crystalline state is up to 25 times (see the [Supplementary Material](#) for details), which is comparatively higher than that of in solution state.

In order to gain more insights into the photosensitivity of **7i** towards blue LED, the X-ray crystallography was sought to examine the possible structural changes at crystalline state during irradiation. A crystal of **7i** was irradiated with blue LED for 24 h and its X-ray ORTEP diagram was obtained (CCDC No 2300435). [Figure 9](#) depicts the superimposition of the ORTEP diagrams of **7i** before and after blue LED irradiation. Some conformational differences in the crystals were noticed, that is, the benzylamine and thiophene moieties were found to be tilted to certain degrees after irradiation. For instance, prior to the blue LED irradiation, the dihedral angle

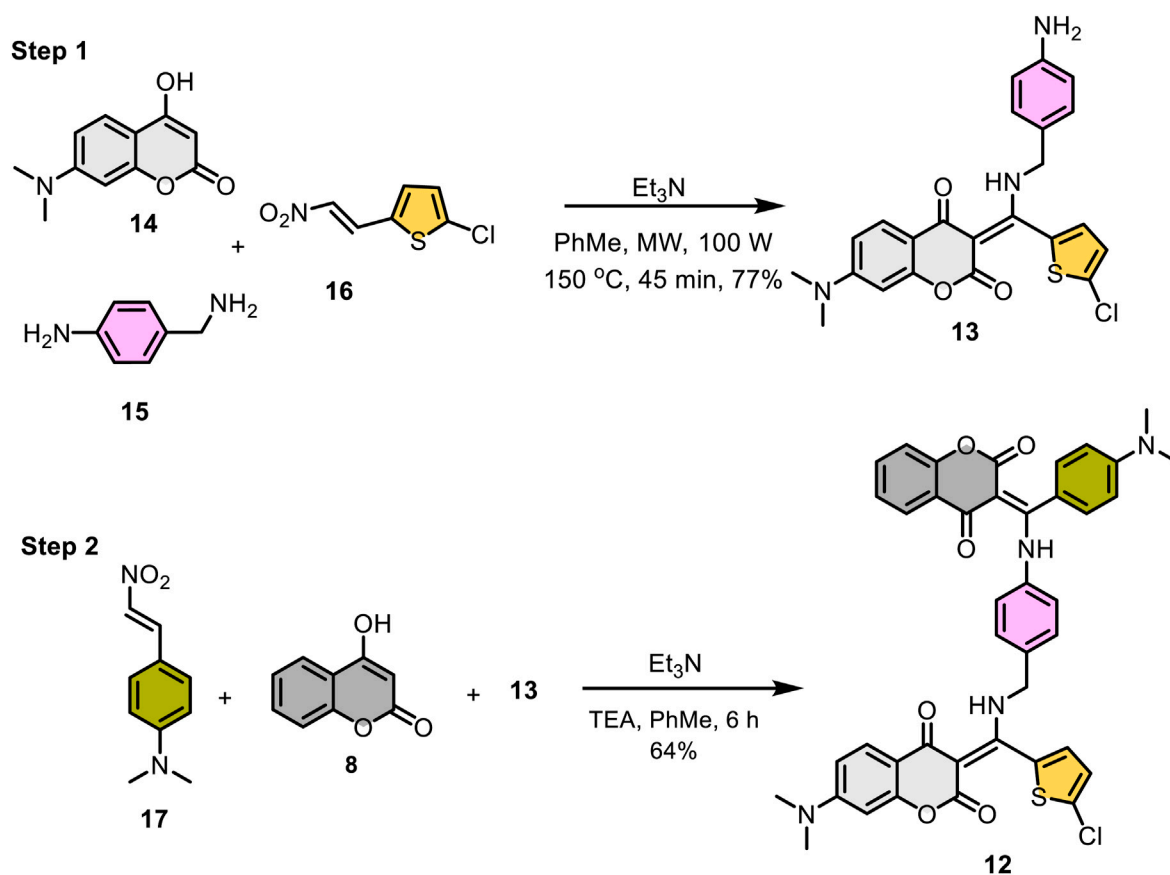
between coumarin and thiophene moieties in **7i** was found to be  $-81.82^\circ$ . After irradiation, however, it changed to  $-70.79^\circ$ . Similarly, the torsion angle between coumarin and benzylamine moieties switched from  $34.35^\circ$  to  $56.09^\circ$  after irradiation. These subtle yet significant conformational variations during blue LED irradiation suggested that the compound **7i** is indeed sensitive to visible light and is capable of undergoing reversible changes upon irradiation with suitable wavelength. Although the mechanistic details for the photochromic switch of **7i** in solution, thin film, and crystalline state remain to be investigated, compound **7i** represents one of the rare examples that exhibit opposite photochromic property under different states ([Funasako et al., 2020](#)), that is, positive photochromism in solution and thin film as well as negative photochromism in crystalline state.

As illustrated in [Figure 1](#), our previous study has demonstrated that coumarin-based *N*-aryl- $\beta$ -enamino diketone **4** exhibits piezochromic behavior ([Figure 1](#)) ([Hsieh et al., 2019](#)). We speculate that by linking this pressure-sensitive molecular scaffold ([Sagara et al., 2007; Sagara and Kato, 2009; Ma et al., 2015; Naumov et al., 2015; Wang et al., 2015; Li et al., 2021; Wei et al., 2023](#)) of **4** with the present light-sensitive moiety of **7i** into one molecule, the resulting hybrid compound may exhibit multi-stimuli responsive properties in solid state ([Zhang et al., 2011; Chiu and Yang, 2020; Vaidya et al., 2021; Martinez-Junquera et al., 2022; Wang et al., 2022](#)). [Scheme 3](#) depicts the conceptual design of the potential dual responsive *N*-aryl- $\beta$ -enamino diketone **12**. Since both piezochromic **4** and photochromic **7i** share a phenyl group on the *N*-substituent, this common phenyl group was then used to connect the two molecular scaffolds to form the hybrid **12**.

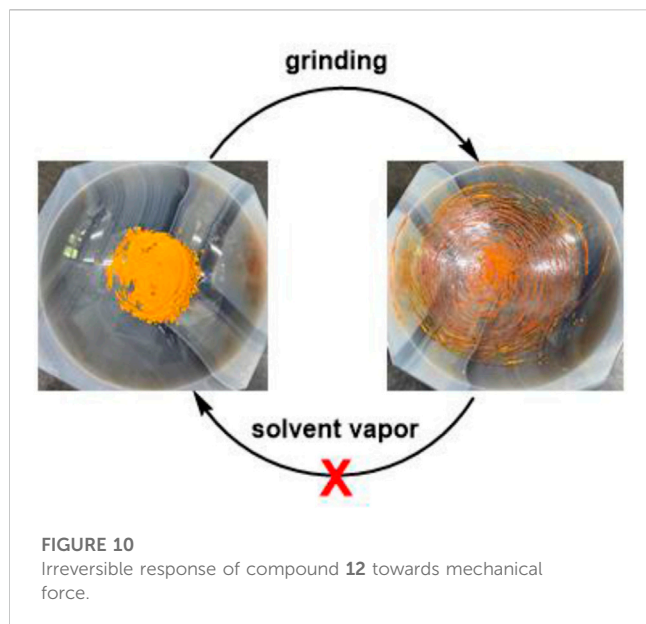
[Scheme 4](#) outlines the two-step synthesis of the target compound **12**. The photochromic unit **13** was synthesized via base-promoted, three-component reaction of 7-*N,N*-dimethylamino-4-hydroxycoumarin (**14**), 4-aminobenzylamine (**15**), and  $\beta$ -nitrostyrene **16** under microwave conditions. As expected, the less nucleophilic aniline nitrogen on 4-aminobenzylamine (**15**) did not participate in the reaction, and the desired  $\beta$ -enamino diketone **13** was isolated as an exclusive product in 77% yield. The subsequent three-component reaction of **13** with 4-hydroxycoumarin



**SCHEME 3**  
Conceptual design of the hybrid **12**.



**SCHEME 4**  
Two-step preparation of  $\beta$ -enamino diketone **12**.



(**8**) and *p*-*N,N*-dimethylamino- $\beta$ -nitrostyrene (**17**) under basic conditions yielded the hybrid  $\beta$ -enaminone **12** in 64% yield.

After realizing compound **12**, we then explored its functional properties by applying external stimuli such as mechanical force and UV irradiation to examine its potential piezochromic and photochromic responses. Upon grinding, compound **12** turned slowly from yellow to dark brown (Figure 10), indicating that the hybrid **12** remained pressure-sensitive. Nevertheless, the ground **12** failed to return to its original color when exposed to various solvent vapors such as methylene chloride, dichloroethane, acetone, chloroform, and THF, etc. This irreversible response of the hybrid **12** towards mechanical force suggests that it is not piezochromic anymore.

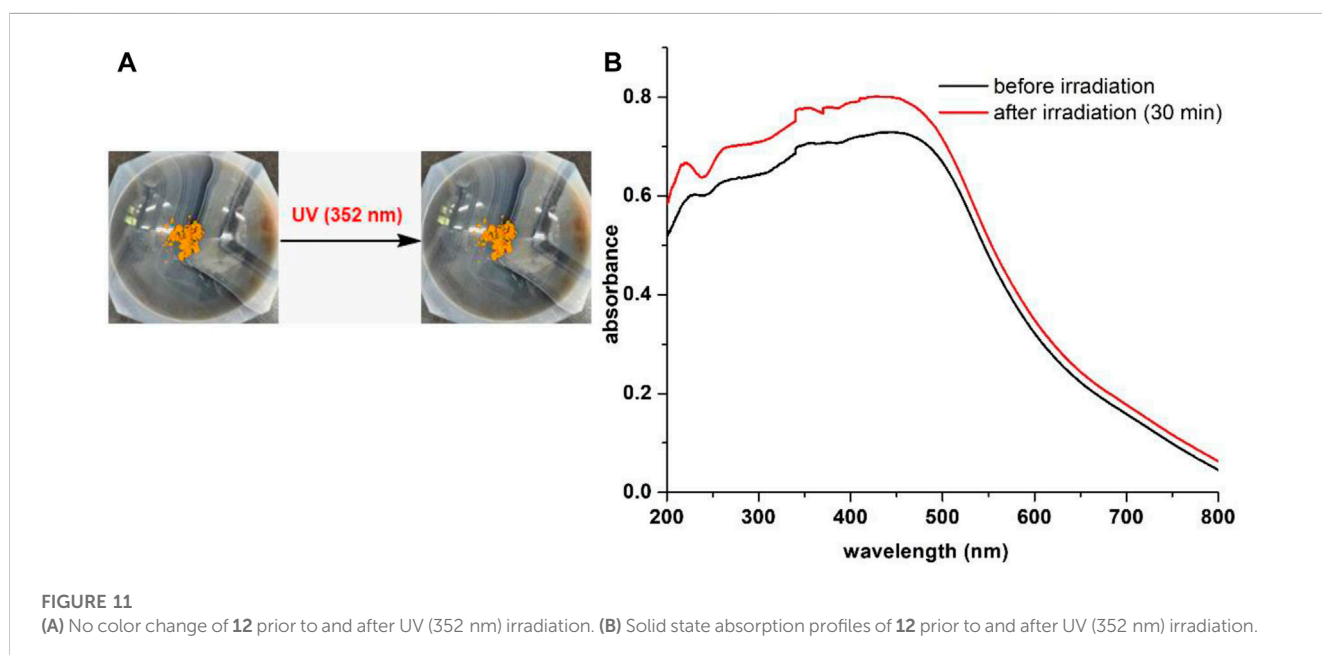
Compound **12** was also subjected to UV (352 nm) irradiation in solid state as it consisted of a light-sensitive  $\beta$ -enamino diketone

moiety. Regrettably, the hybrid **12** failed to respond to UV light in solid state. As shown in Figure 11A compound **12** did not show noticeable color change even after exposed to UV light (352 nm) for 30 min. Further, no major change was observed in the solid-state absorbance spectra of **12** prior to and after UV irradiation (Figure 11B). Our studies suggest that a multi-stimuli responsive molecule cannot be constructed simply through combination of two different chromic moieties into one, even though structures of the two chromic molecular scaffolds are closely related.

### 3 Methods and materials

#### 3.1 General information

Microwave reactions were performed using a CEM Discover unit (operating at 110 V, microwave irradiation of 2.45 GHz, maximum microwave output of 300 W) in 50 mL capacity open round-bottom flasks. Visualization was accomplished by using portable UV light and an iodine chamber. Flash chromatography was performed in columns of various diameters with Merck silica gel (230–400 mesh ASTM 9385 kieselgel 60H) by elution with the solvent systems. Solvents, unless otherwise specified, were reagent grade and distilled once before use. All new compounds exhibited satisfactory spectroscopic and analytical data.  $^1\text{H}$  NMR (400 MHz) and  $^{13}\text{C}$  NMR (100) spectra were recorded on a Bruker 400 spectrometer. Chemical shifts were reported in parts per million on the scale relative to an internal standard (tetramethylsilane, or appropriate solvent peaks) with coupling constants given in hertz.  $^1\text{H}$  NMR multiplicity data are denoted by s (singlet), d (doublet), t (triplet), q (quartet), and m (multiplet). Analytical thin-layer chromatography (TLC) was carried out on Merck silica gel 60G-254 plates (25 mm) and developed with the solvents mentioned. Melting points were





determined on a Mel-Temp melting point apparatus in open capillaries and are uncorrected. High-resolution mass spectra (HRMS) were obtained on a Thermo Fisher Scientific Finnigan MAT95XL spectrometer using a magnetic sector analyzer. Infrared (IR) spectra were recorded using 1725XFT-IR spectrophotometer. Single-crystal structures were determined with a Bruker AXS SMART-1000 X-ray single-crystal diffractometer. The absorption spectra were obtained using a UV/vis/NIR spectrophotometer (Jasco V-770) with a deuterium lamp (190–350 nm) and halogen lamp (300–2,700 nm) light sources and the detector was a photomultiplier tube.

### 3.2 Synthesis of compounds 7a–o, 12, and 13

Mixtures of appropriately substituted 4-hydroxycoumarin (1 equiv.),  $\beta$ -nitrostyrene (1.2 equiv.), substituted amine (1.2 equiv.), and a few drops of triethylamine in toluene (~20 mL) were irradiated under microwave (100 W, 150 C) for 25–30 min (unless otherwise specified). The cooled reaction mixture was concentrated and then re-dissolved in DCM. The solution was washed with water, brine, dried over  $\text{MgSO}_4$ , and evaporated *in vacuo*. The crude product was purified by column chromatography and was further recrystallized from DCM/hexanes.

## 4 Conclusion

In summary, a total of 15 structurally diverse  $\beta$ -enamino diketone derivatives were synthesized in good to excellent yields via microwave-assisted, base-mediated, three-component reaction between 4-hydroxycoumarins, substituted  $\beta$ -nitrostyrene, and primary amines. Among prepared compounds, compound **7i** was found to exhibit positive photochromism in solution/thin film and negative photochromism in crystalline state. Further, compound **12** bearing pressure- and light-sensitive molecular scaffolds was designed and synthesized in two steps as a potential dual-responsive material. Unfortunately, the prepared **12** failed to show any expected functional behavior. The in-depth investigation of the photochromic mechanism of this intriguing thiophene-derived  $\beta$ -enamino diketone **7i** at the molecular level is currently underway and will be reported in due course.

## Data availability statement

The datasets presented in this study can be found in online repositories. The names of the repository/repositories and accession number(s) can be found in the article/**Supplementary Material**.

## References

- Avadanei, M., Cozan, V., Shova, S., and Paixão, J. A. (2014). Solid state photochromism and thermochromism of two related N-salicylidene anilines. *Chem. Phys.* 444, 43–51. doi:10.1016/j.chemphys.2014.10.007
- Budzisz, E., Keppler, B. K., Giester, G., Wozniczka, M., Kufelnicki, A., and Nawrot, B. (2004). Synthesis, crystal structure and biological characterization of a novel

## Author contributions

KBM: Conceptualization, Data curation, Formal Analysis, Funding acquisition, Investigation, Methodology, Supervision, Visualization, Writing–original draft, Writing–review and editing. S-CF: Formal Analysis, Investigation, Methodology, Writing–original draft, DYY: Conceptualization, Funding acquisition, Project administration, Resources, Supervision, Writing–original draft, Writing–review and editing.

## Funding

The author(s) declare financial support was received for the research, authorship, and/or publication of this article. National Science and Technology Council of Taiwan Contract No. NSTC 109-2113-M-029-010-MY3 (DYY) and 108-2113-M-029-004 (KBM).

## Acknowledgments

We thank the National Science and Technology Council of Taiwan for financially supporting this research. Also, the support for the X-ray, mass spectroscopy, and NMR measurements from the Instrument Center of National Chung Hsing University (NCHU) is greatly acknowledged.

## Conflict of interest

The authors declare that the research was conducted in the absence of any commercial or financial relationships that could be construed as a potential conflict of interest.

## Publisher's note

All claims expressed in this article are solely those of the authors and do not necessarily represent those of their affiliated organizations, or those of the publisher, the editors and the reviewers. Any product that may be evaluated in this article, or claim that may be made by its manufacturer, is not guaranteed or endorsed by the publisher.

## Supplementary material

The Supplementary Material for this article can be found online at: <https://www.frontiersin.org/articles/10.3389/fchem.2023.1295347/full#supplementary-material>

palladium(II) complex with a coumarin-derived ligand. *Eur. J. Inorg. Chem.* 22, 4412–4419. doi:10.1002/ejic.200400483

CCDC No (2023). *Crystallographic data (excluding structure factors) for 7b, 7g, 7i (prior Blue LED irradiation), 7i (after blue LED irradiation), and 7m* have been deposited with the Cambridge Crystallographic Data Centre as supplementary

publication number CCDC-1540618, -1540615, -1540617, 2300435 and -1540616, respectively. These data can be obtained free of charge via [www.ccdc.cam.ac.uk/data\\_request/cif](http://www.ccdc.cam.ac.uk/data_request/cif), by emailing [data\\_request@ccdc.cam.ac.uk](mailto:data_request@ccdc.cam.ac.uk), or by contacting The Cambridge Crystallographic Data Centre, 12 Union Road, Cambridge CB2 1EZ, UK; fax: +44 1223 336033.

Chithanna, S., and Yang, D. Y. (2019). Multicomponent synthesis of 1,3-diketone-linked *N*-substituted pyrroles, pyrrolo[1,2-*a*]pyrazines, pyrrolo[1,4]diazepines, and pyrrolo[1,4]diazocines. *J. Org. Chem.* 84, 1339–1347. doi:10.1021/acs.joc.8b02819

Chithanna, S., Vyasamudri, S., and Yang, D. Y. (2020). Application of dimedone enamines as protecting groups for amines and peptides. *Org. Lett.* 22, 2391–2395. doi:10.1021/acs.orglett.0c00586

Chiu, C.-W., and Yang, J.-S. (2020). Photoluminescent and photoresponsive iptycene-incorporated  $\pi$ -conjugated systems: fundamentals and applications. *ChemPhotoChem* 4, 538–563. doi:10.1002/cptc.201900300

Ferraz, H. M. C., de Oliveira, E. O., Payret-Arrua, M. E., and Brandt, C. A. (1995). A new and efficient approach to cyclic  $\beta$ -Enamino esters and  $\beta$ -Enamino ketones by iodine-promoted cyclization. *J. Org. Chem.* 60, 7357–7359. doi:10.1021/jo00127a051

Funasako, Y., Ason, M., Takebayashi, J., and Inokuchi, M. (2019). Solid-state photochromism of salts of cationic spiropyran with various anions: a correlation between reaction cavity volumes and reactivity. *Cryst. Growth Des.* 19, 7308–7314. doi:10.1021/acs.cgd.9b01185

Funasako, Y., Miyazaki, H., Sasaki, T., Goshima, K., and Inokuchi, M. (2020). Synthesis, photochromic properties, and crystal structures of salts containing a pyridinium-fused spiropyran: positive and negative photochromism in the solution and solid state. *J. Phys. Chem. B* 124, 7251–7257. doi:10.1021/acs.jpcc.0c04994

Ghabraie, E., Bararjanian, M., Balalaie, S., Rominger, F., and Bijanzadeh, H. R. (2011). Efficient synthesis of (3*e*)-3-[amino(aryl)methylidene]chromane-2,4-diones (=3*E*)-3-[Amino(aryl)methylene]-2*H*-1-benzopyran-2,4(3*H*)-diones) via a three-component reaction. *Helv. Chim. Acta* 94, 1440–1447. doi:10.1002/hlca.201100001

Helmy, S., Oh, S., Leibfarth, F. A., Hawker, C. J., and Read de Alaniz, J. (2014). Design and synthesis of donor–acceptor stenhouse adducts: a visible light photoswitch derived from furfural. *J. Org. Chem.* 79, 11316–11329. doi:10.1021/jo502206g

Hsieh, W. C., Manjappa, K. B., and Yang, D. Y. (2019). Structural tuning enables piezochromic and photochemical properties in *N*-aryl- $\beta$ -enaminones. *RSC Adv.* 9, 34088–34094. doi:10.1039/C9RA07598D

Irie, M., Fukaminato, T., Matsuda, K., and Kobatake, S. (2014). Photochromism of diarylethene molecules and crystals: memories, switches, and actuators. *Chem. Rev.* 114, 12174–12277. doi:10.1021/cr500249p

Kuo, P. Y., Chuang, R. R., and Yang, D. Y. (2009). Reactions of 3-benzoyl-7-dimethylamino-4-hydroxycoumarin and their potential applications in solution- and solid-phase synthesis. *Mol. Divers.* 13, 253–260. doi:10.1007/s11030-009-9107-2

Li, G., Watson, K., Buckheit, R. W., Zhang, Y., and Zhang, Y. (2007). Total synthesis of anibamine, a novel natural product as a chemokine receptor CCR5 antagonist. *Org. Lett.* 9, 2043–2046. doi:10.1021/ol070748n

Li, A., Xu, S., Bi, C., Geng, Y., Cuib, H., and Xu, W. (2021). Piezochromic mechanism of organic crystals under hydrostatic pressure. *Mater. Chem. Front.* 5, 2588–2606. doi:10.1039/D0QM00975J

Loan, T., Santra, M., and Bradley, M. (2023). Novel class of photochromic molecules exhibiting photo-switching in the solid state. *Front. Chem.* 11, 1205452. doi:10.3389/fchem.2023.1205452

Ma, Z., Wang, Z., Teng, M., Xu, Z., and Jia, M. (2015). Mechanically induced multicolor change of luminescent materials. *ChemPhysChem* 16, 1811–1828. doi:10.1002/cphc.201500181

Manjappa, K. B., Yang, Y.-A., Santhosh, M. S., and Yang, D. Y. (2018). Nitroalkane-mediated multicomponent synthesis of  $\beta$ -enaminones. *ChemistrySelect* 3, 10701–10705. doi:10.1002/slct.201802742

Martinez-Junquera, M., Lalinde, E., and Moreno, M. T. (2022). Multistimuli-responsive properties of aggregated isocyanide cycloplatinated(II) complexes. *Inorg. Chem.* 61, 10898–10914. doi:10.1021/acs.inorgchem.2c01400

Michael, J. P., Koning, C. B., Hosken, G. D., and Stanbury, T. V. (2001). Reformatsky reactions with *N*-arylpiperidine-2-thiones: synthesis of tricyclic analogues of quinolone antibacterial agents. *Tetrahedron* 57, 9635–9648. doi:10.1016/S0040-4020(01)00964-4

Mladenovic, M., Vukovic, N., Niciforovic, N., Sukdolak, S., and Solujic, S. (2009). Synthesis and molecular descriptor characterization of novel 4-Hydroxy-chromene-2-one derivatives as antimicrobial agents. *Molecules* 14, 1495–1512. doi:10.3390/molecules14041495

Naumov, P., Chizhik, S., Panda, M. K., Nath, N. K., and Boldyreva, E. (2015). Mechanically responsive molecular crystals. *Chem. Rev.* 115, 12440–12490. doi:10.1021/acs.chemrev.5b00398

Sagara, Y., and Kato, T. (2009). Mechanically induced luminescence changes in molecular assemblies. *Nat. Chem.* 1, 605–610. doi:10.1038/nchem.411

Sagara, Y., Mutai, T., Yoshikawa, I., and Araki, K. (2007). Material design for piezochromic luminescence: hydrogen-bond-directed assemblies of a pyrene derivative. *J. Am. Chem. Soc.* 129, 1520–1521. doi:10.1021/ja0677362

Sun, F., Xiong, X., Gao, A., Duan, Y., Mao, L., Gu, L., et al. (2022). Fast photochromism in solid: microenvironment in metal-organic frameworks promotes the isomerization of donor-acceptor Stenhouse adducts. *J. Chem. Eng.* 427, 132037. doi:10.1016/j.ccej.2021.132037

Vaidya, S., Sharma, M., Bruckner, C., and Kasi, R. M. (2021). Rhodamine-installed polynorbornenes: molecular design, structure, and stimuli-responsive properties. *ACS Omega* 6, 15017–15028. doi:10.1021/acsomega.1c01160

Valduga, C. J., Braibante, H. S., and Braibante, M. E. F. (1998). Reactivity of *p*-phenyl substituted  $\beta$ -enamino compounds using k-10/ultrasound. I. synthesis of pyrazoles and pyrazolinones. *J. Heterocycl. Chem.* 35, 189–192. doi:10.1002/jhet.5570350136

Vukovic, N., Sukdolak, S., Solujic, S., and Niciforovic, N. (2010). Substituted imino and amino derivatives of 4-hydroxycoumarins as novel antioxidant, antibacterial and antifungal agents: synthesis and *in vitro* assessments. *Food Chem.* 120, 1011–1018. doi:10.1016/j.foodchem.2009.11.040

Wang, Y., Tan, X., Zhang, Y.-M., Zhu, S., Zhang, I., Yu, B., et al. (2015). Dynamic behavior of molecular switches in crystal under pressure and its reflection on tactile sensing. *J. Am. Chem. Soc.* 137, 931–939. doi:10.1021/ja511499p

Wang, J., Zhang, M., Han, S., Zhu, L., and Jia, X. (2022). Multiple-stimuli-responsive multicolor luminescent self-healing hydrogel and application in information encryption and bioinspired camouflage. *Journal of Materials Chemistry* 10, 15565–15572. doi:10.1039/D2TC03072A

Wei, Y., Yang, R., Cui, G., Dai, S., Pan, G., Wang, J., et al. (2023). Low-pressure sensitive piezochromic fluorescence switching of tetraphenylethylene-anthraquinone. *Chem. Eur. J.* 29, e202301070. doi:10.1002/chem.202301070

White, J. D., and Lhle, D. C. (2006). Tandem Photocycloaddition–Retro-mannich fragmentation of enaminones. A route to spiropyrrolines and the tetracyclic core of koumine. *Org. Lett.* 8, 1081–1084. doi:10.1021/ol052955y

Ye, W. J., Li, Y., Zhou, L. X., Liu, J. J., and Wang, C. D. (2015). Three-component reaction between substituted  $\beta$ -nitrostyrenes,  $\beta$ -dicarbonyl compounds and amines: diversity-oriented synthesis of novel  $\beta$ -enaminones. *Green Chem.* 17, 188–192. doi:10.1039/C4GC01234H

Zhang, Z., Yao, D., Zhou, T., Zhang, H., and Wang, Y. (2011). Reversible piezo- and photochromic behaviors accompanied by emission color switching of two anthracene-containing organic molecules. *Chem. Commun.* 47, 7782–7784. doi:10.1039/C1CC11882J

Zhang, L., Deng, Y., Tang, Y., Xie, C., and Wu, Z. (2021). Solid-state spiropyrans exhibiting photochromic properties based on molecular flexibility. *Mater. Chem. Front.* 5, 3119–3124. doi:10.1039/D0QM01086C



## OPEN ACCESS

## EDITED BY

Bing Yu,  
Zhengzhou University, China

## REVIEWED BY

Ge Wu,  
Wenzhou Medical University, China  
Kai Sun,  
Zhengzhou University, China

## \*CORRESPONDENCE

Xingmei Liu,  
✉ 13844973027@163.com

<sup>†</sup>These authors have contributed equally to this work

RECEIVED 26 October 2023

ACCEPTED 02 November 2023

PUBLISHED 22 January 2024

## CITATION

Ouyang B, Chai X, Li Z, Zhang C and Liu X (2024), Aminothiolation of alkenes with azoles and Bunte salts.  
*Front. Chem.* 11:1328441.  
doi: 10.3389/fchem.2023.1328441

## COPYRIGHT

© 2024 Ouyang, Chai, Li, Zhang and Liu. This is an open-access article distributed under the terms of the [Creative Commons Attribution License \(CC BY\)](#). The use, distribution or reproduction in other forums is permitted, provided the original author(s) and the copyright owner(s) are credited and that the original publication in this journal is cited, in accordance with accepted academic practice. No use, distribution or reproduction is permitted which does not comply with these terms.

# Aminothiolation of alkenes with azoles and Bunte salts

Bingqing Ouyang<sup>1†</sup>, Xing Chai<sup>2†</sup>, Zhe Li<sup>1</sup>, Chunling Zhang<sup>1</sup> and Xingmei Liu<sup>1\*</sup>

<sup>1</sup>Department of Pharmacy, The Second Norman Bethune Hospital of Jilin University, Changchun, China,

<sup>2</sup>Outpatient Department, The Second Norman Bethune Hospital of Jilin University, Changchun, China

We have developed an intermolecular aminothiolation of simple olefins using Bunte salt as a thiolating agent. This protocol produces thiyl free radicals under PIDA oxidation conditions, eliminating the need for transition-metal catalysts. The method has a wide range of substrate applicability and is suitable for large-scale preparation and late-stage modification of drug molecules.

## KEYWORDS

aminothiolation, Bunte salts, alkenes, metal-free, multi-component cascade reactions

## Introduction

The simultaneous introduction of sulfur and nitrogen moieties into small molecules is a classical approach for designing new drugs.  $\beta$ -Amino sulfide is an important and widely present scaffold in natural products, best-selling drugs, and small molecular catalysts (Scheme 1A) (Cecchetti et al., 2003; Hosseini-Zare et al., 2011). For a long time, synthetic chemists have devoted considerable effort to develop novel and efficient strategies for the preparation of these significant frameworks (De Paolis et al., 2002; Jiang et al., 2016; Cui et al., 2019). Olefin is a readily available industrial raw material. Direct aminothiolation of olefin, achieved by selecting suitable amination and thiolation reagents, is one of the simplest and most effective strategies for constructing  $\beta$ -amino sulfide compounds (Scheme 1B). This method offers the advantages of high economic feasibility and simplicity of steps. Traditionally, the Ritter-type aminothiolation of alkenes utilizes diaryl disulfides and aryl thiols as thiolation reagents. These reactions are typically carried out in acetonitrile as the solvent, with nucleophile properties, and require stoichiometric amounts of transition-metal or strong acid conditions (Luo et al., 2015; Cui et al., 2016). These reactions proceed first undergo the formation of thiiranium ion intermediates, followed by a subsequent ring-opening reaction with acetonitrile. Soon afterward, Prof. Sun accomplished a breakthrough in  $I_2$ -promoted aminothiolation of alkenes using azoles as nucleophiles (Sun et al., 2017). Recently, *N*-phenyl-sulfonyl phthalimide and ArSCl have also been employed as electrophilic thiolation reagents in the aminothiolation of alkenes [9,10]. Given the significance of  $\beta$ -amino sulfides derivatives, the groups of Zhu and Nishihara demonstrated a copper-catalyzed radical thioamidation of alkenes with NFSI and thiols (Li et al., 2017; Iwasaki et al., 2019). In 2018, Prof. Lei described an electrochemical oxidative aminosulfenylation of alkenes (Yuan et al., 2018). Very recently, Deng's group disclosed that NIS could be used as both a radical initiator and an N-nucleophile, enabling a metal-free amidosulfenylation of alkenes with disulfides (Yao et al., 2023). However, there are common problems associated with these methods. They often require more expensive and toxic transition-metal catalysts. Moreover, they necessitate a large excess amount of Lewis acids, which often leads to the presence of expensive heavy metal residues. Additionally, these methods require complex post-treatment processes and can result in environmental

pollution. At the same time, trace metal ions have a tendency to coordinate with  $\beta$ -amino sulfide compounds, which can affect the purity of the target product. This often necessitates additional filtration steps to remove the metal ions, resulting in reduced economic efficiency and hindering their potential application in the pharmaceutical industry. Therefore, the development of an environmentally friendly and practical protocol for the multi-component aminothioloation of alkenes without the use of catalysts is still a desirable and challenging task.

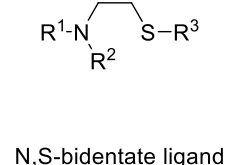
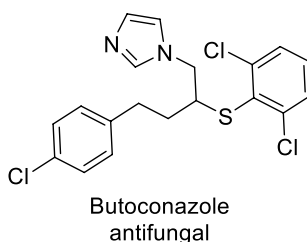
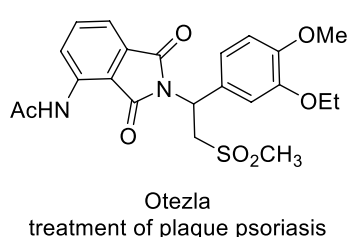
In recent years, Bunte salts have emerged as alternative reagents for thiolation in the formation of new C-S bonds. They have gained popularity due to their ease of preparation and handling. Traditionally, it is frequently used in transition-metal catalyzed cross-coupling reactions (Qiao et al., 2015; Liu and Yi, 2018; Wang et al., 2023; Wu et al., 2023). However, these methods require a toxic transition-metal catalyst, which not only limits the range of substrates but also generates a significant amount of environmentally unfriendly by-products. Herein, we describe an environmentally friendly and practical method for aminothioloation of alkenes using Bunte salts and azoles under metal-free reaction conditions (Scheme 1C). As

per our design, Bunte salts would generate thiyl radicals through a single-electron oxidation. Then, the resultant thiyl radical undergoes region-selective addition with alkenes to produce the alkyl radical intermediate, which is captured by azoles to give the corresponding  $\beta$ -amino sulfides. Therefore, through this radical addition/radical capture process, the use of transition-metal could be completely avoided.

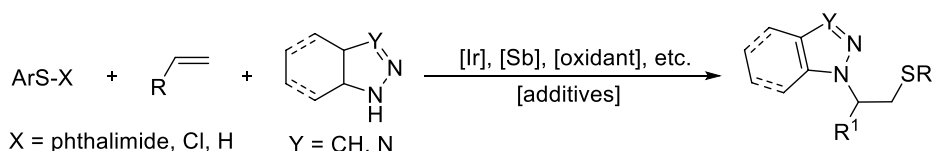
## Results and discussion

Initially, we prepared a 100 mmol scale of  $\text{CH}_3\text{SSO}_3\text{Na}$  through nucleophilic substitution of iodomethane with sodium thiosulfate. We selected styrene (**1a**), benzotriazole (**2a**) and  $\text{CH}_3\text{SSO}_3\text{Na}$  (**3a**) as model substrates to verify the optimal reaction conditions (Table 1). Owing to their high efficiency, broad spectrum, and inward-absorbent properties, benzotriazole compounds are used to prevent epiphyte growth. Therefore, it is particularly important to develop green and efficient methods for constructing benzotriazole derivatives and functionalizing their core skeletons. According to previous literature research, various copper catalysts were preferentially selected. As a result, the desired

### A Important $\beta$ -amino sulfide scaffolds

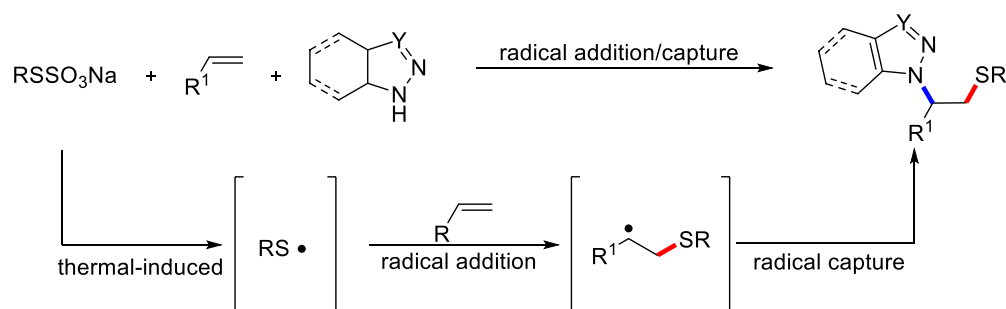


### B Previous works:



● limited to aryl sulfides    ● using stoichiometric amount of oxidant and additive    ● produce a lot of waste

### C Our work: Bunte salt as thiyl radical precursor

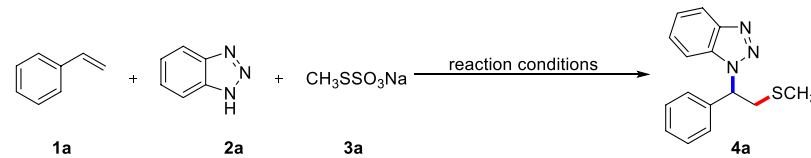


● no transition-metal and additives    ● gram-scale reaction    ● late-stage modification of bioactive molecules

SCHEME 1  
Aminothioloation of alkenes.



TABLE 1 Reaction optimization<sup>a</sup>.

				
Entry	Oxidant	Solvent	Temp (°C)	Yield (%) <sup>b</sup>
1	TBHP	CH <sub>3</sub> CN	80	0
2	K <sub>2</sub> S <sub>2</sub> O <sub>8</sub>	CH <sub>3</sub> CN	80	0
3	DTBP	CH <sub>3</sub> CN	80	0
4	CuBr <sub>2</sub>	CH <sub>3</sub> CN	80	12
5	PIDA	CH <sub>3</sub> CN	80	81
6	NIS	CH <sub>3</sub> CN	80	29
7	PIDA	toluene	80	0
8	PIDA	DCE	80	0
9	PIDA	DMF	80	trace
10	PIDA	THF	80	trace
11	PIDA	MeOH	80	0
12 <sup>c</sup>	PIDA	CH <sub>3</sub> CN	80	43
13 <sup>d</sup>	PIDA	CH <sub>3</sub> CN	70	77
14 <sup>e</sup>	PIDA	CH <sub>3</sub> CN	90	72

<sup>a</sup>Reaction conditions: **1a** (0.2 mmol), **2a** (0.4 mmol), **3a** (0.4 mmol), oxidant (0.4 mmol), solvent (2.0 mL) under O<sub>2</sub>, heated at 80 °C for 24 h.

<sup>b</sup>Isolated yield.

<sup>c</sup>Under N<sub>2</sub> atmosphere.

<sup>d</sup>At 90 °C.

<sup>e</sup>At 70 °C.

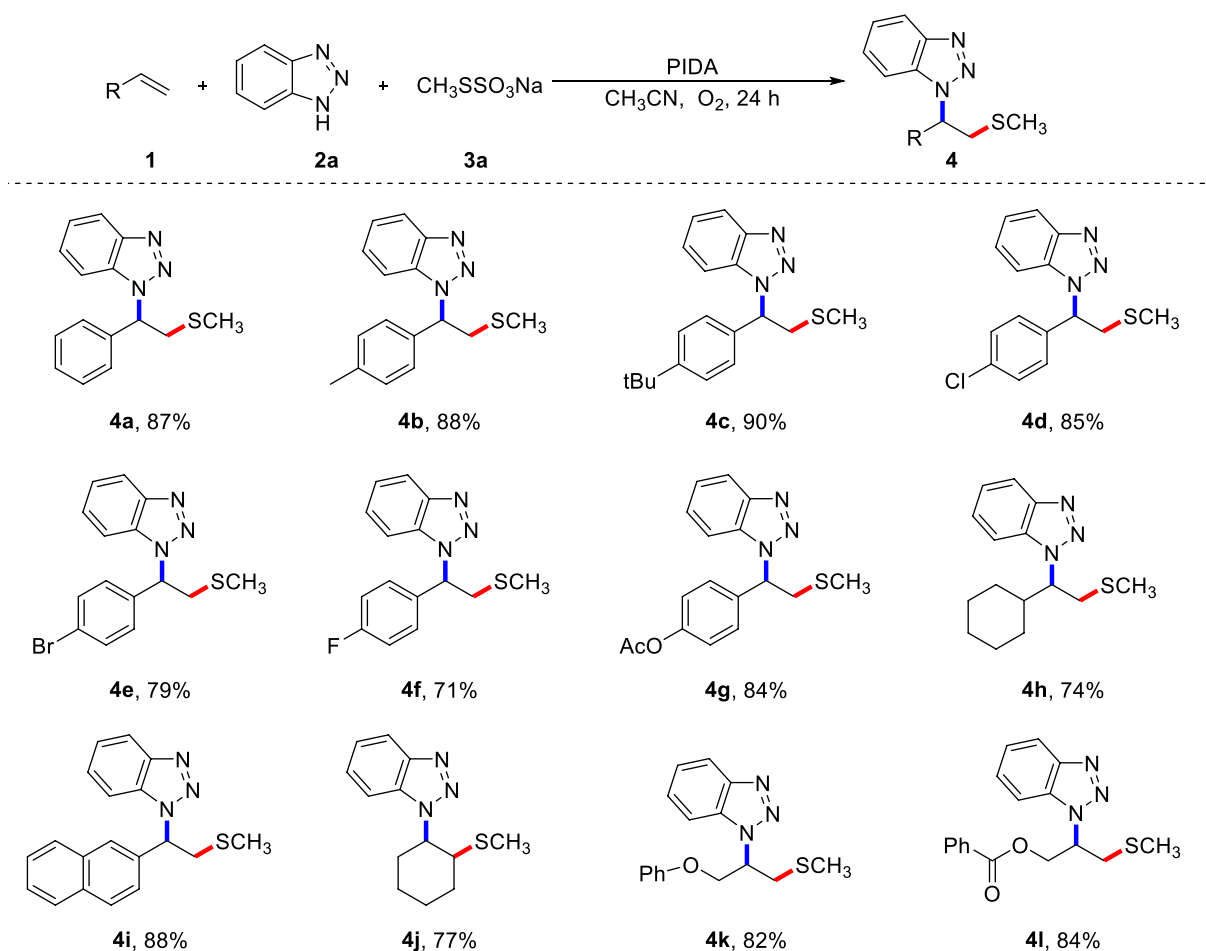
reaction proceeded smoothly, yielding **4a** in 12% yield (entry 4). Inspired by this result, the influences of different oxidants were further examined (entries 1–6). TBHP, K<sub>2</sub>S<sub>2</sub>O<sub>8</sub>, DTBP were not efficient oxidants and could not provide the target product. To our delight, the yield of **4a** increased to 81% using PIDA as an oxidant and CH<sub>3</sub>CN as a solvent at 80 °C under an O<sub>2</sub> atmosphere for 24 h.

Next, we screened different reaction solvents and found that CH<sub>3</sub>CN was the best choice for this transformation. No more satisfactory results were obtained when the reaction was performed with other polar, non-polar, and weak coordination solvents (entries 7–11). It is worth mentioning that the reaction can be carried out in a nitrogen atmosphere, but the yield is reduced (entry 12). Both increasing and decreasing the reaction temperature affect the conversion of the starting material and the yield of the corresponding product (entries 13, 14). Importantly, the hydroamination of alkene with azole is not observed during the process of optimizing reaction conditions.

Next, we examined the generality of this three-component cascade reaction with various alkenes using the optimal reaction conditions (Scheme 2). Methylthio is an essential functional group found in numerous anti-tumor active molecules, candidate drug molecules, and natural products. Therefore, the rapid introduction of methylthio functional groups into small organic molecules is

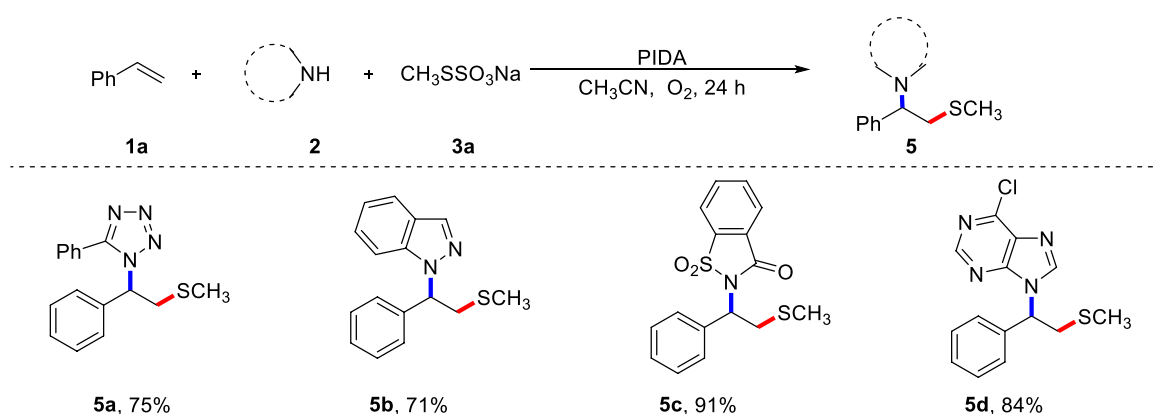
significant for the development and discovery of sulfide drugs. Generally speaking, styrenes bearing both electron-donating and electron-withdrawing functional groups had little impact on the conversion outcome and all resulted in the corresponding products with high yields. Besides the good compatibility of aryl alkenes, alkyl alkenes, such as cyclohexene, also worked well in this transformation (**4h**). 2-Vinylnaphthalene was subjected to a multi-component cascade reaction, and the target product (**4i**) was isolated with an 88% yield. Further tests showed that an internal alkene, such as cyclohexene (**4j**) was a feasible substrate, highlighting the broad applicability of the current strategy. Chained unactivated alkenes, such as allyl phenyl ether and allyl benzoate, were suitable substrates, all producing the desired products (**4k**, **4l**) in high yields.

To further investigate the synthetic application of the current protocol, various azaheterocycles were evaluated, and the results are shown in Scheme 3. Due to their prominent bioelectronic isosteric nature, tetrazoles are particularly significant in the development of pharmaceutical candidates. Therefore, it is important to further investigate this multi-component reaction strategy to diversify and functionalize tetrazoles. To our delight, 5-phenyltetrazole proved to be a feasible azolating reagent, resulting in the desired product **5a**. Importantly, 1H-indazole was effective in the current reaction system and gave the good result (**5b**). Saccharin was also compatible with this



SCHEME 2

Scope of alkenes (A). (A) Reaction conditions: **1** (0.2 mmol), **2** (0.4 mmol), **3a** (0.4 mmol), PIDA (0.4 mmol), CH<sub>3</sub>CN (2.0 mL) under O<sub>2</sub>, heated at 80 °C for 24 h, isolated yield.

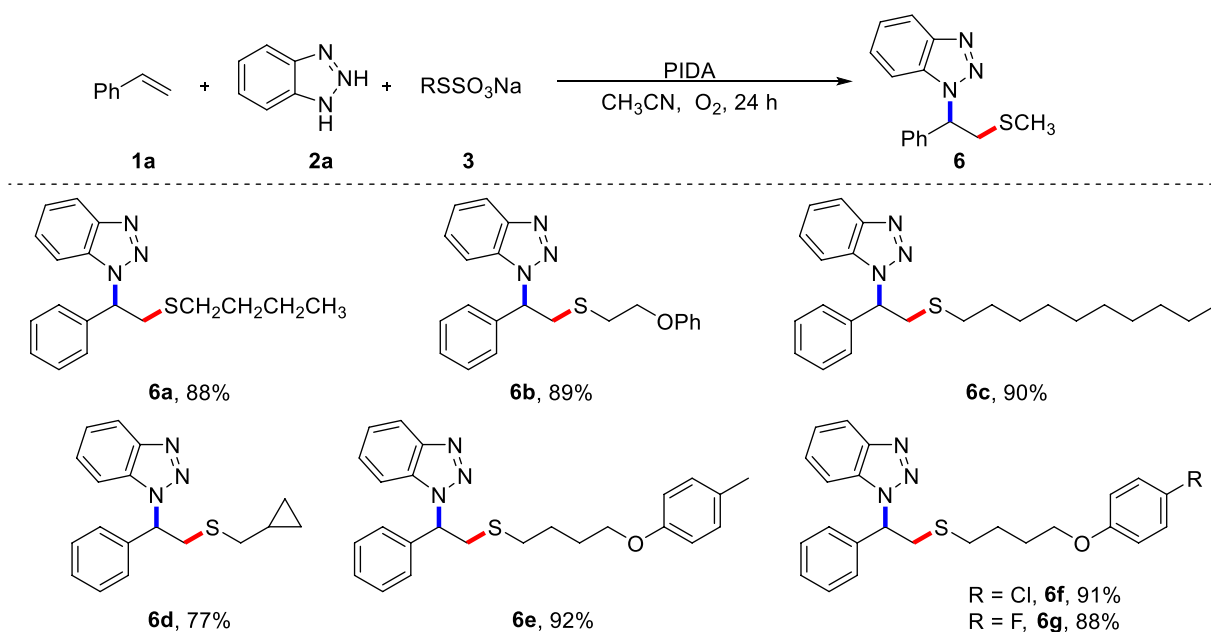


SCHEME 3

Scope of nitrogen nucleophiles (A). (A) Reaction conditions: **1a** (0.2 mmol), **2** (0.4 mmol), **3a** (0.4 mmol), PIDA (0.4 mmol), CH<sub>3</sub>CN (2.0 mL) under O<sub>2</sub>, heated at 80 °C for 24 h, isolated yield.

procedure, resulting in the anticipated product **5c** in excellent yield. 6-Chloropurine could also be tolerated, providing a concise pathway for  $\beta$ -thiomethylated N-alkyl purine **5d**.

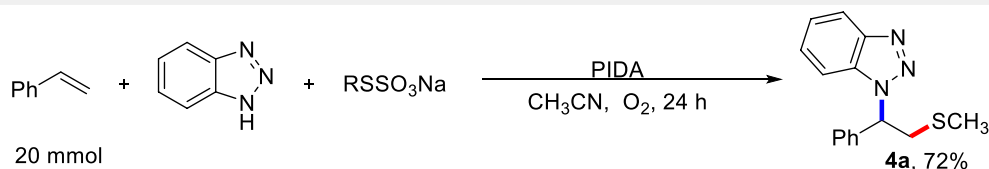
To demonstrate the potential application of this protocol, we prepared and examined various alkyl Bunte salts as thiolation reagents in the metal-free aminothiolation of alkenes (Scheme 4).



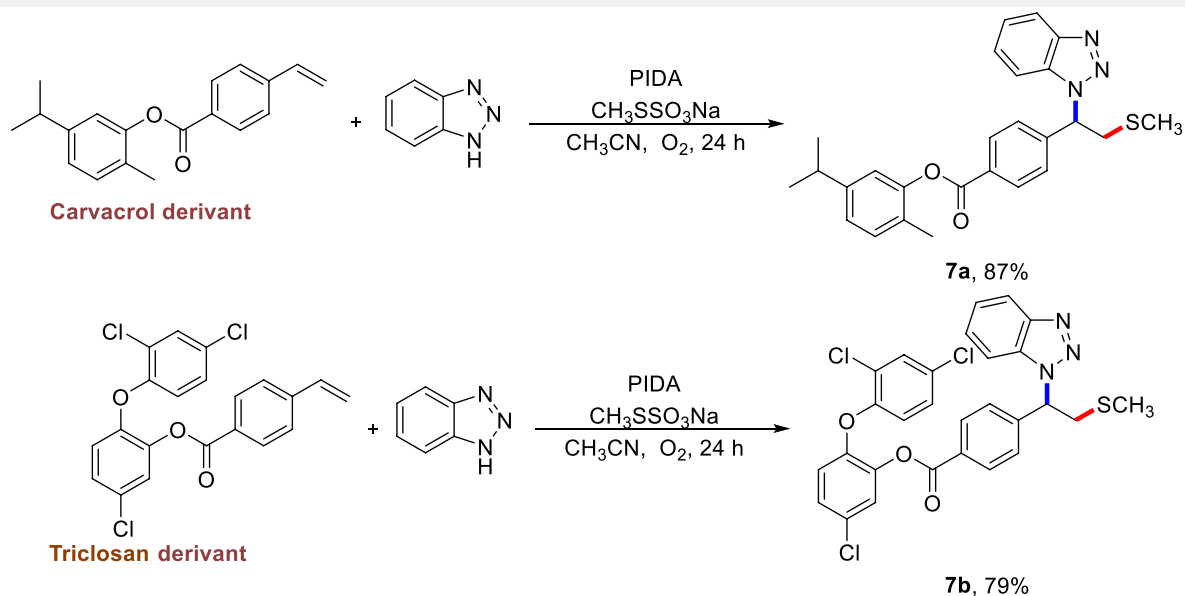
SCHEME 4

Scope of Bunte salts (A). (A) Reaction conditions: **1a** (0.2 mmol), **2a** (0.4 mmol), **3** (0.4 mmol), PIDA (0.4 mmol), CH<sub>3</sub>CN (2.0 mL) under O<sub>2</sub>, heated at 80 °C for 24 h, isolated yield.

### A Gram-scale reaction



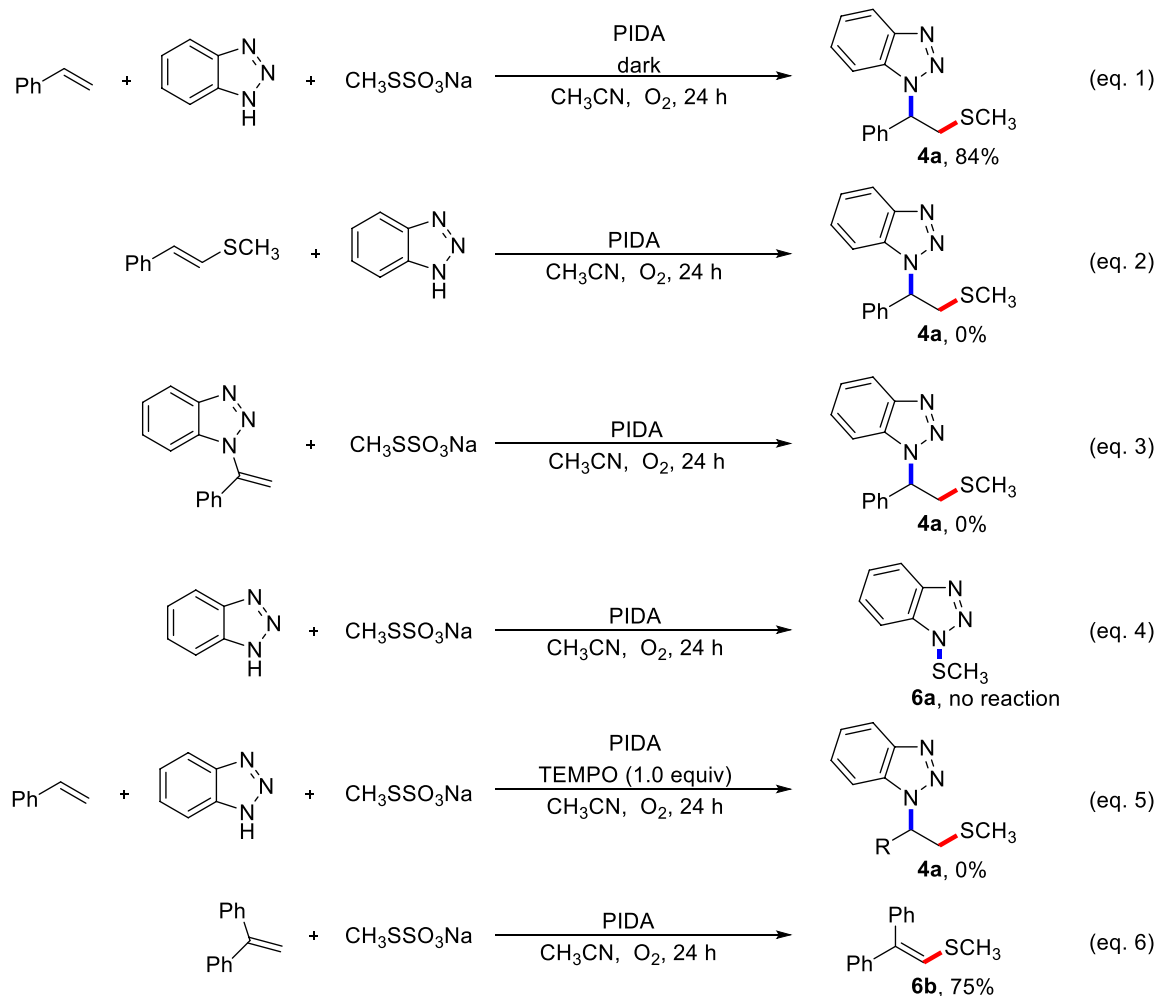
### B Late-stage derivatization of pharmaceuticals



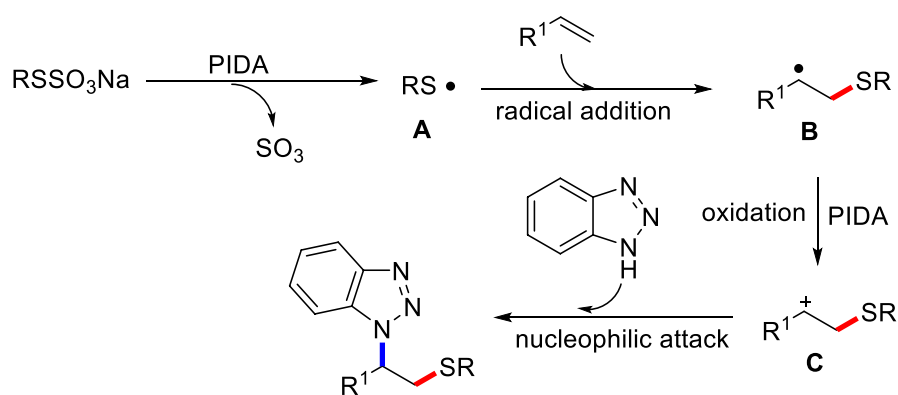
SCHEME 5

Synthetic application.

## Mechanistic experiments:



SCHEME 6  
Mechanistic experiments.



SCHEME 7  
Proposed mechanism.



Significant functional groups, such as alkyl (**6a**, **6c**), ether (**6b**), cyclopropyl (**6d**), methyl (**6e**), and halogen (**6f**, **6g**) were well accommodated, providing a good platform for additional diversification through classical synthetic transformations. Importantly, butanethiol and dimethyl disulfide did not participate in this transformation, which indicates the powerful reactivity of alkyl Bunte salts. It should be emphasized that, in contrast to the use of smelly and unstable dialkyl disulfides for the construction of alkyl sulfides, Bunte salts are odorless reagents that are bench-stable and easy to prepare. This is beneficial for diverse synthesis.

To further demonstrate the potential applicability of this protocol, a scale-up preparation of **4a** and late-stage functionalization of complex compounds were conducted. As shown in Scheme 5A, there was no discernible effect on the 20 mmol-scale reaction, and compound **4a** was still isolated in a 72% yield. Complex alkene molecules could undergo a smooth aminothiolation reaction under standard reaction conditions (Scheme 5B). Remarkably, pharmaceutical derivatives such as carvacrol and triclosan were found to be accommodating and provided the anticipated products (**7a**, **7b**) in excellent yields. This result demonstrates the powerful compatibility of this metal-free reaction system and its potential for use in modifying the structure of various bioactive molecules.

Several carefully designed control experiments were performed to gain a detailed insight into the reaction mechanism (Scheme 6). First, the light shielding experiment showed that the current multi-component cascade reaction only requires the thermodynamic excitation process (entry 1). Next, to verify the possible competent intermediate in the current three-component reaction, we prepared the vinylmethyl sulfide and *N*-vinyl benzotriazole, whether the reaction between vinylmethyl sulfide and benzotriazole or the reaction between *N*-vinyl benzotriazole with CH<sub>3</sub>SSO<sub>3</sub>Na, the desired product **4a** was not observed (entries 2, 3). Subsequently, the treatment of benzotriazole with CH<sub>3</sub>SSO<sub>3</sub>Na did not provide the *N*-SCH<sub>3</sub> benzotriazole (entry 4). These experimental results suggest that the Michael addition and electrophilic aminothiolation of alkenes with sulfenamides were not involved in current aminothiolation process. Finally, the possible radical mechanism of the reaction was studied. When 1.0 equivalent of TEMPO was added to the reaction system, the reaction was completely suppressed (entry 5). Whereas 1,1-diphenylethylene was used as a free radical trapping agent, the product of methyl thiogroup addition was successfully captured (entry 6).

Based on the aforementioned experiments and related literature reports, we proposed a possible mechanism for this aminothiolation of alkenes process in Scheme 7. Firstly, Bunte salt is activated to discharge sulfur trioxide gas to produce alkyl sulfur radical in the presence of PIDA (Prabhakar et al., 2022). Then, electrophilic alkyl sulfur free radicals add to double bonds of olefin to obtain alkyl free radical intermediate **B**.

The resulted radical intermediate **B** could be oxidized to carbon cation **C** in the presence of PIDA. Finally, the active alkyl cation **C** undergoes nucleophilic attack with aza-heterocycle to give the final product.

## Conclusion

In summary, we have developed a heat-induced three-component coupling of alkenes, aza-heterocycles and Bunte

salts for the preparation of  $\beta$ -amino sulfides. The outstanding advantage of this strategy is that it avoids the use of expensive transition metals and additional additives. In addition, a simple reaction system enables readily scaled-up reactions and late-stage modification of drug molecules, which provides an efficient and practical method for the development of thiomethylation drugs. Remarkably, this metal-free aminothiolation of alkenes makes use of readily available and cheap starting materials and shows uniform regioselectivity in all cases.

## Data availability statement

The original contributions presented in the study are included in the article/Supplementary Material, further inquiries can be directed to the corresponding author.

## Author contributions

BQ: Investigation, Methodology, Writing–review and editing. XC: Investigation, Methodology, Writing–review and editing. ZL: Formal Analysis, Writing–review and editing. CZ: Data curation, Writing–original draft. XL: Resources, Supervision, Writing–original draft.

## Funding

The author(s) declare financial support was received for the research, authorship, and/or publication of this article. This work was supported by Project of Jilin Provincial Health Commission (2022JC064).

## Conflict of interest

The authors declare that the research was conducted in the absence of any commercial or financial relationships that could be construed as a potential conflict of interest.

## Publisher's note

All claims expressed in this article are solely those of the authors and do not necessarily represent those of their affiliated organizations, or those of the publisher, the editors and the reviewers. Any product that may be evaluated in this article, or claim that may be made by its manufacturer, is not guaranteed or endorsed by the publisher.

## Supplementary material

The Supplementary Material for this article can be found online at: <https://www.frontiersin.org/articles/10.3389/fchem.2023.1328441/full#supplementary-material>

## References

- Cecchetti, V., Calderone, V., Tabarrini, O., Sabatini, S., Filipponi, E., Testai, L., et al. (2003). Highly potent 1,4-benzothiazine derivatives as  $K_{ATP}$ -channel openers. *J. Med. Chem.* 46, 3670–3679. doi:10.1021/jm030791q
- Cui, H., Liu, X., Wei, W., Yang, D., He, C., Zhang, T., et al. (2016). Molecular iodine-mediated difunctionalization of alkenes with nitriles and thiols leading to beta-acetamido sulfides. *J. Org. Chem.* 81, 2252–2260. doi:10.1021/acs.joc.5b02579
- Cui, Y., Lu, T., Shi, Z., and Feng, J. (2019). Dehydroxylated amination accompanied by 1,2-sulfur immigration. *Org. Chem. Front.* 6, 643–647. doi:10.1039/C8QO01211C
- De Paolis, M. L., Blankenstein, J. R., Bois-Choussy, M., and Zhu, J. P. (2002). N-carbamate-assisted stereoselective synthesis of chiral vicinal amino sulfides. *Org. Lett.* 4, 1235–1238. doi:10.1021/ol025743z
- Hosseini-Zare, M. S., Salehi, F., Seyedi, S. Y., Azami, K., Ghadiri, T., Mobasseri, M., et al. (2011). Effects of pentoxifylline and H-89 on epileptogenic activity of bucladesine in pentylenetetrazol-treated mice. *Eur. J. Pharmacol.* 670, 464–470. doi:10.1016/j.ejphar.2011.09.026
- Iwasaki, M., Nonaka, K., Zou, S., Sawanaka, Y., Shinozaki, T., Fujii, T., et al. (2019). Copper-catalyzed regioselective aminothioloation of aromatic and aliphatic alkenes with N-fluorobenzenesulfonimide and thiols through three-component radical coupling. *J. Org. Chem.* 84 (23), 15373–15379. doi:10.1021/acs.joc.9b02392
- Jiang, Y., Liang, G., Zhang, C., and Loh, T.-P. (2016). Palladium-catalyzed C–S bond formation of stable enamines with arene/alkanethiols highly regioselective synthesis of  $\beta$ -amino sulfides. *Eur. J. Org. Chem.* 2016, 3326–3330. doi:10.1002/ejoc.201600588
- Li, D., Mao, T., Huang, J., and Zhu, Q. (2017). Copper-catalyzed regioselective 1,2-thioamidation of alkenes. *Chem. Commun.* 53, 3450–3453. doi:10.1039/C7CC00083A
- Liu, F., and Yi, W. (2018). A thiol-free synthesis of alkynyl chalcogenides by the copper-catalyzed C–X (X = S, Se) cross-coupling of alkynyl carboxylic acids with Bunte salts. *Org. Chem. Front.* 5, 428–433. doi:10.1039/C7QO00724H
- Luo, J., Zhu, Z., Liu, Y., and Zhao, X. (2015). Diaryl selenide catalyzed vicinal trifluoromethylthioamination of alkenes. *Org. Lett.* 17, 3620–3623. doi:10.1021/acs.orglett.5b01727
- Prabhakar, N. S., Kumar, S., Gupta, P. K., and Singh, K. N. (2022). Visible-light-induced photocatalytic trifluoromethylation of Bunte salts: easy access to trifluoromethylthiolated synthons. *J. Org. Chem.* 87, 11112–11120. doi:10.1021/acs.joc.2c01353
- Qiao, Z., Ge, N., and Jiang, X. (2015).  $CO_2$ -promoted oxidative cross-coupling reaction for C–S bond formation via masked strategy in an odourless way. *Chem. Commun.* 51, 10295–10298. doi:10.1039/C5CC03038B
- Sun, K., Lv, Y., Shi, Z., Mu, S., Li, C., and Wang, X. (2017). A novel metal-free amidosulfonylation of alkenes leading to  $\beta$ -azolyl sulfides. *Org. Biomol. Chem.* 15, 5258–5262. doi:10.1039/C7OB01061C
- Wang, D., Yan, Z., Xie, Q., Zhang, R., Lin, S., and Wang, Y. (2017). Three-component difunctionalization of alkenes leading to beta-acetamido sulfides and beta-acetoxy sulfides. *Org. Biomol. Chem.* 15, 1998–2002. doi:10.1039/C7OB00110J
- Wang, W., Zhao, L., Wu, H., He, Y., and Wu, G. (2023). Divergent trideuteromethylthiolation and aminotrideromethylthiolation of alkenes with N-fluorobenzenesulfonimide and  $CD_3SSO_3Na$ . *Org. Lett.* 25, 7078–7082. doi:10.1021/acs.orglett.3c02329
- Wu, H., He, Y., Sun, K., Xu, Y., Wang, W., and Wu, G. (2023). Iodine(iii)-mediated dehydroaromatization of cyclohexanones with primary amines and  $CD_3SSO_3Na$  to access ortho-SCD<sub>3</sub> anilines. *Org. Chem. Front.* 10, 3213–3218. doi:10.1039/D3QO00481C
- Yao, L., Li, W., Xiao, F., and Deng, G.-J. (2023). Three-component tandem amidosulfonylation of alkenes for the synthesis of  $\beta$ -succinimide sulfides. *J. Org. Chem.* 88, 13956–13966. doi:10.1021/acs.joc.3c01518
- Yuan, Y., Chen, Y., Tang, S., Huang, Z., and Lei, A. (2018). Electrochemical oxidative oxysulfonylation and aminosulfonylation of alkenes with hydrogen evolution. *Sci. Adv.* 4, eaat5312. doi:10.1126/sciadv.aat5312
- Zhu, L.-L., Tian, L., Sun, K., Li, Y., Liu, G., Cai, B., et al. (2022).  $N_2$ -selective  $\beta$ -thioalkylation of benzotriazoles with alkenes. *J. Org. Chem.* 87, 12963–12974. doi:10.1021/acs.joc.2c01519



## OPEN ACCESS

## EDITED BY

Mohamed Saleh Abdelfattah,  
Helwan University, Egypt

## REVIEWED BY

Ajay Kumar Chinnam,  
University of Idaho, United States  
Gourav Kumar,  
Oregon Health and Science University,  
United States

## \*CORRESPONDENCE

Ahmed Alawadi,  
✉ ahmedalawadi85@gmail.com

RECEIVED 22 November 2023

ACCEPTED 15 January 2024

PUBLISHED 16 February 2024

## CITATION

Habeeb Naser I, Thoulfikar A. Alamir H,  
Al-Shukarji AH, Ahmed BA, Qassem TA,  
Kamal M, Almeleebia TM, Alwaily ER,  
Hasan Kadhum E, Alawadi A and Alsalamy A  
(2024), Choline chloride/urea as a green and  
efficient deep eutectic solvent in three-  
component and four-component synthesis of  
novel pyrazole and pyrano[2,3-c] pyrazole  
derivatives with antibacterial and  
antifungal activity.  
*Front. Chem.* 12:1342784.  
doi: 10.3389/fchem.2024.1342784

## COPYRIGHT

© 2024 Habeeb Naser, Thoulfikar A. Alamir, Al-Shukarji, Ahmed, Qassem, Kamal, Almeleebia, Alwaily, Hasan Kadhum, Alawadi and Alsalamy. This is an open-access article distributed under the terms of the [Creative Commons Attribution License \(CC BY\)](#). The use, distribution or reproduction in other forums is permitted, provided the original author(s) and the copyright owner(s) are credited and that the original publication in this journal is cited, in accordance with accepted academic practice. No use, distribution or reproduction is permitted which does not comply with these terms.

# Choline chloride/urea as a green and efficient deep eutectic solvent in three-component and four-component synthesis of novel pyrazole and pyrano[2,3-c] pyrazole derivatives with antibacterial and antifungal activity

Israa Habeeb Naser<sup>1</sup>, Hassan Thoulfikar A. Alamir<sup>2</sup>,  
Ali Hisham Al-Shukarji<sup>3</sup>, Batool Ali Ahmed<sup>4</sup>, Talal Aziz Qassem<sup>5</sup>,  
Maher Kamal<sup>6</sup>, Tahani M. Almeleebia<sup>7</sup>, Enas R. Alwaily<sup>8</sup>,  
Eftikhaar Hasan Kadhum<sup>9</sup>, Ahmed Alawadi<sup>10,11,12\*</sup> and  
Ali Alsalamy<sup>13</sup>

<sup>1</sup>Medical Laboratories Techniques Department, Al-Mustaqbal University, Hillah, Iraq, <sup>2</sup>Faculty of Pharmacy, Department of Pharmaceutics, University of Al-Ameed, Karbala, Iraq, <sup>3</sup>Department of Medical Laboratories Technology, Al-Manara College for Medical Sciences, Maysan, Iraq, <sup>4</sup>Department of Medical Engineering, Al-Nisour University College, Baghdad, Iraq, <sup>5</sup>Department of Medical Laboratory Technics, Al-Noor University College, Nineveh, Iraq, <sup>6</sup>Department of Dentistry, Al-Hadi University College, Baghdad, Iraq, <sup>7</sup>Department of Clinical Pharmacy, College of Pharmacy, King Khalid University, Abha, Saudi Arabia, <sup>8</sup>Microbiology Research Group, College of Pharmacy, Al-Ayen University, Thi-Qar, Iraq, <sup>9</sup>National University of Science and Technology, Dhi Qar, Iraq, <sup>10</sup>College of Technical Engineering, The Islamic University, Najaf, Iraq, <sup>11</sup>College of Technical Engineering, The Islamic University of Al Diwaniyah, Al Diwaniyah, Iraq, <sup>12</sup>College of Technical Engineering, The Islamic University of Babylon, Babylon, Iraq, <sup>13</sup>College of Technical Engineering, Imam Ja'afar Al-Sadiq University, Al-Muthanna, Iraq

In this study, choline chloride/urea was used as a green deep eutectic solvent in the three-component reaction of hydrazine/phenylhydrazine, malononitrile, and aromatic aldehydes for synthesizing pyrazole derivatives, and in the four-component reaction of methyl/ethyl acetoacetate, hydrazine/phenylhydrazine, malononitrile, and aromatic aldehydes for synthesizing pyrano[2,3-c]pyrazole derivatives. Elemental analysis, <sup>1</sup>H, and <sup>13</sup>C NMR spectroscopy were used to confirm the structure of the synthesized pyrazole and pyrano[2,3-c] pyrazole derivatives. The antimicrobial effects of the synthesized pyrazole and pyrano[2,3-c] pyrazole derivatives were investigated. In antimicrobial tests, instructions from clinical and laboratory standards institutes were used. Antimicrobial study was done on pathogenic gram-positive and gram-negative species, and specialized aquatic strains and fungal species. Using choline chloride/urea, novel pyrazole derivatives and pyrano[2,3-c]pyrazole derivatives were synthesized, and other derivatives were synthesized with higher efficiency in less time than some previously reported methods. MIC (minimum inhibitory concentration) and MBC (minimum bactericidal concentration) obtained for derivatives were higher than some antibiotic drugs. Synthesis and reports of new derivatives of pyrazole and pyrano[2,3-c]pyrazole, and investigation and reports of their

antimicrobial properties on gram-positive, gram-negative, and specialized aquatic and fungal species are among the novel and important findings of this study.

#### KEYWORDS

choline chloride/urea, deep eutectic solvent, pyrazole, pyrano[2,3-*c*]pyrazole, biological evaluation, antimicrobial agent

## 1 Introduction

The use of green processes in synthesizing organic and heterocyclic compounds is noteworthy (Nishanth Rao et al., 2021). Green methods in organic synthesis are essential because they are environmentally friendly (Kumar et al., 2020). Among the green techniques in organic chemistry are the synthesis of organic and heterocyclic compounds during multicomponent reactions, the use of recyclable catalysts, and the use of deep eutectic solvents (Calvo-Flores and Mingorance-Sánchez, 2021; Javahershenas, 2023). Multi-component reactions, in which several reactants lead to the synthesis of the desired product in one pot and one step, in addition to being green, are important in the synthesis of organic and heterocyclic compounds due to their high efficiency, cost-effectiveness, and time-saving characteristics (Bhaskaruni et al., 2020; John et al., 2021). There have been several reports of the synthesis of five-membered heterocycles, such as pyrazoles, or two-ring heterocyclic compounds, such as pyranopyrazoles, using multicomponent reactions (Mamaghani and Hossein Nia, 2021; Becerra et al., 2022; Khazaal and Ibraheem, 2022). Pyrazole is a useful heterocyclic compound due to its agricultural and drug-discovery applications (Kumar et al., 2013). There have been reports of this heterocyclic compound in nature, for example, isolation from fungi such as *Colletotrichum gloeosporioides* (Cui et al., 2023). The biological properties of this heterocyclic compound that can be mentioned are its anxiolytic, antidepressant, anti-tubercular, analgesic properties, and anti-malarial activities, etc. (Ramadan et al., 2021). As there is a pyrazole structure in the structure of 4-[5-(4-methylphenyl)-3-(trifluoromethyl)-1*H*-pyrazol-1-yl]benzene-sulfonamide, which is a drug with the brand name Celecoxib, this heterocyclic compound can be used as a medicinal and bioactive compound (Küçükgülzel and Şenkardeş, 2015). Pyrano[2,3-*c*]pyrazole derivatives are one of the pyrazole derivatives that contain two heterocyclic compounds of pyrazole and pyran, which are connected by one facet. Derivatives of pyrano[2,3-*c*] pyrazole can maintain the biological properties of both heterocyclic compounds of pyran and pyrazole. Biological properties, such as cytotoxic, mutagenicity, cancer therapy, and antiviral properties, have been reported for the derivatives of the 6-membered heterocyclic compound of pyran with one oxygen in its structure (Yahiaoui et al., 2022). Biological properties, such as anti-tubercular, anti-malarial, anti-microbial, and anti-cancer properties, have been reported for the derivatives of pyrano[2,3-*c*]pyrazole (Mokariya et al., 2022; Parikh et al., 2022). In addition to the green method of multicomponent reaction, by using other green techniques such as the use of deep eutectic solvents, pyrazole derivatives and pyrano[2,3-*c*]pyrazole derivatives can be synthesized, and reports have been made in this field (Nguyen et al., 2021; Sikandar and Zahoor, 2021). As mentioned, the use of the deep eutectic solvent is one of the important and green methods in synthesizing organic and heterocyclic compounds. With this method, there is no need to use dangerous organic solvents or catalysts in the synthesis of organic and heterocyclic compounds

(Rushell et al., 2019). A deep eutectic solvent plays the role of solvent and catalyst in the synthesizing of heterocyclic and organic compounds (Fekri et al., 2020). Deep eutectic solvents can be used during multicomponent reactions (Calvo-Flores and Mingorance-Sánchez, 2021). In this regard, we can refer to reports such as the use of glycerol: potassium carbonate in the four-component reaction of malononitrile, carbon disulfide, carbonyl, and methylene compounds, which led to the synthesis of [1,3]dithiine derivatives (Moghaddam-Manesh and Hosseinzadegan, 2021). Another deep eutectic solvent system that has been reported so far for the synthesis of pyrazolopyridines derivatives (Vanegas et al., 2019); tetrahydrobenzo [b]pyran and pyrano[2, 3-*d*]pyrimidinone (thione) (Biglari et al., 2020); and pyrazolines, pyrimidines, and naphthyridines (Mohamed et al., 2022) is the use of choline chloride/urea. According to reports, using choline chloride/urea reduces the synthesis time of the desired derivatives and has led to higher efficiency to synthesis of new derivatives. Therefore, choline chloride/urea was used as a deep eutectic solvent to synthesize pyrazole derivatives and pyrano[2,3-*c*] pyrazole derivatives. The synthesis of new derivatives and the experiments of antimicrobial and antifungal properties of the synthesized derivatives were among the other investigations carried out in this study.

## 2 Materials and methods

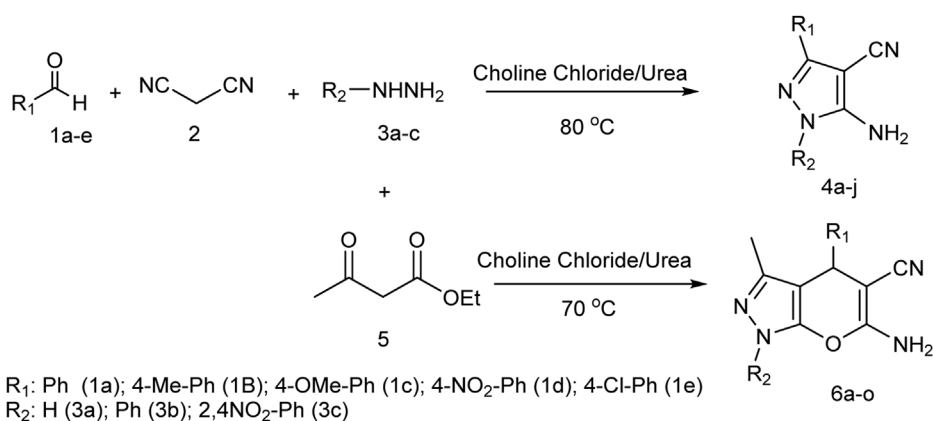
### 2.1 Equipment and materials

The Brookfield DV-II + Pro EXTRA viscometer was used to measure solvent viscosity, and the G LAB melting point apparatus was used to measure the melting point of solvent and derivatives. The <sup>1</sup>H, and <sup>13</sup>C NMR spectra, CHNS/O elemental analyzer, and mass analysis of compounds were prepared using the Varian Inova 500MHz, the EMA 502, and the Agilent technologies 5975C. The Thermo biomate 5 Spectrophotometer was used to prepare the suspension of bacteria. The suspension of bacteria was obtained from the American Type Culture Collection (ATCC). All the reagent materials used for the synthesis of deep eutectic solvent and the synthesis of pyrazole derivatives and pyrano[2,3-*c*] pyrazole derivatives such as choline chloride, urea, malononitrile, aldehyde derivatives, and hydrazine derivatives were obtained from Merck and Sigma.

### 2.2 Solvent preparation

To prepare the choline chloride/urea deep eutectic solvent, choline chloride and urea were weighed in different ratios, 1:1, 1: 2, 1:3, and 1:4, and stirred at 80°C until a colorless homogeneous mixture was observed (Yadav and Pandey, 2014). The prepared mixture was cooled and used for other steps.





SCHEME 1

Using choline chloride/urea as green method for synthesis of pyrazole derivatives and pyrano[2,3-c]pyrazole derivatives.

TABLE 1 Optimization of molar ratio of choline chloride:urea and reaction temperature in synthesis of pyrazole.

Entry	Product	Molar ratio of choline chloride:urea	Reaction temperature (°C)	Tim (min)	Yield (%)
1	4a	0: 1	80	60	N.R
2	4a	1: 0	80	60	N.R
3	4a	1: 1	80	60	67
4	4a	1: 2	80	20	97
5	4a	1: 3	80	30	82
6	4a	1: 4	80	30	55
7	4a	1: 2	50	30	52
8	4a	1: 2	60	30	76
9	4a	1: 2	70	30	88
10	4a	1: 2	90	30	95
11	4a	1: 2	100	30	90

N.R, no reaction.

TABLE 2 Physical parameters of a 1:2 ratio of choline chloride:urea deep eutectic solvent.

Viscosity (25°C, cPa)	Melting point temperature (°C)
17.50	20

## 2.3 Synthesis of pyrazole derivatives

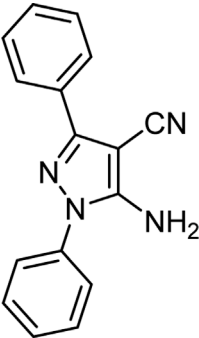
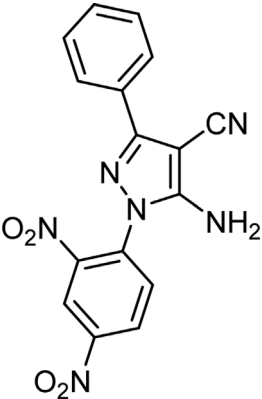
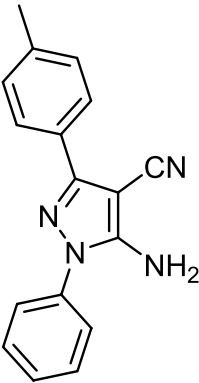
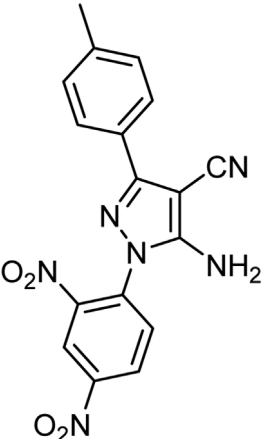
To 1 g choline chloride/urea (1:2) deep eutectic solvent, 1 mmol malononitrile and 1 mmol aldehyde derivatives were added and stirred at 80°C for 5 min. Then 1 mmol hydrazine derivatives was added and stirred at 80°C until the reaction was complete. The completion of the reaction was checked by TLC. Finally, after the completion of the reaction, the temperature was brought to the ambient temperature, and 5 mL of distilled water was added and stirred for 30 min. The sediments, which were the desired product, were separated with filter paper. The desired synthesized product

was purified by recrystallization in a mixture of distilled water and ethanol (1:1).

## 2.4 Synthesis pyrano[2,3-c] pyrazole derivatives

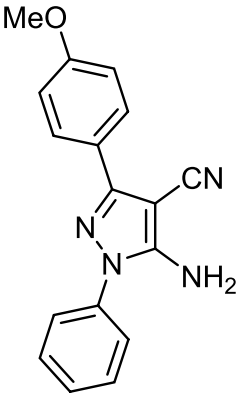
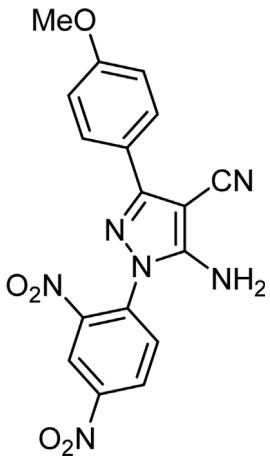
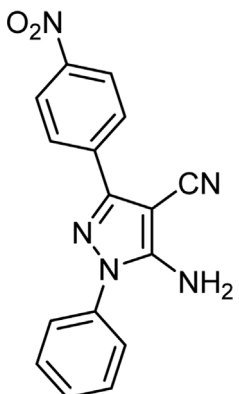
To 1 g choline chloride/urea deep eutectic solvent, 1 mmol malononitrile and 1 mmol aldehyde derivatives were added and stirred at 70°C for 5 min. To 1 g choline chloride/urea deep eutectic solvent, 1 mmol ethyl acetoacetate and 1 mmol hydrazine derivatives were added and stirred at 80°C for 5 min. The mixtures were added together and stirred at 80°C until the reaction was complete. The completion of the reaction was checked by TLC. Finally, after the completion of the reaction, the temperature was brought to the ambient temperature, and 5 mL of distilled water was added and stirred for 30 min. The sediments, which were the desired product, were separated with filter paper.

TABLE 3 Information on synthesized pyrazole derivatives using choline chloride/urea as green method.

Product code	R <sub>1</sub>	R <sub>2</sub>	Product structure	Reported Mp (°C)	Found Mp (°C)	Synthesis time (min)	Yield (%)
4a	Ph	Ph		158-159 (Poonam and Singh, 2019)	159-160	20	97
4b	Ph	2,4-NO <sub>2</sub> -Ph		240-142 (Bakhtiarian and Khodaei, 2022)	240-243		95
4c	4-Me-Ph	Ph		119-121 (Nemati et al., 2021)	120-121		97
4d	4-Me-Ph	2,4-NO <sub>2</sub> -Ph		New	245-247		85

(Continued on following page)

TABLE 3 (Continued) Information on synthesized pyrazole derivatives using choline chloride/urea as green method.

Product code	R <sub>1</sub>	R <sub>2</sub>	Product structure	Reported Mp (°C)	Found Mp (°C)	Synthesis time (min)	Yield (%)
4e	4-OMe-Ph	Ph		107-109 (Abshirini et al., 2020)	108-110		98
4f	4-OMe-Ph	2,4-NO <sub>2</sub> -Ph		New	264-267		86
4g	4-NO <sub>2</sub> -Ph	Ph		165-168 (Nemati et al., 2021)	166-168		97

(Continued on following page)

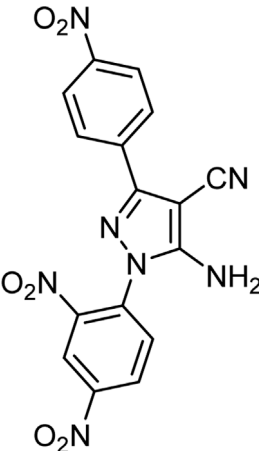
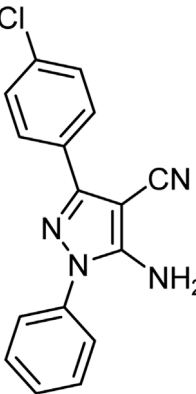
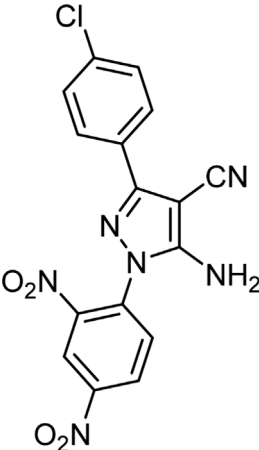
The desired synthesized product was purified by recrystallization in a mixture of distilled water and ethanol (1:1).

## 2.5 Antimicrobial and antifungal activity pyrazole derivatives and pyrano[2,3-c] pyrazole derivatives

Based on previous studies reported according to relevant standards, the antimicrobial activity of synthetic derivatives on *Streptomyces fradiae* (10745), *Staphylococcus aureus* (29213), *Streptococcus*

*pyogenes* (19615), *Streptococcus agalactiae* (12386), *Yersinia enterocolitica* (9610), *Shigella dysenteriae* (13313), *Pseudomonas aeruginosa* (15442), *Acinetobacter baumannii* (19606), *Streptococcus iniae* (29178), *Loctococcus garvieae* (43921), *Yersinia ruckeri* (29473), *Edwardsiella tarda* (15947), *Candida albicans* (10231), *Cryptococcus neoformans* (32045), *Fusarium oxysporum* (7601), and *Aspergillus fumigatus* Fresenius (1022) was investigated and evaluated. For this purpose, first, the half-McFarland concentration of the strains and the initial concentrations of 1, 2, 4, 8, 16, 32, 64, 128, 256, 512, 1024, and 2048 µg/mL of the derivatives were prepared separately. The minimum inhibitory concentration (MIC), minimum bactericidal concentration

TABLE 3 (Continued) Information on synthesized pyrazole derivatives using choline chloride/urea as green method.

Product code	R <sub>1</sub>	R <sub>2</sub>	Product structure	Reported Mp (°C)	Found Mp (°C)	Synthesis time (min)	Yield (%)
4 h	4-NO <sub>2</sub> -Ph	2,4-NO <sub>2</sub> -Ph		New	266-268		84
4i	4-Cl-Ph	Ph		128-130 (Amirnejat et al., 2020)	129-131		98
4j	4-Cl-Ph	2,4-NO <sub>2</sub> -Ph		234-236 (Aryan et al., 2017)	235-236		93

Choline chloride:urea (1: 2); 80°C.

(MBC), minimum fungicidal concentration (MFC), and inhibition zone diameter (IZD) were evaluated (Igei et al., 2016; Suksatan et al., 2022).

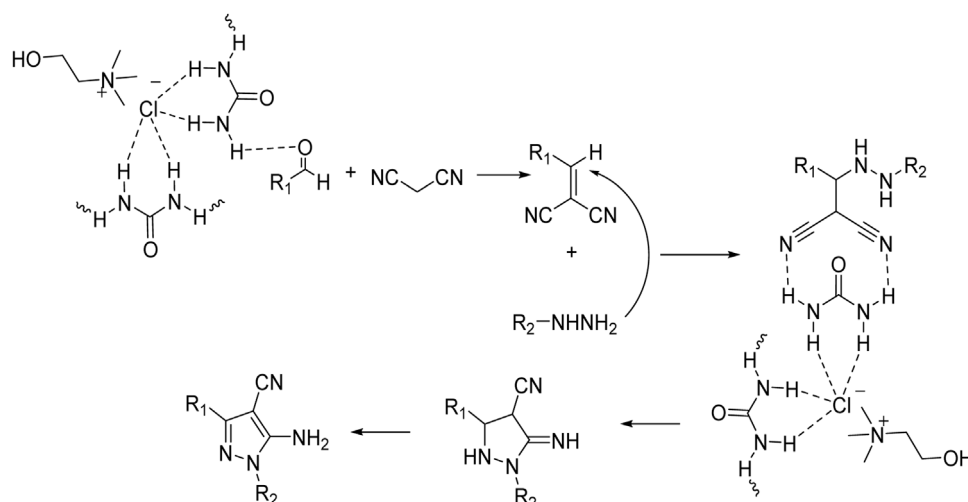
### 3 Results and discussion

In this study, by using choline chloride/urea as a green and environmentally friendly deep eutectic solvent, in the three-component reaction of malononitrile, aldehyde derivatives, and

hydrazine derivatives, novel pyrazole derivatives, and in the four-component reaction of malononitrile, aldehyde derivatives, ethyl acetoacetate, and hydrazine derivatives, novel pyrano[2,3-c]pyrazole derivatives were synthesized (Scheme 1).

In general, the greenness of the reported method, high efficiency, and shorter synthesis time were the advantages of using choline chloride/urea in synthesizing derivatives. Additional information about the synthesis of derivatives is given below.





SCHEME 2  
Mechanism for using choline chloride/urea as green method for synthesis of pyrazole derivatives (4a-j).

TABLE 4 The previously reported conditions and methods in the synthesis of pyrazole compared to the method presented in this study.

Reported year	Product	Condition (catalyst)	Reaction temperature (°C)	Time	Yield (%)	Reference
2023	4a	Sulfonic acid modified 5-aminotetrazole-1,3,5-triazine-(3-aminopropyl)silylated carbon quantum dots-coated Fe <sub>3</sub> O <sub>4</sub> magnetic nanoparticles	70	Not reported	95	Ghorbani et al. (2023)
2022	4a	2,6-diamino-1-(4-sulfobutyl)pyridin-1-ium hydrogen sulfate modified pectin nanoparticles	50	30 min	96	Bakhtiaran and Khodaei (2022)
2021	4a	Sulfonic acid-functionalized polyvinyl alcohol	90	3 h	89	Patki et al. (2021)
2020	4a	1,3-disulfoimidazolium trifluoroacetate	80	50 min	94	Abshirini et al. (2020)
This work	4a	Choline chloride:urea	80	20 min	97	-

### 3.1 Three-component synthesis of pyrazole derivatives using choline chloride/urea

The three-component synthesis of pyrazole derivatives used choline chloride/urea, malononitrile, aldehyde derivatives, and hydrazine derivatives were used as raw materials.

For this purpose, according to the method presented in Section 2.2, different ratios of choline chloride and urea were prepared. For the synthesis of 4a, they were tested according to Table 1.

In obtaining the optimal conditions (Table 1), in addition to using different ratios of choline chloride and urea, temperatures of 50°C, 60°C, 70°C, 80°C, 90°C, and 100°C degrees Celsius were also tested. It was found that the ratio of 1:2 (choline chloride: urea) at 80°C had the highest efficiency in a shorter time for the synthesis.

Physical parameters such as viscosity (according to ASTM D445 testing method) and melting point for 1:2 choline chloride: urea mixture were obtained according to Table 2.

The above optimal conditions were used for synthesizing other derivatives, according to Table 3. Three of the derivatives reported in Table 3 are novel.

The results of <sup>1</sup>H NMR, <sup>13</sup>C NMR, and CHNS/O elemental analyzer of the newly synthesized derivatives that confirm their structure are given in the Supplementary Material.

As the results show, in general, electron-donating substituents attached to hydrazine, such as phenyl, and electron-withdrawing groups attached to the aldehyde, such as nitro, increased the efficiency of the products. Therefore, the following mechanism (Scheme 2) can be proposed for this 3-component reaction, which corresponds to the difference in the results of the product's efficiency.

So far, many studies have been conducted on the three-component reaction of malononitrile, aldehyde derivatives, and hydrazine derivatives, which led to the synthesis of pyrazole derivatives. The conditions of some recent studies (from 2020 to 2023) compared to the conditions used in this study are given in Table 4.

Ease of reaction conditions and no need for catalyst and solvent, reporting of newly synthesized derivatives, being green, and having high efficiency and shorter synthesis time can be mentioned as advantages of using choline chloride/urea to synthesize derivatives compared to recently reported methods.

TABLE 5 Optimization of molar ratio of choline chloride:urea and reaction temperature in synthesis of pyrano[2,3-c] pyrazoles.

Entry	Product	Molar ratio of choline chloride:urea	Reaction temperature (°C)	Tim (min)	Yield (%)
1	6a	0: 1	70	60	N.R
2	6a	1: 0	70	60	N.R
3	6a	1: 1	70	60	42
4	6a	1: 2	70	17	95
5	6a	1: 3	70	30	66
6	6a	1: 4	70	30	54
7	6a	1: 2	50	30	62
8	6a	1: 2	60	30	79
9	6a	1: 2	80	30	90
10	6a	1: 2	90	30	88
11	6a	1: 2	100	30	88

N.R, no reaction.

### 3.2 Four-component synthesis of pyrano [2,3-c]pyrazole derivatives using choline chloride/urea

In the continuation of this study, choline chloride/urea was also used in the 4-component reaction of malononitrile, aldehyde derivatives, hydrazine derivatives, and ethyl acetoacetate for the synthesis of pyrano[2,3-c]pyrazole derivatives.

The steps for synthesizing derivatives here were the first optimization according to Section 3.1, the results of which are given in Table 5.

Here, the optimal conditions for synthesizing pyrano[2,3-c]pyrazole derivatives with high efficiency and shorter time, were the ratio of 1:2 of choline chloride:urea and the reaction temperature of 70°C. With the obtained optimal conditions, other derivatives, including 15 derivatives, of which two were novel, were synthesized (Table 6).

The results of <sup>1</sup>H NMR, <sup>13</sup>C NMR, and CHNS/O elemental analyzer of the newly synthesized derivatives that confirm their structure are given in the Supplementary Material.

Comparing the results of the efficiency with the structure of the raw materials here was also the same as above, and it was observed that electron-donating substituents attached to hydrazine, such as phenyl, and electron-withdrawing groups attached to the aldehyde, such as nitro, increased the efficiency of the products. Therefore, the Scheme 3 mechanism is proposed for this reaction.

The result of the comparison of the method presented in this study to the recent studies in the synthesis of derivatives, as shown in Table 7, is similar to the conclusion for the synthesis of pyrazole derivatives. It can be stated here that ease of reaction conditions, catalyst and solvent not being necessary, newly synthesized derivatives being reported, being green, and having high efficiency and shorter synthesis time can be mentioned as advantages of using choline chloride/urea to synthesize derivatives compared to recently reported methods.

### 3.3 The antimicrobial activity results

In the investigation of antimicrobial and antifungal activity of derivatives, gram-positive, gram-negative, and specialized aquatic strains were used. First, the MIC with a concentration in the range of 1–2048 µg/mL of the derivatives was checked. After obtaining this parameter, its MBC and MFC were acquired. Finally, using the MIC, the IZD parameter of the derivatives on the used strains was obtained.

For further comparison of pyrazole derivatives and pyrano[2,3-c]pyrazole derivatives, the antibacterial properties of gram-positive, gram-negative, and specialized aquatic and fungal strains are shown separately in Tables 8–11.

Table 8 shows the results of investigating the antibacterial properties of the derivatives on the evaluated gram-positive strains.

Table 9 shows the results of investigating the antibacterial properties of the derivatives on the evaluated gram-negative strains.

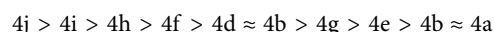
Table 10 shows the results of investigating the antibacterial properties of the derivatives on the evaluated specialized aquatic strains.

Table 11 shows the results of investigating the antibacterial properties of the derivatives on the evaluated fungal strains.

The highest effectiveness in antibacterial activity between pyrazole derivatives and pyrano[2,3-c]pyrazole derivatives was related to 6o.

The IZD value results of some pyrano[2,3-c]pyrazole derivatives compared to *Yersinia ruckeri* are given in Figure 1.

In general, the order of effectiveness of pyrazole derivatives was as follows:



In general, the order of effectiveness of pyrano[2,3-c]pyrazole derivatives was as follows:

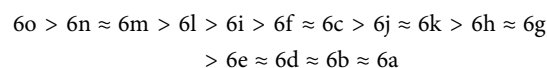
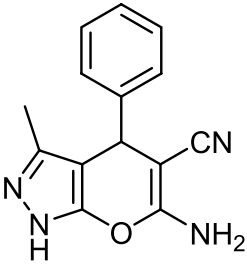
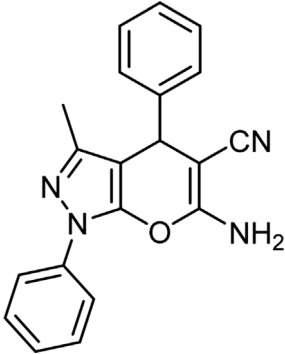
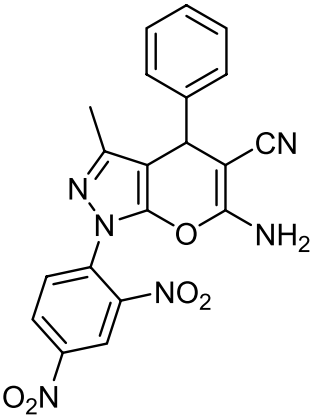
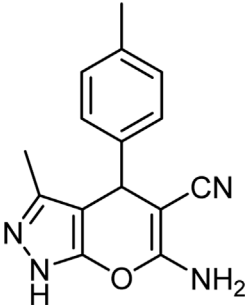
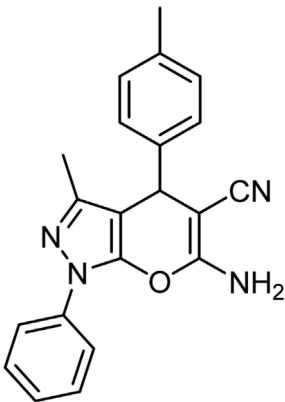
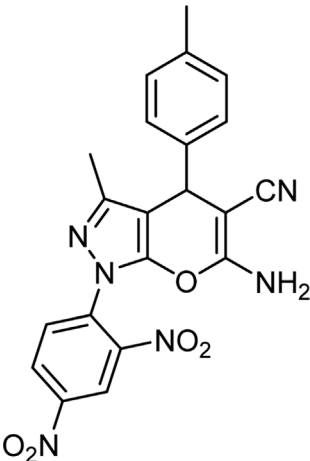
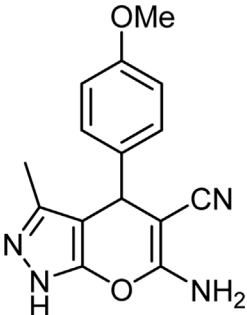
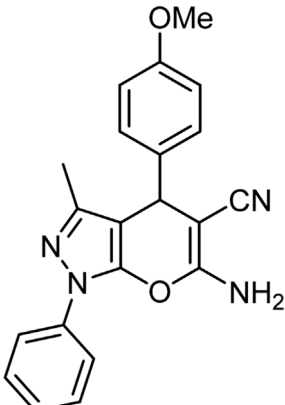


TABLE 6 Information on synthesized pyrano[2,3-c]pyrazole derivatives using choline chloride/urea as green method.

Product code	R <sub>1</sub>	R <sub>2</sub>	Product structure	Reported Mp (°C)	Found Mp (°C)	Synthesis time (min)	Yield (%)
6a	Ph	H		241-243 (Yekke-Ghasemi et al., 2022)	240-242	17	95
6b	Ph	Ph		169-171 (Mathavan and Yamajala, 2023)	170-172	15	95
6c	Ph	2,4-NO <sub>2</sub> -Ph		240-243 (Vasava et al., 2019)	241-242	30	90
6d	4-Me-Ph	H		175-177 (El Mejdoubi et al., 2019)	176-178	25	90

(Continued on following page)

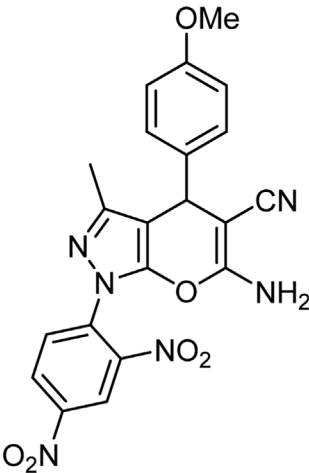
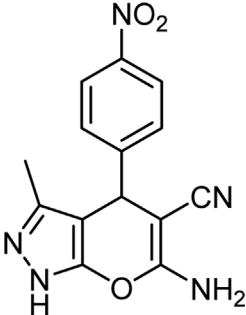
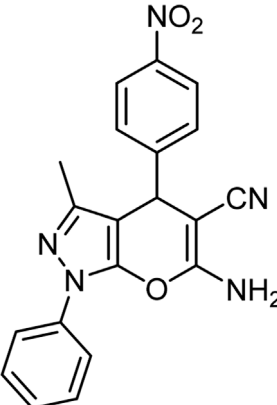
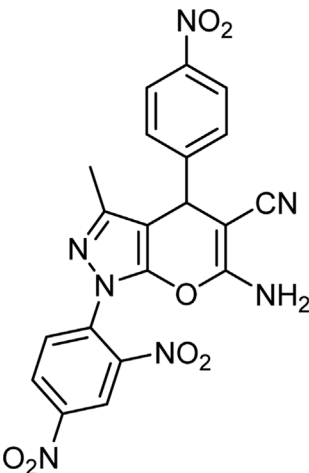
TABLE 6 (Continued) Information on synthesized pyrano[2,3-c]pyrazole derivatives using choline chloride/urea as green method.

Product code	R <sub>1</sub>	R <sub>2</sub>	Product structure	Reported Mp (°C)	Found Mp (°C)	Synthesis time (min)	Yield (%)
6e	4-Me-Ph	Ph		177-179 (Mohamadpour, 2020)	177-180	25	95
6f	4-Me-Ph	2,4-NO <sub>2</sub> -Ph		New	270-273	35	85
6g	4-OMe-Ph	H		209-211 (Yekke-Ghasemi et al., 2022)	209-212	20	92
6 h	4-OMe-Ph	Ph		170 (Suryakumari and Sudhakar, 2023)	169-171	18	95

(Continued on following page)

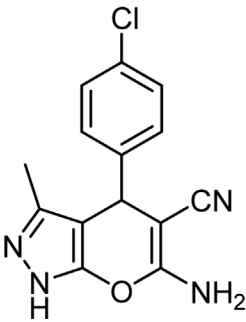
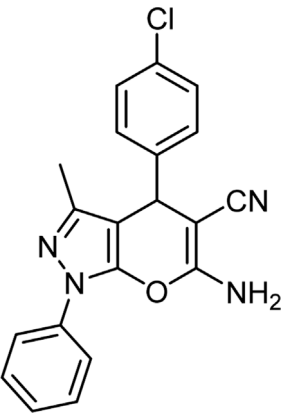
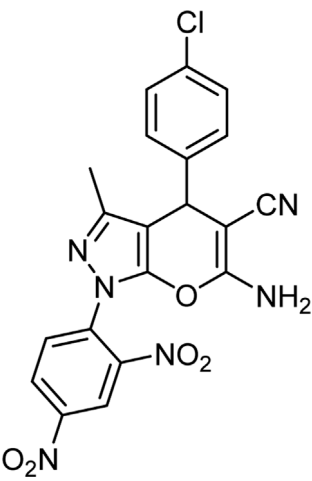


TABLE 6 (Continued) Information on synthesized pyrano[2,3-c]pyrazole derivatives using choline chloride/urea as green method.

Product code	R <sub>1</sub>	R <sub>2</sub>	Product structure	Reported Mp (°C)	Found Mp (°C)	Synthesis time (min)	Yield (%)
6i	4-OMe-Ph	2,4-NO <sub>2</sub> -Ph		New	288-290	36	85
6j	4-NO <sub>2</sub> -Ph	H		249-251 (Moghaddam et al., 2023)	249-251	20	95
6k	4-NO <sub>2</sub> -Ph	Ph		195-197 (Kondabanthini et al., 2022)	194-196	19	95
6L	4-NO <sub>2</sub> -Ph	2,4-NO <sub>2</sub> -Ph		283-285 (Vasava et al., 2019)	284-285	34	88

(Continued on following page)

TABLE 6 (Continued) Information on synthesized pyrano[2,3-c]pyrazole derivatives using choline chloride/urea as green method.

Product code	R <sub>1</sub>	R <sub>2</sub>	Product structure	Reported Mp (°C)	Found Mp (°C)	Synthesis time (min)	Yield (%)
6m	4-Cl-Ph	H		234-236 (Yekke-Ghasemi et al., 2022)	235-236	20	94
6n	4-Cl-Ph	Ph		175-177 (Kondabanthini et al., 2022)	175-177	17	97
6o	4-Cl-Ph	2,4-NO <sub>2</sub> -Ph		260-265 (Vasava et al., 2019)	263-266	35	80

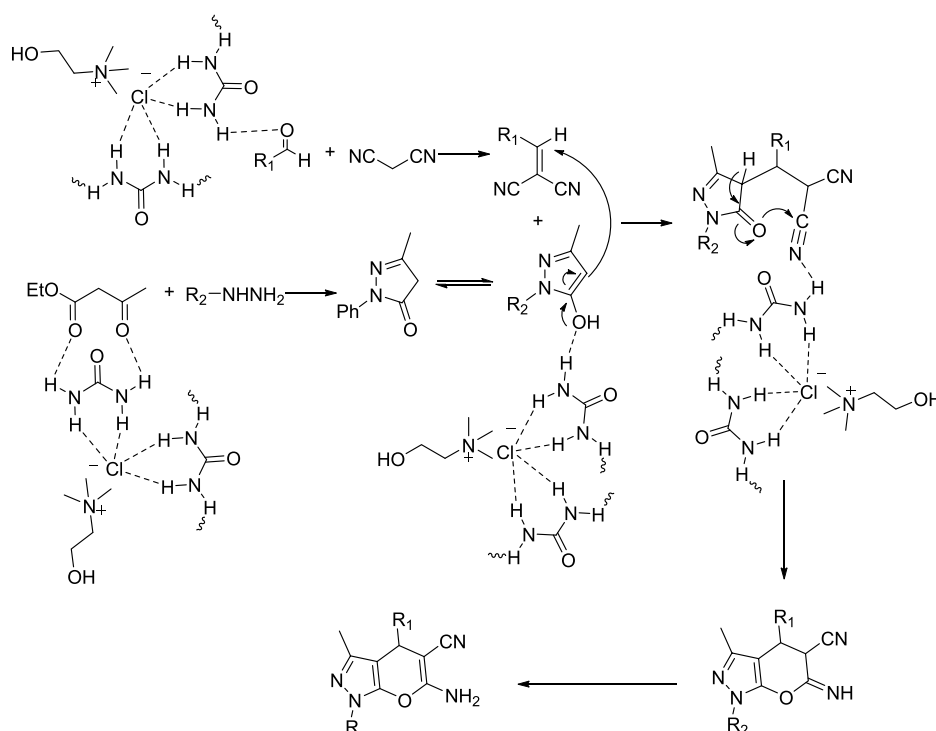
Choline Chloride: Urea (1: 2); 70°C

By comparing the results of Tables 8–11, the pyrano[2,3-c]pyrazole derivatives, in general, are more effective than pyrazole derivatives because pyrano[2,3-c] pyrazoles contain two heterocyclic rings (pyran and pyrazole). Another general conclusion that can be drawn is that the order of effectiveness of derivatives is as described for compounds containing chlorine, nitrogen, and methoxy. These results can be justified based on previous studies on the effectiveness and antimicrobial properties of chlorine and nitrogen. The important point in determining antimicrobial activities is to compare them with commercial drugs, such as penicillin, cefazolin, Tolnaftate, and Terbinafine. As the results of Tables 8–11 show, some derivatives, such as 6o in many studied strains,

are much more effective than tested drugs, which shows the value of synthetic compounds.

## 4 Conclusion

Choline chloride/urea was used as a deep eutectic solvent in the one-pot method and during the multicomponent reaction in synthesizing pyrazole derivatives and pyrano[2,3-c]pyrazole derivatives. The greenness of the synthesis method, the synthesis of new derivatives, and the characteristics of high efficiency and less time were among the advantages and novel findings of this study compared to previously reported methods. The effectiveness on



SCHEME 3

Mechanism for using choline chloride/urea as green method for synthesis of pyrazole pyrano[2,3-c]pyrazole derivatives (6a-o).

TABLE 7 The previously reported conditions and methods in the synthesis of pyrano[2,3-c]pyrazole compared to the method presented in this study.

Reported year	Product	Condition (catalyst)	Reaction temperature (°C)	Time	Yield (%)	Reference
2018	6a	Bael fruit ash	20	15 min	92	Shinde et al. (2018)
2018	6a	Sodium L-ascorbate	Reflux of water	10 min	88	Kiyani and Bamdad (2018)
This work	6a	Choline Chloride: Urea	70	17 min	95	-
2023	6b	Copper(II) oxide incorporated onto montmorillonite-K10 functionalized with tetraethyl orthosilicate, epichlorohydrine, melamine, and 5-sulphosalisilic acid	20	Not reported	90	Karrabi et al. (2023)
2023	6b	Potassium dihydrogenphosphate	100	2 h	95	Mathavan and Yamajala (2023)
2022	6b	Phenylazophenylenediamine-based lanthanum complex supported on silica-coated magnetic nano-Fe <sub>3</sub> O <sub>4</sub> core-shell nanocatalyst	110	12	90	Ghorbani et al. (2022)
2021	6b	Sugarcane bagasse ash-based silica-supported boric acid	80	35 min	86	Pandey et al. (2021)
2022	6b	Tungstic acid immobilized on zirconium-L-aspartate amino acid metal-organic framework-grafted L-(+)-tartaric acid stabilized magnetic Fe <sub>3</sub> O <sub>4</sub> nanoparticles	60	45 min	92	Khademi et al. (2021)
This work	6b	Choline chloride:urea	70	15 min	95	-

gram-positive, gram-negative, and specialized aquatic strains and fungal species is one of the novel findings of this project. In the investigation of antimicrobial activity, the highest effectiveness was

observed in derivative 6o, which contained chlorine and nitrogen, where MIC and MBC values between 2 and 512 µg/mL were observed. In addition, 6o showed higher effectiveness in some

TABLE 8 Antibacterial activity of pyrazole derivatives (4a-j) and pyrazole pyrano[2,3-c]pyrazole derivatives (6a-o) against Gram-positive strains.

Strains		Pyrazole derivatives										Drugs		Pyrano[2,3-c]pyrazole derivatives															
		4a	4b	4c	4d	4e	4f	4g	4h	4i	4j			6a	6b	6c	6d	6e	6f	6g	6h	6i	6j	6k	6l	6m	6n	6o	
10745	(I)	2048	128	-	256	1024	128	512	128	64	64	-	16	512	512	128	1024	256	64	256	128	32	64	64	32	16	16	8	
	(II)	4096	256	-	512	2048	128	1024	128	128	128	-	32	1024	512	128	1024	512	128	256	256	64	64	64	64	16	32	16	
	(III)	12.6	16.8	-	16.2	12.8	17.3	13.7	15.9	18.2	17.3	-	17.3	14.5	14.9	14.3	15.3	14.8	18.9	17.6	18.5	19.1	18.2	21.2	20.3	22.5	19.9	22.4	
29213	(I)	-	-	-	-	-	-	-	-	-	-	16	16	-	-	2048	-	-	512	-	-	256	1024	1024	128	-	-	64	
	(II)	-	-	-	-	-	-	-	-	-	-	32	16	-	-	4096	-	-	1024	-	-	512	2048	1024	256	-	-	128	
	(III)	-	-	-	-	-	-	-	-	-	-	15.1	16.9	-	-	12.2	-	-	13.8	-	-	13.6	12.3	12.9	14.2	-	-	14.1	
19615	(I)	4096	4096	2048	1024	2048	2048	2048	2048	1024	1024	2	8	512	512	16	512	512	8	256	128	4	64	32	4	2	2	2	
	(II)	4096	4096	2048	4096	2048	2048	4096	2048	2048	2048	4	16	1024	1024	16	1024	1024	16	512	128	8	128	64	4	4	2	2	
	(III)	10.4	10.9	10.7	10.2	10.5	11.3	10.4	10.6	11.8	11.5	23.2	18.4	16.4	18.3	20.8	15.9	19.9	19.7	18.8	19.5	23.1	19.4	21.6	22.5	23.1	22.7	22.9	
12386	(I)	-	-	-	-	-	-	-	-	1024	1024	-	4	-	-	64	-	-	32	256	128	16	128	128	8	8	4	2	
	(II)	-	-	-	-	-	-	-	-	4096	2048	-	8	-	-	128	-	-	64	512	256	16	128	128	16	8	8	4	
	(III)	-	-	-	-	-	-	-	-	18.2	17.5	-	19.1	-	-	21.6	-	-	21.0	17.3	16.6	22.1	16.2	19.4	22.4	21.5	21.7	22.3	

(I): Minimum Inhibitory Concentration (µg/mL); (II): Minimum Bactericidal Concentration (µg/mL); (III): Inhibition Zone Diameter (mm); A, penicillin; B, cefazolin.

TABLE 9 Antibacterial activity of pyrazole derivatives (4a-j) and pyrazole pyrano[2,3-c]pyrazole derivatives (6a-o) against gram-negative strains.

Strains		Pyrazole derivatives										Drugs		Pyrano[2,3-c]pyrazole derivatives															
		4a	4b	4c	4d	4e	4f	4g	4h	4i	4j	A	B	6a	6b	6c	6d	6e	6f	6g	6h	6i	6j	6k	6l	6m	6n	6o	
9610	(I)	-	-	-	-	-	-	-	-	-	-	-	64	-	-	-	-	-	-	-	-	-	-	-	-	-	-	-	
	(II)	-	-	-	-	-	-	-	-	-	-	-	128	-	-	-	-	-	-	-	-	-	-	-	-	-	-		
	(III)	-	-	-	-	-	-	-	-	-	-	-	12.0	-	-	-	-	-	-	-	-	-	-	-	-	-	-		
13313	(I)	-	-	-	-	-	-	-	-	1024	1024	-	-	-	-	-	-	-	-	-	-	-	-	-	-	1024	512	512	
	(II)	-	-	-	-	-	-	-	-	4096	2048	-	-	-	-	-	-	-	-	-	-	-	-	-	-	1024	1024	512	
	(III)	-	-	-	-	-	-	-	-	10.7	12.5	-	-	-	-	-	-	-	-	-	-	-	-	-	-	13.6	12.4	12.3	
15442	(I)	-	-	-	-	-	-	-	-	-	-	-	-	-	-	2048	-	-	2048	4096	2048	1024	1024	1024	512	512	256	128	
	(II)	-	-	-	-	-	-	-	-	-	-	-	-	-	-	4096	-	-	2048	4096	4096	1024	2048	2048	1024	512	256	256	
	(III)	-	-	-	-	-	-	-	-	-	-	-	-	-	-	11.8	-	-	11.2	10.1	11.4	12.3	11.9	11.5	12.4	13.6	13.8	13.5	
19606	(I)	-	-	-	-	-	-	-	-	-	1024	-	-	-	-	-	-	-	-	-	-	-	-	-	-	-	-	256	
	(II)	-	-	-	-	-	-	-	-	-	2048	-	-	-	-	-	-	-	-	-	-	-	-	-	-	-	-	512	
	(III)	-	-	-	-	-	-	-	-	-	11.5	-	-	-	-	-	-	-	-	-	-	-	-	-	-	-	-	12.3	

(I): Minimum Inhibitory Concentration (µg/mL); (II): Minimum Bactericidal Concentration (µg/mL); (III): Inhibition Zone Diameter (mm); A, penicillin; B, cefazolin.



TABLE 10 Antibacterial activity of pyrazole derivatives (4a-j) and pyrazole pyrano[2,3-c]pyrazole derivatives (6a-o) against specialized aquatic strains.

Strains			Pyrazole derivatives										Drugs		Pyrano[2,3-c]pyrazole derivatives														
			4a	4b	4c	4d	4e	4f	4g	4h	4i	4j	A	B	6a	6b	6c	6d	6e	6f	6g	6h	6i	6j	6k	6l	6m	6n	6o
Gram-positive	29178	(I)	2048	256	1024	512	1024	512	1024	128	32	32	32	16	4096	-	512	2048	-	256	2048	1024	512	1024	512	128	32	32	32
		(II)	4096	512	2048	1024	2048	512	1024	256	64	64	64	64	4096	-	1024	4096	-	512	4096	2048	512	1024	1024	256	64	64	64
		(III)	11.7	13.8	12.5	11.9	13.0	13.4	11.8	14.2	15.9	16.7	16.6	14.2	10.5	-	1024	11.2	-	13.8	12.1	15.1	14.2	14.4	15.7	13.6	15.7	15.3	15.9
	43921	(I)	-	512	-	1024	2048	512	512	256	256	128	2	-	-	-	128	2048	-	64	512	256	32	256	256	16	4	2	2
		(II)	-	512	-	2048	4096	1024	1024	256	512	256	4	-	-	-	256	4096	-	128	1024	512	128	256	256	32	16	4	2
		(III)	-	12.9	-	11.5	11.9	13.6	14.2	15.4	16.5	17.7	19.7	-	-	-	21.8	10.2	-	20.7	17.6	19.3	21.5	19.8	17.5	22.9	22.6	23.5	23.1
	Gram-negative	29473	(I)	-	-	-	-	-	-	-	2048	2048	-	32	-	-	1024	-	-	1024	4096	4096	1024	4096	2048	512	256	64	64
			(II)	-	-	-	-	-	-	-	4096	4096	-	64	-	-	1024	-	-	2048	4096	4096	1024	4096	4096	512	512	256	128
			(III)	-	-	-	-	-	-	-	11.6	11.1	-	15.9	-	-	12.8	-	-	11.3	12.2	10.3	12.6	10.7	10.9	12.4	13.7	14.5	15.1
		15947	(I)	-	-	-	-	-	-	-	-	-	8	-	-	-	256	-	-	128	2048	1024	64	512	512	16	16	8	4
			(II)	-	-	-	-	-	-	-	-	-	16	-	-	-	512	-	-	128	2048	2048	128	1024	1024	64	16	16	8
			(III)	-	-	-	-	-	-	-	-	-	17.5	-	-	-	17.3	-	-	16.4	15.5	14.9	18.7	17.7	16.2	17.8	19.1	19.5	19.6

(I): Minimum Inhibitory Concentration (µg/mL); (II): Minimum Bactericidal Concentration (µg/mL); (III): Inhibition Zone Diameter (mm);  
A, penicillin; B, cefazolin.

TABLE 11 Antifungal activity of pyrazole derivatives (4a-j) and pyrazole pyrano[2,3-c]pyrazole derivatives (6a-o).

Strains		Pyrazole derivatives										Drugs		Pyrano[2,3-c]pyrazole derivatives														
		4a	4b	4c	4d	4e	4f	4g	4h	4i	4j	A	B	6a	6b	6c	6d	6e	6f	6g	6h	6i	6j	6k	6l	6m	6n	6o
10231	(I)	-	1024	-	4096	2048	1024	2048	1024	512	512	-	32	-	4096	512	-	1024	512	2048	1024	512	1024	512	256	128	128	64
	(II)	-	1024	-	4096	4096	2048	2048	2048	1024	1024	-	64	-	4096	1024	-	2048	1024	2048	2048	512	2048	1024	512	256	256	128
	(III)	-	12.6	-	11.4	11.7	12.1	11.8	13.0	15.9	15.5	-	21.6	-	11.7	16.6	-	12.3	16.9	13.5	14.1	16.3	15.9	16.9	17.8	17.6	17.3	18.4
32045	(I)	-	-	-	-	-	-	-	-	-	-	-	64	-	-	-	-	-	-	-	-	-	-	-	-	-	-	-
	(II)	-	-	-	-	-	-	-	-	-	-	-	128	-	-	-	-	-	-	-	-	-	-	-	-	-	-	-
	(III)	-	-	-	-	-	-	-	-	-	-	-	17.2	-	-	-	-	-	-	-	-	-	-	-	-	-	-	-
7601	(I)	-	-	-	-	-	-	-	-	512	256	-	64	-	-	-	-	-	-	-	-	-	-	-	-	256	256	128
	(II)	-	-	-	-	-	-	-	-	1024	512	-	64	-	-	-	-	-	-	-	-	-	-	-	-	512	256	256
	(III)	-	-	-	-	-	-	-	-	12.7	12.8	-	20.8	-	-	-	-	-	-	-	-	-	-	-	-	13.0	14.6	14.1
1022	(I)	-	512	4096	2048	2048	1024	1024	512	256	256	-	32	2048	-	128	2048	-	64	1024	512	64	512	256	64	16	16	16
	(II)	-	1024	4096	4096	2048	1024	2048	1024	512	256	-	64	4096	-	256	4096	-	128	1024	1024	128	512	512	128	32	32	32
	(III)	-	12.2	14.6	14.8	13.1	13.7	13.8	12.8	15.9	15.5	-	20.3	10.8	-	17.9	11.8	-	18.6	1024	16.3	17.4	17.7	1024	18.2	19.5	19.8	19.3

(I): Minimum Inhibitory Concentration (µg/mL); (II): Minimum Fungicidal Concentration (µg/mL); (III): Inhibition Zone Diameter (mm);  
A, tolnaftate; B, terbinafine.

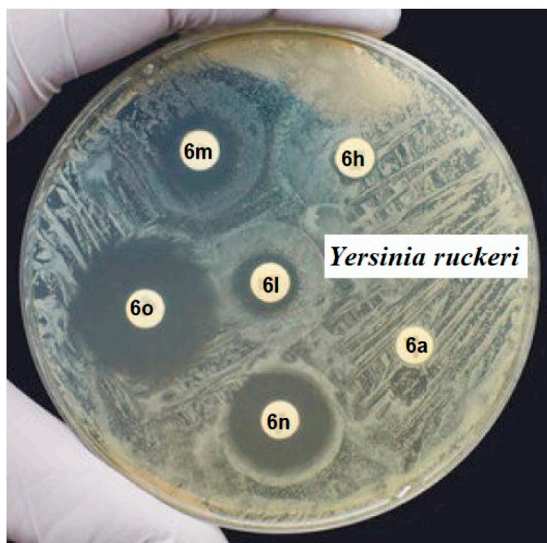


FIGURE 1  
The IZD value results of some pyrano[2,3-c]pyrazole derivatives against *Yersinia ruckeri*.

strains than drugs in the market, such as penicillin, cefazolin, Tolnaftate, and Terbinafine. Finally, the relationship between the antimicrobial properties of the derivatives and their structure were observed and reported.

## Data availability statement

The original contributions presented in the study are included in the article/Supplementary material, further inquiries can be directed to the corresponding author.

## References

- Abshirini, Z., Lotfifar, N., and Zare, A. (2020). A highly effectual and rapid protocol for the synthesis of 5-amino-1, 3-diaryl-1 H-pyrazole-4-carbonitriles using 1, 3-disulfonic acid imidazolium trifluoroacetate as a dual-functional catalyst. *Org. Prep. Proced. Int.* 52, 428–433. doi:10.1080/00304948.2020.1780884
- Amirnejat, S., Nosrati, A., and Javanshir, S. (2020). Superparamagnetic Fe<sub>3</sub>O<sub>4</sub>@Alginate supported L-arginine as a powerful hybrid inorganic–organic nanocatalyst for the one-pot synthesis of pyrazole derivatives. *Appl. Organomet. Chem.* 34, e5888. doi:10.1002/aoc.5888
- Aryan, R., Beyzaei, H., Nojavan, M., and Rezaei, M. (2017). Novel biocompatible glucose-based deep eutectic solvent as recyclable medium and promoter for expedient multicomponent green synthesis of diverse three and four substituted pyrazole-4-carbonitrile derivatives. *Res. Chem. Intermed.* 43, 4731–4744. doi:10.1007/s11164-017-2908-5
- Bakhtiarian, M., and Khodaei, M. M. (2022). Pyridinium-based dual acidic ionic liquid supported on the pectin for efficient synthesis of pyrazoles. *J. Mol. Liq.* 363, 119883. doi:10.1016/j.molliq.2022.119883
- Becerra, D., Abonia, R., and Castillo, J.-C. (2022). Recent applications of the multicomponent synthesis for bioactive pyrazole derivatives. *Molecules* 27, 4723. doi:10.3390/molecules27154723
- Bhaskaruni, S. V., Maddila, S., Gangu, K. K., and Jonnalagadda, S. B. (2020). A review on multi-component green synthesis of N-containing heterocycles using mixed oxides as heterogeneous catalysts. *Arabian J. Chem.* 13, 1142–1178. doi:10.1016/j.arabjc.2017.09.016
- Biglari, M., Shirini, F., Mahmoodi, N. O., Zabihzadeh, M., and Mashhadinezhad, M. (2020). A choline chloride-based deep eutectic solvent promoted three-component synthesis of tetrahydrobenzo [b] pyran and pyrano [2, 3-d] pyrimidinone (thione) derivatives. *J. Mol. Struct.* 1205, 127652. doi:10.1016/j.molstruc.2019.127652
- Calvo-Flores, F. G., and Mingorance-Sánchez, C. (2021). Deep eutectic solvents and multicomponent reactions: two convergent items to green chemistry strategies. *ChemistryOpen* 10, 815–829. doi:10.1002/open.202100137
- Cui, H., Wu, Z., Zhang, L., Ma, Q., Cai, D., Zhang, J., et al. (2023). Design, synthesis, antibacterial activity, and mechanism of novel mesoionic compounds based on natural pyrazole isolated from an endophytic fungus *Colletotrichum gloeosporioides*. *J. Agric. Food Chem.* 71, 10018–10027. doi:10.1021/acs.jafc.3c02908
- El Mejdoubi, K., Sallek, B., Digua, K., Chaair, H., and Oudadesse, H. (2019). Natural phosphate K09 as a new reusable catalyst for the synthesis of dihydropyran [2, 3-c] pyrazole derivatives at room temperature. *Kinet. Catal.* 60, 536–542. doi:10.1134/s0023158419040098
- Fekri, L. Z., Nikpassand, M., Mostaghim, S., and Marvi, O. (2020). Green catalyst-free multi-component synthesis of aminobenzochromenes in deep eutectic solvents. *Org. Prep. Proced. Int.* 52, 81–90. doi:10.1080/00304948.2020.1714319
- Ghorbani, S., Habibi, D., and Heydari, S. (2022). A phenylazophenylenediamine-based La-complex as a superb nanocatalyst for the synthesis of diverse pyrano [2, 3-c] pyrazoles. *J. Mol. Struct.* 1260, 132713. doi:10.1016/j.molstruc.2022.132713
- Ghorbani, S., Habibi, D., Heydari, S., and Ebrahimiasl, H. (2023). The acid modified magnetic carbon quantum dots as a capable nano-catalyst for the synthesis of pyridines and pyrazoles. *Inorg. Chem. Commun.* 156, 111258. doi:10.1016/j.inoche.2023.111258
- Igei, M., Bakavoli, M., Shiri, A., Ebrahimpour, Z., Azizollahi, H., Beyzaei, H., et al. (2016). Synthesis of some new pyrimido [4, 5-e] tetrazolo [5, 1-b] [1, 3, 4] thiadiazine

## Author contributions

IH: Project administration, Writing–review and editing. HT: Conceptualization, Writing–review and editing. AHA-S: Methodology, Writing–original draft. BA: Validation, Writing–original draft. TQ: Formal Analysis, Writing–original draft. MK: Resources, Writing–review and editing. TA: Data curation, Writing–original draft. EA: Methodology, Writing–original draft. EH: Investigation, Writing–original draft. AhA: Supervision, Writing–original draft. ALA: Funding acquisition, Writing–original draft.

## Funding

The author(s) declare financial support was received for the research, authorship, and/or publication of this article. The authors extend their appreciation to the Deanship of Scientific Research at King Khalid University for funding this work through the large research group program under grant number R.G.P.02/535/44.

## Conflict of interest

The authors declare that the research was conducted in the absence of any commercial or financial relationships that could be construed as a potential conflict of interest.

## Publisher's note

All claims expressed in this article are solely those of the authors and do not necessarily represent those of their affiliated organizations, or those of the publisher, the editors and the reviewers. Any product that may be evaluated in this article, or claim that may be made by its manufacturer, is not guaranteed or endorsed by the publisher.

derivatives via an S–N type Smiles rearrangement and their antibacterial evaluation. *J. Chem. Res.* 40, 628–632. doi:10.3184/174751916x14742893137631

Javahershenas, R. (2023). Recent advances in the application of deep eutectic solvents for the synthesis of Spiro heterocyclic scaffolds via multicomponent reactions. *J. Mol. Liq.* 385, 122398. doi:10.1016/j.molliq.2023.122398

John, S. E., Gulati, S., and Shankaraiah, N. (2021). Recent advances in multicomponent reactions and their mechanistic insights: a triennium review. *Org. Chem. Front.* 8, 4237–4287. doi:10.1039/d0qo01480j

Karrabi, M., Malmir, M., Heravi, M. M., and Hosseinnajad, T. (2023). A theoretical and experimental study on ecofriendly-one-pot synthesis of pyrazolopyranopyrimidines catalyzed by CuO functionalized montmorillonite. *Inorg. Chem. Commun.* 149, 110367. doi:10.1016/j.inoche.2022.110367

Khademi, S., Zahmatkesh, S., Aghili, A., and Badri, R. (2021). Tungstic acid ( $H_4WO_6$ ) immobilized on magnetic-based zirconium amino acid metal–organic framework: an efficient heterogeneous Brønsted acid catalyst for 1-(4-phenyl)-2,4-dihydropyrano[2,3-c] pyrazole derivatives preparation. *Appl. Organomet. Chem.* 35, e6192. doi:10.1002/aoc.6192

Khazaal, S., and Ibraheam, S. Y. (2022). One-pot synthesis of new pyranopyrazoles via domino multicomponent reaction. *Egypt. J. Chem.* 65, 259–265. doi:10.21608/EJCHEM.2022.115337.5232

Kiyani, H., and Bamdad, M. (2018). Sodium ascorbate as an expedient catalyst for green synthesis of polysubstituted 5-aminopyrazole-4-carbonitriles and 6-amino-1, 4-dihydropyrano [2, 3-c] pyrazole-5-carbonitriles. *Res. Chem. Intermed.* 44, 2761–2778. doi:10.1007/s11164-018-3260-0

Kondabanthini, S., Katari, N. K., Srimannarayana, M., Gundla, R., Kapavarapu, R., and Pal, M. (2022). Wang resin catalyzed sonochemical synthesis of dihydropyrano [2, 3-c] pyrazole derivatives and their interactions with SIRT1. *J. Mol. Struct.* 1266, 133527. doi:10.1016/j.molstruc.2022.133527

Küçükgüzel, Ş. G., and Şenkardeş, S. (2015). Recent advances in bioactive pyrazoles. *Eur. J. Med. Chem.* 97, 786–815. doi:10.1016/j.ejmech.2014.11.059

Kumar, S., Jain, S., Nehra, M., Dilbaghi, N., Marrazza, G., and Kim, K.-H. (2020). Green synthesis of metal–organic frameworks: a state-of-the-art review of potential environmental and medical applications. *Coord. Chem. Rev.* 420, 213407. doi:10.1016/j.ccr.2020.213407

Kumar, V., Kaur, K., Gupta, G. K., and Sharma, A. K. (2013). Pyrazole containing natural products: synthetic preview and biological significance. *Eur. J. Med. Chem.* 69, 735–753. doi:10.1016/j.ejmech.2013.08.053

Mamaghani, M., and Hossein Nia, R. (2021). A review on the recent multicomponent synthesis of pyranopyrazoles. *Polycycl. Aromat. Compd.* 41, 223–291. doi:10.1080/10406638.2019.1584576

Mathavan, S., and Yamajala, R. B. (2023). Potassium dihydrogen phosphate-catalyzed synthesis of benzylpyrazolyl coumarin and pyrano [2, 3-c] pyrazole derivatives via cascade—one-pot—multicomponent reaction. *J. Heterocycl. Chem.* 60, 123–133. doi:10.1002/jhet.4569

Moghaddam, F. M., Aghili, S., Daneshfar, M., Moghimi, H., and Daneshfar, Z. (2023). Bread waste in the form of  $CoFe_2O_4$ @ TBW catalyst was used as a green biocatalyst to synthesize pyranopyrazole and tetraketone derivatives. *Res. Chem. Intermed.* 49, 1507–1543. doi:10.1007/s11164-022-04934-z

Moghaddam-Manesh, M., and Hosseinzadegan, S. (2021). Introducing new method for the synthesis of polycyclic compounds containing [1, 3] dithiine derivatives, with anticancer and antibacterial activities against common bacterial strains between aquatic and human. *J. Heterocycl. Chem.* 58, 2174–2180. doi:10.1002/jhet.4345

Mohamadpour, F. (2020). Catalyst-free green synthesis of dihydropyrano [2, 3-c] pyrazole scaffolds assisted by ethylene glycol (EG) as a reusable and biodegradable solvent medium. *J. Chem. Sci.* 132, 72–79. doi:10.1007/s12039-020-01775-4

Mohamed, E. A., Abdelmajid, A., Behalo, M., Abel-Maaboud, A., and Hebaish, K. (2022). Green synthesis, cytotoxicity and antimicrobial activities of some new pyrazolines, pyrimidines and naphthyridines based on 1, 3-di (thien-2-yl) prop-2-en-1-one using choline chloride-urea mixture as A deep eutectic solvent. *Egypt. J. Chem.* 65, 651–663.

Mokariya, J. A., Rajani, D. P., and Patel, M. P. (2022). Anomaly of pyrano [2, 3-c] pyrazole synthesis towards pyrazolyl-aryl-methyl-malononitrile derivatives and their antimicrobial activity. *ChemistrySelect* 7, e202201341. doi:10.1002/slct.202201341

Nemati, R., Elhamifar, D., Zarnegaryan, A., and Shaker, M. (2021). Core-shell structured magnetite silica-supported hexatungstate: a novel and powerful nanocatalyst for the synthesis of biologically active pyrazole derivatives. *Appl. Organomet. Chem.* 35, e6409. doi:10.1002/aoc.6409

Nguyen, H. T., Van Le, T., and Tran, P. H. (2021). AC-SO<sub>3</sub>H/[CholineCl] [Urea] 2 as a green catalytic system for the synthesis of pyrano [2, 3-c] pyrazole scaffolds. *J. Environ. Chem. Eng.* 9, 105228. doi:10.1016/j.jece.2021.105228

Nishanth Rao, R., Jena, S., Mukherjee, M., Maiti, B., and Chanda, K. (2021). Green synthesis of biologically active heterocycles of medicinal importance: a review. *Environ. Chem. Lett.* 19, 3315–3358. doi:10.1007/s10311-021-01232-9

Pandey, A., Kumar, A., and Shrivastava, S. (2021). Sugarcane bagasse ash-based silica-supported boric acid (SBA-SiO<sub>2</sub>-H<sub>3</sub>BO<sub>3</sub>): a versatile and reusable catalyst for the synthesis of 1, 4-dihydropyrano [2, 3c] pyrazole derivatives. *Russ. J. Org. Chem.* 57, 653–660. doi:10.1134/s1070428021040229

Parikh, P. H., Timaniya, J. B., Patel, M. J., and Patel, K. P. (2022). Microwave-assisted synthesis of pyrano [2, 3-c]-pyrazole derivatives and their anti-microbial, anti-malarial, anti-tubercular, and anti-cancer activities. *J. Mol. Struct.* 1249, 131605. doi:10.1016/j.molstruc.2021.131605

Patki, A. S., Patil, K. N., Kusuma, S., Muley, D. B., and Jadhav, A. H. (2021). One-pot synthesis of multicomponent pyrazole-4-carbonitrile derivatives under solvent-free condition by using engineered polyvinyl alcohol catalyst. *Res. Chem. Intermed.* 47, 2751–2773. doi:10.1007/s11164-021-04450-6

Poonam, S., and Singh, R. (2019). Facile one-pot synthesis of 5-amino-1 H-pyrazole-4-carbonitriles using alumina–silica-supported MnO<sub>2</sub> as recyclable catalyst in water. *Res. Chem. Intermed.* 45, 4531–4542. doi:10.1007/s11164-019-03847-8

Ramadan, M., Aly, A. A., El-Haleem, L. E. A., Alshammari, M. B., and Bräse, S. (2021). Substituted pyrazoles and their heteroannulated analogs—recent syntheses and biological activities. *Molecules* 26, 4995. doi:10.3390/molecules26164995

Rushell, E., Tailor, Y. K., Khandewal, S., Verma, K., Agarwal, M., and Kumar, M. (2019). Deep eutectic solvent promoted synthesis of structurally diverse hybrid molecules with privileged heterocyclic substructures. *New J. Chem.* 43, 12462–12467. doi:10.1039/c9nj02694k

Shinde, S. K., Patil, M. U., Damate, S. A., and Patil, S. S. (2018). Synergetic effects of naturally sourced metal oxides in organic synthesis: a greener approach for the synthesis of pyrano [2, 3-c] pyrazoles and pyrazolyl-4 H-chromenes. *Res. Chem. Intermed.* 44, 1775–1795. doi:10.1007/s11164-017-3197-8

Sikandar, S., and Zahoor, A. F. (2021). Synthesis of pyrano [2, 3-c] pyrazoles: a review. *J. Heterocycl. Chem.* 58, 685–705. doi:10.1002/jhet.4191

Suksatan, W., Kazemzadeh, P., Afzali, D., Moghaddam-Manesh, M., Chauhan, N. P. S., and Sargazi, G. (2022). A controllable study on ultrasound assisted synthesis of a novel Ni/Zn based hybrid MOF nanostructures for Dextranase immobilization. *Inorg. Chem. Commun.* 139, 109410. doi:10.1016/j.inoche.2022.109410

Suryakumari, A., and Sudhakar, C. (2023). One-pot synthesis of 1, 4 dihydro pyrano [2, 3-c] pyrazole using chitosan-p-toluene sulfonate as a biodegradable catalyst in an aqueous medium. *Lett. Org. Chem.* 20, 596–602. doi:10.2174/1570178620666221216144752

Vanegas, S., Rodríguez, D., and Ochoa-Puentes, C. (2019). An efficient and eco-friendly one-pot synthesis of pyrazolopyridines mediated by choline chloride/urea eutectic mixture. *ChemistrySelect* 4, 3131–3134. doi:10.1002/slct.201900314

Vasava, M. S., Bhoi, M. N., Rathwa, S. K., Shetty, S. S., Patel, R. D., Rajani, D. P., et al. (2019). Novel 1, 4-dihydropyrano [2, 3-c] pyrazole derivatives: synthesis, characterization, biological evaluation and *in silico* study. *J. Mol. Struct.* 1181, 383–402. doi:10.1016/j.molstruc.2018.12.053

Yadav, A., and Pandey, S. (2014). Densities and viscosities of (choline chloride+ urea) deep eutectic solvent and its aqueous mixtures in the temperature range 293.15 K to 363.15 K. *J. Chem. Eng. Data* 59, 2221–2229. doi:10.1021/je5001796

Yahiaoui, A. A., Ghichi, N., Hannachi, D., Djedouani, A., Meskaldji, S., Merazig, H., et al. (2022). Synthesis, XRD/HSA-interactions, biological activity, optical and nonlinear optical responses studies of new pyran derivative. *J. Mol. Struct.* 1263, 133161. doi:10.1016/j.molstruc.2022.133161

Yekke-Ghasemi, Z., Heravi, M. M., Malmir, M., Jahani, G., Bisafar, M. B., and Mirzaei, M. (2022). Fabrication of heterogeneous-based lacunary polyoxometalates as efficient catalysts for the multicomponent and clean synthesis of pyrazolopyranopyrimidines. *Inorg. Chem. Commun.* 140, 109456. doi:10.1016/j.inoche.2022.109456



## OPEN ACCESS

## EDITED BY

Raha Orfali,  
King Saud University, Saudi Arabia

## REVIEWED BY

Abdallah M. A. Hassane,  
Al-Azhar University, Egypt  
Ishtiaq Jeelani,  
University of California, San Diego,  
United States

## \*CORRESPONDENCE

Susana Rodríguez-Couto,  
✉ susana.rodriguez.couto@lut.fi

RECEIVED 30 December 2023

ACCEPTED 04 March 2024

PUBLISHED 13 March 2024

## CITATION

Pinar O and Rodríguez-Couto S (2024),  
Biologically active secondary metabolites from  
white-rot fungi.  
*Front. Chem.* 12:1363354.  
doi: 10.3389/fchem.2024.1363354

## COPYRIGHT

© 2024 Pinar and Rodríguez-Couto. This is an open-access article distributed under the terms of the [Creative Commons Attribution License \(CC BY\)](#). The use, distribution or reproduction in other forums is permitted, provided the original author(s) and the copyright owner(s) are credited and that the original publication in this journal is cited, in accordance with accepted academic practice. No use, distribution or reproduction is permitted which does not comply with these terms.

# Biologically active secondary metabolites from white-rot fungi

Orkun Pinar and Susana Rodríguez-Couto\*

Department of Separation Science, LUT School of Engineering Science, Lappeenranta-Lahti University of Technology LUT, Mikkeli, Finland

In recent years, there has been a considerable rise in the production of novel metabolites derived from fungi compared to the ones originating from bacteria. These organic substances are utilized in various sectors such as farming, healthcare, and pharmaceutical. Since all dividing living cells contain primary metabolites, secondary metabolites are synthesized by utilizing intermediate compounds or by-products generated from the primary metabolic pathways. Secondary metabolites are not critical for the growth and development of an organism; however, they exhibit a variety of distinct biological characteristics. White-rot fungi are the only microorganisms able to decompose all wood components. Hence, they play an important role in both the carbon and nitrogen cycles by decomposing non-living organic substrates. They are ubiquitous in nature, particularly in hardwood (e.g., birch and aspen) forests. White-rot fungi, besides ligninolytic enzymes, produce different bioactive substances during their secondary metabolism including some compounds with antimicrobial and anticancer properties. Such properties could be of potential interest for the pharmaceutical industries. Considering the importance of the untapped biologically active secondary metabolites from white-rot fungi, the present paper reviews the secondary metabolites produced by white-rot fungi with different interesting bioactivities.

## KEYWORDS

white-rot fungi, secondary metabolites, biologically active compounds, bioactive properties, therapeutic substances

## 1 Introduction

Biologically active compounds are synthesized mostly by fungi, bacteria, archaea, and plants. These compounds possess different properties that make them suitable for various applications including drug development with anti-glycaemic, anticancer, antibiotic, antiviral, anti-inflammatory, enzyme inhibiting, hypercholesteremic, immunomodulator, immunosuppressant, cardiovascular, antithrombotic, antidiabetic, antihypertensive, neuropathic, and anti-infective characteristics for humans (Basit et al., 2021; Conrado et al., 2022; Kijpornyongpan et al., 2022). Starting from the 1940s, microorganisms have played a significant role in uncovering important sources of various natural products used in the agrochemical, cosmetic, pharmaceutical, and food industries (Baltz, 2019; Gakuubi et al., 2022). Because of their exceptional biological activities, these compounds have gained the attention of researchers in various fields, including those investigating natural product-derived medicines as well as chemists, biochemists, and microbiologists. In addition, recently, metabolic engineers seek to enlighten regulations, pathways, and gene clusters to produce bioactive compounds efficiently using suitable host organisms with the assistance of genome sequencing to bioinformatics, transcriptomics, metabolomics, and proteomics (Tsukada et al., 2020; Kijpornyongpan et al., 2022). In this sense, microbial



secondary metabolites are beneficial for human wellbeing, owing to their extensive usage in various biological processes spanning across agriculture, medical sciences, food technology, and chemical industry (Yadav, 2021). More specifically, among the different existing microorganisms, fungi have emerged as promising candidates for the discovery of novel biologically active compounds because of their varied pharmacological activities.

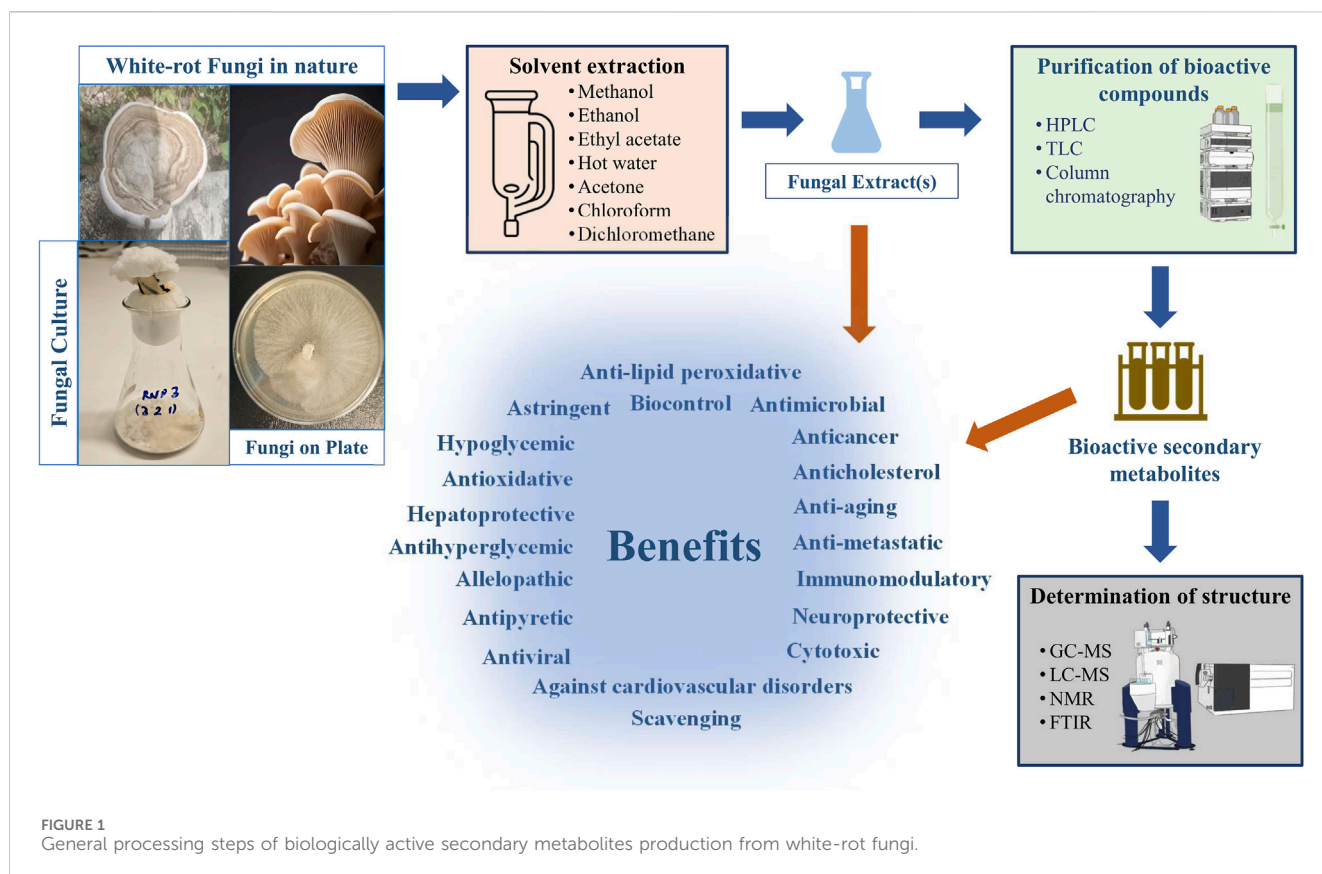
The advantageous effects of fungi on human health have been mainly associated with the abundance of various bioactive compounds, including carbohydrates, proteins, amino acids, unsaturated fatty acids, vitamins, and minerals (Gebreyohannes and Sbhatu, 2023) together with bioactive secondary metabolites. The therapeutic use of fungal species can be traced back to as early as 3000 BC. Thus, macrofungi such as *Ganoderma lucidum* (G. *lucidum*), *Lentinus edodes* (L. *edodes*), *Fomes fomentarius*, and *Fomitopsis officinalis* were used as remedies for different diseases in some East countries (Wasser, 2002). Medical professionals have been aware for over five thousand years regarding the presence of immune-enhancing and defensive attributes in fungal species (Ribka et al., 2021). In the literature, reports indicate that a significant number of approved medications are sourced from nature, with approximately 25% of the one million natural compounds examined showing biological activities. Among these compounds, around 60% originated from plants, while the remaining is derived from microbes. Notably, fungi contribute to approximately 42% of microbial resources, underscoring their significance in the exploration and identification of novel molecules (Bharatiya et al., 2021). Furthermore, until 2019, approximately 35% of the naturally derived products approved by the US Food and Drug Administration (FDA) contributed to the development of pharmaceuticals (Shankar and Sharma, 2022). Moreover, fungi are also able to synthesize various biologically active compounds such as pigments, dyes, antioxidants, nutraceuticals, dietary supplements, polysaccharides, and industrial enzymes (Al-Mousa et al., 2022a; Al-Mousa et al., 2022b; Hassane et al., 2022; Mohamed et al., 2022). These fungal products are not only crucial for functional food and nutrition but also serve as important sources of pharmacological/medicinal substances (Keller, et al., 2005; Hoeksma et al., 2019; Fukushima-Sakuno, 2020; Elhusseiny et al., 2021; Bhambri et al., 2022; Krupodorova et al., 2022). These intriguing scientific discoveries have garnered significant interest from researchers who are exploring the potential applications of these metabolites.

Metabolites are small and intermediate metabolism products that serve various purposes in organisms. These products are classified into primary and secondary metabolites. In this sense, primary metabolites are produced for growth, development, and survival and consist of amino acids, sugars, vitamins, lipids, nucleotides, and carbohydrates, which have critical duties in different metabolic processes including respiration and nutrient consumption. On the other hand, secondary metabolites are not integral components of the metabolic pathways; instead, they are synthesized as byproducts in terms of defense mechanisms and derived from primary metabolism. These compounds exhibit diverse biological functions and result from metabolic reactions that are non-essential for growth and reproduction of organisms. The production of secondary metabolites provides a competitive advantage to the organism by increasing the tolerance to

environmental stresses and extreme conditions, and thereby indirectly influencing ecological dynamics (Devi and Krishnakumari, 2015; Daley et al., 2017; Thirumurugan et al., 2018; Conrado et al., 2022; Rodríguez-Berrios et al., 2023; Sharma et al., 2023). “Secondary metabolites” term was first introduced by the Nobel Prize laureate Albrecht Kossel in 1891 and the botanist Friedrich Czapek further created the term “secondary modifications” in his work related to plant nitrogen metabolism in the 1920s (Henriksen et al., 2022). Secondary metabolites are a diverse group of organic compounds primarily derived from various sources such as plants, fungi, and bacteria. These bioactive molecules are generally low molecular weight compounds (Molecular weight <1,500 Da) (Zerva et al., 2020a). They present scientific interest due to their multiple applications in industries (e.g., textile, functional food innovation, flavoring, glues, oil). Additionally, they hold promising potential for the development of novel pharmaceuticals, antibiotics, insecticides for pest control, and herbicides targeting unwanted plant growth (Devi and Krishnakumari, 2015; Devi et al., 2022; Shankar and Sharma, 2022).

The biosynthesis of fungal secondary bioactive metabolites is typically based on the mevalonic acid pathway, the acetate pathway, and carbohydrate/polysaccharide synthesis (Kundu, 2021). These fungal-derived bioactive compounds can be divided into high and low molecular weight. The former predominantly comprises polysaccharides and enzymes, while the latter encompasses terpenoids, phenols, and indoles, among others (Ziaja-Softys et al., 2022). Conrado et al. (2022) reported that out of the 500,000 secondary metabolites, approximately 70,000 are sourced from microorganisms. Among these compounds, around 33,500 exhibit bioactive properties, and about 47% of these bioactive compounds originate from fungal strains. Up to date, numerous fungal species, particularly filamentous fungi found within the basidiomycetes class, can be considered for an extensive range production of secondary metabolites with significant biological activities (Teoh et al., 2011; Patel and Goyal, 2012). Basidiomycetes are known for their ability to produce numerous secondary metabolites that exhibit antioxidant (Jayakumar et al., 2009), antimicrobial (Bala et al., 2011), anti-inflammatory (Liu et al., 2015), antifungal (Sidorova and Voronina, 2019), and antiviral (Krupodorova et al., 2014) properties. Moreover, they can also produce cytotoxic compounds with the potential use as anticancer agents and immunomodulating polysaccharides. Additionally, some of these metabolites have hallucinogenic effects while others serve as sources for plant growth regulators or flavors (Prasher and Manju, 2019; Halabura et al., 2023).

In recent years, microorganisms belonging to basidiomycetes have become very promising for red (medical) biotechnology (Mizerska-Dudka et al., 2015) and cosmeceuticals (Zerva et al., 2020b). In this sense, white rot fungi are a prominent group within the phylum basidiomycota, which are saprotrophic organisms in the fungal kingdom, encompassing approximately 30%–32% of fungal diversity with an estimated 30,000 distinct species. These fungi can degrade all components of plant cell wall through various mechanisms including extracellular enzymatic processes as well as non-enzymatic ones such as reactive oxygen species (Kijpornyongpan et al., 2022). Due to the



distinct characteristics of white rot fungi, these microorganisms and their extracellular enzymes that primarily include lignin peroxidases (LiPs, EC 1.11.1.14), manganese-dependent peroxidases (MnPs, EC 1.11.1.13), and laccases (benzenediol: oxygen oxidoreductases, EC 1.10.3) along with additional enzymes such as peroxidase-generating oxidases and mycelium-associated dehydrogenases (Martínez et al., 2005) have been recognized for their potential in various biotechnological applications. With the aid of these enzymes, white-rot fungi possess the capacity to break down intricate plant cell wall polymers such as cellulose, hemicellulose, and lignin. White-rot fungi represent the only known group of organisms that have evolved to effectively break down lignin into carbon dioxide (CO<sub>2</sub>) and water (H<sub>2</sub>O) which contributes significantly to Earth's ecosystem (Floudas et al., 2012; Kundu, 2021; Llanos-López et al., 2023).

White rot fungi possess a significant capacity to produce numerous enzymes and secondary metabolites, exhibiting potential in the fields of nutrition, medicine, and degradation. These secondary metabolites, including terpenoids, polyphenols, sterols, flavonoids, alkaloids, derivatives of benzoic acid, quinolones, anthraquinones, and lactones possess bioactive characteristics (Jaszek et al., 2013; Jaszek et al., 2014; Fernando et al., 2016; Bogale, 2020; Kundu and Khan, 2021; Mahuri et al., 2023). Moreover, considering the economic significance and the intention of applications based on biologically active secondary metabolites, there has been a rising global interest in these compounds produced by white rot fungi. Thus, recognizing the great potential of biologically active secondary metabolites from white-rot fungi, this

review focuses on exploring the secondary metabolites generated by them, emphasizing their fascinating bioactive properties.

## 2 Biologically active secondary metabolites produced by white-rot fungi

Secondary bioactive metabolites produced by white rot fungi have significant potential of applicability in various sectors such as pharmaceutical production (Zheng et al., 2010), biobleaching processes in pulp and paper industries (Jerusik, 2010), wastewater treatment approaches (Muszyńska et al., 2019), enhancing digestibility of cellulose and lignin in animals (Yilkal, 2015), generation of renewable resources from lignocellulosic materials, and bioremediation technologies (Korcan et al., 2012; Contreras et al., 2023) (Figure 1). In the literature, several works have revealed the production of biologically active secondary metabolites of white-rot fungi (Table 1). Moreover, the chemical structures of some bioactive secondary metabolites from white-rot fungi are illustrated in Table 2. Considering this, the *Schizophyllum* genus has been an important white-rot fungal genus with the capability of producing bioactive secondary metabolites. The combined treatment of radiotherapy and sizofiran, a polysaccharide extract from the culture broth of *Schizophyllum commune* (*S. commune*), resulted in a significantly higher 5-year survival rate with 90 patients compared to 82 patients treated with radiotherapy alone. Sizofiran demonstrated promising potential as an

TABLE 1 Bioactive secondary metabolites from white-rot fungi and their benefits.

Strain name	Bioactive compound(s)	Benefits	References
<i>S. commune</i>	Sizofiran	Anticancer	Miyazaki et al. (1995)
<i>S. commune</i>	Schizostatin	Anticholesterol	Tanimoto et al. (1996)
<i>S. commune</i>	Phenyl benzoate (C <sub>13</sub> H <sub>10</sub> O <sub>2</sub> ), 4-(phenyl methoxy) phenol (C <sub>13</sub> H <sub>12</sub> O <sub>2</sub> ), pyrrolo (1, 2-a) piperazine-3, 6-dione (C <sub>7</sub> H <sub>10</sub> O <sub>2</sub> N <sub>2</sub> ), gallic acid, and L-ascorbic acid	Antioxidative Antibacterial	Tripathi and Tiwary (2013)
<i>S. commune</i>	Gallic acid, catechin, chlorogenic acid, epicatechin, caffeic acid, coumaric acid, rutin quercetin, and kaempferol	Antioxidative Biocontrol agent	Kaur et al. (2018)
<i>S. commune</i>	Phenolics, flavonoids, alkaloids, tannins, and saponins	Antioxidative	Kumar et al. (2018)
<i>S. commune</i>	Schizostatin	Antimicrobial	Dutta et al. (2019)
<i>P. ostreatus</i>	Lovastatin	Anticholesterol	Alam et al. (2009)
<i>P. sajor-caju</i>			
<i>P. florida</i>			
<i>P. florida</i>	Not determined	Antibacterial	Fagade and Oyelade (2009)
<i>P. fulvus</i>			
<i>P. pulmonarius</i>	Total phenols and flavonoids	Antioxidative Antimicrobial	Ramesh and Pattar (2010)
<i>P. ostreatus</i>	Not determined	Antihyperglycemic	Ghaly et al. (2011)
<i>P. ostreatus</i>	Polysaccharides	Antioxidative	Zhang et al. (2012)
<i>P. sajor-caju</i>	Exopolysaccharide (EPS) and intracellular polysaccharides (IPs)	Anticancer	Assis et al. (2013)
<i>P. ostreatus</i>	β-glucan	Antioxidative	Mitra et al. (2013)
<i>P. cystidiosus</i>	Alkaloids, flavonoids, saponins, and terpenoids	Antimicrobial	Kalaw and Albinto (2014)
		Antioxidative	
<i>P. ostreatoroseus</i>	Free sugars, organic acids, phenolic compounds, and tocopherols	Antioxidative	Corrêa et al. (2015)
		Anti-inflammatory Antimicrobial	
<i>P. sajor caju</i>	Phenols, flavonoids, tannins, and alkaloids	Antimicrobial	Devi and Krishnakumari (2015)
		Anticancer	
		Antipyretic	
		Astringent	
		Antiviral	
<i>P. ostreatus</i>	Phenols and flavonoids	Antioxidative Antimicrobial	Chowdhury et al. (2015)
<i>P. ostreatus</i>	Phenolic acids, resveratrol, triterpenic compounds, and ergosterol	Antioxidative	Koutrotsios et al. (2018)
<i>P. eryngii</i>			
<i>P. nebrodensis</i>			
<i>P. ostreatus</i>	Flavonoids, total phenols	Antioxidative	Beltrán Delgado et al. (2021)
<i>P. pulmonarius</i>	Exopolysaccharides	Antioxidative	Ogidi et al. (2020)
		Antimicrobial	
<i>P. ostreatus</i>	Phenolics, and flavonoids including catechin, kaempferol, apigenin	Anticancer, antiviral, antioxidative	Elhusseiny et al. (2021)
<i>C. indica</i>	Phenol, glycerine, pimelic ketone, D-ribonic acid, methyl myristate, palmitic acid methyl ester, oleic acid ethyl ester, lauramide, oleic acid amide, 1,2-cyclododecanediol, resorcinol, and phytol	Antimicrobial	Ogidi et al. (2020)
		Antioxidative	
		Anti-inflammatory	

(Continued on following page)

TABLE 1 (Continued) Bioactive secondary metabolites from white-rot fungi and their benefits.

Strain name	Bioactive compound(s)	Benefits	References
		Immunomodulator	
		Antitumor	
<i>L. edodes</i>	Lentinan	Anticancer	Oba et al. (2009)
<i>L. edodes</i>	High phenols and flavonoids	Antioxidative	Chowdhury et al. (2015)
		Antimicrobial	
<i>L. edodes</i>	Ergosterol and trilinolein	Antioxidative	Resurreccion et al. (2016)
		Anticancer	
		Against cardiovascular disorders	
<i>L. tigrinus</i>	Not determined	Antioxidative	Sevindik (2018a)
		Antimicrobial	
<i>L. edodes</i>	Catechin and quercetin	Anticancer	Elhusseiny et al. (2021)
		Antiviral	
		Antioxidative	
<i>L. swartzii</i>	Not determined	Antioxidative	Austria et al. (2021)
		Antidiabetic	
<i>L. squarrosulus</i>	Not determined	Antioxidative	Muslihin et al. (2022)
<i>C. versicolor</i>	Extracellular polysaccharopeptides (PSP)	Immunomodulator	Lin et al. (2008)
<i>P. strigellus</i>	Panapophenanthrin, panepophenanthrin, and dihydrohypnophilin	Antimicrobial, anticancer	Llanos-López et al. (2023)
<i>H. tessulatus</i>	Phenols and flavonoids	Antioxidative	Chowdhury et al. (2015)
		Antimicrobial	
<i>C. cylindracea</i>	Not determined	Antioxidative	Sevindik et al. (2018)
		Anti-inflammatory	
		Anticancer	
<i>G. frondosa</i>	Not determined	Anticancer	Masuda et al. (2008)
		Anti-metastatic	
<i>G. frondosa</i>	Not determined	Anticancer	Masuda et al. (2009)
		Anti-metastatic	
<i>G. frondosa</i>	Not determined	Anticancer	Deng et al. (2009)
<i>G. frondosa</i>	Water-soluble polysaccharides	Anti-inflammatory	Su et al. (2020)
		Anticancer	
<i>O. leariis</i>	Irofulven	Anticancer	Eckhardt et al. (2000)
<i>P. chrysosporium</i> <i>P. brevispora</i> <i>P. floridensis</i>	Not determined	Antioxidative	Chandra et al. (2019)
<i>H. erinaceus</i>	Erinacine A	Neuroprotective	Lee et al. (2014)
<i>H. erinaceus</i>	Hericenones C, D, and F	Anti-inflammatory	Lee et al. (2016)
<i>H. erinaceus</i>	Erinacine A	Neuroprotective	Chang et al. (2016)
<i>H. erinaceus</i>	Terpenoid backbones, diterpenoids, sesquiterpenes, and polyketides	Neuroprotective	Chen et al. (2017)
<i>H. erinaceus</i>	4-chloro-3,5-dimethoxybenzoic methyl ester, 3-(hydroxymethyl)-2-furaldehyde, erinacine A, erinacine G, herierin III, and herierin IV	Neuroprotective Neuritogenic	Zhang et al. (2017)

(Continued on following page)

TABLE 1 (Continued) Bioactive secondary metabolites from white-rot fungi and their benefits.

Strain name	Bioactive compound(s)	Benefits	References
<i>H. erinaceus</i>	Erinacine A and S	Anti-neurodegenerative Neuroprotective	Tzeng et al. (2018)
<i>H. erinaceus</i>	Erinacine A, hericenone C, and hericenones D	Anti-aging	Ratto et al. (2019)
<i>H. erinaceus</i>	Erinacine A, hericenone C, hericenone D, and ergothioneine	Anti-aging, Neuroprotective	Roda et al. (2021)
<i>H. erinaceus</i>	Ergothioneine	Anti-aging, Neuroprotective	Roda et al. (2022)
<i>H. erinaceus</i>	Ergothioneine	Anti-aging, Neuroprotective	Roda et al. (2023)
<i>I. lacteus</i>	Irpexlacte A-D, irlactin E, and 3 $\beta$ -hydroxycinnamolide	Antioxidative	Duan et al. (2019)
		Antimicrobial	
<i>P. pini</i>	Gallic acid, catechin, chlorogenic acid, epicatechin, caffeic acid, umbelliferone, coumaric acid, tert-butyl-hydroquinone, and quercetin	Antioxidative	Devi et al. (2022)
<i>B. adusta</i>	Not determined	Antioxidative	İldiz et al. (2022)
		Antimicrobial	
<i>H. myxotricha</i>	Not determined	Antioxidative	Krupodorova et al. (2022)
		Antimicrobial	
<i>C. unicolor</i>	Crude endopolysaccharides (c-EPL) and low molecular weight compound (ex-LMS)	Antioxidative	Jaszek et al. (2013)
		Antibacterial	
<i>C. unicolor</i>	Endopolysaccharides (c-EPL) and a low molecular weight metabolites (ex-LMS)	Antiviral	Mizerska-Dudka et al. (2015)
		Anticancer Immunostimulatory Antiproliferative	
<i>C. unicolor</i>	Not determined	Antioxidative	Sevindik (2018b)
		Antimicrobial	
<i>C. unicolor</i>	Low molecular weight compounds	Anticancer	Matuszewska et al. (2019)
		Antioxidative	
<i>A. fuscosuccinea</i>	Alkaloids and tannins glycosides	Antimicrobial	Romorosa et al. (2017)
<i>C. comatus</i>	Alkaloids, flavonoids, saponins, and terpenoids, steroids and cardiac glycosides	Antimicrobial	Kalaw and Albinto (2014)
		Antioxidative	
<i>C. comatus</i>	4-hydroxybenzoic acid, protocatechuic acid, cinnamic acid, p-coumaric acid, caffeic acid, and quinic acid	Antioxidative	Stilinović et al. (2020)
		Hepatoprotective	
<i>P. ribis</i>	Carbohydrates, proteins, amino acids, lipids, alkaloids, glycosides, cardiac glycerides, flavonoids, phenols, terpenoids, steroids, sterols, saponins, tannins, and phosphate	Antimicrobial	Ribka et al. (2021)
<i>P. gramocephalus</i>	Alkaloids, flavonoids, triterpenes, essential oils, phenols, fatty acids, anthraquinones, coumarins, anthrones, tannins, and steroids	Antioxidative	Aquino et al. (2018)
<i>A. alternata</i>	Not determined	Antimicrobial	Chatterjee et al. (2019)
		Antioxidative	
<i>Alternaria</i> sp	Sinapate, 4-hydroxystyrene, piceatannol, and taxifolin	Antimicrobial	Lu et al. (2020a)
		Antioxidative	
<i>I. obliquus</i>	Not determined	Antihyperglycemic	Sun et al. (2008)
		Anti-lipid peroxidative	
		Antioxidative	
<i>I. obliquus</i>	Lanosterol, 3 $\beta$ -hydroxy-8,24-dien-21-al, ergosterol, inotodiol, ergosterol peroxide, and trametenolic acid	Anti-inflammatory	Ma et al. (2013)

(Continued on following page)



TABLE 1 (Continued) Bioactive secondary metabolites from white-rot fungi and their benefits.

Strain name	Bioactive compound(s)	Benefits	References
		Anticancer	
<i>I. obliquus</i>	Epicatechin-3-gallate, epigallocatechin-3-gallate, naringin, ferulic acid and gallic acid properties	Antioxidative	Xu et al. (2016)
<i>I. obliquus</i>	3 $\beta$ -hydroxy lanosta-8,24-dien-21, (+)-fuscoporianol C, inonotsutriol E, inotodiol, inonotsutriol A, trametenolic acid, saponaceous acid I, and chagabusone A.	Cytotoxicity	Baek et al. (2018)
		Anticancer	
<i>I. obliquus</i>	3 $\beta$ -hydroxy-8,24-dien-21-al, inotodiol, betulin, betulinic acid-3-O-caffeate, trametenolic acid, and melanin	Anti-inflammatory	Wold et al. (2020)
		Immunological	
		Anticancer	
<i>I. obliquus</i>	Betulin, betulinic acid, inotodiol, and trametenolic acid	Anti-proliferative	Kim et al. (2020)
		Anticancer	
<i>I. obliquus</i>	3 $\beta$ ,22,24-trihydroxy-lanosterol-8,25-diene, oleanolic acid, 3 $\beta$ -hydroxy-lanoster-8,24-dien-21-acid, 3 $\beta$ ,21-Dihydroxy-lanosterol-8,24 diene, betulin, inotodiol, 3 $\beta$ -Hydroxy-lanoster-8,24 dien-21-aldehyde, and lanosterol	Anti-hyperuricemic	Luo et al. (2021)
		Anti-inflammation	
<i>I. obliquus</i>	Gallic acid, ferulic acid, flavonoids epicatechin-3-gallate, epigallocatechin-3-gallate, naringin, rutin, naringenin, phelligrudin G, inoscavin B, and davallialektone	Antioxidative	Zhao et al. (2021)
<i>I. obliquus</i>	Seven lanostane-type triterpenoids	Anti-neuroinflammatory	Kou et al. (2021)
<i>I. obliquus</i>	Gallic acid, protocatechuic acid, salicylic acid, vanillic acid, 2,3-dihydroxybenzaldehyde, 2,5-dihydroxyterephthalic acid, coumaric acid, caffeic acid, 4-methoxycinnamic acid, hispidin, ferrulic acid, isorhamnetin, myricetin, quercetin, syringic acid, ellagic acid, hispolon, 3,4-dihydroxybenzalacetone, and 3-O-methylellagic acid	Antioxidative	Abu-Reidah et al. (2021)
<i>I. obliquus</i>	Phelligrudin D	Antioxidative	Li et al. (2021)
		Antidiabetic	
<i>I. obliquus</i>	Procyanidin, caffeic acid, p-coumaric acid, isorhamnetin-3-O-glucoside, astilbin, tangeretin, gallic acid, kaempferol, quercetin, and catechin	Antioxidative	Wang et al. (2021)
<i>I. obliquus</i>	Forty-six triterpenoids	Antihyperglycemic	Chen et al. (2021)
<i>I. obliquus</i>	Inotodiol, lanosterol, and trametenolic acid	Improved lipid accumulation	Peng et al. (2022)
<i>L. quercina</i>	Phenol and flavonoid content	Antioxidative	Ogidi et al. (2018)
<i>P. nuda</i>	Tricaproin and 13-Docosenamide, (Z)-	Antioxidative	Prasher and Manju (2019)
		Anti-tumor	
		Antibacterial	
		Immunostimulant Lipoxigenase-inhibitor	
		Anti-aging	
		Analgesic	
		Antidiabetic	
		Anti-inflammatory	
		Antidermatitic	
		Antileukemic	
		Anticancer	
		Hepatoprotective	
		Hypocholesterolemic	

(Continued on following page)

TABLE 1 (Continued) Bioactive secondary metabolites from white-rot fungi and their benefits.

Strain name	Bioactive compound(s)	Benefits	References
		Antitumor	
		Anticancer	
		Antibacterial	
		Antifungal	
<i>F. flavus</i>	Phenolics and flavonoids	Antioxidative	Fernando et al. (2016)
<i>X. feejeensis</i>	Phenolics and flavonoids	Antioxidative	Fernando et al. (2016)
<i>F. torulosa</i>	Pentacyclic triterpenoids (fusicortones A and B)	Antimicrobial	Noji et al. (2021)
<i>G. lucidum</i>	Triterpenes, steroids, and polysaccharides	Antihyperglycemic	Baby et al. (2015)
<i>G. lucidum</i>	Triterpenes, steroids, and polysaccharides	Antihyperglycemic	Baby et al. (2015)
<i>G. applanatum</i>	Exopolymer	Antihyperglycemic	Yang et al. (2007)
<i>G. lucidum</i>	Lucidenic acids	Anticancer	Weng et al. (2007)
<i>G. lucidum</i>	Ethyl lucidenate (ethyl 7 $\beta$ -hydroxy-4,4,14 $\alpha$ -trimethyl-3,11,15-trioxo-5 $\alpha$ -chol-8-en-24-oate)	Antitumor	Li et al. (2013)
<i>G. applanatum</i>	Exopolysaccharides	Anticancer	Osińska-Jaroszuk et al. (2014)
		Antibacterial	
<i>G. lucidum</i>	Ganoderic acids	Anticancer	Upadhyay et al. (2014)
		Antibacterial	
<i>G. lucidum</i>	Polysaccharides	Anticancer	Li et al. (2018)
<i>G. sinense</i>			
<i>G. lucidum</i>	Lanostane triterpene, and aromatic meroterpenoids	Antioxidant	Wang et al. (2019a)
		Neuroprotective	
<i>G. lucidum</i> Lurongzhi	Ganoderic acids	Anticancer	Zhang et al. (2019)
<i>G. sinensi</i>			
<i>G. lucidum</i>	Polysaccharides	Antitumor	Bhat et al. (2021)
		Antioxidant	
		Immunomodulator	
		Antibacterial	
		Neuroprotective	
		Hypoglycemic	
		Hepatoprotective	
<i>G. lucidum</i>	Fucoxyloolmannan	Anticancer	Milhorini et al. (2022)
<i>G. applanatum</i>	Not determined	Antibiotic	Hassan et al. (2019)
<i>G. lucidum</i>	Polysaccharides, triterpenoids	Antimicrobial	Uma Gowrie et al. (2014)
<i>G. lucidum</i>	Not determined	Antimicrobial	Hleba et al. (2014)
<i>G. boninense</i>	Dodecanoic acid, cyclododecane, octadecanoic acid, 9-octadecenoic acid, hexadecanoic acid, methyl tetradecanoate, 9, 12-octadecadienoic acid, dodecyl acrylate, and hexadecanoic acid	Antibacterial	Ismail et al. (2014)
<i>G. lucidum</i>	Not determined	Antioxidant	Hoque et al. (2015)
		Antibacterial	
		Cytotoxicity	

(Continued on following page)

TABLE 1 (Continued) Bioactive secondary metabolites from white-rot fungi and their benefits.

Strain name	Bioactive compound(s)	Benefits	References
<i>G. lucidum</i>	Alkaloids, tannins, glycosides, and saponins	Antimicrobial	Romorosa et al. (2017)
<i>G. lucidum</i>	Triterpenoids, polysaccharides	Antiviral	Ahmad et al. (2021)
<i>G. boninense</i>	Not determined	Antibacterial	Chan and Chong (2022)
<i>G. neo-japonicum</i>	Flavonoids	Antioxidant	Ayimbila et al. (2023)
<i>G. lucidum</i>		Antibacterial	
<i>G. lucidum</i>	Polysaccharides, triterpenes, peptides, and polysaccharide peptides	Anti-aging	Wang et al. (2017)
<i>T. versicolor</i>	Not determined	Antimicrobial	Hleba et al. (2014)
<i>T. hirsuta</i>	Flavonoids	Antimicrobial	Romorosa et al. (2017)
<i>T. gibbosa</i>	Cerevisterol	Antibiotic	Appiah et al. (2020)
<i>T. elegans</i>			
<i>T. elegans</i>	Flavonoids, tannins, phenols, steroids, alkaloids, anthraquinones, anthrones, coumarins, essential oils, and fatty acids	Scavenging	Nanglihan et al. (2018)
		Antibacterial	
		Cytotoxicity	
<i>Trametes</i> spp.	Not determined	Antimicrobial	Gebreyohannes et al. (2019)
<i>T. versicolor</i>	Sesquiterpenes	Antimicrobial	Gebreyohannes et al. (2019)
<i>T. versicolor</i>	Not determined	Antibiotic	Hassan et al. (2019)
<i>T. versicolor</i>	Phenolics, flavonoids, ascorbic acid, β-carotene, and lycopene	Antimicrobial	Bains and Chawla (2020)
		Anti-inflammatory	
<i>T. polyzona</i>	Caprylic acid methyl ester, tridecanoic acid methyl ester, myristoleic acid methyl ester, cis-10 pentadecanoic acid methyl ester, palmitoleic acid methyl ester, heptadecanoic acid methyl ester, stearic acid methyl ester, elaidic acid methyl ester, oleic acid methyl ester, linolelaidic acid methyl ester, g- linoleic acid methyl ester, x-linolenic acid methyl ester, heneicosanoic acid methyl ester, and cis-11-14-eicosadienoic acid methyl ester	Antimicrobial	Oyetayo and Akingbesote (2022)
<i>T. hirsuta</i>	Not determined	Antimicrobial	Begum et al. (2023)
<i>T. versicolor</i>	Sesquiterpenes	Antimicrobial	Wei et al. (2023)
<i>T. versicolor</i>	Not determined	Anti-leishmanial	Leliebre-Lara et al. (2015)
<i>T. versicolor</i>	Not determined	Anti <i>Fusarium langsethiae</i> (cereal pathogen)	Parroni et al. (2019)
<i>T. versicolor</i>	Polysaccharopeptide	Anti morphine addiction	Wang et al. (2019b)
<i>T. orientalis</i>	Polysaccharide	Chemoprotective	Zheng et al. (2017)
<i>T. versicolor</i>	Polysaccharides	Anticancer	Roca-Lema et al. (2019)
<i>T. versicolor</i>	Musarin	Anticancer	He et al. (2021)

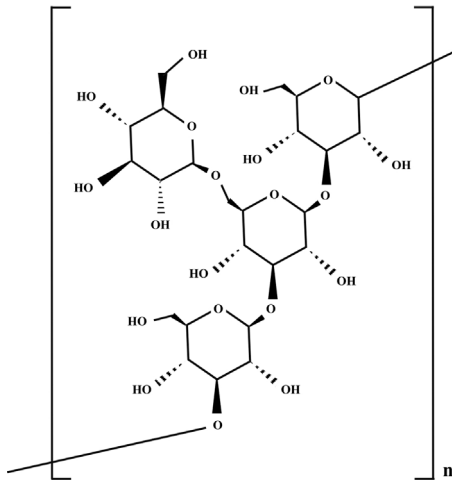
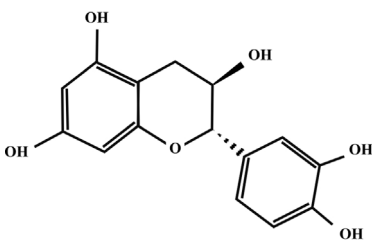
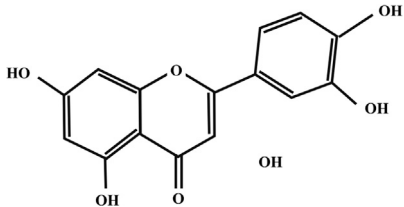
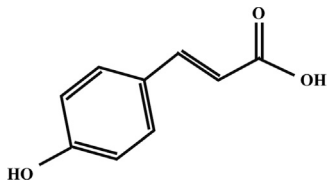
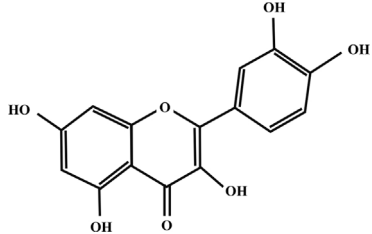
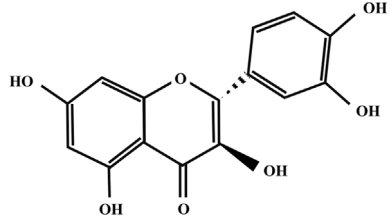
immunotherapeutic agent in the treatment of cervical carcinoma (Miyazaki et al., 1995).

Tanimoto et al. (1996) extracted and identified a novel metabolite, schizostatin, from *S. commune* with the ability to inhibit rat liver microsomal squalene synthase to control cholesterol levels. However, in terms of antimicrobial effects, schizostatin showed no antimicrobial activity at a concentration of 1 mg/mL against many microorganisms including *Bacillus subtilis* (*B. subtilis*), *Candida albicans* (*C. albicans*), *Escherichia coli* (*E. coli*),

*Mycobacterium smegmatis*, *Mycoplasma mycoides*, *Proteus vulgaris*, *Proteus mirabilis*, and *Staphylococcus aureus* (*S. aureus*).

Tripathi and Tiwary (2013) investigated the production of bioactive compounds from the solvent extracts (methanol, ethanol, acetone, ethyl acetate, and hot water) of *S. commune* isolated from the Achanakmar-Amarkantak Biosphere Reserve of Central India. In that work, phenolic compounds (i.e., phenyl benzoate (C<sub>13</sub>H<sub>10</sub>O<sub>2</sub>) and 4-(phenyl methoxy) phenol (C<sub>13</sub>H<sub>12</sub>O<sub>2</sub>)) with antioxidant activity and the antibacterial

TABLE 2 Illustration of chemical structures of some bioactive secondary metabolites from white-rot fungi.

Bioactive compound	Chemical structure
Sizofiran	
Catechin	
Kaempferol	
Coumaric acid	
Quercetin	
Taxifolin	

(Continued on following page)

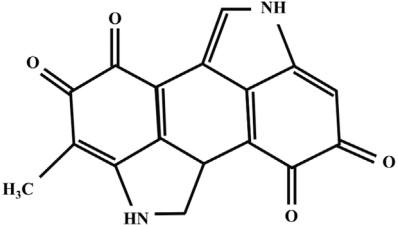
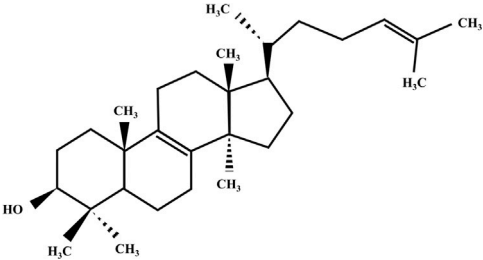
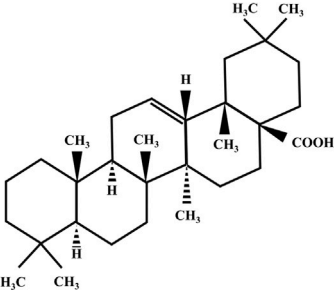
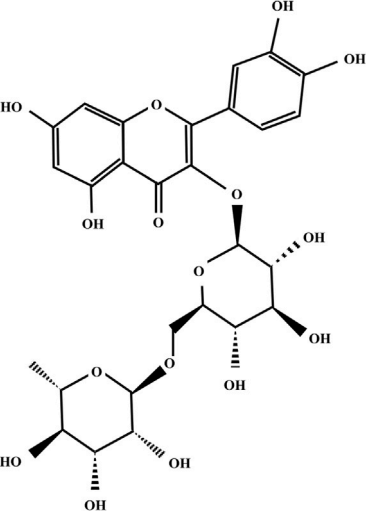
TABLE 2 (Continued) Illustration of chemical structures of some bioactive secondary metabolites from white-rot fungi.

Bioactive compound	Chemical structure
$\beta$ -glucan	
Betulin	
Betulinic acid	
Inotodiol	
Trametenolic acid	

(Continued on following page)



TABLE 2 (Continued) Illustration of chemical structures of some bioactive secondary metabolites from white-rot fungi.

Bioactive compound	Chemical structure
Melanin	
Lanosterol	
Oleanolic acid	
Rutin	

compound pyrrolo (1, 2-a) piperazine-3, 6-dione ( $C_7H_{10}O_2N_2$ ) were identified from the ethanolic and methanolic extracts, respectively. Moreover, they also detected gallic acid and L-ascorbic acid as antioxidant metabolites of both *S. commune* ethanol and methanol extracts. Therefore, it was suggested that *S. commune* could be used for the production of valuable therapeutic agents having antimicrobial and antioxidant activities.

Among several fungal isolates tested for the insecticidal potential against the tobacco cutworm *Spodoptera litura* (*S. litura*), ethyl acetate extracts of *S. commune*, isolated from Aloe vera, showed the strongest

insecticidal activity (Kaur et al., 2018). The HPLC analysis of the fungal extract indicated that it contained various phenolic compounds such as gallic acid, catechin, chlorogenic acid, epicatechin, caffeic acid, coumaric acid, rutin quercetin, and kaempferol. Larvae of *S. litura* treated with that *S. commune* extract exhibited a notable decrease in the occurrence of living haemocytes with 40.00%–73.33% mortality, as well as an elevated incidence of apoptotic and necrotic cells through the cytotoxic effect of the fungal extract. Moreover, the effect of the fungal extract on tetrazolium dye mammalian viability assay (MTT) on Chinese Hamster Ovary (CHO) cell lines was carried out with a cell viability of 81.82%

which was higher than the control (below 60%) consisting of doxorubicin treated cells. Additionally, the evaluation of the genotoxic effect of the *S. commune* ethyl acetate extract at various exposition times using the comet assay showed that the increasing oxidative stress triggered more DNA damage in haemocytes of *S. litura*. As a result of all the findings, the *S. commune* extract was proposed as a potential biocontrol agent.

Water, acetone, and ethanol extracts of *S. commune* exhibited a free radical scavenging activity of 19.65% at a concentration of 100 µg/mL (Kumar et al., 2018). Moreover, at the same concentration, the superoxide anion scavenging activity and the hydroxyl radical scavenging activity for *S. commune* extract was determined as 4.84% and 7.50%, respectively, whereas the total antioxidant capacity (TAC) of *S. commune* extract was found to be 12.15% using ascorbic acid as a reference standard. According to the quantitative analysis of *S. commune* mycochemicals, phenolics, flavonoids, alkaloids, tannins, and saponins were found to be  $10.80 \pm 0.76$ ,  $4.67 \pm 0.23$ ,  $4.26 \pm 0.54$ ,  $1.24 \pm 0.16$ , and  $23.83 \pm 0.84$  (mg/g), respectively. Compared to the edible fungi *Tricholoma nudum* and *Psalliota campestris*, a higher number of bioactive compounds (except for the content in phenolics) was obtained from *S. commune*. Overall, those results indicated that *S. commune* can serve as a valuable source of antioxidants for human health, and it was proposed that their extracts had the potential to be used for the development of drugs to lower the oxidative stress in the body.

Culture filtrate and bioactive metabolites from chloroform extracts of *S. commune* were investigated for their antimicrobial properties against different types of plant pathogens (Dutta et al., 2019). In that work, pepper fruits were treated with schizostatin and then infected with *Colletotrichum gloeosporioides* (*C. gloeosporioides*) or *Botrytis cinerea* (*B. cinerea*). For *C. gloeosporioides* infection (for anthracnose), significant effect for the control of the disease was observed from the treatment with 10 µg/mL and reached maximum with 97.8% and 100.0% by 100 µg/mL and 150 µg/mL treatment, respectively. Moreover, the control of the disease for *B. cinerea* (cause of gray mold disease) was 83.2% and 94.6% by treatment with 100 mg/mL and 150 mg/mL, respectively. The incidence of anthracnose in field conditions showed a decrease when treated with a diluted solution (12.5%) of a culture filtrate derived from *S. commune*. In that paper, the compound responsible for its antifungal and disease-control activity was identified as schizostatin. On the other hand, the growth of fungal pepper plant pathogens was inhibited by *S. commune* culture filtrate, while bacterial pathogens *Ralstonia solanacearum* and *Pectobacterium carotovorum* were unaffected by schizostatin. Thus, it was proposed that schizostatin had the potential to be utilized as a biochemical pesticide for controlling fungal infections, including anthracnose and gray mold, in various types of vegetables.

Alam et al. (2009) discovered that feeding hypercholesterolemic rats with a 5% of fruiting body powders of *Pleurotus ostreatus* (*P. ostreatus*), *Pleurotus sajor-caju* (*P. sajor-caju*), and *Pleurotus florida* (*P. florida*) resulted in substantial reductions in total cholesterol levels (by 37.0%, 21.0%, and 16.0%, respectively) and triglyceride levels (by 45.0%, 24.0%, and 14.0%, respectively) in plasma which were attributed to the content of lovastatin in the fungal powders. Also, they compared the effect of *P. sajor-caju* on plasma and fecal lipid profiles as well as liver and kidney function in rats with high

and normal cholesterol levels. The low-density lipoproteins (LDL)/high-density lipoproteins (HDL) ratio also exhibited significant decreases of 64.0%, 45.0%, and 41.0% for *P. sajor-caju*, *P. ostreatus*, and *P. florida*-fed rats, respectively. These findings based on mice studies suggested that consumption of the aforementioned *Pleurotus* species could bring notable health advantages by modulating physiological functions, particularly in addressing various atherogenic lipid profiles in cases of hypercholesterolemia, potentially serving as a nutritious source and a preventative measure against related complications and known risk factors for atherosclerosis.

Fagade and Oyelade (2009) identified and assessed 12 different species including *Auricularia auricula*, *Coriolus versicolor* (*C. versicolor*), *Daedalea elegans*, *Fomes lignosus*, *G. lucidum*, *Lentinus subnudus*, *Leptoporus* sp., *S. commune*, *Panus fulvus* (*P. fulvus*), *P. florida*, *Trametes saepiaria*, and *Trametes betulina* for antibacterial activity. Among them, the ethanol extracts of *P. florida* and *P. fulvus* exhibited the strongest antibacterial activity against a range of bacteria including *S. aureus*, *Streptococcus* sp., *Streptococcus pyogenes* (*S. pyogenes*), *E. coli*, *Klebsiella pneumoniae* (*K. pneumoniae*), *Flavobacterium* sp., and the yeast *C. albicans* at a concentration of 1 g/mL for each microorganism. Additionally, *P. florida* displayed the lowest minimum inhibitory concentrations (MIC) value (0.01 g/mL) when tested against the yeast *C. albicans*, whereas the highest MIC was observed for *P. florida* (1 g/mL) against *Flavobacterium* sp. However, ethanolic extracts of *S. commune* and *C. versicolor* showed no inhibition against any of the tested bacteria.

The predominant bioactive component, total phenols, of the methanolic extract of *Pleurotus pulmonarius* (*P. pulmonarius*) was found to be  $5.79 \pm 0.03$  mg/mL expressed as milligrams of gallic acid equivalent (GAE) per Gram of fruiting body (Ramesh and Pattar, 2010). The extract also contained flavonoids at a concentration of  $1.76 \pm 0.06$  mg/mL and a minimal amount of ascorbic acid at  $0.13 \pm 0.00$  mg/mL. The radical scavenging activity (RAS) on 2,2-diphenyl-1-picrylhydrazyl (DPPH) radical was measured at  $1.62 \pm 0.2$  mg/mL for *P. pulmonarius*. Antimicrobial activity against a range of standard pathogenic Gram-positive and Gram-negative bacteria, along with yeast, was assessed demonstrating a notable antibacterial effect. MIC values indicated antimicrobial activity even at low concentrations (from 1 to 5 mg/mL). The methanolic extract of *P. pulmonarius* showed promising biopharmaceutical potential with its antioxidant and antimicrobial properties. However, additional research is essential to assess its effectiveness as a therapeutic compound. It is also crucial to identify the bioactive compounds and understand their mechanisms of action before considering practical applications.

Ghaly et al. (2011) evaluated the antihyperglycemic properties of an ethanol extract from *P. ostreatus* and its influence on potential DNA damage, chromosome aberrations, and sperm abnormalities in diabetic rats induced by streptozotocin. The research involved five groups of adult male albino rats, with the control group consisting of normal animals and the remaining groups comprising hyperglycemic animals. These hyperglycemic groups were orally administered with the antidiabetic drug Amaryl and different levels of mushroom extract doses: low (100 mg/kg.body weight/dL), or high (200 mg/kg.body weight/dL) for 30 days. According to their findings, the application of a higher dosage of *P. ostreatus* extract exhibited superior therapeutic effects compared to the treatment

with a lower dosage. Notably, *P. ostreatus* extract, especially at high concentration, effectively lowered blood glucose levels in hyperglycemic rats, though to a lesser extent than Amaryl treatment. Significantly, mushroom treatments exhibited greater efficacy in reducing genetic alterations and sperm abnormalities in diabetic conditions compared to Amaryl treatment. In conclusion, this study highlighted the potential of *P. ostreatus* extract, particularly at higher concentration, to alleviate elevated blood glucose levels and mitigate genetic and reproductive abnormalities associated with diabetes, offering a promising alternative to conventional treatments.

Two polysaccharide fractions, namely PSPO-1a (composed of mannose, glucose, galactose, xylose, and rhamnose) and PSPO-4a (composed of rhamnose, mannose, and galactose), both containing protein and uronic acid, were isolated from ethanol extracts of *P. ostreatus* (Zhang et al., 2012). These fractions demonstrated stronger DPPH and superoxide anion radical scavenging activities, which increased with concentrations up to 2.1 mg/mL and 3.0 mg/mL, respectively. However, their efficacy in scavenging hydroxyl radicals was comparatively lower compared to DPPH and superoxide anion radical scavenging activities. Consequently, PSPO-1a proved to be a more potent free-radical scavenger than PSPO-4a which could be resulted from their different polysaccharide compositions and their varied molar ratios.

A study conducted by Mitra et al. (2013) focused on exploring the antioxidant potential and nitric oxide synthase (NOS) activation properties of water-soluble crude polysaccharides derived from *P. ostreatus*. Their results indicated that the polysaccharides, primarily composed of carbohydrates, notably  $\beta$ -glucan, displayed good antioxidant activity, demonstrating superiority in free radical scavenging and NOS activation compared to other components including low levels of protein and phenolic compounds. The yield from hot water extraction of dried fruit bodies revealed a total polysaccharide content of  $62.67 \pm 7.67$  mg/100 mg, with the total glucan component as  $43.9 \pm 1.2$  mg/100 mg. Furthermore, the polysaccharides exhibited significant NOS activation properties. Moreover, considering the antioxidant activity, the  $EC_{50}$  (the concentration required to obtain a 50% antioxidant effect) values for scavenging hydroxyl radicals, superoxide radicals, and chelating ferrous ions were 665, 390, and 370  $\mu$ g/mL, respectively. That study highlighted the potential of *P. ostreatus* as a valuable source of bioactive compounds, suggesting that its crude polysaccharides, rich in  $\beta$ -glucan, could serve as an effective antioxidant food additive or find applications in the pharmaceutical industry.

Assis et al. (2013) investigated the antitumor activity of the exopolysaccharides (EPSs) and the mycelial biomass (intracellular polysaccharides, IPSs) of *P. sajor-caju* against Sarcoma 180 (S180) cells. According to that test, the antitumor efficacy of the produced EPS was 86%, and two IPSs from the mycelial biomass showed 80% and 82%. Since the chemical characterization of these bioactive compounds was not determined within that study, the main concern surrounding these exo- and intracellular polysaccharides lies in the lack of identification of bioactive secondary metabolites presented in EPS and IPS produced by *P. sajor-caju*. Therefore, after further investigation, that findings could aid in the exploration of new bioactive substances, introducing innovative perspectives to the medical and pharmaceutical fields.

Corrêa et al. (2015) focused on the chemical characterization and bioactivity of ethanol extracts of fruiting bodies and submerged mycelia from *Pleurotus ostreatoroseus* (*P. ostreatoroseus*). The fruiting body and mycelia extracts contained a minimum of five free sugars, four organic acids, four phenolic compounds, and two tocopherols. The culture filtrates from submerged cultivation exhibited superior reducing activity only for fruiting body ( $1.79 \pm 0.01$  mg/mL). Furthermore, DPPH scavenging activity ( $4.78 \pm 0.02$  mg/mL for fruiting body and  $15.62 \pm 0.13$  mg/mL for mycelia),  $\beta$ -carotene bleaching inhibition ( $0.40 \pm 0.01$  mg/mL for fruiting body and  $7.62 \pm 0.25$  for mycelia), and lipid peroxidation inhibition ( $0.29 \pm 0.00$  mg/mL for fruiting body and  $2.34 \pm 0.08$  mg/mL for mycelia) in porcine (*Sus scrofa*) brain homogenates were detected in terms of bioactivity. Additionally, *P. ostreatoroseus* demonstrated higher anti-inflammatory and antimicrobial activities, while showing no hepatotoxicity in porcine liver primary cells. These functional responses could be associated with varying levels of bioactive metabolites in the fruiting body extract and the submerged culture filtrate, including phenolic acids, organic acids, and tocopherols. These bioactive compounds can be utilized to create dietary supplements for nutraceutical purposes.

*P. sajor caju*, a medicinal fungus, was reported as a notable source of secondary metabolites such as phenols ( $3.35 \pm 0.20$  mg/g), flavonoids ( $5.36 \pm 0.31$  mg/g), tannins ( $6.84 \pm 0.12$  mg/g), and alkaloids ( $2.81 \pm 0.61$  mg/g), in addition to carbohydrates, protein, amino acids, and vitamins (A, C, and E) (Devi and Krishnakumari, 2015). These secondary metabolites could have significant potential for exhibiting antimicrobial, anticancer, antipyretic, astringent, and antiviral properties. The findings in that work strongly indicated the commercial and pharmaceutical significance of the secondary bioactive compounds found in *P. sajor caju*.

Chowdhury et al. (2015) studied the antimicrobial and antioxidant properties of methanolic extracts from three edible mushrooms (*P. ostreatus*, *Lentinula edodes* (formerly *Lentinus edodes*) (*L. edodes*), and *Hypsizygus tessulatus* (*H. tessulatus*)) isolated from Bangladesh. Antimicrobial activity against 8 microbial strains was evaluated, revealing substantial effectiveness with diameters of inhibition zone (DIZ) ranging from  $7 \pm 0.2$  to  $20 \pm 0.1$  mm. MIC values exhibited notable activity at concentrations ranging from 1 mg/mL to 9 mg/mL, with *L. edodes* exhibiting the most potent antimicrobial activity. *Pseudomonas aeruginosa* (*P. aeruginosa*) showed the maximum resistance, while *Saccharomyces cerevisiae* (*S. cerevisiae*) was more sensitive for the three fungal tested extracts. To reveal the antioxidant efficiency, free radical scavenging activity ( $EC_{50}$ ,  $\mu$ g/ml) on DPPH was determined as  $100 \pm 1.20$ ,  $105.0 \pm 1.23$ , and  $110.0 \pm 1.24$   $\mu$ g/mL respectively for *P. ostreatus*, *H. tessulatus*, and *L. edodes* (with ascorbic acid as a control,  $5.25 \pm 0.21$   $\mu$ g/mL). The total phenols, a major bioactive component, ranged from  $3.20 \pm 0.05$  to  $10.66 \pm 0.52$  mg/mL expressed as mg of GAE per Gram of fruiting bodies. Furthermore, the flavonoid concentration detected spectrophotometrically in all isolates ranged from  $2.50 \pm 0.008$  mg/mL to  $4.76 \pm 0.11$  mg/mL. The potential of these extracts to serve as effective therapeutic agents requires further investigation and a detailed study of their mechanisms of action prior to application.

Koutrotsios et al. (2018) cultivated *P. ostreatus*, *Pleurotus eryngii* (*P. eryngii*), and *Pleurotus nebrodensis* (*P. nebrodensis*) on unconventional substrates such as grape marc (GMC) and olive mill byproducts (OMB), with wheat straw (WHS) serving as the control. GMC-based media demonstrated comparable or superior mushroom productivity compared to WHS for *P. eryngii* and *P. nebrodensis*, while *P. eryngii* exhibited enhanced cultivation performance in OMB-based media. Both GMC and OMB substrates led to a substantial increase in the content of fruiting bodies in phenolic acids, resveratrol, triterpenic compounds, and ergosterol. Specifically, *P. eryngii* methanol extract displayed significantly high total phenolics, showing a substantial 2- to 8-fold increase in antioxidant activity based on DPPH and ferric reducing/antioxidant power assays. Moreover, substrates containing GMC or OMB resulted in up to a 27.0% increase in mushroom  $\beta$ -glucans. *Pleurotus* species responded differentially and mostly in a substrate-specific manner, selectively absorbing organic compounds. The phenolics and squalene content in substrates showed a strong correlation with the antioxidant activity of fungi and ergosterol, respectively. Similarly, a comparable correlation was noted between the triterpene content in substrates and fungi.

In a study by Beltrán Delgado et al. (2021), the aqueous extract of mature fruiting bodies of *P. ostreatus* exhibited higher levels of proteins, reducing sugars, and flavonoids than those in the extract of early-stage fungus. However, carbohydrates and total phenols were higher in the extract from the early stage of fungal development than in mature fruiting body extract. According to that work, the antioxidant characteristics of *P. ostreatus* aqueous extractions (earliest stage of fungal development and mature fruiting bodies) were influenced by changes in the levels of bioactive compounds, considering the physiological attributes during different growth phases. These findings could be valuable for developing protocols to obtain bioproducts from *P. ostreatus* with potential applications as antioxidants in food and medical-pharmaceutical industries and for the design and formulation of new related therapeutic products.

Ogidi et al. (2020) focused on the production of EPSs by submerged cultures of *P. pulmonarius*, containing diverse agricultural wastes. The highest EPS yield (5.60 g/L) was achieved by *P. pulmonarius* submerged cultures supplemented with groundnut shells (20.0 g/L) (EPS-B). The observed zones of inhibition by EPS-A (without agro-waste), EPS-B (groundnut shell), EPS-C (coconut husk), and EPS-D (pineapple peel) against *Shigella dysenteriae* and *E. coli* did not show significant differences. All the obtained EPS variants inhibited the growth not only of Gram-positive bacteria, including *B. subtilis* and *S. aureus*, but also against *C. albicans* and Gram-negative bacteria. All the obtained EPS exhibited DIZs (5.00–14.00 mm) against different tested microorganisms. The MIC also ranged from 0.25 to 1.00 mg/mL against the tested microorganisms. The EPS-A to D demonstrated scavenging activity within the ranges of 67.80%–81.80%, 60.60%–81.20%, 70.40%–84.70%, and 78.40%–88.50% against DPPH, OH,  $\text{Fe}^{2+}$ , and NO radicals, respectively. The potential applications of the EPS, obtained from submerged cultures of *P. pulmonarius* supplemented with different agro-wastes, make it a promising natural product with the possibility of being utilized as a preservative in the food industry. Additionally, the method of generating natural bioactive compounds through fungal submerged culture using agricultural waste offers a potential

solution to the unregulated disposal of agricultural waste into the environment.

Aqueous extracts from *P. ostreatus* and *L. edodes* (shiitake mushroom) exhibited the expression of 753 and 432 proteins, respectively (Elhusseiny et al., 2021). Common bioactive peptides such as Rab GDP dissociation inhibitor, superoxide dismutase, thioredoxin reductase, serine proteinase, and lectin were identified in both white rot fungal extracts. Additionally, *P. ostreatus* extract contained phenolics and flavonoids, such as catechin, kaempferol, and apigenin, whereas catechin and quercetin were detected in the extract of *L. edodes*. Vitamins, including ascorbic acid, nicotinic acid, nicotinamide, and pyridoxine, together with various amino acids were also detected in both extracts. The antioxidant impact of both fungi can be ascribed to the existence of numerous bioactive elements, such as flavonoids, phenolics, bioactive peptides, and vitamin C. Notably, both extracts demonstrated significant antiviral activities, particularly *P. ostreatus* extract exhibited a selectivity index (SI) of 4.5 and 2.0 against adenovirus (Ad7) and herpes simplex virus-II, respectively, while *L. edodes* extract showed values of 2.7 and 2.5 for the respective viruses. The aqueous extracts from *L. edodes* and *P. ostreatus* demonstrated an approximately 20.0% reduction in viability among the tested cancer cell lines LS-513 (cecum carcinoma), HepG2 (hepatocellular carcinoma), DU-145 (prostate cancer), and PC-3 (prostate cancer). Cytotoxicity analysis was conducted on aqueous fungal extracts against leukemia (CCR-CEM, NB-4, THP-1) and lymphoma (U937) cells. The *L. edodes* extract exhibited a viability decrease of 66.02% in THP1 cells, while the *P. ostreatus* extract reduced the viability of CCRF-CEM cells to 70.64%. Additionally, minimal cytotoxic effects on normal human peripheral blood mononuclear cells (PBMC) from the extracts with untreated cells and doxorubicin treated cells as negative and positive controls, respectively, was observed. Considering the effects of a wide range of bioactive compounds in the aqueous extracts of the white rot fungi *P. ostreatus* and *L. edodes*, the study suggested the potential pharmacological application of these fungal strains. It underscored their minimal cytotoxicity on normal PBMCs, while also emphasizing their beneficial properties in terms of antiviral, antitumor, and antioxidant properties.

Oba et al. (2009) assessed the impact of immunochemotherapy using lentinan derived from *L. edodes* in comparison to chemotherapy alone in individuals with advanced gastric cancer through a meta-analysis of 650 individual patient data. Based on their findings, lentinan demonstrated a potentially higher efficacy in patients with lymph node metastasis in contrast to those without such metastasis. Moreover, the proportion of hepatic metastasis in the group receiving chemotherapy plus lentinan was smaller than that in the group receiving chemotherapy alone, with percentages of 34.5% and 43.1%, respectively. It was indicated that lentinan extended the overall survival period of the patients. In summary, the inclusion of lentinan alongside standard chemotherapy showed a notable and significant advantage over chemotherapy alone in terms of survival for individuals having advanced gastric cancer.

Resurreccion et al. (2016) reported the isolation of ergosterol and trilinolein from dichloromethane extracts of *L. edodes*, obtained from the Mushroom Burger in Tagaytay City, Philippines. Their structures were identified by comparing their NMR data with those of the existing literature. Ergosterol from the water extract of



*Polyporus* showed significant protective properties against bladder tumor promotion in Wistar rats (Yazawa et al., 2000). Previous research also indicated that ergosterol in *P. ostreatus* extracts had the potential to inhibit lipid peroxidation (Dissanayake et al., 2009). On the other hand, trilinolein exhibited protective effects against cardiovascular disorders, including its ability to inhibit ischemia-induced ventricular arrhythmias and display antioxidant properties (Chan et al., 2002; Chan et al., 2005). In addition, trilinolein from the water extract of *Polyporus* inhibited the growth of human non-small cell lung carcinoma A549 and induce programmed cell death, with the effects being contingent on both the dosage and duration of exposure (Chou et al., 2011).

Sevindik (2018a) evaluated the antioxidant capacity of the *Lentinus tigrinus* (*L. tigrinus*) by determining the total antioxidant status (TAS), the total oxidant status (TOS), and the oxidative stress index (OSI) as  $1.748 \pm 0.071$  mmol/L,  $19.294 \pm 0.237$   $\mu$ mol/L, and  $1.106 \pm 0.031$ , respectively. Additionally, the antimicrobial properties of ethanol, methanol, and dichloromethane extracts of *L. tigrinus* were investigated against several bacterial and yeast strains, including *S. aureus*, *Enterococcus faecalis* (*E. faecalis*), *E. coli*, *P. aeruginosa*, *C. albicans*, *Candida krusei* (*C. krusei*) and *Candida glabrata* (*C. glabrata*) in a range from 800 to 100 MIC ( $\mu$ g/mL) values with highest anticandidal activity. In that paper, it was proposed that *L. tigrinus* could serve as a natural antioxidant and antimicrobial source. On the other hand, since *L. tigrinus* is an edible mushroom (Mohammadnejad et al., 2019), the restriction of over-consumption of this white-rot fungus could be necessary because of its high level of antioxidants. Moreover, the fungal extracts should be analyzed to determine the responsible bioactive secondary metabolites for its antimicrobial and antioxidant activities.

The antioxidant and antidiabetic properties of mycelium and fruiting body ethanol extracts of *Lentinus swartzii* (*L. swartzii*) was examined by Austria et al. (2021). The inhibition of  $\alpha$ -amylase, which is an enzyme responsible for breaking down carbohydrates during digestion, has the potential to cause a decrease in blood sugar levels (Tundis et al., 2010). Considering this, the ethanolic extract of *L. swartzii* mycelium demonstrated a notable  $\alpha$ -amylase inhibitory activity of 81.98%, while the fruiting body ethanolic extract exhibited an  $\alpha$ -amylase inhibitory activity of 71.08%. The mycelial extract contained essential oils, triterpenes, sugars, tannins, flavonoids, fatty acids, and phenols, while the fruiting body extract presented the same components except for fatty acids and sugars. At a concentration of 1,000  $\mu$ g/mL, the mycelial ethanolic extract showed scavenging effects against DPPH (35.29%) and NO (36.04%), contained 20.25 mg GAE/g sample, and demonstrated high inhibitory activity against  $\alpha$ -amylase (81.98%). Similarly, the fruiting body ethanolic extract, at the same concentration, scavenged 43.69% of DPPH, 31.75% of nitric oxide, contained 16.92 mg GAE/g sample, and exhibited high inhibitory activity against  $\alpha$ -amylase (71.08%). Consequently, both *L. swartzii* mycelia and fruiting body ethanolic extracts held promise as valuable sources of bioactive compounds with antioxidant and antidiabetic activities. A notable observation in that paper was that mycelia grown in coconut water exhibited superior activities compared to the fruiting body cultivated in sawdust and rice straw substrate. This signifies that the chemical properties and biological effects are impacted not just by elements like species, strain type, growth media, and solvents for extraction

but also by the specific medium composition used for fungal cultivation. Further steps, including the isolation and characterization of the compounds responsible for these significant bioactivities, are crucial for a comprehensive understanding of the extracts' potential in different applications.

Muslihin et al. (2022) reported that the wild mushroom *Lentinus squarrosulus* (*L. squarrosulus*) possessed notable characteristics such as rapid mycelium growth, having potential to be a food source, and various other benefits. Notably, it serves as a source of bioactive compounds. The ethyl acetate extract from *L. squarrosulus* was analyzed at 516.8 nm using a UV-Vis spectrophotometer and it revealed a strong antioxidant activity with an EC<sub>50</sub> of 54.93 mg/L. This highlights its possible utility in various applications.

Lin et al. (2008) investigated the impact of *Lycium barbarum* (*L. barbarum*) fruit extract on the growth and extracellular polysaccharopeptide (ePSP) production by *C. versicolor* (now *Trametes versicolor* (*T. versicolor*)) in a 20-L fermenter under submerged fermentation conditions. The addition of *L. barbarum* extract (LBE) into the culture medium led to a notable increase in ePSP production as from 0.61 g/L to 1.66 g/L. Significantly, ePSP from *C. versicolor* cultured with supplemental *L. barbarum* extract demonstrated noteworthy immunomodulatory activity, influencing the production of nitric oxide and various cytokines by murine RAW264.7 cells. The approach in that work can open up new possibilities for the future advancement of dietary supplements centered around *C. versicolor* LH1 polysaccharopeptides.

From a submerged culture of *Panus strigellus* (*P. strigellus*), Llanos-López et al. (2023) isolated three metabolites, including a new bioactive compound called panapophenanthrin and two known compounds identified as panepophenanthrin and dihydrohynophillin which are defined in an uncommon group of oligocyclic terpenoidal metabolites, exclusively identified in the *Panus* genus. While panapophenanthrin and dihydrohynophillin exhibited not a very strong antimicrobial effect with MIC ranging from 33.3 to 66.6 g/mL on various fungal strains together with Gram-positive and Gram-negative bacteria, panepophenanthrin showed no activity against any of the tested microorganisms. Moreover, panapophenanthrin showed strong cytotoxic effects on mammalian cell lines including mouse fibroblast (L929) and human endocervical adenocarcinoma (KB3.1) with 13.2 and 17.9 EC<sub>50</sub> ( $\mu$ M) values, respectively. *Panus* species are predominantly found in tropical and subtropical areas. Hence, this discovery emphasized the significance of examining tropical species to uncover new bioactive compounds, but additional research is necessary to thoroughly understand the bioactivity of these compounds and explored their potential uses in different applications.

*Cyclocybe cylindracea* (*C. cylindracea*) ethanol extract was investigated to determine its phenolic content, heavy metal content, and antioxidant activity to evaluate possible medical benefits (Sevindik et al., 2018). In that work, TAS, TOS, and OSI values were determined as 4.325 mmol/L, 21.109  $\mu$ mol/L, and 0.488. Phenolic compounds including gallic acid, hesperidin, catechin, syringic acid, and hydroxybenzoic acid, were detected in the ethanolic extracts of *C. cylindracea*. These bioactive compounds presented diverse health advantages, encompassing antioxidant properties, anti-inflammatory effects, and potential anti-cancer properties (Sevindik et al., 2018). Despite possible benefits, since *C. cylindracea* is edible (Landingin et al., 2020), its levels of Pb ( $16.54 \pm 0.93$  mg/kg) and TOS values should be considered.



Masuda et al. (2008) explored the antimetastatic properties of *Grifola frondosa* (*G. frondosa*) (maitake mushroom) extracts, using an experimental mice model of lung metastasis. The observed inhibition of lung metastasis by *G. frondosa* extract was attributed to the activation of NK cells. Additionally, the *G. frondosa* extract demonstrated inhibition of ICAM-1 (Intercellular Adhesion Molecule 1) expression in vascular endothelial cells, suggesting that its mechanism of action involved blocking the adhesion of tumor cells to lung tissue, thereby inhibiting metastasis. Their findings suggested that *G. frondosa* extract was effective for cancer prevention and the inhibition of tumor metastasis when consumed regularly.

Masuda et al. (2009) explored the ability of an extract from *G. frondosa* to enhance the immune system by antitumor and antimetastatic activities together with cisplatin, a well-known anticancer drug. Based on their findings, the increased antitumor and antimetastatic effectiveness observed in the combination of cisplatin with *G. frondosa* extract was attributed to a synergistic interaction. This synergy was sourced from the dual action of cisplatin's cytotoxic impact on tumor cells and the simultaneous activation of the immune response in antigen-presenting cells (APC) and natural killer (NK) cells by *G. frondosa* extract. Moreover, this combination not only exhibited antitumor and antimetastatic activity but also caused a decrease in cisplatin-induced myelotoxicity and nephrotoxicity. Consequently, the joint administration of *G. frondosa* extract with cisplatin holds promise as a beneficial approach to cancer treatment.

The clinical evaluation of the immunological effects of hot water and alcohol extract from the fruit body of *G. frondosa* at different oral dosage levels was first investigated for a group of 34 eligible study subjects in the work performed by Deng et al. (2009). Based on their results, it was shown that the administration of *G. frondosa* extract was linked to notable alterations in specific immunologic parameters within the peripheral blood. According to their findings, this extract was recognized for its role as an immunomodulator rather than simply an immune enhancer. Moreover, cancer patients should be aware of that *G. frondosa* extracts may have complex effects on immune function, and while the clinical impact on cancer prevention or treatment remains uncertain, it is crucial to conduct experimental investigations to clarify its potential anticancer effects.

Su et al. (2020) prepared a *G. frondosa* extract through a process involving hot water extraction from the fruiting body, followed by enzymatic digestion and dialysis, resulting in high and low molecular weight fractions. They examined the water-soluble polysaccharides of *G. frondosa* to understand their impact on inflammation and receptor interactions using parental RAW264.7 macrophages and Dectin-1-expressing RAW264.7 macrophages. The results of cell-based assays indicated that the high molecular weight fraction (1,260 kDa) as the major bioactive fraction demonstrated inhibitory effects on tumor necrosis factor- $\alpha$  (TNF- $\alpha$ ) and interleukin-6 (IL-6) production, while also reducing NF- $\kappa$ B (important transcription factor regulating inflammatory responses in eukaryotes) activation in lipopolysaccharide-induced macrophages. That research suggested that the nondigestible  $\beta$ -(1 $\rightarrow$ 6)-branched (1 $\rightarrow$ 4)- $\beta$ -D-glucan found in high molecular weight fraction might be responsible for its anti-inflammatory properties by interacting with TLR2 receptors rather than Dectin-1 or CR3 receptors. The

discovered polysaccharide was identified as a non-digestible glucan with a  $\beta$ -linked core and side groups. Moreover, the receptor-binding properties and anti-inflammatory activity of *G. frondosa* polysaccharides may be influenced by their molecular weight and arrangement of linkages.

Eckhardt et al. (2000) reported the impact of a bioactive fungal compound on pancreatic cancer in humans. This involved a phase I trial and a pharmacokinetic examination of irofulven (a fungal cytotoxin) (doses ranging from 1.0 to 17.69 mg/m<sup>2</sup>) and a novel cytotoxin derived from the white-rot fungus *Omphalotus olearius* (*O. olearius*), which was conducted on 46 patients (given daily for 5 consecutive days every 4 weeks) with advanced solid malignancies. According to the trial, evidence of antitumor activity was observed in an individual with advanced pancreatic cancer, coupled with the remarkable preclinical antitumor effects demonstrated by irofulven.

Chandra et al. (2019) assessed the antioxidant activity of the white-rot fungi *Phanerochaete chrysosporium* (*P. chrysosporium*), *Phlebia brevispora* (*P. brevispora*), and *Phlebia floridensis* (*P. floridensis*) against various free radicals, including DPPH, nitric oxide, ferrous ion, and ferric ion, in addition to their total phenolic content. All the studied fungal strains produced phenolics ranging from 5.2 to 16.7 mg/mL and exhibited diverse free radical and metal ion scavenging activities. The growth medium significantly influenced these activities. Thus, all the studied fungi presented similar antioxidant activity (approximately 72.0% DPPH scavenging) in yeast extract glucose medium, while it was lower in Czapek dox's medium (ranging from 60.0% to 45.0%). The fungal extracts showed no mutagenic or cytotoxic effects, highlighting the fungi's potential as a new source for the rapid production of extracellular antioxidants. These white rot fungi displayed strong antioxidant potential and could serve as a valuable source of natural antioxidant compounds. Further studies are recommended to isolate and characterize the bioactive compounds for potential use in new therapeutic approaches.

*Hericium erinaceus* (*H. erinaceus*) is a well-known traditional medicinal fungus acclaimed for its anti-dementia properties, Alzheimer's disease, depression, Parkinson's disease, and spinal cord injuries together with the production of cyathane diterpenoids (erinacines). Numerous structurally diverse bioactive compounds, exceeding 80 types, have been extracted from both the fruiting bodies and mycelia of *H. erinaceus*. These compounds, including terpenoids (erinacines), phenols (hericenone AE), pyrones (erinapyrones AC), sterols (erinanol, hericerins, hericenones), fatty acids, and non-ribosomal peptides, exhibit various therapeutic effects such as anti-tumor, antibacterial, hypoglycemic, and neuroprotective activities. Around 20 of the 25 isolated diterpenoids extracted from *H. erinaceus* share a characteristic 5-6-7 tricyclic fused core structure (Kawagishi et al., 1992; Kawagishi et al., 1996; Lee et al., 2000; Li et al., 2001; Kenmoku et al., 2002; Kawagishi et al., 2006; Kobayashi et al., 2014; Lu et al., 2014; Friedman, 2015; Li et al., 2015; Wang et al., 2015; Brandalise et al., 2023).

Lee et al. (2014) reported that erinacine A from the ethanolic extract of *H. erinaceus* was able to inhibit inflammatory cytokine expression as a neuroprotective effect in adult male Sprague-Dawley rats having ischemia injury. In that work, it was also shown that the brain tissue trauma effectors of nitrotyrosine (RNS) via inducible nitric oxide synthase (iNOS) (Alderton et al., 2001)/p38 mitogen-

activated protein kinase (MAPK) (Darling and Cook, 2014; Han et al., 2020)/a transcription factor (i.e., CHOP) (Bruhat et al., 1997) contributed to the neuroprotective effect. Furthermore, in a stroke animal model, erinacine A led to the suppression of reactive nitrogen species and the downregulation of iNOS, p38 MAPK, and CHOP, which are factors involved in ischemia injury.

*H. erinaceus* methanolic extracts inhibited the inflammatory activity induced by lipopolysaccharide/interferon- $\gamma$  in murine RAW264.7 cells, with a maximum decrease in nitric oxide production of 39.6% (Lee et al., 2016). The bioactive metabolites in these methanol extracts were identified as three different hericenones, C, D, and F. Consequently, they suggested that the anti-inflammatory effect of the *H. erinaceus* extract was likely based on the hericenones F. Also, ethanolic extracts of *H. erinaceus* mycelia effectively inhibited glutamate-induced apoptosis in PC12 cells against 20 mM glutamate-induced damage (Chang et al., 2016). The following biochemical parameters glutathione at  $2.5 \pm 0.7$  nmol/mg protein, glutathione peroxidase at  $28.2 \pm 3.2$  mU/mg protein, glutathione reductase at  $2.3 \pm 0.4$  mU/mg protein, calcium influx at  $360 \pm 23$  nmol/L, reactive oxygen species at  $140.0\% \pm 7.0\%$ , superoxide dismutase at  $23.2 \pm 4.2$  U/mg protein,  $H_2O_2$  at  $20.4 \pm 3.5$  nmol/mg protein, and thiobarbituric acid reactive substances (malondialdehyde) at  $13.3 \pm 2.5$  mmol/mg protein, were affected by glutamate insult. Overall, their findings underlined the potential neuroprotective effect of erinacine A from *H. erinaceus* ethanolic extracts.

Despite the elucidation of chemical synthesis, the biosynthetic pathway and gene regulation remain unknown. A comparative genome analysis of 42 basidiomycota fungal species, including *H. erinaceus*, revealed abundant gene clusters related to terpenoid and polyketide biosynthesis (Chen et al., 2017). The genome analysis of *H. erinaceus* will provide important understanding into the biosynthetic pathways of bioactive secondary compounds, which is crucial for improving the production of these compounds.

Zhang et al. (2017) explored the neuroprotective and neuritogenic properties of several secondary metabolites, including 4-chloro-3,5-dimethoxybenzoic methyl ester, 3-(hydroxymethyl)-2-furaldehyde, erinacine A, erinacerin G, herierin III, and herierin IV from the methanol extract of *H. erinaceus* mycelium. Among them, 4-chloro-3,5-dimethoxybenzoic methyl ester and erinacine A metabolites not only enhanced nerve growth factor-induced neurite outgrowth but also protected neuronally differentiated cells against lack of nerve growth factor in PC12 pheochromocytoma cells. Erinacine A additionally stimulated neuritogenesis in primary rat cortex neurons. Their findings suggest that *H. erinaceus* holds promise as a potential therapeutic agent for reducing the risk of various neurodegenerative diseases.

Erinacine A and S, isolated from of *H. erinaceus* mycelia, displayed anti-neurodegenerative and neuroprotective effects in the cerebrum of transgenic mice (Tzeng et al., 2018). Thus, 30-days application of erinacine A and S attenuated cerebral plaque loading by inhibiting plaque growth, diminishing glial cell activation, and promoting hippocampal neurogenesis in transgenic mice as Alzheimer's disease model. Additionally, it was showed that erinacine A recovered behavioral deficits in transgenic mice. These findings suggested the possibility that erinacine A may have therapeutic potential for treating Alzheimer's disease.

Ratto et al. (2019) reported that ethanol extract of *H. erinaceus*, containing erinacine A, hericenone C, and hericenone D bioactive metabolites, was able to partially revert the cognitive and locomotor frailty index during physiological aging in a mice model. They observed an increase in proliferating cell nuclear antigen (PCNA) and doublecortin (DCX) levels in the hippocampus and cerebellum of mice supplemented (2 months) with *H. erinaceus* extract orally, indicating the occurrence of neurogenesis in elderly frail mice. Therefore, it was demonstrated that the supplementation of *H. erinaceus* extract reversed the age-related decline in recognition memory.

Roda et al. (2021) demonstrated that a two-month oral supplementation of ethanol extract from *H. erinaceus*, which contained erinacine A, hericenone C, hericenone D, and ergothioneine, could reverse age-induced cerebellar alterations in C57BL-6J wild-type male mice. These alterations included volume reduction, molecular layer thickness decrease, and dwindled neurons. Additionally, the supplementation led to a decrease in inflammation, oxidative stress, and reactive gliosis. In another study, they investigated the preventive effects of *H. erinaceus* ethanol extract, which contained a high amount of ergothioneine, on cognitive and locomotor decline during physiological aging in C57BL-6J mice. The ergothioneine-rich extract exhibited neuroprotective and preventive actions, mitigating age-dependent deficiencies (Roda et al., 2022). Moreover, same extract was shown to reduce oxidative stress and inflammation in the hippocampus, prevent recognition memory decline, and increase the expression of specific receptors crucially involved in glutamatergic neurotransmission in the same mice (Roda et al., 2023).

A tremulane sesquiterpene, named irpexlacte A (yellowish needle crystals), along with three novel furan derivatives, identified as irpexlacte B (yellowish oil), irpexlacte C (yellowish powder), irpexlacte D (brown flaky solid), were obtained from the fungus *Irpex lacteus* (*I. lacteus*) isolated from waterlogging tolerant plant *Distylium chinense* by Duan et al. (2019). Furthermore, they also isolated two known metabolites, irilactin E and  $\beta$ -hydroxycinnamolide. Irpexlacte A and D demonstrated robust antioxidant activity, with  $EC_{50}$  values of 2.50 and 5.75  $\mu$ M, respectively. Moreover, in contrast to gentamicin (0.18  $\mu$ M) as the positive control, four new compounds, irpexlacte A, B, C and D, demonstrated moderate activity, displaying MIC values of 24.1, 32.3, 35.5, and 23.8  $\mu$ M, respectively, against *P. aeruginosa*. On the other hand, the isolated compounds showed no activity against tested cancer cell lines. However, irpexlacte A-D displayed significant antioxidant activity, underscoring the need for further investigations to evaluate their importance and clarify underlying mechanisms.

*Porodaedalea pini* (*P. pini*) has been an esteemed traditional mushroom known for its therapeutic properties against various diseases. In this context, Devi et al. (2022) determined the antioxidant potential of hexane, chloroform, ethyl acetate, and methanol extracts of *P. pini* using DPPH assay ( $EC_{50}$ , 253.98  $\mu$ g/mL, maximum with hexane extraction), total antioxidant capacity ( $231.04 \pm 1.75$   $\mu$ g ascorbic acid equivalents/g of dried extract, maximum with methanol extraction), total phenolic content ( $277.67 \pm 9.46$   $\mu$ g GAE/g of the sample, maximum with methanol extraction), and total flavonoid content ( $4.95 \pm .013$   $\mu$ g rutin equivalent/g of dried extract, maximum with methanol

extraction). The presence of 12 polyphenolic metabolites, including gallic acid, catechin, chlorogenic acid, epicatechin, caffeic acid, umbelliferone, coumaric acid, tert-butyl-hydroquinone, and quercetin was revealed. However, rutin, elagic acid, and kaempferol were not detected. The identified polyphenols of *P. pini* could potentially contribute to its antioxidant activity. Moreover, further exploration of *P. pini* extracts is necessary to unveil its nutraceutical and pharmacological potential.

Ildiz et al. (2022) employed molecular techniques to analyze the total phenolic compound content, antioxidant activity using the DPPH scavenging method, and antimicrobial activity for *Bjerkandera adusta* (*B. adusta*). Ethanol and methanol were used for extraction and the methanolic extract of *B. adusta* exhibited a total phenolic content of 772.28 µg GAE/mL. The ethanol extract demonstrated a substantial 79.66% scavenging activity against a 0.1 mM DPPH solution. For antimicrobial activity, the ethanolic extract exhibited significant antimicrobial activity, showing the largest DIZ of  $28 \pm 1$  mm against *P. aeruginosa*. In contrast, the methanol extract displayed the lowest antimicrobial efficacy, with a DIZ of  $8.7 \pm 1.2$  mm against *Salmonella typhimurium* (*S. typhimurium*). These findings suggested that both ethanolic and methanolic extracts of *B. adusta* possess antioxidant and antibacterial properties. More comprehensive investigations into wild-collected fungal strains should be done for an extensive exploration of the bioactive constituents present in fungi, drawing attention to their potential applications in the development of functional foods and other potential uses.

The antioxidant and oxidant potentials of the ethanolic extracts of *Hohenbuehelia myxotricha* (*H. myxotricha*) was determined for the first time by Krupodorova et al. (2022). The highest recorded TAS, TOS, and OSI values for *H. myxotricha* were  $5.416 \pm 0.150$  mmol/L,  $1.320 \pm 0.156$  µmol/L, and  $0.024 \pm 0.003$ , respectively. The ethanolic extracts of *H. myxotricha* exhibited antimicrobial activities with concentrations ranging from 25 to 200 µg/mL against various bacteria and yeasts. The extract demonstrated a better antifungal activity compared to its antibacterial activity. The antioxidant, oxidant, and antimicrobial potentials of *H. myxotricha* mycelia exhibited variations based on the culture media employed. According to their findings, glucose peptone yeast (GPY) medium was found more suitable for the synthesis of antibacterial bioactive metabolites against *E. coli*, while Sabouraud dextrose broth (SDB) medium was more proper for the production of antioxidant and antifungal bioactive metabolites. Thus, their findings underscored the importance of identifying an optimal cultivation medium to maximize antimicrobial and antioxidant activities. Overall, the ethanolic extract of *H. myxotricha* mycelia presented significant pharmacological potential, serving as a natural source of antioxidants and antimicrobials with potential health benefits. Like various studies in the literature, further research is required to isolate and identify the bioactive secondary metabolites responsible for the observed antioxidant and antimicrobial effects, offering potential sources for pharmacological drug designs.

Jaszek et al. (2013) isolated bioactive compounds (crude endopolysaccharides - c-EPL, and low molecular secondary metabolites - ex-LMS) extracted from *Cerrena unicolor* (*C. unicolor*) submerged cultures that exhibited antioxidant and antibacterial properties. Ex-LMS demonstrated the highest

antioxidant capability (39.0%–90.0% for chemiluminometric measurement, 20.0%–90.0% for ABTS, and 10.0%–59.0% for DPPH reduction at 6.25–800 µg/mL). Moreover, c-EPL scavenging abilities ranged from 36.0% to 70.0% for chemiluminometric measurement, 2%–60% for ABTS, and 28.0%–32.0% for DPPH reduction at 6.25–800 µg/mL. Preliminary data for the toxic effect against *Vibrio fischeri* (*V. fischeri*) were found to be 85.37% for c-EPL, and 99.8% for ex-LMS. In this sense, c-EPL showed antibacterial activity against *S. aureus* with an  $18.96 \pm 0.4$  mm DIZ while ex-LMS displayed activity with  $11.83 \pm 0.2$  and  $25.86 \pm 0.2$  mm DIZs, respectively, against *E. coli* and *S. aureus*. These compounds have the potential to serve as a novel and easily producible source of effective antioxidants within laboratory-scale conditions. Additionally, further investigation of the aforementioned bioactive secondary metabolites is crucial in terms of applications, as they may play a critical role in new therapies and serve as a natural source of antioxidative molecules.

Mizerska-Dudka et al. (2015) explored the antiviral, immunostimulatory, cytotoxic, and antitumor effects of bioactive compounds from *C. unicolor*, specifically endopolysaccharides (c-EPL) and an extracellular low molecular weight compound (ex-LMS) obtained from the culture filtrate below 10 kDa. The study employed THP-1-derived macrophages to assess immunomodulatory activity, revealing that the fungal c-EPL stimulated the production and secretion of TNF-α and IL-6. Antitumor activity was evaluated using cervical carcinoma cell lines SiHa and CaSki, with SiHa showing cytotoxic EC<sub>50</sub> (µg/mL) value of 1.2 for ex-LM, and CaSki values of 2.3 for ex-LMS. The research highlighted the promising immunomodulatory effect of c-EPL samples and the need for further investigations into these multifaceted bioactive compounds.

The antioxidant and antimicrobial properties of ethanol, methanol, and dichloromethane extracts of *C. unicolor* were studied by Sevindik (2018b). Considering antioxidant effects, TSS, TOS, and OSI were measured as  $6.706 \pm 0.059$  mmol/L,  $19.308 \pm 0.114$  µmol/L, and  $0.288 \pm 0.003$ . Additionally, all the extracts presented antimicrobial efficacy within the concentration range of 25–400 µg/mL, spanning a spectrum of MIC values from 400 to 50 µg/mL against *S. aureus*, *E. faecalis*, *E. coli*, *P. aeruginosa*, *Acinetobacter baumannii*, *C. albicans*, *C. glabrata*, and *C. krusei* with higher anticandidal activity. The primary issue about these extracts is their unidentified contents regarding the bioactive secondary metabolites.

Matuszewska et al. (2019) explored the anticancer and antioxidant properties of low molecular weight secondary metabolites produced by *C. unicolor*. These secondary metabolites consisted of protein, sugars, and phenolic compounds. The findings revealed that the low molecular weight compounds displayed inhibitory effects on human colon cancer cells HT-29 within the concentration range of 25–200 µg/mL and demonstrated dose-dependent inhibition of cell proliferation, ranging from 47.5% to 9.2% at the highest concentrations. Microscopic observations indicated that all compounds induced programmed cell death, specifically apoptosis (up to 44.4% for a compound in HT-29 and less than 20.0% for most compounds in CCD 841 CoTr), with minimal or significantly low levels of necrosis observed in both cell lines simultaneously.

Romerosa et al. (2017) found that distilled water, aqueous, and acetonitrile extracts of *Auricularia fuscusuccinea* (*A. fuscusuccinea*)

fruiting bodies contained alkaloids and tannins glycosides, while saponins and flavonoids were absent. The antibacterial properties of the aqueous and acetonitrile extracts were evaluated against *S. aureus* and *E. coli*. The results indicated low antibacterial activity against *S. aureus* for all the fungal extracts with DIZs of 5.0 mm, 13.5 mm, and 5.0 mm, respectively, compared to cotrimoxazole (control) with a 33.54 mm DIZ. For *E. coli*, the corresponding DIZs were 5.0 mm, 22.98 mm, and 22.41 mm, which were lower than the control with a 32.00 mm zone.

Kalaw and Albinto (2014) evaluated the antibacterial properties, phytochemical composition, and antioxidant activity of ethanol and acetone extracts of *Coprinus comatus* (*C. comatus*) and *Pleurotus cystidiosus* (*P. cystidiosus*). Both ethanol and acetone extracts exhibited antibacterial activity against *S. aureus*. The ethanol extract of *C. comatus* displayed a slightly larger DIZ ( $14.09 \pm 4.65$  mm) compared to the acetone extract ( $13.16 \pm 3.39$  mm). Conversely, in *P. cystidiosus*, the acetone extract exhibited a larger DIZ ( $15.25 \pm 2.76$  mm) than the ethanol extract ( $13.43 \pm 0.15$  mm). There was no inhibition against *E. coli* for both fungal extracts. Moreover, phytochemical screening of the extracts revealed the presence of alkaloids, flavonoids, saponins, and terpenoids in both fungal species. Steroids and cardiac glycosides were absent in *P. cystidiosus* while tannins were not detected in any of the studied species. *P. cystidiosus* registered higher DPPH radical scavenging activity ( $72.97\% \pm 0.68\%$  to  $66.59\% \pm 0.83\%$ ) indicating its potential antioxidant capacity, and lower total phenolic content ( $3.41 \pm 0.12$  mg GAE/g) than *C. comatus* ( $17.82 \pm 0.51$  mg GAE/g).

In a research conducted by Stilinović et al. (2020), it was reported that *C. comatus* methanol extract contained significant amounts of proteins ( $23.07 \pm 0.28$  g/100 g dry matter), carbohydrates ( $40.42 \pm 0.48$  g/100 g dry matter), dietary fibers ( $21.13 \pm 0.34$  g/100 g dry matter) and fats ( $2.04 \pm 0.03$  g/100 g dry matter). Furthermore, methanol extract of *C. comatus* served as a valuable flavonoid content ( $0.39 \pm 0.08$  (mg quercetin equivalents (QE))/g dry weight extract) and a total phenolic source ( $107.02 \pm 2.42$  mg GAE/g dry weight extract) including 4-hydroxybenzoic acid, protocatechuic acid, cinnamic acid, p-coumaric acid, caffeic acid, and quinic acid with concentrations of  $11.41 \pm 1.17$ ,  $0.13 \pm 0.03$ ,  $4.34 \pm 0.27$ ,  $10.48 \pm 0.94$ ,  $0.15 \pm 0.02$ , and  $9.10 \pm 1.39$   $\mu$ g/g, respectively, based on spectrometric analysis. According to the findings of experiments involving rats having liver damage induced by carbon tetrachloride, the administration of *C. comatus* orally for 42 days exhibited hepatoprotective effects in oxidative stress-induced liver damage by triggering repair mechanisms. Based on the results indicated in that paper, *C. comatus* had the potential to be utilized as a readily available food source with high levels of natural antioxidants. It also can be used as an additive or component for producing nutraceuticals and functional foods. Considering the reported work, an important issue arises regarding the complex composition of *C. comatus* extracts. Additional investigation is needed to ascertain whether the positive effects result from a singular active compound, or the synergistic activities of various metabolites present in the extract.

*Phylloporia ribis* (*P. ribis*), traditionally used in China for natural medicine, is recognized for its functional ingredients beneficial in treating conditions like pharyngitis, laryngitis, tonsillitis, and hyperglycemia. Ribka et al. (2021) reported bioactive compounds, and antifungal activity of methanolic (from 5% to 25%) extracts of *P.*

*ribis*. Such extracts contained a diverse array of bioactive compounds, including carbohydrates, proteins, amino acids, lipids, alkaloids, glycosides, cardiac glycerides, flavonoids, phenols, terpenoids, steroids, sterols, saponins, tannins, and phosphate. The methanolic extract of *P. ribis* presented superior antifungal activity, particularly against *Aspergillus niger* (*A. niger*), causing soft rot in carrots, with 100% inhibition observed in all methanolic extracts except at 5% concentration. The diverse components present in *P. ribis* hold promise for applications as immunity boosters, food supplements, and in the field of drug discovery. Further investigations are also required to isolate the bioactive compounds responsible for immunity-boosting, drug development, antioxidant, anti-inflammatory, antibiotic, and antimicrobial activities in their pure form.

*Polyporus gramocephalus* (*P. gramocephalus*) ethanol extract was studied for its nutraceutical potential considering its bioactive metabolites. Aquino et al. (2018) identified sugars, alkaloids, flavonoids, triterpenes, essential oils, phenols, fatty acids, anthraquinones, coumarins, anthrones, tannins, and steroids, while terpenoids, cardiac glycosides, whereas saponins were not present in the *P. gramocephalus* ethanol extract. The ethanol extract of *P. gramocephalus* displayed DPPH radical scavenging activity (26.37%) and total phenolic content of 38.58 mg GAE/g. Brine shrimp toxicity assay indicated high toxicity with an  $LC_{50}$  value of 73.78  $\mu$ g/mL. These findings suggested that *P. gramocephalus* extract was rich in bioactive compounds with significant pharmacological activities, including antioxidant properties and cytotoxic effects.

The antioxidant and antimicrobial properties of ethyl acetate extracts from *Alternaria alternata* (*A. alternata*) were investigated by Chatterjee et al. (2019). The ethyl acetate extracts showed MIC ranging from 300 to 400  $\mu$ g/mL against both Gram-positive and Gram-negative bacteria. Moreover, the ethyl acetate extract of *A. alternata* displayed antibacterial inhibition on *B. subtilis*, *Listeria monocytogenes*, *S. aureus*, *E. coli*, and *S. typhimurium* with up to  $14 \pm 1.5$  mm DIZ. Furthermore, a reduction in the activity of key metabolic pathways, including the EMP pathway, TCA cycle, and gluconeogenic enzymes, suggested interference with the central carbohydrate metabolism. Additionally, *A. alternata* extract demonstrated strong antioxidant potential through DPPH and superoxide radical scavenging assays, with  $EC_{50}$  values of  $38.0 \pm 1.7$   $\mu$ g/mL and  $11.38 \pm 1.2$   $\mu$ g/mL, respectively. Within this analysis, ascorbic acid, used as a positive control, had an  $EC_{50}$  value of  $20.23 \pm 2.3$   $\mu$ g/mL. These results suggest that *A. alternata* showed potential as a source of bioactive compounds with medicinal importance, demonstrating strong antibacterial effects.

Phenylpropanoid (PPPN) compounds are widely utilized in various industries due to their diverse bioactivities, including applications in agriculture, medicine, food, and cosmetics. In this sense, *Alternaria* sp., which is, a novel natural source of PPPNs, was isolated from grapes by Lu J. et al. (2020). However, starvation is known to stimulate the PPPN pathway in plants, its impact on fungi remains underexplored. In that study, metabolomics analysis revealed that starvation treatment significantly increased the accumulation of shikimate and PPPN compounds in *Alternaria* sp. Notably, the study also identified additional PPPNs, such as sinapate, 4-hydroxystyrene, piceatannol, and taxifolin, under starvation conditions. These findings indicated that starvation



treatment offers an effective strategy to enhance PPPN production and unveil compounds undetectable under non-starvation conditions. Overall, subjecting *Alternaria* sp. to starvation treatment during cultivation resulted in the robust activation of both the shikimate and PPPN pathways. These findings can shed light on the potential for optimizing the production of PPPN compounds by fungi, offering insights into the genetic resources and secondary metabolite pathways of *Alternaria* sp. for future functional studies.

*Inonotus obliquus* (*I. obliquus*), naturally grows on the trunks of birch wood trees in colder northern climates and is a medicinal fungus that has been used for therapeutic purposes since the 16th century (Ern et al., 2023). To investigate the antihyperglycemic and anti-lipid peroxidative effects of the dry matter of the culture broth (DMCB) of *I. obliquus*, Sun et al. (2008) utilized normal, glucose-induced hyperglycemic, and alloxan-induced diabetic mice. The DMCB exhibited a mild hypoglycemic effect in normal mice and achieved euglycemia in glucose-loaded mice after 2 h at a higher dose (1,000 mg/kg compared to 500 mg/kg). In alloxan-induced diabetic mice, the DMCB significantly reduced blood glucose levels, with a notable reduction observed for 21 days. The treatment also decreased serum levels of free fatty acids, total cholesterol, triglycerides, and LDL-cholesterol, while increasing HDL-cholesterol, insulin levels, and hepatic glycogen contents. Additionally, the DMCB enhanced antioxidant enzyme activities and histologically restored pancreas tissues in diabetic mice. Overall, the DMCB of *I. obliquus* demonstrated significant antihyperglycemic, anti-lipid peroxidative, and antioxidant effects in alloxan-induced diabetic mice.

Ma et al. (2013) identified the anti-inflammatory and anticancer compounds present in ethanol, petroleum ether, ethyl acetate, n-butyl alcohol, and water extracts of *I. obliquus*. Among all extracts, the petroleum ether extract was the most active one against human prostatic carcinoma cells and breast carcinoma cell lines with 64.66% and 63.26% inhibitory percentages, respectively. They also isolated lanosterol, 3 $\beta$ -hydroxy-8,24-dien-21-al, ergosterol, inotodiol, ergosterol peroxide, and trametenolic acid from both petroleum ether and ethyl acetate extracts. Among these metabolites, ergosterol, ergosterol peroxide, and trametenolic acid exhibited anti-inflammatory properties, while ergosterol peroxide and trametenolic acid demonstrated cytotoxic effects on human prostatic carcinoma cells and breast carcinoma cell lines. Additionally, these metabolites significantly inhibited nitric oxide production and nuclear factor kappa-light-chain-enhancer of activated B cells (NF- $\kappa$ B) luciferase activity in murine macrophage RAW 264.7 cells.

Xu et al. (2016) discovered flavonoids from ethanol, chloroform, ethyl acetate and n-butanol extracts of *I. obliquus*. In these extracts epicatechin-3-gallate, epigallocatechin-3-gallate, and naringin, as well as phenolic acids, such as ferulic acid and gallic acid were identified. DPPH radical-scavenging abilities were significantly higher in Tween 20 medium (minimum EC<sub>50</sub>; 40.63  $\pm$  0.89 mg/L) and linoleic acid medium (minimum EC<sub>50</sub>; 43.54  $\pm$  0.92 mg/L) than the control medium (minimum EC<sub>50</sub>; 95.80  $\pm$  1.99).

Baek et al. (2018) isolated triterpenoids from the methanol extract of *I. obliquus* to assess its cytotoxic effects on four human lung adenocarcinoma cell lines, each one with a different p53 tumor protein conditions (human lung adenocarcinoma cell lines A549,

H1264, H1299, and Calu-6). They identified several metabolites including 3 $\beta$ -hydroxylanosta-8,24-dien-21, (+)-fuscoporianol C, inonotsutriol E, inotodiol, inonotsutriol A, trametenolic acid, saponaceous acid I, and a novel lanostane-type triterpenoid, chagabusone A from methanol extracts from *I. obliquus*. Among these, 3 $\beta$ -hydroxylanosta-8,24-dien-21, trametenolic acid, and chagabusone A exhibited the most potent cytotoxicity against all human lung cancer cell lines tested, with EC<sub>50</sub> values ranging from 75.1 to 227.4  $\mu$ M. Notably, these compounds reduced the viability of human adenocarcinoma cell lines regardless of p53 mutations or null phenotype. This suggests that the cytotoxic effects observed against human lung cancer cells were independent of p53-related pathways, but rather mediated by apoptosis with caspase-3 activation.

Wold et al. (2020) identified melanin and six triterpenoids from dichloromethane and ethanol extracts of *I. obliquus*, chemically characterized, and evaluated for their anti-inflammatory, immunological, antimicrobial, anticancer, and cytotoxic effects. Among these compounds, melanin, and the triterpenoids 3 $\beta$ -hydroxy-8,24-dien-21-al and inotodiol significantly inhibited the hemolysis of antibody-sensitized sheep red blood cells by human sera. Specifically, 3 $\beta$ -hydroxy-8,24-dien-21-al and inotodiol activated the complement cascade, while the melanin fraction inhibited it. Inotodiol, betulinic acid, and betulin demonstrated anti-proliferative effects against the methotrexate-resistant human adenocarcinoma cell line HT29-MTX (viability: 3.8  $\pm$  0.8  $\mu$ M, 0.8  $\pm$  0.3  $\mu$ M, and 1.6  $\pm$  0.4  $\mu$ M, respectively) and the human lung carcinoma cell line NCI-H460 (viability: 4.7  $\pm$  1  $\mu$ M, 2.1  $\pm$  0.5  $\mu$ M, and 2.8  $\pm$  0.4  $\mu$ M, respectively). Additionally, the melanin fraction and betulinic acid-3-O-cafeate reduced the nitric oxide production in primary murine macrophages. However, these metabolites showed no antimicrobial activity against the tested four bacterial strains (*E. coli*, *S. aureus*, *B. subtilis*, and *P. aeruginosa*) and the yeast *C. albicans*.

Betulin, betulinic acid, inotodiol, and trametenolic acid, extracted with methanol from inner and outer parts (the sclerotium) of *I. obliquus* fruiting bodies, were tested against cancer cell lines (HT-29, AGS, MCF-7, and PC3) by Kim et al. (2020). The MTT assay was conducted to test the effect of triterpenoids on cancer cell lines. They found that the triterpenoids from the outer part extract showed significantly higher anti-proliferative activity against AGS, MCF-7, and PC3 cells compared to the inner part extract.

The hypouricemic properties of triterpenoid acids isolated from *I. obliquus* in mice with hyperuricemia were investigated by Luo et al. (2021). They identified various triterpenoid acids, including 3 $\beta$ ,22,24-trihydroxy-lanosterol-8,25-diene, oleanolic acid, 3 $\beta$ -hydroxy-lanoster-8,24-dien-21-acid, 3 $\beta$ ,21-dihydroxy-lanosterol-8,24 diene, betulin, inotodiol, 3 $\beta$ -Hydroxy-lanoster-8,24 dien-21-aldehyde, and lanosterol. Their research demonstrated that triterpenoid acids extracted from ethanol extracts of *I. obliquus* effectively inhibited xanthine oxidase activity (with an EC<sub>50</sub> of 0.065  $\pm$  0.01 mg/mL), displaying a mixed and reversible inhibition pattern. These triterpenoid acids also significantly reduced uric acid levels, hepatic xanthine oxidase, and serum blood urea nitrogen activities in mice with hyperuricemia. This suggests that triterpenoid acids from *I. obliquus* may help suppress kidney damage, lower inflammation in hyperuricemic mice, and



exhibit inhibitory effects on xanthine oxidase activity. These findings underscore the potential of triterpenoids derived from *I. obliquus* as a promising dietary or medicinal supplement for managing hyperuricemia.

Zhao et al. (2021) identified flavonoids, including gallic acid, ferulic acid, flavonoids epicatechin-3-gallate, epigallocatechin-3-gallate, naringin, rutin, naringenin, phelligradin G, inoscavin B, and davallialectone, from the ethanol extract of *I. obliquus*. Moreover, they showed that cultivating *I. obliquus* on wheat straw led to increased levels of inoscavin B and davallialectone. In that work, the degradation of lignocellulose boosted the synthesis of flavonoids such as epicatechin-3-gallate, epigallocatechin-3-gallate, rutin, and naringin, thereby enhancing the antioxidative capabilities of *I. obliquus*. The highest antioxidant potential was observed in the extract obtained on day 9 (EC<sub>50</sub> of 30.96 mg/L) against DPPH radicals.

In a study by Kou et al. (2021), seven newly discovered lanostane-type triterpenoids, named inotusols H to N, were identified from the ethanol extract of *I. obliquus*. These metabolites exhibited significant inhibition of nitric oxide production in lipopolysaccharide-stimulated BV-2 microglial cells, with EC<sub>50</sub> values ranging from 2.32 to 23.83  $\mu$ M. At the concentration of 25.0  $\mu$ M of these metabolites, no cytotoxicity was observed towards lipopolysaccharide-stimulated BV2 cells. Through molecular docking and Western blotting studies, two of the inotusols showed the most potent inhibitory effects on iNOS and nitric oxide production. These findings suggest that these bioactive metabolites hold promise for development into therapeutic agents for neurodegenerative disorders, including Alzheimer's disease.

Abu-Reidah et al. (2021) identified phenolics and flavonoids, including gallic acid, protocatechuic acid, salicylic acid, vanillic acid, 2,3-dihydroxybenzaldehyde, 2,5-dihydroxyterephthalic acid, coumaric acid, caffeic acid, 4-methoxycinnamic acid, hispidin, ferulic acid, isorhamnetin, myricetin, quercetin, syringic acid, ellagic acid, hispolon, 3,4-dihydroxybenzalacetone, and 3-O-methylellagic acid, from *I. obliquus* extract using the modified Swiss water method. These metabolites showed hydrophilic, lipophilic, and total antioxidant activities.

Li et al. (2021) reported that phelligradin D, extracted from *I. obliquus* using both petroleum ether and ethyl acetate, presented good antioxidant properties. This metabolite reduced reactive oxygen species and malondialdehyde levels while increasing the activity of superoxide dismutase and catalase in human glomerular mesangial cells under high glucose concentration (30 mM). Additionally, it enhanced the capacity of the nuclear factor erythroid 2-related factor 2 (Nrf2), a master transcription factor that upregulates antioxidant response elements (ARE) (Zhao et al., 2017), to promote the transcription of ARE. It was also shown that phelligradin D activated Nrf2 in mesangial cells exposed to high glucose concentration, contributing to its protective effects. Their findings indicated the potential discovery of novel therapies targeting diabetic nephropathy and the applications of *I. obliquus* metabolites in clinical practices.

Wang et al. (2021) identified polyphenol compounds from ethanol extracts of *I. obliquus* such as procyanidin, caffeic acid, p-coumaric acid, isorhamnetin-3-O-glucoside, astilbin, tangeretin, gallic acid, kaempferol, quercetin, and catechin. According to the

antioxidant activity of these polyphenols, their DPPH radical scavenging activity increased from 45.12% to 85.64% as the concentration increased from 1.0 to 5.0 mg/mL, respectively. As for their hydroxyl radical scavenging activity, it was found to be 38.76% at 1.0 mg/mL. When the concentration of polyphenols increased from 1.0 to 5.0 mg/mL, its stronger ferric-reducing antioxidant power increased from 0.11 to 0.39 mmol/mL. Their findings suggested that polyphenols from *I. obliquus* possessed promising potential as natural antioxidants.

Chen et al. (2021) extracted forty-six triterpenoids, twelve of which were newly discovered, from *I. obliquus* using ethanol and ethyl acetate stepwise. Among these 46 triterpenoids, thirteen of them showed strong  $\alpha$ -glucosidase inhibition, with EC<sub>50</sub> values from 11.5 to 81.8  $\mu$ M. This study highlighted the significance of triterpenoids in clarifying the hypoglycemic effects associated with *I. obliquus*.

Peng et al. (2022) showed that ethanol extracts from *I. obliquus*, containing inotodiol, lanosterol, and trametenolic acid, significantly improved lipid accumulation in mouse livers induced by a methionine-choline deficient diet or in human LO2 hepatocyte cells lines induced by oleic acid. These metabolites exhibited protective properties against non-alcoholic fatty liver disease (NAFLD) by mitigating lipid deposition effects, reversing liver weight loss, and reducing liver triglyceride content together with restoring lower levels of alanine transaminase (ALT) and aspartate aminotransferase (AST). Inotodiol specifically demonstrated its anti-NAFLD properties by regulating the lipid metabolism pathway, farnesoid X receptor (FXR)/small heterodimer partner (SHP)/sterol regulatory element-binding protein-1c (SREBP-1c) (Liu et al., 2016). Their findings suggested that these bioactive compounds hold promise as potential drugs for NAFLD treatment.

Ogidi et al. (2018) analyzed raw and fermented ethyl acetate and ethanol extracts of *Lenzites quercina* (*L. quercina*) for their total phenol and flavonoid contents, alongside assessments of their antioxidant properties. The scavenging efficacy of fungal extracts was found against various free radicals, including DPPH, OH<sup>-</sup>, nitric oxide, and Fe<sup>2+</sup> ranging from 0.12 to 1.80 mg/mL EC<sub>50</sub> values. Furthermore, petroleum ether, ethyl acetate, and ethanol extracts exhibited EC<sub>50</sub> lower than the positive controls butylated hydroxytoluene (BHT) and ethylenediaminetetraacetic acid (EDTA). The ethyl acetate extract from fermented *L. quercina* exhibited a higher phenolic content of 67.6 mg GAE/g extract, while the ethyl acetate extract from raw *L. quercina* displayed the highest flavonoid content of 51.4 mg QE/g extract. The antioxidant property, measured by FeCl<sub>3</sub> reducing power, ranged from 18.1 (fermented *L. quercina* extracted with petroleum ether) to 127.6 mg (raw *L. quercina* extracted with petroleum ether) Ascorbic Acid Equivalent (AAE)/g extract for extracts obtained from both raw and fermented *L. quercina*. Fermented *L. quercina* demonstrated pronounced scavenging properties against nitric oxide and ferrous ion radicals, and it also exhibited superior inhibition of thiobarbituric acid reactive species (TBARS) with the highest inhibitory effect of 109.3%. The study suggested that the high total phenol and flavonoid content in *L. quercina* extracts positioned them as effective antioxidant agents, potentially serving as alternative therapy in healthcare.

A study by Prasher and Manju (2019) analyzed the active constituents present in ethyl acetate, methanol, and hexane

extracts of *Peniophora nuda* (*P. nuda*) isolated from mango twigs. GC-MS chromatograms revealed 60, 9, and 60 major peaks in the ethyl acetate, methanol, and hexane crude extracts, respectively. The ethyl acetate extract exhibited 29 peaks with area percentages greater than one, with 13-docosenamide, (Z)- occupying the highest at 12.88%. In the methanolic extract, all 9 peaks had area percentages exceeding 1%, with tricaproin being the highest at 49.82%. The hexane extract displayed 28 peaks with area percentages greater than 1, and 13-docosenamide, (Z)- was the highest at 14.46%. According to their GC-MS findings, *P. nuda* was found to contain significant bioactive compounds with known antioxidant, anti-tumor, antibacterial, immunostimulant, lipoxygenase-inhibitor, anti-aging, analgesic, antidiabetic, anti-inflammatory, antidermatitic, antileukemic, anticancer, hepatoprotective, hypocholesterolemic, antiulcerogenic, vasodilator, antispasmodic, and antibronchitic properties (Prasher and Manju, 2019). These results could serve for identifying and understanding the nature of various bioactive components, with potential applications in biotechnological processes. Further isolation of individual phytochemicals may lead to the discovery of novel drugs. An extensive study of the pharmacological importance, diversity, and chemical composition can provide valuable insights and advance knowledge in this area. Further isolation of bioactive compounds has the potential to reveal new drugs.

The antioxidant properties of terrestrial *Flavodon flavus* (*F. flavus*) and *Xylaria feejeensis* (*X. feejeensis*), harvested from the dry zone forest from Sri Lanka were investigated by Fernando et al. (2016). The study also aimed to determine the contribution of phenolic and flavonoid substances to the antioxidant capabilities of these white rot fungi. Both species exhibited strong antioxidant capacity, indicating the presence of an effective antioxidative system. *F. flavus* demonstrated potent antioxidant activity with an  $EC_{50}$  of  $77.00 \pm 0.18 \mu\text{g/mL}$  based on DPPH radical scavenging capacity, while *X. feejeensis* exhibited promising antioxidant capacity with an  $EC_{50}$  value of  $98.4 \pm 0.28 \mu\text{g/mL}$ . Additionally, both analyzed species contained high levels of phenolic and flavonoid substances, suggesting their contribution to the prominent antioxidant activity. *F. flavus* and *X. feejeensis* showed higher total phenol contents of  $55.7 \pm 10.89 \mu\text{g gallic acid/mg}$  and  $31.33 \pm 8.87 \mu\text{g gallic acid/mg}$ , respectively. They also exhibited elevated levels of total flavonoids, with values of  $82.4 \pm 4.0 \mu\text{g epicatechin/mg}$  and  $23.35 \pm 7.0 \mu\text{g epicatechin/mg}$ , respectively. Notably, *F. flavus* exhibited a higher amount of total phenolics and flavonoids compared to *X. feejeensis*.

*Fuscoporia torulosa* (*F. torulosa*) is a fungus that develops woody fruiting bodies on both living and deceased trees. From methanol extract of *F. torulosa* fruiting bodies, two distinctive pentacyclic triterpenoids, namely fuscotorunones A and B, were isolated using ethyl acetate and purification by Noji et al. (2021). *In vitro* antimicrobial testing against *B. subtilis*, *S. aureus*, and *C. albicans* was conducted for fuscotorunones A and B. However, the ethyl acetate extract of *F. torulosa* demonstrated antimicrobial activity, with a MIC of  $25 \mu\text{g/mL}$  against *S. aureus* and MIC of  $100 \mu\text{g/mL}$  against *B. subtilis*, fuscotorunones A and B exhibited no activity against all tested microorganisms.

The *Ganoderma* genus belongs to the basidiomycota division, agaricomycetes class, polyporales order and ganodermataceae family. Among them, the species *G. lucidum* (Ling-Zhi in

Chinese, Reishi in Japanese and Yeongji in Korean) is an outstanding medicinal mushroom having different therapeutical properties. Thus, this fungus is being cultivated worldwide, especially in Southeast Asian countries and many health products are being produced and sold (Bijalwan et al., 2020). Even in Europe there is a biotechnology company named *Hifas da Terra* (<https://hifasdaterra.com/en/>) that grow some white-rot fungi, *G. lucidum* among them, to extract active biomolecules that are commercialized in different products with diverse benefits for human health (e.g., immune system, oncology, mental health).

Several research works have reported different secondary metabolites from the *Ganoderma* genus, particularly from the *G. lucidum* species (Zhou et al., 2012; Sharma et al., 2019; Lu Y. et al., 2020; Wu et al., 2024), with interesting bioactivities. In this context, Baby et al. (2015) reviewed the biologically active secondary metabolites produced by different species belonging to the *Ganoderma* genus. They stated that phytochemical studies resulted in the isolation of 431 secondary metabolites, from which 240 were isolated from *G. lucidum*. Most of the isolated biologically active secondary metabolites were triterpenes, steroids, and polysaccharides (Seo et al., 2009; Cör et al., 2018). The latter showed to diminish the levels of serum glucose in normal fasted mice after 3 and 6 h of administration (Zhang and Lin, 2004). Likewise, Yang et al. (2007) observed that the administration of a *Ganoderma applanatum* (*G. applanatum*) exopolymer to induced diabetic rats reduced the glucose levels in plasma by 22%. Additionally, it decreased the total levels of cholesterol and triglycerides in plasma by 20.3% and 22.5%, respectively. Also, the activity of alanine transaminase and aspartate transaminase was reduced by 23.2% and 20.7%. Therefore, these compounds could find application to treat diabetes in animals.

Other researchers found that *Ganoderma* extracts presented interesting anti-cancer activities. Thus, for example, lucidenic acids, isolated from triterpenoids of ethanolic extracts of a new *G. lucidum* strain, exhibited anti-invasive activity on human hepatoma carcinoma cells (Weng et al., 2007). Similarly, Li et al. (2013) identified a new triterpenoid, named ethyl lucidenate (ethyl 7 $\beta$ -hydroxy-4,4,14 $\alpha$ -trimethyl-3,11,15-trioxo-5 $\alpha$ -chol-8-en-24-oate) from ethyl acetate extracts of *G. lucidum* with cytotoxicity against the cancer cell lines HL-60 and CA46. Also, exopolysaccharides obtained from *G. applanatum* presented antitumor activity against carcinoma cell lines (Osińska-Jaroszuk et al., 2014). In addition, *G. lucidum* ganodermic acid was able to inhibit the proliferation of HeLa and U87 human glioma cells, indicating its potential utilization as an anticancer drug (Upadhyay et al., 2014). Li et al. (2018) found that the polysaccharides from *G. lucidum* and *Ganoderma sinense* (*G. sinense*) presented similar chemical characteristics and tumor suppressive activity in mice, which indicated that polysaccharides from *Ganoderma* are therapeutic agents. Also, Wang K. et al. (2019) isolated from ethanolic extracts of *G. lucidum* fruiting bodies 1 new lanostane triterpene and 2 known aromatic meroterpenoids showing high antioxidant and neuroprotective activities. Zhang et al. (2019) showed that ganoderic acids from chloroform extracts of three *Ganoderma* species presented high antiproliferative activity (inhibition percentages from 70.8% to 80.7%) against three cancer cell lines (i.e., gastric carcinoma, liver carcinoma, and colon carcinoma). Bhat et al. (2021) reviewed the bioactivities of

polysaccharides produced by different *Ganoderma* genera, mainly by *G. lucidum*, and stated that they presented antitumor, antioxidant, immunomodulatory, antibacterial, neuroprotective, hypoglycemic, and hepatoprotective activities. Therefore, they hold promise for further research to formulate natural efficient drugs to prevent and treat several diseases. More recently, Milhorini et al. (2022) isolated a fucoxylomannan from *G. lucidum* fruiting bodies by alkaline extraction with important antimelanomic properties.

On the other hand, there are many research papers reporting antimicrobial activities of *Ganoderma* strains. Thus, Hassan et al. (2019) reported the high antibiotic activity of water extracts from *G. applanatum* against *P. aeruginosa*, *Pseudomonas fluorescens* (*P. fluorescens*), *B. subtilis*, *Staphylococcus epidermidis* (*S. epidermidis*), and *Micrococcus luteus* (*M. luteus*) strains. In addition, chloroform extracts of *G. lucidum* basidiocarp displayed high antibacterial activity against *Salmonella typhi* (*S. typhi*) ( $18 \pm 2.1$  mm DIZ for 100  $\mu$ L extract) and *B. subtilis* ( $17 \pm 1.9$  mm DIZ for 100  $\mu$ L extract) and high antifungal activity against the yeast *C. albicans* ( $17 \pm 1.7$  mm DIZ for 100  $\mu$ L extract) which was related to their content in polysaccharides and triterpenoids. In addition, *G. lucidum* chloroform extracts also presented high antioxidant activity (Uma Gowrie et al., 2014). Also, methanolic extracts of *G. lucidum* exhibited strong antimicrobial activity against the yeast *S. cerevisiae* (MIC<sub>50</sub> value 3  $\mu$ g/mL) but low antimicrobial activities against Gram-positive bacteria (*S. epidermidis* and *Enterococcus raffinosus* (*E. raffinosus*)) and no activity against Gram-negative bacteria (*E. coli* and *P. aeruginosa*) and the yeast *C. albicans* (Hleba et al., 2014). Also, Ismail et al. (2014) studied the antimicrobial activities of methanol, chloroform, dichloromethane, and hexane extracts of *Ganoderma boninense* (*G. boninense*). The methanol and chloroform extracts showed significant antibacterial activities against different food-borne and skin disease bacterial pathogens (i.e., *E. coli*, *B. subtilis*, *Bacillus cereus* (*B. cereus*), *P. aeruginosa*, *S. pyogenes*, *Streptococcus pneumoniae*, *S. aureus*, and *Klebsiella* spp.). Further, GC-MS results confirmed that *G. boninense* contained bioactive compounds such as dodecanoic acid, cyclododecane, octadecanoic acid, 9-octadecenoic acid, hexadecanoic acid, methyl tetradecanoate, 9, 12-octadecadienoic acid, dodecyl acrylate and hexadecanoic acid. In addition, exopolysaccharides from *G. applanatum* presented antibacterial activity against *S. aureus* ( $17.98 \pm 0.4$  mm DIZ and MIC value 1 mg/mL) and toxicity against *V. fischeri* (82.8% cell damage) (Osińska-Jaroszuk et al., 2014). Moreover, ganodermic acid from *G. lucidum* presented antibacterial properties against the Gram-negative bacteria *E. coli* and *P. aeruginosa* (MIC 1 mg/mL) and the Gram-positive bacteria *S. aureus* and *S. epidermidis* (MIC 0.25 mg/mL), pointing out its potential use as a broad-spectrum antibiotic (Upadhyay et al., 2014). Hoque et al. (2015) investigated the antioxidant, antimicrobial and cytotoxic potential of pet ether, chloroform, and methanol extracts of a *G. lucidum* strain collected from Bangladesh. Their results revealed that all the extracts presented high antioxidant activity, low to moderate antibacterial activity (DIZs ranging from 7 mm to 21 mm) against different strains of both Gram-positive (*Sarcina lutea*, *Bacillus megaterium*, *B. subtilis*, *S. aureus*, and *B. cereus*) and Gram-negative bacteria (*P. aeruginosa*, *S. typhi*, *E. coli*, *Vibrio parahaemolyticus*, *Vibrio mimicus*, *Shigella boydii*, and *Shigella dysenteriae*) and weak cytotoxic activity (brine

shrimp nauplii bioassay). However, Romorosa et al. (2017) showed that aqueous extracts of *G. lucidum*, isolated from decaying logs in Isabela State University, Philippines, contained alkaloids, tannins, glycosides and in less extent saponins but not flavonoids. Nevertheless, these extracts had low antimicrobial activity against *E. coli* and especially against *S. aureus*. This was likely because they were devoid in flavonoids. According to the review by Ahmad et al. (2021), *G. lucidum* has a wide range of pharmacological activities, including antiviral activities, due to its content in triterpenoids and polysaccharides. Nonetheless, further studies on the clinical application of the biologically active compounds of this strain are needed. More recently, Chan and Chong (2022) reported the strong antibacterial activity against methicillin-resistant *S. aureus* (MRSA) (DIZ  $41.08 \pm 0.04$  mm and MIC 0.078 mg/mL) of ethyl acetate extracts of a *G. boninense* strain collected from Malaysia. This strong antibacterial activity against MRSA was attributed to its content in aristolochic acid and tamoxifen, which are known to be effective against MRSA (Flores et al., 2016; Bartha et al., 2019), as well as its content in other metabolites with reported antimicrobial properties (i.e., aminoimidazole ribotide, lysine sulfonamide, carbocyclic puromycin, fenbendazole, acetylcaranine, and tigecycline) (Vince et al., 1986; Livermore, 2005; Stranix et al., 2006; Kim et al., 2015; Ločárek et al., 2015; Qadir et al., 2016; Miro-Canturri et al., 2019; de Oliveira et al., 2020). Hence, it could be a promising solution to develop drugs able to fight against multi-antibiotic resistant bacteria. In another recent work, it was shown that hot water extracts of *Ganoderma neo-japonicum* (*G. neo-japonicum*) exhibited 2-fold higher antioxidant and antimicrobial activities (against *S. typhimurium*, *Salmonella enteritidis*, and *E. coli*) than those of *G. lucidum* ones. This was presumably related to the higher content in flavonoids of the *G. neo-japonicum* extracts (Ayimbila et al., 2023).

Additionally, Wang et al. (2017) reported anti-aging activities of *G. lucidum* extracts which were mainly exerted through anti-oxidation, immunomodulation, and anti-neurodegeneration. The bioactive compounds responsible for these antiaging effects consisted of polysaccharides, triterpenes, peptides, and polysaccharide peptides. More studies are needed to clarify the mechanisms involved in these antiaging properties.

The *Trametes* genus belongs to the basidiomycota division, agaricomycetes class, polyporales order and family polyporaceae. Different research studies have reported the production of secondary metabolites with various biological activities by several strains of the *Trametes* genus. Among them, *T. versicolor* (also known as *C. versicolor*) is the most studied species. Thus, methanolic extracts of *T. versicolor* exhibited strong antimicrobial activity against the yeast *S. cerevisiae* (MIC<sub>50</sub> value 24  $\mu$ g/mL), low against Gram-positive bacteria (*S. epidermidis* and *E. raffinosus*) and no activity against Gram-negative bacteria (*E. coli* and *P. aeruginosa*) and the yeast *C. albicans* (Hleba et al., 2014). Also, acetonitrile and aqueous extracts of *Trametes hirsuta* (*T. hirsuta*), isolated from decaying logs in Isabela State University, Philippines, presented strong antimicrobial activity against *E. coli* (DIZ 26.36 mm) and *S. aureus* (DIZ 13.87 mm). This could be related to the flavonoid content in the extracts (Romorosa et al., 2017). Furthermore, isolated cerevisterol (ergosta-7, 22E-diene-3 $\beta$ 5 $\alpha$ , 6 $\beta$ -triol) from methanol extracts of *Trametes gibbosa* (*T. gibbosa*) and *Trametes elegans* (*T. elegans*), collected from farms and forests in Ghana, exhibited a broad-spectrum antibiotic activity. Thus, the



isolated cerevisterol from *T. gibbosa* and *T. elegans* inhibited the growth of *S. typhi* (MIC<sub>25</sub> and MIC<sub>50</sub>,  $\mu\text{g/mL}$ , respectively), *S. aureus* (MIC<sub>25</sub> and 100  $\mu\text{g/mL}$ , respectively), *A. niger* (MIC<sub>25</sub> and 100  $\mu\text{g/mL}$ , respectively) and *E. faecalis* (MIC<sub>50</sub> and 200  $\mu\text{g/mL}$ , respectively) (Appiah et al., 2020). Nanglihan et al. (2018) showed that the ethanol extracts of *T. elegans*, collected from the Lingap Kalikasan Park of Central Luzon State University, Philippines, contained flavonoids, tannins, phenols, steroids, alkaloids, anthraquinones, anthrones, coumarins, essential oils, and fatty acids. Also, *T. elegans* extracts presented significant scavenging activity, antibacterial activities against *S. aureus* (DIZ 8.30 mm) and *E. coli* (DIZ 8.07 mm) and high cytotoxicity (brine shrimp nauplii bioassay). Gebreyohannes et al. (2019) found that chloroform, ethanol and hot extracts of two wild fungi, collected from National Reserve Forests, in Kenya, and further identified as *Trametes* spp. showed interesting antimicrobial activities against different test strains (*E. coli*, *K. pneumoniae*, *P. aeruginosa*, *S. aureus*, MRSA, *C. albicans*, and *Candida parapsilosis*), the highest one being obtained for *S. aureus* (MIC values  $0.83 \pm 0.29$ ,  $0.67 \pm 0.29$ , and  $0.67 \pm 0.29$  for chloroform, ethanol and hot water extracts, respectively). In addition, Hassan et al. (2019) reported the high antibiotic activity of water extracts from *T. versicolor* against *P. aeruginosa*, *P. fluorescens*, *B. subtilis*, *S. epidermidis*, and *M. luteus* strains. Bains and Chawla (2020) reported that the methanolic extracts from *T. versicolor*, collected from the forest of Chail in India, contained phenolics as the main compounds followed by flavonoids, ascorbic acid,  $\beta$ -carotene, and lycopene and presented significant antimicrobial activities against *S. aureus*, *P. aeruginosa*, *K. pneumoniae*, and *E. coli* (DIZs ranging from 24.14 to 30.18 mm). It also showed anti-inflammatory activities presumably due to its content in glycopeptides. Furthermore, Oyetayo and Akingbesote (2022) tested the antimicrobial properties of acetone and methanolic extracts from raw and submerged and solid-state fermented *Trametes polyzona* (*T. polyzona*), collected from dead wood in Nigeria, against *S. aureus* isolated from blood, soil, water, and urine. The methanolic extract from submerged fermented *T. polyzona* showed the highest antimicrobial activity against blood isolated *S. aureus* (DIZ 28 mm), probably due to its ability to dissolve the endogenous compounds of the fungus. However, the acetonic extracts presented low antimicrobial activity. GC-MS analysis of *T. polyzona* methanolic extracts showed the following 14 bioactive compounds: caprylic acid methyl ester, tridecanoic acid methyl ester, myristoleic acid methyl ester, cis-10 pentadecanoic acid methyl ester, palmitoleic acid methyl ester, heptadecanoic acid methyl ester, stearic acid methyl ester, elaidic acid methyl ester, oleic acid methyl ester, linolelaidic acid methyl ester, g-linoleic acid methyl ester, x-linolenic acid methyl ester, heneicosanoic acid methyl ester, and cis-11-14-eicosadienoic acid methyl ester. Recently, Begum et al. (2023) reported that the aqueous extracts of *T. hirsuta* exhibited antimicrobial activity against *S. aureus* (DIZ  $16.00 \pm 0.66$  mm for 20 mg/mL extract), *K. pneumoniae* (DIZ  $14.66 \pm 0.88$  mm for 20 mg/mL extract) and *Salmonella enterica* (DIZ  $13.00 \pm 0.88$  mm for 20 mg/mL extract). They also related that ethanolic extracts of *T. hirsuta* had significant analgesic, anti-inflammatory and antispasmodic activities. Therefore, *T. hirsuta* could be a valuable source of bioactive compounds to develop new drugs to treat pain, fever and anti-inflammatory disorders, bacterial infections, and gastrointestinal problems. Moreover, Wei et al.

(2023) characterized four new sesquiterpenes (three bisabolane sesquiterpenes and one drimane sesquiterpene) from *T. versicolor*, one of them (drimarene sesquiterpene) showing antimicrobial activity against *S. aureus* (MIC<sub>50</sub> value 22.2  $\mu\text{M}$ ).

On the other hand, Leliebre-Lara et al. (2015) found that n-hexane, dichloromethane, ethyl acetate, and ethanol extracts of *T. versicolor*, collected from a dead and dry trunk in Cuba, presented anti-leishmanial activity against the parasite *Leishmania amazonensis*, being higher in ethyl acetate and ethanol extracts. Also, a partially purified exoproteome of *T. versicolor* culture filtrates highly inhibited the growth and the T2 toxin production of the cereal pathogen *Fusarium langsethiae* (Parroni et al., 2019). Wang K. et al. (2019) reported that the bioactive macromolecule polysaccharopeptide from *T. versicolor* (TPSP), purchased from Fujian Fuzhou Green Valley Biopharmaceutical Technology Research, inhibited the development of morphine addiction in rats. They pointed out that TPSP could be used as an adjunctive therapy approach for the alleviation of morphine resistance in the clinic.

Additionally, a polysaccharide from *Trametes orientalis* (*T. orientalis*) presented chemoprotective effects against cyclophosphamide-induced immunosuppression and oxidative stress in mice (Zheng et al., 2017). Furthermore, Roca-Lema et al. (2019) assessed the anticancer effects of polysaccharide-rich extracts from *T. versicolor* on LoVo and HT-29 human colon cancer cells. Their studies showed that *T. versicolor* extracts inhibited human colon proliferation and cause cytotoxicity. Moreover, blending the extracts with the known anticancer drug 5-fluorouracil boosted cell cytotoxicity. More recently, He et al. (2021) purified a protein named musarin from *T. versicolor* extract which strongly inhibited the growth of human colorectal cancer cell lines *in vitro*. Therefore, musarin protein holds promise to develop drugs against colorectal cancers, especially against the chemo-resistant ones.

### 3 Concluding remarks

In the evolving landscape of natural bioactive metabolite discovery, white-rot fungi have emerged as prolific sources of novel metabolites, offering versatile applications, including agriculture, healthcare, and pharmaceuticals. These compounds constitute a rich reservoir of bioactive substances, synthesized during secondary metabolism by utilizing intermediate compounds or by-products from primary metabolic pathways. While secondary metabolites are non-essential for an organism's growth, they show diverse biological characteristics, underscoring their potential significance. White-rot fungi exhibit a unique ability to decompose all wood components, contributing to carbon and nitrogen cycles and producing bioactive substances with several effects, such as antioxidant, antimicrobial, and anticancer properties. In light of explanations, this article reviews the potential application of biologically active secondary metabolites from white-rot fungi in different fields like nutrition, medicine, and degradation. As shown, the diversity of these compounds highlights their importance in forthcoming research, advancements, and practical applications across various industries. This underscores the crucial contribution that white-rot fungi can make in influencing the field of biotechnology and sustainable development. Nevertheless, scaling up production on a large scale is necessary to assess the feasibility of commercial applications.

## Author contributions

OP: Conceptualization, Visualization, Writing–original draft, Writing–review and editing. SR-C: Conceptualization, Funding acquisition, Project administration, Supervision, Visualization, Writing–original draft, Writing–review and editing.

## Funding

The author(s) declare that financial support was received for the research, authorship, and/or publication of this article. This work was funded by the Mikkeli University Consortium (MUC) with the project number 23B350E6YT10.

## References

- Abu-Reidah, I. M., Critch, A. L., Manful, C. F., Rajakaruna, A., Vidal, N. P., Pham, T. H., et al. (2021). Effects of pH and temperature on water under pressurized conditions in the extraction of nutraceuticals from chaga (*Inonotus obliquus*) mushroom. *Antioxidants* 10 (8), 1322. doi:10.3390/antiox10081322
- Ahmad, M. F., Ahmad, F. A., Khan, M. I., Alsayegh, A. A., Wahab, S., Alam, M. I., et al. (2021). *Ganoderma lucidum*: a potential source to surmount viral infections through  $\beta$ -glucans immunomodulatory and triterpenoids antiviral properties. *Int. J. Biol. Macromol.* 187, 769–779. doi:10.1016/j.ijbiomac.2021.06.122
- Alam, N., Amin, R., Khan, A., Ara, I., Shim, M. J., Lee, M. W., et al. (2009). Comparative effects of oyster mushrooms on lipid profile, liver, and kidney function in hypercholesterolemic rats. *Mycobiology* 37 (1), 37–42. doi:10.4489/MYCO.2009.37.1.037
- Alderton, W. K., Cooper, C. E., and Knowles, R. G. (2001). Nitric oxide synthases: structure, function and inhibition. *Biochem. J.* 357 (3), 593–615. doi:10.1042/bj3570593
- Al-Mousa, A., Abo-Dahab, N. F., Hassane, A. M. A., Gomaa, A. E. F., Aljuriss, J. A., and Dahmash, N. D. (2022a). Harnessing *Mucor* spp. for xylanase production: statistical optimization in submerged fermentation using agro-industrial wastes. *Biomed. Res. Int.* 2022, 1–17. doi:10.1155/2022/3816010
- Al-Mousa, A., Hassane, A. M. A., Gomaa, A. E. F., Aljuriss, J. A., Dahmash, N. D., and Abo-Dahab, N. F. (2022b). Response-surface statistical optimization of submerged fermentation for pectinase and cellulase production by *Mucor circinelloides* and *M. hiemalis*. *Fermentation* 8, 205. doi:10.3390/fermentation8050205
- Appiah, T., Agyare, C., Luo, Y., Boamah, V. E., and Boakye, Y. D. (2020). Antimicrobial and resistance modifying activities of *cervisterol* isolated from *Trametes* species. *Curr. Bioact. Compd.* 16 (2), 115–123. doi:10.2174/1573407214666180813101146
- Aquino, Y. K. D. C., Vega, L. D. P., Medrano, N. R. M., and Dulay, R. M. R. (2018). Mycochemicals, antioxidant and cytotoxic activities of *Polyporus grammopcephalus* Berk (BIL7749). *Int. J. Biol. Pharm. Allied. Sci.* 7 (6), 966–975. doi:10.31032/IJBPA/2018/7.6.4455
- Assis, I. S., Chaves, M. B., Silveira, M. L. L., Gern, R. M. M., Wisbeck, E., Júnior, A. F., et al. (2013). Production of bioactive compounds with antitumor activity against sarcoma 180 by *Pleurotus sajor-caju*. *J. Med. Food.* 16 (11), 1004–1012. doi:10.1089/jmf.2012.0267
- Austria, A. B., Dulay, R. M. R., and Pambid, R. C. (2021). Mycochemicals, antioxidant and anti-diabetic properties of Philippine sawgill mushroom *Lentinus swartzii* (Higher Basidiomycetes). *Asian J. Agric. Biol.* 2, 1–8. doi:10.35495/ajab.2020.06.365
- Ayimbila, F., Siri Wong, S., Chaiyama, V., Srihanant, N., and Keawsompong, S. (2023). Comparative study of bio-functional profile and bioactivities of polysaccharides from *Ganoderma lucidum* and *Ganoderma neo-japonicum*. *Biocatal. Agric. Biotechnol.* 53, 102875. doi:10.1016/j.bcab.2023.102875
- Baby, S., Johnson, A. J., and Govindan, B. (2015). Secondary metabolites from *Ganoderma*. *Phytochemistry* 114, 66–101. doi:10.1016/j.phytochem.2015.03.010
- Baek, J., Roh, H. S., Baek, K. H., Lee, S., Lee, S., Song, S. S., et al. (2018). Bioactivity-based analysis and chemical characterization of cytotoxic constituents from Chaga mushroom (*Inonotus obliquus*) that induce apoptosis in human lung adenocarcinoma cells. *J. Ethnopharmacol.* 224, 63–75. doi:10.1016/j.jep.2018.05.025
- Bains, A., and Chawla, P. (2020). *In vitro* bioactivity, antimicrobial and anti-inflammatory efficacy of modified solvent evaporation assisted *Trametes versicolor* extract. *3 Biotech.* 10 (9), 404. doi:10.1007/s13205-020-02397-w
- Bala, N., Aitken, E. A., Fechner, N., Cusack, A., and Steadman, K. J. (2011). Evaluation of antibacterial activity of Australian basidiomycetous macrofungi using a high-throughput 96-well plate assay. *Pharm. Biol.* 49, 492–500. doi:10.3109/13880209.2010.526616
- Baltz, R. H. (2019). Natural product drug discovery in the genomic era: realities, conjectures, misconceptions, and opportunities. *J. Ind. Microbiol. Biotechnol.* 46, 281–299. doi:10.1007/s10295-018-2115-4
- Bartha, G. S., Tóth, G., Horváth, P., Kiss, E., Papp, N., and Kerényi, M. (2019). Analysis of aristolochic acids and evaluation of antibacterial activity of *Aristolochia clematitis* L. *Biol. Futur.* 70 (4), 323–329. doi:10.1556/019.70.2019.36
- Basit, A., Shah, S. T., Ullah, I., Ullah, I., and Mohamed, H. I. (2021). “Microbial bioactive compounds produced by endophytes (bacteria and fungi) and their uses in plant health,” in *Plant growth-promoting microbes for sustainable biotic and abiotic stress management*. Editors S. T. Shah, and M. H. I. Mohamed (Berlin, Germany: Springer Cham), 285–318.
- Begum, H. A., Ahmad, W., Rafiq, N., Ali, H., Hussain, S., Ali, B., et al. (2023). Exploring the pharmacological potential of *Trametes hirsuta* (White Rot Fungi): analgesic, anti-inflammatory, antispasmodic and antimicrobial activities. *Pure Appl. Biol.* 12 (2), 1183–1193. doi:10.19045/bspub.2023.120121
- Beltrán Delgado, Y., Morris Quevedo, H., Domínguez, O. D., Batista Corbal, P., and Llaurodó Maury, G. (2021). Composición microquímica y actividad antioxidante de la seta *Pleurotus ostreatus* en diferentes estados de crecimiento. *Acta Biológica Colomb.* 26 (1), 89–98. doi:10.15446/abc.v26n1.84519
- Bhambri, A., Srivastava, M., Mahale, V. G., Mahale, S., and Karn, S. K. (2022). Mushrooms as potential sources of active metabolites and medicines. *Front. Microbiol.* 13, 837266. doi:10.3389/fmicb.2022.837266
- Bharatiya, P., Rathod, P., Hiray, A., and Kate, A. S. (2021). Multifarious elicitors: invoking biosynthesis of various bioactive secondary metabolite in fungi. *Appl. Biochem. Biotechnol.* 193 (3), 668–686. doi:10.1007/s12010-020-03423-6
- Bhat, Z. A., Wani, A. H., War, J. M., and Bhat, M. Y. (2021). Major bioactive properties of *Ganoderma* polysaccharides: a review. *Asian J. Pharm. Clin. Res.* 14 (3), 11–24. doi:10.22159/ajpcr.2021.v14i3.40390
- Bijalwan, A., Bahuguna, K., Vasisht, A., Singh, A., Chaudhary, S., Tyagi, A., et al. (2020). Insights of medicinal mushroom (*Ganoderma lucidum*): prospects and potential in India. *Biodivers. Int. J.* 4 (5), 202–209.
- Bogale, T. T. (2020). Biotechnological applications of white rot fungi: a review. *GSC Adv. Res. Rev.* 5 (2), 97–103. doi:10.30574/gscarr.2020.5.2.0043
- Brandalise, F., Roda, E., Ratto, D., Gargano, M. L., Cirilione, F., et al. (2023). *Herichium erinaceus* in neurodegenerative diseases: from bench to bedside and beyond, how far from the shoreline? *J. Fungus* 9 (5), 551. doi:10.3390/jof9050551
- Bruhat, A., Jousse, C., Wang, X. Z., Ron, D., Ferrara, M., and Fafournoux, P. (1997). Amino acid limitation induces expression of CHOP, a CCAAT/enhancer binding protein-related gene, at both transcriptional and post-transcriptional levels. *J. Biol. Chem.* 272 (28), 17588–17593. doi:10.1074/jbc.272.28.17588
- Chan, P., Kao, P. F., and Tomlinson, B. (2005). Cardiovascular effects of trilineolein, a natural triglyceride isolated from the herb sanchi (*Panax notoginseng*). *Acta Cardiol. Sin.* 21 (2), 71–76.
- Chan, P., Thomas, G. N., and Tomlinson, B. (2002). Protective effects of trilineolein extracted from *Panax notoginseng* against cardiovascular disease. *Acta Pharmacol. Sin.* 23 (12), 1157–1162.
- Chan, Y. S., and Chong, K. P. (2022). Bioactive compounds of *Ganoderma boninense* inhibited methicillin-resistant *Staphylococcus aureus* growth by affecting their cell



membrane permeability and integrity. *Molecules* 27 (3), 838. doi:10.3390/molecules27030838

Chandra, P., Arora, D. S., Pal, M., and Sharma, R. K. (2019). Antioxidant potential and extracellular auxin production by white rot fungi. *Appl. Biochem. Biotechnol.* 187, 531–539. doi:10.1007/s12010-018-2842-z

Chang, C. H., Chen, Y., Yew, X. X., Chen, H. X., Kim, J. X., Chang, C. C., et al. (2016). Improvement of erinacine A productivity in *Hericium erinaceus* mycelia and its neuroprotective bioactivity against the glutamate-insulted apoptosis. *LWT - Food Sci. Technol.* 65, 1100–1108. doi:10.1016/j.lwt.2015.08.014

Chatterjee, S., Ghosh, R., and Mandal, N. C. (2019). Production of bioactive compounds with bactericidal and antioxidant potential by endophytic fungus *Alternaria alternata* AE1 isolated from *Azadirachta indica* A. Juss. *PLoS One* 14 (4), e0214744. doi:10.1371/journal.pone.0214744

Chen, J., Zeng, X., Yang, Y. L., Xing, Y. M., Zhang, Q., Li, J. M., et al. (2017). Genomic and transcriptomic analyses reveal differential regulation of diverse terpenoid and polyketides secondary metabolites in *Hericium erinaceus*. *Sci. Rep.* 7 (1), 10151. doi:10.1038/s41598-017-10376-0

Chen, S. D., Yong, T. Q., Xiao, C., Gao, X., Xie, Y. Z., Hu, H. P., et al. (2021). Inhibitory effect of triterpenoids from the mushroom *Inonotus obliquus* against  $\alpha$ -glucosidase and their interaction: inhibition kinetics and molecular stimulations. *Bioorg. Chem.* 115, 105276. doi:10.1016/j.bioorg.2021.105276

Chou, P. Y., Huang, G. J., Pan, C. H., Chien, Y. C., Chen, Y. Y., Wu, C. H., et al. (2011). Trilinolein inhibits proliferation of human non-small cell lung carcinoma A549 through the modulation of PI3K/Akt pathway. *Am. J. Chin. Med.* 39 (4), 803–815. doi:10.1142/S0192415X11009214

Chowdhury, M. M. H., Kubra, K., and Ahmed, S. R. (2015). Screening of antimicrobial, antioxidant properties and bioactive compounds of some edible mushrooms cultivated in Bangladesh. *Ann. Clin. Microbiol. Antimicrob.* 14 (1), 8–6. doi:10.1186/s12941-015-0067-3

Conrado, R., Gomes, T. C., Roque, G. S. C., and De Souza, A. O. (2022). Overview of bioactive fungal secondary metabolites: cytotoxic and antimicrobial compounds. *Antibiotics* 11 (11), 1604. doi:10.3390/antibiotics11111604

Contreras, E., Flores, R., Gutiérrez, A., Cerro, D., and Sepúlveda, L. A. (2023). Agro-industrial wastes revalorization as feedstock: production of lignin-modifying enzymes extracts by solid-state fermentation using white rot fungi. *Prep. Biochem. Biotechnol.* 53 (5), 488–499. doi:10.1080/10826068.2022.2109048

Cör, D., Knez, Ž., and Knez Hrncic, M. (2018). Antitumour, antimicrobial, antioxidant and antiacetylcholinesterase effect of *Ganoderma lucidum* terpenoids and polysaccharides: a review. *Molecules* 23, 649. doi:10.3390/molecules23030649

Corrêa, R. C. G., de Souza, A. H. P., Calhelha, R. C., Barros, L., Glamoclija, J., Sokovic, M., et al. (2015). Bioactive formulations prepared from fruiting bodies and submerged culture mycelia of the Brazilian edible mushroom *Pleurotus ostreatus* Singer. *Food Funct.* 6 (7), 2155–2164. doi:10.1039/c5fo00465a

Daley, D. K., Brown, K. J., and Badal, S. (2017). “Fungal metabolites,” in *Pharmacognosy*. Editors S. Badal, and R. Delgoda (United States: Academic Press), 413–421.

Darling, N. J., and Cook, S. J. (2014). The role of MAPK signalling pathways in the response to endoplasmic reticulum stress. *Biochim. Biophys. Acta, Mol. Cell Res.* 1843 (10), 2150–2163. doi:10.1016/j.bbamcr.2014.01.009

Deng, G., Lin, H., Seidman, A., Fournier, M., D’Andrea, G., Wesa, K., et al. (2009). A phase I/II trial of a polysaccharide extract from *Grifola frondosa* (Maitake mushroom) in breast cancer patients: immunological effects. *J. Cancer Res. Clin. Oncol.* 135, 1215–1221. doi:10.1007/s00432-009-0562-z

de Oliveira, H. C., Joffe, L. S., Simon, K. S., Castelli, R. F., Reis, F. C., Bryan, A. M., et al. (2020). Fenbendazole controls *in vitro* growth, virulence potential, and animal infection in the *Cryptococcus* model. *Antimicrob. Agents Chemother.* 64, 002866–e320. doi:10.1128/AAC.00286-20

Devi, M. R., and Krishnakumari, S. (2015). Quantitative estimation of primary and secondary metabolites in hot aqueous extract of *Pleurotus sajor caju*. *J. Pharmacogn. Phytochem.* 4 (3), 198–202.

Devi, R., Sharma, P., Rajput, A., Kaur, J., and Arora, S. (2022). Evaluation of taxonomic, phytochemical and antioxidant characteristics of wild mushroom *Porodaedalea pini*. *Pharmacol. Res. - Mod. Chin.* 5, 100189. doi:10.1016/j.prmcm.2022.100189

Dissanayake, D. P., Abeytunga, D. T. U., Vasudewa, N. S., and Ratnasooriya, W. D. (2009). Inhibition of lipid peroxidation by extracts of *Pleurotus ostreatus*. *Pharmacogn. Mag.* 5 (19), 266–271.

Duan, X. X., Qin, D., Song, H. C., Gao, T. C., Zuo, S. H., Yan, X., et al. (2019). Irpexlactone AD, four new bioactive metabolites of endophytic fungus *Irpex lacteus* DR10-1 from the waterlogging tolerant plant *Distylium chinense*. *Phytochem. Lett.* 32, 151–156. doi:10.1016/j.phytol.2019.06.001

Dutta, S., Woo, E. E., Yu, S. M., Nagendran, R., Yun, B. S., and Lee, Y. H. (2019). Control of anthracnose and gray mold in pepper plants using culture extract of white-rot fungus and active compound schizostatin. *Mycobiology* 47 (1), 87–96. doi:10.1080/12298093.2018.1551833

Eckhardt, S. G., Baker, S. D., Britten, C. D., Hidalgo, M., Siu, L., Hammond, L. A., et al. (2000). Phase I and pharmacokinetic study of ifofulven, a novel mushroom-derived cytotoxin, administered for five consecutive days every four weeks in patients with advanced solid malignancies. *J. Clin. Oncol.* 18 (24), 4086–4097. doi:10.1200/JCO.2000.18.24.4086

Elhusseiny, S. M., El-Mahdy, T. S., Awad, M. F., Elleboudy, N. S., Farag, M. M., Yassein, M. A., et al. (2021). Proteome analysis and *in vitro* antiviral, anticancer and antioxidant capacities of the aqueous extracts of *Lentinula edodes* and *Pleurotus ostreatus* edible mushrooms. *Molecules* 26 (15), 4623. doi:10.3390/molecules26154623

Ern, P. T. Y., Quan, T. Y., Yee, F. S., and Yin, A. C. Y. (2023). Therapeutic properties of *Inonotus obliquus* (Chaga mushroom): a review. *Mycology* 2023, 1–18. doi:10.1080/21501203.2023.2260408

Fagade, O. E., and Oyelade, A. A. (2009). A comparative study of the antibacterial activities of some wood-decay fungi to synthetic antibiotic discs. *Elec. J. Env. Agric. Food Chem.* 8, 184–188.

Fernando, M. D. M., Wijesundera, R. L. C., Soysa, S. S. B. D. P., de Silva, E. D., and Nanayakkara, C. M. (2016). Antioxidant potential and content of the polyphenolic secondary metabolites of white rot macrofungi; *Flavodon flavus* (Klotzsch.) and *Xylaria fjeeensis* (Berk.). *SDRP J. Plant Sci.* 1 (1), 1–6. doi:10.25177/jps.1.1.2

Flores, R., Insel, P. A., Nizet, V., and Corriden, R. (2016). Enhancement of neutrophil antimicrobial activity by the breast cancer drug tamoxifen. *FASEB J.* 30, 969–1014. doi:10.1096/fasebj.30.1\_supplement.969.14

Floudas, D., Binder, M., Riley, R., Barry, K., Blanchette, R. A., Henrissat, B., et al. (2012). The Paleozoic origin of enzymatic lignin decomposition reconstructed from 31 fungal genomes. *Science* 336 (6089), 1715–1719. doi:10.1126/science.1221748

Friedman, M. (2015). Chemistry, nutrition, and health-promoting properties of *Hericium erinaceus* (Lion’s Mane) mushroom fruiting bodies and mycelia and their bioactive compounds. *J. Agric. Food Chem.* 63 (32), 7108–7123. doi:10.1021/acs.jafc.5b02914

Fukushima-Sakuno, E. (2020). Bioactive small secondary metabolites from the mushrooms *Lentinula edodes* and *Flammulina velutipes*. *J. Antibiot.* 73 (10), 687–696. doi:10.1038/s41429-020-0354-x

Gakuubi, M. M., Ching, K. C., Munusamy, M., Wibowo, M., Liang, Z. X., Kanagasundaram, Y., et al. (2022). Enhancing the discovery of bioactive secondary metabolites from fungal endophytes using chemical elicitation and variation of fermentation media. *Front. Microbiol.* 13, 898976. doi:10.3389/fmicb.2022.898976

Gebreyohannes, G., Nyerere, A., Bii, C., and Berhe Sbhatu, D. (2019). Determination of antimicrobial activity of extracts of indigenous wild mushrooms against pathogenic organisms. *Evid. Based Complement. Altern. Med.* 2019, 1–7. doi:10.1155/2019/6212673

Gebreyohannes, G., and Sbhatu, D. B. (2023). Wild mushrooms: a hidden treasure of novel bioactive compounds. *Int. J. Anal. Chem.* 2023, 6694961–6695020. doi:10.1155/2023/6694961

Ghaly, I. S., Ahmed, E. S., Booles, H. F., Farag, I. M., and Nada, S. A. (2011). Evaluation of antihyperglycemic action of oyster mushroom (*Pleurotus ostreatus*) and its effect on DNA damage, chromosome aberrations and sperm abnormalities in streptozotocin-induced diabetic rats. *Glob. Vet.* 7 (6), 532–544.

Halabura, M. I. W., Avelino, K. V., Araújo, N. L., Kassem, A. S. S., Seixas, F. A. V., Barros, L., et al. (2023). Light conditions affect the growth, chemical composition, antioxidant and antimicrobial activities of the white-rot fungus *Lentinus crinitus* mycelial biomass. *Photochem. Photobiol. Sci.* 22 (3), 669–686. doi:10.1007/s43630-022-00344-7

Han, J., Wu, J., and Silke, J. (2020). An overview of mammalian p38 mitogen-activated protein kinases, central regulators of cell stress and receptor signaling. *F1000Research* 9, 653. doi:10.12688/f1000research.22092.1

Hassan, F., Ni, S., Becker, T. L., Kinstedt, C. M., Abdul-Samad, J. L., Actis, L. A., et al. (2019). Evaluation of the antibacterial activity of 75 mushrooms collected in the vicinity of Oxford, Ohio (USA). *Int. J. Med. Mushrooms* 21 (2), 131–141. doi:10.1615/IntJMedMushrooms.2018029710

Hassane, A. M. A., Hussien, S. M., Abouelela, M. E., Taha, T. M., Awad, M. F., Mohamed, H., et al. (2022). *In vitro* and *in silico* antioxidant efficiency of bio-potent secondary metabolites from different taxa of black seed-producing plants and their derived mycoendophytes. *Front. Bioeng. Biotechnol.* 10, 930161. doi:10.3389/fbioe.2022.930161

He, Y., Liu, S., and Newburg, D. S. (2021). Musarin, a novel protein with tyrosine kinase inhibitory activity from *Trametes versicolor*, inhibits colorectal cancer stem cell growth. *Biomed. Pharmacother.* 144, 112339. doi:10.1016/j.biopha.2021.112339

Henriksen, N. N., Lindqvist, L. L., Wibowo, M., Sonnenschein, E. C., Bentzon-Tilia, M., and Gram, L. (2022). Role is in the eye of the beholder—the multiple functions of the antibacterial compound tropodithietic acid produced by marine *Rhodobacteraceae*. *FEMS Microbiol. Rev.* 46 (3), fuac007. doi:10.1093/femsre/fuac007

Hleba, L., Vuković, N., Petrová, J., and Kačaniová, M. (2014). Antimicrobial activity of crude methanolic extracts from *Ganoderma lucidum* and *Trametes versicolor*. *Anim. Sci. Biotechnol.* 47, 89–93.

Hoeksma, J., Misset, T., Wever, C., Kemmink, J., Kruijtz, J., Versluis, K., et al. (2019). A new perspective on fungal metabolites: identification of bioactive compounds

from fungi using zebrafish embryogenesis as read-out. *Sci. Rep.* 9 (1), 17546. doi:10.1038/s41598-019-54127-9

Hoque, N., Ahmed, I., Akanda, M. R. U. Z., and Chowdhury, N. S. (2015). *In vitro* antioxidant, antimicrobial and cytotoxic activities of the various extracts of *Ganoderma lucidum* available in Bangladesh. *J. Pharmacogn. Phytochem.* 4 (3), 42–46.

Ildiz, E., Canpolat, Ş., İşlek, C., Canpolat, E. Y., İşlek, Y., and Akata, I. (2022). Bjerkandera adusta collected from nigde: analysis of total phenolic compound, antioxidant, vnd antimicrobial properties. *TURJAF* 10, 2996–3000. doi:10.24925/turjaf.v10isp2.2996-3000.5750

Ismail, K., Abdullah, S., and Chong, K. P. (2014). Screening for potential antimicrobial compounds from *Ganoderma boninense* against selected foodborne and skin disease pathogens. *Int. J. Pharm. Pharm. Sci.* 6 (2), 771–774.

Jaszek, M., Kos, K., Matuszewska, A., Grąz, M., Stefaniuk, D., Osińska-Jaroszuk, M., et al. (2014). Effective stimulation of the biotechnological potential of the medicinal white rot fungus: *Phellinus pini* by menadione-mediated oxidative stress. *Appl. Biochem. Biotechnol.* 174, 644–656. doi:10.1007/s12010-014-1064-2

Jaszek, M., Osińska-Jaroszuk, M., Janusz, G., Matuszewska, A., Stefaniuk, D., Sulej, J., et al. (2013). New bioactive fungal metabolite with high antioxidant and antimicrobial capacity isolated from *Cerrena unicolor* idiophasic cultures. *Biomed. Res. Int.* 2013, 1–11. doi:10.1155/2013/497492

Jayakumar, T., Thomas, P. A., and Geraldine, P. (2009). *In-vitro* antioxidant activities of an ethanolic extract of the oyster mushroom, *Pleurotus ostreatus*. *Innov. Food Sci. Emerg. Technol.* 10 (2), 228–234. doi:10.1016/j.ifset.2008.07.002

Jerusik, R. J. (2010). Fungi and paper manufacture. *Fungal Biol. Rev.* 24 (1–2), 68–72. doi:10.1016/j.fbr.2010.04.003

Kalaw, S. P., and Albinto, R. F. (2014). Functional activities of Philippine wild strain of *Coprinus comatus* (OF Müll.; Fr.) Pers and *Pleurotus cystidiosus* OK Miller grown on rice straw based substrate formulation. *Mycosphere* 5 (5), 646–655. doi:10.5943/mycosphere/5/5/5

Kaur, M., Chadha, P., Kaur, S., Kaur, A., Kaur, R., Yadav, A. K., et al. (2018). *Schizophyllum commune* induced genotoxic and cytotoxic effects in *Spodoptera litura*. *Sci. Rep.* 8 (1), 4693. doi:10.1038/s41598-018-22919-0

Kawagishi, H., Masui, A., Tokuyama, S., and Nakamura, T. (2006). Erinacines J and K from the mycelia of *Heridium erinaceum*. *Tetrahedron* 62 (36), 8463–8466. doi:10.1016/j.tet.2006.06.091

Kawagishi, H., Shimada, A., Hosokawa, S., Mori, H., Sakamoto, H., Ishiguro, Y., et al. (1996). Erinacines E, F, and G, stimulators of nerve growth factor (NGF)-synthesis, from the mycelia of *Heridium erinaceum*. *Tetrahedron Lett.* 37 (41), 7399–7402. doi:10.1016/0040-4039(96)01687-5

Kawagishi, H., Shirai, R., Sakamoto, H., Yoshida, S., Ojima, F., and Ishiguro, Y. (1992). Erinapyrones A and B from the cultured mycelia of *Heridium erinaceum*. *Chem. Lett.* 21 (12), 2475–2476. doi:10.1246/cl.1992.2475

Keller, N. P., Turner, G., and Bennett, J. W. (2005). Fungal secondary metabolism from biochemistry to genomics. *Nat. Rev. Microbiol.* 3, 937–947. doi:10.1038/nrmicro1286

Kenmoku, H., Shimai, T., Toyomasu, T., Kato, N., and Sassa, T. (2002). Erinacine Q, a new erinacine from *Heridium erinaceum*, and its biosynthetic route to erinacine C in the basidiomycete. *Biosci. Biotechnol. Biochem.* 66 (3), 571–575. doi:10.1271/bbb.66.571

Kijpornyongpan, T., Schwartz, A., Yaguchi, A., and Salvachúa, D. (2022). Systems biology-guided understanding of white-rot fungi for biotechnological applications: a review. *iScience* 25 (7), 104640. doi:10.1016/j.isci.2022.104640

Kim, A., Wolf, N. M., Zhu, T., Johnson, M. E., Deng, J., Cook, J. L., et al. (2015). Identification of *Bacillus anthracis* PurE inhibitors with antimicrobial activity. *Bioorg. Med. Chem.* 23 (7), 1492–1499. doi:10.1016/j.bmc.2015.02.016

Kim, J., Yang, S. C., Hwang, A. Y., Cho, H., and Hwang, K. T. (2020). Composition of triterpenoids in *Inonotus obliquus* and their anti-proliferative activity on cancer cell lines. *Molecules* 25 (18), 4066. doi:10.3390/molecules25184066

Kobayashi, S., Tamanoi, H., Hasegawa, Y., Segawa, Y., and Masuyama, A. (2014). Divergent synthesis of bioactive resorcinols isolated from the fruiting bodies of *Heridium erinaceum*: total syntheses of hericenones A, B, and I, hericenols B–D, and erinacerins A and B. *J. Org. Chem.* 79 (11), 5227–5238. doi:10.1021/jo500795z

Korcan, S. E., Cigerci, İ. H., and Konuk, M. (2012). “White-rot fungi in bioremediation,” in *Fungi as bioremediators*. Editors E. M. Goltapeh, Y. R. Danesh, and A. Varma (Heidelberg: Springer-Verlag Berlin Heidelberg), 371–390.

Kou, R. W., Han, R., Gao, Y. Q., Li, D., Yin, X., and Gao, J. M. (2021). Anti-neuroinflammatory polyoxygenated lanostanoids from Chaga mushroom *Inonotus obliquus*. *Phytochemistry* 184, 112647. doi:10.1016/j.phytochem.2020.112647

Koutrotsios, G., Kalogeropoulos, N., Kaliora, A. C., and Zervakis, G. I. (2018). Toward an increased functionality in oyster (*Pleurotus*) mushrooms produced on grape marc or olive mill wastes serving as sources of bioactive compounds. *J. Agric. Food Chem.* 66 (24), 5971–5983. doi:10.1021/acs.jafc.8b01532

Krupodorova, T., Barshteyn, V., and Sevidik, M. (2022). Antioxidant and antimicrobial potentials of mycelial extracts of *Hohenbuehelia myxotricha* grown in

different liquid culture media. *BioTechnologia* 103 (1), 19–28. doi:10.5114/bta.2022.113912

Krupodorova, T., Rybalko, S., and Barshteyn, V. (2014). Antiviral activity of basidiomycete mycelia against influenza type A (serotype H1N1) and herpes simplex virus type 2 in cell culture. *Virol. Sin.* 29 (5), 284–290. doi:10.1007/s12250-014-3486-y

Kumar, A., Ali, S., Lal, S. B., and Sinha, M. P. (2018). Mycochemical screening and determination of nutritive potency and antioxidant activity of edible macrofungi *Dacryopinax spathularia* (Schwein) and *Schizophyllum commune* (Fries). *World J. Pharm. Res.* 7 (16), 1311–1321. doi:10.20959/wjpr201816-13240

Kundu, S. (2021). Study of Secondary Metabolites Produced by White rot fungi for knowing their antimicrobial properties. *J. Emerg. Technol. Innov. Res.* 8 (2), 1–12.

Kundu, S., and Khan, M. A. (2021). Diversity of metabolites produced by White rot fungi possess different biological properties: a review. *Eco. Env. Cons.* 27 (2021), S165–S177.

Landingin, H. R. R., Francisco, B. E., Dulay, R. M. R., Kalaw, S., and Reyes, R. (2020). Optimization of culture conditions for mycelial growth and basidiocarp production of *Cyclocybe cylindracea* (Maire). *CLSUIJST* 4 (1), 1–17. doi:10.22137/ijst.2020.v4n1.01

Lee, D. G., Kang, H. W., Park, C. G., Ahn, Y. S., and Shin, Y. (2016). Isolation and identification of phytochemicals and biological activities of *Heridium erinaceus* and their contents in *Heridium* strains using HPLC/UV analysis. *J. Ethnopharmacol.* 184, 219–225. doi:10.1016/j.jep.2016.02.038

Lee, E. W., Shizuki, K., Hosokawa, S., Suzuki, M., Suganuma, H., Inakuma, T., et al. (2000). Two novel diterpenoids, erinacines H and I from the mycelia of *Heridium erinaceum*. *Biosci. Biotechnol. Biochem.* 64 (11), 2402–2405. doi:10.1271/bbb.64.2402

Lee, K. F., Chen, J. H., Teng, C. C., Shen, C. H., Hsieh, M. C., Lu, C. C., et al. (2014). Protective effects of *Heridium erinaceus* mycelium and its isolated erinacine A against ischemia-injury-induced neuronal cell death via the inhibition of iNOS/p38 MAPK and nitrotyrosine. *Int. J. Mol. Sci.* 15 (9), 15073–15089. doi:10.3390/ijms150915073

Leliebre-Lara, V., García, M., Nogueiras, C., and Monzote, L. (2015). Qualitative analysis of an ethanolic extract from *Trametes versicolor* and biological screening against *Leishmania amazonensis*. *Emir. J. Food Agric.* 592, 592–595. doi:10.9755/efja.2015.05.194

Li, J. L., Lu, L., Dai, C. C., Chen, K., and Qiu, J. Y. (2001). A comparative study on sterols of ethanol extract and water extract from *Heridium erinaceus*. *Zhongguo Zhong Yao Za Zhi= Zhongguo Zhongyao Zazhi= China J. Chin. Materia Medica* 26 (12), 831–834.

Li, L. F., Liu, H. B., Zhang, Q. W., Li, Z. P., Wong, T. L., Fung, H. Y., et al. (2018). Comprehensive comparison of polysaccharides from *Ganoderma lucidum* and *G. sinense*: chemical, antitumor, immunomodulating and gut-microbiota modulatory properties. *Sci. Rep.* 8 (1), 6172. doi:10.1038/s41598-018-22885-7

Li, P., Deng, Y. P., Wei, X. X., and Xu, J. H. (2013). Triterpenoids from *Ganoderma lucidum* and their cytotoxic activities. *Nat. Prod. Res.* 27 (1), 17–22. doi:10.1080/14786419.2011.652961

Li, W., Zhou, W., Kim, E. J., Shim, S. H., Kang, H. K., and Kim, Y. H. (2015). Isolation and identification of aromatic compounds in Lion's Mane Mushroom and their anticancer activities. *Food Chem.* 170, 336–342. doi:10.1016/j.foodchem.2014.08.078

Li, Y., Zhou, Y., Wu, J., Li, J., and Yao, H. (2021). Phelligradin D from *Inonotus obliquus* attenuates oxidative stress and accumulation of ECM in mesangial cells under high glucose via activating Nrf2. *J. Nat. Med.* 75 (4), 1021–1029. doi:10.1007/s11418-021-01534-w

Lin, F. Y., Lai, Y. K., Yu, H. C., Chen, N. Y., Chang, C. Y., Lo, H. C., et al. (2008). Effects of *Lycium barbarum* extract on production and immunomodulatory activity of the extracellular polysaccharopeptides from submerged fermentation culture of *Coriolus versicolor*. *Food Chem.* 110 (2), 446–453. doi:10.1016/j.foodchem.2008.02.023

Liu, C., Dunkin, D., Lai, J., Song, Y., Ceballos, C., Benkov, K., et al. (2015). Anti-inflammatory effects of *Ganoderma lucidum* triterpenoid in human Crohn's disease associated with downregulation of NF-κB signaling. *Inflamm. Bowel. Dis.* 21 (8), 1918–1925. doi:10.1097/MIB.0000000000000439

Liu, N., Zhao, J., Wang, J., Teng, H., Fu, Y., and Yuan, H. (2016). Farnesoid X receptor ligand CDCa suppresses human prostate cancer cells growth by inhibiting lipid metabolism via targeting sterol response element binding protein 1. *Am. J. Transl. Res.* 8 (11), 5118–5124.

Livermore, D. M. (2005). Tigecycline: what is it, and where should it be used? *J. Antimicrob. Chemother.* 56, 611–614. doi:10.1093/jac/dki291

Llanos-López, N. A., Ebada, S. S., Vasco-Palacios, A. M., Sánchez-Giraldo, L. M., López, L., Rojas, L. F., et al. (2023). Panapophenanthrin, a rare oligocyclic diterpene from *Panus strigellus*. *Metabolites* 13 (7), 848. doi:10.3390/metabo13070848

Ločárek, M., Nováková, J., Klouček, P., Hošťálková, A., Kokoška, L., Gábrlová, L., et al. (2015). Antifungal and antibacterial activity of extracts and alkaloids of selected *Amaryllidaceae* species. *Nat. Prod. Commun.* 10, 1934578X1501000–1540. doi:10.1177/1934578X1501000912

Lu, J., He, R., Sun, P., Zhang, F., Linhardt, R. J., and Zhang, A. (2020a). Molecular mechanisms of bioactive polysaccharides from *Ganoderma lucidum* (Lingzhi), a review. *Int. J. Biol. Macromol.* 150, 765–774. doi:10.1016/j.ijbiomac.2020.02.035

- Lu, Q. Q., Tian, J. M., Wei, J., and Gao, J. M. (2014). Bioactive metabolites from the mycelia of the basidiomycete *Herichium erinaceum*. *Nat. Prod. Res.* 28 (16), 1288–1292. doi:10.1080/14786419.2014.898145
- Lu, Y., Che, J., Xu, X., Pang, B., Zhao, X., Liu, Y., et al. (2020b). Metabolomics reveals the response of the phenylpropanoid biosynthesis pathway to starvation treatment in the grape endophyte *Alternaria* sp MG1. *J. Agric. Food Chem.* 68 (4), 1126–1135. doi:10.1021/acs.jafc.9b05302
- Luo, L. S., Wang, Y., Dai, L. J., He, F. X., Zhang, J. L., and Zhou, Q. (2021). Triterpenoid acids from medicinal mushroom *Inonotus obliquus* (Chaga) alleviate hyperuricemia and inflammation in hyperuricemic mice: possible inhibitory effects on xanthine oxidase activity. *J. Food Biochem.* 46 (3), 13932. doi:10.1111/jfbc.13932
- Ma, L., Chen, H., Dong, P., and Lu, X. (2013). Anti-inflammatory and anticancer activities of extracts and compounds from the mushroom *Inonotus obliquus*. *Food Chem.* 139 (1–4), 503–508. doi:10.1016/j.foodchem.2013.01.030
- Mahuri, M., Paul, M., and Thatoi, H. (2023). A review of microbial laccase production and activity toward different biotechnological applications. *Syst. Appl. Microbiol.* 3, 533–551. doi:10.1007/s43393-023-00163-6
- Martínez, A. T., Speranza, M., Ruiz-Dueñas, F. J., Ferreira, P., Camarero, S., Guillén, F., et al. (2005). Biodegradation of lignocelluloses: microbial, chemical, and enzymatic aspects of the fungal attack of lignin. *Int. Microbiol.* 8 (3), 195–204.
- Masuda, Y., Inoue, M., Miyata, A., Mizuno, S., and Nanba, H. (2009). Maitake  $\beta$ -glucan enhances therapeutic effect and reduces myelosuppression and nephrotoxicity of cisplatin in mice. *Int. Immunopharmacol.* 9 (5), 620–626. doi:10.1016/j.intimp.2009.02.005
- Masuda, Y., Murata, Y., Hayashi, M., and Nanba, H. (2008). Inhibitory effect of MD-Fraction on tumor metastasis: involvement of NK cell activation and suppression of intercellular adhesion molecule (ICAM)-1 expression in lung vascular endothelial cells. *Biol. Pharm. Bull.* 31 (6), 1104–1108. doi:10.1248/bpb.31.1104
- Matuszewska, A., Stefaniuk, D., Jaszek, M., Pięć, M., Zajac, A., Matuszewska, Ł., et al. (2019). Antitumor potential of new low molecular weight antioxidative preparations from the white rot fungus *Cerrena unicolor* against human colon cancer cells. *Sci. Rep.* 9 (1), 1975. doi:10.1038/s41598-018-37947-z
- Milhorini, S. D., Bellan, D., Zavadinack, M., Simas, F. F., Smiderle, F. R., de Santana-Filho, A. P., et al. (2022). Antimelanoma effect of a fucosylomannan isolated from *Ganoderma lucidum* fruiting bodies. *Carbohydr. Polym.* 294, 119823. doi:10.1016/j.carbpol.2022.119823
- Miro-Canturri, A., Ayerbe-Algaba, R., and Smani, Y. (2019). Drug repurposing for the treatment of bacterial and fungal infections. *Front. Microb.* 10, 41–12. doi:10.3389/fmicb.2019.00041
- Mitra, P., Khatua, S., and Acharya, K. (2013). Free radical scavenging and NOS activation properties of water-soluble crude polysaccharide from *Pleurotus ostreatus*. *Asian J. Pharm. Clin. Res.* 6 (3), 67–70.
- Miyazaki, K., Mizutani, H., Katabuchi, H., Fukuma, K., Fujisaka, S., and Okamura, H. (1995). Activated (HLA-DR+) T-lymphocyte subsets in cervical carcinoma and effects of radiotherapy and immunotherapy with sifozifiran on cell-mediated immunity and survival. *Gynecol. Oncol.* 56 (3), 412–420. doi:10.1006/gyno.1995.1073
- Mizerska-Dudka, M., Jaszek, M., Blachowicz, A., Rejczak, T. P., Matuszewska, A., Osinska-Jaroszk, M., et al. (2015). Fungus *Cerrena unicolor* as an effective source of new antiviral, immunomodulatory, and anticancer compounds. *Int. J. Biol. Macromol.* 79, 459–468. doi:10.1016/j.ijbiomac.2015.05.015
- Mohamed, H., Awad, M. F., Shah, A. M., Nazir, Y., Naz, T., Hassane, A., et al. (2022). Evaluation of different standard amino acids to enhance the biomass, lipid, fatty acid, and  $\gamma$ -linolenic acid production in *Rhizomucor pusillus* and *Mucor circinelloides*. *Front. Nutr.* 9, 876817. doi:10.3389/fnut.2022.876817
- Mohammadnejad, S., Pourianfar, H. R., Drakhshan, A., Jabaleh, I., and Rezayi, M. (2019). Potent antiproliferative and pro-apoptotic effects of a soluble protein fraction from culinary-medicinal mushroom *Lentinus tigrinus* on cancer cells. *J. Food Meas. Charact.* 13 (4), 3015–3024. doi:10.1007/s11694-019-00222-4
- Muslihin, A. M., Rifai, Y., and Rante, H. (2022). Isolation and identification of endophytic fungi producing antioxidant compound from *Azadirachta indica* A. juss based on gen 18S rRNA. *Teikyo Med. J.* 45 (1), 3635–3644.
- Muszyńska, B., Dąbrowska, M., Starek, M., Żmudzi, P., Lazur, J., Pytko-Polończyk, J., et al. (2019). *Lentinula edodes* mycelium as effective agent for piroxicam mycoremediation. *Front. Microbiol.* 10, 313. doi:10.3389/fmicb.2019.00313
- Nanglihan, K. E. M. V., Dulay, R. M. R., and Kalaw, S. P. (2018). Myko-actives and functional activities of Philippine wild mushroom *Trametes elegans*. *Int. J. Biosci.* 13 (5), 402–408. doi:10.12692/ijb/13.5.402-408
- Noji, M., Yoneyama, T., Nishihama, K., Elshamy, A. I., Hashimoto, T., and Umeyama, A. (2021). Pentacyclic triterpenoids, fuscotorunones A and B, with  $\epsilon$ -caprolactone in ring E from *Fuscoporia torulosa*. *Phytochem.* 187, 112748. doi:10.1016/j.phytochem.2021.112748
- Oba, K., Kobayashi, M., Matsui, T., Kodera, Y., and Sakamoto, J. (2009). Individual patient based meta-analysis of lentinan for unresectable/recurrent gastric cancer. *Anticancer Res.* 29 (7), 2739–2745.
- Ogidi, C. O., Oyeyayo, V. O., and Akinyele, B. J. (2018). Estimation of total phenolic, flavonoid contents and free radical scavenging activity of a wild macrofungus, *Lenzites quercina* (L.) P. Karsten. *Curr. Res. Environ. Appl.* 8 (4), 425–437. doi:10.5943/cream/8/4/2
- Ogidi, C. O., Ubaru, A. M., Ladi-Lawal, T., Thonda, O. A., Aladejana, O. M., and Malomo, O. (2020). Bioactivity assessment of exopolysaccharides produced by *Pleurotus pulmonarius* in submerged culture with different agro-waste residues. *Heliyon* 6 (12), e05685. doi:10.1016/j.heliyon.2020.e05685
- Osinska-Jaroszk, M., Jaszek, M., Mizerska-Dudka, M., Blachowicz, A., Rejczak, T. P., Janusz, G., et al. (2014). Exopolysaccharide from *Ganoderma applanatum* as a promising bioactive compound with cytostatic and antibacterial properties. *Biomed. Res. Int.* 2014, 1–10. doi:10.1155/2014/743812
- Oyeyayo, V. O., and Akingbesote, E. T. (2022). Assessment of the anti-staphylococcal properties and bioactive compounds of raw and fermented *Trametes polyzona* (Pers.) Justo extracts. *Microb. Biosyst.* 7 (1), 1–7. doi:10.21608/mb.2022.129214.1054
- Parroni, A., Bellabarba, A., Beccaccoli, M., Scarpari, M., Reverberi, M., and Infantino, A. (2019). Use of the secreted proteome of *Trametes versicolor* for controlling the cereal pathogen *Fusarium langsethiae*. *Int. J. Mol. Sci.* 20 (17), 4167. doi:10.3390/ijms20174167
- Patel, S., and Goyal, A. (2012). Recent developments in mushrooms as anti-cancer therapeutics: a review. *3 Biotech.* 2 (1), 1–15. doi:10.1007/s13205-011-0036-2
- Peng, A., Liu, S., Fang, L., Zhu, Z., Zhou, Y., Yue, S., et al. (2022). *Inonotus obliquus* and its bioactive compounds alleviate non-alcoholic fatty liver disease via regulating FXR/SHP/SREBP-1c axis. *Eur. J. Pharmacol.* 921, 174841. doi:10.1016/j.ejphar.2022.174841
- Prasher, I. B., and Manju, (2019). Screening of *Peniophora nuda* (a white rot fungus) for the presence of commercially important bioactive metabolites. *Vegetos* 32 (3), 307–315. doi:10.1007/s42535-019-00038-z
- Qadir, M. A., Ahmed, M., and Khaleeq, A. (2016). Synthesis, antibacterial and antifungal possession of amino acids containing sulfonamide moieties. *Pak. J. Pharm. Sci.* 29, 1609–1613.
- Ramesh, C. H., and Pattar, M. G. (2010). Antimicrobial properties, antioxidant activity and bioactive compounds from six wild edible mushrooms of western ghats of Karnataka, India. *Pharmacogn. Res.* 2 (2), 107. doi:10.4103/0974-8490.62953
- Ratto, D., Corana, F., Mannucci, B., Priori, E. C., Cobelli, F., Roda, E., et al. (2019). *Herichium erinaceus* improves recognition memory and induces hippocampal and cerebellar neurogenesis in frail mice during aging. *Nutrients* 11 (4), 715. doi:10.3390/nu11040715
- Resurreccion, N. G. U., Shen, C. C., and Ragasa, C. Y. (2016). Chemical constituents of *Lentinus edodes*. *Der Pharm. Lett.* 8 (4), 117–120.
- Ribka, T., Nagadesi, P. K., Ponnuru, V., Thatha, V., and Pratyusha, A. V. (2021). Phenotypical, mycochemicals, proximate composition and antifungal activity of *Phylloporia ribis* (schumacher) ryvarden from India. *J. Chem. Pharm. Res.* 13 (2), 20–28.
- Roca-Lema, D., Martínez-Iglesias, O., de Ana Portela, C. F., Rodríguez-Blanco, A., Valladares-Ayerbes, M., Díaz-Díaz, A., et al. (2019). *In vitro* anti-proliferative and anti-invasive effect of polysaccharide-rich extracts from *Trametes versicolor* and *Grifola frondosa* in colon cancer cells. *Int. J. Med. Sci.* 16 (2), 231–240. doi:10.7150/ijms.28811
- Roda, E., De Luca, F., Ratto, D., Priori, E. C., Savino, E., Bottone, M. G., et al. (2023). Cognitive healthy aging in mice: boosting memory by an ergothioneine-rich *Herichium erinaceus* primordium extract. *Biology* 12 (2), 196. doi:10.3390/biology12020196
- Roda, E., Priori, E. C., Ratto, D., De Luca, F., Di Iorio, C., Angelone, P., et al. (2021). Neuroprotective metabolites of *Herichium erinaceus* promote neuro-healthy aging. *Int. J. Mol. Sci.* 22 (12), 6379. doi:10.3390/ijms22126379
- Roda, E., Ratto, D., De Luca, F., Desiderio, A., Ramieri, M., Goppa, L., et al. (2022). Searching for a longevity food, we bump into *Herichium erinaceus* primordium rich in ergothioneine: the “longevity vitamin” improves locomotor performances during aging. *Nutrients* 14 (6), 1177. doi:10.3390/nu14061177
- Rodríguez-Berrios, R. R., Ríos-Delgado, A. M., Perdomo-Lizardo, A. P., Cardona-Rivera, A. E., Vidal-Rosado, Á. G., Narváez-Lozano, G. A., et al. (2023). Extraction, Isolation, characterization, and bioactivity of polypropionates and related Polyketide metabolites from the Caribbean region. *Antibiotics* 12 (7), 1087. doi:10.3390/antibiotics12071087
- Romeros, E. S., De Guzman, C. T., Martin, J. R. G., and Jacob, J. K. S. (2017). Preliminary investigation on the pharmacological properties of wood-rotting mushrooms collected from Isabela State University, Echague, Isabela, Philippines. *Int. J. Agric. Technol.* 13 (7), 2591–2596.
- Seo, H. W., Hung, T. M., Na, M., Jung, H. J., Kim, J. C., Choi, J. S., et al. (2009). Steroids and triterpenes from the fruit bodies of *Ganoderma lucidum* and their anti-complement activity. *Arch. Pharm. Res.* 32, 1573–1579. doi:10.1007/s12272-009-2109-x
- Sevindik, M. (2018a). Investigation of antioxidant/oxidant status and antimicrobial activities of *Lentinus tigrinus*. *Adv. Pharmacol. Pharm. Sci.* 2018, 1–4. doi:10.1155/2018/1718025
- Sevindik, M. (2018b). Antioxidant and antimicrobial activity of *Cerrena unicolor*. *Mycopath* 16 (1), 11–14.
- Sevindik, M., Akgul, H., Bal, C., and Selamoglu, Z. (2018). Phenolic contents, oxidant/antioxidant potential and heavy metal levels in *Cyclocybe cylindracea*. *Indian J. Pharm. Educ. Res.* 52 (3), 437–441. doi:10.5530/ijper.52.3.50



- Shankar, A., and Sharma, K. K. (2022). Fungal secondary metabolites in food and pharmaceuticals in the era of multi-omics. *Appl. Microbiol. Biotechnol.* 106 (9–10), 3465–3488. doi:10.1007/s00253-022-11945-8
- Sharma, C., Bhardwaj, N., Sharma, A., Tuli, H. S., Batra, P., Beniwal, V., et al. (2019). Bioactive metabolites of *Ganoderma lucidum*: factors, mechanism and broad spectrum therapeutic potential. *J. Herb. Med.* 17, 100268. doi:10.1016/j.hermed.2019.100268
- Sharma, N., Takkur, S., Bhatia, K., Vardhan, H., Tripathi, M., Iqbal, K., et al. (2023). “Recent advances in fungal secondary metabolites and their applications,” in *Fungal resources for sustainable economy: current status and future perspectives*. Editors I. Singh, V. R. Rajpal, and S. S. Navi (Singapore: Springer), 411–432.
- Sidorova, I., and Voronina, E. (2019). “Bioactive secondary metabolites of basidiomycetes and its potential for agricultural plant growth promotion,” in *Secondary metabolites of plant growth promoting rhizomicroorganisms*. Editors H. Singh, C. Keswani, M. Reddy, E. Sansinenea, and C. García-Estrada (Singapore: Springer), 3–26.
- Stilinović, N., Čapo, I., Vukmirović, S., Rašković, A., Tomas, A., Popović, M., et al. (2020). Chemical composition, nutritional profile and *in vivo* antioxidant properties of the cultivated mushroom *Coprinus comatus*. *R. Soc. Open Sci.* 7 (9), 200900. doi:10.1098/rsos.200900
- Stranix, B. R., Lavalée, J. F., Sévigny, G., Yelle, J., Perron, V., LeBerre, N., et al. (2006). Lysine sulfonamides as novel HIV-protease inhibitors: Ne-acyl aromatic  $\alpha$ -amino acids. *Bioorg. Med. Chem. Lett.* 16 (13), 3459–3462. doi:10.1016/j.bmcl.2006.04.011
- Su, C. H., Lu, M. K., Lu, T. J., Lai, M. N., and Ng, L. T. (2020). A (1→6)-branched (1→4)- $\beta$ -D-glucan from *Grifola frondosa* inhibits lipopolysaccharide-induced cytokine production in RAW264.7 macrophages by binding to TLR2 rather than dectin-1 or CR3 receptors. *J. Nat. Prod.* 83 (2), 231–242. doi:10.1021/acs.jnatprod.9b00584
- Sun, J. E., Ao, Z. H., Lu, Z. M., Xu, H. Y., Zhang, X. M., Dou, W. F., et al. (2008). Antihyperglycemic and antilipidperoxidative effects of dry matter of culture broth of *Inonotus obliquus* in submerged culture on normal and alloxan-diabetes mice. *J. Ethnopharmacol.* 118 (1), 7–13. doi:10.1016/j.jep.2008.02.030
- Tanimoto, T., Onodera, K., Hosoya, T., Takamatsu, Y., Kinoshita, T., Tago, K., et al. (1996). Schizostatin, a novel squalene synthase inhibitor produced by the mushroom, *Schizophyllum commune*. I. Taxonomy, fermentation, isolation, physico-chemical properties and biological activities. *J. Antibiot.* 49 (7), 617–623. doi:10.1016/j.antibiotics.49.617
- Teoh, Y. P., Don, M. M., and Ujang, S. (2011). Media selection for mycelia growth, antifungal activity against wood-degrading fungi, and GC-MS study by *Pycnoporus sanguineus*. *BioResources* 6 (3), 2719–2731. doi:10.15376/biores.6.3.2719-2731
- Thirumurugan, D., Cholarajan, A., Raja, S. S., and Vijayakumar, R. (2018). “An introductory chapter: secondary metabolites,” in *Secondary metabolites-sources and applications*. Editors R. Vijayakumar, and S. S. S. Raja. London, United Kingdom: (IntechOpen), 3–21.
- Tripathi, A. M., and Tiwary, B. N. (2013). Biochemical constituents of a wild strain of *Schizophyllum commune* isolated from Achanakmar-Amrarkantak Biosphere Reserve (ABR), India. *World J. Microbiol. Biotechnol.* 29, 1431–1442. doi:10.1007/s11274-013-1306-4
- Tsukada, R., Shinki, S., Kaneko, A., Murakami, K., Irie, K., Murai, M., et al. (2020). Synthetic biology based construction of biological activity-related library of fungal decalin-containing diterpenoid pyrones. *Nat. Commun.* 11, 1830. doi:10.1038/s41467-020-15664-4
- Tundis, R., Loizzo, M. R., and Menichini, F. (2010). Natural products as  $\alpha$ -Amylase and  $\alpha$ -Glucosidase inhibitors and their hypoglycaemic potential in the treatment of diabetes: an update. *Mini-Rev. Med. Chem.* 10 (4), 315–331. doi:10.2174/138955710791331007
- Tzeng, T. T., Chen, C. C., Chen, C. C., Tsay, H. J., Lee, L. Y., Chen, W. P., et al. (2018). The cyanthrin diterpenoid and sesterterpene constituents of *Hericium erinaceus* mycelium ameliorate Alzheimer's disease-related pathologies in APP/PS1 transgenic mice. *Int. J. Mol. Sci.* 19 (2), 598. doi:10.3390/ijms19020598
- Uma Gowrie, S., Chaturvedi, G., and Rani, K. (2014). Evaluation of bioactive potential of basidiocarp extracts of *Ganoderma lucidum*. *Int. J. Pharm. Res. Allied Sci.* 3, 36–46.
- Upadhyay, M., Shrivastava, B., Jain, A., Kidwai, M., Kumar, S., Gomes, J., et al. (2014). Production of ganoderic acid by *Ganoderma lucidum* RCKB-2010 and its therapeutic potential. *Ann. Microbiol.* 64 (2), 839–846. doi:10.1007/s13213-013-0723-9
- Vince, R., Daluge, S., and Brownell, J. (1986). Carbocyclic purmocyin: synthesis and inhibition of protein biosynthesis. *J. Med. Chem.* 29, 2400–2403. doi:10.1021/jm00161a044
- Wang, C., Liu, X., Lian, C., Ke, J., and Liu, J. (2019b). Triterpenes and aromatic meroterpenoids with antioxidant and neuroprotective activity from *Ganoderma lucidum*. *Molecules* 24 (23), 4353. doi:10.3390/molecules24234353
- Wang, J., Cao, B., Zhao, H., and Feng, J. (2017). Emerging roles of *Ganoderma lucidum* in anti-aging. *Aging Dis.* 8 (6), 691. doi:10.14336/AD.2017.0410
- Wang, K., Bao, L., Qi, Q., Zhao, F., Ma, K., Pei, Y., et al. (2015). Erinacerins C–L, isoidolin-1-ones with  $\alpha$ -glucosidase inhibitory activity from cultures of the medicinal mushroom *Hericium erinaceus*. *J. Nat. Prod.* 78 (1), 146–154. doi:10.1021/np5004388
- Wang, K., Wang, Z., Cui, R., and Chu, H. (2019a). Polysaccharopeptide from *Trametes versicolor* blocks inflammatory osteoarthritis pain-morphine tolerance effects via activating cannabinoid type 2 receptor. *Int. J. Biol. Macromol.* 126, 805–810. doi:10.1016/j.ijbiomac.2018.12.212
- Wang, Y., Ouyang, F., Teng, C., and Qu, J. (2021). Optimization for the extraction of polyphenols from *Inonotus obliquus* and its antioxidant activity. *Prep. Biochem. Biotechnol.* 51 (9), 852–859. doi:10.1080/10826068.2020.1864642
- Wasser, S. P. (2002). Medicinal mushrooms as a source of antitumor and immunomodulating polysaccharides. *Appl. Microbiol. Biotechnol.* 60, 258–274. doi:10.1007/s00253-002-1076-7
- Wei, W. K., Chi, M. J., Yang, Y. L., and Feng, T. (2023). Bisabolane and drimane sesquiterpenes from the fungus *Trametes versicolor*. *Phytochem. Lett.* 57, 73–77. doi:10.1016/j.phytol.2023.07.015
- Weng, C. J., Chau, C. F., Chen, K. D., Chen, D. H., and Yen, G. C. (2007). The anti-invasive effect of lucidenic acids isolated from a new *Ganoderma lucidum* strain. *Mol. Nutr. Food Res.* 51 (12), 1472–1477. doi:10.1002/mnfr.200700155
- Wold, C. W., Gerwick, W. H., Wangenstein, H., and Inngjerdigen, K. T. (2020). Bioactive triterpenoids and water-soluble melanin from *Inonotus obliquus* (Chaga) with immunomodulatory activity. *J. Funct. Foods.* 71, 104025. doi:10.1016/j.jff.2020.104025
- Wu, S., Zhang, S., Peng, B., Tan, D., Wu, M., Wei, J., et al. (2024). *Ganoderma lucidum*: a comprehensive review of phytochemistry, efficacy, safety and clinical study. *Food Sci. Hum. Wellness.* 13 (2), 568–596. doi:10.26599/FSHW.2022.9250051
- Xu, X., Zhao, W., and Shen, M. (2016). Antioxidant activity of liquid cultured *Inonotus obliquus* polyphenols using tween-20 as a stimulatory agent: correlation of the activity and the phenolic profiles. *J. Taiwan Inst. Chem. Eng.* 69, 41–47. doi:10.1016/j.jtice.2016.10.011
- Yadav, A. N. (2021). Microbial biotechnology for bio-prospecting of microbial bioactive compounds and secondary metabolites. *J. App. Biol. Biotech.* 9 (2), 1–6. doi:10.7324/JABB.2021.92ed
- Yang, B. K., Jung, Y. S., and Song, C. H. (2007). Hypoglycemic effects of *Ganoderma applanatum* and *Collybia confluens* exo-polymers in streptozotocin-induced diabetic rats. *Phytother. Res.* 21 (11), 1066–1069. doi:10.1002/ptr.2214
- Yazawa, Y., Yokota, M., and Sugiyama, K. (2000). Antitumor promoting effect of an active component of *Polyporus*, ergosterol and related compounds on rat urinary bladder carcinogenesis in a short-term test with concanavalin A. *Biol. Pharm. Bull.* 23 (11), 1298–1302. doi:10.1248/bpb.23.1298
- Yilkal, T. (2015). Role of white rot fungi as a biological treatment of low-quality animal feeds. *Sch. J. Agric. Sci.* 5 (7), 247–255.
- Zerva, A., Tsfantakis, N., and Topakas, E. (2020a). Production of biocatalysts and bioactive compounds from Greek basidiomycete wild strains grown in different induction media. *Proceedings* 2020, 1–7.
- Zerva, A., Tsfantakis, N., and Topakas, E. (2020b). Greek basidiomycete wild strains for the production of bioactive compounds and enzymes with applications in cosmetic and biocatalysis industries. *Chem. Proc.* 1, 1–7.
- Zhang, C., Fu, D., and Guo, M. (2019). Comparative and chemometric analysis of correlations between the chemical fingerprints and anti-proliferative activities of ganoderic acids from three *Ganoderma* species. *Phytochem. Anal.* 30 (4), 474–480. doi:10.1002/pca.2830
- Zhang, C. C., Cao, C. Y., Kubo, M., Harada, K., Yan, X. T., Fukuyama, Y., et al. (2017). Chemical constituents from *Hericium erinaceus* promote neuronal survival and potentiate neurite outgrowth via the TrkA/Erk1/2 pathway. *Int. J. Mol. Sci.* 18 (8), 1659. doi:10.3390/ijms18081659
- Zhang, H. N., and Lin, Z. B. (2004). Hypoglycemic effect of *Ganoderma lucidum* polysaccharides. *Acta Pharmacol. Sin.* 25 (2), 191–195.
- Zhang, Y., Dai, L., Kong, X., and Chen, L. (2012). Characterization and *in vitro* antioxidant activities of polysaccharides from *Pleurotus ostreatus*. *Int. J. Biol. Macromol.* 51 (3), 259–265. doi:10.1016/j.ijbiomac.2012.05.003
- Zhao, H., Eguchi, S., Alam, A., and Ma, D. (2017). The role of nuclear factor-erythroid 2 related factor 2 (Nrf-2) in the protection against lung injury. *Am. J. Physiol. Lung Cell Mol.* 312 (2), L155–L162. doi:10.1152/ajplung.00449.2016
- Zhao, W., Huang, P., Zhu, Z., Chen, C., and Xu, X. (2021). Production of phenolic compounds and antioxidant activity via bioconversion of wheat straw by *Inonotus obliquus* under submerged fermentation with the aid of a surfactant. *J. Sci. Food Agric.* 101 (3), 1021–1029. doi:10.1002/jsfa.10710
- Zheng, W., Miao, K., Liu, Y., Zhao, Y., Zhang, M., Pan, S., et al. (2010). Chemical diversity of biologically active metabolites in the sclerotia of *Inonotus obliquus* and submerged culture strategies for up-regulating their production. *Appl. Microbiol. Biotechnol.* 87, 1237–1254. doi:10.1007/s00253-010-2682-4
- Zheng, Y., Zong, Z. M., Chen, S. L., Chen, A. H., and Wei, X. Y. (2017). Ameliorative effect of *Trametes orientalis* polysaccharide against immunosuppression and oxidative stress in cyclophosphamide-treated mice. *Int. J. Biol. Macromol.* 95, 1216–1222. doi:10.1016/j.ijbiomac.2016.11.013
- Zhou, X. W., Su, K. Q., and Zhang, Y. M. (2012). Applied modern biotechnology for cultivation of *Ganoderma* and development of their products. *Appl. Microbiol. Biotechnol.* 93, 941–963. doi:10.1007/s00253-011-3780-7
- Ziaja-Soltys, M., Kołodziej, P., Stefaniuk, D., Matuszewska, A., Jaszek, M., and Bogucka-Kocka, A. (2022). Low-molecular-weight secondary metabolites from fungi: *Cerrena unicolor* as a new proposal of an effective preparation against rhabditis nematodes. *Molecules* 27 (5), 1660. doi:10.3390/molecules27051660

# Frontiers in Chemistry

Explores all fields of chemical science across the periodic table

Advances our understanding of how atoms, ions, and molecules come together and come apart. It explores the role of chemistry in our everyday lives - from electronic devices to health and wellbeing.

## Discover the latest Research Topics

[See more →](#)

### Frontiers

Avenue du Tribunal-Fédéral 34  
1005 Lausanne, Switzerland  
[frontiersin.org](https://frontiersin.org)

### Contact us

+41 (0)21 510 17 00  
[frontiersin.org/about/contact](https://frontiersin.org/about/contact)

